

AD-A229 589

MATERIALS
RESEARCH
SOCIETY
SYMPOSIUM PROCEEDINGS



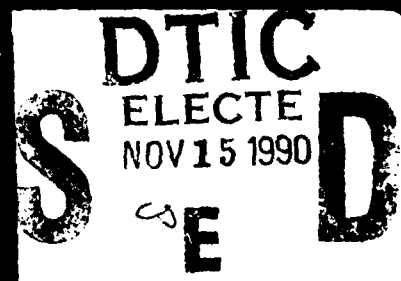
VOLUME 161

**Properties of
II-VI Semiconductors:
Bulk Crystals, Epitaxial
Films, Quantum Well
Structures, and Dilute
Magnetic Systems**

EDITORS

F.J. Bartoli, Jr.
H.F. Schaake
J.F. Schetzina

DTIC FILE COPY



DISTRIBUTION STATEMENT A

Approved for public release;
Distribution Unlimited

REPORT DOCUMENTATION PAGE			Form Approved OMB No. 0704-0188	
<small>Please forwarding burden for this collection of information is estimated to average 1 hour per response, including the time for reviewing instructions, searching existing data sources, gathering and maintaining the data needed, and completing and reviewing the collection of information. Send comments regarding this burden estimate or any other aspect of this collection of information, including suggestions for reducing this burden, to Washington Headquarters Services, Directorate for Information Operations and Reports, 1215 Jefferson Davis Highway, Suite 1204, Arlington, VA 22202-4302, and to the Office of Management and Budget, Paperwork Reduction Project (0704-0188), Washington, DC 20503.</small>				
1. AGENCY USE ONLY (Leave blank)	2. REPORT DATE	3. REPORT TYPE AND DATES COVERED		
		Final Report 22 Nov 89-21 Nov 90		
4. TITLE AND SUBTITLE		5. FUNDING NUMBERS		
1989 Materials Research Society Fall Meeting		2306/A2		
6. AUTHOR(S)				
Dr John Ballance				
7. PERFORMING ORGANIZATION NAME(S) AND ADDRESS(ES)		8. PERFORMING ORGANIZATION REPORT NUMBER		
Material Reserach Society 9800 McKnight Road, Suite 327 Pittsburgh, PA 15237-6005		AFOSR TR- 001 1050		
9. SPONSORING/MONITORING AGENCY NAME(S) AND ADDRESS(ES)		10. SPONSORING/MONITORING AGENCY REPORT NUMBER		
AFOSR/NE Bldg 410 Bolling AFB DC 2033206448		AFOSR-90-0081		
11. SUPPLEMENTARY NOTES				
12a. DISTRIBUTION / AVAILABILITY STATEMENT		12b. DISTRIBUTION CODE		
UNLIMITED				
13. ABSTRACT (Maximum 200 words)				
<p>CONFERENCE WAS HELD ON THE FOLLWING AREA</p> <p>(158) In Situ Patterning: Selective Area Deposition and Etching</p> <p>(161) Properties of II-VI Semiconductors: Bulk Crystals, Expitaxial Films, Quantum We'l Structures, and Dilute Magnetic Systems</p> <p>(163) Impurties, Defects and Diffusion in Semiconductors: Bulk and Layered Structures</p> <p>(168) Chemical Vapor Deposition of Refractory Metals and Ceramics</p> <p>(170) Tailored Interfaces in Composite Materials.</p>				
14. SUBJECT TERMS		15. NUMBER OF PAGES		
		16. PRICE CODE		
17. SECURITY CLASSIFICATION OF REPORT	18. SECURITY CLASSIFICATION OF THIS PAGE	19. SECURITY CLASSIFICATION OF ABSTRACT	20. LIMITATION OF ABSTRACT	
UNCLASS	UNCLASS	UNCLASS	UNLIMITED	

DTIC
ELECTE
NOV 15 1990
S E D

AFOSR-TR-

AFOSR-TR-84-0101

AFOSR-TR-84-0101

AFOSR-TR-84-0101

Properties of II-VI Semiconductors: Bulk Crystals, Epitaxial Films, Quantum Well Structures, and Dilute Magnetic Systems

Symposium held November 27-December 2, 1989, Boston,
Massachusetts, U.S.A.

EDITORS:

F.J. Bartoli, Jr.

Naval Research Laboratory, Washington, DC, U.S.A.

H.F. Schaake

Texas Instruments, Dallas, Texas, U.S.A.

J.F. Schetzina

North Carolina State University, Raleigh, North Carolina, U.S.A.



MATERIALS RESEARCH SOCIETY
Pittsburgh, Pennsylvania

This work was supported in part by the U.S. Army Research Office under Grant Number DAAL03-90-G-0014. The views, opinions, and/or findings contained in this report are those of the authors and should not be construed as an official Department of the Army position, policy, or decision unless so designated by other documentation.

This work was supported by the Air Force Office of Scientific Research, Air Force Systems Command, USAF, under Grant Number AFOSR 90-0081.

Single article reprints from this publication are available through University Microfilms Inc., 300 North Zeeb Road, Ann Arbor, Michigan 48106

CODEN: MRSPDH

Copyright 1990 by Materials Research Society.
All rights reserved.

This book has been registered with Copyright Clearance Center, Inc. For further information, please contact the Copyright Clearance Center, Salem, Massachusetts.

Published by:

Materials Research Society
9800 McKnight Road
Pittsburgh, Pennsylvania 15237
Telephone (412) 367-3003
Fax (412) 367-4373

Library of Congress Cataloging in Publication Data

Properties of II-VI semiconductors : bulk crystals, epitaxial films, quantum well structures, and dilute magnetic systems / editors, F.J. Bartoli, Jr., H.F. Schaake, J.F. Schetzina.

p. cm. — (Materials Research Society symposium proceedings : ISSN 0272-9172 ; v. 161)

"Symposium held November 27-December 1, 1989, Boston, Massachusetts, U.S.A."

Includes bibliographical references and index.

ISBN 1-55899-049-6

1. Compound semiconductors—Congresses. 2. Crystals—Growth—Congresses. 3. Epitaxy—Congresses 4. Quantum wells—Congresses 5. Magnetic semiconductors—Congresses. I. Bartoli, F.J. (Fil J.) II. Schaake H.F. (Herb F.) III. Schetzina, J.F. (Jan F.) IV. Materials Research Society. Meeting (1989 : Boston, Mass.) V. Series: Materials Research Society symposium proceedings : v. 161.

QC611.8.C64P76 1990
537.6'22—dc20

90-6261
CIP

Manufactured in the United States of America

Contents

PREFACE	xiii
MATERIALS RESEARCH SOCIETY SYMPOSIUM PROCEEDINGS	xv
PART I: BULK CRYSTAL GROWTH AND PROPERTIES	
<p>*GROWTH OF LARGE-DIAMETER CdZnTe AND CdTeSe BOULES FOR $Hg_{1-x}Cd_xTe$ EPITAXY: STATUS AND PROSPECTS S. Sen, S.M. Johnson, J.A. Kiele, W.H. Konkel, and J.E. Stannard</p>	3
<p>*GROWTH AND CHARACTERIZATION OF CdTe AND CdTe ALLOYS S. McDevitt, D.R. John, J.L. Sepich, K.A. Bowers, J.F. Schetzina, R.S. Rai, and S. Mahajan</p>	15
<p>PHOTOLUMINESCENCE DETECTION OF NATIVE DEFECTS IN THE SURFACE REGION OF BULK CdTe P.M. Amirtharaj and N.K. Dhar</p>	27
<p>ANNEALING BEHAVIOR OF THE PHOTOLUMINESCENCE LINES IN CdTe AND $Zn_xCd_{1-x}Te$ SINGLE CRYSTALS J. González-Hernandez, A. Reyes-Mena, Elias Lopez-Cruz, D.D. Allred, and Worth P. Allred</p>	33
<p>NONDESTRUCTIVE COMPOSITIONAL AND DEFECT CHARACTERIZATION OF CdZnTe ALLOYS USING PHOTOLUMINESCENCE SPECTROSCOPY W.M. Duncan, R.J. Koestner, J.H. Tregilgas, H.-Y. Liu, and M.-C. Chen</p>	39
<p>ION-IMPLANTATION GETTERING OF IMPURITIES IN CdTe M.H. Jin, K.M. James, C.E. Jones, and J.L. Merz</p>	45
<p>PREPARATION AND CHARACTERISATION OF $(ZnTe)_x(CdSe)_{1-x}$ SINGLE CRYSTALS V.K. Madhu Smitha Rani, R.P. Vijayalakshmi, D. Raja Reddy, and B.K. Reddy</p>	51
PART II: OPTICAL AND ELECTRICAL PROPERTIES	
<p>DEEP LEVEL LUMINESCENCE MEASUREMENTS OF MBE CdTe GROWTH QUALITY AND PROCESSING J.L. Shaw, L.J. Brillson, S. Sivananthan, and J.P. Faurie</p>	59
<p>HIGH RESOLUTION AND ANALYTICAL ELECTRON MICROSCOPY OF MULTILAYER HETEROEPIITAXIAL SEMICONDUCTORS H.-J. Kleebe, W.J. Hamilton, W.L. Ahlgren, S.M. Johnson, and M. Rühle</p>	63

*Invited Paper

*SOLUBILITY OF IMPURITIES AND DEFECT IMPURITY INTERACTION IN II-VI SEMICONDUCTORS Y. Marfaing	69
-----------------------------------------------------------------------------------------------------	----

THICKNESS MEASUREMENT OF THIN FILMS BY X-RAY ABSORPTION J. Chaudhuri and S. Shah	83
-------------------------------------------------------------------------------------	----

PART III: DOPING OF II-VI MATERIALS

*MOCVD GROWTH AND DOPING OF ZnSe AND RELATED II-VI MATERIALS Hiroshi Kukimoto	91
-------------------------------------------------------------------------------------	----

*GROWTH AND DOPING OF ZINC SELENIDE BY MOLECULAR BEAM EPITAXY J.M. DePuydt, H. Cheng, M.A. Haase, and J.E. Potts	97
------------------------------------------------------------------------------------------------------------------------	----

DEPOSITION OF ZINC SELENIDE BY ATOMIC LAYER EPITAXY FOR MULTILAYER X-RAY OPTICS J.K. Shurtleff, D.D. Allred, R.T. Perkins, and J.M. Thorne	109
-----------------------------------------------------------------------------------------------------------------------------------------------------	-----

EFFECT OF GaAs SURFACE STOICHIOMETRY ON THE INTERFACE OF AS-GROWN EPITAXIAL ZnSe/EPITAXIAL GaAs HETEROSTRUCTURES J. Qiu, R.L. Gunshor, M. Kobayashi, D.R. Menke, Q.-D. Qian, D. Li, and N. Otsuka	115
---------------------------------------------------------------------------------------------------------------------------------------------------------------------------------------------------------------	-----

PSEUDOMORPHIC ZnTe/AlSb/GaSb HETEROSTRUCTURES BY MOLECULAR BEAM EPITAXY D.L. Mathine, J. Han, M. Kobayashi, R.L. Gunshor, D.R. Menke, M. Vaziri, J. Gonsalves, N. Otsuka, Q. Fu, M. Hagerott, and A.V. Nurmikko	121
-----------------------------------------------------------------------------------------------------------------------------------------------------------------------------------------------------------------------------	-----

TRANSMISSION ELECTRON MICROSCOPY OF II-VI/III-V SEMICONDUCTOR HETEROEPITAXIAL INTERFACES D. Li, N. Otsuka, J. Qiu, J. Glenn Jr., M. Kobayashi, and R.L. Gunshor	127
--------------------------------------------------------------------------------------------------------------------------------------------------------------------------	-----

*PROPERTIES OF CHLORINE-DOPED ZINC SELENIDE GROWN BY MOLECULAR BEAM EPITAXY S. Kwang, J. Ren, K.A. Bowers, J.W. Cook, Jr., and J.F. Schetzina	133
--------------------------------------------------------------------------------------------------------------------------------------------------------	-----

PART IV: THIN FILMS AND HETEROSTRUCTURES

SURFACE MORPHOLOGY AND PHOTOLUMINESCENCE SPECTRA OF ZnSe (Na) AFTER EXCIMER LASER ANNEALING Guan-Jiun Yi, G.F. Neumark, Z. Lu, P.R. Newbury, C.F. Yu, B.J. Fitzpatrick, M. Shone, and A. Sicignano	141
----------------------------------------------------------------------------------------------------------------------------------------------------------------------------------------------------------------	-----

PLASMA-ASSISTED EPITAXIAL GROWTH OF ZnSe FILMS IN HYDROGEN PLASMA S. Yamauchi and T. Hariu	147
--------------------------------------------------------------------------------------------------	-----

*Invited Paper

GROWTH OF $\text{ZnS}_x\text{Se}_{1-x}$ BY MBE USING AN ELECTROCHEMICAL SULPHUR SOURCE	153
J.M. Wallace, K.A. Prior, B.C. Cavenett, J.J. Hunter, S.J.A. Adams, and M.J.L.S. Haines	
SELECTIVE AREA DEPOSITION OF PASSIVANTS, INSULATORS, AND EPITAXIAL FILMS OF II-VI COMPOUND SEMICONDUCTORS	159
D.L. Dreifus, Y. Lansari, J.W. Han, S. Hwang, J.W. Cook, Jr., and J.F. Schetzina	
SPATIAL LIGHT MODULATOR USING A CDS THIN FILM PHOTOCAPACITOR	165
Joseph Reichman	
PHOTOLUMINESCENCE PROPERTIES OF GRADED COMPOSITION $\text{Mg}_x\text{Zn}_{1-x}\text{Se}$ CRYSTALS	171
H.J. Lozykowski, X.D. Jiang, and J.L. Merz	
*ATOMIC LAYER EPITAXY OF WIDE BANDGAP II-VI COMPOUND SEMICONDUCTOR SUPERLATTICES	177
M. Konagai, Y. Takemura, R. Kimura, N. Teraguchi, and K. Takahashi	
GROWTH OF LATTICE-MATCHED ZnSe-ZnS STRAINED-LAYER SUPERLATTICES ONTO GaAs AS AN ALTERNATIVE TO ZnSSe ALLOYS	187
H. Oniyama, S. Yamaga, and A. Yoshikawa	
U.S. POLYCRYSTALLINE THIN FILM SOLAR CELLS PROGRAM	193
Harin S. Ullal, Kenneth Zweibel, and Richard L. Mitchell	
EXCITONIC PROPERTIES OF ZnSe-ZnS STRAINED-LAYER SUPERLATTICES AND A FIBONACCI SEQUENCE	199
Tsunemasa Taguchi and Yoichi Yamada	
OPTICAL PROPERTIES OF CdZnS-ZnS STRAINED-LAYER SUPERLATTICES	211
Yasuyuki Endoh and Tsunemasa Taguchi	
PRECISE MEASUREMENTS OF TRANSIENT EXCESS CARRIER LIFETIMES IN II-VI FILMS AND SUPERLATTICES	217
W.O. Doggett, Michael W. Thelander, and J.F. Schetzina	
PART V: NOVEL GROWTH AND CHARACTERIZATION	
*PHOTOASSISTED MBE OF II-VI SEMICONDUCTOR FILMS AND SUPERLATTICES	227
N.C. Giles, R.L. Harper, J.W. Han, and J.F. Schetzina	
GROWTH AND INITIAL CHARACTERIZATION OF NOVEL HgTe -BASED II-VI MATERIALS	239
F.G. Moore, J.C. Abele, and R.E. Kremer	

*Invited Paper

ELECTRICAL PROPERTIES OF MBE-GROWN HgCdTe S. Hwang and J.F. Schetzina	245
FIRST AND SECOND ORDER RAMAN STUDIES OF COMPOSITION AND STRUCTURAL ORDERING IN $\text{Hg}_{1-x}\text{Cd}_x\text{Te}$ A. Compaan and R.C. Bowman, Jr.	251
TEMPERATURE-DEPENDENT INFRARED ABSORPTION OF Hg-BASED II-VI SEMICONDUCTOR SUPERLATTICES Z. Yang, Y. Lansari, W. Han, Z. Yu, and J.F. Schetzina	257
PROPERTIES OF MODULATION-DOPED HgCdTe SUPERLATTICES S. Hwang, Z. Yang, Y. Lansari, J.W. Han, J.W. Cook, Jr., N.C. Giles, and J.F. Schetzina	263
PART VI: HgCdTe: SURFACES, PASSIVANTS, AND PROCESSING	
THE EFFECT OF SURFACE LAYERS IN EPITAXIAL n-TYPE $\text{Hg}_{1-x}\text{Cd}_x\text{Te}$ K.K. Parat, N.R. Taskar, I.B. Bhat, and S.K. Ghandi	271
SURFACE ELECTRONS IN INVERTED LAYERS OF p-HgCdTe Samuel E. Schacham and Eliezer Finkman	277
ELECTRICAL CHARACTERISATION OF P-TYPE $\text{Cd}_x\text{Hg}_{1-x}\text{Te}$ GROWN BY MOVPE Anne Royle, J.S. Gough, S.J.C. Irvine, and J.B. Mullin	285
SURFACE ROUGHNESS THEORY AND LOW-TEMPERATURE EPITAXY Srinivasan Krishnamurthy, M.A. Berding, A. Sher, and A.-B. Chen	291
ENHANCED METALLIZATION STABILITY ON MERCURY-CADMIUM- TELLURIDE A. Räsänen, G. Haugstad, X. Yu, G. Ceccone, and A. Franciosi	297
GROWTH OF HIGH QUALITY LWIR FILMS BY LIQUID PHASE EPITAXY Dipankar Chandra	303
EFFECTS OF DEFECTS ON METAL-INSULATOR-SEMICONDUCTOR PROPERTIES OF HgCdTe FILMS GROWN BY LIQUID PHASE EPITAXY Dipankar Chandra and Michael W. Goodwin	313
LOW TEMPERATURE DEVICE PROCESSING TECHNOLOGY FOR II-VI SEMICONDUCTORS D.L. Dreifus, R.M. Kolbas, B.P. Sneed, and J.F. Schetzina	323

PART VII: HgCdTe: EPITAXIAL GROWTH

*RECENT PROGRESS IN THE OMVPE GROWTH OF HgCdTe Sorab K. Gandhi	331
VAPOUR PRESSURE MEASUREMENTS ON ORGANOTELLURIUM PRECURSORS FOR MOVPE J.E. Hails, S.J.C. Irvine, and J.B. Mullin	343
STRUCTURAL AND ELECTRICAL PROPERTIES OF HETEROEPITAXIAL HgCdTe/CdZnTe/GaAs/Si S.M. Johnson, W.L. Ahlgren, M.H. Kalisher, J.B. James, and W.J. Hamilton, Jr.	351
PROPERTIES OF HgTe:ZnTe STRAINED LAYER SUPERLATTICES GROWN BY MOVPE J.T. Mullins, P.A. Clifton, P.D. Brown, D.O. Hall, and A.W. Brinkman	357
MBE GROWTH AND CHARACTERIZATION OF SMALL BAND GAP HgTe-HgCdTe SUPERLATTICES Y. Lansari, Z. Yang, S. Hwang, J.W. Cook, Jr., and J.F. Schetzina	363
ON THE FIELD EMISSION FROM HgTe-CdTe SUPERLATTICES WITH GRADED STRUCTURES UNDER MAGNETIC QUANTIZATION Kamakhya P. Ghatak and Sambhu N. Biswas	371
MBE GROWTH AND CHARACTERIZATION OF LWIR HgCdTe M.B. Lee, J. DeCarlo, D. DiMarzio, and M. Kesselman	377

PART VIII: Hg-BASED SUPERLATTICES

*FREE-CARRIER INDUCED OPTICAL NONLINEARITIES IN NARROW BANDGAP SEMICONDUCTORS D. Walrod, S.Y. Auyang, and P.A. Wolff	385
NARROW-GAP NONLINEAR OPTICAL MATERIALS E.R. Youngdale, C.A. Hoffman, J.R. Meyer, F.J. Bartoli, J.W. Han, J.W. Cook Jr., J.F. Schetzina, and A. Martinez	397
*TRANSPORT PROPERTIES OF NARROW GAP II-VI SUPERLATTICES C.A. Hoffman, J.R. Meyer, and F.J. Bartoli	403
HgTe-CdTe MULTIPLE QUANTUM WELLS C.A. Hoffman, D.J. Arnold, J.R. Meyer, F.J. Bartoli, Y. Lansari, J.W. Cook, Jr., J.F. Schetzina, and J.N. Schulman	413
QUANTUM-CONFINED STARK EFFECT IN II-VI SEMICONDUCTOR COUPLED QUANTUM WELLS Z. Yang and J.F. Schetzina	419

*Invited Paper

PART IX: DILUTE MAGNETIC SEMICONDUCTORS

*RECENT DEVELOPMENTS IN II-VI DILUTED MAGNETIC SEMI- CONDUCTORS N. Samarth and J.K. Furdyna	427
TEM STUDY OF DEFECTS IN CdTe/CdMnTe SUPERLATTICES ON (100) InSb S.J. Diamond, J.W. Steeds, D. Ashenford, and B. Lunn	437
Ga AND In AUTODOPING OF Cd _{1-x} Mn _x Te EPITAXIAL LAYERS GROWN ON GaAs AND InSb SUBSTRATES J.J. Dubowski, J.M. Wrobel, S. Rolfe, J.A. Jackman, J.H. Mazur, and J. Noad	443
PHOTOLUMINESCENCE STUDIES OF DILUTED MAGNETIC SEMICONDUCTORS UNDER HYDROSTATIC PRESSURE: Cd _{1-x} Mn _x Te Maneesha Prakash, Meera Chandrasekhar, H.R. Chandrasekhar, I. Miotkowski, and A.K. Ramdas	449
OBSERVATION OF Mn ²⁺ TRIPLET CLUSTERS AND NON-NEAREST- NEIGHBOR EXCHANGE EFFECT IN (Cd,Mn)Te Xiaomei Wang, D. Heiman, S. Foner, and P. Becla	455
IN-SITU STUDIES OF SEMIMAGNETIC HETEROJUNCTION FILAMETERS Xiaohua Yu, N. Troullier, A. Raisanen, G. Haugstad, and A. Franciosi	459
PULSED LASER EVAPORATION AND EPITAXY GROWTH OF Cd _{1-x} Mn _x Te X.L. Zheng, C.A. Huber, P. Becla, M. Shih, and D. Heiman	465
PHOTOLUMINESCENCE OF ZnSe EPILAYERS ON GaAs UNDER HYDROSTATIC PRESSURE Judah A. Tuchman, Zhifeng Sui, Irving P. Herman, R.L. Gunshor, L.A. Kolodziejski, D.A. Cammack, and M. Shone	471
3d TRANSITION METALS IN II-VI SEMICONDUCTORS D. Heiman, M. Dahl, X. Wang, P.A. Wolff, P. Becla, A. Petrou, and A. Mycielski	479
MAGNETIZATION STUDY OF Fe-BASED II-VI DILUTED MAGNETIC SEMICONDUCTORS W.J.M. de Jonge, H.J.M. Swagten, and A. Twardowski	485
ENERGY LEVEL SPECTRA OF TRANSITION METAL IONS IN DILUTED MAGNETIC SEMICONDUCTORS Murielle Villeret, S. Rodriguez, and E. Kartheuser	491
RAMAN SPECTROSCOPY OF A NOVEL DILUTED MAGNETIC SEMICONDUCTOR: CUBIC Cd _{1-x} Mn _x Se R.G. Alonso, E.-K. Suh, H. Pascher, E. Oh, A.K. Ramdas, N. Samarth, H. Luo, and J.K. Furdyna	497

*Invited Paper

FREE EXCITON MAGNETOSPECTROSCOPY OF CdFeSe DILUTED MAGNETIC SEMICONDUCTOR A. Twardowski, K. Pakula, M. Arciszewska, and A. Mycielski	503
AUTHOR INDEX	509
SUBJECT INDEX	513
MATERIALS RESEARCH SOCIETY SYMPOSIUM PROCEEDINGS	517

Preface

The II-VI compound semiconductors possess characteristics which, as a group, are unique. Among the most active areas of investigation in these materials today are blue light emitters based on ZnSe, infrared detectors based on mercury-containing compounds such as HgCdTe, and the properties of dilute magnetic semiconductors. Each of these areas is represented by several papers included in this volume. The symposium at which the papers in this volume were orally presented was attended by 250 researchers from across the globe. Of the nearly 100 papers presented, 69 are contained in these proceedings.

The symposium organizers would like to give special thanks to those institutions which provided financial support: the Air Force Office of Scientific Research, the Army Research Office, the Defense Advanced Research Projects Agency, the Office of Naval Research, and Texas Instruments. Thanks also to the many who refereed the manuscripts contained herein, and to North Carolina State University, the Naval Research Laboratory, and Texas Instruments for the resources which the organizers used before, during, and after the symposium.

F.J. Bartoli, Jr.
H.F. Schaake
J.F. Schetzina

April 1990

MATERIALS RESEARCH SOCIETY SYMPOSIUM PROCEEDINGS

Recent Materials Research Society Symposium Proceedings

- Volume 145—III-V Heterostructures for Electronic/Photonic Devices, C.W. Tu, V.D. Matterna, A.C. Gossard, 1989, ISBN: 1-55899-018-6
- Volume 146—Rapid Thermal Annealing/Chemical Vapor Deposition and Integrated Processing, D. Hodul, J. Gelpey, M.L. Green, T.E. Seidel, 1989, ISBN: 1-55899-019-4
- Volume 147—Ion Beam Processing of Advanced Electronic Materials, N.W. Cheung, A.D. Marwick, J.B. Roberto, 1989, ISBN: 1-55899-020-8
- Volume 148—Chemistry and Defects in Semiconductor Heterostructures, M. Kawabe, T.D. Sands, E.R. Weber, R.S. Williams, 1989, ISBN: 1-55899-021-6
- Volume 149—Amorphous Silicon Technology-1989, A. Madan, M.J. Thompson, P.C. Taylor, Y. Hamakawa, P.G. LeComber, 1989, ISBN: 1-55899-022-4
- Volume 150—Materials for Magneto-Optic Data Storage, C.J. Robinson, T. Suzuki, C.M. Falco, 1989, ISBN: 1-55899-023-2
- Volume 151—Growth, Characterization and Properties of Ultrathin Magnetic Films and Multilayers, B.T. Jonker, J.P. Heremans, E.E. Marinero, 1989, ISBN: 1-55899-024-0
- Volume 152—Optical Materials: Processing and Science, D.B. Poker, C. Ortiz, 1989, ISBN: 1-55899-025-9
- Volume 153—Interfaces Between Polymers, Metals, and Ceramics, B.M. DeKoven, A.J. Gellman, R. Rosenberg, 1989, ISBN: 1-55899-026-7
- Volume 154—Electronic Packaging Materials Science IV, R. Jaccodine, K.A. Jackson, E.D. Lillie, R.C. Sundahl, 1989, ISBN: 1-55899-027-5
- Volume 155—Processing Science of Advanced Ceramics, I.A. Aksay, G.L. McVay, D.R. Ulrich, 1989, ISBN: 1-55899-028-3
- Volume 156—High Temperature Superconductors: Relationships Between Properties, Structure, and Solid-State Chemistry, J.R. Jorgensen, K. Kitazawa, J.M. Tarascon, M.S. Thompson, J.B. Torrance, 1989, ISBN: 1-55899-029
- Volume 157—Beam-Solid Interactions: Physical Phenomena, J.A. Knapp, P. Borgesen, R.A. Zuhr, 1989, ISBN 1-55899-045-3
- Volume 158—In-Situ Patterning: Selective Area Deposition and Etching, R. Rosenberg, A.F. Bernhardt, J.G. Black, 1989, ISBN 1-55899-046-1
- Volume 159—Atomic Scale Structure of Interfaces, R.D. Bringans, R.M. Feenstra, J.M. Gibson, 1989, ISBN 1-55899-047-X
- Volume 160—Layered Structures: Heteroepitaxy, Superlattices, Strain, and Metastability, B.W. Dodson, L.J. Schowalter, J.E. Cunningham, F.H. Pollak, 1989, ISBN 1-55899-048-8
- Volume 161—Properties of II-VI Semiconductors: Bulk Crystals, Epitaxial Films, Quantum Well Structures and Dilute Magnetic Systems, J.F. Schetzina, F.J. Bartoli, Jr., H.F. Schaake, 1989, ISBN 1-55899-049-6
- Volume 162—Diamond, Boron Nitride, Silicon Carbide and Related Wide Bandgap Semiconductors, J.T. Glass, R.F. Messier, N. Fujimori, 1989, ISBN 1-55899-050-X
- Volume 163—Impurities, Defects and Diffusion in Semiconductors: Bulk and Layered Structures, J. Bernholc, E.E. Haller, D.J. Wolford, 1989, ISBN 1-55899-051-8
- Volume 164—Materials Issues in Microcrystalline Semiconductors, P.M. Fauchet, C.C. Tsai, K. Tanaka, 1989, ISBN 1-55899-052-6
- Volume 165—Characterization of Plasma-Enhanced CVD Processes, G. Lucovsky, D.E. Ibbotson, D.W. Hess, 1989, ISBN 1-55899-053-4
- Volume 166—Neutron Scattering for Materials Science, S.M. Shapiro, S.C. Moss, J.D. Jorgensen, 1989, ISBN 1-55899-054-2

MATERIALS RESEARCH SOCIETY SYMPOSIUM PROCEEDINGS

- Volume 167—Advanced Electronic Packaging Materials, A. Barfknecht, J. Partridge, C-Y. Li, C.J. Chen, 1989, ISBN 1-55899-055-0
- Volume 168—Chemical Vapor Deposition of Refractory Metals and Ceramics, T.M. Besmann, B.M. Gallois, 1989, ISBN 1-55899-056-9
- Volume 169—High Temperature Superconductors: Fundamental Properties and Novel Materials Processing, J. Narayan, C.W. Chu, L.F. Schneemeyer, D.K. Christen, 1989, ISBN 1-55899-057-7
- Volume 170—Tailored Interfaces in Composite Materials, C.G. Pantano, E.J.H. Chen, 1989, ISBN 1-55899-058-5
- Volume 171—Polymer Based Molecular Composites, D.W. Schaefer, J.E. Mark, 1989, ISBN 1-55899-059-3
- Volume 172—Optical Fiber Materials and Processing, J.W. Fleming, G.H. Sigel, S. Takahashi, P.W. France, 1989, ISBN 1-55899-060-7
- Volume 173—Electrical, Optical and Magnetic Properties of Organic Solid-State Materials, L.Y. Chiang, D.O. Cowan, P. Chaikin, 1989, ISBN 1-55899-061-5
- Volume 174—Materials Synthesis Utilizing Biological Processes, M. Alper, P.D. Calvert, P.C. Rieke, 1989, ISBN 1-55899-062-3
- Volume 175—Multi-Functional Materials, D.R. Ulrich, F.E. Karasz, A.J. Buckley, G. Gallagher-Daggitt, 1989, ISBN 1-55899-063-1
- Volume 176—Scientific Basis for Nuclear Waste Management XIII, V.M. Oversby, P.W. Brown, 1989, ISBN 1-55899-064-X
- Volume 177—Macromolecular Liquids, C.R. Safinya, S.A. Safran, P.A. Pincus, 1989, ISBN 1-55899-065-8
- Volume 178—Fly Ash and Coal Conversion By-Products: Characterization, Utilization and Disposal VI, F.P. Glasser, R.L. Day, 1989, ISBN 1-55899-066-6
- Volume 179—Specialty Cements with Advanced Properties, H. Jennings, A.G. Landers, B.E. Scheetz, I. Odler, 1989, ISBN 1-55899-067-4

MATERIALS RESEARCH SOCIETY MONOGRAPH

Atom Probe Microanalysis: Principles and Applications to Materials Problems,
M.K. Miller, G.D.W. Smith, 1989; ISBN 0-931837-99-5

Earlier Materials Research Society Symposium Proceedings listed in the back.

PART I

Bulk Crystal Growth
and Properties

GROWTH OF LARGE-DIAMETER CdZnTe AND CdTeSe BOULES
FOR $Hg_{1-x}Cd_xTe$ EPITAXY: STATUS AND PROSPECTS

S. SEN, S.M. JOHNSON, J.A. KIELE, W.H. KONKEL AND J.E. STANNARD
Santa Barbara Research Center, 75 Coromar Dr., B2/8, Goleta, CA 93117

ABSTRACT

Single crystals of CdTe or dilute alloys of $Cd_{1-y}Zn_yTe$ ($y \leq 0.04$) and $CdTe_{1-z}Se_z$ ($z \leq 0.04$) with low defect density and large single-crystal area ($>30 \text{ cm}^2$) are required as substrates for high-quality epitaxial $Hg_{1-x}Cd_xTe$ thin films in the infrared (IR) detector industry. Bridgman or gradient freeze has been the most common current technique used for growing these materials. This paper reviews the current status and the evolution at SBRC of one variation of the Bridgman technique, viz., vertical-modified Bridgman (VMB), for producing large-area substrates with excellent uniformity and reproducibility. CdTe, $Cd_{1-y}Zn_yTe$ ($y \leq 0.04$) and $CdTe_{1-z}Se_z$ ($z \leq 0.04$) boules of 5- to 7.5-cm diameter have been grown unseeded in the present version of the VMB growth system. In general, under optimum growth conditions, the boules have the smallest grain structure (several grains) at the tip end with enhancement of grain selection as the cylindrical body of the boule is approached, resulting in one predominant and large grain occupying 70 to 80 percent of the entire boule volume; $\{111\}$ -oriented $Cd_{1-y}Zn_yTe$ and $CdTe_{1-z}Se_z$ substrates with single-crystal areas as large as 50 to 60 cm^2 have been obtained from these boules. Crystal quality characterized by x-ray rocking curve, IR transmission (2.5 to 20 μm), low-temperature photoluminescence, and Hall-effect measurements as a function of temperature, showed a strong correlation with the starting material quality (especially that of elemental Te and Se). Analyses of the thermal history during growth reveals that the presence of the ampoule (with charge) increases the temperature inside the furnace by 10 to 15 degrees. The temperature gradient at the tip was measured to be 8 to 10°C/cm and it dropped to 4 to 5°C/cm beyond 2.5 cm from the tip - where rapid enhancement of grain selection takes place in most boules. The effect of this temperature rise on the initial crystallization near the tip of a boule can be explained from the numerical thermal model that was developed for the growth process with radiative and conductive heat transfer included and using a temperature profile similar to that existing in the actual growth furnace. Conditions for maximizing the fraction solidifying with a slightly convex interface, hence maximizing the single-crystal yield are discussed.

INTRODUCTION

Various growth methods have been applied in the past to the bulk growth of CdTe. This is mainly due to the difficulty of obtaining high quality single-crystal material of large size. In comparison with the highly developed group IV and III-V materials, there are several factors, viz., higher ionicity, reactivity and lower stacking fault energy in II-VI materials which in general make it more difficult for achieving large single crystals with low defects. Although different growth methods, viz., vapor phase growth, solution growth, and melt growth have all been used for growing bulk CdTe crystals, Bridgman and gradient freeze techniques of the melt growth process are the two most common current techniques used for growing large-diameter CdTe and dilute alloys of $Cd_{1-y}Zn_yTe$ ($y \leq 0.04$) and $CdTe_{1-z}Se_z$ ($z \leq 0.04$) boules.

The use of lattice-matched substrates for growth of $Hg_{1-x}Cd_xTe$ epitaxial layers has been shown to reduce the interfacial dislocation density and improve layer morphology. Both CdZnTe and CdTeSe have been used as substrates for the growth of HgCdTe by liquid-phase epitaxy (LPE) [1,2]. CdZnTe succeeded the binary compound CdTe several years ago because of greater hardness, lower dislocation density, and the advantage of lattice matching (resulting in fewer misfit dislocations at the substrate-layer interface). Recently, the growth of HgCdTe on lattice-matched substrates of CdTeSe by metal-organic chemical vapor deposition (MOCVD) has been reported [3], supporting the importance of close lattice matching for improved HgCdTe layer quality for MOCVD growth.

Although alternative ("foreign") substrate materials, such as GaAs with an intervening CdTe buffer layer, have been used for the growth of HgCdTe by both MOCVD and molecular beam epitaxy (MBE), the lattice mismatch between HgCdTe and CdTe generates dislocations at the interface and can degrade the HgCdTe layer properties. Current investigation of the growth of lattice-matched CdZnTe layers grown on GaAs by MOCVD indicates promise of a possible replacement for bulk substrates of CdZnTe (and perhaps also CdTeSe) in the future. However, current development of next-generation hybrid infrared detector arrays relies upon active layers of HgCdTe grown by LPE, and the substrate materials required, at least at the present time, are in bulk crystal form with large single-crystal area ($>30 \text{ cm}^2$) and low defect density.

It is expected from the phase diagrams of the two alloy systems (Cd-Zn-Te and Cd-Te-Se) that composition control can be maintained over longer boule lengths for CdTeSe than for CdZnTe, because the equilibrium distribution coefficient of CdSe is about 0.97 in CdTe compared with 1.31 for ZnTe in CdTe.

In this paper, results are reported of CdTeSe and CdZnTe boules $\geq 5 \text{ cm}$ in diameter grown vertically and unseeded in a specially designed multiple-zone furnace assembly with a computerized control and monitoring system [4]. Parameters required for improved crystal quality based on growth experiments and numerical thermal model of the growth process are reviewed. Finally, factors influencing reproducibility of single crystal yield and quality are discussed.

CRYSTAL GROWTH AND EVALUATION

The crystal growth apparatus, optimum thermal conditions from thermal modeling of growth process, crystal growth procedure, and evaluation of grown crystal are described in this section.

Growth Apparatus

The crystal growth furnace assembly is shown schematically in Figure 1. The furnace can accommodate growth ampoule up to 7.5 cm in diameter. Temperature profiling of the furnace assembly was accomplished with a thermocouple array consisting of 11 thermocouple junctions 0.5 in. apart. The thermocouple array was positioned inside the middle furnace (melt or hot zone, Figure 1) to monitor temperature distribution both circumferentially and along the vertical axis (longitudinally). Temperature was displayed in real time on the video screen and all measured data were available for printout or storage on hard disk. Temperature profile data were obtained as a function of time with loaded ampoule in position, to monitor temperature distribution and fluctuations in temperature during the entire crystal growth period.

Thermal Modeling of Growth Process

From fundamental heat-transfer considerations it is known that for crystal growth from the melt in the vertical Bridgman configuration a slightly convex (toward the melt) liquid-solid interface is favorable for grain selection and helps to prevent spontaneous nucleation at the ampoule wall. Although the thermal conditions at the interface can be controlled to a large extent by furnace design features and furnace parameters, the thermal properties of the charge will have a major influence on the interface shape and position. The most important of the thermal properties of the charge is its thermal conductivity. While the magnitude of the thermal conductivity influences the thermal coupling between the furnace and the charge, a difference in thermal conductivity values for the solid crystal and the melt at the interface can lead to unfavorable interface shape (i.e., concave toward the melt).

Thermal diffusivity (α), which is related to the thermal conductivity (k) by $k = \alpha \rho C_p$, where ρ and C_p are density and specific heat (at constant pressure), respectively, was measured for both solid and liquid CdTe and $\text{Cd}_{0.96}\text{Zn}_{0.04}\text{Te}$. Results of the thermal diffusivity measurements [4] as a function of temperature for both CdTe and CdZnTe, showed only a 20% increase in

the thermal diffusivity values of the liquid compared with the solid near the vicinity of the melting point.

For evaluation of the parametric effects on the solid-liquid interface shape in the growth of CdTe, CdZnTe and CdTeSe boules by the VMB process, heat transfer analysis using a finite-element numerical analysis code, ANSYS [5], was performed. Calculations were made using a two-dimensional axisymmetric model for the ampoule containing the charge, with both conductive and radiative modes of heat transfer between the furnace wall and the ampoule. Convective fluid flow was neglected. The crystal diameter used was 2 in., ampoule wall thickness 0.08 in. and crystal length 12 in. (sufficiently long to be considered thermally infinite). Measured temperature profiles in the growth furnace and thermal diffusivity values for liquid and solid CdTe and $\text{Cd}_{0.96}\text{Zn}_{0.04}\text{Te}$ were used in the model to provide guidance in determining the optimum position of the solid-liquid interface within the growth furnace. A sample numerical solution with the hot-zone temperature at 1110°C , cold-zone temperature at 925°C and the gradient-zone (insulated) length of 1 in. is shown in Figure 2. The model shows that the interface is convex, lies inside the hot-zone and is 1.5 in. from the center of the insulated zone. Similar thermal conditions were used in the actual growth experiments described below.

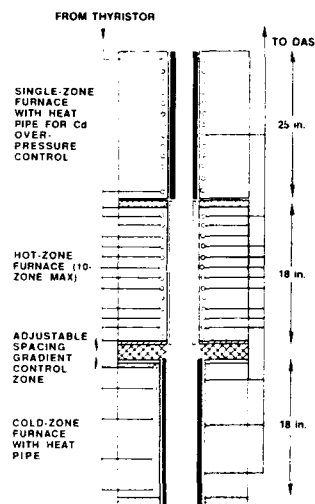


Figure 1. Schematic diagram of multiple-segment VMB furnace assembly.

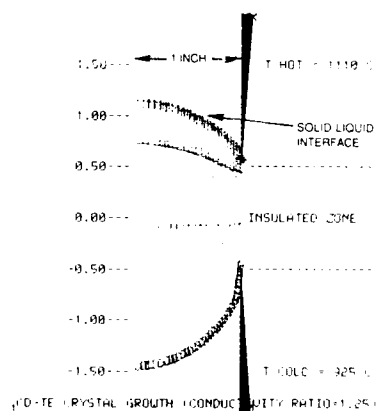


Figure 2. Numerical heat transfer model of VMB process showing optimum position of solid-liquid interface (see text).

Crystal Growth

Crystals of $\text{Cd}_{0.96}\text{Zn}_{0.04}\text{Te}$ and $\text{CdTe}_{0.96}\text{Se}_{0.04}$ 2 to 3 in. in diameter and up to 6 in. in length have been grown unseeded from melts, using vapor-reacted pre-synthesized CdTe, ZnTe, and CdSe charges. Charge masses up to 3.0 kg (3-in. diameter) have been utilized for CdZnTe growth and up to 1.1 kg (2-in. diameter) for CdTeSe growth. Both materials were grown under similar conditions, that is, melt temperature approximately 1110°C , Cd overpressure approximately 1 atmosphere, temperature gradient without the growth ampoule approximately $5^\circ\text{C}/\text{cm}$, and a furnace travel rate of 1 mm/hr.

Since commercially available Se is not as pure as the readily available electronic grade Zn (6 9's purity), prereacted CdSe was twice sublimed to effect separation of some impurities; the final sublimate was used in the preparation of the CdTeSe boules. {111}-oriented single-crystal substrates sawed from the boules were used for characterization of the bulk properties of the

material and for epitaxial $\text{Hg}_{1-x}\text{Cd}_x\text{Te}$ growth by SBRC's vertical liquid-phase epitaxial (VLPE) process [6] for evaluation of the substrate quality.

Crystal Evaluation

Macroscopic Structure

The characteristic crystal grain structure of $\text{Cd}_{0.96}\text{Zn}_{0.04}\text{Te}$ boules of different diameters are shown in Figures 3 and 4. Photographs of 2- and 2.5-in. diameter CdZnTe boules and {111} slices cut almost parallel to the growth axis from those boules are shown in Figure 3a and 3b, respectively. Figure 4 shows a photograph of a recently grown 3-in. diameter CdZnTe boule, that shows very similar macroscopic surface grain structure as seen in the smaller diameter boules. For the 2.5- and 3-in. diameter boules, the furnace travel rate was reduced to 0.75 mm/hr and 0.5 mm/hr, respectively, from the typical speed of 1 mm/hr used for 2-in. diameter boules. Post growth cooling rate was also reduced from 25°C/hr to 10°C/hr for these larger diameter boules.

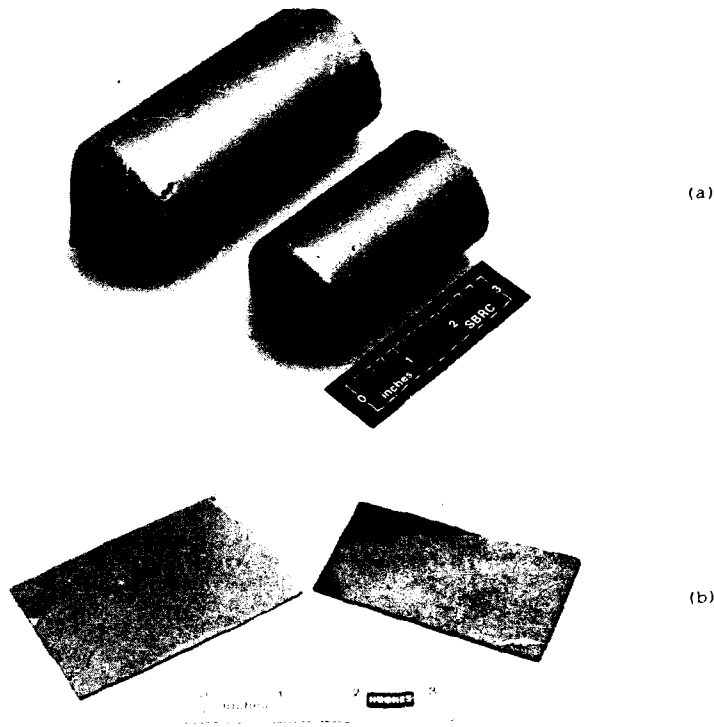


Figure 3. (a) $\text{Cd}_{0.96}\text{Zn}_{0.04}\text{Te}$ boules 2- and 2.5-in. diameters; (b) {111} oriented substrates from 2- and 2.5-in. diameter boules showing large ($>40\text{ cm}^2$) single-crystal area.

Under these growth conditions $\text{Cd}_{0.96}\text{Zn}_{0.04}\text{Te}$ boules, for which 75% of the boule volume was single crystal, were achieved. Single crystal area as large as approximately 50 cm^2 was obtained from the 2.5-in. diameter boule. Usually

a few lamellar twins on the surface of the boule are found that propagate either parallel to or at a slight angle (approximately 15 to 30°) to the growth axis. Generally it is seen that crystal growth begins with several grains near the tip, but after 0.5 to 1 in. of growth the grains grow out and no additional grains are nucleated. This is indirect evidence of a favorable solid-liquid interface shape for grain selection throughout the growth period.

Analysis of the thermal history during growth reveals that the presence of the ampoule (with charge) increases the temperature inside the

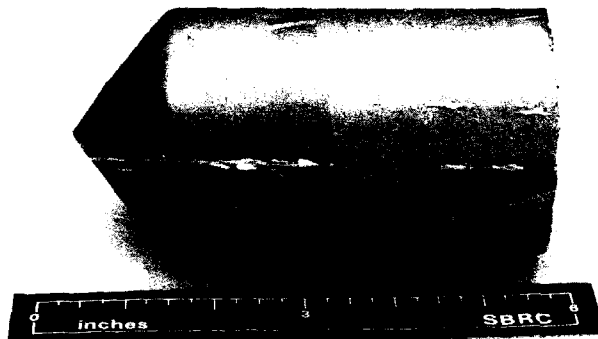


Figure 4.
 $\text{Cd}_{0.96}\text{Zn}_{0.04}\text{Te}$ boule
3-in. diameter
shows similar grain
structure as in
smaller diameter
boules.

furnace by 10 to 15 degrees. The temperature gradient at the tip of the ampoule was measured to be 8 to 10°C/cm and it dropped to 4 to 5°C/cm beyond 2.5 cm from the tip - where rapid enhancement of grain selection takes place in most boules. The initial temperature rise of 10 to 15 degrees is expected to shift the interface position towards the cold-zone, changing the interface shape from convex to concave which will promote spontaneous grain nucleation near the ampoule wall. As growth progresses and the temperature drops, the interface position can move upward toward the hot-zone and the shape changing to convex favoring grain selection.

Figure 5 shows the characteristic crystal grain structure of $\text{Cd}_{0.96}\text{Zn}_{0.04}\text{Te}$ and $\text{CdTe}_{0.96}\text{Se}_{0.04}$ for comparison. Longitudinal sections from each boule cut parallel (as for CdTeSe) or nearly parallel (as for CdZnTe) to the growth axis demonstrate comparable grain selection and large single-crystal area ($\geq 17 \text{ cm}^2$) in both cases.

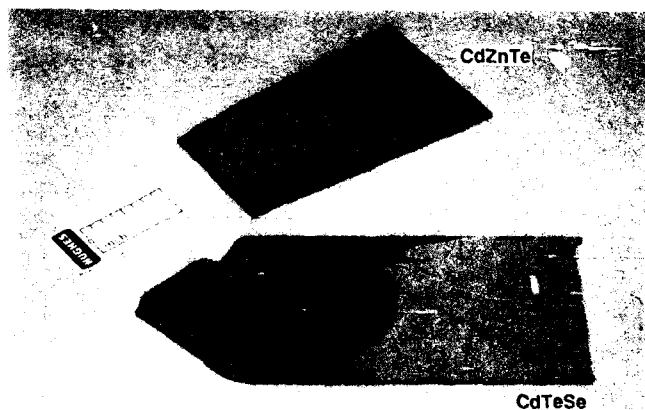


Figure 5. Characteristic crystal grain structure in CdZnTe and CdTeSe.

Microscopic Structure

Although the etch-pit density for these CdTeSe boules was similar to that of typical CdZnTe (10^4 to low 10^5 cm $^{-2}$), the precipitate size and density were significantly reduced (factor of 10) in CdTeSe compared with that in CdZnTe. Since Se substitutes for the Te site in CdTeSe it is quite possible that it reduces the slope in the retrograde solubility curve of the Te-rich side in CdTe, thereby reducing precipitation of the Te during cool-down after growth. It is also perhaps significant that clustering of etch pits around precipitates typically seen in CdTe and CdZnTe was not present in CdTeSe.

(333) x-ray topographs and x-ray rocking curve (CuK α_1 , Si 4-crystal monochromator) values of full width at half-maximum (FWHM) for the two materials are shown in Figure 6. The FWHM values are indicated in the figure for various locations at which they were measured. The uniformity of both the topographs and the FWHM values measured at different locations in the two substrates demonstrate excellent structural quality of both materials.

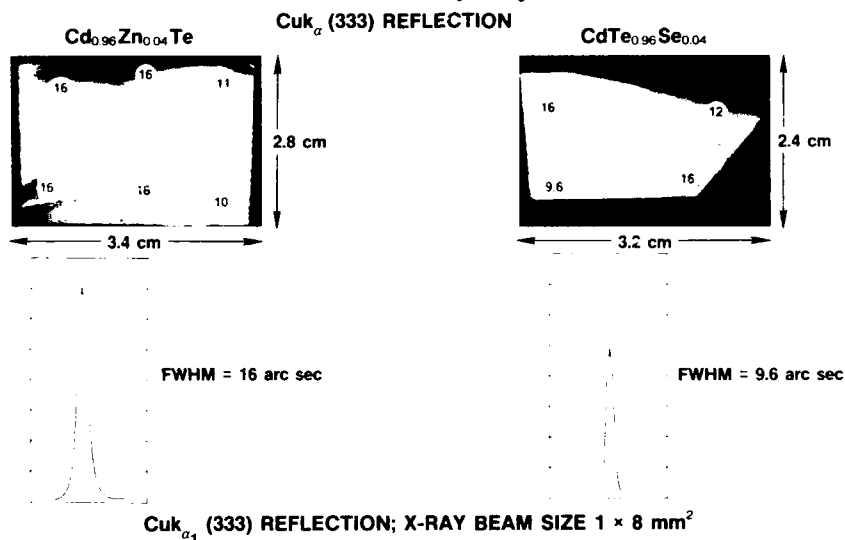


Figure 6. X-ray reflection topograph and double-crystal rocking curve on CdZnTe and CdTeSe substrate.

Composition Variation

Variation in composition (y -value) along the growth axis in Cd $_{1-y}$ Zn $_y$ Te and CdTe $_{1-y}$ Se $_y$ boules was measured by high resolution photoluminescence at 4.2K where bound-exciton (BE) peak positions were used to determine relative changes in composition. The 5145Å line of an Ar-ion laser was used as the excitation source and the samples were immersed in liquid He (4.2K). A Spex 1404 double spectrometer (using a resolution of 0.8Å) and a Hamamatsu R943 photomultiplier tube (GaAs photocathode) were used for the measurements. The shift in the BE peak position corresponds to a change in the bandgap of the crystal. This change in bandgap was used to determine the change in composition, y , assuming that, for small variations, the variation in bandgap with composition (dE_g/dx) is linear and equal to difference in bandgap between the two end binaries, CdTe-ZnTe and CdTe-CdSe. Figure 7 shows the composition change (from a nominal melt composition of 4 percent for both CdZnTe and CdSeTe boules) versus distance along the growth axis. For CdTeSe the composition remains relatively constant along the growth axis, whereas for CdZnTe the composition is seen to vary downward to as low as approximately 1.2 percent

along the length of the boule, consistent with a distribution coefficient for ZnTe which is greater than unity. The variation in composition of CdZnTe near the tip of the boule and up to 4 cm from the tip is probably due to transient effects, such as temperature fluctuations and associated spontaneous nucleation, at the beginning of growth as discussed before.

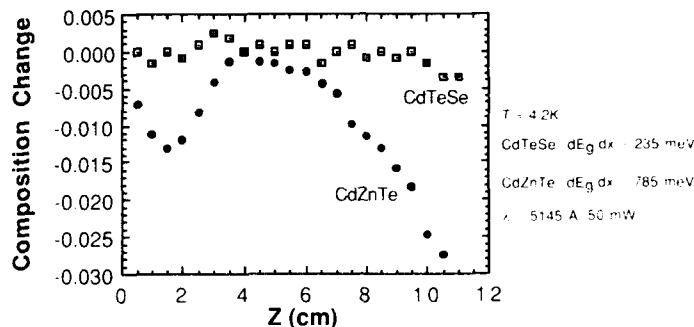


Figure 7. Photoluminescence BE peak positions used to determine relative changes in composition along growth axis.

Epitaxial $\text{Hg}_{1-x}\text{Cd}_x\text{Te}$ Layer on CdZnTe and CdTeSe

Epitaxial $\text{Hg}_{1-x}\text{Cd}_x\text{Te}$ ($x = 0.26$, $t = 8 \mu\text{m}$) layers grown on (111) CdTeSe and CdZnTe substrates by SBRC's VLPE process from Hg-rich melts showed comparable surface morphology and electrical properties. However, the structural quality of $\text{Hg}_{1-x}\text{Cd}_x\text{Te}$ on CdTeSe was more uniform than that on CdZnTe, as shown in Figures 8 and 9. The structural quality of the HgCdTe layer on CdZnTe, as measured by x-ray rocking-curve FWHM values and shown in Figure 8, indicates a systematic broadening of the rocking curve across the width of the layer. As displayed in Figure 9, for the HgCdTe layer on CdTeSe the FWHM values did not vary as much as in the case for the CdZnTe substrates. In both cases, however, the underlying substrate had very uniform and narrow x-ray FWHM values (10 to 16 arc-sec).

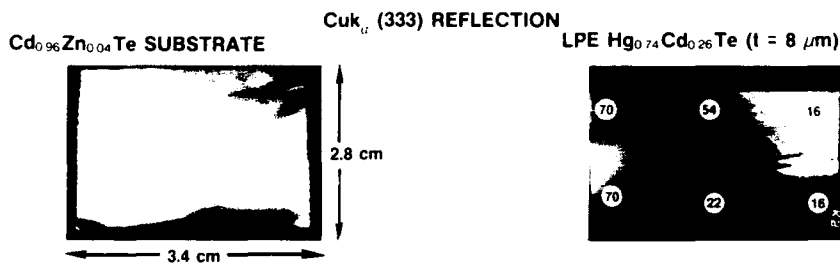


Figure 8. X-ray scanning reflection topographs of (111) CdZnTe substrate and LPE HgCdTe layer showing FWHM values from x-ray double-crystal rocking curves at different locations in the LPE HgCdTe layer.

To determine if this variation in the structural quality of epitaxial HgCdTe on CdZnTe was due to the variation in the Zn concentration of the underlying substrate, PL measurements were made along the lengths of the same two substrates. As described earlier, bound-exciton peak positions were measured from the PL spectra and the corresponding composition changes determined as a function of position across the two substrates. The results are plotted in Figure 10. It was found that the composition of CdTeSe remained unchanged along the length, whereas for CdZnTe the composition varied from 4- to 5-mole percent from one side of the substrate to the other. Thus, the broadening of

the rocking curve in the case of LPE HgCdTe on CdZnTe is most probably due to this gradual change of composition from 4 to 5 percent across the CdZnTe substrate.



Figure 9. X-ray scanning reflection topographs of {111} CdTeSe substrate and LPE HgCdTe layer showing FWHM values from x-ray double-crystal rocking curves at different locations in the LPE HgCdTe layer.

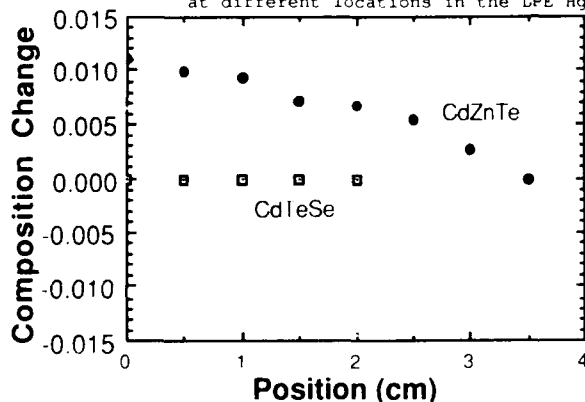


Figure 10. Photoluminescence BE peak positions used to determine compositional uniformity of CdZnTe and CdTeSe substrates.

Optical and Electrical Properties of CdZnTe

Infrared (IR) optical transmission measurements of polished CdZnTe wafers can provide useful information about excess impurities in the material. Considering only reflectance losses at two surfaces, the theoretical transmission should be approximately 63% over the typical range of 2.5 to 20 μm covered by most FTIR spectrometers. Figure 11a shows the transmission spectrum from a CdZnTe wafer which has an excess Cd vacancy concentration. Figure 11b shows the transmission of this same sample is restored after a 72-hr isothermal anneal at 600°C in Cd overpressure to fill these excess vacancies. Figure 12 shows the absorption coefficient versus wavelength, determined from Figure 11a, increases rapidly at first then as $\lambda^{0.85}$ for $\lambda > 7 \mu\text{m}$. This absorption behavior is clearly not free-carrier absorption but is another mechanism apparently related to the nonstoichiometry (Cd vacancies).

An example of CdZnTe material exhibiting free-carrier absorption is Figure 13 which shows the IR transmission expanded in the region from 8 to 20 μm (spectrum is flat from 2.5 to 8 μm) from three different regions, separated by approximately 0.4 cm, taken progressively closer to the tail end of a boule. The absorption coefficient from each of these regions was plotted as a function of wavelength and varies as $\alpha = k\lambda^{2.7}$ from 8 to 20 μm ; this plot for region 3 is shown in Figure 12. The value of the coefficient k , derived from the α versus λ plots, was found to be linearly related to the n-type carrier concentration, determined from 300K Hall-effect measurements as shown in Figure 14; Figure 14 shows that $k = (8.6 \times 10^{-9})N_d$.

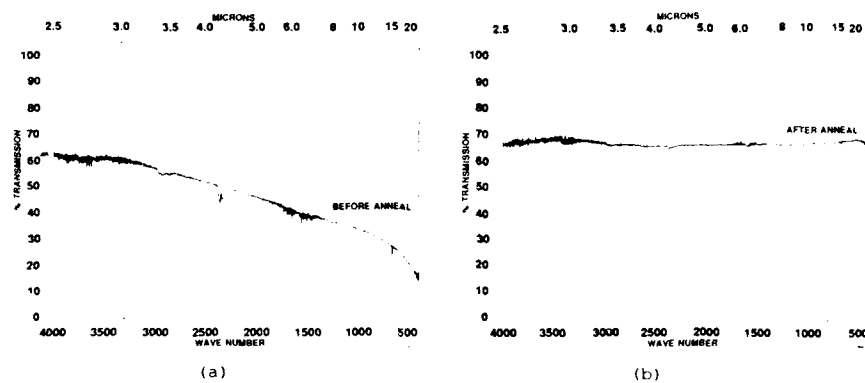


Figure 11. (a) IR transmission spectrum from a CdZnTe wafer with an excess Cd vacancy concentration; (b) IR transmission spectrum from same wafer after a 72-hr anneal at 600°C in Cd overpressure.

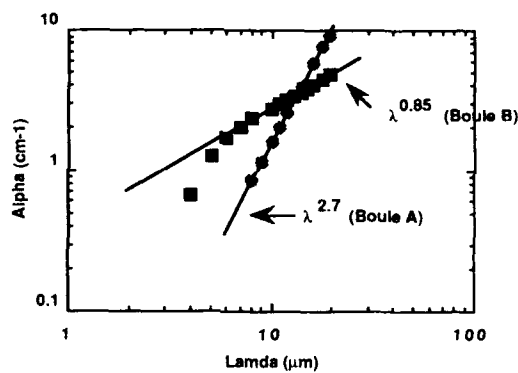


Figure 12. Absorption coefficient versus wavelength in CdZnTe wafers from two different boules. Boule B shows effect due to excess Cd vacancies ($\lambda^{0.85}$), Boule A shows effect due to free carrier absorption.

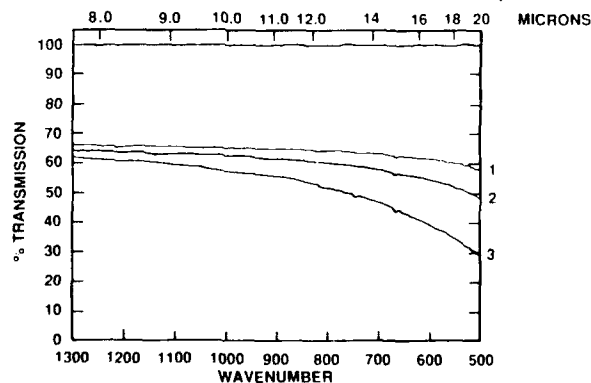


Figure 13. IR transmission spectra near tail end of a CdZnTe boule showing effect due to free carrier absorption.

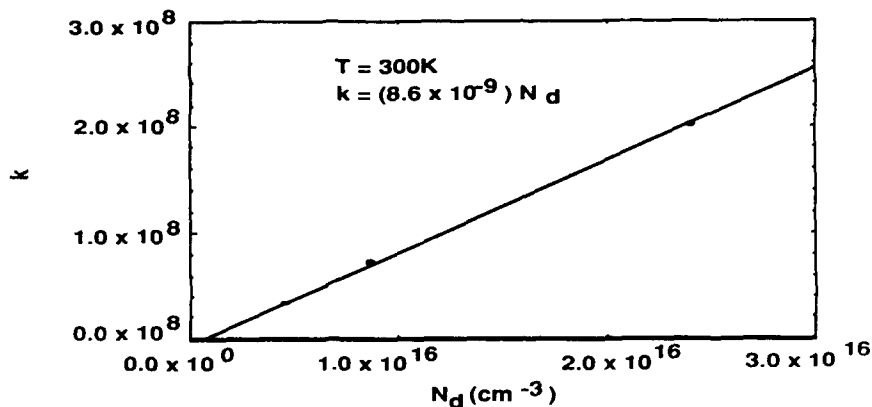


Figure 14. Coefficient k plotted against n-type carrier concentration N_d (300K) from Hall effect shows linear dependence, with $k = 8.6 \times 10^{-9} N_d$.

Figure 15 shows n-type carrier concentration and mobility versus temperature for a CdZnTe sample taken from the same region of the boule which showed free-carrier absorption. The overall mobility is low and decreases somewhat at lower temperatures which indicates disorder in this region of the boule. However, similar measurement on a sample from the tip region of this boule show lower carrier concentration ($1.7 \times 10^{15} \text{ cm}^{-3}$) and higher mobility (approximately $1000 \text{ cm}^2/\text{V}\cdot\text{s}$) at room temperature, which agrees with negligible free carrier absorption from this part of the boule. The formation of ohmic contacts to p-type CdZnTe is an area that needs further work to allow more routine characterization of these materials by Hall-effect measurements.

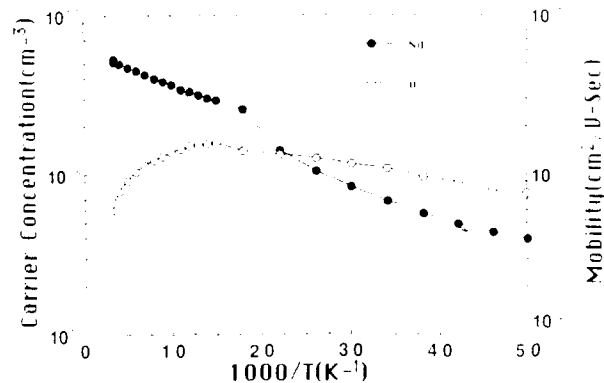


Figure 15. Carrier concentration (n-type) and mobility versus temperature for a CdZnTe sample taken from same region of boule that showed free-carrier absorption.

Low temperature (4.2K) photoluminescence (PL) measurements made at the tail end and tip end of this same boule are shown in Figures 16a and 16b, respectively. A comparison of these figures shows the decrease in the bandgap due to a lower concentration of Zn at the tail end of the boule as described earlier. At the tail end, shown in Figure 16b, the donor-acceptor band or "defect" band at 1.45 eV is exceptionally intense in comparison to this same

band in Figure 16a for the tip end of the boule. The luminescence intensity of the bound exciton peaks at $E > 1.6$ eV is approximately twice as large for the tip region of this boule which also indicates better material quality. We were unable to quantitatively relate the Hall-effect data in the tail end of the boule with absolute intensities or intensity ratios of either the donor-acceptor band or the bound exciton peaks. Quantitative measurement of shallow impurity concentration by PL, which is common for Si, is still elusive for CdZnTe materials and needs further research.

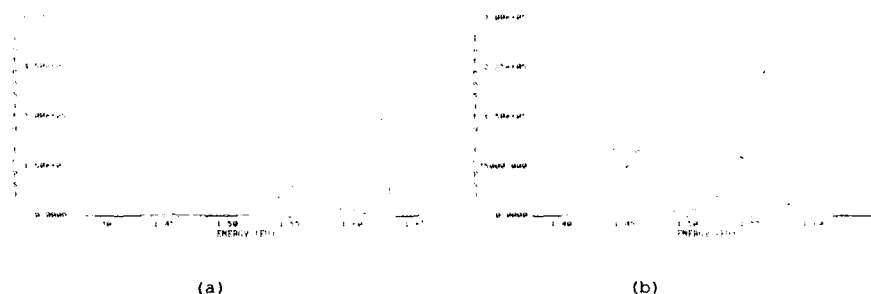


Figure 16. Low temperature PL spectra on samples from (a) tip and (b) tail end of a boule that showed free carrier absorption.

REPRODUCIBILITY OF BOULE QUALITY

Assessing the current status of these crystals, although large-area single-crystal substrates of CdTe, CdZnTe, and CdTeSe with excellent quality are achieved, a major issue still remains that affects the reproducibility of substrate quality. Based on numerous growth results in recent years at SBRC, it is found that once the crystal growth conditions were optimized, a major factor affecting the single-crystal quality is the quality of the elemental starting materials. Starting materials as received from commercial sources has been found to be variable. Reduced purity of input raw materials (Cd, Te, Zn, Se) has affected the substrate quality in two ways: (1) reduced optical transmission and (2) higher density of twins and microtwins. Both effects can limit the usable single-crystal yield in a boule.

Presence of excess substitutional impurities in a boule can give rise to free carrier absorption as discussed before. Additionally, impurities, oxides, or particulates such as carbon - which is sometimes detected in large concentrations in the substrate can initiate twins and microtwins during crystal growth in these materials. In the diamond or zinc blend structure, such as in these II-VI crystals, twinning is always observed with one of the {111} family of lattice planes acting as a twin plane. There are four types of such octahedral planes belonging to the same family included at $70^\circ 32'$ to each other. Twinning about a {111} plane is a simple stacking fault. It is characterized by a perfect fit of the lattices on either side of the fault; i.e., it leaves all distances between nearest neighbors and all bond angles undisturbed. Very little energy is therefore required to initiate twinning, only that due to interaction between second-nearest neighbors. Therefore, a single crystal growing with a certain crystallographic orientation can swing readily over to one of four other orientations by this mechanism. Since very little energy is required to initiate such a twin, small sudden temperature fluctuations in the melt or local disturbances at the interface, such as those caused by the presence of foreign particles or excess solute species might initiate twins in these materials.

Thus reliability of quality (purity) of input raw materials needs to be improved to assure improved reproducibility of boule quality in these materials.

PROSPECTS

Large-area single crystals of $\text{Cd}_{0.96}\text{Zn}_{0.04}\text{Te}$ or $\text{CdTe}_{0.96}\text{Se}_{0.04}$ with low defect density are required as substrates for large-scale production of high-quality epitaxial HgCdTe layers for hybrid focal plane arrays in the infrared detector industry. Bulk substrates of CdZnTe continues to play a major role in HgCdTe epitaxy either by liquid phase epitaxial (LPE) or vapor phase epitaxial (VPE) techniques such as MOCVD or MBE, despite future trend toward alternative "foreign" substrates, viz, Al_2O_3 , GaAs, or Si.

As reviewed in previous sections the quality and single crystal size of both CdZnTe and CdTeSe have improved significantly in recent years to provide impetus for further development of these materials in bulk crystal form. Of particular significance is the improvement in structural quality as measured by x-ray topography and x-ray rocking curve analysis. X-ray rocking curve FWHM as low as 8 arc-sec and with a typical value of ≤ 20 arc-sec and excellent uniformity have been achieved in these materials. These results are comparable to that of bulk GaAs. Improvements in compositional uniformity in CdTeSe compared with CdZnTe have shown corresponding improvement of structural uniformity in epitaxial HgCdTe layers grown by VLPE.

The aforementioned improvements in crystal quality and size is attributed to a combination of several parameters established experimentally and through the aid of a numerical thermal model of the growth process. The critical parameters are: favorable solid-liquid interface shape, promoting grain selection; improved temperature stability with time in the melt zone (± 0.1 to 0.2°C); axial temperature uniformity in the melt zone (approximately 3°C maximum variation over 6 inches); low axial temperature gradient at the growth interface ($< 15^\circ\text{C}/\text{in.}$); and low furnace travel rate ($\leq 1 \text{ mm/h}$).

However, reproducibility of boule quality still remains a critical issue. Analysis of boule growth results at SBRC points toward a strong correlation of boule quality with starting raw materials.

As discussed in the previous section, excess impurities by themselves or in the form of oxides, can degrade substrate quality as well as single crystal yield in a boule. Thus for improvement in reproducibility of boule quality, it is imperative that the reliability of starting material (purity) is assured.

ACKNOWLEDGEMENTS

We wish to thank all our colleagues at SBRC who have contributed to the substrate growth technology over the past several years. We also thank U.S. Naval Research Laboratory and SBRC IR&D for financial support.

REFERENCES

1. S.L. Bell and S. Sen, J. Vac. Sci. Technol. **A 3**(1), 112 (1985).
2. R.A. Wood, J.L. Schmit, H.K. Chung, T.J. Maye, and G.R. Woolhouse, J. Vac Sci, Technol. **A 3**(1), 93 (1985).
3. S.K. Ghandi, I.E. Bhat, and H. Fardi, App. Phys. Lett. **52**, 5 (1988).
4. S. Sen, W.H. Konkel, S.J. Tighe, L.G. Bland, S.R. Sharma, and R.E. Taylor, J. Crystal Growth **86**, 111 (1988).
5. G.J. Desalvo and J.A. Swanson, ANSYS Engineering Analysis System Users Manual, Swanson Analysis Systems, Inc., Houston, PA, 1985.
6. T. Tung, J. Crystal Growth **86**, 161 (1988).

GROWTH AND CHARACTERIZATION OF CDTE AND CDTE ALLOYS

S. MCDEVITT*, D.R. JOHN*, J.L. SEPICH*, K.A. BOWERS**,
J.F. SCHETZINA**, R.S. RAI***, AND S. MAHAJAN***
*II-VI Incorporated, 375 Saxonburg Boulevard, Saxonburg, PA
16056

**North Carolina State University, Department of Physics,
Raleigh, NC 27695

***Carnegie Mellon University, Department of Metallurgical
Engineering and Materials Science, Pittsburgh, PA 15023

ABSTRACT

Methods used to grow bulk, CdTe crystals, effects of alloying on their perfection and typical single crystal properties are reviewed in this paper. Crystals grown by a modified horizontal Bridgman technique have lower dislocation densities than those grown by a modified vertical Bridgman method. Dislocation densities of the order of $1 \times 10^3/\text{cm}^2$ have been observed in CdTeSe crystals grown by the former technique. Due to the difference in the distribution coefficients of Zn and Se in CdTe, CdTeSe ingots are chemically more uniform than CdZnTe ingots. Purity studies of starting materials indicate that Se substitutions may introduce more impurities than Zn additions.

INTRODUCTION

CdTe and CdTe alloys are used as substrates to grow HgCdTe, HgZnTe and HgMnTe epitaxial layers. These epitaxial materials are being developed for infrared detection and optoelectronic applications. Although HgCdTe can be grown by bulk crystal growth methods [1,2], the demand for large-area infrared (IR) devices has increased dependence on epitaxial HgCdTe to produce large scale, detector grade material. A variety of epitaxial growth techniques, such as liquid phase epitaxy (LPE), organo-metallic vapor phase epitaxy (OMVPE), and molecular beam epitaxy (MBE), have been used to deposit epitaxial layers. In addition, since the perfection of CdTe substrates is not very high, alternative substrates, InSb, GaAs, and Si, have been used. However, CdTe and CdTe alloys have the advantage of chemical compatibility and closer lattice match.

BULK CRYSTAL GROWTH

It is well documented that the performance of heterostructure devices is strongly influenced by the quality of the underlying substrate [3]. Dislocations present in the substrates are observed to be replicated into epitaxial layers grown by MBE [4], OMVPE [5], and LPE [6]. Therefore in addition to growing large area single crystals, a bulk crystal growth method should be optimized to produce material with low dislocation density, high IR transmission, high resistivity, and absence of second phase particles. Vertical Bridgman with OverPressure (VBOP) and Horizontal Bridgman with OverPressure (HBOP) have the advantages of producing large area, high quality, and stoichiometric crystals as compared to the three other growth

techniques - heat exchanger method (HEM), traveling heater method (THM) and high pressure Bridgman. THM offers the advantage of lower processing temperatures to produce a "purer" material. This method has been used advantageously in the growth of $\text{Cd}_{1-x}\text{Mn}_x\text{Te}$, where $x \geq 0.15$, to avoid a high temperature hexagonal to cubic phase transformation which leads to extensive twinning [7].

A schematic of a VBOP furnace is shown in Figure 1. The furnace contains ten independently controlled thermal zones with a heat pipe providing additional stability in the overpressure control zone. The ampoule is positioned on a vibration free stand and remains stationary during growth. The furnace travels at a speed of 0.5-5mm/hr with a temperature gradient of 4-8°C/cm. The temperature gradient and overpressure control during growth and cooldown are critical operating parameters which influence defect density and stoichiometry of the crystals. Ingots grown to date have diameters of 60 to 75mm and masses between 1.2 and 2.5kg. The largest, rectangular single crystals we have fabricated from VBOP ingots had areas of 40mmx60mm or 50mmx50mm.

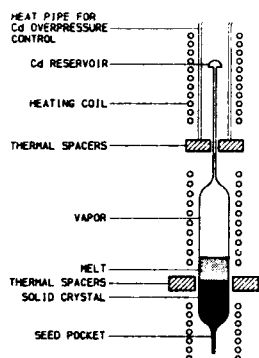


Figure 1. Schematic of a multizone VBOP furnace.

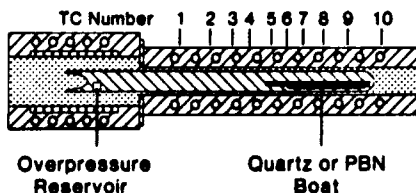


Figure 2. Schematic of a multizone HBOP furnace.

A schematic of an HBOP furnace is shown in Figure 2. The furnace has 10 independently controlled zones in addition to an overpressure zone containing a heat pipe. One advantage of HBOP technology as compared to VBOP technology is that there is no ampoule confinement on top of the melt. This leads to lower thermomechanical stress in that direction. In addition, we use a gradient freeze technique so that neither the crystal or furnace are in motion during growth. By using this horizontal technique, we have consistently grown crystals with lower dislocation densities than by our vertical technique. Currently, the ingots are 50mm diameter half-round and weigh approximately 700g. The largest rectangular single crystal fabricated had an area of 20mmx30mm.

EFFECTS OF ALLOYING CDTE

Lattice Matching

The benefits of lattice matching include improved epilayer morphology, decrease in misfit dislocation densities, and reduced epilayer strain [8]. Because the binary compounds CdTe, ZnTe, CdSe, ZnSe and MnTe are highly miscible in one another, nearly any desired value of band gap or lattice parameter can be achieved. The lattice constant of CdTe is $a_0 = 6.482 \text{ \AA}$, mismatched by approximately 0.3% with respect to $\text{Hg}_{0.8}\text{Cd}_{0.2}\text{Te}$, $a_0 = 6.464 \text{ \AA}$ [9]. A region of high dislocation density is known to exist at the HgCdTe/CdTe interface [10]. If Zn and/or Se are alloyed with CdTe, the lattice constant is decreased from 6.482 Å and can be adjusted to equal that of the HgCdTe composition. Lattice parameter as a function of alloy composition for CdZnTe and CdTeSe can be written as:

$$\text{Cd}_{1-y}\text{Zn}_y\text{Te}: a_0 = 6.482 - 0.381y \quad (1)$$

$$\text{CdTe}_{1-w}\text{Se}_w: a_0 = 6.482 - 0.3987w \quad (2)$$

as in references [11] and [12]. By combining (1) and (2), the lattice parameter of CdZnTeSe can be expressed as:

$$\text{Cd}_{1-y}\text{Zn}_y\text{Te}_{1-w}\text{Se}_w: a_0 \approx 6.482 - 0.381y - 0.3987w \quad (3)$$

We have grown two CdZnTeSe ingots. The lattice parameters measured agree with this equation to within $\pm 0.03\%$ [13].

Segregation Effects

When growing an alloy such as CdZnTe or CdTeSe, one must study the effects of solute distribution in order to approximate the alloy concentration relative to the volume fraction solidified. We assume normal freezing and use Pfann's equation:

$$C = kC_0(1-g)^{k-1} \quad (4)$$

where C is the concentration of the freezing material, C_0 is the nominal concentration, g is the fraction solidified, and k is the effective distribution coefficient [14]. If $k=1$ then $C=C_0$, and the alloy concentration remains constant and equal to that loaded. We have measured the chemical concentration, calculated k, and measured the lattice parameter of samples from CdZnTe and CdTeSe ingots [13]. Chemical concentration was measured by direct current plasma emission spectrometry and lattice parameter was measured with a Siemens D500 diffractometer.

Samples from a $\text{Cd}_{1-y}\text{Zn}_y\text{Te}$ ingot, where the nominal Zn concentration was equal to 0.045, were selected on the basis of fraction solidified. The chemical concentration was measured and plotted as shown in Figure 3. The distribution coefficient, k, was calculated to be approximately 1.1. It is interesting to note that the first data point, where the fraction solidified was close to 10%, is very close to the nominal Zn concentration that

was loaded. This indicates that non-equilibrium freezing is likely to have occurred. We have measured other k values for Zn in CdTe and find them to be in the range of 1.1-1.25. The lattice parameter was measured for samples companion to the chemical samples. Lattice parameter vs. chemical concentration is plotted in Figure 4. Although the data does not fit exactly with equation (1), we feel that the equation can be used as a first approximation in determining the nominal Zn concentration needed for lattice matching.

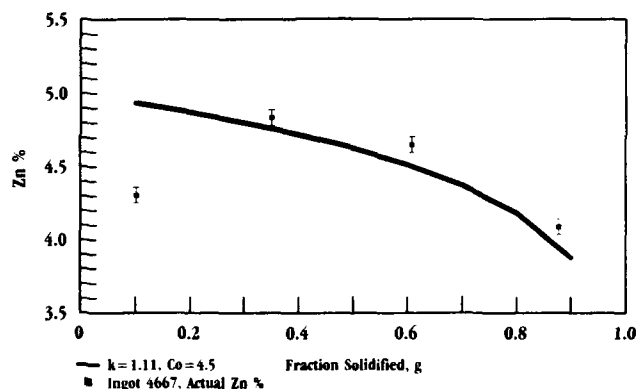


Figure 3. Distribution of Zn in a Cd_{0.955}Zn_{0.045}Te ingot.

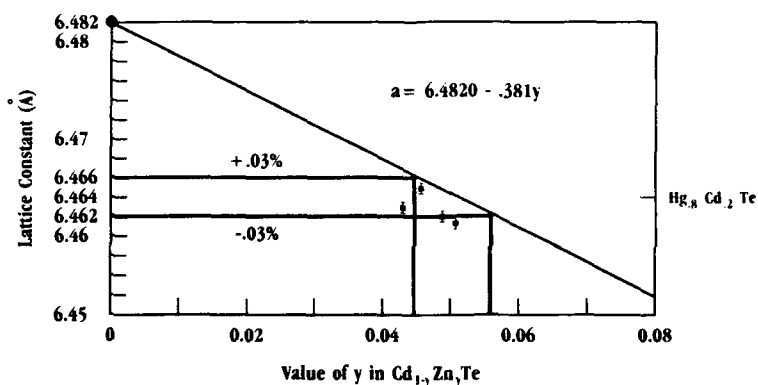


Figure 4. Lattice parameter vs. chemical composition of a Cd_{0.955}Zn_{0.045}Te ingot.

The chemical concentrations of samples from a CdTe_{1-w}Se_w ingot, where the nominal concentration of Se was equal to 0.04, were also measured and the results plotted in Figure 5. We calculated k to be ≈ 0.97 . Figure 6 is a plot of the lattice constants measured for the companion samples. With the exception

of one datum point the results closely agree with those predicted from equation (2).

Figure 7 is a plot of lattice constant vs. chemical composition for a $\text{Cd}_{1-y}\text{Zn}_y\text{Te}_{1-w}\text{Se}_w$ ingot where $y = w = 0.02$. We conclude that $\text{Cd}_{1-y}\text{Zn}_y\text{Te}_{1-w}\text{Se}_w$ can be used as an effective lattice matching alloy.

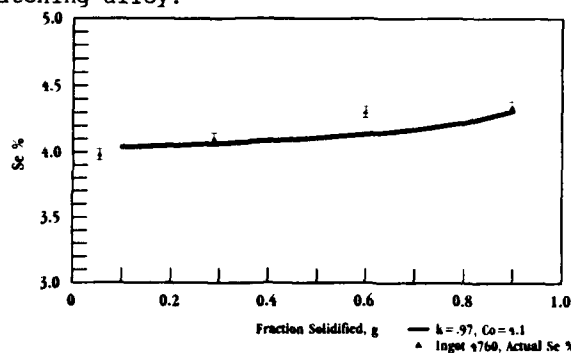


Figure 5. Distribution of Se in a $\text{CdTe}_{.959}\text{Se}_{.041}$ ingot.

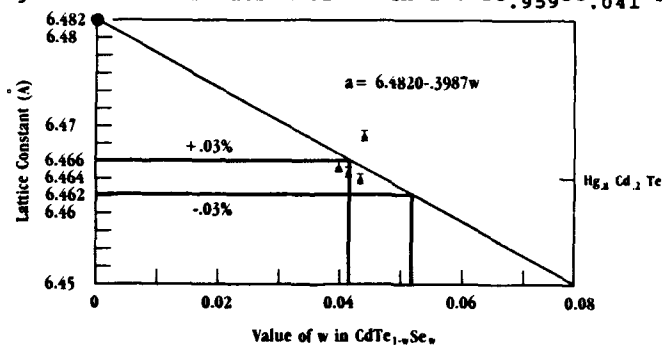


Figure 6. Lattice parameter vs. chemical composition of a $\text{CdTe}_{.959}\text{Se}_{.041}$ ingot.

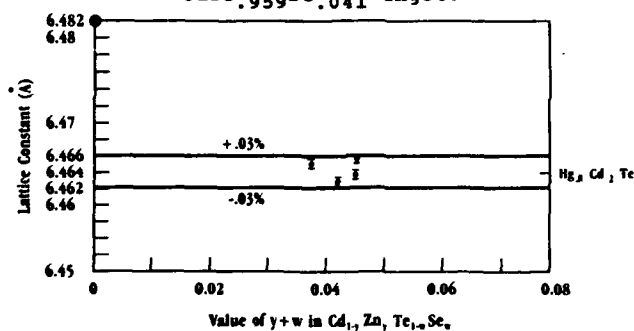


Figure 7. Lattice parameter vs. chemical composition of a $\text{Cd}_{.98}\text{Zn}_{.02}\text{Te}_{.98}\text{Se}_{.02}$ ingot.

Recently, there has been a limited requirement for lattice matched substrates for HgZnTe [15]. This alloy, analogous to HgCdTe, can be "tuned" to yield semiconductors with a band gap that reduces to zero at an intermediate alloy concentration. $\text{Cd}_{1-y}\text{Zn}_y\text{Te}$ substrates, where $0.20 \leq y \leq 0.24$, are lattice matched to $\text{Hg}_{1-x}\text{Zn}_x\text{Te}$, where $0.16 \leq x \leq 0.19$. Chemical composition measurements of samples from a $\text{Cd}_{0.8}\text{Zn}_{0.2}\text{Te}$ ingot were plotted and k was calculated to be 1.25.

Strengthening

In addition to changing the lattice constant of CdTe, the addition of Zn and/or Se strengthens the material. Mechanisms for alloy strengthening have been modeled by Sher and co-workers using bond length and energy changes of the constituents relative to pure crystal values [16]. The shorter bond length of ZnTe increases the dislocation energy and the hardness of CdZnTe alloys. We have found that CdZnTe and CdTeSe crystals grown at II-VI Incorporated are harder and have lower etch pit densities, as revealed by the Nakagawa etch [17], than CdTe grown under similar conditions. A cellular dislocation structure, due to glide and climb caused by thermal gradient induced stresses, is less pronounced with CdTe containing Zn [18] and/or Se. Epitaxial crystal growth on these substrates with lower dislocation densities has resulted in films with superior crystallinity and morphology [19].

Purity

The purity of Cd and Te has been extensively studied and reported [20]. However, the purity levels of Zn and Se are not as well documented. Glow Discharge Mass Spectrometry (GDMS) provides detection limits for most elements on the order of one to fifteen parts per billion atomic (ppba) with accuracies of $\pm 20\%$ [21]. Trace Elements via Solid Sampling Analysis (TESSA) is a reengineered Graphite Furnace Atomic Absorption (GFAA) technique. One advantage of TESSA is that it requires no special sample size. However, a broad elemental survey by this technique would be very expensive. The TESSA technique has detection limits of 10-100 ppba for most elements with accuracies of $\pm 20\%$ [22].

The Zn which we utilize in our CdZnTe ingots is sublimed with Te to form ZnTe in a process separate from the crystal growth. The Se is either reacted with Cd to produce CdSe prior to growth or purchased in the form of a sublimed, solid CdSe material. Zn, Te, sublimed ZnTe, Cd, reacted CdSe and sublimed CdSe were submitted for GDMS analysis to Charles Evans & Assoc., Redwood City, CA for a 66 elemental impurity survey. Because of the shape of the Se material the fabrication of a pin was impossible and the GDMS technique could not be used. We submitted the Se sample to VHG Labs, Manchester, N.H. for TESSA determination of 3 elemental impurities. The raw Cd and Se materials used in the sublimed CdSe were not available for analysis. Results of the purity testing are shown in Table I. The major impurities in the Se were Fe and Si and these were

present in the reacted CdSe. The major impurity in the sublimed CdSe was S and it is unknown if this was present in the starting material or was introduced during the sublimation process.

TABLE I. PURITY OF ALLOY STARTING MATERIALS (PPMA)

Impurity	Zn ¹	Te ¹	ZnTe ¹ (sublimed)	Cd ¹	Se ²	CdSe ¹ (reacted)	CdSe ¹ (sublimed)
Li	ND	ND	.36	ND	NM	ND	ND
B	0.02	ND	0.04	0.02	NM	0.07	0.18
Na	0.02	0.32	ND	0.01	NM	1.33	.07
Mg	ND	0.01	0.03	ND	NM	0.02	0.02
Al	0.01	0.13	0.08	0.01	NM	0.20	0.03
Si	0.04	0.01	0.16	0.03	11.52	3.00	ND
P	ND	ND	ND	0.003	NM	ND	ND
S	ND	ND	ND	0.004	NM	1.70	10.15
K	ND	0.04	0.02	ND	NM	ND	0.001
Ti	0.001	0.02	ND	ND	NM	0.28	ND
Cr	ND	ND	ND	ND	NM	0.01	0.08
Mn	ND	ND	ND	ND	NM	0.14	ND
Fe	0.05	0.004	0.13	ND	8.34	3.77	0.23
Ni	ND	0.01	0.01	ND	NM	0.05	0.07
Cu	ND	ND	0.36	0.01	NM	0.23	ND
Zn	-	ND	-	0.02	NM	0.44	2.63
Ga	ND	ND	0.05	ND	NM	0.008	0.052
Ge	ND	ND	ND	ND	NM	ND	0.08
Se	ND	0.60	0.98	ND	-	-	-
Te	ND	-	-	ND	0.37	0.54	5.26
Total	0.15	1.15	2.22	0.11	20.24	11.52	18.85

¹ GDMS - 66 elements surveyed
² TESSA - 3 elements surveyed
 ND - Not Detected
 NM - Not Measured

CHARACTERIZATION

Single Crystal Properties

IR spectrometry, chemical etching, microhardness, double crystal x-ray diffractometry, and IR microscopy are used to characterize CdTe and CdTe alloys. Table II compares 4 different materials grown by either vertical Bridgman (VB) or horizontal Bridgman (HB) methods with typical attainable properties. Dislocation density is lowered with the addition of Zn or Se and hardness is increased. HBOP CdTeSe consistently has the lowest dislocation densities and the sharpest double crystal rocking curves. We believe this is due to the addition of Se combined with the modified horizontal Bridgman growth process.

TABLE II. SINGLE CRYSTAL PROPERTIES

	VB CdTe	VB $\text{Cd}_{1-y}\text{Zn}_y\text{Te}$ $y \approx 0.045$	VB $\text{Cd}_{1-y}\text{Zn}_y\text{Te}$ $y \approx 0.20$	HB $\text{CdTe}_{1-w}\text{Se}_w$ $w \approx 0.043$
IR Transmission (2.5 - 25 μm)	> 50%	> 50%	> 50%	> 50%
Nakagawa Etch Pit Density ($\times 10^4/\text{cm}^2$)	20-50	4-20	5-7	.1 - 6
DCRC FWHM (arcsec) CuK α (333) or (400) 2mm x 2mm spot size	13-150	10-100	13-100	8-30
Microhardness (Knoop 50g)	45	54	90 (tip) 80 (heel)	54

Photoluminescence

Photoluminescence (PL) has proven to be a powerful technique for assessing the quality of semiconducting materials. It can be used to determine the band gap of the material, making it useful in determining the composition of ternary alloys such as CdZnTe . It can be used to determine the nature and identity of impurities in the material. In addition, such information as PL linewidths and intensities, the presence of strong phonon replication, and the presence of deep level "defect-band" emission is useful in determining the structural perfection of semiconductor crystals. In general, narrow linewidths, strong phonon replication and the absence of deep level emission indicate a high degree of structural perfection.

One of the effects of increasing the Zn content in CdTe is the shift in band gap to increasingly higher energies. The Zn concentration in $\text{Cd}_{1-y}\text{Zn}_y\text{Te}$ can be determined from the luminescence data using the following equation;

$$\text{FE} (5^\circ\text{K}, y) = 1.5964 + 0.445y + 0.33y^2 \text{ (eV)} \quad (5)$$

where FE is the peak position of the free exciton and y is the molar fraction of Zn. This formula is a modification of a previously reported equation written for 80°K [23]. The free excitons (FE) represent the lowest intrinsic excitation energy of electrons and holes in pure materials at low excitation density. This intrinsic recombination is seldom the dominant process at low temperatures. The presence of impurities in most semiconductors is unavoidable and extrinsic recombinations (bound excitons) are usually dominant. Figure 8 is a characteristic spectrum of a $\text{Cd}_{1-y}\text{Zn}_y\text{Te}$ substrate. At 1.6188, the free exciton peak can be observed. Using equation (5), the peak energy corresponds to $y \approx 0.05$. In order to identify the rest of the

peaks, the assumption is made that they are related to the corresponding peak positions in CdTe shifted in energy by

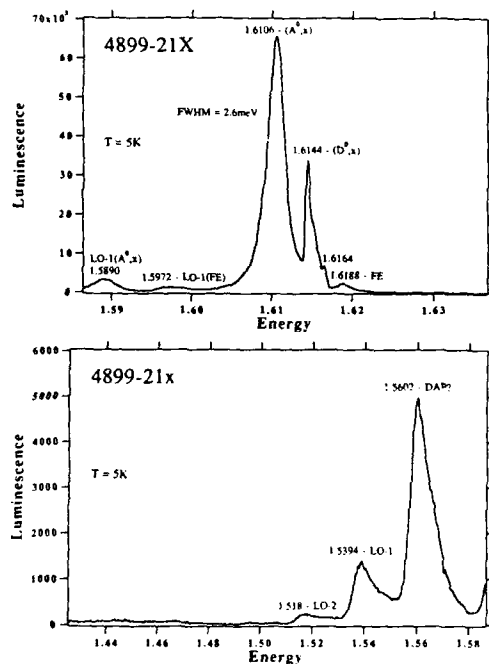


Figure 8. Characteristic PL spectrum of a CdZnTe substrate.

suggests it could be due to donor-to-acceptor pair recombination (DAP). However, a more thorough study, one that includes power and temperature dependence measurements, is needed to further clarify this identification.

INFRARED MICROSCOPY

Precipitates form in CdTe and CdTe alloys during cooling of the crystals from high temperatures due to retrograde solubility of Te in CdTe. The size and density of these precipitates vary from ingot to ingot. It is desirable to minimize the formation of precipitates as they may be responsible for epitaxial defects if they are present on the growth surface. Infrared (IR) transmission optical microscopy is a technique used to non-destructively view bulk material that is transparent in a particular wavelength range. Precipitates that are opaque to IR light are photographed as dark shapes against the IR transparent matrix. The resolution of the microscope is $1\mu\text{m}$ at 400X. Figure 9 is a group of micrographs from four different samples. To date, we have been more successful at controlling precipitate

approximately the same amount as the free exciton. The near edge region is dominated by two bright narrow excitonic peaks. The peak at 1.6144eV can be identified as a neutral donor-bound exciton (D^0, x). The emission line at 1.6106 is in the region for a neutral acceptor-bound exciton (A^0, x). These peaks are quite bright and sharp, having FWHM's of 1.0meV and 2.6meV respectively. Sharp excitonic lines such as these are typical of high quality bulk CdZnTe. At 1.5972eV and 1.5890eV the first order LO-phonon replicas for the free exciton and (A^0, x) transition can be observed. Further below the band edge, a peak at 1.5602eV is present, accompanied by first and second order LO-phonon replicas. This peak is in a position that

size and density by HBOP as compared to VBOP possibly due to the geometry and smaller mass of HBOP ingots.

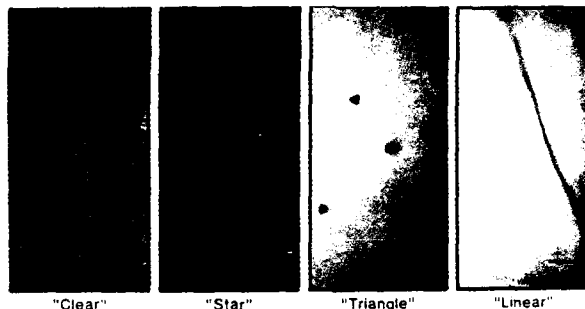


Figure 9. Variety of infrared opaque precipitates and clear region.

TRANSMISSION ELECTRON MICROSCOPY (TEM)

In order to better understand the chemistry and nature of IR opaque precipitates, samples were examined in a Philips EM420 electron microscope operating at 120keV. Samples for TEM were polished mechanically followed with a thinning procedure using 1% bromine in methanol solution.

Figure 10 is an electron micrograph obtained from a CdTe specimen. This is an example of an array of dislocations associated with a slip band. The dislocations in this configuration are nearly all parallel and most of them have the same Burgers vector. Contrast analyses, performed from weak beam and bright field images using different diffraction vectors, here revealed that dislocations are dissociated into two Shockley partials having Burgers vectors of the type $a/6\langle 112 \rangle$. A stacking fault fringe contrast is observed at F. The small particles exhibiting black contrast are precipitates in the matrix of CdTe. On the basis of selected area electron diffraction, these particles have been identified as Te precipitates. This is consistent with earlier published results [24,25,26]. Under the appropriate diffracting condition, Moire fringes are seen in some of the Te precipitates. This is a result of differences in the structure factors between precipitate and matrix. Figure 11 is an example of stress-induced dislocations. Contrast analyses, performed from weak beam and bright field images using different diffraction vectors, have shown that dislocations are also dissociated into Shockley partials. Observation of dislocations as seen in Figures 10 and 11 indicates that the crystal experiences thermal gradient induced stresses during cooling, and this causes slip to occur on parallel slip planes.

SUMMARY

CdTe and CdTe alloys grown by VBOP and HBOP methods are used as substrates for epitaxial growth of HgCdTe and HgZnTe. With the addition of Zn and/or Se, the lattice constant of CdTe is

reduced leading to improved lattice matching. Due to segregation effects, a CdTeSe ingot has a more uniform chemical composition than a CdZnTe ingot. Zn and/or Se strengthen the CdTe matrix resulting in harder materials with lower dislocation densities. To date, the lowest dislocation densities and the sharpest rocking curves have been found in HBOP CdTeSe material. Purity testing shows that Se is contributing more impurities to the matrix as compared with Zn. Photoluminescence can be used to assess the quality and determine alloy concentration in $\text{Cd}_{1-y}\text{Zn}_y\text{Te}$. TEM has been used to identify Te precipitates. Dislocation arrays suggest the presence of thermal gradient induced stress during crystal growth.



Figure 10. Bright field electron micrograph showing a slipband. A stacking fault is marked F. Moire fringes are marked with double arrows. The diffraction vector is $02\bar{2}$ and zone axis is $[111]$.

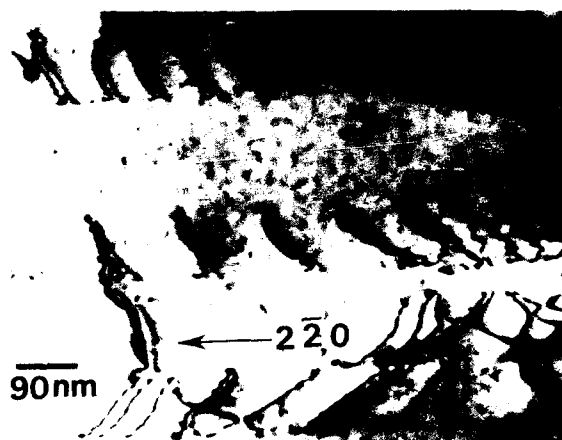


Figure 11. Bright field electron micrograph showing arrays of dislocations and precipitates. The diffraction vector is $2\bar{2}0$ and zone axis is $[111]$.

REFERENCES

1. R. Triboulet, T. Nguyen Duy and A. Durand, J. Vac. Sci. Technol. A3 (1), 95 (1985).
2. Luigi Colombo, A.J. Syllaos, R.W. Perlaky, and M.J. Brau, Ibid., 100 (1985).
3. B.V. Dutt, S. Mahajan, R.J. Roedel, G.P. Schwartz, D.C. Miller and L. Derick, J. Electrochem Soc. 128 (1981) 1573.
4. J.P. Faurie, A. Million and J. Piagnet, J. Crystal Growth 59 (1982) 10.
5. P.D. Brown, J.E. Hails, G.J. Russell and J. Woods, Appl. Phys. Letters 50 (1987) 1144.
6. L.O. Bubulac, W.E. Tennant, D.D. Edwall, E.R. Gertner and J.C. Robinson, J. Vacuum Sci. Technol. A3 (1985) 163.
7. R. Triboulet, Presented at Fourth International Conference on II-VI Compounds, Berlin (West), September 1989.
8. R.A. Wood, J.L. Schmit, H.K. Chung, T.J. Magee and G.R. Woolhouse, J. Vac. Sci. Tech. A3 93 (1985); G.R. Woolhouse, T.J. Magee, H.A. Kawayashi, C.S.H. Leung, and R.D. Ormond, ibid., A3 83 (1985).
9. Wooley and Ray, J. Phys. Chem. Solids 13, 151 (1960).
10. G.R. Woolhouse, H. Kawayashi, and T.J. Magee, Proceedings of the Sixth Conference on Crystal Growth/AACG, Fallen Leaf Lake, CA, 1982.
11. A. Ebina and T. Takahashi, J. Cryst. Growth 59, 51 (1982).
12. R.A. Carlson, R.J. Hager, and R.A. Wood, J. Vac. Sci. Technol. A5, 3048 (1987).
13. S. McDevitt, B. Dean, D. Nichols, T.H. Myers, R.W. Green, presented at the Second Eastern Regional Conference on Crystal Growth/AACG-East, Atlantic City, NJ, 1988 (unpublished).
14. W.G. Pfann, Zone Melting, Robert El Krieger Publishing Co., Huntington NY, 11 (1978).
15. Ariel Sher, D. Eger and A. Raizman, J. Crystal Growth 43, 507 (1987).
16. Arden Sher, An-Ban Chen, W.E. Spicer, and C-K Shih, J. Vac. Sci. Technol. A3, 105 (1985).
17. K. Nakagawa, K. Maeda, and S. Takeuchi, J. Phys. Soc. Japan 49, 1909 (1980).
18. S. McDevitt, B.E. Dean, D.G. Ryding, F.J. Scheltens and S. Mahajan, Materials Letters 4, 451 (1986).
19. S.L. Bell and S. Sen, J. Vac. Sci. Tech. A3, 112 (1985).
20. B.E. Dean, C.J. Johnson, F.J. Kramer, Evaluation of Techniques for Purity Analysis of II-VI Compound Materials, presented at the AACG/ Third Workshop on Purification of Materials for Crystal Growth and Glass Processing, Orlando, FL, 1989 (unpublished).
21. Charles Evans & Associates, Redwood City, CA.
22. VHG Labs., Inc., Manchester, NH.
23. K.Y. Lay, N.C. Giles-Taylor, J.F. Schetzina, and K.J. Bachmann, J. Electrochem. Soc. 133 5, 1049 (1986).
24. M.A. Shahid, S. McDevitt, S. Mahajan and C.J. Johnson, Inst. Phys. Conf. 87, 321 (1987).
25. S.H. Shin, J. Bajaj, L.A. Moudy and D.T. Cheung, Apply. Phys Lett. 43, 68 (1983).
26. H.F. Schaake, J.H. Tregilas, A.J. Lewis and P.M. Evert, J. Vac. Sci. Technol. A1, 1625 (1983).

PHOTOLUMINESCENCE DETECTION OF NATIVE DEFECTS IN THE SURFACE
REGION OF BULK CdTe

P.M. AMIRTHARAJ AND N.K. DHAR
U.S. Army Center for Night Vision and Electro-Optics
Fort Belvoir, VA-22060

ABSTRACT

The native defects introduced by $\text{Br}_2/\text{CH}_3\text{OH}$ etching and aging under atmospheric conditions have been investigated in In doped, bulk CdTe using photoluminescence (PL) spectroscopy. The results indicate a large enhancement of the Cd vacancy related 1.5896 eV excitonic feature with chemical treatment and aging. Hence, the primary perturbation is interpreted to be a small loss of Cd within the sampling region. This result is compared and contrasted with previous studies of etching induced modifications. The implications of Cd depletion on interpreting PL spectra, device processing and long term stability are considered.

INTRODUCTION

The presence of native defects such as vacancies, interstitials, etc. can have a significant influence on the electronic behavior of semiconductor materials. However, detection of specific defects and studying their microscopic properties is nontrivial. The traditional methods of microscopic chemical detection is inapplicable; and an indirect study of properties such as the transport behavior lacks sufficient information on both the microscopic details and spatial resolution. Photoluminescence (PL) spectroscopy, in comparison, is almost ideal for this study since sharp well defined optical features associated with many native defects can be investigated with acceptable spatial resolution. It is the intent of this paper to provide examples of the applicability of PL: the results of an investigation of the native defects introduced as a result of chemical treatment and aging in CdTe are presented. The results are also important in improving the capability of PL in the analysis of defects in CdTe since it identifies those features introduced as a result of the modification of the surface region.

Chemical etching is widely used for cleaning semiconductor surfaces and in processing applications. Deleterious effects may be caused as a result and hence, it is important to understand the consequences to the near surface region and perturbations in the physical properties of the sample.

Several previous investigators have used photoluminescence (PL) to study the electronic behavior of impurities, dopants and electrically active native defects in CdTe [1-12]. However, the results can be ambiguous. Residual impurities, self compensating native defects [2] and those introduced as a result of the chemical treatment may interfere with the interpretation.

A large proportion of the published results on bulk CdTe used surfaces that were chemically etched, the most common etchant being a solution of Br_2 and CH_3OH with concentrations in the range of 0.1 to 20% by volume. It is well known that $\text{Br}_2/\text{CH}_3\text{OH}$

leads to a preferential loss of Cd from the surface region [14-16]. In comparison to earlier conclusions, the results of this study strongly suggest that the depletion of Cd may extend deeper than the $\sim 10\text{\AA}$ previously expected [14,15] and is likely to modify the electronic behavior of the surface region. The inherent ability of PL in detecting very small quantities of an impurity or native defect in a large matrix should be contrasted with the capability techniques such as XPS, Raman scattering and ellipsometry which are sensitive to large stoichiometric changes over relatively thin regions.

The investigation is confined to the near edge region of 1.55 to 1.61 eV. In the samples used in this study, a sharp peak at 1.5896 eV, at 10K, is shown to increase significantly in intensity after the $\text{Br}_2/\text{CH}_3\text{OH}$ etch. This feature has been observed previously and assigned to originate from an exciton bound to a neutral Cd vacancy or a complex defect involving a Cd vacancy [3-5]. Hence our results strongly suggest that Cd vacancies are being introduced into the near surface region by the chemical treatment. Samples that were stored for several weeks without any chemical treatment were also observed to form a Cd vacancy feature. Implications of these results on the spectroscopic behavior, device fabrication and long term stability of CdTe are considered in the following sections.

II EXPERIMENTAL DETAILS

The PL measurements were conducted in a conventional facility that used a spectrometer with a resolution of 0.1 meV. The excitation was provided by a 6328A He-Ne laser line with a power density of 40 mW.cm^{-2} at the sample surface. The measurements reported were performed in the temperature range of 8 - 40K.

The samples used were grown by the Bridgman method and were doped with In to a density of $\sim 1 \times 10^{15}\text{ cm}^{-3}$. Large slices with {111} oriented parallel faces, cut from the ingot, were cleaved to expose the {110} just prior to the measurement or chemical treatment. Cleaving, chemical etching and loading of the samples in the dewar were all performed in an inert atmosphere of Ar or N_2 [16].

The $\text{Br}_2/\text{CH}_3\text{OH}$ etch solution concentrations used were 0.5, 2 and 5% by volume. Post treatment of the samples with 1N $\text{KOH}/\text{CH}_3\text{OH}$ which is known to remove the surface Te layer [14] was also investigated. The effects of aging was investigated by rerecording the PL spectrum from the unetched face after ~ 10 weeks. All the PL measurements, except in the case of the aged sample, were performed immediately after the chemical treatment and sample refrigeration.

RESULTS

The PL spectra measured in the range of 1.55 to 1.61 eV from a set of four cleaved and $\text{Br}_2/\text{CH}_3\text{OH}$ etched samples are presented in Fig. 1. The spectral intensities displayed in the figure were normalized to the integrated intensity in the near edge region in order to account for overall changes due to modifications of the near surface electronic properties such as the electric field and the surface recombination velocity as well as slight unavoidable changes in the measurement conditions. The spectra display

several sharp and distinct features that are usual for good quality CdTe. Shoulders, weak features, and subtle sidebands on some of the peaks are also observable. The expected position of the band edge [6] (E_g) is indicated at 1.605 eV as is the location of the free exciton [6,7] (FE) recombination at 1.597 eV. The peaks are labeled D_μ at 1.5930 eV; A_0-X at 1.5896 eV; I_1 at 1.5850 eV; I_2 at 1.581 eV; and I_1, I_2-LO at 1.564-1.56 eV; the nomenclature will be discussed in the following section.

Fig. 1: The near edge PL spectra from the Br_2/CH_3OH samples and a reference unetched sample are shown. The etched spectra are magnified by a factor 2.5 for clarity. The etch concentration is indicated on the high energy end of the curves. Note the overall increase in the A_0-X feature with etch concentration.

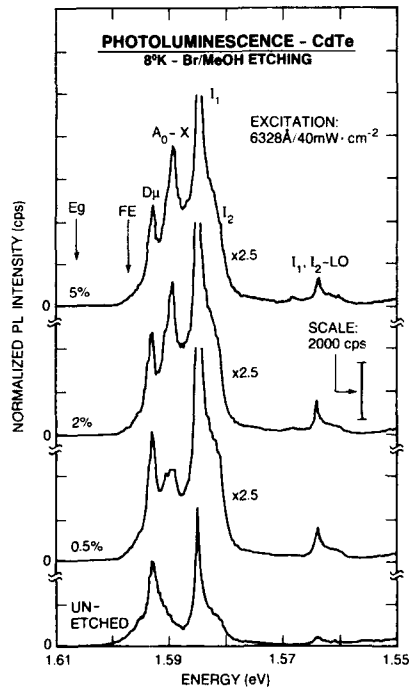


Fig 1.

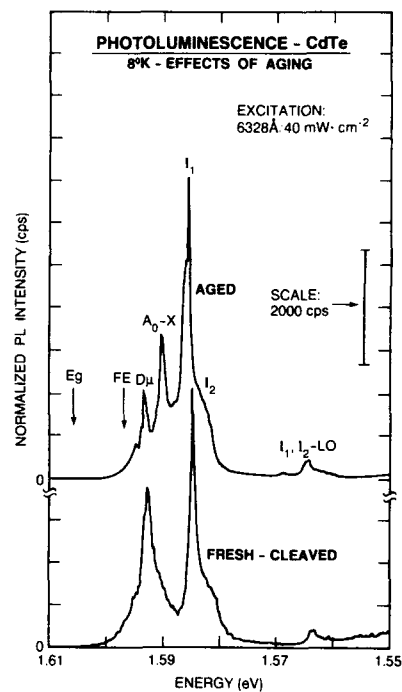


Fig. 2

Fig. 2: PL spectra measured from a fresh cleaved and an aged surface are presented. The presence of the intense A_0-X feature in the aged surface is indicative of Cd vacancies in the surface region.

The spectra measured from the freshly cleaved surface and the aged sample are presented in Fig. 2. As in Fig. 1, E_g , FE,

D_{μ} , A_0-X , I_1 , I_2 and I_1, I_2-LO are indicated. A discussion of the spectra follows.

The spectra observed from samples that were subjected to both the Br_2/CH_3OH and the KOH/CH_3OH treatments were qualitatively similar to those presented in Fig. 1, i.e., no significant change was introduced by the KOH/CH_3OH in either the A_0-X feature or the overall spectrum.

DISCUSSION

Chemical Etching

It is clear from the spectra displayed in Fig. 1 that the dominant effect of etching is the introduction of a distinct feature with the peak energy at 1.5896 eV; a weak shoulder is discernible on the high energy side of the peak for the 2 and 5% etched samples. The 1.5896 eV peak has been observed by several investigators in the past [1,3-5,8-10]; it is the most dominant feature in the PL spectrum of Bridgman grown, undoped, bulk CdTe [4,10]. Previous investigators have demonstrated that its intensity reduces substantially when the as-grown, undoped crystals are annealed in Cd vapor [4,10] and is correlated with Cd vacancies produced using electron irradiation [3,5]. Hence, it has been assigned to originate in a defect involving a Cd vacancy: namely a simple Cd vacancy that acts as a doubly ionizable acceptor [5], $[V_{Cd}^{2-}]$, or a complex defect made up of a vacancy and a donor [4], i.e., $[V_{Cd}^{2-}, D^+]$. The annihilation of an exciton bound to a neutral state of the acceptor described above is responsible for the feature denoted by A_0-X . On this basis, the occurrence of the 1.5896 eV feature is interpreted as arising from the introduction of Cd vacancies in the chemically etched surface region. It is also apparent from the spectra shown in Fig. 1 that the normalized intensity of the A_0-X peak increases with the concentration of the etching solution pointing to an etch related origin.

Previous studies have indicated a severe loss of Cd from the surface region of CdTe etched in Br_2/CH_3OH [14-16]. Ellipsometric [15] and Raman scattering [14] measurements have indicated the presence of a $\sim 10\text{\AA}$ thick Te layer. It has been reported that the Te overlayer can be stripped using a 1N KOH/CH_3OH surface treatment. The effect of the 1N KOH/CH_3OH treatment was investigated and found not to alter the PL spectrum in any appreciable fashion. In addition, the spectra observed from the etched surfaces imply only a small perturbation, i.e., the spectra are indicative of nearly stoichiometric CdTe with the change in the Cd to Te ratio of $< 1\%$. The apparent contradiction can be understood if one considers the depth sensitivity for the various techniques. The observed PL spectral intensity arises from a region extending from the surface to a depth of $> 2000\text{\AA}$ which is much larger than that of XPS ($< 25\text{\AA}$) and the sensitivity for ellipsometry ($< 2\text{\AA}$). Both observations may be explained on the basis of a qualitative model that allows for a severely Cd depleted region near the surface as well as a deeper region where the depletion is less intense. The expected modifications of the electronic properties of the deeper region and its implications for device applications are considered in the next section.

The peak denoted by D_{μ} at 1.593 eV has been investigated by Feng et al [7] and assigned to originate from a structural defect or impurity-defect complex. The peak denoted by I_1 at 1.5850 eV

is due to an In impurity [5,11]. The I_2 feature at 1.581 eV probably also originates in an In related electronic defect. The longitudinal optical (LO) phonon replicas of I_1 and I_2 are indicated by I_1, I_2 -LO.

Effects of Aging

The PL spectrum measured from a sample that was stored under atmospheric conditions for ~ 10 weeks is displayed in Fig. 2. For comparison, the spectrum obtained from the freshly cleaved face is also shown. The A_0 -X peak at 1.5896 eV is clearly evident in the aged surface.

The presence of the A_0 -X peak strongly suggests the loss of Cd from the near surface region from the aged face. Reaction with the atmospheric oxygen [17] as well as an inherent surface reactivity and/or instability may be responsible for the formation of Cd vacancies. It has been reported that anodic oxidation followed by electrochemical etching leads to an enhancement of the A_0 -X feature [13].

A comparison of the A_0 -X peak line shapes from the aged surface and the Br_2/CH_3OH etched surfaces brings out a subtle difference: the former contains no shoulder and is therefore much narrower, whereas the chemically etched face clearly indicates an additional contribution. This may signify the differences in the centers created by the two processes, indicating perhaps the occurrence of complex defects involving $[V_{Cd}^{2-}]$ and Br under Br_2/CH_3OH treatment as opposed to $[V_{Cd}^{2-}]$ during aging.

Implications for Device Fabrication

The tendency of bulk CdTe to form $[V_{Cd}^{2-}]$ in the surface region as a result of chemical treatment as well as aging has significant consequences in the device fabrication area. The foremost of these is the formation of metallic contacts with controlled physical properties. The formation of a large density of $[V_{Cd}^{2-}]$, a known acceptor, will modify the electronic properties and may dominate the surface electrical properties. For instance, the fabrication of a simple Schottky barrier on an etched n-type CdTe may be impossible if a thin p-type layer, resulting from the Cd vacancies, were present near surface region. Devices that use exposed CdTe are likely to degrade in electrical performance due to modifications introduced as a result of the formation of $[V_{Cd}^{2-}]$. The former may be corrected by a suitable annealing step whereas the latter would require the use of proper encapsulation.

CONCLUSION

In conclusion, the perturbation caused as a result of Br_2/CH_3OH etching have been investigated. A sample aged under atmospheric conditions was also studied to determine the long term stability of CdTe. The reference for all the measurements was the PL spectrum obtained from a sample cleaved in an inert atmosphere. The results demonstrate the introduction of a strong feature at 1.5896 eV as a result of the chemical treatment as well as aging. On the basis of previous analysis that has identified the peak to be caused by Cd vacancies, it is strongly

suggested that Cd vacancies are formed in the near surface region. The implications of these results are two fold: The presence of the 1.5896 eV excitonic peak in the PL spectrum may be just a consequence of the surface preparation and not any intrinsic chemical or electronic property of the sample; the conclusions of all previous studies that relied on this PL feature and used chemically treated samples may have to be reevaluated. Next, the formation of Cd vacancies may interfere with the fabrication of devices and have a deleterious consequence on the long term stability of those that contain exposed surfaces.

ACKNOWLEDGEMENT

The authors wish to acknowledge Mr. Philip R. Boyd of the U.S. Army Center for Night Vision and Electro-Optics for helpful discussions.

REFERENCES

1. E. Molva, J.L. Pautrat, K. Saminadayar, G. Milchberg and N. Magnea, Phys. Rev. B 30, 3344 (1984).
2. J.L. Pautrat, J.M. Francou, N. Magnea, E. Molva and K. Saminadayar, J. Crystal Growth 72, 194 (1985).
3. F.J. Bryant and D.H.J. Totterdell, Radiation Effects 9, 115 (1971).
4. S. Seto, A. Tanaka, Y. Masa, S. Dairaku and M. Kawashima, Appl. Phys. Lett. 53, 1524 (1928).
5. C.E. Barnes and K. Zanio, J. Appl. Phys. 46, 3659 (1975).
6. R. Triboulet and Y. Marfaing, J. Electrochem. Soc. 120, 1260 (1973).
7. Z.C. Feng, M.G. Burke and W.J. Choyke, Appl. Phys. Lett. 53, 128 (1988).
8. K.M. James, J.D. Flood, J.L. Merz, and C.E. Jones, J. Appl. Phys. 59, 3596 (1986).
9. J.P. Laurenti, G. Bastide, M. Rouzeyre and R. Triboulet, Solid State Commun. 67, 1127 (1988).
10. D.E. Cooper, J. Bajaj and P.R. Newman, J. Crystal Growth 86, 544 (1988).
11. N.C. Giles, R.N. Bicknell and J.F. Schetzina, J. Vac. Sci. Technol. A 5, 3064 (1987).
12. Z.C. Feng, A. Mascarenhas and W.J. Choyke, J. Luminescence 35, 329 (1986).
13. J.M. Figueroa, F. Sanchez-Sinencio, J.G. Mendoza-Alvarez, O. Zelaya, C. Vazquez-Lopez and J.S. Helman, J. Appl. Phys. 60, 452 (1986).
14. P.M. Amirtharaj and F.H. Pollak, Appl. Phys. Lett. 45, 789 (1984).
15. D.E. Aspnes and H. Arwin, J. Vac. Sci. and Technol A 2, 1309 (1984).
16. J.P. Haring, J.G. Werthen and R.H. Bube, J. Vac. Sci. Technol. A 1, 1469 (1983).
17. F. Wang, A. Schwartzman, A.L. Fahrenbruch, R. Sinclair, R.H. Bube and C.M. Stahle, J. Appl. Phys. 62, 1469 (1987).

ANNEALING BEHAVIOR OF THE PHOTOLUMINESCENCE LINES IN CdTe AND
 $\text{Zn}_x\text{Cd}_{1-x}\text{Te}$ SINGLE CRYSTALS

J. GONZALEZ-HERNANDEZ*, A. REYES-MENA*, ELIAS LOPEZ-CRUZ⁺, D.D. ALLRED[#]
 AND WORTH P. ALLRED[&]

*Departamento de Física, Centro de Investigación y de Estudios Avanzados del IPN, Apdo. Postal 14-740, 07000 México, D. F.

+Departamento de Física del Instituto de Ciencias, Universidad Autónoma de Puebla, Apdo. Postal J-48, Puebla 72570, Pue. México.

[#]Physics and Astronomy Department, Brigham Young University, Provo, UT.
[&]Galtech Semiconductor Materials Corp., Mt. Pleasant, UT.

ABSTRACT

The main lines in the photoluminescence spectra of $\text{Zn}_x\text{Cd}_{1-x}\text{Te}$ single crystals grown by a modified Bridgman method in the compositional range of $0 \leq x \leq 0.25$ have been identified. All crystals show only near-band-edge emission. To assist in the identification, various samples with different compositions were annealed under a Cd atmosphere. In the pure crystals, the prominent (A^0, X) bound exciton line, as well as the doublet at longer wavelengths, disappear after the annealing. In contrast, the treatments do not change significantly the PL spectra of the mixed crystals.

INTRODUCTION

Large area cadmium telluride (CdTe) and zinc cadmium telluride ($\text{Zn}_x\text{Cd}_{1-x}\text{Te}$) single crystal substrates have many potential applications in the fabrication of electronic and optoelectronic devices [1]. Interest in this wide-gap material has also developed due to its chemical compatibility and close lattice match to the important infrared detector material HgCdTe. However, the understanding of the native defects and their complex with residual impurities is important in order to have a better control of both their optical and electrical properties. In the last few years numerous studies on the photoluminescent (PL) properties of CdTe crystals have been reported [2-5] and only few on $\text{Zn}_x\text{Cd}_{1-x}\text{Te}$ [6-8].

In the present paper we report on the PL from as-prepared and Cd vapor annealed $\text{Zn}_x\text{Cd}_{1-x}\text{Te}$ ($0 \leq x \leq 0.25$) single crystals. For all the investigated values of x , the prominent emission lines occur in the exciton region indicating a high crystalline quality. In pure CdTe crystals, the 15K PL spectra exhibit two main lines in this region at 778.2 nm (1.5934eV) and 779.5 nm (1.5907eV). The former line occurs in the energy range where recombination of excitons bound to shallow neutral donors (D^0, X) has been reported [9]. Our studies on annealed CdTe samples under Cd atmosphere indicate that the 1.5907 eV line is related with recombination of excitons bound to cadmium vacancies [5]. We also observed that in the mixed crystals exciton recombination mainly occurs via neutral donor states.

EXPERIMENTAL

All samples were grown from the melt by a modified Bridgman method at Galtech Semiconductor Materials Corporation. The composition of the $\text{Zn}_x\text{Cd}_{1-x}\text{Te}$ samples was determined from electron microprobe analysis and from the energy of the main exciton line observed in the 15K PL spectra [6]. All as-prepared crystals were unintentionally doped and have an appro-

ximate room-temperature resistivity of 5×10^6 and $8 \times 10^8 \Omega \text{ cm}$ for the mixed and pure crystals, respectively. All spectra in the as-prepared samples were taken on (110) cleaved surfaces at 15K. The laser power, from an argon ion laser, impinging on the sample was of 0.5 mW with the laser beam focused using cylindrical optics. The PL emission was spectrally analyzed with a double monochromator, with slits set to achieve a resolution of less than 1Å.

Annealing was carried out in a sealed quartz ampoule under Cd saturated isothermal conditions at 600°C for two hours. Before the PL was measured all annealed samples were chemically etched to remove the surface damage. The chemical treatment was as follows: immersion in a 1% bromine in methanol solution for 30 seconds followed by a 60 seconds immersion in a solution of 3.5M KOH in 1 liter of H_2O .

RESULTS AND DISCUSSION

Figure 1 shows typical 15K PL spectra for three as-prepared $\text{Zn}_x\text{Cd}_{1-x}\text{Te}$ cleaved surfaces with $x=0, 0.10$ and 0.25 . All three spectra are plotted with the same abscissa. Considering the origin of the emission lines, the PL spectra in the figure can be divided into three regions: a) the exciton region, for wavelengths near the band-gap; b) the free to bound (F-A) and bound to bound (D-A) transitions, for intermediate λ 's and, c) emission at longer λ 's associated with crystal imperfections and deeper impurity levels [6,10]. This latter emission generally appears in the PL spectra as a broad band at approximately 50 to 100 nm above the exciton lines. Notice that none of the three spectra in Fig. 1 shows any significant emission in this latter region, which is an indication of high crystalline quality.

The identification of the emission lines in the intermediate region, as due to electron-acceptor and donor-acceptor transitions has been reported in a previous study [11].

In the exciton region, free exciton recombination results in the emission of photons with an energy 10.5 meV less than the band gap, which, at 15K is at 772 nm (1.606 eV), 743.5 nm (1.668 eV) and 695.9 nm (1.7819 eV) for $x=0, 0.10$ and 0.25 , respectively. This line is denoted by (X) $n=1$ in the figure. The existence of several different donors and acceptors in CdTe has already been pointed out [12]. Free excitons can get trapped by the potential of the impurities becoming bound excitons. The two main lines in the exciton region of our pure CdTe crystals at 778.2 nm (1.5934 eV) and at 779.5 nm (1.5907 eV) have been identified as due to the recombination of excitons bound to shallow neutral donors (D^0, X) [9] and to neutral acceptor (A^0, X) states, respectively.

The identification of the 1.5907 eV line as due to a (A^0, X) process is based on the changes observed in the PL spectra induced by the annealing under Cd atmosphere, which are shown in Fig. 2. The complete PL spectra as well as the resolved exciton regions are shown for as-prepared (a) and for annealed (b) samples. As can be seen, two drastic changes occur upon annealing: one is that the lines in the range of 790-800 nm denoted by (F-A) and (D-A) have been drastically reduced and the other is the disappearance of the (A^0, X) line. The broader bands found at 790-800 nm are generally accepted to involve deep acceptorlike levels associated with a complex center [3], and more recently their origin has been related with cadmium vacancies [13]. In a recent publication Seto et al [5] have seen that, under similar annealing conditions, the intensity of a bound exciton

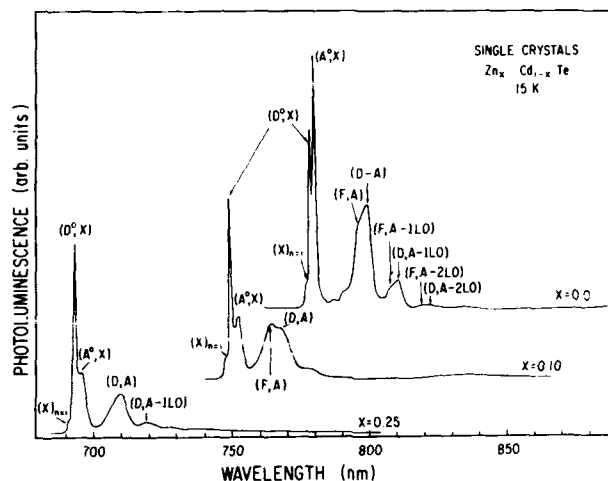


Fig. 1. Photoluminescence spectra of $\text{Zn}_x\text{Cd}_{1-x}\text{Te}$ single crystals with $x=0$, 0.10 and 0.25. Details on the assignments and identification of various lines can be found in the text.

line at 1.5896 eV in their 4.2K PL spectra of high quality p-type CdTe is drastically reduced after the annealing; their results strongly suggest that this line can be ascribed to the recombination of excitons trapped at Cd vacancies. Our results in annealed CdTe crystals under a Cd atmosphere provide further evidence for the previously proposed assignments for the PL bands in the region of 790–800 nm as well as for the origin of the (A^0, X) line at 1.5907 eV. The identification of the 1.5907 eV line is also consistent with its temperature dependence because the PL intensity of acceptor-bound excitons decreases very rapidly with increasing temperature [11].

Figure 3 shows the PL spectra of an as-prepared (a) and Cd vapor annealed (b) $\text{Zn}_x\text{Cd}_{1-x}\text{Te}$ with $x=0.09$. Similar to the pure CdTe crystals, the PL spectra of the as-prepared mixed crystals show a dominant near-band-edge emission. In the exciton region the line at 753.2 nm (1.6463 eV) has the same exciton binding energy of 2 meV as the line labeled with (D^0, X) in the PL spectra of pure CdTe, lending evidence that this feature is due to the same transition in both cases. The line at 756 nm (1.6402 eV) has been identified with a (A^0, X) transition based on a variety of evidence. In the first place, the exciton binding energy of 7.5 meV is close to the calculated binding energy of excitons bound to acceptors of 7 meV [14]. In the second place, this line is thermally quenched at temperatures exceeding 50K. This assignment is also in agreement with previous observations in other alloyed compound semiconductors showing that the (A^0, X) lines are much more sensitive to alloying and that the linewidth increases at a rate much greater than that of the (D, X) levels [15]. We have observed that in the exciton region, the PL spectra of the mixed crystals look very similar regardless of x in the range investigated.

The result of the annealing under Cd atmosphere for $\text{Zn}_x\text{Cd}_{1-x}\text{Te}$ crystals is quite different than that observed in the pure crystals. In the

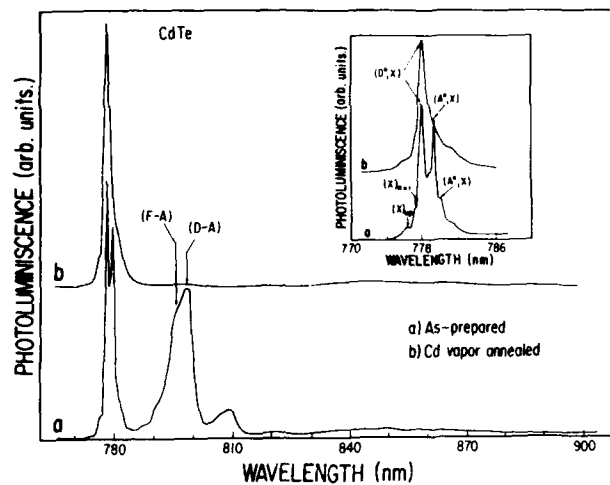


Fig. 2. Photoluminescence spectra of a CdTe single crystal, before (a) and after (b) annealing at 600C/2hrs. in a saturated Cd vapor atmosphere. The insert shows the resolved exciton region.

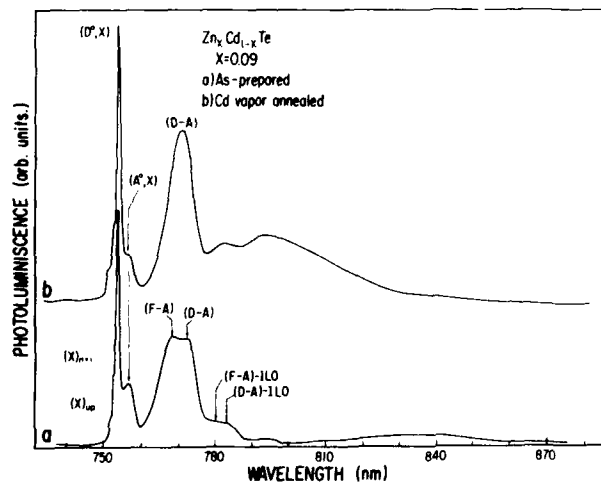


Fig. 3. Photoluminescence spectra of as-prepared (a) and Cd vapor annealed (b) $\text{Zn}_x\text{Cd}_{1-x}\text{Te}$ single crystals with $x=0.09$.

mixed crystal a small decrease in the amplitude of the (A^0, X) line and a change in the shape of the broader emission line located at about 20-30 nm above the exciton range are observed. Before annealing the well defined doublet labeled as (F-A) and (D-A) becomes a single line with a position at 769.5 nm (1.6114 eV) in between the (F-A) and (D-A) doublet. From the dependence on temperature and excitation intensity we have identified this line with a (D-A) transition. We have also observed that as a result of Cd annealing a new broad emission band appears at about 795 nm (1.5597 eV) probably originated at deeper defect levels created during the thermal annealing, however, further studies are needed in order to have a better understanding about the origin of this band.

Based on the annealing behavior of the PL spectra of CdTe and $Zn_xCd_{1-x}Te$ crystals, one can conclude that, in contrast to pure CdTe, the free to bound, the bound to bound and the (A^0, X) bands in the mixed crystals are probably not related with recombination involving cadmium vacancy levels. These results provides further support for the observation that Zn addition to CdTe improves crystal quality [16,17], particularly reducing the density of group II (Cd or Zn) vacancies.

CONCLUSIONS

The photoluminescent properties of $Zn_xCd_{1-x}Te$ single crystals for $0 \leq x \leq 0.25$ have been studied. To assist in the identification of the lines in the spectra, as-prepared and annealed (under Cd atmosphere) samples were measured. In all crystals, the dominant emission occurs at the near-band-edge region, indicating good crystalline quality. In the pure crystal, the two main exciton lines are identified with recombination of excitons at neutral shallow donors (778.2 nm) and at neutral donors (779.5 nm). The assignment of the latter line was deduced from its annealing behavior under a saturated Cd atmosphere. We also observed that the doublet in the wavelength range of 790-800 nm disappears after the annealing, which indicates that the levels involved in that transition are also related to cadmium vacancies.

In the as-prepared mixed crystals, we observed that the PL spectra is qualitatively similar regardless of the values of x . By analogy with the pure crystal, the main exciton line is identified with a (D^0, X) transition and a weak (A^0, X) line is also observed. From the observed changes in the PL spectra of Cd annealed mixed crystals, we concluded that the main lines in the spectra are not related with transitions involving Cd vacancies.

REFERENCES

1. K.Zanio, in Semiconductors and Semimetals, edited R.K. Willardson and A.C. Beer (Academic, N.Y. 1978), Vol.13.
2. J.L.Pautrat, J.M.Francou, N.Magnea, E.Molva and K.Saminadayar, J. of Cryst. Growth, 72,194(1985).
3. N.C.Giles-Taylor, R.N.Bicknell, D.K.Blanks, T.H.Myers and J.F.Schetzina, J. Vac. Sci. Technol. A3,76(1985).
4. J.P.Laurenti, G.Bastide, M.Rouzeyre and R.Triboulet, Sol. State Comm., 67,1127(1988).

5. S.Seto, A. Tanaka, Y.Masa, S.Dairaku and M.Kawashima, Appl. Phys. Lett., 53,1524(1989).
6. D.J.Olego, J.P.Faurie, S.Sivanathan and P.M.Raccah, Appl. Phys. Lett., 47,1172(1985).
7. E.Cohen, R.A.Street and A.Muranevich, Phys. Rev. 828,7115(1983).
8. J.H.Dinan and S.B.Qadri, J. Vac. Sci. Technol. A3,851(1985).
9. J.L.Pautrat, J.M.Francou, N.Magnea, E.Molva and K.Saminadayar, J. of Cryst. Growth, 72,194(1985).
10. V.N.Babentsov, S.I.Gorban, E.A.Salkov and N.I.Torbaev, Sov. Phys. Semicond., 21,1043(1987).
11. J.González-Hernández, E.López-Cruz, D.D.Allred and W.P.Allred, submitted to J. of Vac. Sci. and Technol. (1989).
12. P.A.Simmonds, R.A.Stradling, J.R.Birch and C.C.Bradley, Phys. Status Solidi (b) 64,195(1974).
13. J.M.Figueroa, F.Sánchez-Sinencio, J.G.Mendoza-Alvarez, O.Zelaya, C.Vázquez-López and J.S.Helman, J. Appl. Phys. 60,452(1986).
14. R.E.Halsted and M.Aven, Phys. Rev. Lett., 14,64(1965).
15. C.Mikkelsen and J.B.Boyce, Phys. Rev. Lett., 49,1412(1982).
16. S.L.Bell and S.Sen, J. Vac. Sci. Technol., A3,112(1985).
17. A.Sher, A.B.Chen, W.E.Spicer and C.K.Shih, J. Vac. Sci. Technol., A3,105(1985).

NONDESTRUCTIVE COMPOSITIONAL AND DEFECT CHARACTERIZATION OF CdZnTe ALLOYS USING PHOTOLUMINESCENCE SPECTROSCOPY

W.M. DUNCAN, R.J. KOESTNER, J.H. TREGILGAS, H.-Y. LIU and M.-C. CHEN
Central Research Laboratories, Texas Instruments, Inc., Dallas, TX 75265

ABSTRACT

Results from high resolution helium temperature photoluminescence (PL) spectroscopy have been correlated to precision lattice constant and transport measurements and to theoretical band gap versus composition behavior. It is found that low temperature PL spectra provide precise determination ($\pm 0.02\%$) of ZnTe mole fraction as well as carrier type, relative impurity concentration and point defect properties of these substrates. In addition helium and room temperature PL results are correlated to determine the accuracy of room temperature measurements for composition determination.

INTRODUCTION

Alloys of CdZnTe are important substrate materials for growth of epitaxial thin films of HgCdTe for infrared detector and focal plane array applications. In order to attain thin films of high crystalline quality, it is known that close lattice match is needed between the film and substrate. For matching to nominally $10 \mu\text{m}$ HgCdTe, substrates of CdZnTe alloys containing a few percent of ZnTe are needed. Although photoluminescence has been used widely for evaluation of II-VI binary materials [1] only more recently has CdZnTe films [2,3] and bulk crystals been studied [4]. In the current work the photoluminescence optical properties of a large sampling of CdZnTe ingots with ZnTe fractions of 0 to about 8% been studied and correlated to electrical and precision X-ray lattice constant measurements.

EXPERIMENTAL

The crystals of CdZnTe studied in this work were prepared in sealed ampoules by the horizontal Bridgman method. Stoichiometric melt charges were precompounded from the elements. Unseeded crystals 3-4 kg in mass were grown. Etch pit counts range from 5×10^4 to $2 \times 10^5 \text{ cm}^{-2}$ in these crystals. Unoriented samples were rough cut from the boules, chemomechanically polished and etched in Br/methanol prior to study. Samples typically were taken at 3 inch intervals along the 15 inch boules.

Precision lattice parameter measurements were made using a Siemens D-500 powder diffractometer. Silicon was used as an internal standard. Compositions were calculated based on the JCPDS [5] lattice constants for pure ZnTe (6.1026 \AA) and CdTe (6.4810 \AA).

Photoluminescence measurements were made at room temperature and at 4.2 K with samples immersed in liquid helium. Although different spectrometers were used for analyzing the emission at room and helium temperatures, nearly identical excitation conditions and backscattering sampling geometries were used for both cases. Samples were excited using 5145 \AA argon ion radiation at a power density of approximately 0.2 W/cm^2 (6mW). The room temperature emission was analyzed with a conventional scanning dispersive monochromator and cooled GaAs photocathode photomultiplier whereas the low temperature spectra were analyzed interferometrically [6] using a Michelson interferometer and 77 K Ge pin diode detector. For room temperature measurements, a spectral

resolution of 0.8 meV was used with a spectral sampling interval of 0.2 meV. At helium temperature resolution and sampling intervals were 0.2 and 0.1 meV, respectively.

DISCUSSION

Results discussed in the following are representative of the trends observed for about 15 boules. Shown in Fig. 1 is a 4.2 K PL spectra of a compensated CdZnTe sample illustrating the dominant near band gap spectral features. The 13,000 to 13,200 cm^{-1} (1.612 - 1.636 eV) region of the spectrum is dominated by recombination of excitons. Because the band gap of this material is a function of alloy composition, the identification of these excitonic transitions must be derived a priori. In CdTe, the neutral acceptor bound exciton ($A^\circ X$) transition occurs at 16 meV from the band edge and the neutral donor bound exciton ($D^\circ X$) transition occurs at 12 meV from the edge [1]. The excitonic feature observed at 1.6169 eV (13,043 cm^{-1}) in Fig. 1 is observed to dominant in p-type material and the feature at 1.6210 eV (13,076 cm^{-1}) is dominate in n-type material. Hence due the relative position and 4 meV spacing of these two strong features and the correlation of features with carrier type, the line at 1.6169 eV is identified as the neutral acceptor bound exciton ($A^\circ X$) and the line at 1.6210 eV as the the neutral donor bound exciton ($D^\circ X$). It should also be noted that as in CdTe, the $A^\circ X$ is strongly vibronically coupled in CdZnTe, with an $A^\circ X$ -LO replica occurring at 21 meV below the $A^\circ X$ feature. All of the samples studied exhibited the same quartet of no phonon exciton lines with spacings equal to those observed in Fig 1. Based on the identification of the $A^\circ X$ feature and the $A^\circ X$ binding energy of 16 meV, a band gap of 1.6329 eV can be calculated for the sample in Fig 1. The binding energies of the two weak excitonic features X at 1.6231 eV (13093 cm^{-1}) and X_2 at 1.6252 eV (13110 cm^{-1}) in Fig. 1, are then calculated as 9.8 meV and 7.7 meV, respectively. From these binding energies, the feature labeled X is assigned to the free exciton. The feature labeled X_2 has not been conclusively identified but is likely due to $n=2$ exciton transitions.

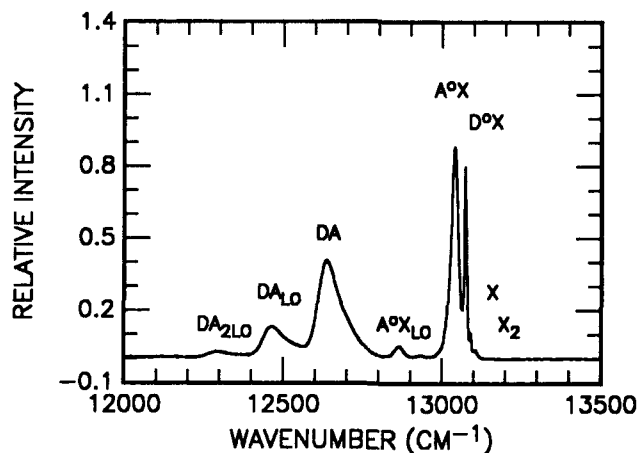


Figure 1: Near band gap PL spectrum at 4.2 K of a compensated CdZnTe sample.

As shown in Fig. 1, donor-to-acceptor (D-A) transitions are also evident in the spectra of these samples. Based on the band gap calculated from the position of the A^0X transition, the no phonon D-A transition occurs at 66 meV from the band edge. The D-A center also exhibits strong vibronic coupling with 1LO and 2LO replicas clearly visible spaced by 21 meV. At the excitation intensities employed (0.2 W/cm^2), the D-A bands exhibit asymmetric lineshapes, rising steeply on the low energy side and more gradually to high energy. Although an asymmetric lineshape is suggestive of a free-electron-to-acceptor (F-A) transition, power dependence studies clearly demonstrate that these bands shift to higher energy with increasing excitation intensity, demonstrating that they are in fact due to D-A transitions. The broadening on the high energy side of these bands results from the presence of the unresolved F-A transition.

Low temperature photoluminescence also yields information about the optically active point defect centers in these CdZnTe samples. In some of the boules studied, a deep center is observed at 1.1 eV. Whereas the atomistic identity of this center is uncertain, we observe that the 1.1 eV center is associated with either high initial ZnTe mole fraction or high Te precipitate concentration. Boules exhibiting the 1.1 eV center have lower PL quantum yields at room and helium temperature than boules free of this center. The intensity of the 1.1 eV center remains nearly constant along the boule length when observed. Also in the tail most sample of many of these boules, a band at 1.4 eV is observed. This band in CdTe, described as the metal vacancy donor center, V_M-D , has been studied in detail [1].

Perhaps the most important correlation established in this work is that between the band gap from low temperature PL and the precision lattice constant. Shown in Figure 2 is the measured 4.2 K PL band gap versus composition determined from the X-ray powder diffraction pattern.

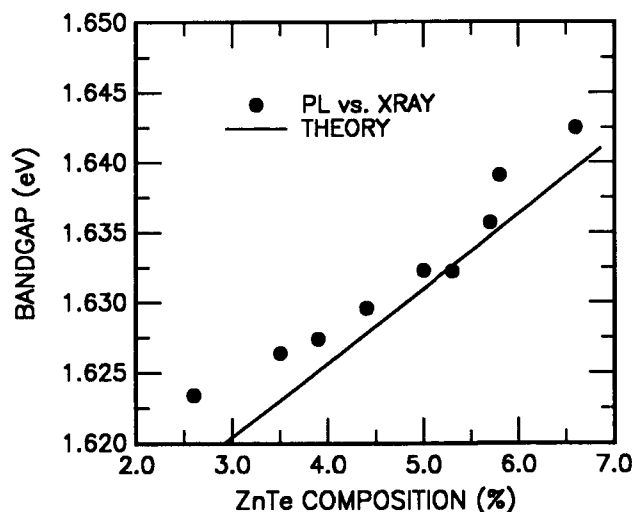


Figure 2: PL band gap versus composition determined from X-ray powder diffraction.

The CdZnTe band gap is calculated from the low temperature PL based on the identification of the A^oX feature in the spectrum and the 16 meV A^oX binding energy. The solid line is the band gap versus composition relationships of Magnea, et al. [3]. The uncertainty in lattice constant as determined from X-ray translates to an uncertainty of $\pm 0.2\%$ in ZnTe mole fraction. The uncertainty in low temperature PL is that of the 0.1 meV sampling interval. From the sampling interval and the band gap to composition relationship of Magnea et al., [3] an uncertainty of $\pm 0.02\%$ in ZnTe mole fraction can be determined. Hence the scatter in the experimental data in Fig. 2 is expected to be limited by the X-ray measurements and by the uniformity of the samples. In addition to scatter in the experimental data in Fig 2, there appears to be a systematic offset between the present experimental data and the calculated behavior from [3]. It should be noted that the band gap to composition relationship determined in reference [3] was determined from a comparison of the 4.2 K band gap calculated from the LO phonon replica of the free exciton in photoluminescence and composition determined from X-ray fluorescence.

The compositional dependence of these boules versus sample position was also examined and is presented in Fig. 3. Compositions were determined as described above from the position of the A^oX band and the relationship of Magnea, et al. [3]. The initial concentration in these boules agrees well with the initial charge composition. The decrease in ZnTe composition with sample position is also expected from consideration of melt segregation.

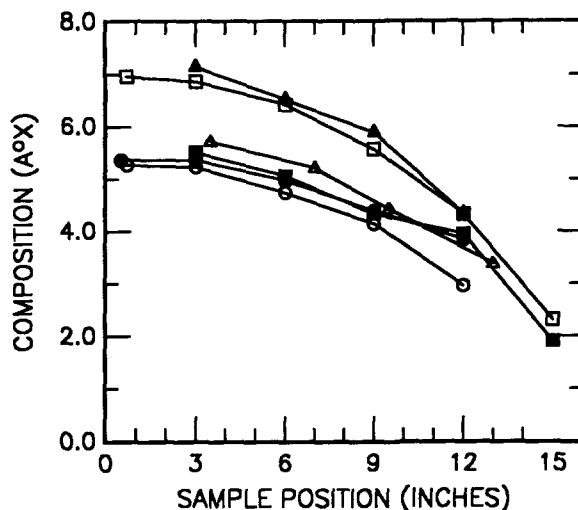


Figure 3: Composition determined from A^oX peak energy versus sample position.

One of the goals of this work has been to evaluate the potential of room temperature PL measurements for the evaluation of CdZnTe composition. Shown in Fig. 4 is a representative room temperature CdZnTe PL spectra. The band exhibits an asymmetric lineshape, rising steeply on the low energy side and more gradually on the high energy side.

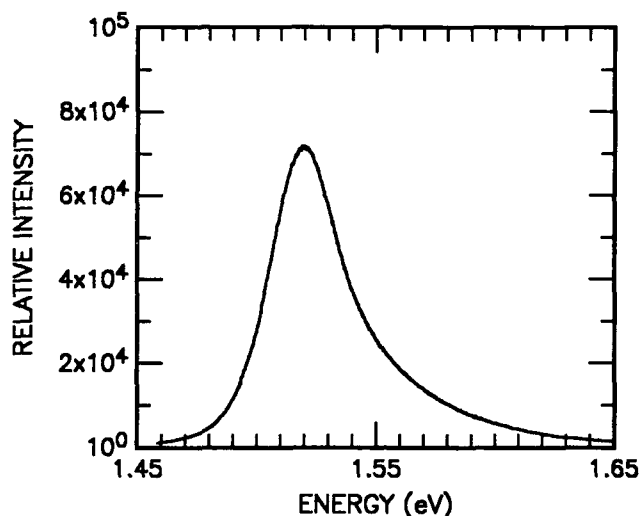


Figure 4: Room temperature PL spectrum of a CdZnTe sample.

Room temperature peak energies were determined using a parabolic fit of the band. The recombination energy, $h\nu$, at room temperature is given by, $h\nu = E_g + kT$, where E_g is the band gap of the material, k is Boltzman's constant, and T the electron temperature in Kelvin. Presented in Fig. 5 is the relationship between room temperature peak energy and the A^oX band position at 4.2 K. It should be noted that the scatter in the data is much larger than the uncertainty in the low temperature (0.1 meV) or the room temperature energy measurement (0.8 meV). Because the electron temperature is expected to contribute primarily to the high energy side of the room temperature band, we also evaluated the data using the energy at half height on the low energy side of the band. However a nearly constant difference was found between the energy at the peak maximum and the energy at the low energy half height, indicating that the scatter in the data in Fig. 5 is not due to variations in electron temperature. It was found, however, that the samples falling to the lower right in the distribution are n-type samples whereas the samples falling to the upper left are p-type samples. Because of the relative large activation energy of acceptors in CdZnTe (58 meV or greater), the acceptors are partially neutral at room temperature. Hence the recombination energy at room temperature is likely modified by the population of neutral acceptors. Stated differently, the peak energy at room temperature is dependent on both the composition of the material and the position of the Fermi energy.

CONCLUSIONS

In this work, photoluminescence spectroscopy has been shown to be a powerful method for nondestructive contactless determination of impurity, defect and compositional properties of CdZnTe alloys. Compositional measurements based on low temperature PL are shown to have an accuracy of (+/- 0.02%) in ZnTe mole fraction based on the identification of the A^oX transition. CdZnTe boules are also found to be of high quality as indicated by the dominance of excitonic recombination and the general absence of optically

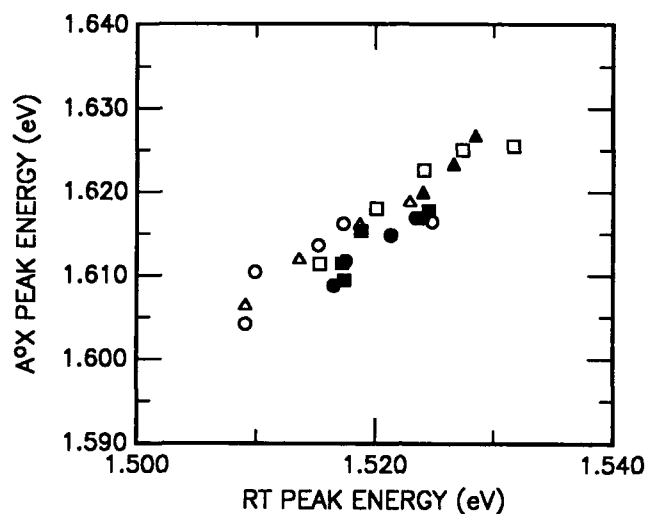


Figure 5: Relationship between room temperature peak energy and A°X peak position.

active point defects in 4.2 K photoluminescence. Compositional measurements using room temperature PL are shown less accurate than low temperature measurements due to contributions of the Fermi energy to the measured band position.

REFERENCES

1. J.L. Pautrat, J.M. Francou, N.Magnea, E.Molva and K.Saminadayar, *J. Crystal Growth* **72**, 194(1985) and references therein.
2. D.J. Olego, J.P. Faurie, S Sivananthan, and P.M. Racciah, *Appl. Phys. Lett.* **47**, 1172(1985).
3. N. Magnea, F. Dal'bo, J.L. Pautrat, A.Million, L. Dicioccio and G. Feuillet, *Mat. Res. Soc. Symp. Proc.* **90**, 455(1987).
4. K.Y. Lay, N.C. Giles-Taylor, J.F. Schetzina and K.J. Bachmann, *J. Electrochem. Soc.* **133**, 1049(1986).
5. Joint Committee of Powder Diffraction Standards, Swarthsmore, PA. ZnTe file 15-746 and CdTe file 15-770.
6. W.M. Duncan and M.L. Eastwood, in *Proceedings of the International Conference on Raman and Luminescence Spectroscopy in Technology*, J.E. Griffiths and F. Adar, editors, *Proc. of SPIE*, **822**, 172(1987).

ION-IMPLANTATION GETTERING OF IMPURITIES IN CdTe

M. H. Jin, K. M. James, C. E. Jones¹ and J. L. Merz
Department of Electrical and Computer Engineering, University of California, Santa Barbara, CA 93106

ABSTRACT

This is the first reported use of ion-implantation damage gettering of impurities in CdTe to provide high-quality substrates for the epitaxial growth of appropriate binary or ternary compounds, or for related applications. We describe the results of photoluminescence (PL) measurements performed on samples of Bridgman-grown CdTe to study both the annealing behavior and gettering effects in this material. From the PL results, it was found that impurity gettering occurs at temperatures at which liquid phase epitaxy takes place ($\sim 500^\circ\text{C}$) so that these two fabrication procedures are compatible. It was also found that the optimum anneal time at this temperature is four hours.

INTRODUCTION

CdTe is an extremely useful material for optical devices which require a direct bandgap in the near infrared. Bulk CdTe is of interest as a substrate for the epitaxial growth of HgCdTe, and for the formation of superlattices in combination with other II-VI compounds. However, in order to properly control the liquid phase epitaxial (LPE) growth of HgCdTe on CdTe, a knowledge of the annealing behavior of the CdTe substrate is important. It is also necessary to identify and eliminate unwanted impurities in the CdTe that would diffuse into epitaxial layers during growth.

One technique for the removal of impurities involves gettering. Considerable work has been done with both ion-implantation damage gettering and surface gettering on Si and on GaAs [1,2,3]. However, this technique has not yet been applied to CdTe. It is possible that ion-implantation damage gettering could be useful in providing better substrates for epitaxial growth or for other applications. It is especially important to study the annealing behavior and gettering effects at the growth temperatures used for LPE.

EXPERIMENTAL TECHNIQUES

Eight samples studied in this investigation were taken from the same slice of a Bridgman-grown boule of CdTe. The crystals were not intentionally doped and they are high purity p-type ($\sim 1 \times 10^{14} \text{cm}^{-3}$). All surfaces are of (111) orientation. Low temperature (1.4K) PL experiments were performed on all of these samples in order to study the uniformity of the original samples. The samples were illuminated with the 5145Å line of an Ar⁺ laser with an incident power of 1.2mW focused on the samples. The diameter of the focused laser spot was approximately 200 μm . The PL data on as-received samples showed that there was no significant variation either along the surface of the samples or as a function of depth below the surface, which was determined by step-etching the surface.

Three of these samples were ion-implanted with 200keV Kr⁺⁺ ions on one side of the wafer at room temperature, to a dose of $1 \times 10^{16} \text{cm}^{-2}$; the equivalent energy for Kr⁺ ions was therefore 400keV. These samples were then annealed at 500°C, which is in the temperature range used for liquid epitaxial layer growth, for times of 2, 4 and 6 hours. The anneals were done for both an implanted and a unimplanted sample (i.e., a control or reference sample), sealed together in one tube with a purified Ar atmosphere. Following annealing, both the implanted and non-implanted samples were etched in 0.5, 1, 2, 4, 14, 34, 52, 70 μm steps, using 2% Br in ethylene glycol.

¹ Santa Barbara Research Center, Goleta CA 93117 (present address: Santa Barbara Focalplane, Goleta, CA 93117).

PL experiments were performed on both the implanted and control samples following each step of the etching, as described above. The results of these measurements were used to determine the effect of impurity gettering.

EXPERIMENTAL RESULTS

CdTe has a direct bandgap of 1.6eV at 1.8K. Typical low temperature luminescence data commonly show a peak at approximately 1.5930eV, which is associated with the recombination of excitons bound to shallow neutral donors (D^0X), and four narrow bands, at approximately 1.5897, 1.5894, 1.5890 and 1.5886eV, which are attributed to neutral-acceptor bound exciton recombination (A^0X). These four spectral features have been associated with four different impurities, Cu, Li, Na and Ag [4, 5]. Fig. 1 shows PL data from an unimplanted and unannealed sample, that is a reference sample, and an implanted sample that has been annealed for four hours and etched to 14 μ m. Very weak D^0X lines and sharp A^0X peaks were seen in the spectra of all samples studied, and are the main features used for studying the quality of this material. In particular, significant changes were noted in the intensities of the A^0X lines as a result of treatment.

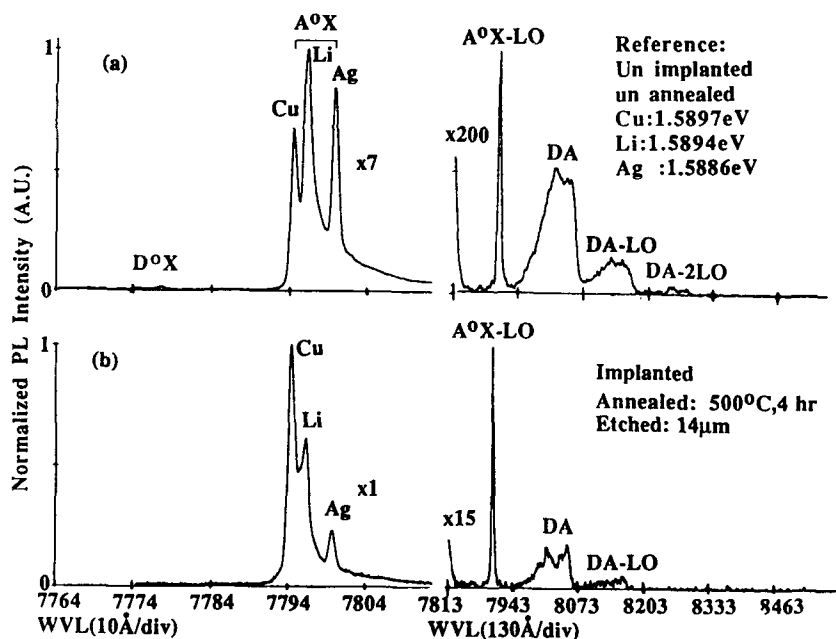


Fig. 1. Typical PL spectra observed from CdTe samples at 1.4K. (a) Spectrum from reference sample, which is unimplanted and unannealed. (b) Spectrum from implanted sample after 4-hour anneal and 14 μ m etching.

There are two main mechanisms by which the intensity of A⁰X lines might increase in bulk semiconductors. One is an increase in the concentration of radiative shallow acceptors capable of binding excitons, while the other is a decrease in the concentration of deep centers, which provide competing non-radiative pathways for recombination. The latter mechanism, i.e., variations in the non-radiative component, has been identified as the most important effect controlling the luminescence intensity of several materials [6,7]. Therefore, we suggest that PL intensities of the A⁰X lines provide a good indication of the effectiveness of various annealing and gettering procedures.

Fig. 2 shows the PL intensity variations of three of the common acceptors, Cu, Li and Ag, as a function of depth below the surface, for the implanted sample after a 4-hour anneal. All three lines have a similar behavior: low intensity near the surface and dramatically increased intensity from about 10 μm to approximately 60 μm . Beyond this, the intensities keep decreasing with increasing depth from the surface. A possible explanation for this behavior is the gettering of non-radiative (NR) deep centers. These NR centers might be likely to accumulate in the region of high implant defect density in order to relieve lattice strain. The low PL intensities near the surface might result from a number of factors: a high density of NR deep centers diffusing to the implant-damage region, shallow impurity gettering, or surface Cd loss; on the other hand, the high PL intensities between 10 μm and 60 μm is most likely due to a decrease in the concentration of NR deep centers. The decrease of the intensities in the deeper region might result from a gradual increase in NR deep centers as the gettering effect becomes weaker far from the implant.

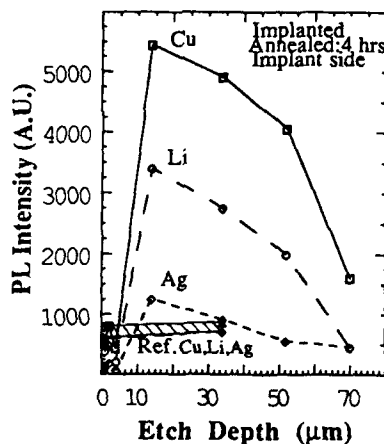


Fig. 2. Intensity variation vs depth from the implanted surface. Cu, Li and Ag neutral bound exciton lines have a similar annealing behavior; the Cu line is the most significant one, and will be used to study gettering in subsequent results in this paper.

The change in the intensity of the Cu line is most significant. Cu is of particular interest because it is a common contaminant in CdTe. For example, Cu and alkali ion diffusion from CdTe substrates into HgCdTe epilayers during epitaxial growth has been suspected of causing high acceptor concentrations in the epitaxial material [8]. We have used the Cu A⁰X line as representative of the general band-edge luminescence intensity in most of this study.

In particular, Cu luminescence is used in Fig. 3 to show the effect of the annealing time for the implant side of the implanted sample. Compared to the intensity of the reference sample (also shown in Fig. 3), the intensities of all the annealed samples are considerably higher in the gettering region (i.e. between 14 and approximately 60 μm below the surface). The 4-hour annealed sample shows more than ten times higher intensity than that of the reference sample at the optimum depth (14 μm), and therefore represents the optimum annealing conditions.

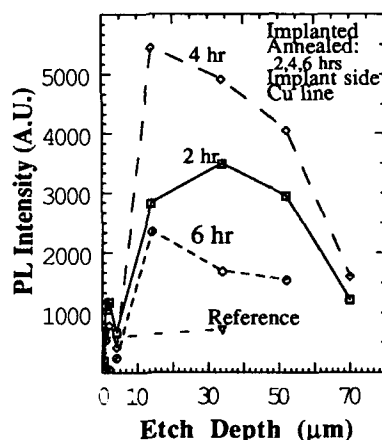


Fig. 3. Effect of annealing time. 4-hour annealing is optimum, which shows more than ten times higher PL intensity compared to that of the reference sample.

Fig. 4 shows spectra from implanted samples annealed for 4 and 6 hours after 1 μm etching. The low intensity of the 6-hour annealed sample might result from "over annealing" the sample. It is significant that this decrease in intensity is correlated with the appearance of a new, high-intensity peak at approximately 1.584 eV, which dominated the exciton region, as shown in Fig. 4(b). This new peak labeled "X" in Fig. 4(b), is suspected to be due to the formation of new vacancy-related defects resulting from out-diffusion of Cd during the long annealing [9].

The ion-implant damage gettering effect is compared with surface defect gettering in Fig. 5, which shows the PL intensity variation as a function of depth after 4-hour annealing of an implanted and unimplanted sample. The similar variation of the Cu line intensity for the unimplanted sample indicates that some gettering occurs without implantation due to surface defects on the unimplanted samples. However, the luminescence intensity in the implanted sample is 2 to 5 times stronger than the unimplanted sample, and the gettering region is deeper. These data imply that the increased luminescence intensity in the implanted sample does not result solely from the annealing of deep impurities or the release of impurities from macroscopic defects such as dislocations and precipitates (all of which can take place in unimplanted samples), but that damage-induced gettering is a significant mechanism in the implanted sample. Therefore, ion-implantation damage gettering of the NR deep centers is more efficient.

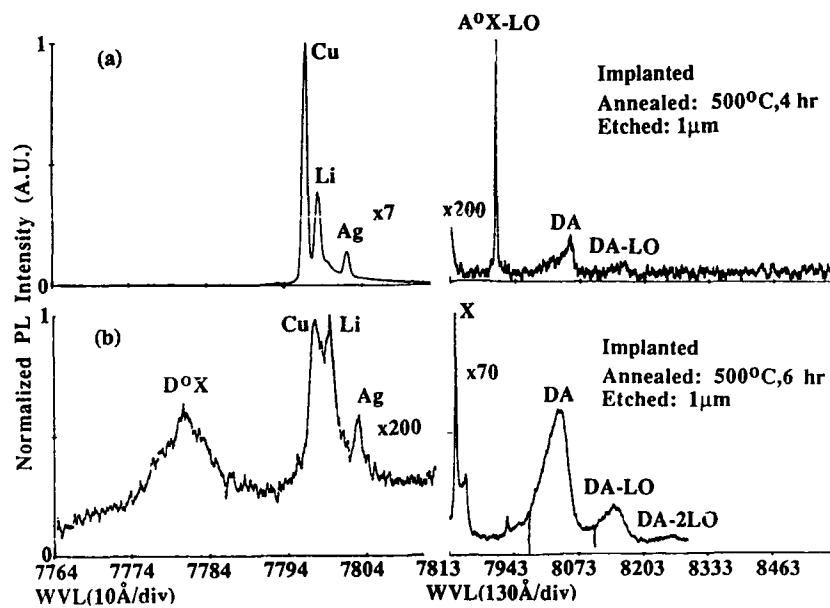


Fig. 4. PL spectra from implanted samples that have been annealed for 4 and 6 hours. The domination of a new vacancy-related peak, denoted "X" in (b), shows that the sample is overannealed in 6 hours.

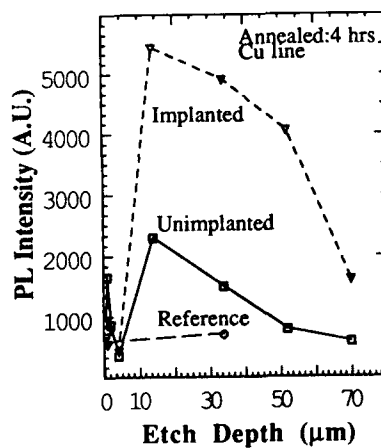


Fig. 5. Comparison of the annealing behavior between implanted and non implanted samples. The results show that surface gettering occurs without implantation, but that implant-induced damage gettering is considerably more efficient.

CONCLUSION

From PL experiments the annealing behavior of bulk CdTe material was studied with and without implantation. Implantation and annealing at the temperature at which liquid phase epitaxy takes place ($\sim 500^\circ\text{C}$) can be explained by a reduction of the concentration of deep non-radiative centers, possibly due to gettering of these centers at implantation damage and at the surface. The region effected by gettering covers a depth of approximately $50\mu\text{m}$. The surface gettering effect is observed to be much weaker. It was found that the optimum anneal time is four hours at this temperature.

ACKNOWLEDGMENT

We would like to thank Scott Johnson of Santa Barbara Research Center for help with the processing of these samples.

REFERENCES

1. Impurity Diffusion and Gettering in Silicon, MRS Symposia Proceedings, Vol. 36. Edited by Richard B. Fair, Charles W. Pearce and Jack Washburn. (Boston, Massachusetts, 1984).
2. T.E. Seidel and R.L. Meek, Proceedings of the 3rd International Conference on Ion Implantation in Semiconductors and Other Materials, edited by B. L. Crowder (Plenum, New York, 1973), p. 305.
3. C. O. Bozler, J. P. Donnelly, W. T. Lindley and R. A. Reynolds. "Impurity Gettering in Semi-Insulating Gallium Arsenide Using Ion-Implantation Damage." Appl. Phys. Lett., Vol. 29, No. 11, (1 Dec. 1976).
4. D. E. Nobel, Philips Res. Rep. **14**, 361 (1959).
5. E. Molva, J. P. Chamonal and J. L. Pautrat "Shallow Acceptors in Cadmium Telluride" Phys. Stat. Sol. (b) **102**, 635 (1982).
6. H. J. Hovel and D. Guidotti. "Correlations of Photoluminescence with Defect Densities in Semi-Insulating GaAs." IEEE Transaction on Electron Devices, Vol. ED-32, No. 11 Nov., 198D
7. P. M. Petroff, R. A. Logan and A. Savage. "Nonradiative Recombination at dislocations in III-V Compound Semiconductors." Phys. rev. let. Vol. 44, No. 4, 28 Jan., 1980
8. E. H. Cirlin. Intl. Conference on II-VI Compounds, Monterey, CA 1987.
9. Juan M. Figueroa, F. Sanchez-Sinencio, etc. "Influence of CdTe Vacancies on the Photoluminescence of CdTe." J. Appl. Phys. **60** (1), 1 July, 1986.

PREPARATION AND CHARACTERISATION OF
 $(\text{ZnTe})_x(\text{CdSe})_{1-x}$ SINGLE CRYSTALS

V.K.MADHU SMITHA RANI, R.P.VIJAYALAKSHMI, D.RAJA REDDY AND B.K.REDDY
 Department of Physics, S.V.University College, Tirupati 517 502 India.

ABSTRACT

The title material is one of the least studied among the II-VI alloy systems. So far it has not been possible to prepare ZnTe in n-type and CdSe in p-type with appreciable conductivities. Moreover ZnTe crystallises in zincblende whereas CdSe crystallises in wurtzite structure. Because of the varied nature of the end compounds, an attempt has been made to prepare single crystals of $(\text{ZnTe})_x(\text{CdSe})_{1-x}$ in the entire range of 'x'. The alloy material in the entire range of composition in the single crystalline form was grown by a modified Piper-Plich method. The grown crystals of this alloy system have been subjected to chemical analysis. DTA and DTG studies carried out on these alloys did not show any phase transitions. However two exothermic peaks associated with increase in mass were noticed. This has been attributed to oxidation effects of Se/Te or Cd/Zn. XRD data though showed some regularity near end compositions there is still some ambiguity for the middle compositions. Energy gap obtained from reflection spectra and also photocurrent spectral response showed bowing. However, there is a marked different feature at one of the end regions. The growth and the results of all the above mentioned investigations are presented and discussed in this paper.

INTRODUCTION

Method of alloying semiconductors in single crystalline form is ostensibly of both basic and applied interest. While the former interest tries to see the coherent behaviour of atomic systems, the latter engineers physical properties of materials for feasible technological use. All II-VI semiconductors crystallise either in cubic zincblende or hexagonal wurtzite structure. Among these CdTe is the only semiconductor which can be prepared in both n and p types with appreciable conductivities. Careful analysis of autocompensation phenomenon based on the stringent experimental conditions [1] used to prepare the other II-VI compounds in both types did not lead to any simple method of preparing these in both n and p types with desired conductivities. Therefore, to bridge the gap alloys are used to tailor some of the physical parameters of II-VI compounds. In general sulphides and tellurides are not completely miscible. This is due to the incompatible ionic radii of sulphur and tellurium in the same lattice [2]. The end compounds of $(\text{ZnTe})_x(\text{CdSe})_{1-x}$ quaternary system have diverse properties. Their structure and conductivity type normally obtained are different. Also the mutual quaternary system $(\text{ZnSe})_x(\text{CdTe})_{1-x}$ has already been studied in detail by many workers [2,3,4,5]. Vitrikhovskii [6], Vitrikhovskii et al [7] and Olenik et al [8] have reported some interesting conflicting results on the miscibility and the nature of these mutual systems. Therefore, in the present investigation single crystals of $(\text{ZnTe})_x(\text{CdSe})_{1-x}$ in the entire range of 'x' have been prepared and characterised. The results are compared with the earlier results on melt grown crystals.

EXPERIMENTAL

Single crystals of $(\text{ZnTe})_x(\text{CdSe})_{1-x}$ in the entire range of 'x' ($x=0.0, 0.2, 0.4, 0.5, 0.6, 0.8, 1.0$) have been prepared using a modified Piper-Polich vapour phase growth method (Fig.1) described elsewhere in detail [3].

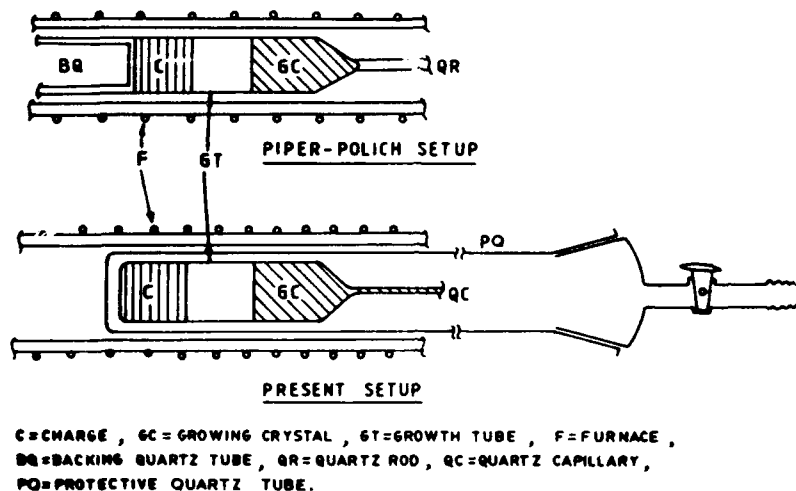


FIG.1. EXPERIMENTAL SETUP FOR VAPOUR PHASE GROWTH

The source material for crystal growth is prepared by sintering the appropriate quantities of 99.99% pure (Balzers, Switzerland) ZnTe and CdSe in an atmosphere of argon at about 750°C for two to three days. After the necessary ampoule preparation the growth is carried out at about 1100°C in argon atmosphere for 7 to 10 days. Good crystals of 1cm diameter are obtained when pull rates of less than 1cm/day are used. Single crystallinity is confirmed by the observation of spots in X-ray backreflection photographs.

The chemical analysis of Cd and Zn has been carried out by atomic absorption spectroscopy using Varian AA 575 atomic absorption spectrometer with an accuracy of about 1%. DTA and DTG are carried out in the temperature range 30-900°C with a heating rate of 10°/min. Alumina crucible is used as reference and Pt/Pt-Rh10% thermocouple is used for temperature sensing. XRD data is obtained from a computerised Philips diffractometer with Cu K α radiation. Diffuse reflectance spectra (300-900nm) is obtained using a Cary 2390 spectrophotometer. The photon energy corresponding to the point of intersection of the two linear reflectance regions near the band edge is taken as the band gap. The band gap is also determined by noticing the peak in photoconductivity spectral response (200-900nm). A CEL monochromator with 600W halogen lamp is used for this study.

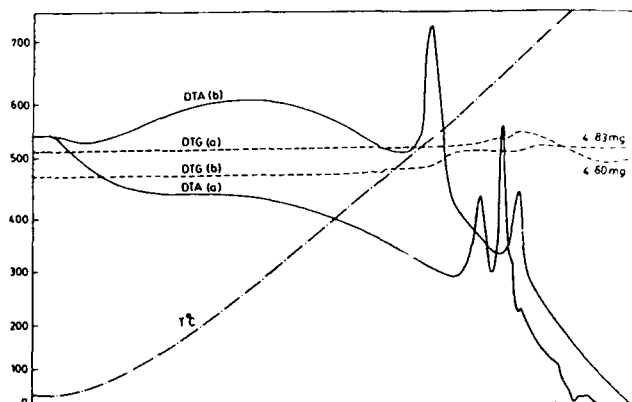
RESULTS AND DISCUSSION

The source and the estimated compositions of Zn and Cd in the grown crystals are given in table.I.

Table.I. Chemical composition of $(\text{ZnTe})_x(\text{CdSe})_{1-x}$ crystals

X	0.0	0.2	0.4	0.5	0.6	0.8	1.0
Target Zn Wt%	--	6.82	13.62	17.00	20.39	27.15	33.88
Estimated "	--	6.92	13.76	16.68	20.12	26.77	33.88
Target Cd Wt%	58.74	46.91	35.13	29.25	23.38	11.67	--
Estimated "	58.74	46.56	34.88	29.43	23.40	11.43	--

It is clear from the table that the deviations from the target compositions are not very significant. Therefore in the discussion only target composition is used. DTA and DTG of two compositions ($x=0.5$ and 0.8) are shown in Fig.2. Apart from the usual endothermic vaporisation process distinct exothermic peaks associated with increase in mass in DTG were noticed. The peak positions of all the compositions are given in Table.II.

Fig.2. DTA and DTG of $(\text{ZnTe})_x(\text{CdSe})_{1-x}$ crystals
 $x=0.5$ (a) $x=0.8$ (b)Table.II; DTA peaks of $(\text{ZnTe})_x(\text{CdSe})_{1-x}$ single crystals($^{\circ}\text{C}$)

X	0.0	0.2	0.4	0.5	0.6	0.8	1.0
	258	300	235	236	258	258	--
	754	747	654	619	662	539	
			688	654	705	663	
			729	680	742		

These peaks can not be attributed to structural changes similar to those found in $(\text{ZnSe})_x(\text{CdTe})_{1-x}$ because these occur at still higher

temperatures [5] and also increase in mass (DTG) has been observed. These might be due to the formation of oxides of Se/Te; Cd/Zn and selenates and tellurates of Cd/Zn. But the oxides of Se/Te and selenates and tellurates of Zn/Cd have low melting/dissociation temperatures and hence can not account for the increase in mass. Oxides of Zn and Cd are stable even at high temperatures and therefore the peaks might be due to oxidation of Zn/Cd. However, this has to explain the sharpness of the DTA peaks also. It is also clear from Fig.2 that the evaporation process is faster than the heating rate.

The structures of specimens of all the compositions have been determined by analysing the XRD data. This showed cubic structure for $x > 0.4$. For $0.0 \leq x \leq 0.4$ the structure is hexagonal. Fig. 3 shows the corresponding lattice constants of all the compositions. The transition from hexagonal to cubic is sharp and takes place near $x=0.4$.

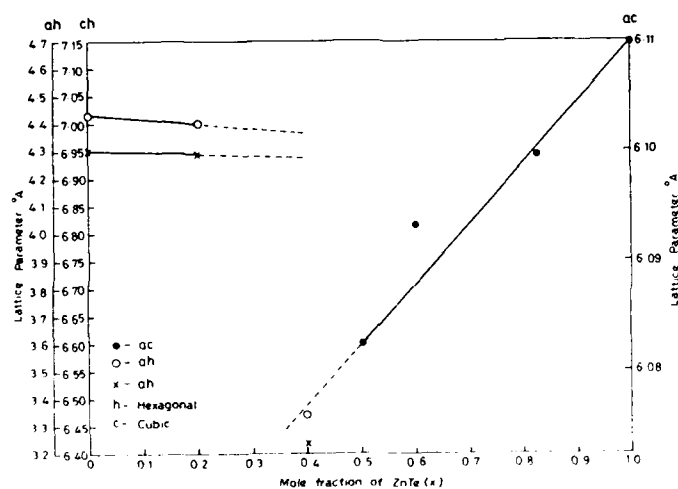


Fig. 3 Variation of Lattice Parameter with composition in $(\text{ZnTe})_{1-x}(\text{CdSe})_x$ single crystals

Sharp deviation in lattice constants from linearity (Vegard's law) is also found in samples with $x=0.4$. However, Vitrikhovski [6] reported structural ambiguities in the range $0.35 \leq x \leq 0.4$ in the melt grown crystals.

The band gap values obtained from diffuse reflectance and Photoconductivity spectral response are not significantly different. These values are marked in Fig.4 as functions of composition. Band gap varied nonlinearly. The data is fitted to the usual second order equation in x and found to satisfy the equation.

$$E_g(x) = 1.706 - 0.156x + 0.724x^2 \quad (1)$$

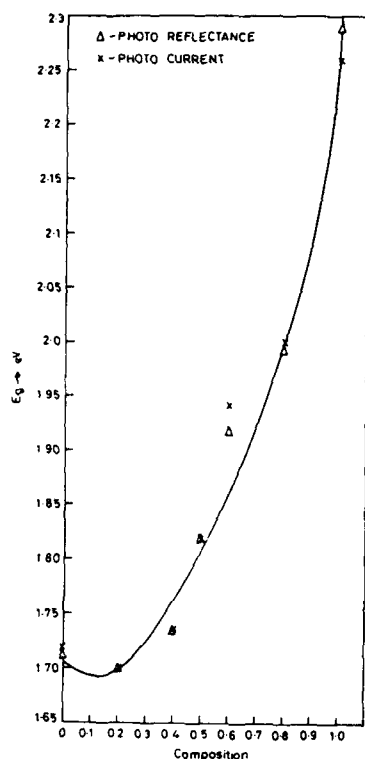


Fig. 4
Energy gap variation with composition 'x' of
 $\text{ZnTe}_x\text{CdSe}_{1-x}$ crystals

The curve in Fig. 4 is drawn according to the above equation. The bowing parameter (coefficient of x^2) is 0.724. This shows that the energy gap passes through a minimum at about $x=0.1$. However, Vitrikhovskii's data [6] shows that it occurs near about $x=0.4$. By taking the variation of bowing parameter with composition, $b(x)$ as per the pseudopotential approach it is found that the bowing parameter increases with increase of lattice constant thereby showing that constancy of $b(x) \times a(x)^4$ [9] is not maintained in support of pseudopotential model. This might be due to the structural intricacies involved in this system. At $x=0.5$ $(\text{ZnTe})_x(\text{CdSe})_{1-x}$ and $(\text{ZnSe})_x(\text{CdTe})_{1-x}$ systems are identical in chemical composition. The structures of both are cubic zincblende with lattice constants of 6.08 \AA and 6.07 \AA [4] and are almost equal within experimental errors. However, the energy gap of $(\text{ZnTe})_{0.5}(\text{CdTe})_{0.5}$ is 1.82 eV and that of $(\text{ZnSe})_{0.5}(\text{CdTe})_{0.5}$ is 1.68 eV [4]. The above data

is for vapourphase grown crystals prepared using the respective binary compounds as source materials. Therefore the nature of the source material seems to control the position of atoms and hence their properties. The reported splitting of ZnTe - CdSe system into CdTe - ZnSe [8] is not found to occur in the vapour grown crystals.

CONCLUSIONS

Single crystals of $(\text{ZnTe})_x(\text{CdSe})_{1-x}$ solid solutions in the entire range of 'x' without any phase splitting can be obtained by vapourphase method. The DTA peaks are due to chemical rather than structural phase changes. The crystals are cubic for $x > 0.4$. The energy gap passes through minimum around $x=0.1$. The bowing can not completely be accounted by pseudopotential model and more structural intricacies have to be taken into account.

REFERENCES

1. R.Baubinas, Z. Januskevicius, A.Sakalas and J.Viscakas, Solid State Commun. 15, 1731 (1974).
2. W.M.Yim, J.P.Dismukes, E.J.Stoko and R.J.Ulmer, Phys.Stat.Solidi (a), 13, K57 (1972).
3. P.Chandrasekharam, D.Raja Reddy and B.K.Reddy, J.Cryst.Growth, 63, 304 (1983).
4. P.Chandrasekharam, D.Raja Reddy and B.K.Reddy, Phys. Stat.Sol.(b) 119, K5 (1983).
5. H.Tai and S.Hori, J.Jap.Inst. Met., 41, 33 (1977).
6. N.I.Vitraikhovskii, Neorg. Mater. 13, 437 (1977)
7. N.I.Vitrikhovskii, M.P.Lisitsa, S.F.Terekhova and G.G.Tsebulya, Sov.Phys.Semicond., 7 1498 (1974).
8. G.S.Oleinik, V.N.Tomashik and I.B.Mizetskaya (Russian), Poliprovodn Tekh. and Mikroelectron., 28, 56 (1978).
9. R.Hill and D.Richardson, J.Phys. C, 6, L115 (1973).

PART II

Optical and Electrical Properties

DEEP LEVEL LUMINESCENCE MEASUREMENTS OF MBE CdTe GROWTH QUALITY AND PROCESSING

J. L. SHAW*, L. J. BRILLSON**, S. SIVANANTHAN***, and J. P. FAURIE***

*Naval Research Laboratory, Washington D. C. 20375

**Xerox Webster Research Laboratory, Webster, NY 14580

***Microphysics Laboratory, Physics dept., University of Illinois at Chicago, Chicago, IL 60680

ABSTRACT

We used photoluminescence spectroscopy to monitor CdTe in-situ during surface processing in order to optimize the surface electronic quality. Spectra of *optimally-prepared* (100) films grown by molecular beam epitaxy reveal low intensity emission from deep states relative to typical bulk-grown material.

INTRODUCTION

CdTe is used as a substrate for epitaxial growth of II-VI compounds as well as an active part of various electronic devices [1]. The characteristics of such devices are often sensitive to the surface and interface properties of CdTe as well as the bulk properties. Photoluminescence (PL) is widely used as a characterization tool for CdTe, and is sensitive to the presence of a variety of mid-gap as well as shallow states, which may be local to the CdTe surface [2,3]. The presence of deep states at the surface can increase the recombination rate, alter the surface band bending, and influence the Schottky barrier height, all of which may influence the PL spectrum [2,4]. Thus to ensure reliable comparison of bulk-related features, the surface condition must be controlled. High quality (110) CdTe surfaces may be obtained by cleaving the crystals in ultra high vacuum (UHV) [2-4]. However, characterization of epitaxially-grown material or orientations other than (110) require an alternative preparation method. Here we report the use of PL to optimize (100) CdTe surfaces prepared by chemical etching followed by thermal desorption in UHV [5].

EXPERIMENTAL DETAILS

We grew CdTe films from CdTe sources on (100), (111), and (211) CdTe substrates (GalTech) in an Riber 2300 MBE machine. In some cases a Te source as well as a CdTe source was used. Substrate preparation involved etching in 0.05% Br:methanol (to remove ~0.4 $\mu\text{m/min}$), rinsing in methanol, blowing dry with N_2 , and transferring to UHV; all under N_2 atmosphere. This process leaves excess Te on the surface but no contamination. Heating to the growth temperature (250-335 C) in UHV desorbs the excess Te. The finished films were stored in air for several weeks, then re-etched in the same way prior to analysis in a second UHV chamber.

PL spectra were measured with the films held at 80 K. The focused beam of either a HeCd (442 nm, extinction length 100 nm) or HeNe laser (extinction length 200 nm) provided excitation. Only the blue HeCd laser was used for the spectra reported here. Luminescence in the range 0.4-1.6 eV was dispersed by flint glass or CaF_2 prisms and phase-detected with Ge or InSb photodiodes. The response function of the detection system was deconvolved from the spectra. Auger electron spectra (AES) were measured at room temperature with a normal incidence, 2 kV, 0.5 mA, 1 μm electron beam and a cylindrical mirror analyzer (CMA) modulated through 2 eV at 10 kHz. To avoid electron beam damage, the position of the electron beam was not allowed to dwell on any portion of the surfaces used to measure PL spectra. The University of Wisconsin's Aladdin synchrotron light source and the Mark V Grasshopper monochromator combined with a double pass CMA provided <0.3 eV resolution for the soft x-ray photoemission (SXPS) measurements. The SXPS measurements were made with the specimen at 80 K in order to allow in-situ PL measurements.

RESULTS

Figure 1 shows PL spectra of air-exposed (111) CdTe films grown under various conditions. The spectra contain near band edge (NBE) emission plus bands peaked at 0.5, 0.9, 1.3 and 1.4 eV. The spectral shape varied across the surface, with the red vs. blue laser, and with the specimen. Similar variations were noted in spectra of (100) and (211) CdTe films. The surface variations were probably due to changes in band bending across the surface (discussed below), whereas the changes observed between specimens probably reflect various concentrations of mid-gap states. The temperature we used (80K) was too high to allow resolution of the individual features near the band edge, however changes in the shape and position of the NBE peak were noted.

Figure 2 shows PL spectra of three air-exposed (100) CdTe films. The (100) films were selected for further study based on their low luminescence intensity at energies below 1.4 eV. The substrate used to grow these films had relatively intense luminescence near 1.4 eV, which may have contributed to the observed emission in that region.

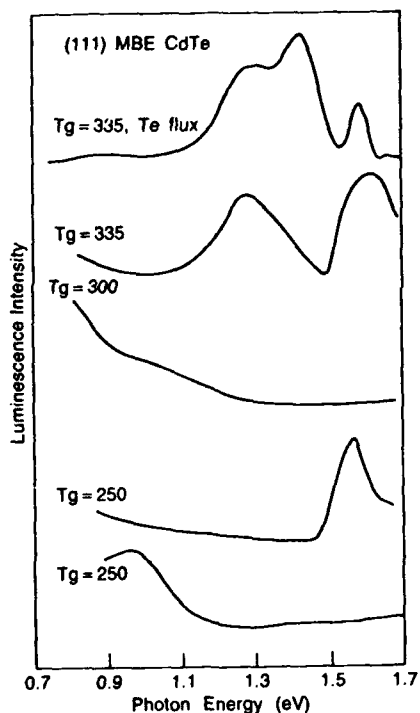


Figure 1. PL spectra of air-exposed (111) CdTe films grown as indicated.

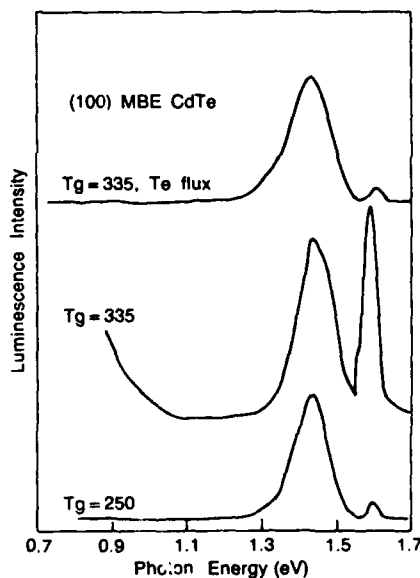


Figure 2. PL spectra of air-exposed (100) MBE CdTe films grown as indicated.

Figure 3 shows PL spectra of the (100) film grown at 335 C with additional Te flux. Treatment of the film grown without Te flux yielded similar results. The surface was cleaned using the procedure described above for MBE substrates, except that the desorption was carried out incrementally, with PL and AES spectra measured after each 60 second heat treatment. The AES spectra of these surfaces showed no C or O contamination, and verified that the Te/Cd ratio was reduced to that of a UHV-cleaved (110) surface after heating to 200-250 C, depending on the time at elevated temperature. To within our experimental error (<5%), no further change in Te/Cd ratio

was observed after additional heat treatments up to 500 C. The initial Te-rich surface showed no detectable luminescence, however intense NBE emission developed quickly with Te desorption. The NBE peak intensity and energy, as well as the intensity of the 1.4 eV band all increased with heat treatments up to 250 C. These changes were reversed by additional heat treatments above 250 C. Both the time and temperature of the heat treatments contribute to the optimal desorption conditions, thus longer or shorter heat treatments will require lower or higher temperatures to achieve similar results.

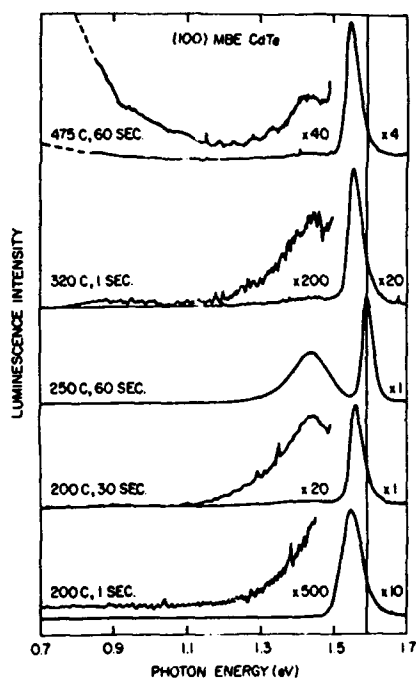


Figure 3. PL spectra of a (100) CdTe film grown 335 C after etching and heat treatment at the temperatures indicated.

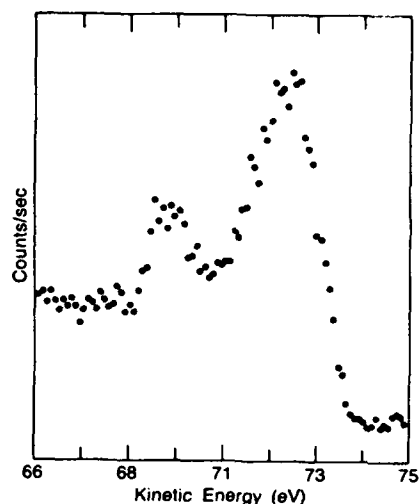


Figure 4. SXPS valence band spectrum ($h\nu=80$ eV) of a (100) MBE CdTe film grown at 335 C after etching and heat treatment.

The increase in both the NBE peak energy and the intensity at 1.4 eV may be explained by a reduction of the band bending near the surface as Te is desorbed. The initial Te-rich surface produced no NBE recombination because the surface band bending was large enough to form a depletion layer deeper than the layer where electron-hole pairs are created, and thus separate all loosely bound electron-hole pairs. (The Te-rich surface layer might also cause increased non-radiative surface recombination.) Lower energy emission from deep level recombination might still have been produced, hence the lack of any observed low energy luminescence (in any of the spectra) indicates that few deep trap states exist near the surface, and attests to the high quality of the MBE material. After the first desorption at 200 C, the band bending is reduced sufficiently to permit some NBE recombination, however the low energy of the NBE peak (~ 1.55 eV) indicates that the electric field near the surface is still large enough to favor recombinations from more tightly bound electron-hole pairs, such as those bound to acceptor states, over the higher energy transitions. The relative intensity from the higher energy transitions, and thus the energy position

of the NBE peak, increased further after heat treatments at 225 C and 250 C, where the NBE peak energy reached its maximum of ~1.59 eV. We have previously observed a similar change in the PL NBE peak position after Au deposition induced band bending (measured with SXPS) at a UHV-cleaved (110) CdTe surface [4].

The anomalously high intensity of the PL band near 1.4 eV measured after the 250 C desorption indicates that the band bending at both the surface and at the substrate-epilayer interface was small enough to allow diffusion of electrons and holes into the substrate (or the interface region), where the recombination producing the 1.4 eV luminescence occurred. Thus the presence of the 1.4 eV band in the spectrum measured after the 250 C heat treatment shows that the carriers in the MBE layer had long enough recombination times to diffuse through several (~5) μm of material to the substrate interface, as well as flat band conditions at both the surface and bulk interfaces.

Heating to 450 C and above produced a new deep level luminescence band peaked at 0.5 eV. The same low energy band also developed after exposing the surface to a 1 kV, 1 mA electron beam focused into a 100 μm spot for 5 min. The electron beam damage also reduced the NBE emission to a small fraction of its original intensity. The electron beam damage was removed by re-etching and re-heating the surface, indicating that it was confined to the near surface region.

Figure 4 shows a valence band spectrum of a (100) MBE CdTe film measured after etching the surface and optimal heat treatment as monitored by PL. The spectrum shows the double peaked structure routinely observed for UHV-cleaved (110) CdTe and other semiconductors. This structure is not observed when the surface contains small amounts of contamination or excessive step density, and is often used as a standard of surface quality. Thus our observation of the valence band structure verifies the high electronic quality of the surfaces.

CONCLUSIONS

We have demonstrated that the significant changes in the PL spectrum which occur due to surface effects can be used to optimise the CdTe surface electronic properties by monitoring surface processing in-situ with PL. Optimising CdTe surface preparation in this way may lead to improved and more controlled interfaces between CdTe and both metals and semiconductors.

ACKNOWLEDGEMENTS

The work at Xerox was supported in part by the Army Research Office under contract No. DAAL03-86-C-0003. The work at the University of Illinois at Chicago was supported by Defense Advanced Research Projects Agency (DARPA) contract No. F49620-87-0021 monitored by the Air Force Office for Scientific Research.

References

1. K. R. Zanio, in *Semiconductors and Semimetals*, edited by R. K. Willarsen and C. Beer (Academic, New York, 1978), Vol. 13.
2. I. M. Dharmadasa, J. M. Thornton, and R. H. Williams, *Appl. Phys. Lett.* **54**, 137 (1989); Z. Sobiesierski, I. M. Dharmadasa, and R. H. Williams, *Appl. Phys. Lett.* **53**, 2623 (1988); I. M. Dharmadasa, W. G. Herrindon-Harker, and R. H. Williams, *Appl. Phys. Lett.* **48**, 1802 (1986).
3. J. L. Shaw, R. E. Viturro, L. J. Brillson, D. Kilday, M. K. Kelly, and G. Margaritondo, *J. Vac. Sci. Technol. A* **6**, 2752 (1988); J. L. Shaw, R. E. Viturro, L. J. Brillson, D. Kilday, and G. Margaritondo, *J. Electron. Mater.* **17**, 149 (1988).
4. J. L. Shaw, R. E. Viturro, L. J. Brillson, and D. LaGraffe, *Appl. Phys. Lett.* **53**, 1723 (1988).
5. J. P. Faurie, A. Million, and G. Jacquier, *Thin Solid Films* **90**, 107 (1982); J. P. Faurie, C. Hsu, J. Reno, S. Sivananthan, and M. Boukerche, *Third Int. Conf. Solid Films and Surfaces* (Sydney, 1984) (unpublished); J. P. Faurie, DARPA Contract MDA 903-83-K-0251 (1983-86), Final Report (unpublished).

HIGH RESOLUTION AND ANALYTICAL ELECTRON MICROSCOPY OF MULTILAYER HETEROEPITAXIAL SEMICONDUCTORS

H.-J. KLEEBE*, W.J. HAMILTON**, W.L. AHLGREN**, S.M. JOHNSON**, and
M. RÜHLE*+

*UCSB, Materials Dept., Eng. III, Santa Barbara, CA;

**Santa Barbara Research Center, Goleta, CA.

+Now at MPI für Metallforschung, Stuttgart, FRG.

ABSTRACT

Thin-film epitaxial layers on silicon substrates are being actively developed as an alternative to bulk substrates for infrared detectors. Success in this development is expected to yield improvements in size, strength, monolithic signal processing, and cost of the detector arrays. To provide feedback to the thin-film growth process, this study has investigated the structural and chemical properties of these films. CdTe or CdZnTe was grown on GaAs on Si wafers by metalorganic chemical vapor deposition (MOCVD) followed by the growth of HgCdTe by liquid-phase epitaxy (LPE). Development of TEM specimen preparation techniques permitted investigation of materials with up to four layers. Cross sectional TEM and AEM investigations resulted in the following observations: Selected area diffraction and CTEM show relations between the layers and structural defects. High resolution imaging of the multilayers reveals that most of the heteroepitaxial misfit is accommodated by misfit dislocations. Many, but not all, stacking faults and dislocations which propagate across the films appear to be related to structural interface defects. The evidence indicates that there is little, if any, contamination at MOCVD and LPE interfaces. Interface defects mainly appear to be extremely minute pits or hillocks. AEM investigations of interface regions have demonstrated a redistribution of material close to the CdZnTe / HgCdTe interface.

INTRODUCTION

A key issue in the reliability of infrared detectors is their survival under repeated thermal cycling from room temperature to cryogenic operating temperatures. Thermal mismatch between the II-VI detector elements and the silicon chips used for signal readout causes destructive stresses during cycling. In addition, significant cost savings should be realized with the use of silicon wafer automated processing technology. However, growth of single crystal, high-quality HgCdTe materials directly upon silicon has been found to be extremely difficult. Therefore, thin-film buffer layers have been grown on the silicon prior to growth of the active detector layers.¹ Single-crystal, thin-film layers of GaAs have been successfully grown on silicon and are now available commercially (Kopin Corporation). The large lattice mismatch between GaAs and HgCdTe (HCT) requires first a growth of a CdTe or CdZnTe (CZT) layer as a lattice-matching buffer layer. These films have been prepared by molecular beam epitaxy (MBE)¹, hot-wall epitaxy², evaporation^{1,3}, and metalorganic chemical vapor deposition (MOCVD).^{4,5} HgCdTe thin-film layers for IR detectors have been grown on CdTe or CZT by liquid-phase epitaxy (LPE),⁶ MOCVD⁷ and MBE.⁸

Previously, TEM has been used successfully to characterize thin-layers of CdTe grown on GaAs by MBE and MOCVD.⁹⁻¹⁴ LPE growths of HgCdTe on CdTe or CZT have been examined by TEM.^{15,16} This paper covers the results accomplished by TEM and AEM of multilayer, heteroepitaxial structures. X-ray rocking curve analysis and measurement of electrical properties of the same films have been performed by Johnson et al.¹⁷ The structures investigated here also have been processed recently into 128 X 128 detector arrays, which show good electrical performance and imaging performance.¹⁸

EXPERIMENTAL PROCEDURE

The investigated structures consisted of a buffer layer of CdZnTe grown by MOCVD on a commercially available GaAs thin film deposited on Si. In addition, films of HgCdTe were grown by LPE on some of the buffer layers.

MOCVD layers of nominally $\text{Cd}_{0.96}\text{Zn}_{0.04}\text{Te}$ were grown on a GaAs/Si {100} 4° to $\langle 111 \rangle$ substrate.¹ MOCVD growth of the CZT layer was done by a standard pyrolytic process at a substrate temperature of 441 C. In the reactor, the substrate was heated to 600 C under flowing hydrogen for 20 minutes, then cooled to the growth temperature. The reactants used for CZT deposition were dimethyl cadmium, diethyl zinc, and diethyl telluride. Typically, deposition was performed for about 3 hrs at a rate of $1.8 \mu\text{m h}^{-1}$ forming a 6 μm thick layer.

An LPE layer of $\text{Hg}_{0.7}\text{Cd}_{0.3}\text{Te}$ was grown on top of the above structure from a Hg-rich, In-doped melt containing about 6.5% Te and 0.003% Cd. The material was first prepared with a ultraviolet light and ozone treatment followed by etching in a solution of 0.2% bromine in methanol. The growth occurred by ramping temperature between 474 and 469 C and resulted in an approximately 5 μm thick layer. The morphological properties tended to replicate that of the underlying material. The entire structure was subsequently annealed in a saturated Hg atmosphere at 250 C for 4 hrs. The electrical properties were measured on a small sample by using the van der Pauw method of Hall-effect measurement. This measurement indicated that the material was about $4 \times 10^{15}/\text{cm}^3$ n-type with a mobility of about $4 \times 10^4 \text{ cm}^2/\text{V}\cdot\text{s}$ at a temperature of 77 K.

In order to retain the integrity of the multi-layer structure throughout the specimen preparation for TEM, a ceramic cylindrical rod and tubing assembly of alumina was used. A sandwich of two substrates with the thin-film regions face to face was cemented (M-Bond 610, Measurements Group, Raleigh, N.C.) into a slit in the alumina rod and held in place by the outer alumina cylinder. Discs were cut perpendicular to the rod axis and mechanically ground and polished down to 100 μm thickness. The discs were dimpled from one side and subsequently ion-thinned to perforation using a liquid-nitrogen cold stage. The specimens were carbon-coated to provide conductivity.

TEM and AEM studies were performed in a 400 kV analytical high resolution instrument (JEOL 4000 FX). Energy dispersive x-ray spectroscopy (EDS, Tracor Northern) and parallel electron energy loss spectroscopy (PEELS, Gatan) instruments were used for AEM studies. During all investigations a double tilting specimen holder with a low-temperature stage to reduce contamination was used. Spot sizes used for microanalysis were typically 10 to 20 nm diameter.

RESULTS AND DISCUSSION

The low magnification image in Fig. 1 shows a typical region of the four layer structure consisting of an LPE HCT film grown on an MOCVD CZT buffer layer deposited on an MOCVD GaAs layer on a Si substrate. The portion of the study reported here concentrated on the microstructural and microchemical characterization of the GaAs / CdZnTe and CdZnTe / HgCdTe interfacial regions in the multilayer structures. A number of the features observed are related to the processing techniques used during growth of the layers.

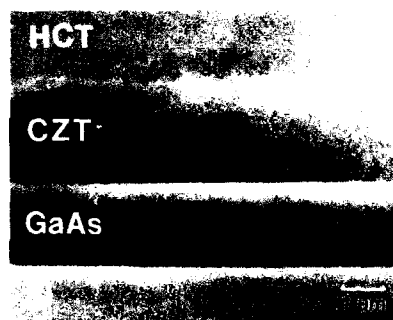


Fig. 1. Low magnification image of a typical four layer structure.

Characterization of the GaAs / CdZnTe interface

The MOCVD deposition of the CdZnTe buffer layer on the GaAs substrate material forms a sharp, planar interface, as shown in Fig. 2. A high dislocation density is visible near the interface in the CZT layer. Within about 2 μm of growth of the CZT, the dislocation density has diminished significantly and only a few threading dislocations (Lomer-Cottrell type^{9,11}) propagate into the HCT layers. The annihilation of the dislocations by intersection with others appears to be the primary mechanism for the improving defect density as growth continues. In many cases, threading dislocations are associated with micropits at the interface (Fig. 2b), but there is no consistent relationship between the observed pits and the threading dislocations generated at the interface.

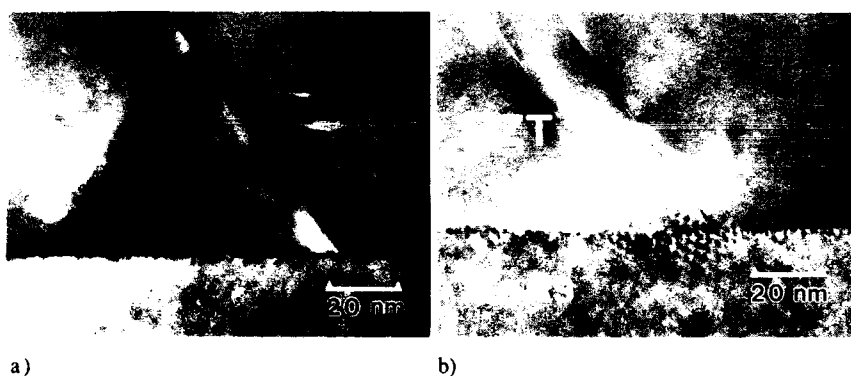


Fig. 2 Threading dislocations (a) independent and (b) associated with micropits at the [100] GaAs / [100] CdZnTe interface.

Chemical analysis combining EDS and PEELS techniques of this interface gave results related to the GaAs surface treatment prior to the MOCVD CZT deposition. No contaminants were detectable at or near the interface using EDS, and no oxygen, carbon, nitrogen, or other light elements were detected with PEELS analysis. Moreover, no contamination, segregation, or amorphous layer at the interface could be detected, indicating that the cleaning and heat treatment prior to deposition of the CZT do not result in significant amounts of impurities. A careful examination near the interface showed that no enrichment of Ga or As depletion occurred during the elevated temperature pre-treatment. Although Ponce et al¹¹ suggest that the micropitting is a result of this high temperature processing, the presence of very small hillocks as well as the pits indicates that this may not be the mechanism of pit formation (Fig. 3a). These interface features may be the result of the pre-deposition chemical etch. The dimensions of the pits and hillocks were too small (typically < 20 nm) to detect any chemical contaminants which might have been associated with them. Although the growth conditions for the layers studied here had previously produced CZT layers of 2 wt.% zinc, Zn was undetectable by EDS analysis in these layers. That this was not an artefact of the TEM preparation or observation was verified independently on one of the samples with a scanning electron microscope and EDS.

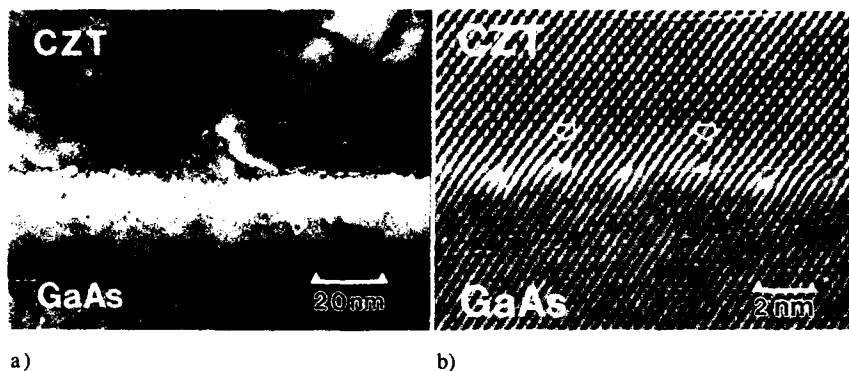


Fig. 3 High resolution images of the GaAs / CdZnTe interface; (a) hillock and (b) misfit dislocation (observed along [011] orientation).

Primary misfit dislocations adapt the lattice mismatch between CdZnTe and GaAs of 14.7% (Fig. 3b). Ponce et al.^{9,11} reported a misfit dislocation distance of 3.1 nm in MBE-deposited CdTe as is predicted from calculations assuming the strain is entirely accommodated by these dislocations. In the present material relief of the stresses appears to be shared (i) by the misfit dislocation period of about 3.6 nm, (ii) by an approximately 3 degree lattice tilt of the CdZnTe relative to the GaAs, (iii) remaining strain in the lattice, and (iv) Zn interdiffusion in the lattice.

Characterization of the CZT / HCT interface

As a result of the liquid-phase growth temperatures, melting and interdiffusion causes the CdZnTe / HgCdTe boundary be a diffuse interface. PEELS analysis over this region did not detect any light element contaminants. EDS analysis determined the concentration distribution shown in Fig. 4a. This distribution is not substantially different from that given by Nouruzi-Khorasani et al.¹⁶ for LPE HCT grown on bulk {111} CdTe and CZT.

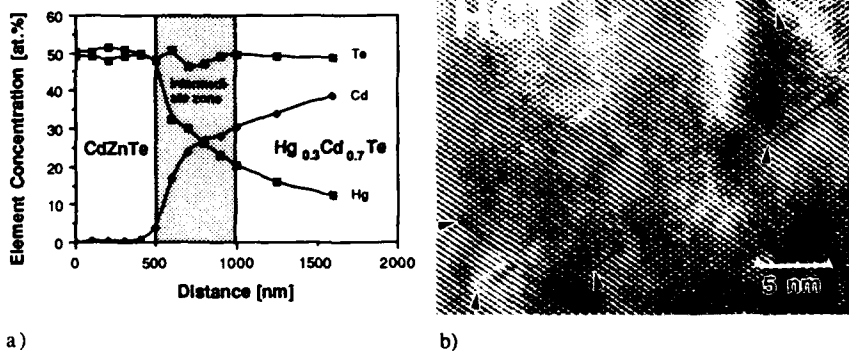


Fig. 4 CZT / HCT interface region: (a) elemental distribution, and (b) high resolution image of intermediate region (incident beam parallel [011]).

High-quality HgCdTe detectors for infrared radiation require high-quality material of low defect density. Although the defect density in the CZT / HCT interface region is rather high (Fig 4b) outside the first few nanometers in the HCT layer, very few defects can be located by TEM. This is consistent with a measured surface etch-pit density of about 10^6 cm^{-2} . Because the defect density is of this magnitude, too few defects are present to accurately verify the density by TEM. The primary defect observed near the interface and in the HCT layer was stacking faults (Fig. 5a). One possible explanation for the source of these stacking faults is that they may arise from the condensation of vacancies, most probably Hg vacancies on close-packed {111} lattice planes. The bound size of the stacking faults observed would be determined by the energy equilibrium between 1) reduced strain energy of continued vacancy condensation and 2) increased energy produced when enlarging the dislocation loop defining the borders of the stacking fault. This interpretation is consistent with the reduction in numbers of the faults near the surface of the HCT. The reduction would occur by annihilation of these faults by Hg diffusing into the bulk during the annealing process resulting in the nearly perfect lattice shown in Fig. 5b.

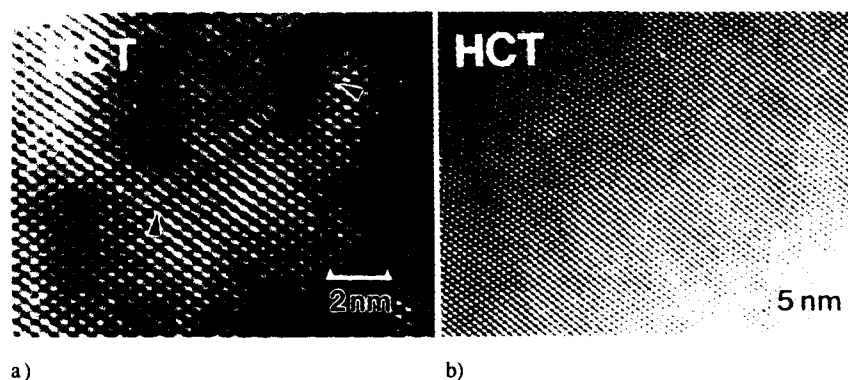


Fig. 5 (a) Stacking fault loop in [111] in interfacial region and (b) perfect HCT lattice in near surface region (observed along [011] orientation).

CONCLUSIONS

The near-term future of HgCdTe hybrid infrared detectors requires improvements in size, strength, reliability, signal processing, and cost. Growth of multilayer, heteroepitaxial thin films is expected to yield significant advances in these areas. In this study, TEM and AEM observations of these materials have provided feedback to the development of MOCVD and LPE multilayer processing.

The results show that the films have retained their structural integrity throughout the processing. Although the material properties observed are similar to those previously reported for single-layer thin films, it is important to note that subsequent processing has not severely modified the previously grown layers. Extremely small micropits and hillocks have been seen in the CZT / GaAs interface, but no consistent correlation could be made to defects present in the CZT layer. A number of threading dislocations penetrate from substrate through successive epitaxial layers, while others appear to be the result of interface defects. Dislocations in the CZT / GaAs interface are reduced within 2 to 3 μm of growth to a small fraction of the near-interface dislocation density. The bulk of the misfit in this interface is accommodated by misfit dislocations. EDS and PEELS analytical techniques were used to determine the chemical properties of multilayer epitaxial films

made by sequential growths: Chemical contaminants are not detectable in the interfacial regions; There are no oxide boundaries or amorphous carbon contamination detectable. A high density of stacking fault defects at the HCT / CZT interface is observed to be markedly reduced within the first micrometer of growth. It is believed the reduction in the stacking faults observed was due to annihilation of vacancies by Hg atoms during the post-growth diffusion. Finally, the HgCdTe layer was shown to have a low dislocation density observed over a large area near the surface which approaches the high crystal perfection required for fabrication of IR diode detectors.

REFERENCES

1. K. R. Zanio and R. C. Bean, SPIE Infrared Detectors and Arrays, V930, 44 (1988).
2. K. Lischka, D. J. Fantner, T. W. Ryan and H. Sitter, Appl. Phys. Lett. 55, 1309 (1989).
3. J. T. Cheung and T. Magee, J. Vac. Sci. Technol. A 1, 1604 (1983).
4. J. J. Zinck, P. D. Brewer, J. E. Jensen, G. L. Olson and L. W. Tutt, Appl. Phys. Lett. 52, 1434 (1988).
5. W. L. Ahlgren, S. M. Johnson, W. J. Hamilton and S. Szilagyi, Mat. Res. Soc. Symp. these proceedings (1989).
6. T. Tung, M. H. Kalisher, A. P. Stevens, P. E. Herning, Mat. Res. Soc. Symp. Proc. 90, 321 (1987).
7. C. G. Bethea, B. F. Levine, P.-Y. Lu, L. M. Williams and M. H. Ross, Appl. Phys. Lett. 53, 1629 (1988).
8. R. F. C Farrow, J. Vac. Sci. Technol. A 3, 60 (1985).
9. F. A. Ponce, G. B. Anderson and J. M. Ballingall, Surf. Sci. 168, 564 (1986).
10. A. J. Noreika, R. F. C. Farrow, F. A. Shirland, W. J. Takei, J. Gregg, Jr., S. Wood and W. J. Choyke, J. Vac. Sci. Technol. A 4, 2081 (1986).
11. F. A. Ponce, G. B. Anderson and J. M. Ballingall, Mat. Res. Soc. Symp. Proc. 90, 199 (1987).
12. J. Petruzzello, D. Olego, Sk. K. Ghandhi, N. R. Tasker and I. Bhat, Appl. Phys. Lett. 50, 1423 (1987).
13. P. D. Brown, J. E. Hails, G. J. Russell and J. Woods, J. Cryst. Growth 86, 511 (1988).
14. S. R. Glanvill, C. J. Rossouw, M. S. Kwietniak, G. N. Pain, T. Warminski and L.S. Warminski, J. Appl. Phys. 66, 619 (1989).
15. T. W. James and R. E. Stoller, Appl Phys Lett. 44, 56 (1984).
16. A. Nouruzi-Khorasani, I. P. Jones, P. S. Dobson, D. J. Williams and M. G. Astles, J. Cryst. Growth 96, 348 (1989).
17. S. M. Johnson, W. L. Ahlgren, M. H. Kalisher, W. J. Hamilton, Jr. and J. B. James, Mat. Res. Soc. Symp. Proc. these proceedings (1989).
18. S. M. Johnson, M. H. Kalisher, W. L. Ahlgren, J. B. James, C. A. Cockrum, submitted to Appl. Phys. Lett., (1989).

SOLUBILITY OF IMPURITIES AND DEFECT IMPURITY INTERACTION IN II-VI SEMICONDUCTORS

Y. MARFAING

Laboratoire de Physique des Solides de Bellevue,
C.N.R.S. - 92195 Meudon-Cedex, France

ABSTRACT

A description of incorporation and solubility limit of substitutional impurities is made using the alloy $\text{Cd}_x\text{Hg}_{1-x}\text{Te}$ as a model of analysis and a source of experimental data.

Then non-equilibrium incorporation of impurities under light excitation is considered. A model of photo assisted doping is presented which accounts for the high doping efficiency reported for the donor indium in photoassisted grown CdTe.

1. INTRODUCTION

Impurity doping of II-VI semiconductors poses particular problems : strong interaction of impurities with native defects often occurs leading to self-compensation phenomena ; moreover the solubility of electrically active impurities is in any case not very high, limited to a few 10^{18} cm^{-3} . This result is in contrast with impurity doping of Si or III-V compounds where active concentrations above 10^{19} cm^{-3} are commonly obtained.

In the past, the attention to these problems has mainly been focused on wide band gap II-VI compounds (ZnSe , ZnTe , CdS) for the reason that very severe self-compensation phenomena prevent the conversion of conductivity type in these materials. Theoretical models have been worked out based on the chemical and electrical relations which link impurities and native defects under the conditions of thermodynamic equilibrium [1] [2] [3]. They provide an interpretation of compensation effects in terms of lattice defect properties : energy of formation, electronic energy levels. As these quantities are not a priori known, comparison with experiments does not lead to firm and definite conclusions.

Another way of approach is to consider the low band gap materials - essentially the alloy $\text{Cd}_x\text{Hg}_{1-x}\text{Te}$ - for which a larger amount of data is available. Incorporation of impurities has been carried out in a wide range of temperature and mercury vapour pressure, either during growth (Bridgman, LPE, MOCVD, MBE) or in post-growth anneals. In the first part of this paper we will show that a detailed analysis of these results provides a general understanding of the solubility limits in II-VI materials, in terms of impurity-defect interaction.

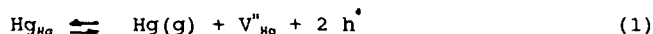
Putting the problem of effective solubility in this way leads to the idea of non-equilibrium incorporation, where the feedback between impurities and defects might be relaxed. Photoassisted doping could reach such a result according to experiments recently reported in the literature. We will present a simple model of incorporation of impurities during epitaxial growth under light excitation which is able to explain some of the observed effects. This could open up the way to more systematic studies aiming to dope reproducibly the reluctant wide band gap materials.

2. DEFECT IMPURITY INTERACTION IN $\text{Cd}_x\text{Hg}_{1-x}\text{Te}$ ALLOYS

Due to the large number of data available $\text{Cd}_x\text{Hg}_{1-x}\text{Te}$ is an exemplary medium for studying defect-impurity interaction. Through specific examples we will show how the defects first control the incorporation of impurities and second determine their (maximum) solubility.

2.1. Role of defects in undoped material

Mercury-rich $\text{Cd}_x\text{Hg}_{1-x}\text{Te}$ alloy ($x \leq 0.4$) is the best example, and perhaps the only one, of a II-VI material where the electrical conductivity is readily dependent upon the concentration of a simple native defect. This well known behaviour derives from solid-vapour equilibrium involving mercury vacancies in the solid. Using Kroger's notations [1].



The mercury vacancy V_{Hg}'' is supposed to be in a doubly ionized negatively charged state. Application of mass-action law leads to the defect concentration at the equilibration temperature (HT).

$$[\text{V}_{\text{Hg}}'']_{\text{HT}} = \frac{K_{\text{VH}}''}{P_{\text{HT}}^2 P_{\text{Hg}}} \quad (2)$$

If the semiconductor is extrinsic at HT, which is valid for $x = 0.4$, the hole concentration p_{HT} is equal to $2[\text{V}_{\text{Hg}}'']_{\text{HT}}$, so that the ionized vacancy concentration is given by :

$$[\text{V}_{\text{Hg}}'']_{\text{HT}} = \left(\frac{K_{\text{VH}}''}{4P_{\text{Hg}}} \right)^{1/3} \quad (3)$$

Assuming that this defect concentration is frozen in when quenching the material to room temperature, the hole concentration measured in a low temperature extrinsic state is :

$$p_{\text{LT}} = 2 [\text{V}_{\text{Hg}}'']_{\text{HT}} \sqrt[3]{P_{\text{Hg}}} \quad (4)$$

Such a dependence on the mercury vapour pressure has indeed been observed by Vydyanath et al [4] which gives a good evidence of the presence of doubly ionized mercury vacancies.

This simple defect model has been extended to different alloy compositions by the same authors and a number of others. As an example, Fig. 1 shows the phase limits for the widespread alloy $\text{Hg}_{0.8}\text{Cd}_{0.2}\text{Te}$ measured and calculated in a wide temperature range [5] : on the Te-saturated side as well as on the Hg-saturated one, the low temperature hole concentration is determined by the mercury vacancy concentration, according to the equation (4).

A questionable aspect is the assumption of complete defect freezing during cooling from the equilibration state. In wide band gap compounds, vacancy migration and annihilation are often postulated to explain the differences between the room

temperature state and the modelled or measured high temperature equilibration state [6] [7]. For instance it is known that excess zinc vacancies introduced in ZnSe by electron bombardment annihilate at 400 K by forming complexes with impurities and defects [8]. A better understanding of the particularly simple behaviour of $\text{Cd}_x\text{Hg}_{1-x}\text{Te}$ remains an open question.

2.2. Group V acceptors on Te sites.

We start by analysing the incorporation process under solid/liquid equilibrium, and first give some definitions. Let I_l designate the impurity in the liquid phase and I_s , I_nD_m , the impurity in the solid in the electrically active soluble form I_s or associated with defects D.

The distribution coefficient is defined as :

$$k_d = \frac{[I_s] + \sum [I_nD_m]}{[I_l]} \quad (5)$$

and can be determined from chemical analysis. The solubility coefficient is :

$$k_s = \frac{[I_s]}{[I_l]} \quad (6)$$

and can be reached from complementary electrical measurements. Finally the doping efficiency is given by :

$$\eta = \frac{[I_s]}{[I_s] + \sum [I_nD_m]} = \frac{k_s}{k_d} \quad (7)$$

The "solubility" of the impurity I is the maximum value of the concentration $[I_s]$. It depends on temperature and also vapour pressure. The last dependence is a particular feature of compounds compared to elementary semiconductors like silicon.

We now write the incorporation reaction of, to be specific, arsenic on Te sites.



$$[\text{As}_{\text{Te}}^{\times}] = K_l [V_{\text{Te}}^{\times}] \gamma_l [\text{As}(l)] \quad (9)$$

Eq. 9 comes from the application of the mass action law to (8). γ_l is the activity coefficient of As in the liquid phase and $\gamma_l [A_l]$ is the corresponding activity. To this basic incorporation reaction we add reactions describing :

- the exchange with the gas phase



$$[V_{\text{Te}}^{\times}] = K_{\text{VT}} P_{\text{Hg}} \quad (11)$$

- the ionization of the acceptor arsenic and of the tellurium vacancies supposed to be single donors :

$$p[As'_{Te}] = K_A [As^x_{Te}] \quad (12)$$

$$n[V_{Te}^{\bullet}] = K_D [V_{Te}^x] \quad (13)$$

- global electroneutrality and electron-hole equilibrium :

$$p + [V_{Te}^{\bullet}] = n + [As'_{Te}] + 2 [V_{Hg}^{\bullet}] \quad (14)$$

$$np = n_i^2 \quad (15)$$

$[V_{Hg}^{\bullet}]$ is given by (2) and n_i is the intrinsic carrier concentration. The system of equations (9), (11) - (15) can be solved to give the concentration of arsenic in solution $[As'_{Te}]$. A particular situation is that of high mercury pressure, which after (9) and (11) corresponds to a large incorporation rate. Then the concentration of mercury vacancies can be neglected and one get :

$$[As'_{Te}] = (K_1 P_{Hg} \gamma_i [As(l)]^{1/2} \left[\frac{1 + \frac{K_2 P_{Hg}}{n_i^2}}{1 + \frac{n_i^2}{K_1 P_{Hg} \gamma_i [As(l)]}} \right]^{1/2} \quad (16)$$

$$K_1 = K_l K_{VT} K_A \quad (17)$$

with

$$K_2 = K_D K_{VT}$$

In these conditions the low temperature hole concentration is given by :

$$p_{LT} = [As'_{Te}] - [V_{Te}^{\bullet}] \quad (18)$$

These theoretical expressions can be used to analyse the results of the doping experiments performed by Kalisher [9] on $Cd_{1-x}Hg_xTe$ ($0.2 < x < 0.4$) grown by LPE from a Hg melt. First, electrical measurements indicate a doping efficiency of one for arsenic concentrations in the solid up to a few 10^{17} cm^{-3} [10] (Fig. 2). From (18) this shows that the concentration of ionized tellurium vacancies is at least one order of magnitude smaller. Second, chemical analysis makes to appear a square root dependence of arsenic concentration in the solid versus arsenic concentration in the melt (Fig. 3).

Such a dependence is predicted by (16) if the material is extrinsic at the growth dependence ($x \approx 0.4$) and if γ_i is constant in the explored concentration range.

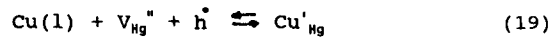
Fig. 3 also displays the results of Hall measurements performed on layers grown from a Te melt with phosphorus added in it [11]. These samples were given a post-growth anneal at 500°C under high mercury vapour pressure. The small solubility coefficient observed here has two origins : incorporation under conditions of high tellurium activity and consequently a low concentration of tellurium vacancies ; small values of the activity coefficient of phosphorus in Te melts.

Efficient incorporation of As and P has recently been reported in MOCVD grown CdTe and CdHgTe layers in the temperature range 350 - 410°C [12] [13].

The highest incorporation ratio is obtained under high Cd activity in accordance with (16) and a doping efficiency of unity was measured up to a concentration of a few 10^{17} cm^{-3} [13].

2.3. Group I acceptors on metal sites.

We refer here to the incorporation of copper from a liquid Te melt as recently studied by Sarusi et al [14]. The basic incorporation relations are directly written as :



$$[\text{Cu}'_{\text{Hg}}] = K_1 p \cdot [V_{\text{Hg}}''] \gamma_1 [\text{Cu}(1)] \quad (20)$$

and the neutrality equation at the growth temperature is :

$$p = [\text{Cu}'_{\text{Hg}}] + 2 [V_{\text{Hg}}''] + n \quad (21)$$

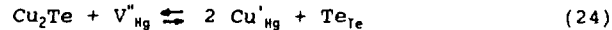
$$p = [\text{Cu}'_{\text{Hg}}] + \frac{2 K_{\text{VH}}''}{p^2 P_{\text{Hg}}} + \frac{n_i^2}{p} \quad (22)$$

Finally the low temperature hole concentration is :

$$p_{\text{LT}} = [\text{Cu}'_{\text{Hg}}] + 2 [V_{\text{Hg}}''] \quad (23)$$

Since the quantities K_{VH}'' and n_i^2 are known [5] the system of equations (20), (22), (23) can be solved to predict the dependence of p_{LT} on the product $K_1 \gamma_1 [\text{Cu}(1)]$, proportional to the activity of Cu in Te melt (Fig. 4). This is to be compared with the experimental results of [14] reproduced in Fig. 5. The trend is similar but the measurements show a steeper dependence of p_{LT} as a function of the copper concentration in the melt, which could be due to a variation of the activity coefficient

γ_1 . Also a limit hole concentration appears which decreases after annealing under Hg saturated conditions. These saturation values correspond to the solubility limits for the conditions used in this work. We analyse the attainment of the solubility limit by postulating that some internal equilibrium exists with a precipitated second phase. Assuming that this second phase is Cu_2Te , we write :



$$[\text{Cu}'_{\text{Hg}}]^2_L = K_p [V_{\text{Hg}}''] a_{\text{Cu}_2\text{Te}} \quad (25)$$

where $a_{\text{Cu}_2\text{Te}}$ is the activity of Cu_2Te in the solid.

Introducing (2) and the neutrality equation $p = [\text{Cu}'_{\text{Hg}}]$ valid at high copper concentration we get :

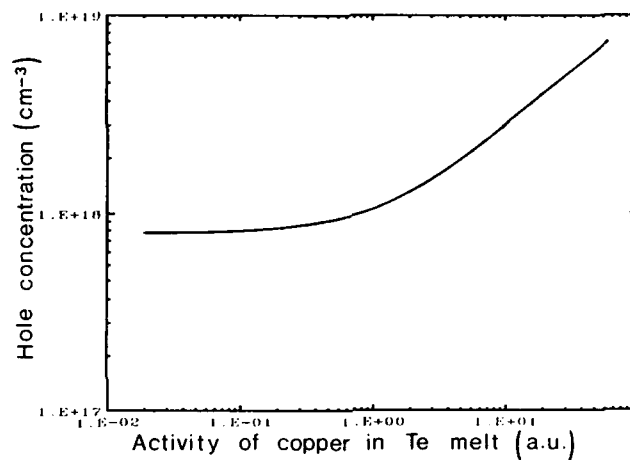


Fig. 4 Theoretical variation of hole concentration (77 K) in $\text{Cd}_{0.2}\text{Hg}_{0.8}\text{Te}$ layers versus copper activity in Te-rich growth solution.

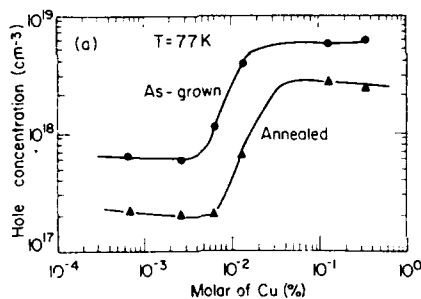


Fig. 5 Experimental hole concentration in $\text{Cd}_{0.2}\text{Hg}_{0.8}\text{Te}$ layers versus copper concentration in Te-rich growth solution [14].

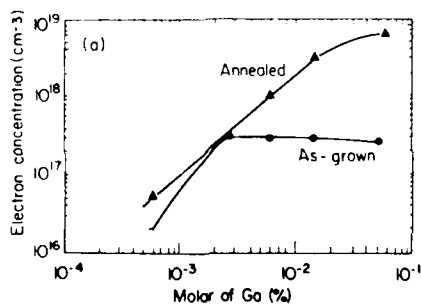


Fig. 6 Electron concentration in $\text{Cd}_{0.2}\text{Hg}_{0.8}\text{Te}$ layers versus gallium concentration in Te-rich growth solution [14].

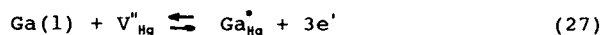
$$p_{LT} = [Cu'_{Hg}]_L = \left[\frac{K_p K''_{vH} a_{Cu_2Te}}{P_{Hg}} \right]^{1/4} \quad (26)$$

If Cu_2Te really forms a precipitated second phase the corresponding activity is unity and $[Cu'_{Hg}]$ depends only on temperature and vapour pressure. This predicted dependence of copper solubility upon mercury vapour pressure is in rough quantitative agreement with that observed in Fig. 5.

2.4. Group III donors on metal sites.

We consider first the case of incorporation from a melt, taking Ga as a specific donor impurity.

The incorporation reactions are now :



$$[Ga'_{Hg}] = \frac{K_1 [V''_{Hg}] \gamma_1 [Ga(1)]}{n^3} \quad (28)$$

and the neutrality equation is :

$$n + 2 [V''_{Hg}] = p + [Ga'_{Hg}] \quad (29)$$

At low temperature this relation reduces to :

$$n_{LT} = [Ga'_{Hg}] - 2 [V''_{Hg}] \quad (30)$$

As in the case of copper incorporation it is possible to solve the system of equations (28) - (30) to get n_{LT} as a function of the product $K_1 \gamma_1 [Ga(1)]$. For incorporation under a high mercury vapour pressure the concentration of ionized mercury vacancy is negligible and the solution is :

$$n_{LT} = [Ga'_{Hg}] = \frac{K_3 [Ga(1)] \gamma_1 / P_{Hg}}{[n_i^2 + K_3 [Ga(1)] \gamma_1 / P_{Hg}]}^{1/2} \quad (31)$$

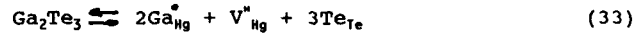
with

$$K_3 = K_1 K''_{vH} / n_i^4 \quad (32)$$

Using liquid phase epitaxy from a Hg melt which corresponds to the above conditions, Kalisher [9] has determined distribution coefficients above unity for Ga and In (Fig. 3). This points out that the activity coefficients of these elements in mercury melt is indeed large. A doping efficiency of 100 % is measured for In concentration up to 10^{17} cm^{-3} [15].

Incorporation of Ga from a Te melt has recently been reported by Sarusi et al [14]. Fig. 6 shows that a solubility limit of $2 \cdot 10^{17} \text{ cm}^{-3}$ appears in the as-grown material.

This phenomenon can be explained in the same framework as above by postulating the presence of a precipitated second phase such as Ga_2Te_3 . Internal equilibrium is expressed by :



$$[\text{Ga}_{\text{Hg}}^{\bullet}]^2_L = \frac{K_p n_i^4}{K_{\text{VH}}^{\prime\prime} n^2} P_{\text{Hg}} a_{\text{Ga}_2\text{Te}_3} \quad (34)$$

introducing the activity of the second phase $a_{\text{Ga}_2\text{Te}_3}$.

This material is intrinsic at the growth temperature so that $n = n_i$. One deduces the low temperature electron concentration :

$$n_{\text{LT}} = [\text{Ga}_{\text{Hg}}^{\bullet}] - 2[\text{V}_{\text{Hg}}^{\prime\prime}] \quad (35)$$

$$n_{\text{LT}} = \left(\frac{K_p n_i^2}{K_{\text{VH}}^{\prime\prime}} P_{\text{Hg}} a_{\text{Ga}_2\text{Te}_3} \right)^{1/2} - \frac{2 K_{\text{VH}}^{\prime\prime}}{P_{\text{Hg}} n_i^2} \quad (36)$$

Since $a_{\text{Ga}_2\text{Te}_3} = 1$ for a precipitated second phase the solubility limit only depends on temperature and pressure. The above expression shows that n_{LT} increases with increasing P_{Hg} as it is observed in Fig. 6 for the sample annealed under saturated mercury pressure.

Incorporation of indium from a Te melt in the Cd-rich alloy $\text{Cd}_{0.7}\text{Hg}_{0.3}\text{Te}$ was studied by Lusson [16]. The results presented in Fig. 7 clearly show the difference between distribution and solubility coefficients. The distribution coefficient is large, around unity, and constant in the investigated concentration range, while the electron concentration, which is a measure of $[\text{In}_{\text{Cd}}]$ is small and increases very slowly with increasing indium activity in the melt.

The donor indium is also commonly used as a dopant in vapour phase epitaxy. An electron concentration saturating at 10^{17} cm^{-3} has been measured for CdTe grown by OMCVD at 420°C [17]. The lack of data does not allow to attribute this saturation to a solubility limit or to a limiting transfer of indium from the gas phase. More detailed results were reported for $\text{Cd}_x\text{Hg}_{1-x}\text{Te}$ ($0.2 < x < 0.3$) grown by MBE at 200°C and doped with indium during growth [18]. Fig. 8 gives the measured low temperature electron concentration versus the indium concentration in the solid, after the results of this work.

This curve is interesting because it shows the approach to the solubility limit. This variation was modeled in [19] by assuming the presence of two indium related species : In and In_2Te_3^x . A more detailed analysis is given below. Internal equilibrium can be described by an equation similar to (34) :

$$[\text{In}^{\bullet}]^2 = \frac{K}{n^2} \gamma [\text{In}_2\text{Te}_3^x] \quad (37)$$

where γ is the activity coefficient of the species (In_2Te_3) and the reaction constant K depends on temperature and mercury vapour pressure only. The electroneutrality and mass conservation relations are :

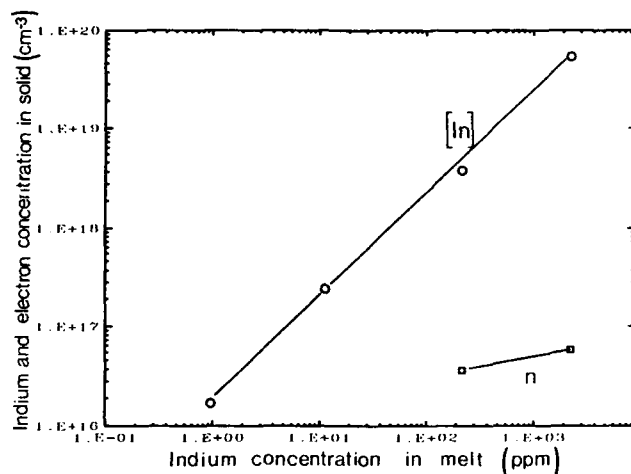


Fig. 7 Indium and electron concentration in $\text{Cd}_{0.7}\text{Hg}_{0.3}\text{Te}$ layers versus indium concentration in Te-rich growth solution [16].

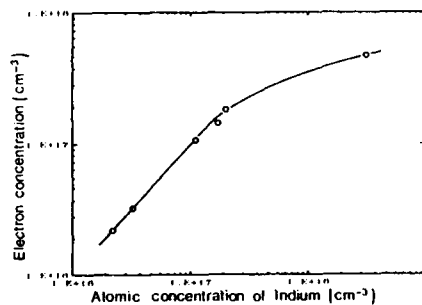


Fig. 8 Electron concentration at 77 K versus indium concentration in CdHgTe layers grown by MBE [18].

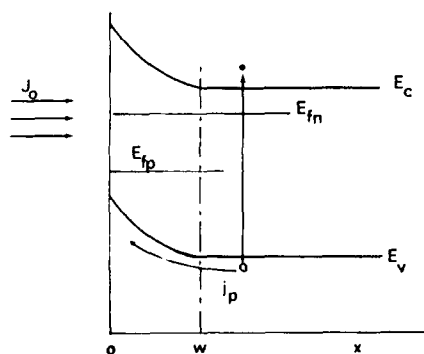


Fig. 9 Surface energy band diagram and photoelectronic processes considered for the model of photoassisted doping.

$$n = [In^{\bullet}] - [2V_{Hg}^{\bullet}] - p \quad (38)$$

$$[In_T] = [In^{\bullet}] + 2 [In_2Te_3^x] \quad (39)$$

(In_T) is the total concentration of indium in the solid. It can be shown that the concentration of mercury vacancies is negligible in (38). Hence the low temperature electron concentration is simply :

$$n_{LT} = [In^{\bullet}] \quad (40)$$

Solving this system of equations gives n_{LT} as a function of $[In_T]$. A fit to the experimental variation can be obtained with $K = 4.5 \cdot 10^{53} \text{ cm}^{-9}$ and an activity coefficient γ decreasing from 1 to 0.12 when $[In_2Te_3]$ increases in the range $10^{16} - 4 \cdot 10^{18} \text{ cm}^{-3}$. A variable activity coefficient means that the solution between In_2Te_3 and $Cd_{x-1}Hg_xTe$ is non ideal. Precipitation of In_2Te_3 and attainment of the solubility limit would be observed at higher indium concentrations.

3. PHOTOASSISTED DOPING

Recent reports on efficient doping of CdTe films grown by photoassisted MBE have raised a strong interest [20] [21]. In these experiments indium, antimony or arsenic were incorporated from effusion sources during growth while the substrate was illuminated using an argon ion laser (514 - 528 nm). The laser power density at the substrate was around 150 mW/cm^2 . These first announcements were followed by others dealing with CdTe [22] and the higher band gap compounds ZnSe [23] and ZnS [24].

All these experiments show that impurity doping is enhanced under light excitation, which could originate in enhanced impurity incorporation, increased doping efficiency or both. In the following we present a model able to account for one aspect : the photoenhanced doping efficiency. Specifically we consider the case of CdTe doped with indium during MBE growth [20]. Without illumination the as-grown films are reported to be semi-insulating with a photoluminescence spectrum dominated by a broad band centered at about 1.44 eV. This band is always observed in compensated crystals and is associated with In-defect complexes [25]. Thus In is indeed incorporated in the films. The compensation of indium can be described by a chain of reactions:



Basically there is a transfer of electrons from the indium donors to the cadmium vacancies. The complex $(In_{Cd}V_{Cd})^{\bullet}$ is believed to be a deep acceptor compensating the shallow donor In_{Cd}^{\bullet} .

The electron transfer can be described by the following rate equation :

$$\frac{\partial n_t}{\partial t} = \alpha_n n p_t - \alpha_n n_1 n_t \quad (42)$$

n is the free electron concentration coming from the ionized donors. n_t and p_t are the concentrations of electrons and holes trapped on the vacancy level E_t . n_1 is related to this energy level by the usual expression :

$$n_i = N_c \exp [-(E_c - E_i)/kT] \quad (43)$$

where N_c is the density of states in the conduction band of minimum energy E_c . α_n is the capture coefficient for electrons. For the sake of simplicity we assume now that the vacancy has two charge states only, V_{cd}^x and V_{cd}' . Then $p_t = [V_{cd}^x]$. At thermodynamic equilibrium this quantity only depends on temperature and cadmium vapour pressure :

$$[V_{cd}^x] = K_{vc} / P_{cd} \quad (44)$$

At any time $n + n_i = N_0$, the concentration of incorporated donors. The asymptotic ($t \rightarrow \infty$) solution of (42) is

$$n_t = \frac{N_0 p_t}{n_i + p_t} \quad (45)$$

Taking $E_c - E_i = 0.85$ eV, we have $n_i = 10^9$ cm⁻³. p_t is not known and is probably not given by equilibrium thermodynamics (44). However if $p_t > n_i$ we get $n_t \approx N_0$; which describes the state of compensation between donors and cadmium vacancies. Note that self-compensation occurs because there is a continuous supply of cadmium vacancies in order to keep constant the neutral fraction p_t . We now consider the film growing under light illumination with a flux of photons J_0 . Fig. 9 represents the electronic processes occurring near the growing surface. A surface potential barrier is present due to the Fermi level pinning in the gap. Photogenerated holes diffuse to the barrier and are accelerated towards the surface. The rate equation (42) now becomes :

$$\frac{\partial n_t}{\partial t} = \alpha_n n p_t - \alpha_n n_i n_t - \alpha_p n_t \Delta p + \alpha_p p_t p_i \quad (46)$$

where Δp is the concentration of excess holes at the surface and α_p is the capture coefficient of holes. p_i is given by :

$$p_i = N_v \exp [-(E_i - E_v)/kT] \quad (47)$$

where N_v is the density of states in the valence band of maximum energy E_v . In steady state we now have :

$$n_t = \frac{\alpha_n N_0 p_t + \alpha_p p_i p_t}{\alpha_n (p_t + n_i) + \alpha_p \Delta p} \approx \frac{N_0}{\left(1 + \frac{\alpha_p \Delta p}{\alpha_n p_t}\right)} \quad (48)$$

Δp is evaluated by solving the continuity equation of photogenerated holes with appropriate boundary conditions. This is a classical treatment which leads to the condition of current continuity at the surface :

$$q S_p \Delta p = i_{ph} - q \frac{D_p}{L_p} \cdot \Delta p (w) \quad (49)$$

The right hand term proportional to the recombination velocity S_p is the current due to surface recombination. i_{ph} is the short circuit photocurrent of the barrier.

$$i_{ph} = q J_0 (1 - R) \left[1 - \frac{\exp(-\alpha w)}{\alpha L_p + 1} \right] \quad (50)$$

where R and α are the coefficients of reflexion and absorption. D_p and L_p are the diffusion constant and diffusion length of holes in the bulk. The concentration of holes Δp and $\Delta p(w)$ on both sides of the space charge layer are related to each other by assuming that the quasi-Fermi level of holes is constant through the barrier. The solution can be put in two limiting forms. When $S_p \geq D_p/L_p$.

$$\Delta p = i_{ph}/qS_p \quad (51)$$

and when $S_p \ll D_p/L_p$

$$\Delta p = \left(\frac{i_{ph} L_p n_b}{q D_p} \right)^{1/2} \quad (52)$$

where n_b is the bulk electron concentration.

Introducing the values : $i_{ph} = 3 \times 10^{-2} \text{ A.cm}^{-2}$ (corresponding to 150 mWcm^{-2} illumination), $S_p = 10^4 \text{ cm s}^{-1}$, $L_p = 5 \cdot 10^{-5} \text{ cm}$, $D_p = 0.4 \text{ cm}^2 \text{ s}^{-1}$, $n_b = 10^{17} \text{ cm}^{-3}$, we estimate the variation range of p

$$2 \cdot 10^{13} \text{ cm}^{-3} < \Delta p < 10^{15} \text{ cm}^{-3} \quad (53)$$

As the ratio $\Delta p/p_i$ is much larger than unity (perhaps between 10 and 10^3) the relation (48) shows that the concentration of ionized vacancies has been reduced well below N_D . As a result the incorporated donors are not or only slightly compensated leading to a high doping efficiency as it was observed. More generally it is seen that such a photochemical process causes a decrease of the total concentration of vacancies, which could also improve the crystalline quality of the epitaxial layers.

4. CONCLUSIONS.

It has been shown how native defects control the incorporation and solubility of substitutional impurities in low band gap $\text{Cd}_{1-x}\text{Hg}_x\text{Te}$ alloys. Near the solubility limit impurities and vacancies interact to form complex defects which ultimately precipitate as a second phase in the lattice. This process is well exemplified in the case of cation-substituted impurities where mercury vacancies are involved. These findings could be generalized to wider band gap II-VI compounds.

Thus the control of defect impurity interaction is a determining factor to obtain a large solubility and consequently a high doping efficiency. In this respect photoassisted doping appears to be a promising technique. A model of interpretation has been presented which is based on the neutralization of

vacancies by photogenerated carriers drifting towards the growing surface. As this area of photoassisted doping and growth is developing new results will soon appear which will allow us to refine and extend the simple proposed model.

5. REFERENCES.

- [1] F.A. Kröger and H.J. Vink in Solid State Physics, edited by F. Seitz and D. Turnbull (Academic Press Inc, New York, 1956), p. 310.
- [2] G. Mandel, Phys. Rev. **134 A**, 1073 (1964).
- [3] Y. Marfaing, Progress in Crystal Growth and Characterization, **4**, 317 (1981).
- [4] H.R. Vydyanath, J.C. Donovan and D.A. Nelson, J. Electrochem. Soc. **128**, 2625 (1981).
- [5] H.R. Vydyanath and C.H. Hiner, J. Appl. Phys. **65**, 3080 (1989).
- [6] S.S. Chern, H.R. Vydyanath and F.A. Kröger, J. Solid State Chem. **14**, 33 (1975).
- [7] J.C. Pfister, Revue Phys. Appl. **15**, 707 (1980).
- [8] G.D. Watkins, in Radiation Effects in Semiconductors, edited by N.B. Urli and J.W. Corbett (Inst. Phys. Conf. Ser. n° 31, London 1977) p. 95.
- [9] M.H. Kalisher, J. Crystal Growth, **70**, 365 (1984).
- [10] T. Tung, J. Crystal Growth, **86**, 161 (1988).
- [11] H.R. Vydyanath, J.A. Ellsworth and C.M. Devaney, J. Electron. Mater., **16**, 13 (1987).
- [12] S.K. Ghandhi, N.R. Taskar and I.B. Bhat, Appl. Phys. Lett. **50**, 900 (1987). S.K. Ghandhi, N.R. Taskar, K.K. Parat, D. Terry and J.B. Bhat, Appl. Phys. Lett. **53**, 1641 (1988).
- [13] P. Capper, P.A.C. Whiffin, B.C. Easton, C.D. Maxey and I. Kenworthy, Mater. Letters, **6**, 365 (1988).
- [14] G. Sarusi, A. Zemel, D. Eger and Y. Shapira, J. Appl. Phys. **65**, 672 (1989).
- [15] L.E. Lapidés, R.L. Whitney and C.A. Crasson, Mat. Res. Soc. Symp. **48** (Materials Research Society, Pittsburg, PA 1985), p. 365.
- [16] A. Lusson, Doctorate thesis, Paris VI University, 1987.
- [17] N.R. Taskar, V. Natarajan, I.B. Bhat and S.K. Ghandhi, J. Crystal Growth, **86**, 228 (1988).
- [18] M. Boukerche, J. Reno, I.K. Sou, C. Hsu and J.P. Faurie, Appl. Phys. Lett. **48**, 1733 (1986).
- [19] M. Boukerche, S. Sivananthan, P.S. Wijewarnasuriya, I.K. Sou and J.P. Faurie, J. Vac. Sci. Technol. **A7**, 311 (1989).
- [20] R.N. Bicknell, N.C. Giles and J.F. Schetzina, Appl. Phys. Lett. **49**, 1095 (1986).
- [21] R.L. Harper, Jr, S. Hwang, N.C. Giles, J.F. Schetzina, D.L. Dreifus and T.H. Myers, Appl. Phys. Lett. **54**, 170 (1989).
- [22] R.N. Bicknell-Tassius, presented at the 4th Int. Conf. on II-VI Compounds, Berlin, Sept. 1989.
- [23] S. Fujita, A. Tanabe, T. Kiroshita and S. Fujita, presented at the 4th Int. Conf. on II-VI Compounds, Berlin, Sept. 1989.
- [24] Z. Kawazu, T. Ohno and T. Taguchi, presented at the 4th Int. Conf. on II-VI Compounds, Berlin, Sept. 1989.
- [25] C.B. Norris and K.R. Zanio, J. Appl. Phys. **53**, 6347 (1982).

THICKNESS MEASUREMENT OF THIN FILMS BY X-RAY ABSORPTION
 J. CHAUDHURI AND S. SHAH
 The Wichita State university, Wichita, KS 67208

ABSTRACT

An x-ray diffraction method is described for determining thicknesses of thin films grown on single crystal substrates. The equations, based on the kinematical theory of x-ray diffraction and the mosaic crystal model, were developed. The thickness of the thin film was computed from the absorption of the integrated diffracted x-ray intensity from the single crystal substrate by the film. Since the diffracted intensity from the film is not required, the film does not have to be single crystal in nature. Thus, thicknesses of less ordered, polycrystalline or even amorphous films can be measured with high precision by this technique.

INTRODUCTION

A substantial amount of current research activity in materials is focused on thin films. It is desirable to know thicknesses precisely to assist in the investigation of growth and kinetics of these films. X-ray diffraction offers a simple and nondestructive means to measure thicknesses. Coulman et al attempted to determine film thicknesses by an x-ray diffraction technique but could not provide an absolute value of thickness [1].

In the previous study, a simple x-ray diffraction method was utilized to determine thicknesses of thin films from the ratio of the integrated diffracted intensities from the film to the substrate [2]. Thus, it was not necessary to measure the direct beam intensity. This method works very well when thin films are single crystal in nature and are of extremely good quality. Often, grown films are less ordered or have polycrystalline or amorphous structure. Thus the diffracted intensity from the film can not be used.

In the present study, thicknesses of thin films, grown on single crystal substrates, were determined from the attenuation of the integrated diffracted intensity due to double traverses through the film. The kinematical expression for the integrated diffracted intensity was corrected for the curvature effect which arises due to the deposition of the film and, also for the primary and secondary extinction effects by assuming a mosaic crystal model [3]. A comparison of these x-ray measurements was made with reflection high-energy electron diffraction (i. e. RHEED) data to demonstrate the extreme usefulness of this x-ray technique.

As it well explained by Zachariasen as well as Guinier, among others, the reflecting power of a real crystal is in between that of an ideally imperfect crystal and a perfect crystal [3,4]. Thus, to account for the reflecting power of a real crystal, the mosaic structure model was first proposed by Darwin [5]. This model assumes that either the atoms are arranged in layers which are not quite parallel, or they are arranged in blocks, each block being itself an ideal crystal, but with adjacent blocks not accurately fitted together.

Extinction in a mosaic crystal structure is a power loss in

an x-ray beam that is caused by the production of a diffracted beam. The extinction within any one ideal crystal block is called primary extinction. The power loss due to diffraction in the blocks that are traversed by the incident x-ray beam before it reaches the particular block under consideration is referred to as secondary extinction.

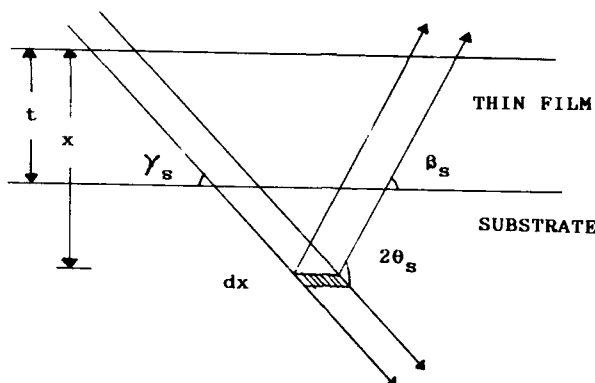


Figure 1. Bragg Case X-Ray Diffraction from the Substrate Underlying the Film.

THICKNESS CALCULATION

Figure 1 shows the Bragg case x-ray diffraction from the substrate. The attenuation of the incident and the diffracted beam by the film is

$$\exp - \mu_f t (1/\sin \gamma_s + 1/\sin \beta_s) \quad (1)$$

where t is the thickness of the film, μ_f is the mass absorption coefficient of the film, γ_s is the angle between the incident beam and the substrate and β_s is the angle between the diffracted beam and the substrate. Then, the kinematic integrated diffracted intensity from the substrate is [6]

$$I_s = \left(\frac{e^2}{mc^2} \right)^2 \frac{I_0 |F_s|^2 \lambda^3}{\sin \gamma_s v_s^2} \frac{1 + \cos^2 2\theta_s}{2 \sin 2\theta_s} \exp - \mu_f t (1/\sin \gamma_s + 1/\sin \beta_s)$$

$$\int_{x=0}^{x=\infty} \exp - \mu_s x (1/\sin \gamma_s + 1/\sin \beta_s) dx, \quad (2)$$

where e^2/mc^2 is the classical electron radius, I_0 is the incident x-ray intensity, F_s is the structure factor for the substrate, v_s is the unit cell volume of the substrate, μ_s is the mass absorption coefficient of the substrate and θ_s is the Bragg angle

for the substrate. After integration, equation (2) becomes

$$I_s = \left(\frac{e^2}{mc^2}\right)^2 \frac{I_0 |F_s|^2 \lambda^3}{\sin^2 \theta_s} \frac{1 + \cos^2 2\theta_s}{2 \sin 2\theta_s} \frac{e^{-\mu_f \alpha_s t}}{\mu_s \alpha_s}, \quad (3)$$

where

$$\alpha_s = \frac{1}{\sin \gamma_s} + \frac{1}{\sin \delta_s}$$

Applying the primary extinction correction of a mosaic crystal model, the integrated reflected intensity, I^P , can be written as shown by Zachariasen [3]

$$I^P = I f(A), \quad (4)$$

where I is the kinematic diffracted intensity, and the Bragg case primary extinction correction is

$$f(A) = \frac{\tanh A + \cos 2\theta_s \tanh |A \cos 2\theta_s|}{A(1 + \cos^2 2\theta_s)}, \quad (5)$$

where

$$A = \frac{e^2}{mc^2} \frac{|F| \lambda t}{v \sin \theta_s} \frac{1 + \cos 2\theta_s}{2}, \quad (6)$$

The secondary extinction correction of a mosaic crystal model is applied by replacing the mass absorption coefficient of the substrate, μ_s , by $\mu_s + g_s Q_s$ in the expression for the integrated reflected intensity [3]. Here

$$Q_s = \left(\frac{e^2}{mc^2}\right)^2 |F|^2 \frac{\lambda^3}{v^2} \frac{1 + \cos^2 2\theta_s}{2 \sin 2\theta_s}, \quad (7)$$

and

$$g_s = \frac{1}{2\eta/\pi}, \quad (8)$$

where η is the standard deviation of the block tilts in the mosaic crystal model. After applying the appropriate primary and secondary extinction corrections, the expression for the integrated diffracted intensity from the substrate becomes

$$I_s = \left(\frac{e^2}{mc^2} \right)^2 \frac{I_0 f(\lambda_f) |F_s|^2 \lambda^3}{\sin \gamma_s v_s^2} \frac{1 + \cos^2 2\theta_s}{2 \sin 2\theta_s} \frac{e^{-\mu_f \alpha_s t}}{(\mu_s + g_s Q_s) \alpha_s}, \quad (9)$$

If the direct beam intensity, I_0 , and the integrated diffracted beam intensity from the substrate, I_s , are known, the thickness of the thin film can be computed.

APPLICATION

As an illustration of the application of the method, thicknesses of AlGaAs thin films on GaAs substrates (001) were determined. These films were grown by molecular beam epitaxy. The integrated reflected intensities from the substrates were measured by utilizing a Blake Industries double crystal diffractometer in the (+,-) parallel setting [3]. A perfect crystal of germanium (001) was used as the first crystal. The rocking curves of (004) reflection were measured by using $\text{CuK}\alpha_1$ radiation. The direct beam intensity, I_0 , was obtained by multiplying the direct beam in counts per second with the total time through which the samples were rotated to get the integrated diffracted intensity. For best results, the system was calibrated for a film of known thickness, 2μ . I_s/I_0 values for three samples are listed in Table I.

TABLE I. Intensity Ratios, I_s/I_0 , and Thickness Values, t , of AlGaAs Thin Films.

SAMPLE NO.	I_s/I_0	t (μm)		% DIFFERENCE
		X-RAY	RHEED	
1	.00004244	0.48	0.5	4
2	.00004032	1.57	1.6	2
3	.00003287	3.33	3.5	2

The structure factor of GaAs was calculated using appropriate atomic scattering factors and dispersion corrections [7]. Figure 2 shows the dependence of the Bragg case primary extinction coefficient $f(\lambda)$ of GaAs, on the block thickness in the mosaic crystal model. In the present study, $f(\lambda)$ corresponding to $2\mu\text{m}$ block thickness of GaAs was considered. The secondary extinction correction was applied considering standard deviations in block tilts, η , as equal to the full width at half maximum of the x-ray rocking curves. The values are approximately 10 arc secs but varied from sample to sample. The correction for the curvature was added (Table II) by getting data from another set of experiment in which a GaAs crystal was bent in cantilever mode to different curvatures and the corresponding integrated diffracted intensity for the (004) reflection was obtained each time. Thicknesses for three samples, as calculated are listed in Table I. An attempt was made to compare the results obtained from x-ray measurement with RHEED oscillation [8-10] data as shown in Table I. There was excellent agreement between the results from these two different methods, with the percentage

difference being less than 4%.

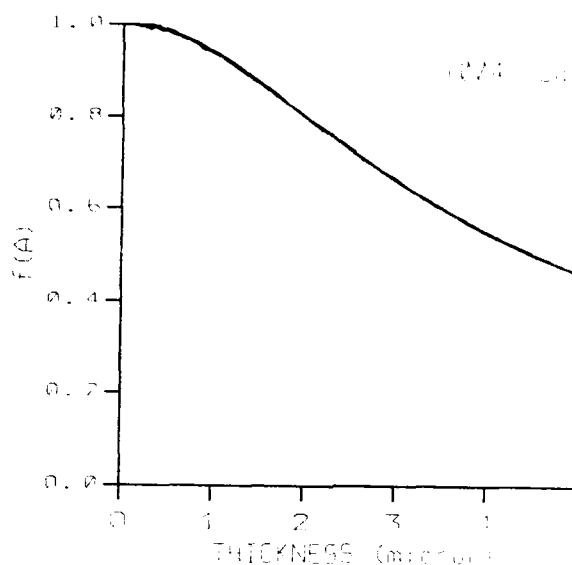


Figure 2. Dependence of Bragg Case Primary Extinction Coefficient of GaAs on the Block Thickness in the Mosaic Model.

Thickness values as calculated, without any extinction corrections or curvature corrections, are shown in Table II. It can be seen that, for this system, the effect of curvature correction is quite small and the extinction corrections play an important role. Nevertheless, there could be errors in the determination of thickness values when there are no particular reasons for expecting either of the correction factors to be negligible.

TABLE II. Radius of Curvature, R, Curvature Correction, Thickness Values without the Extinction Corrections or Curvature Correction.

SAMPLE NO.	R (m)	CURVATURE CORR.	t (μ m)	
			WITHOUT CURV. CORR.	WITHOUT EXTINC. CORR.
1	100	1.00	.48	1.095
2	20	1.07	1.65	1.72
3	14	1.11	3.60	3.01

CONCLUSIONS

An x-ray method was described for determining the thicknesses of thin films grown on crystalline substrates. This method is highly sensitive, rapidly performed, repeatable, nondestructive and inexpensive, and does not need any sample preparation. The technique utilizes the ratio of the integrated diffracted intensity from the substrate to the direct beam intensity. Since the diffracted intensity from the film is not needed, thicknesses of films not highly perfect in nature or thicknesses of polycrystalline or amorphous films can be determined by this method. X-ray results were in excellent agreement with RHEED oscillation data. Applications of primary and secondary extinction corrections of a mosaic crystal model and effect of curvature were found to be extremely useful in determining the correct thickness. It was anticipated that the results could be further improved using a weaker reflection or a shorter wavelength, since the extinction corrections tend to become negligible in either case.

ACKNOWLEDGMENT

Authors were thankful to Dr. J. P. Harbison at Bellcore, NJ for providing samples and the RHEED oscillation data. This work was supported in part by the National Science Foundation, NSF Grant #DMR-8605564.

REFERENCES

1. B. Coulman, H. Chen and L. E. Rehn, *J. Appl. Phys.* **57** (2), 643 (1985).
2. J. Chaudhuri, S. Shah and J. P. Harbison, *J. Appl. Physics* (to be published in Nov. 15, 1989).
3. W. H. Zachariasen, Theory of X-Ray Diffraction in Crystals (John Wiley and Sons, Inc., New York, 1945), pp. 147-175.
4. A. Guinier, X-Ray Diffraction in Crystals, Imperfect Crystals and Amorphous Bodies (Freeman, San Francisco, 1963) pp. 97-119.
5. C. G. Darwin, *Philos. Mag.*, **27**, 315 (1914), **27**, 657 (1914), **43**, 800, 1922.
6. B. D. Cullity, Elements of X-Ray Diffraction (Addison-Wesley Publ. Co., Inc., Reading, Massachusetts, 1978), pp. 133-135.
7. J. A. Ibers and W.C. Hamilton, eds., International Tables for X-Ray Crystallography, Vol IV (Kynock, Birmingham, 1974).
8. J. J. Harris, B. A. Joyce, and P. J. Dobson, *Surf. Sci.* **103** (1), L90 (1981).
9. J. H. Neave, B. A. Joyce, P. J. Dobson, and N. Norton, *Appl. Phys.* **A31**, 1 (1983).
10. J. P. Harbison, D. E. Aspnes, A. A. Studna, L. T. Florez, and M. K. Kelly, *Apple Phys. Lett.* **52** (24), 2046 (1988).

PART III

Doping of II-VI Materials

MOCVD GROWTH AND DOPING OF ZnSe AND RELATED II-VI MATERIALS

HIROSHI KUKIMOTO

Imaging Science and Engineering Laboratory, Tokyo Institute of Technology, 4259 Nagatsuda, Midori-ku, Yokohama 227, Japan

ABSTRACT

Recent progress in metalorganic chemical vapor deposition (MOCVD) of wide bandgap II-VI materials, especially of ZnSe, ZnS and their alloys, is discussed with emphasis on the general principles for obtaining uniform and high quality epitaxial layers and the current major issue of impurity doping for achieving conductivity control. The surface morphology and crystalline quality can be improved by a suitable choice of source materials and by lattice-matching the epitaxial layer to the substrate. By using appropriate sources, high conductivity n-type epitaxial layers of ZnSe and ZnS doped with impurities from group III and VII of the periodic table have been successfully grown by low temperature MOCVD. We have also grown p-type ZnSe layers with carrier concentration ranging from low 10^{16} to high 10^{17} cm⁻³ using Li₃N as the dopant. Extensive studies are now focussed on the better p-type control. High purity source materials, appropriate p-type dopants and low temperature growth are important keys.

INTRODUCTION

Wide bandgap II-VI materials of ZnSe, ZnS and their alloys potentially offer optical devices operating in the short wavelength spectral region which cannot be covered by III-V materials other than nitrides. The II-VI devices expected along this line includes blue light-emitting diodes and short-wavelength (green to blue) lasers. The studies of these wide bandgap II-VI materials were extensively performed in the past, but encountered two major problems. One was the difficulty in growing high quality epitaxial layers on commercially available large-area substrates such as GaAs, GaP, InP and Si by the conventional techniques established for III-V epitaxial growth. Neither liquid phase epitaxy by using a variety of solvent metals nor conventional vapor phase epitaxy by using hydrogen carrier transport of constituent elements or by sublimation of compounds met a significant success, primarily owing to high vapor pressure of constituent elements (Zn, Se and S) at growth temperature. The other was the hardship of conductivity control by doping with donor and acceptor impurities due to so-called self-compensation which is typical of these wide bandgap materials. Upon doping with a donor impurity in ZnSe or ZnS for achieving n-type conductivity control, for example, a Zn-vacancy acting as an acceptor tends to be generated, resulting in charge compensation. Similarly, p-type conductivity control is hampered by the formation of S- or Se-vacancies which act as the donors compensating doped acceptor impurities.

Metalorganic chemical vapor deposition (MOCVD) has proven in recent years to be a very effective method for growing a variety of epitaxial layers of III-V materials and their devices. The versatility of MOCVD has already been suggested in the early pioneering work of Manasevit [1]. The application of MOCVD for the growth of ZnSe was first demonstrated by Stutius [2] in 1978. Since then, MOCVD growth of wide bandgap II-VI materials, especially of ZnSe, has been extensively studied in many research groups, and recently a significant progress has been made towards a solution to the problems mentioned above.

This paper is concerned with general principles for growing high quality epitaxial layers of ZnSe and related materials and the current major issue of impurity doping for achieving conductivity control, primarily based on the results obtained in our research group. In improving the surface morphology and crystalline quality of epitaxial layers it has been found that a suitable choice of source materials is essential. Further improvements can be obtained by lattice-matching the epitaxial layer to the substrate, which is a common principle for all epitaxial layers. The MOCVD features low-temperature and nonequilibrium growth, and is in principle capable of stoichiometry control by controlling vapor pressures of constituent elements. By taking advantage of these features and by using appropriate sources, n-type epitaxial layers of ZnSe and ZnS with sufficiently high carrier concentration can be successfully grown by low temperature MOCVD by doping impurities from group III and VII of the periodic table during growth. The growth of p-type ZnSe layers doped with Li and N has also become possible recently, but there remains the problem with reproducibility.

GENERAL GROWTH PRINCIPLES

Sources

Among wide bandgap II-VI compounds, ZnSe has been most extensively grown by using dialkylzinc (dimethyl or diethyl zinc; DMZn or DEZn) and hydrogen selenide (H_2Se) as source materials [2-8]. The source combination is quite analogous to that for growing GaAs, i.e., trialkyl gallium (trimethyl or triethyl gallium; TMGa or TEGa) and arsine (AsH_3). With these sources for the ZnSe growth, however, there was a serious problem; that is a premature reaction between these sources taking place even at room temperature. DMZn (or DEZn) and H_2Se introduced in a growth chamber easily react to form ZnSe-like powder, resulting in unwanted deposition on the chamber wall before they reach the substrate on which epitaxial layers are to be grown, as schematically shown in Fig. 1(a).

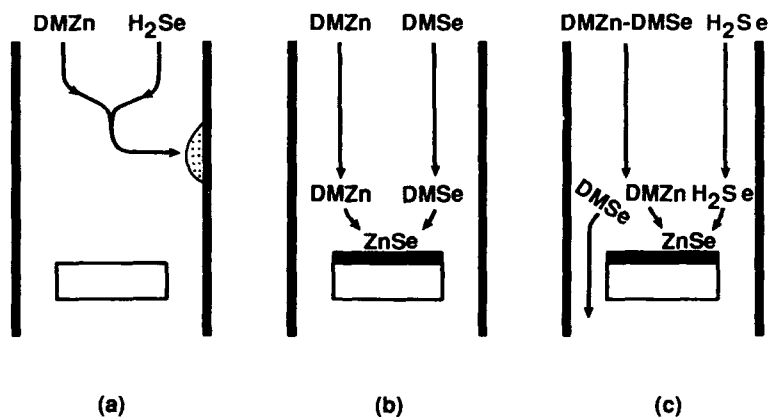


Fig. 1. Schematic illustration of the processes involved in MOCVD growth of ZnSe using different source combinations.

Such a reaction was reduced by introducing zinc alkyl just above the substrate surface in the low pressure reactor [2,7,8]. However, uniform growth in large area cannot be expected with this source transport configuration. A better source combination to eliminate the premature reaction is DMZn (or DEZn) and DMSe (or DESe) [9]. These sources can be transported effectively to the substrate, as shown in Fig.1(b), resulting in uniform growth of epitaxial layers with satisfactory surface morphology. With such alkyl zinc and alkyl selenide combinations (DMZn/DMSe, DMZn/DESe, DEZn/DMSe and DEZn/DESe), a mass-transport limited growth region, where the growth rate is temperature-independent above 500°C, and a surface kinetic limited growth region, where the growth rate changes exponentially with temperature below 500°C, have been clearly observed, indicating that the combinations are ideal. However, the temperature of mass-transport limited growth, which is related to the high decomposition temperature of dialkyl selenides, seems to be too high to overcome the self-compensation effect which prevents effective donor and acceptor doping. The growth temperature can be reduced to about 300°C by using Lewis acid-base adducts of dialkyl zinc with dialkyl selenide (DMZn-DMSe, DMZn-DESe, DEZn-DMSe and DEZn-DESe) and H_2Se , although the premature reaction is not completely eliminated with these source combinations. We believe that DMSe in the DMZn-DMSe adduct plays an important role in protecting DMZn from a premature reaction with H_2Se , and hence the source materials can be transported effectively onto the substrate, as shown in Fig. 1(c), resulting in a uniform growth throughout the substrate.

Similar arguments about source combination is also applicable to the growth of related materials, ZnS_xSe_{1-x} . ZnS epitaxial layers of high uniformity have been grown using an adduct of DEZn-DES and H_2S at temperature ranging from 250°C to 370°C [10], while using DEZn, DESe and DES epitaxial layers of ZnS_xSe_{1-x} have been successfully grown at 500°C [11,12].

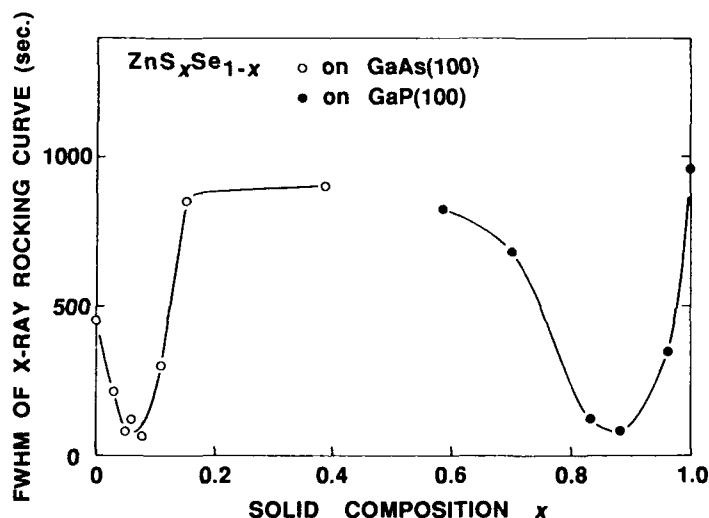


Fig. 2. Line width (full width at half maximum) of X-ray rocking curves as a function of composition x in ZnS_xSe_{1-x} epitaxial layers grown on GaAs (100) and GaP (100) substrates.

Lattice match

Further improvements in surface morphology and crystalline quality must rely on the lattice match between epilayers and substrates, as is the case with all kinds of epitaxial growth. The mismatches between ZnSe and GaAs and between ZnS and GaP are about 0.3% and 0.8%, respectively. ZnSe layers thinner than 0.15 μm grow coherently on GaAs substrates involving strains due to the lattice mismatch to the substrate, but thicker layers contain misfit dislocations introduced by the relaxation of strain [13]. A similar trend is observable for ZnS layers grown on GaAs and GaP substrates. However, there is an apparently unusual phenomenon that largely mismatched (4.3%) ZnS layers on GaAs show better surface morphology than less mismatched (0.8%) ZnS layers on GaP. This phenomenon has been ascribed to the strain relaxation taking place at an earlier stage of epitaxial growth on GaAs than on GaP [14].

$\text{ZnS}_x\text{Se}_{1-x}$ alloys are lattice matched to GaAs and GaP at $x = 0.06$ and $x = 0.83$, respectively. High crystalline quality of lattice matched layers grown using DEZn, DES, and DESe is evident from the surface morphology and the line width of double crystal X-ray diffraction which is shown in Fig. 2 [11,12].

IMPURITY DOPING

n-Type doping

Extensive studies of n-type impurity doping have been performed since the first work of Stutius [15], where Al was doped in ZnSe using triethylaluminum (TEAl) during growth. The doping elements studied include Al and Ga substituted on the Zn site of ZnSe lattice, and Cl, Br, and I substituted on the Se site. ZnSe layers of high n-type carrier concentration have been grown using dopant sources including TEAl [15], TEGa [16], octylchloride ($1-\text{C}_8\text{H}_{17}\text{Cl}$) [17], HCl [18], ethylbromide ($\text{C}_2\text{H}_5\text{Br}$) [19], ethyliodide ($\text{C}_2\text{H}_5\text{I}$) [20,21], and normal-butyliodide ($n-\text{C}_4\text{H}_9\text{I}$) [21]. The controllability of carrier concentration over a wide range from 10^{15} to 10^{19} cm^{-3} is noticed for the iodine doping.

ZnS layers of n type have also been successfully grown using TEAl [10] and HCl as dopants [22]. Recently, we have found that ethylbromide ($\text{C}_2\text{H}_5\text{Br}$) is also an appropriate dopant for obtaining ZnS layers with high carrier concentrations of mid 10^{18} cm^{-3} which show efficient blue photoluminescence at room temperature.

A general principle for obtaining high carrier concentration is to grow layers at low temperatures, typically below 350°C . The decrease of carrier concentrations in Al-doped ZnSe and ZnS layers with increasing growth temperature above 350°C is primarily due to the self-compensation, since the increase in self-activated photoluminescence (so called SA photoluminescence), which is ascribed to the donor (Al)-acceptor (Al-Zn vacancy complex) pair emission, is observable for such samples [10,23]. For halogen-doped layers, a decrease in impurity incorporation efficiency also takes place with increasing growth temperature, resulting in decrease of carrier concentration.

One should note here that the SA photoluminescence in MOCVD grown ZnSe is not completely eliminated at present for high carrier concentration samples. The SA photoluminescence of ZnSe is orange at room temperature, while band edge emission is blue. Therefore, it is very important to suppress the SA emission of ZnSe layers for its application to blue light-emitting devices. On the other hand, the high conductivity ZnS layers doped with n-type impurities generally exhibit efficient blue SA photoluminescence, which is favorable for its device application for blue LEDs.

p-Type doping

The impurities for p-type doping of ZnSe by MOCVD first noted were group V elements of N, P and As which are to be substituted on the Se site of the ZnSe lattice, presumably because their conventional sources of NH_3 , PH_3 and AsH_3 were available. Stutius grew ZnSe layers by MOCVD in the presence of NH_3 and PH_3 and found from photoluminescence that N acts as a shallow acceptor and P as a deep acceptor, but no direct proof of p-type behavior was obtained [24]. Okajima et al. suggested that As in the ZnSe layers grown using AsH_3 as a dopant forms both shallow and deep states [25]. Our samples of arsenic-doped ZnSe grown in a similar manner have only shown deep level photoluminescence.

We have paid attention to the fact that high quality epitaxial layers of wide bandgap materials are typically grown under high VI vapor pressure, e.g., VI/II flow ratio is larger than 10. Under this growth condition, high concentration doping with group V acceptors to be substituted on the Se site cannot be expected. Instead, group Ia elements which act as acceptors to be substituted on the Se site would be more effectively incorporated. By using Li_3N as the dopant, we have succeeded, for the first time, in growing p-type ZnSe with sufficiently high carrier concentrations ranging from low 10^{16} to high 10^{17} cm^{-3} [26]. The problems with this dopant are a reaction with H_2Se and its low vapor pressure. Therefore, we were forced to use the source combination of alkyl zinc and alkyl selenide instead of adduct and H_2Se at the expense of low growth temperature of the latter, and to locate the dopant at a part of the susceptor in the reactor. Typical substrate and dopant temperatures were 450°C and 400°C , respectively. This resulted in low controllability of carrier concentration. Low temperature photoluminescence of the samples suggests that N is also incorporated together with Li. We believe that Li and N co-doping is effective for obtaining high hole concentration and stabilizing mobile Li atoms.

Nitrogen-doped p-type ZnSe layers with carrier concentration of about 10^{14} cm^{-3} have been grown using NH_3 [27]. Lithium-doped p-type ZnSe layers grown using tertiary-butyllithium, which show reproducible carrier concentrations in a range of 10^{15} cm^{-3} , have been reported quite recently [28]. Although these concentrations are not sufficiently high, we could expect a reproducible growth of ZnSe layers with higher concentrations by co-doping of Li and N using these dopants.

Our preliminary growth of ZnS using cyclopentadienyl lithium as a dopant has demonstrated that Li act as a shallow acceptor.

It is obvious that high purity sources and low temperature growth are two keys for achieving better p-type conductivity control of wide bandgap II-VI materials. Our recent results of high purity ZnSe layers grown using the DMZn source which involves extremely low concentration of chlorine impurities and the low temperature growth of ZnSe achieved by photo-assisted MOCVD using alkyl zinc and alkyl selenide sources are quite encouraging [29].

CONCLUSION

General principles for growing high quality layers of ZnSe and related materials on GaAs and GaP substrates by MOCVD have been described, with emphasis on the appropriate choice of source materials and lattice match between epilayers and substrates. Recent progress in impurity doping during MOCVD has demonstrated that n-type control of ZnSe and ZnS layers can be achieved satisfactorily. It has been shown that p-type ZnSe layers can be grown by doping with lithium and/or nitrogen during growth, but further studies are necessary to improve controllability.

REFERENCES

1. H. M. Manasevit, Appl. Phys. Lett. **12**, 1536 (1968).
2. W. Stutius, Appl. Phys. Lett. **33**, 656 (1978).
3. P. Blanconnier, M. Cerclet, P. Henoc and A. M. Jean-Louis, Thin Solid Films **55**, 375 (1978).
4. P. J. Wright and B. Cockayne, J. Cryst. Growth **59**, 148 (1982).
5. F. A. Ponce, W. Stutius and J. G. Werthen, Thin Solid Films **104**, 133 (1983).
6. P. J. Wright, R. J. M. Griffiths and B. Cockayne, J. Cryst. Growth **66**, 26 (1984).
7. S. Fujita, Y. Matsuda and A. Sasaki, Jpn. J. Appl. Phys. **23**, L360 (1984).
8. A. Yoshikawa, K. Tanaka, S. Yamaga and H. Kasai, Jpn. J. Appl. Phys. **23**, L773 (1984).
9. H. Mitsuhashi, I. Mitsuishi and H. Kukimoto, J. Cryst. Growth **77**, 219 (1986).
10. T. Yasuda, K. Hara and H. Kukimoto, J. Cryst. Growth **77**, 485 (1986).
11. H. Mitsuhashi, I. Mitsuishi and H. Kukimoto, Jpn. J. Appl. Phys. **24**, L8-4 (1985).
12. I. Mitsuishi, H. Mitsuhashi and H. Kukimoto, Jpn. J. Appl. Phys. **28**, L275 (1989).
13. H. Mitsuhashi, I. Mitsuishi, M. Mizuta and H. Kukimoto, Jpn. J. Appl. Phys. **24**, L578 (1985).
14. I. Mitsuishi, H. Mitsuhashi and H. Kukimoto, Jpn. J. Appl. Phys. **27**, L15 (1988).
15. W. Stutius, Appl. Phys. Lett. **38**, 352 (1981).
16. Sz. Fujita, K. Terada, T. Sakamoto and Sg. Fujita, J. Cryst. Growth **94**, 102 (1989).
17. A. Kamata, T. Uemoto, M. Okajima, K. Hirahara, M. Kawachi and T. Beppu, J. Cryst. Growth **86**, 185 (1988).
18. A. Kamata, T. Uemoto, K. Hirahara, and T. Beppu, J. Appl. Phys. **65**, 2561 (1989).
19. H. Kukimoto, in *Growth and Optical Properties of Wide-Gap II-VI Low-Dimensional Semiconductors*, edited by T. C. McGill, C. M. Sotomayor Torres and W. Gebhardt (Plenum Press, New York, 1989), p. 119.
20. A. Yoshikawa, H. Nomura, S. Yamaga and H. Kasai, Jpn. J. Appl. Phys. **27**, L1948 (1988).
21. N. Shibata, A. Ohki and A. Katsui, J. Cryst. Growth **94**, 703 (1988).
22. S. Yamaga, A. Yoshikawa and H. Kasai, J. Cryst. Growth **86**, 252 (1988).
23. T. Yasuda, I. Mitsuishi, Y. Koyama and H. Kukimoto, in *Electroluminescence*, edited by S. Shionoya and H. Kobayashi (Springer-Verlag, Berlin Heidelberg, 1989), p. 362.
24. W. Stutius, Appl. Phys. Lett. **40**, 246 (1982).
25. M. Okajima, M. Kawachi, T. Sato, K. Hirahara, A. Kamata and T. Beppu, Extended Abstracts of the 18th (1986 International) Conference on Solid State Devices and Materials, Tokyo, 1986, p. 647.
26. T. Yasuda, I. Mitsuishi and H. Kukimoto, Appl. Phys. Lett. **52**, 57 (1988).
27. A. Ohki, N. Shibata and S. Zembutsu, Jpn. J. Appl. Phys. **27**, L909 (1988).
28. H. Mitsuhashi, A. Yahata, T. Uemoto, A. Kamata, M. Okajima, K. Hirahara and T. Beppu, presented at the 4th International Conference on II-VI Compounds, Berlin, 1989 (to be published in J. Cryst. Growth).
29. H. Kukimoto, presented at the 4th International Conference on II-VI Compounds, Berlin, 1989 (to be published in J. Cryst. Growth).

GROWTH AND DOPING OF ZINC SELENIDE BY MOLECULAR BEAM EPITAXY

J.M. DePUYDT, H. CHENG, M.A. HAASE AND J.E. POTTS
3M Company, 201-1N-35 / 3M Center, St. Paul, MN 55144.

Recently, with the advent of thermal nonequilibrium growth techniques like molecular beam epitaxy and metalorganic chemical vapor deposition, great progress has been made in overcoming some of the problems traditionally encountered in the growth and doping of ZnSe. Breakthroughs have been made in several areas including the growth of high quality undoped films, in intentional n-type doping and, most importantly, in p-type doping. In this paper we will review the progress made in the growth and doping of ZnSe by molecular beam epitaxy.

In addition, we will present some of our recent results. We will describe the growth of ZnSe at temperatures as low as 150°C using thermally cracked selenium. We will discuss our production of low resistivity p-ZnSe and will describe the junction characteristics and injection electroluminescence obtained from ZnSe p-n junctions. Finally, some problems which we feel are limiting the performance of our ZnSe light emitting diodes and the approaches which may be used to overcome these problems will be discussed.

Introduction

Zinc selenide (ZnSe) has several properties which make it an attractive material for optoelectronic device applications; it has a direct band gap of about 2.7eV at room temperature, is transparent over a wide range of the visible spectrum and has relatively large nonlinear optical coefficients. Some devices which take advantage of these properties include blue light emitting diodes, injection laser diodes, electroluminescent displays, second harmonic generators, frequency mixers and optical modulators.

Construction of the types of devices described above places very stringent requirements on the crystalline quality of the materials used to fabricate the devices. Unfortunately the growth of large, single crystals of ZnSe with low dislocation and twin densities using melt growth techniques has proved to be extremely difficult, if not impossible.¹

In addition to excellent crystalline perfection, some of the proposed optoelectronic devices also require high quality p-n junctions. The difficulty in producing high quality p-n junctions in ZnSe primarily lies in the inability to produce conductive p-type material. The physics behind this difficulty is the mechanism of self-compensation.² Since self-compensation is a direct consequence of thermodynamics, many groups have turned to growth techniques in which growth is controlled by kinetics rather than equilibrium thermodynamics; one such technique is molecular beam epitaxy (MBE).³

In this paper we wish to focus on the growth and doping of ZnSe by MBE. We will review some of the advances which have been made since this growth technique has been applied to ZnSe and will try to emphasize the more significant results. Furthermore, we will describe some of our recent efforts such as the production of highly conductive p-type films through Li doping, the growth of single crystals at very low temperatures using cracked Se, and the fabrication of blue LED's. We will finish by describing some of the outstanding problems limiting the performance of our blue LED's and potential solutions to these problems.

REVIEW OF MBE GROWTH

The growth of ZnSe by MBE was first reported by Smith and Pickhardt in 1975.⁴ They found that substrate choice and preparation had a significant effect on the crystallographic quality of the resulting films; they showed that (100) oriented GaAs was preferred over the other substrates they studied. The MBE growth of ZnSe on ZnSe⁵⁻⁷, Ge⁸ and Si⁹ have also been reported, but routine use of these alternative substrates has not gained widespread acceptance. The advantages of GaAs over other potential substrates are: (1) GaAs is nearly lattice-matched to ZnSe ($\Delta a/a \approx 0.25\%$), (2) large, high quality GaAs substrates are readily available, (3) GaAs, like ZnSe, is a polar material, and (4) surface preparation techniques for GaAs are well developed.

In order to produce conductive, n-type ZnSe crystals using conventional bulk growth techniques it was necessary to subject the samples to a post-growth anneal in molten Zn ($\approx 1000^\circ\text{C}$) for several hours.¹⁰ The observation of very conductive n-type epitaxial films grown by MBE without the "Zn-extraction" treatment clearly demonstrated the superiority of this technique over conventional growth methods.¹¹ Films with resistivities about $1\ \Omega\text{-cm}$ and room temperature carrier mobilities comparable to that of Zn-extracted bulk ZnSe were successfully grown. The good quality of these films was further evidenced by the dominant near-band-edge emission in the photoluminescence (PL) at room temperature.

Studies of the effects of growth conditions on film properties began soon after the demonstration that device quality epitaxial films could be deposited by MBE. The parameters which were independently controlled during these investigations were the substrate temperature (T_G) and the molecular beam fluxes. When using elemental sources evaporated from standard effusion cells it was shown that the acceptable window for the growth of device quality ZnSe was $250^\circ\text{C} < T_G < 400^\circ\text{C}$.¹² Samples grown at temperatures outside this window generally exhibited much lower electron mobilities and defect-related features appeared in their PL. A more complete study in which both the substrate temperature and Zn/Se beam pressure ratio were varied revealed four growth regimes in the growth space defined by these two variables.¹⁴ During this two dimensional growth space study, the Zn/Se beam pressure ratio was varied from 0.25 to 2.0 and the growth temperature was varied over $250\text{-}400^\circ\text{C}$. Reflection high energy electron diffraction (RHEED) patterns observed during growth revealed two transition lines: (1) a transition from Zn- to Se-stabilized growth and (2) a transition from 2- to 3-dimensional growth. The intersection of these two transition lines provides a fundamental reference point in growth space. The electrical and optical properties of these films were correlated with the transition lines and the best growth conditions for undoped ZnSe were found to occur under slightly Zn-stabilized conditions near the transition between two-dimensional to three-dimensional growth.

Up to this point, most unintentionally doped films grown under reasonable conditions were strongly n-type. The next major step taken was the identification and the elimination of the unintentional donors. Several proposals were put forth as to the origin of the unwanted donors; these included: (1) uncontrolled, intrinsic point defects, (2) extrinsic impurities emanating from the sources, (3) outdiffusion of Ga from the GaAs substrate, (4) vapor transport of In which is used for substrate bonding and (5) a combination of the above. A partial resolution of this issue resulted from a series of secondary ion mass spectrometry (SIMS), selectively-excited photoluminescence (SPL) and electrical transport studies.¹⁵ From these studies it was concluded that the n-type conductivity was primarily due to the unintentional incorporation of Cl.

The growth of undoped, high purity, high resistivity ZnSe was achieved using extremely pure Se source materials.^{16,17} In their report, Yoneda et al. showed that repeated distillation of the Se source resulted in a

dramatic reduction of the residual donor density as evidenced by the gradual elimination of the donor bound excitons (DBE) in the PL and a reduction of the residual electron density from 10^{17}cm^{-3} to less than $7 \times 10^{14}\text{cm}^{-3}$ (Fig. 1). This result clearly demonstrated that the donor impurities were emanating from the Se source and that they could be eliminated by cyclic sublimation of that source. The need to carry out in-house Se purification was subsequently shown to be unnecessary when undoped, highly resistive ($\rho > 10^4 \Omega\text{-cm}$) ZnSe could be routinely grown using ultra pure Se from Osaka Asahi Metals Company.^{18,15}

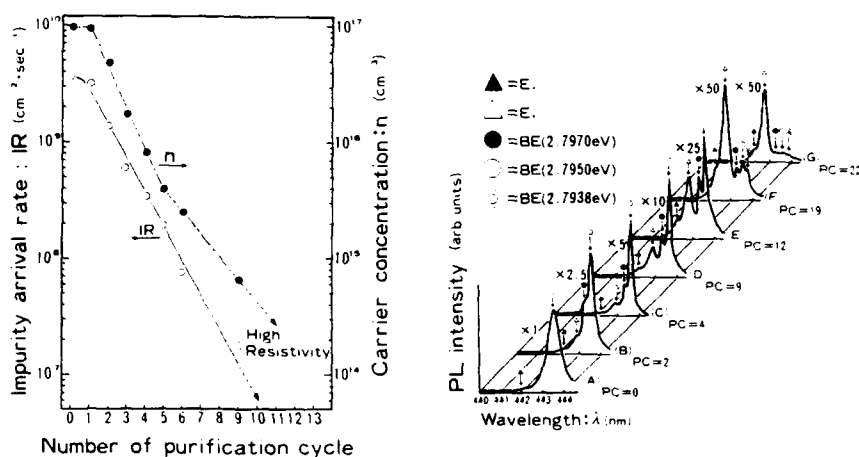


Fig.1 Dependence of the carrier concentration and excitonic emission intensity as a function of Se purification cycles. Reproduced with permission from the authors and Applied Physics Letters.

Intentional n-type Doping

The interpretation of intentional doping studies was made much more transparent with the elimination of inadvertent doping. With the ability to grow high quality, intrinsic ZnSe films it was no longer necessary to deconvolute the effects of intentional doping from those resulting from unintentional dopant incorporation. The conventional wisdom in choosing donor impurities has been to substitute either group III elements for Zn or group VII elements for Se. The dopants which have been studied include In¹⁹, Ga^{20,21}, Al²², Cl^{18,23}, I²⁴ and Br²⁵. Of these Cl has produced the most spectacular results.^{18,23}

Chlorine doping has allowed the highest electron concentrations to date. The only reported source which has been used to achieve Cl doping was 99.999% pure ZnCl_2 . The ZnCl_2 is evaporated from a standard effusion cell at temperatures typically from 130 to 225°C.^{18,23} During our initial Cl-doping study a series of films were grown with a substrate temperature of 300°C and a Zn-to-Se beam pressure ratio of 1/4. The growth rates were 0.8 $\mu\text{m/hr}$. The PL of the undoped films was dominated by free exciton recombination and the resistivity of these films was greater than $1 \times 10^4 \Omega\text{-cm}$. As we started doping we observed two prominent features in the PL spectra: (1) the DBE at 2.7945 eV and (2) a very broad band with an intensity maximum

near 2.0 eV. At low Cl concentrations, the DBE intensity increased with Cl concentration becoming the dominant feature until it reached a maximum when $[Cl] \approx 1 \times 10^{18} \text{ cm}^{-3}$. After this point the DBE intensity decreased with heavier doping. The intensity of the broad band centered at 2.0 eV increased from an undetectable level in the lightly doped films up to where it became the dominant feature in the photoluminescence (Fig. 2a).

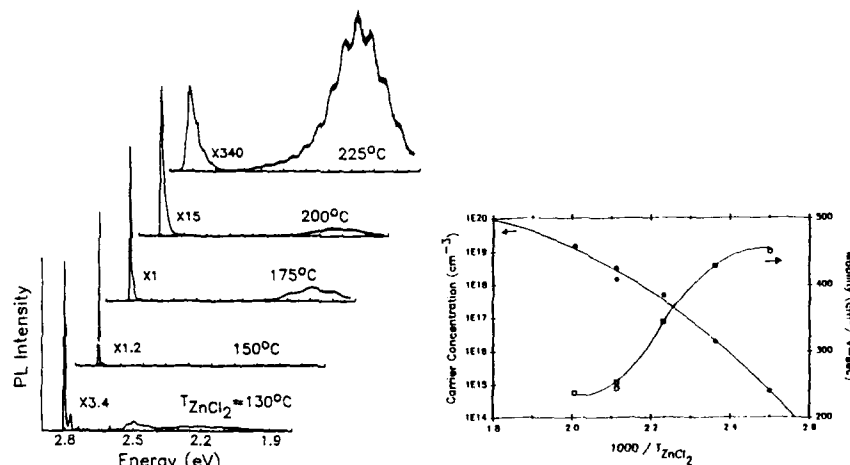


Fig. 2a The PL from Cl-doped ZnSe samples. The most intense feature in the lightly doped films is from the DBE whereas a deep level becomes dominant as doping levels increase.

Fig. 2b The electron concentration and mobility are shown versus the reciprocal of the temperature of the dopant source.

The carrier concentrations were measured in the Cl-doped films using Hall measurements (Fig. 2b). We found that we could reproducibly dope films with carrier concentrations less than 10^{15} cm^{-3} up to $1.5 \times 10^{19} \text{ cm}^{-3}$. The room temperature electron mobilities in our studies decreased from $430 \text{ cm}^2/\text{V-sec}$ in the lightly doped films to $240 \text{ cm}^2/\text{V-sec}$ in the heavily doped films.

Another major concern when considering intentional n-type doping is whether or not the dopant source will contaminate the bell jar producing the so-called memory effect. ZnCl_2 appears to also be a very well-behaved dopant in this respect. We have grown undoped ZnSe with dominant free exciton emission and high resistivity immediately following the growth of heavily Cl-doped layers.

Controllable p-type Doping

Controllable p-type doping represents the next major obstacle in development of the MBE growth of ZnSe. The standard approach for p-type doping is to substitute with group V elements on the Se site or to substitute with group I elements on the Zn site. The dopants most commonly used include Li^{26} , Na^{27} , Ag^{28} , $\text{N}^{29,30}$, $\text{P}^{31,32}$, As^{33} and Sb^{34} . In addition to the conventional dopants, there recently have been efforts to dope with oxygen.^{35,36} Of the dopants studied so far Li, N and O have produced the most promising results.

Although oxygen is isoelectronic with Se, Akimoto et al. reported the observation of a shallow acceptor level in ZnSe after doping with O.^{35,36} While this phenomenon is not well understood it is believed that oxygen's large electronegativity causes a charge transfer from the host lattice to the substitutional O impurity. In his studies Akimoto used 99.999% pure ZnO as the source of O, the growth temperature was fixed at 240°C and the Zn-to-Se beam pressure ratio was held at unity. The temperature of the ZnO source was varied from 650°C to 900°C. Two peaks were observed at 443.7 and 455.1 nm in the PL taken from a sample doped with O at $2.2 \times 10^{17} \text{ cm}^{-3}$. These peaks were assigned to emissions from a neutral acceptor bound exciton (ABE) and the zero phonon peak in a donor-acceptor pair series (DAP). From the positions of the ABE and DAP the oxygen-related acceptor ionization energy was estimated to be 80 meV. ZnSe p-n junction diodes were fabricated from a sample grown on a Si-doped GaAs substrate with an O-doped p-layer and Ga-doped n-layer. Although Hall measurements on the p-layers were not possible, capacitance-voltage (C-V) profiles of the p-n junctions were completed. From the C-V measurements the hole concentration was determined to be $1.2 \times 10^{16} \text{ cm}^{-3}$ and the built in potential was estimated to be 2.3V. Blue emission was obtained at room temperature and 77K when the diodes were forward biased at 3.5V (200 ma). The electroluminescence (EL) showed a very pronounced peak at 466nm at room temperature and two peaks at 446 and 459nm when operated at 77K.

Reports describing N-doping of ZnSe have demonstrated that N forms a shallow acceptor with ionization energy of approximately 110 meV. Nitrogen doping of ZnSe by MBE has been achieved using NH_3 , N_2 and low-energy ionized beams of NH_3 as dopant sources.^{29,30} In all cases PL spectra obtained from the N-doped films showed ABE emissions near 2.790 eV and DAP series with a zero phonon peaks near 2.700 eV. Although the PL studies clearly showed the formation of an acceptor level, no evidence of p-type conversion could be obtained through electrical measurements. One of the major complications when attempting to dope with N is that N_2 and NH_3 have very low sticking coefficients. Park et al. required N_2 or NH_3 overpressures of about 10^{-4} mbar in order to incorporate even modest amounts of N. In an attempt to circumvent this problem, Mitsuyu et al. used an ionized source of nitrogen. While some improvement over doping with unionized sources was demonstrated, conductive p-type ZnSe was not achieved.

To date, the most spectacular demonstrations of p-type conductivity in ZnSe grown by MBE have been with Li doping.^{37,38} We have studied three types of Li sources: (1) Li alkali metal dispensers, (2) Li_3N and (3) elemental Li. Of these elemental Li provides the most usable source in terms of flux stability, active acceptor incorporation and reproducibility. The lithium metal we use is 99.95% pure and no additional purification is attempted. The Li is evaporated from a standard 2cc Knudsen cell whose temperature is varied from 220 to 320°C. During the Li-doping studies we used growth temperatures from 250-375°C and Zn-to-Se beam pressure ratios from 1/4 to 2. SIMS measurements have shown that Li concentrations up to $5 \times 10^{19} \text{ cm}^{-3}$ have been achieved without detectable incorporation of other inadvertent impurities. We have not observed any type of memory effect in our system.

The typical near-band-edge PL spectrum taken at 9K from our undoped samples is shown in figure 3. The spectrum is dominated by emission from free excitons at 2.803 and 2.799 eV indicating very low residual impurity concentrations. There is very little emission from DBE's (2.795 to 2.798 eV). Also shown in figure 3 is the spectrum taken at 9K from one of our Li-doped films. The growth temperature for this sample was 350°C, the Zn/Se flux ratio was unity and the Li doping concentration was $1.2 \times 10^{17} \text{ cm}^{-3}$. The dominant feature is an ABE doublet with peaks at 2.7908 and 2.7891 eV. A weak DAP series is also present with its zero-phonon peak at 2.691 eV. From the positions of the ABE and DAP we obtain an acceptor ionization energy of approximately 115 meV.

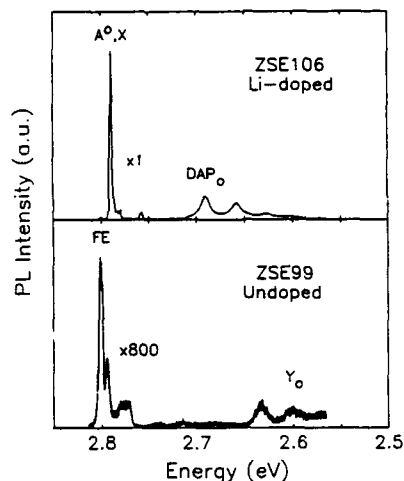


Fig. 3 Typical PL spectra obtained from undoped and Li-doped films.

We have measured the net acceptor densities in our films by C-V profiling. In these measurements we formed the diodes either with $300\mu\text{m}$ diameter evaporated Au dots or with a $900\mu\text{m}$ diameter Hg electrode in a standard mercury probe; we used ring dot patterns so that the C-V profiles were asymmetric with respect to voltage bias. A C-V profile for a sample grown at 300°C with Zn/Se beam pressure ratio of 1/2 and Li concentration of $8.6 \times 10^{16} \text{cm}^{-3}$ is shown in figure 4. This film was determined to be p-type from the bias polarity needed to increase the width of the space charge region. The net acceptor concentration was determined to be $8.2 \times 10^{16} \text{cm}^{-3}$ from the slope of $1/C^2$ vs V ; this represents our best effort to date. We are able to routinely produce samples with $N_A - N_D > 1 \times 10^{16} \text{cm}^{-3}$ when the Li concentrations are in the mid- 10^{16} to low- 10^{17}cm^{-3} over a wide range of growth conditions. As the Li concentration is increased above mid- 10^{17}cm^{-3} the films become compensated. The origin of the compensating centers is not known at this time.

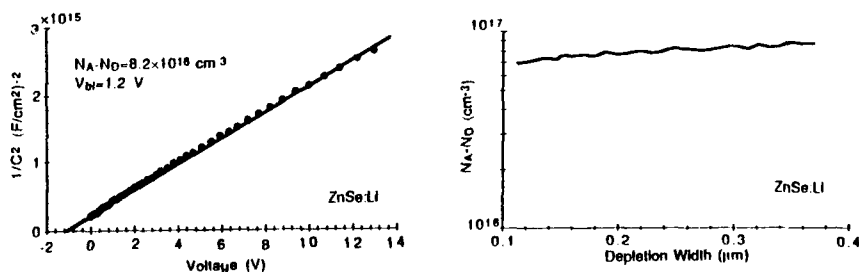


Fig. 4 This figure shows the $1/C^2$ vs V and depth profile for our best p-type ZnSe film to date.

ZnSe Blue LED's

We have fabricated ZnSe p-n junction diodes where the p-layers were produced by Li-doping and the n-layers were produced by Cl-doping. These layers were grown on (100) oriented p+ GaAs substrates. The diode structure we typically use is shown in figure 5. Under forward bias blue electroluminescence (EL) centered at about 461nm is observed at room temperature; the FWHM of this peak is approximately 9.9nm. At 77K two peaks at approximately 444 and 459nm can be seen in the EL spectrum. The 459nm peak has a long wavelength shoulder indicating another peak at 464nm. The splitting between these peaks suggests that these emissions may be due to band-to-band, band-to-acceptor, and donor-to-acceptor transitions. Very little deep level EL was observed either at room temperature or at 77K. The light emission we observe is not uniform across the diode. Instead the light is emitted from numerous spots, this phenomenon is likely a result of filamentary breakdown at the ZnSe/GaAs interface. In our better diodes, the bright spots nearly cover the entire mesa giving the appearance of uniform emission.

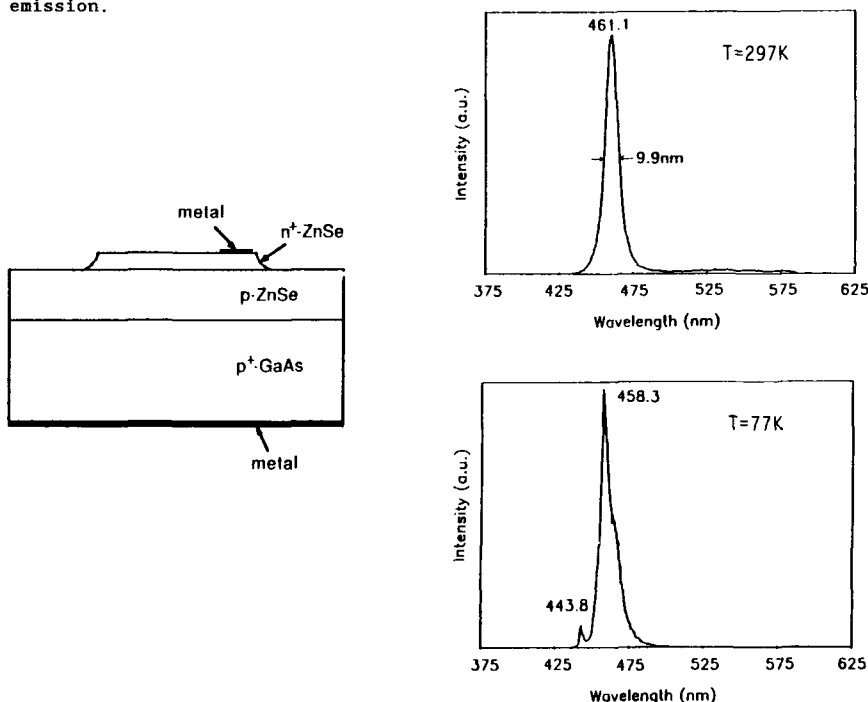


Fig. 5 This figure shows the structure of our LED's. Also shown are the EL spectra obtained at room temperature and 77K.

Very Low Temperature Growth

As was pointed out earlier the lowest growth temperature that allows the MBE growth of ZnSe single crystals is approximately 250°C when the Se is evaporated from a standard effusion cell. The ability to grow ZnSe at still lower temperatures may be beneficial for several reasons. It should

suppress interdiffusion at the interface, allow the production of more abrupt doping profiles, and enhance the sticking of highly volatile dopant species. Growth at lower temperatures may also prove to be necessary in order to further increase the incorporation of uncompensated acceptors; this phenomenon has already been observed in certain III-V semiconductors.³⁹

Recently, we demonstrated that device quality, single crystal ZnSe can be grown at temperatures as low as 150°C when using a thermally cracked Se source.⁴⁰ In our studies we use a cracker cell which consists of a bulk evaporator and a high temperature cracking zone of custom design. The design and capabilities of this furnace are discussed in detail elsewhere.⁴¹ We typically operate the cracking zone at 600°C. By passing the beam through the hot cracking zone we observe a significant reduction in the number of large molecular species ($\text{Se}_n, n \geq 2$) of Se.

The PL spectra obtained at 9K from three layers grown at low temperatures are shown in figure 6. Sample (a) was grown at 200°C using uncracked Se. As can be seen from the PL spectrum, the film is of very poor quality; the spectrum is dominated by defect-related bands at 2.6, 2.5 and 2.2 eV. The RHEED pattern observed during the growth of this film indicated that the film was partially polycrystalline. Sample (b) was also grown at 200°C, but this time the Se was thermally cracked. The PL spectrum for this sample is dominated by near-band-edge emission and is comparable to the spectra obtained from samples grown at higher temperatures using uncracked Se. Sample (c) was grown at 150°C using thermally cracked Se. The PL spectrum is again dominated by NBE emission, but this time the DBE emission (2.794-2.797 eV) is slightly more intense than the free exciton emission (2.799-2.803 eV); this may indicate that extrinsic impurities are more efficiently incorporated into the growing film when lower growth temperatures are used. Attempts to grow at temperatures less than 150°C have produced only polycrystalline samples up to this time.

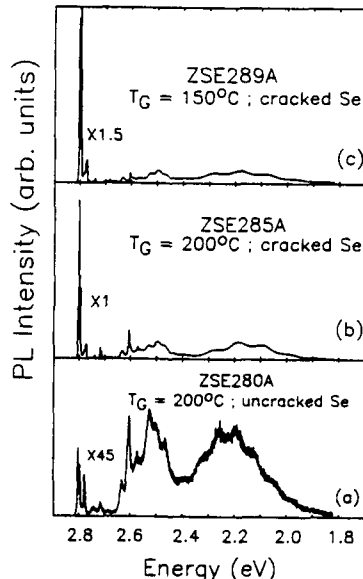


Fig. 6. The PL from three samples grown at low temperatures are shown here. Sample (a) was grown at 200°C using uncracked Se. Samples (b) and (c) were grown using cracked Se at 200°C and 150°C, respectively.

Our undoped films grown with uncracked Se at 250-350°C are normally fully depleted. This was also the case for the undoped layers grown at 150-200°C with cracked Se. In order to determine whether or not the carrier mobilities would be diminished by growing at these low temperatures we grew a sample intentionally doped with Cl. Hall measurements demonstrated the electron mobility at room temperature to be $399 \text{ cm}^2/\text{V}\cdot\text{sec}$ in a sample with electron density of $2.6 \times 10^{16} \text{ cm}^{-3}$. These values are comparable to what we would expect for samples grown at temperatures greater than 250°C similarly doped with Cl.

We have also recently shown that Li can be better confined in samples grown at low temperatures. In figure 7 we show SIMS profiles from modulation doped samples grown at 350°C and 150°C. The growth schedule for both of these samples was such that a Li-doped layer ($0.5 \mu\text{m}$ thick) was to have been sandwiched between two undoped layers ($1.0 \mu\text{m}$ thick). However, SIMS measurements showed the lithium concentration to be nearly uniform in the sample grown at 350°C; this is likely the result of solid state diffusion of Li. The lithium profile in the sample grown at 150°C, however, shows very little diffusion into the underlying undoped layer. The continued incorporation of Li after closing the Li cell shutter is likely a result of the surface segregation of Li; a similar observations have been made in Sn doping of GaAs⁴² and Na doping of ZnSe.⁴³ This preliminary result indicates that Li-diffusion may be controlled by moving to lower growth temperatures.

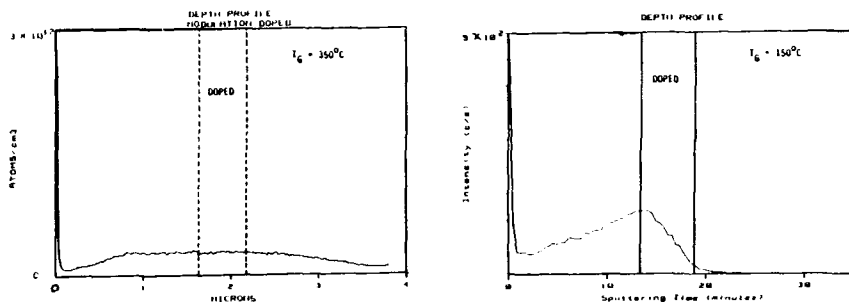


Figure 7 The SIMS profiles of Li doped samples grown at 350°C and 150°C. The dashed lines indicate the region where the Li source shutter was open.

Existing Problems

Reliable resistivity and Hall effect measurements on p-type ZnSe have not been possible in our labs because of the inability to form ohmic contacts. Even more importantly, the performance of our LED's has been greatly diminished because of losses at the p-layer contact; in all cases we rely on the reverse breakdown of barriers either at the metal contact or at the heterointerface. However, not all labs report difficulty in making

ohmic contacts. Akimoto has reported ohmic contact to p-ZnSe with Au³⁵; the discrepancy is not understood at this time. Ultraviolet photoemission spectroscopy has shown that surface states are not important in determining the barrier height at the metal-semiconductor interface in ZnSe.⁴⁴ Instead, the barrier at the interface obeys the classical Schottky barrier model. Since the valence band maximum is more 6.8 eV from the vacuum level it is not possible to form a simple ohmic contact since no metal has a work function greater than 5.7 eV. Nevertheless, we have attempted to form contacts using a wide variety of metals, alloys and compounds deposited by vacuum evaporation and RF sputtering onto surfaces which had been prepared by a wide variety of techniques; post-deposition thermal, rapid thermal, and laser anneals were also studied. To date, vacuum evaporation of Au onto untreated films have produced the best results in which contacts with barrier heights of approximately 1 eV are formed.

A second approach to making contact to p-ZnSe is to inject holes from the substrate through the heterointerface. In this approach the quality of the interface is of critical importance. Several issues must be addressed when attempting to control or modify interface properties: (1) lattice mismatch, (2) difference in thermal expansion coefficients, (3) band offsets and (4) interface charges and dipoles. Although ZnSe is nearly lattice matched to GaAs, misfit dislocations are formed to accommodate the slight difference in lattice parameters. The effect of the dislocation network on transport across the interface is not well understood. One solution to this problem is to grow on lattice matched substrates; growth of ZnSe on InGaAs has been shown to greatly reduce problems associated with lattice mismatch.⁴⁵ Not only should the substrate and epilayer be lattice matched at growth temperature, they should also have similar lattice parameters at room temperature. Since it is difficult to greatly modify the thermal expansion coefficient of any potential substrate material, the approach to reducing strain from differential thermal expansion must rely on minimizing the difference between the growth temperature and the temperature at which the device must operate. A significant step has already been taken in this direction by developing growth techniques at 150°C. By growing at 150°C the strain due to differential thermal contraction is reduced by about 50% as compared to the situation when using standard growth temperatures. Another fundamental problem is that the valence band discontinuity at the GaAs-ZnSe interface is about 1.0 eV. While this represents an already large barrier, the unfavorable band lineup may also be aggravated by uncontrolled interface charge or dipoles. It has been shown in other systems that interface layers can be used to influence transport across heterointerfaces.⁴⁶ This approach usually relies on the difference in average electro-negativity of the two materials. Since the average electronegativity of ZnSe is very similar to that of GaAs, the usefulness of this approach is questionable. It should also be noted that intentional modification of the transport properties at heterointerfaces is at a primitive stage in all semiconductor systems at this time.

Conclusions

Very significant progress has been made in the growth and doping of ZnSe by MBE in recent years. It is now possible for crystal growers to routinely produce very pure, undoped ZnSe films. The PL spectra obtained from ZnSe films grown using ultra high purity Se typically show dominant free exciton recombination and very little deep level emission. These films also have very low free carrier densities and often their resistivities exceed $10^4 \Omega\text{-cm}$. It is now possible to intentionally dope ZnSe layers n-type with electron densities greater than 10^{19}cm^{-3} when using Cl. The carrier mobilities observed in the Cl-doped films are high and even exceed $230 \text{ cm}^2/\text{V}\cdot\text{sec}$ at room temperature in samples with $n=1.5 \times 10^{19}\text{cm}^{-3}$. Zinc chloride

is most often used as the source of Cl since it provides a stable and reproducible beam flux. Great progress has also been made in producing p-type ZnSe. Free hole densities greater than 10^{16}cm^{-3} have been reported in both Li- and O-doped films. We have studied Li-doping extensively and find that we can routinely produce layers with N_A-N_D up to, but not exceeding, $8.6 \times 10^{16}\text{cm}^{-3}$. We have found that the most usable source of Li is lithium metal since it provides a well controlled beam flux and does not produce the memory effect. Blue-light emitting diodes have been realized from ZnSe p-n junctions where the p-layer was produced either through oxygen or lithium doping. In both cases the electroluminescence showed a single, narrow peak at approximately 461 nm at room temperature with very little deep level emission. A new avenue of research has also recently opened with the demonstration of ZnSe growth at very low temperatures with the use of thermally cracked Se. While the full impact of the ability to grow at temperatures as low as 150°C is not known, it has already been shown to be useful when trying to confine Li.

We feel that the most critical issues which remain to be addressed are with contact formation to p-type ZnSe and with improving the properties of the heterointerface. If these issues can be properly resolved then we are confident that marketable optoelectronic devices made from ZnSe will soon become possible.

References

- 1 B. Fitzpatrick, J. Crystal Growth **86**, 106 (1988).
- 2 H. Hartman, R. Mach and B. Selle, in Current Topics in Materials Science, edited by E. Kaldis (North-Holland, Amsterdam, 1982), Vol. 9.
- 3 P. Jewsbury and S. Holloway, J. Phys. C **9**, 3205 (1976).
- 4 D. Smith and V. Pickhardt, J. Appl. Phys. **46**, 2366 (1975).
- 5 R.M. Park, H.A. Mar and N.M. Salansky, J. Vac. Sci. Technol. **B3**, 1637 (1985).
- 6 M. Ohishi, K. Ohmori, Y. Fujii, H. Saito and S. Tiong, Proceed. of the 3rd Int. Conf. on II-VI Compounds, 324 (1987).
- 7 K. Menda, I. Takayasu, T. Minato and M. Kawashima, Proceed. of the 3rd Int. Conf. on II-VI Compounds, 342 (1987).
- 8 J. Werthen, W. Stutius and F. Ponce, J. Vac. Sci. Technol. **B1**, 656 (1983).
- 9 R. Park and H. Mar, Appl. Phys. Lett **48**, 529 (1986).
- 10 M. Aven and H. Woodbury, Appl. Phys. Lett. **1**, 53 (1962).
- 11 T. Yao, Y. Makita and S. Maekawa, Appl. Phys. Lett. **35**, 97 (1979).
- 12 T. Yao, M. Ogura, S. Matsuoaka and T. Morishita, Jpn. J. Appl. Phys. **22**, L144 (1983).
- 14 J. DePuydt, H. Cheng, J. Potts, T. Smith and S. Mohapatra, J. Appl. Phys. **62**, 4756 (1987).
- 15 J. DePuydt, T. Smith, J. Potts, H. Cheng and S. Mohapatra, J. Cryst. Growth **86**, 318 (1988).
- 16 K. Yoneda, Y. Hishida, T. Toda, H. Ishii and T. Niina, Appl. Phys. Lett. **45**, 1300 (1984).
- 17 L. Kolodziejski, R. Gunshor, T. Bonsett, R. Venkata-subramanian, S. Datta, R. Bulsma, W. Becker and N. Otsuka, Appl. Phys. Lett. **47**, 169 (1985).
- 18 K. Ohkawa, T. Mitsuyu and O. Yamazaki, Extended Abs. of the 18th Conf. on Solid State Dev. and Mat., 635 (1986).
- 19 T. Yao, T. Sera, Y. Makita and S. Maekawa, Surface Science **86**, 120 (1979).
- 20 T. Niina, T. Minato and K. Yoneda, Jpn. J. Applied Phys. **21**, L387 (1982).

- 21 M. Vaziri, R. Reifenberger, R. Gunshor, L. Kolodziejski, S. Venkatasana and R. Pierrel, J. Vac. Sci. and Technol. B7, 253 (1989).
- 22 A. Kamata, T. Uemoto, M. Okajima, K. Hirahara, M. Kawachi and T. Beppu, J. Crystal Growth 86, 285 (1988). Note: The samples in this report were deposited by MOCVD. Please contact J. DePuydt if you have information on Al-doping of ZnSe by MBE.
- 23 H. Cheng, J. DePuydt, J. Potts and M. Haase, J. Cryst. Growth 95, 512 (1988).
- 24 T. Nakajima, M. Matsubara, S. Tamura, K. Yokota and S. Katayama, Abstracts of the Spring meeting of the Japanese Society of Applied Physics, Vol. 1, p.374, April 1989, Chiba, Japan. Note: The films in this report were deposited by an ion-beam method. Please contact J. DePuydt if you have information on Br-doping of ZnSe by MBE.
- 25 N. Shibata, A. Ohki and S. Zembutsu, Jpn. J. Appl. Phys. 27, L251 (1988). Note: The films in this report were grown by MOVPE. Please contact J. DePuydt if you have information on I-doping of ZnSe by MBE.
- 26 H. Cheng, J. DePuydt, J. Potts and T. Smith, Appl. Phys. Lett. 52, 147 (1987).
- 27 J. Potts, H. Cheng, J. DePuydt and M. Haase, Fourth Int'l. Conf. on II-VI Compounds, Technische Universitat, Berlin, 17-22 Sept. 1989 (to be published in J. Cryst. Growth).
- 28 T. Miyajima, K. Akimoto and Y. Mori, Abstracts of the Spring Meeting of the Japanese Society of Applied Physics, Vol. 1, p.376, April 1989, Chiba, Japan.
- 29 T. Mitsuyu, K. Ohkawa, and O. Yamazaki, Appl. Phys. Lett. 49, 1348 (1986).
- 30 R. Park, H. Mar and N. Salansky, J. Appl. Phys. 58, 1047 (1985).
- 31 T. Yao and Y. Okada, Jpn. J. Appl. Phys. 25, 821 (1986).
- 32 J. DePuydt, T. Smith, J. Potts, H. Cheng and S. Mohapatra, J. Cryst. Growth, 86, 318 (1988).
- 33 S. Shibli, M. Tamargo, B. Skromme, S. Schwartz, C. Schwartz, R. Nahory and R. Martin, 10th MBE Workshop, North Carolina State University, Raleigh, NC (to be published in the J. Vac. Sci. and Technol.).
- 34 R. Park, J. Kleiman, H. Mar and T. Smith, J. Appl. Phys. 63, 2851 (1988).
- 35 K. Akimoto, T. Miyajima and Y. Mori, Jpn. J. Appl. Phys. 28, L531 (1989).
- 36 K. Akimoto, T. Miyajima and Y. Mori, Phys. Rev. B 39, 3138 (1989).
- 37 J. DePuydt, M. Haase, H. Cheng and J. Potts, Appl. Phys. Lett. 55, 1103 (1989).
- 38 M. Haase, H. Cheng, J. DePuydt and J. Potts, (to be published in J. Appl. Phys., Jan. 1, 1990).
- 39 R. Hamm, M. Panish, R. Nottenburg, Y. Chen and D. Humphrey, Appl. Phys. Lett. 54, 2586 (1989).
- 40 H. Cheng, J. DePuydt, M. Haase and J. Potts, (submitted to Appl. Phys. Lett.)
- 41 H. Cheng, J. DePuydt, M. Haase and J. Potts, 11th MBE workshop Raleigh, NC; Sept. 1989 (to be published in J. Vac. Sci. and Technol.)
- 42 J. Harris, D. Ashenford, C. Foxon, P. Dobson and B. Joyce, Appl. Physics A, 33, 87 (1984).
- 43 H. Cheng, J. DePuydt, J. Potts and M. Haase, J. Crystal Growth 95, 512 (1989).
- 44 F. Xu, M. Vos, J. Weaver, and H. Cheng, Phys. Rev. B38, 13418 (1988).
- 45 N. Shibata, A. Ohki, H. Nakanishi and S. Zembutsu, J. Crystal Growth 86, 273 (1988).
- 46 F. Capasso, A. Cho, K. Mohammed and P. Foy, Appl. Phys. Lett. 46, 664 (1985).

DEPOSITION OF ZINC SELENIDE BY ATOMIC LAYER EPITAXY FOR MULTILAYER X-RAY OPTICS

J.K. Shurtleff, D.D. Allred, R.T. Perkins and J.M. Thorne
Center for X-ray Imaging, Brigham Young University, Provo, Utah, 84602

ABSTRACT

Thin film deposition techniques currently being used to produce multilayer x-ray optics (MXOs) have difficulty producing smooth, uniform multilayers with d-spacings less than about twelve angstroms. We are investigating atomic layer epitaxy (ALE) as an alternative to these techniques.

ALE is a chemical vapor deposition technique which deposits an atomic layer of material during each cycle of the deposition process. The thickness of a film deposited by ALE depends only on the number of cycles. Multilayers deposited by ALE should be smooth and uniform with precise d-spacings which makes ALE an excellent technique for producing multilayer x-ray optics.

We have designed and built an ALE system and we have used this system to deposit ZnSe using diethyl zinc and hydrogen selenide.

MULTILAYER X-RAY OPTICS

Multilayer x-ray optics (MXOs) are designed so that x rays which are diffracted from each interface of the multilayer constructively interfere to give a large total reflectivity. The maximum reflectivity is obtained when the interfaces between the layer pairs are abrupt and the layers are uniform and smooth with precise d-spacings, as depicted in Figure 1.

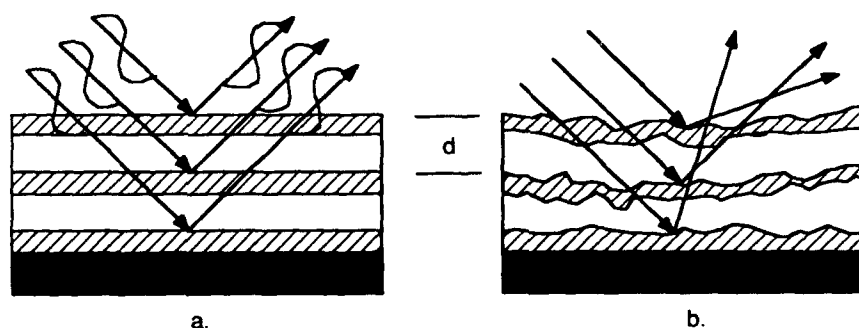


Figure 1. a. A good multilayer x-ray mirror which gives the maximum reflectivity. b. A poor multilayer x-ray mirror. Layers are rough and nonuniform so that the diffracted x rays do not constructively interfere.

ATOMIC LAYER EPITAXY

ALE was developed at the Lohja Corporation in Finland for producing large-area thin film electroluminescent displays [1]. It is currently being used to produce quantum well devices [2]. The ability of ALE to produce high quality thin films has prompted a great deal of research on ALE in the electronics industry. We are the first research group to apply ALE to the production of MXOs.

ALE is a thin film deposition technique which deposits an atomic layer of material during each cycle of the deposition process. The thickness of the deposited film depends only on the total number of cycles and is independent of other process parameters so that the thickness of a film deposited by ALE can be controlled to within one atomic layer [3-5].

ALE is possible due to the difference in bond energies of chemisorbed atoms and physisorbed atoms.

Chemisorption vs Physisorption

A chemisorbed atom shares electrons with atoms of the previous layer to form strong chemical bonds. A physisorbed atom is attracted to atoms of the previous layer by weak dipole-dipole interactions or Van der Waals forces. Covalent bonds are typically ten times stronger than Van der Waals forces, as depicted in Figure 3.

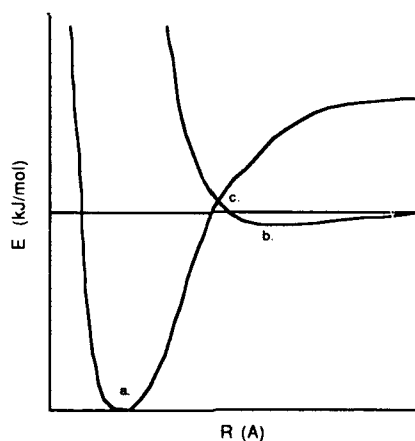


Figure 3. Interaction energy as a function of internuclear separation. a. Chemisorbed atoms form a strong chemical bond with atoms of the previous layer. b. Physisorbed atoms are only weakly bound to atoms of the previous layer c.. Energy barrier may or may not exist depending on the type of atoms being adsorbed.

Theory of ALE

To successfully deposit materials by ALE, the bond between the adatom and the previous layer must be stronger than the interaction between the molecules containing the adatom. For example, the bond between a selenide atom in the previous layer and the zinc atom in diethyl zinc is many times stronger than the weak interaction between molecules of diethyl zinc. The deposition temperature must also be selected so that the atoms which have been chemisorbed remain strongly bound to the surface while the atoms which have been physisorbed are evaporated, leaving only the single layer of chemisorbed atoms.

Deposition process

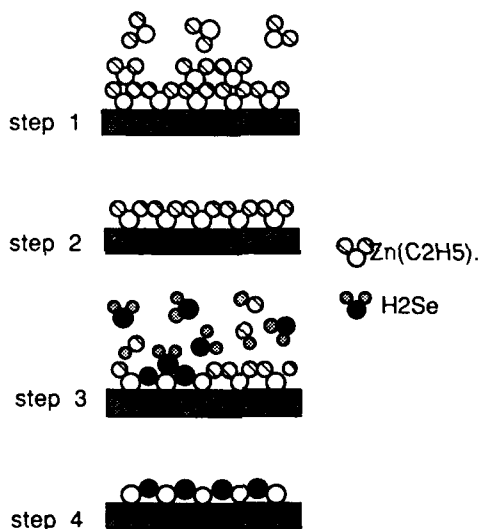


Figure 4. One cycle of the deposition process for depositing zinc selenide by ALE.

In the first step, diethyl zinc is introduced into the system. The diethyl zinc molecules react with the selenide atoms in the previous layer and are chemisorbed until a complete layer of zinc atoms is deposited. Once the chemisorbed layer has formed, diethyl zinc molecules can only be physisorbed.

During the second step, the gas flow is shut off and the system is evacuated so that any physisorbed diethyl zinc molecules will evaporate.

Hydrogen selenide is introduced into the system during the third step. The hydrogen selenide molecules react with the chemisorbed diethyl zinc molecules to form a single zinc selenide layer and ethane gas.

In the fourth and final step, the gas flow is again shut off and the system is evacuated so that unreacted hydrogen selenide and the ethane gas products are removed.

The cycle is repeated until the desired thickness of zinc selenide has been deposited. The layer growth in ALE is epitaxial which means that a complete atomic layer is deposited before the next atomic layer begins to grow, with the result that the structure of the deposited layer resembles that of the previous layer or substrate. To produce the required multilayers for use as MXOs, the reactant gases are switched and a different material deposited. Figure 5 depicts a ZnSe/CdS superlattice which could be used as a MXO.

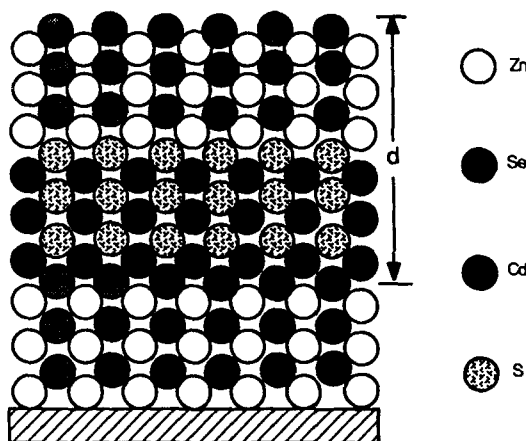


Figure 5. ZnSe/CdS superlattice which can be deposited by ALE and used as a MXO.

ZINC SELENIDE DEPOSITION

We recently completed construction of an ALE reactor. The system design has been described elsewhere [6]. We selected zinc selenide as the first material we would deposit by ALE, because other researchers have successfully deposited many of the II-VI and III-V semiconductor materials using metal-organic and hydride reactants[7] and we are interested in eventually producing a ZnSe/CdS superlattice for use as a MXO.

We report that we have successfully deposited zinc selenide on a polished [111] silicon substrate using diethyl zinc and hydrogen selenide. The deposition temperature was 250 C. The diethyl zinc was introduced

into the deposition chamber by bubbling 200 ml/min of hydrogen through the liquid diethyl zinc. The hydrogen selenide was introduced directly into the deposition chamber at 200 ml/min. During each cycle the reactant gases were introduced for 2 seconds and the system was then evacuated for 8 seconds to a pressure of 3×10^{-4} torr before the next reactant gas was introduced. The total deposition consisted of 500 cycles.

We determined the thickness of the zinc selenide film to be approximately 360 Å using ellipsometry. The thickness of the zinc selenide film indicates that we deposited less than one layer of zinc selenide during each cycle. We believe that the explanation for this result is that we depleted the diethyl zinc supply before the 500 cycles were completed. We have modified the gas system so that we can now monitor the amount of diethyl zinc in the bubbler during the deposition.

X-ray Diffraction Results

We performed x-ray diffraction measurements on the film using the Cu K α line at 1.54 Å. The results are given in Figure 6 and clearly show that the film on the Si substrate is crystalline ZnSe.

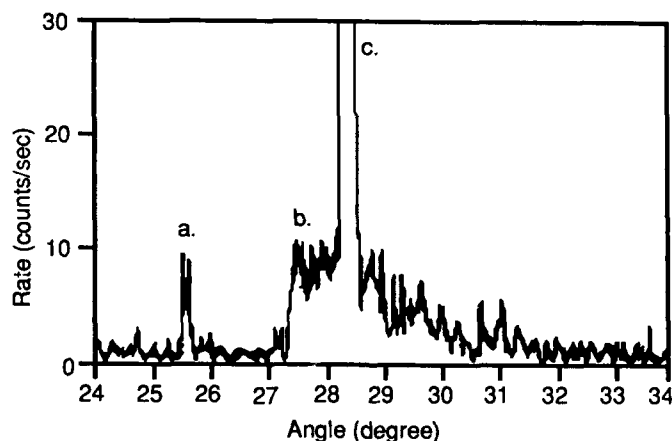


Figure 6. a. CuK β from Si[111]. b. CuK α from ZnSe[111]. c. CuK α from Si[111].

Electron Microscopy Results

To confirm the results of the x-ray diffraction measurements, we examined the film using a scanning electron microscope. The x-ray emission spectrum we obtained from the film and show in Figure 7 proves that the film is indeed ZnSe.

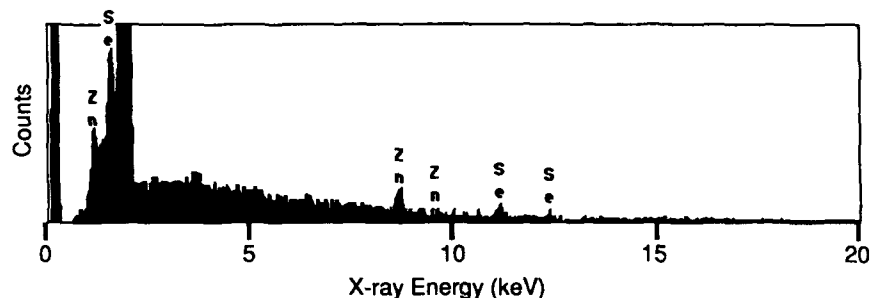


Figure 7 X-ray emission spectra of the film obtained using SEM. The largest peak is due to the Si substrate.

CONCLUSIONS

We have investigated the use of ALE as a new technique for producing MXOs. Our research suggests that ALE we be able to produce high quality MXOs with smooth, uniform layers and small d-spacings.

We have designed and built an ALE reactor and we have used this reactor to deposit crystalline zinc selenide. In the future, we will deposit a ZnSe/CdS superlattice for use as a MXO.

ACKNOWLEDGEMENTS

This research was supported by a grant from the National Science Foundation under their small business innovative research program. The authors wish to thank Larry Knight, director of the Center for X-ray Imaging at Brigham Young University for his support.

REFERENCES

1. T. Suntola and J. Hyvarinen, *Ann. Rev. Mater. Sci.* **15**, 177-95 (1985).
2. S.P. DenBars, C.A. Beyler, A. Hairz and P.D. Dapkus, *Appl. Phys. Lett.* **51** (19), 1530-2 (1987).
3. C.H.L. Goodman and M.V. Pessa, *J. Appl. Phys.* **60** (3), R65-71 (1986).
4. M. Simpson and P. Smith, *Chemistry in Britain* **1987**.
5. M.A. Tischler and S.M. Bedair, *Appl. Phys. Lett.* **48** (24), 1681-3 (1986).
6. J.K. Shurtleff, D.D. Allred, R.T. Perkins, J.M. Thorne, *SPIE* **1160** (34) (1989).
7. M.A. Tischler and S.M. Bedair, *Journal of Crystal Growth* **77**, 89-94 (1986).

EFFECT OF GaAs SURFACE STOICHIOMETRY ON THE INTERFACE OF AS-GROWN EPITAXIAL ZnSe/EPITAXIAL GaAs HETEROSTRUCTURES

J. Qiu, R.L. Gunshor, M. Kobayashi, D.R. Menke, and Q.-D. Qian
School of Electrical Engineering, Purdue University, West Lafayette,
Indiana 47907

D. Li, and N. Otsuka
Materials Engineering, Purdue University, West Lafayette, Indiana 47907

ABSTRACT

In the study reported here, the GaAs surface stoichiometry was systematically varied prior to the nucleation of ZnSe to form epitaxial ZnSe/epitaxial GaAs interfaces. The structures were grown by molecular beam epitaxy and evaluated by several techniques including capacitance-voltage (C-V) measurements. A dramatic reduction of interface state density occurred when the GaAs epilayer was made As deficient. The resulting interface state densities of as-grown structures are comparable to values obtained with (Al,Ga)As/GaAs interfaces.

INTRODUCTION

The wide band gap of ZnSe (2.67 eV) when compared to (Al,Ga)As (2.0 eV for an Al mole fraction of 0.5), as well as a close lattice parameter match to GaAs, indicated that ZnSe/GaAs could provide an alternative to (Al,Ga)As/GaAs in a variety of device applications. In recent publications [1,2] we have reported the occurrence of both hole accumulation (for p-type GaAs) and inversion (for n-type GaAs) in post-growth annealed structures. The C-V characteristics of the annealed structures were nearly ideal, exhibiting an integrated interface state density of $2.5 \times 10^{11} \text{ cm}^{-2}$ a value which compared favorably with the densities reported [3] for typical (Al,Ga)As/GaAs interfaces. In this paper we describe a growth technique, involving the selection of an appropriate GaAs surface stoichiometry prior to nucleation of ZnSe, that resulted in as-grown samples exhibiting nearly ideal C-V characteristics, without requiring post-growth annealing.

DISCUSSION OF EXPERIMENTS

The ZnSe and GaAs epilayers were grown in separate growth chambers of a modular MBE system in order to avoid cross-contamination. Transfer between growth chambers occurred in an

ultrahigh vacuum ($<3 \times 10^{-10}$ Torr) transfer module. The Be doped p-type ($1.0 \times 10^{17} \text{cm}^{-3}$) GaAs epilayers were grown on (100) oriented Zn doped GaAs substrates at a substrate temperature of 582°C . Reflection high energy electron diffraction (RHEED) was used to monitor the film growth; a (2x4) reconstruction pattern was observed throughout the GaAs epilayer growth. When the temperature of the GaAs epilayer was lowered after the growth, an As-rich c(4x4) reconstruction pattern was observed. Following the growth of the GaAs epilayer, samples were transferred to the second growth chamber for the nucleation of ZnSe.

A series of experiments were performed in the ZnSe growth chamber wherein the GaAs epilayer surface stoichiometry was altered prior to the nucleation of ZnSe. The GaAs epilayers were heated to different temperatures to reduce the surface As content, resulting in two different ZnSe/GaAs interfaces. When the GaAs was heated to approximately 510°C , a (4x6) surface reconstruction pattern was observed. In some cases the presence of this reconstruction resulted in a quasi two-dimensional (2D) [4] nucleation of ZnSe; on other occasions 2D nucleation has been observed on the (4x6) reconstructed surface. (Two-dimensional nucleation of ZnSe is always observed [5,6,7] on an As-stabilized GaAs surface.) As the GaAs epilayer temperature continued to be raised above the temperature where the (4x6) pattern was observed, in the vicinity of 550°C the reconstruction again changed. Although one might expect that a (4x2) Ga-stabilized pattern would be seen as the temperature was increased [8], the reconstruction pattern recorded following the (4x6) was a (4x3), sometimes changing to (2x3). (The occurrence of the (4x3) and the (2x3) reconstructions were very close together in temperature and time.) The (4x3 and (2x3) reconstructions, differing from conventionally reported GaAs surface reconstruction patterns, may have resulted from the "decoration" [9] of the heated GaAs surface by high vapor pressure species, most likely Se. (The (4x3) reconstruction has recently been observed by Kobayashi et al under similar conditions[10].) Such a modification of the GaAs reconstruction pattern seemed not unlikely since the background chamber pressure increased from about 5×10^{-11} to 5×10^{-9} Torr as the GaAs epilayers (and contiguous substrate mounting hardware) were heated to temperatures as high as 570°C .

Following the growth of the epitaxial ZnSe/GaAs heterojunctions, circular capacitors with Al metallization were fabricated. All of the data reported here were taken in the dark. Figure 1 shows the room temperature, 1 MHz C-V characteristics of Al/ZnSe/p-GaAs capacitors for various GaAs surface reconstructions. For comparison, ideal (neglecting the effect of interface states) theoretical C-V curves were calculated corresponding to the doping densities obtained from C-V profiling and the ZnSe thicknesses measured from TEM images. In all cases the flat-band voltages of the theoretical curves were shifted to facilitate comparison with the experimental data. (The variation in the flat band voltage, caused by the presence of fixed charge at the interfacial region,

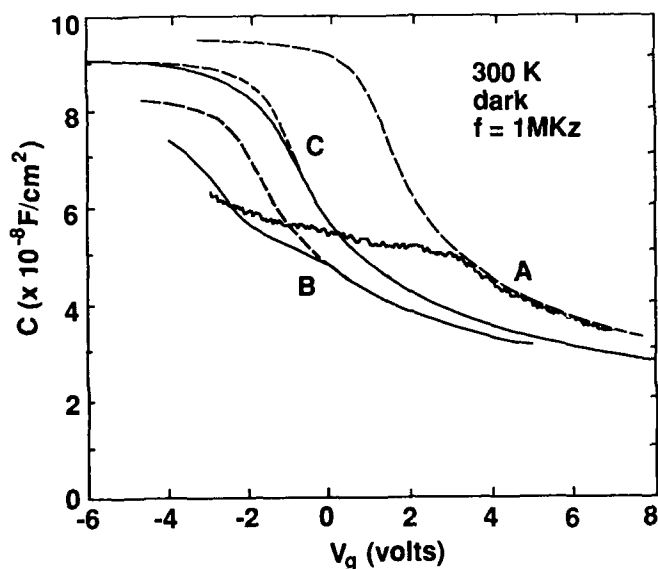


Figure 1: Experimental (solid line) and theoretical (dashed line) C-V characteristics of the as-grown ZnSe/p-GaAs heterojunctions at room temperature. All of the data were taken at 1 MHz in the dark with a sweep rate of 0.1 V/sec. The GaAs epilayer surfaces for sample types A, B, and C, respectively, were made increasingly As deficient before nucleation. The discrepancy between the experimental and theoretical curves diminished as the surface As content decreased. Hole accumulation was achieved only in the type C samples. All samples showed deep depletion at large positive gate bias.

did not affect the total range of band bending.) As shown in Fig. 1, a sample typical of the (4x3) reconstructed surface, as-grown, exhibited a clear accumulation ledge; the thickness of the ZnSe epilayer calculated from the accumulation capacitance was 840 Å, a value which agreed closely with the TEM measurement. The samples formed from a (4x6) reconstructed surface showed a tendency to form a hole accumulation layer before current started to flow across the ZnSe layers. For the latter samples some interface state-related stretching could be seen clearly from the depletion portion of the C-V curve, with the C-V characteristics of such samples improving to nearly ideal following the same thermal

annealing procedure as described above [1]. Among the three types of samples, those involving nucleation on an As-stabilized surface exhibited the most pronounced interface state-induced stretching near the mid-gap, while those for which ZnSe was nucleated on the most As-deficient surface had no indication of such stretching, indicating a virtual elimination of interface states in this region of the band gap. Because of the reduction in interface states obtained for the As deficient samples, the Fermi level was free to move, and the band bending spanned the entire GaAs band gap. The only remaining interface states were distributed near the valence band edge. The C-V characteristics of the optimally grown samples were virtually independent of frequency from 1 kHz to 4 MHz. At large positive voltages, all the ZnSe/p-GaAs samples tested exhibited deep depletion instead of electron inversion, suggesting the existence of a small conduction band discontinuity [1,2,11,12].

The interface state density distributions were measured using Terman's method [13] at 1 MHz. The parameters used for calculating the interface state density were the same as those used in generating the theoretical curves of Fig.1. By comparing the interface state densities near the mid-gap for the series of samples, a clear trend was seen showing a reduction in the interface state density as the GaAs epilayer surface became increasingly As deficient. For the samples formed on As-deficient GaAs the integrated interface state density was $2.5 \times 10^{11} \text{ cm}^{-2}$.

At this point there is no clear model to explain the improvement in interface quality reported in this work. One possibility is that a degree of As deficiency of the GaAs surface is inherently required for a good electrical interface [14]. A second possibility is that a chemical reaction occurs between the As-deficient GaAs epilayer and the II-VI elemental flux [15,16]. An example of such a reaction would be the formation of a III-VI compound such as Ga_2Se_3 . Recent TEM studies tend to indicate the presence of 1 or 2 monolayers of a strained interfacial compound at the interface [17]. In the structures grown on As-rich surfaces, similar interfacial layers have been observed, although they appeared to be considerably less distinct compared to those observed in the samples grown on As-deficient surfaces.

CONCLUSIONS

In conclusion, it is shown that the interface state density can be reduced by orders of magnitude when an appropriate GaAs epilayer surface stoichiometry is chosen for the subsequent nucleation of a ZnSe epilayer. Although the specific mechanism of the interface formation is not understood, it is clear that the interface state reduction for as-grown samples is important for the fabrication of heterojunctions involving the ZnSe/GaAs interface.

ACKNOWLEDGEMENT

The authors are grateful to L.A. Kolodziejski for her extensive involvement in the Purdue work involving ZnSe/GaAs interfaces. The authors would also like to acknowledge the contributions to this work by M. R. Melloch, J. A. Cooper, Jr., M. Vaziri, D. Lubelski, S. Durbin, and D. Mathine. This work was supported by Air Force Office of Scientific Research (AFOSR-85-0185), and the Defense Advanced Research Projects Agency/Office of Naval Research University Research Initiative Program (N00014-86-K0760).

REFERENCES

- [1] Q.-D. Qian, J. Qiu, M.R. Melloch, J.A. Cooper, Jr., L.A. Kolodziejski, M. Kobayashi, and R.L. Gunshor, *Appl. Phys. Lett.* **54**, 1359 (1989).
- [2] Q.-D. Qian, J. Qiu, M. Kobayashi, R.L. Gunshor, M.R. Melloch, and J.A. Cooper, Jr., *J. Vac. Sci. Technol.* **B7**, 793 (1989).
- [3] S.K. Chung, Y. Wu, K.L. Wang, N.H. Sheng, C.P. Lee, and D.L. Miller, *IEEE Trans. Electron Devices* **ED-34**, 149 (1987).
- [4] Quasi two-dimensional is used to describe nucleation which is predominantly two-dimensional, but shows some 3D characteristics. At the instant of nucleation, the streaky pattern, although largely remaining streaked, is superimposed by a spotty pattern (3D nucleation feature). The pattern becomes completely streaked in less than 10 seconds as the growth proceeds.
- [5] R.L. Gunshor, L.A. Kolodziejski, M.R. Melloch, M. Vaziri, C. Choi, and N. Otsuka, *Appl. Phys. Lett.* **50**, 200 (1987).
- [6] R.L. Gunshor, L.A. Kolodziejski, M.R. Melloch, N. Otsuka and A.V. Nurmikko, NATO Advanced Workshop on Wide Bandgap Semiconductors, Regensburg, W.Germany, August 1988.
- [7] M.C. Tamargo, J.L. de Miguel, D.M. Hwang, and H.H. Farrell, *J. Vac. Sci. Technol.* **B6**, 784 (1988).
- [8] A.Y. Cho, *J. Appl. Phys.* **47**, 2841 (1976).
- [9] L.A. Kolodziejski, R.L. Gunshor, N. Otsuka and C. Choi, *J. Vac. Sci. Technol.* **A4**, 2150 (1986).
- [10] N. Kobayashi, *Appl. Phys. Lett.* **55**, 1235 (1989).
- [11] S.P. Kowalczyk, E.A. Kraut, J.R. Waldrop, and R.W. Grant, 1982 *J. Vac. Sci. Technol.* **21**, 482 (1982).
- [12] J. Tersoff, *Phys. Rev. Lett.* **56**, 2755 (1986).
- [13] M.L. Terman, *Solid-State Electron.* **5**, 285 (1962).
- [14] R.E. Viturro, J.L. Shaw, L.J. Brillson, J.M. Woodall, P.D. Kirchner, G.D. Pettit, and S.L. Wright, *J. Vac. Sci. Technol.* **B6**, 1397 (1988).
- [15] I. Suemune, K. Ohmi, T. Kanda, K. Yukutake, Y. Kan, and M. Yamanishi, *Jpn J. Appl. Phys.* **25**, L827 (1986).
- [16] N. Kobayashi, *Jpn J. Appl. Phys.* **27**, L1597 (1988).
- [17] D. Li, N. Otsuka, J. Qiu, M. Kobayashi and R. L. Gunshor, to be published; see also this conference.

**Pseudomorphic ZnTe/AlSb/GaSb Heterostructures
by Molecular Beam Epitaxy**

D.L.Mathine*, J. Han* M.Kobayashi*, R.L.Gunshor*,D.R.Menke*, M. Vaziri*,
J.Gonsalves**, N.Otsuka**, Q.Fu***, M.Hagerott***, and A.V.Nurmikko***

*School of Electrical Engineering, Purdue University, West Lafayette,
Indiana 47907

**Materials Engineering, Purdue University, West Lafayette, Indiana 47907

***Division of Engineering, Brown University Providence, Rhode Island
02912

ABSTRACT

A series of pseudomorphic ZnTe/AlSb/GaSb epilayer/epilayer heterostructures, aimed at the realization of novel wide bandgap light emitting devices, were grown by molecular beam epitaxy. The low temperature photoluminescence (PL) spectra of ZnTe epilayers showed dominant near-band-edge features related to free, and shallow impurity bound excitons. The PL could be seen at room temperature. Both GaSb and AlSb were doped n-type using a PbSe source.

INTRODUCTION

Wide-gap II-VI semiconductors provide an opportunity to realize optoelectronic devices operating in the visible portion of the spectrum. To achieve this objective, experiments are under way to examine the epitaxial growth and materials properties of a variety of layered structures which incorporate both II-VI and III-V compounds that are grown on suitable substrates. One heterojunction that might be suitable for carrier injection and wide-bandgap light emission consists of p-ZnTe/n-AlSb [1,2]; a structure expected to have a favorable band line-up for carrier injection [3]. In this paper we describe epilayer/epilayer ZnTe/AlSb/GaSb heterostructures grown by molecular beam epitaxy (MBE) on GaSb substrates. The layer thicknesses were kept pseudomorphic (or nearly pseudomorphic) in order to minimize interfacial dislocations.

DISCUSSION OF EXPERIMENTS

To avoid unintentional doping during the growth of the II-VI/III-V structures, two isolated MBE growth chambers, connected by an ultra high vacuum (UHV) transfer tube, were used. The active interface was preserved by transferring the sample between growth chambers in the UHV transfer module. All of the epilayers for this study were grown on GaSb (001) substrates. The substrates were given an initial degrease followed by etching in HCl [4]. ZnTe was grown at a substrate temperature of 320°C using elemental sources, and flux ratios were measured by means of a quartz crystal monitor placed at the substrate position. Pseudomorphic ZnTe layers were nucleated on pseudomorphic AlSb layers; the AlSb in turn was grown on homoepitaxial GaSb buffer layers. The substrate temperature was 550°C, and the Sb_4 to Ga and Sb_4 to Al flux ratios were approximately 2:1 during the growth of both GaSb and AlSb undoped epilayers layers; the growth rates were about 1 Å/s. The RHEED patterns of the GaSb and AlSb surfaces during growth showed $c(2 \times 6)$ and (1×3) reconstructions, respectively [5,6].

The evolution of the RHEED diffraction pattern during the nucleation of ZnTe on an MBE-grown GaSb epilayer contrasts the behavior observed during nucleation on a GaSb substrate. For both cases, a 3-fold surface reconstruction is observed in the $[110]$ prior to nucleation of the ZnTe. For the nucleation on the substrate, one observes a spotty RHEED pattern indicative of three-dimensional nucleation, followed first by elongation of the spots into streaks after about 1 minute, then by the appearance of a (2×1) surface reconstruction, with the 2-fold pattern observed in the $[110]$. On the other hand, the observation, at nucleation, of a strongly streaked RHEED pattern, and the early presence (after about 15 seconds) of diffraction from surface reconstruction, suggests a more two-dimensional character for the nucleation of ZnTe on GaSb (or AlSb) epilayers. The two-dimensional nucleation is confirmed by the observation of strong RHEED intensity oscillations. The oscillations, which are characteristic of layer-by-layer growth, are present from the start of the nucleation of ZnTe on GaSb/AlSb epilayers.

Microstructural quality was examined using TEM and x-ray diffraction. TEM images revealed a range of strain relaxation in various samples. A small number of misfit dislocations were observed in the plan-view specimen of a sample with 2200 Å thick ZnTe and 540 Å thick AlSb layers. These misfit dislocations lie predominantly along one of the $\langle 110 \rangle$ directions, appearing as scattered groups, each consisting of several dislocations. The specific interface having the misfit dislocations could not be identified by the observation of plan-view specimens. Cross-sectional images did not show any misfit dislocations because of the very low density of misfit dislocations in the sample. A preliminary estimation of

the average spacing of misfit dislocations indicated that only a small percentage of the strain caused by the lattice mismatch is relaxed by misfit dislocations in this sample. No misfit dislocations were observed in the case of a plan-view specimen of a sample with 1380 Å thick ZnTe and 300 Å thick AlSb layers, implying the perfect pseudomorphic nature of this heterostructure. Despite the presence of a finite (but low) density of misfit dislocations, the x-ray rocking curve of a nearly pseudomorphic sample with 2200 Å of ZnTe shows a full width at half maximum (FWHM) of 82 arc sec, close to the theoretically expected broadening due to the finite layer thickness (74 arc sec). No dislocations or stacking faults were found in the examined area of the plan view specimen (over a few thousand square microns.), suggesting that the defect density in the epilayers is similar to that of the GaSb substrate.

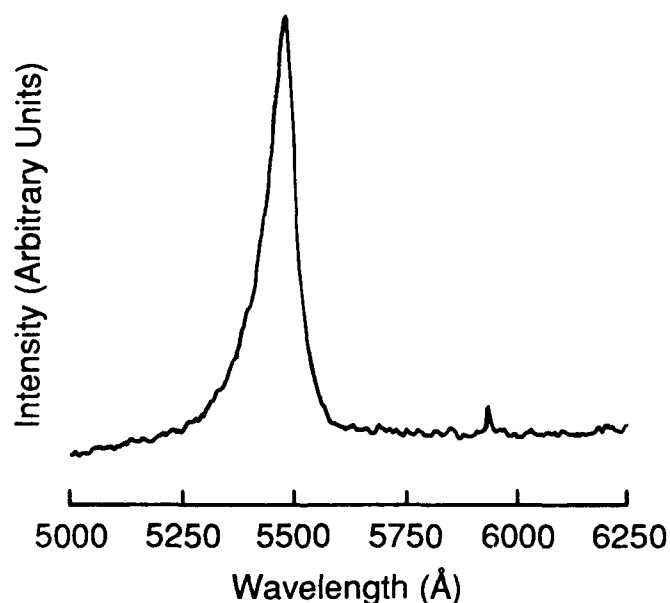


Fig. 1. Room temperature photoluminescence of a 2 μm ZnTe epitaxial layer on a GaSb substrate. The luminescence was excited with a wavelength of 4579 Å and a power density of 3 W/cm².

Photoluminescence (PL), reflectance, and Raman spectroscopies are applied to study the optical properties of the heterostructures. Intense, sharp exciton-related features are observed in photoluminescence for both thick (strain-relaxed) and pseudomorphic ZnTe epilayers; for the thick layers, PL is found to persist to room temperature (Fig.1). Dominant features in the low temperature luminescence corresponds to near bandedge transitions, and only weak deep level features are observed. The dominant portion of the low temperature PL spectrum shows features which can be associated with shallow bound excitons (with line widths $<1\text{meV}$) as well as free-exciton like components [7,8,9]. The presence of the latter can be identified through their spectral position which overlaps the pronounced reflectance excursions commonly encountered at the exciton bandgap. Transition energies for the free exciton of pseudomorphic samples are split shifted by lattice strain to higher values when compared to thick ($\sim 2\mu\text{m}$) ZnTe epilayers. Raman spectra show distinct, sharp contributions, especially from optical phonons from the various portions of the heterostructures.

Good optical fingerprints, in both photoluminescence and reflectance, are also obtained from the GaSb portions of our structures. (AlSb, as an indirect gap material, has weak optical resonances at the E_0 edge.) The reflectance excursions are sharp, consistent with the good interfacial quality. (Comparable traces are also obtained from the ZnTe/GaSb heterostructures.)

Se doping of both GaSb and AlSb have been achieved by employing PbSe as a dopant source. Contrary to previous reports [10,11], the doping efficiency of Se in GaSb can be similar to GaAs using a Sb/Ga flux ratio of unity at a growth temperature of 450°C . An example of room temperature carrier concentration and electron mobility for highly doped $2\mu\text{m}$ thick GaSb epilayers grown on GaAs substrates are $5.5 \times 10^{17}\text{cm}^{-3}$ and $1500\text{cm}^2/\text{V-sec}$, respectively. The Se doping of AlSb appears to present more of a challenge, although n-type levels in the low 10^{16}cm^{-3} range have been obtained in our laboratory. Preliminary experiments involving the Se doping of AlSb suggest a decreased incorporation efficiency for Se when compared to results for GaSb epilayers. Evaluation of the doping behavior and electrical properties for ZnTe epilayers is in progress.

SUMMARY

In summary, the potentially important pseudomorphic epilayer/epilayer heterojunction MBE consisting of ZnTe on AlSb has been grown for the first time by MBE, and characterized by several techniques. The nucleation characteristics of ZnTe on GaSb substrates and epilayers

were compared, with consistent two-dimensional nucleation observed in the case of epilayers. Microstructural and optical evaluations indicated a high structural quality, and the potential for developing novel light emitting device structures. Preliminary studies support the feasibility of Se doping of GaSb and AlSb. Future efforts will be directed at optimization of the electrical properties of this II-VI/III-V heterojunction.

ACKNOWLEDGEMENTS

The authors would like to acknowledge L.A. Kolodziejski for numerous discussions, L.R. Dawson for discussing unpublished results concerning Se doping, and Y.R. Lee, and A.K. Ramdas for measurements of modulated reflectance. The authors also thank Z. Pei, S.M. Durbin, J. Qiu, S. Karthik, R. Venkatasubramanian and D.A. Lubelski for contributions to the project. The Pb-enriched PbSe source material was provided by D.L. Partin. Research support was provided by DARPA/ONR URI contract N00014-86-K0760, AFOSR grant AFOSR-85-0185, National Science Foundation (NSF)-MRG Grant DMR-8520866, and NSF Equipment grant ECS-8606241.

REFERENCES

1. D.L. Mathine, S.M. Durbin, R.L. Gunshor, M. Kobayashi, D.R. Menke, Z. Pei, J. Gonsalves, N. Otsuka, Q. Fu, M. Hagerott, and A.V. Nurmikko. *Appl. Phys. Lett.* **55**, 268 (1989).
2. J.O. McCaldin, and T.C. McGill, *J. Vac. Sci. Technol.* **B6**, 1360 (1988).
3. W.A. Harrison, and J. Tersoff, *J. Vac. Sci. Technol.* **B4**, 1068 (1986).
4. H. Muneoka (private communication).
5. T.H. Chiu and W.T. Tsang, *J. Appl. Phys.* **57**, 4572 (1985).
6. C.A. Chang, H. Takaoka, L.L. Chang, and L. Esaki, *Appl. Phys. Lett.* **40**, 983 (1982).
7. M.S. Brondin, V.M. Bandura, and M.G. Matsko, *Phys. Stat. Sol. (b)* **125**, 613 (1984).
8. Y. Hishida, H. Ishii, T. Toda, and T. Niina, *J. Cryst. Growth* **95**, 517 (1989).
9. R.D. Feldman, R.F. Austin, P.M. Bridenbaugh, A.M. Johnson, W.M. Simpson, B.A. Wilson, and C.E. Bonner, *J. Appl. Phys.* **64**, 1191 (1988).
10. T.D. McLean, T.M. Kerr, D.I. Westwood, C.E.C. Woos, and D.F. Howell, *J. Vac. Sci. Technol. B* **4**, 601 (1986).
11. S. Subbanna, G. Tuttle, and H. Kroemer, *J. Electron. Mat.* **17**, 797 (1988).

TRANSMISSION ELECTRON MICROSCOPY OF II-VI/III-V SEMICONDUCTOR HETEROEPITAXIAL INTERFACES

D. LI, AND N. OTSUKA

School of Materials Engineering, Purdue University, West Lafayette, IN 47907

J. QIU, J. GLENN Jr., M. KOBAYASHI, AND R. L. GUNSHOR

School of Electrical Engineering, Purdue University, West Lafayette, IN 47907

ABSTRACT

Interfaces of pseudomorphic (100)ZnSe/GaAs and (100)CdTe/InSb heterostructures grown by molecular beam epitaxy have been studied by transmission electron microscopy. High resolution electron microscope images show dark bands with thicknesses of one or two monolayers at the interfaces. The interfaces appear as bright lines in dark field images of the 200 type reflections, while they become dark lines in dark field images of the 400 type reflections. These observations are explained by assuming the existence of interface layers of III_2VI_3 compounds which have structural vacancies in the sublattices of the group III atoms.

1. INTRODUCTION

In recent years, a significant progress has been made in the growth of II-VI/III-V semiconductor heterostructures by molecular beam epitaxy (MBE) and metalorganic chemical vapor deposition (MOCVD). Heterostructures having high structural qualities are grown by utilizing closely lattice matched systems such as ZnSe/GaAs, CdTe/InSb, and ZnTe/GaSb. The growth of these heterostructures has raised a possibility of the development of new novel electronic devices. In addition, the possibility of the development of light emitting devices of wide-gap II-VI semiconductors are presently being explored by utilizing these heterostructures.

The realization of II-VI/III-V semiconductor heterojunction devices, however, requires the preparation of heteroepitaxial interfaces having extremely good electronic properties. For achieving this goal, important results have been obtained in a recent study by Qian, et al. [1]. This study has demonstrated the feasibility of the preparation of ZnSe/GaAs heterojunctions whose interface state densities are comparable to those of GaAs/(Al, Ga)As heterojunctions. For the preparation of these heterojunctions, the growth of pseudomorphic ZnSe epilayers on GaAs epilayers and post-growth annealing were employed. In a more recent development, as-grown heterostructures having interfaces with the similar quality have been obtained by growing ZnSe on As-deficient GaAs surfaces without the need for the post-growth annealing [2]. These results, which have shown the change of the interface electronic properties by the post-growth annealing or by the change of the surface stoichiometry of GaAs epilayers, suggest a certain form of modification of ZnSe/GaAs interface from the abrupt one.

Earlier studies of ZnSe/GaAs [3,4] and CdTe/InSb [5] heterostructures have suggested the formation of stable III_2VI_3 compounds such as Ga_2Se_3 and In_2Te_3 at these interfaces. These studies have utilized spectroscopic techniques for the analysis of the interfaces; to date, no structural study of these heteroepitaxial interfaces has been reported. In this paper, we present transmission electron microscope (TEM) observations of ZnSe/GaAs and CdTe/InSb heteroepitaxial interfaces which directly show the existence of interface layers. The analysis of dark field images suggests that the interface layers have structures identical to those of Ga_2Se_3 and In_2Te_3 .

2. EXPERIMENTAL PROCEDURE

(100)ZnSe/GaAs and (100)CdTe/InSb heterostructures were grown by using a Perkin-Elmer model 430 modular MBE system. For both heterostructure systems, III-V semiconductor epilayers were grown first on III-V semiconductor substrates and transferred through an ultra high vacuum (3×10^{-10} Torr) tube to another growth chamber for the growth of II-VI semiconductor epilayers. Details of growth procedures of these heterostructures are described in other reports [2, 6, 7]. Thicknesses of II-VI semiconductor epilayers were kept smaller than the critical thicknesses expected from lattice mismatch between the II-VI and III-V semiconductor crystals. Interfaces of these heterostructures, therefore, are free from misfit dislocations. For the growth of ZnSe/GaAs heterostructures, the surfaces of GaAs epilayers were varied from As-rich to As-deficient conditions among samples by heating prior to the deposition. The following three ZnSe/GaAs heterostructures are examined in the present study: the sample grown on the As-rich surface which exhibits a $c(4 \times 4)$ reconstruction structure, the sample grown on the As-deficient surface which exhibits a (4×3) reconstruction structure, and the sample grown on the surface whose As coverage is intermediate between the above two and exhibits a (4×6) reconstruction structure.

For the TEM observation, (011) and (010) cross-sectional samples were prepared by ion thinning at low temperatures. Iodine ions were used at the final thinning stage in order to reduce damages in the samples [8]. A JEM 2000 EX electron microscope equipped with an ultra-high resolution objective lens pole piece was used at an operating voltage of 200kV. The spherical aberration coefficient of the pole piece is 0.7mm which yields a point resolution of 2.0 Å.

3. RESULTS AND DISCUSSION

Two ZnSe/GaAs samples grown on the (4×6) and (4×3) surfaces show TEM images which suggest the existence of an interface layer. From the sample grown on the $c(4 \times 4)$ surface, on the other hand, no distinct image of the interface layer is observed. In the following, observations of the sample grown on the (4×6) surface are explained.

Fig. 1 is a [010] high resolution electron microscopy (HREM) image of the ZnSe/GaAs interface. The image was taken at a defocusing of about -600 Å with an objective lens aperture having a diameter of 0.7 Å^{-1} . The thickness of the observed area is about 50 Å. In the image, a dark band with a width of about two monolayers is seen along the ZnSe/GaAs interface. This dark band is seen along the interface in all observed area except very thin parts close to edges of the sample. Compared to [010] HREM images, [011] HREM images do not show a clear dark band along the interface, which may be attributed to the dominance of $\{111\}$ -type lattice fringes in the lattice images.

Fig. 2(a) is a dark field image of the 400 reflection. The image was taken under the exact Bragg condition of the 400 reflection with the excitation of only h00 type reflections. The thickness of the observed area is about 400 Å which was estimated with locations of thickness contours. In the image, a distinct dark line is seen at the ZnSe/GaAs interface. This dark line appears along the interface in all parts of observed areas except those crossed by dark thickness contours where the interface appears as a bright line. Similar dark lines are observed in $\bar{4}00$, 004, and $00\bar{4}$ dark field images taken under the exact Bragg conditions. Fig. 2(b) is a dark field image of the 200 reflection which is taken from the same area. Similarly to Fig. 2(a), the image was taken under the exact Bragg condition of the 200 reflection with the excitation of only h00 type reflections. In this image, unlike the 400 type images, the ZnSe/GaAs interface appears as a bright line. The bright line along the interface is seen in all observed areas from edges of the sample to thicker parts. Dark field images of 002, $00\bar{2}$, and $\bar{2}00$ reflections also show similar bright lines under the exact Bragg conditions.

As described earlier, these bright and dark lines are observed from the sample grown on the (4x6) and (4x3) surfaces, but the sample grown on the c(4x4) surface does not show distinct images suggesting the existence of an interface layer. In particular, 200 dark field images reveal a clear difference among these samples [9]. Distinct bright lines are observed in both samples grown on the (4x6) and (4x3) surfaces, the latter of which appears to have a more continuous bright line than the former one. The images of the sample grown on the c(4x4) surface either have no bright line or exhibit a very weak thin bright line. The difference among the images of these samples suggests that As-deficient surfaces may be more preferable for the formation of the interface layer than As-rich surfaces.

The crystal structure factor of the 200 type reflection of the zincblende structure is given by a difference of scattering factors of atoms occupying two different face centered cubic (fcc) sublattices, while the crystal structure factor of the 400 type reflection is given by an addition of scattering factors of these two types of atoms. With this difference of crystal structure factors, one can derive the following model of the interface layer. Between ZnSe and GaAs crystals, a very thin layer having a zincblende structure exists by maintaining coherent interfaces. One of the fcc sublattices is occupied by cations, i.e., Zn or Ga, and the other by anions, i.e., Se or As. Unlike the GaAs and ZnSe crystals, one of the fcc sublattices in the thin layer has a high concentration of vacancies, due to which interplanar spacing of the layer in the [100] direction becomes slightly smaller than those of GaAs and ZnSe. Because of vacancies in one of the fcc sublattices, the crystal structure factor of the 200 reflection of the thin layer becomes much greater than those of GaAs and ZnSe which are very small due to nearly equal values of scattering factors of constituent atoms. The thin layer, therefore, will appear with a bright contrast in the 200 dark field images. In the 400 dark field images, on the other hand, the thin layer will appear as a dark line as a result of the smaller crystal structure factor than those of ZnSe and GaAs.

As described previously, early studies [3,4] has suggested the formation of a (Ga, Se) compounds at the ZnSe/GaAs heteroepitaxial interface. One of the stable phases of (Ga, Se) compounds, named Ga_2Se_3 , is known to have a structure identical to that suggested by the present observations [10]. It has a zincblende structure, and one third of Ga sites are left as structural vacancies. As a result of these structural vacancies, the lattice parameters of Ga_2Se_3 is about 5% smaller than those of GaAs and ZnSe. This lattice contraction may give rise to a shift of (202) type lattice fringes at the interface in [010] HREM images. The shift, however, is too small to be detected unambiguously in HREM images such as the images shown in Fig. 1, if the thickness of the layer is only two or three monolayers. The difference of the interface images among three samples also suggests that the interface layer may be a compound close to Ga_2Se_3 ; As-deficient surfaces are expected to be preferable for the formation of Ga_2Se_3 than As-rich surfaces.

Based on the model of a thin Ga_2Se_3 interface layer, intensities of 200 and 400 dark field images are calculated. Fig. 3 schematically illustrates this model. The calculation were made based on the two beam dynamical theory with the column approximation. Fig. 4(a) and (b) are calculated intensity profiles of 400 and 200 dark field images, respectively. The thickness of the crystal is 400 Å, and the incident beam is set at the exact Bragg condition in both cases. As seen in figures, the calculations are in good agreement with observed images despite the use of simple approximations.

Similarly to the ZnSe/GaAs interfaces, HREM images and dark field images of the CdTe/InSb heterostructure suggest the existence of an interface layer. Fig. 5 is a [011] HREM image of the CdTe/InSb interface. Unlike the ZnSe/GaAs interface, a distinct dark band is observed in both [011] and [010] HREM images as seen in this image. Fig. 6(a) and (b) are dark field images of the CdTe/InSb interface which were taken with the 400 and 200 reflections, respectively. In both cases, the reflection was set at the exact Bragg condition with the excitation of only h00 type reflections. The 200 dark field image shows a distinct bright line, and the 400 dark field image exhibits a

dark line at the interface, similarly to the images of the ZnSe/GaAs interfaces. The bright and dark lines in this case, however, are more distinct than those observed at the ZnSe/GaAs interface, which, along with the observation of a dark band in [011] HREM images, suggests the formation of a more developed interface layer in the CdTe/InSb heterostructure; the interface layer may be more continuous or may have a greater thickness than those in ZnSe/GaAs heterostructures.

As explained in Introduction, earlier studies have suggested the formation of In_2Te_3 in CdTe/InSb heteroepitaxial interfaces [5]. Similarly to Ga_2Se_3 , In_2Te_3 crystallizes in a zincblende structure with one third of its cation sites being structural vacancies [11]. It is, therefore, expected that an In_2Te_3 layer appears as a bright line in 200 dark field images and as a dark line in 400 dark field images. The existence of In_2Te_3 in the CdTe/InSb interfaces is also suggested by X-ray diffraction studies of CdTe/InSb multilayer structures [12]. The shift of the 0-th peaks of the multilayer structures due to the lattice contraction of In_2Te_3 are observed in X-ray diffraction patterns.

The results of the present study suggest that III_2VI_3 compound layers form at the II-VI/III-V heteroepitaxial interfaces under certain growth conditions. One can also suggest the formation of interface layers of these compounds with thermodynamic data, which show that these compounds are highly stable phases despite the existence of a high concentration of vacancies in their structures. For example, the heat of atomization of Ga_2Se_3 , which corresponds to the energy required to break all chemical bonds in the compound, is 308 kcal for one mole at 298 K [13,14]. This value is comparable to that of ZnSe which is 357 kcal for three moles [14]. Such a high stability of III_2VI_3 compounds is explained by the matching of valences of constituent atoms in their structures. One cannot, therefore, consider the present model of the interface layer energetically unstable simply because of the existence of a high concentration of vacancies. It is also important to point out that the systematic dependence of the interface contrast on the reflections used for dark field images can be explained only by the present model without adding any artificial modification.

ACKNOWLEDGEMENT

The authors wish to thank L. A. Kolodziejski, J. M. Gonsalves, Y. Nakamura, D. Lubelski, D. R. Menke, Sungki O, and Q. E. Qian for their contribution to this work. The research was supported by DARPA/ONR-URI Program N0014-86-k0760. AFOSR grant No. 85-0185, and NSF-MRG, grant DMR-8520866.

REFERENCES

1. Q. D. Qian, J. Qiu, M. R. Melloch, J. A. Cooper, Jr., L. A. Kolodziejski, M. Kobayashi, and R. L. Gunshor, *Appl. Phys. Lett.*, 54 (1989) 1359.
2. J. Qiu, Q. D. Qian, R. L. Gunshor, M. Kobayashi, D. R. Menke, D. Li, and N. Otsuka, submitted to *Appl. Phys. Lett.*
3. D. W. Tu and A. Kahn, *J. Vac. Sci. Technol. A* 3 (1985) 922.
4. I. Suemune, K. Ohmi, T. Kanda, K. Yatake, Y. Kan, and M. Yamanishi, *Jap. J. Appl. Phys.*, 25 (1986) 1827.
5. D. R. T. Zahn, K. J. Mackey, R. H. Williams, H. Munder, J. Gearts, and W. Richter, *Appl. Phys. Lett.*, 50 (1987) 742.
6. R. L. Gunshor, L. A. Kolodziejski, M. R. Melloch, M. Vaziri, C. Choi, and N. Otsuka, *Appl. Phys. Lett.*, 50 (1987) 200.
7. J. L. Glenn, Jr., Sungki O, L. A. Kolodziejski, R. L. Gunshor, M. Kobayashi, D. Li, N. Otsuka, M. Haygerott, N. Pelekanos, and A. V. Nurmikko, *J. Vac. Sci. Technol. B* 7 (1989) 249.
8. A. G. Cullis, N. G. Chew, and J. L. Hutchison, *Ultramicroscopy*, 17 (1985) 203.
9. D. Li, N. Otsuka, J. Qiu, M. Kobayashi, and R. L. Gunshor, submitted to *Appl. Phys. Lett.*

10. H. Hahn, and W. Klingler, *Z. anorg. Chemie.*, 259 (1949) 135
11. B. Grzeta-Plenkovic, S. Popovic, B. Celustka, Z. Ruzic-toros, B. Santic, and D. Sold, *J. Appl. Cryst.* 16 (1983) 415.
12. J. L. Glenn, Jr., Sungki, O, M. Kobayashi, R. L. Gunshor, L. A. Kolodziejski, D. Li, N. Otsuka, M. Haggerott, N. Pelekanos, and A. V. Nurmikko, submitted to *Appl. Phys. Lett.*
13. K. V. Mills, the thermodynamic Data for Inorganic Sulphides, Selenides, and Tellurides (Butterworth, 1974).
14. H. Hartmann, R. Mach, and G. Selle, *Current Topics in Materials Science*, Vol. 9, ed. E. Kaldis, (North-Holland, Amsterdam, 1981), Chap. 1.

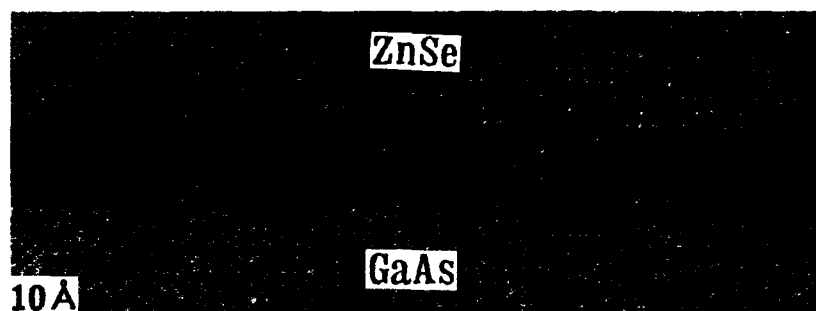


Fig. 1. [010] HREM image of the ZnSe/GaAs interface.

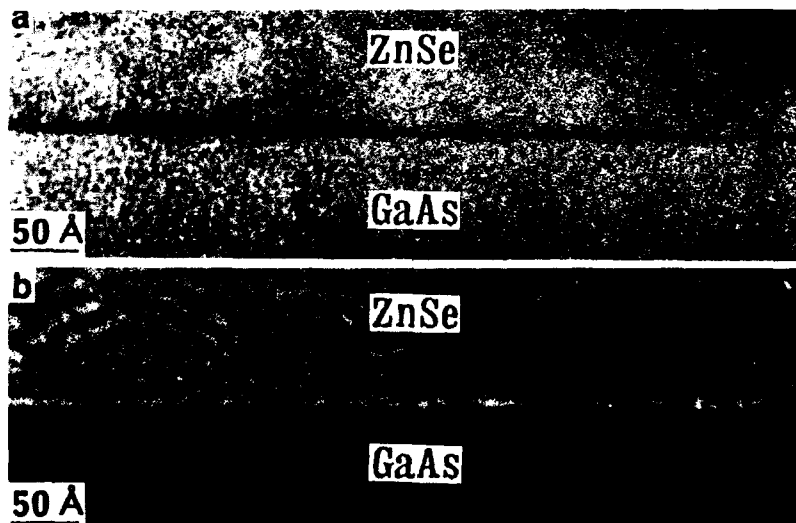


Fig. 2. Darkfield images of the ZnSe/GaAs interface, (a) 400 reflection, and (b) 200 reflection.

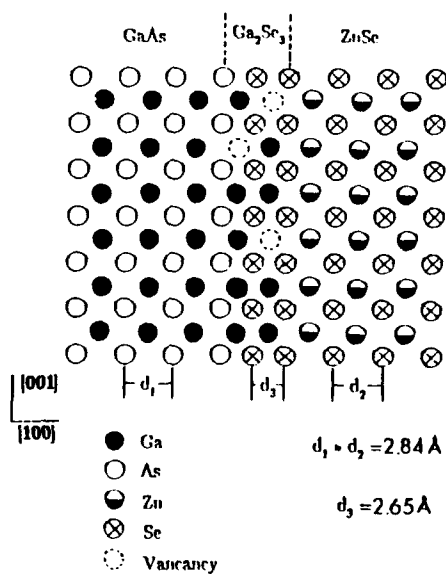


Fig. 3. Model of the interface layer.

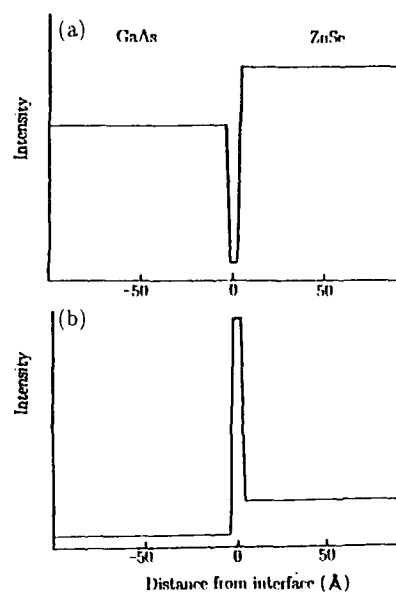


Fig. 4. Calculated intensity profiles of dark field images, (a) 400 reflection, and (b) 200 reflection.

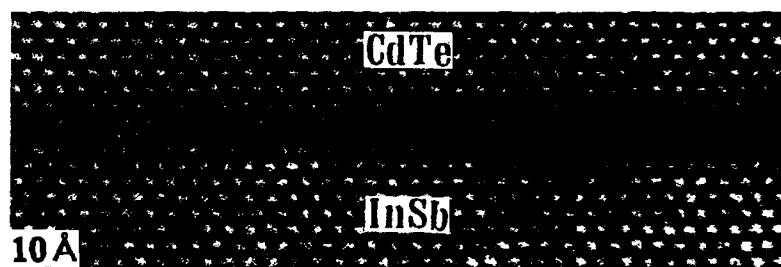
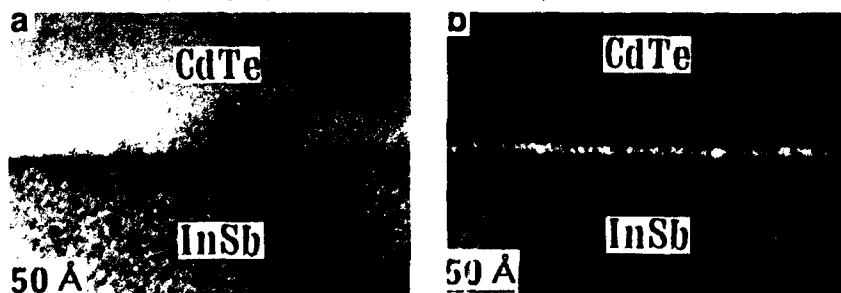
Fig. 5. $[011]$ HREM image of the CdTe/InSb interface

Fig. 6. Dark field images of the CdTe/InSb interfaces. (a) 400 reflection, and (b) 200 reflection.

PROPERTIES OF CHLORINE-DOPED ZINC SELENIDE
GROWN BY MOLECULAR BEAM EPITAXY

S. HWANG, J. REN, K.A. BOWERS, J.W. COOK, JR., and J.F. SCHETZINA
Department of Physics, North Carolina State University, Raleigh,
North Carolina 27695-8202

ABSTRACT

ZnSe:Cl epilayers have been grown on (100) GaAs by MBE using a Zn to Se beam flux ratio of 2:1 and substrate temperatures as low as 225°C. The ZnSe:Cl epilayers are highly conducting and exhibit bright blue-violet edge luminescence at 300 K. A mobility of 2480 cm²/V-s at 40 K was measured for an n-type ZnSe:Cl film that was Cl-doped to $\sim 2.3 \times 10^{17}$ cm⁻³ and for which a compensation ratio (N_A/N_D) of $\sim 3\%$ was calculated. Carrier concentrations as large as 6.7×10^{18} cm⁻³ were obtained by increasing the temperature of the MBE oven containing the Cl dopant.

INTRODUCTION

ZnSe is a wide band gap II-VI semiconductor that has attracted considerable attention in recent years. Its room temperature band gap of ~ 2.7 eV makes it an attractive candidate for the fabrication of blue light emitting devices [1,2]. Although p-type doping is currently the major obstacle in making such devices, efficient activation of n-type dopants is of equal importance, especially if semiconductor lasers are to be developed. High n-type doping is also required for other related devices such as optical modulators, transistor amplifiers, and diode detectors which might form the basis of a new blue-green optoelectronics technology. Recent investigations by MBE [3] and MOVPE [4] have shown that very high n-type doping levels can be achieved in ZnSe films using group VII elements as dopants. However, the samples reported to date generally exhibit low Hall mobilities compared to n-type ZnSe:Ga doped films [2]. In spite of this, we consider the group VII elements as the most promising n-type dopants. In this paper we report the successful MBE growth of n-type ZnSe:Cl films at low temperatures. The films exhibit excellent electrical and optical properties.

II. EXPERIMENTAL DETAILS

The ZnSe:Cl samples were grown in an MBE system designed and built at North Carolina State University (NCSU) [5]. The growth chamber has a base pressure of 6×10^{-11} torr and is equipped with seven MBE sources. The MBE sources feature special two-temperature-zone furnaces, designed and constructed at NCSU specifically for the growth of II-VI materials, which are capable of producing highly stable beam fluxes [6]. High purity (6N grade) Zn and Se were used as primary source materials, and ultra dry ZnCl₂ (5N grade) was used as the dopant source. To calibrate the molecular beam flux density from each of the primary MBE ovens, films were deposited at room temperature and their thicknesses were measured. The beam flux was calculated assuming unity sticking coefficient and correlated with the beam equivalent pressure (BEP) measured with a nude ion gauge at the exact location of the substrate [5]. Both the Zn and Se source beams

were calibrated in this way so that an accurate beam flux ratio (BFR) could be obtained.

Semi-insulating (100) GaAs wafers were used as substrates. Prior to MBE film growth, the GaAs substrate was first degreased in standard solvents and then etched in an $\text{H}_2\text{SO}_4:\text{H}_2\text{O}_2:\text{H}_2\text{O}$ (6:1:1) solution at 40°C for 3 minutes. The substrate was preheated to 580°C for 10 minutes in the MBE system to desorb the surface oxide. A $2.5\ \mu\text{m}$ thick undoped ZnSe buffer layer was first grown. Doping was then initiated by opening the shutter of the ZnCl_2 source.

Electrical characterization of the epilayers consisted of standard van der Pauw Hall effect measurements over the temperature range 20–300 K. Ohmic contacts to the samples were made with an In-based solder. Photoluminescence (PL) was excited using the 360 nm UV output from an Ar^+ ion laser and was measured using a SPEX 1403 double monochromator equipped with a GaAs photomultiplier tube and computer-controlled photon counting electronics. A Janis Super-Varitemp cryostat was used to cool the ZnSe:Cl films to liquid helium temperatures.

RESULTS AND DISCUSSION

It is essential that the surface stoichiometry of ZnSe be maintained during MBE film growth in order to achieve high quality electrical and optical properties. The growth mechanisms of II-VI materials have been studied by several groups [7,8]. In a recent study, Zhu et. al. showed that while the growth rate is influenced by the Se desorption from the growing surface into the precursor states when the Zn to Se BFR is greater than 1, when the BFR is equal or smaller than 1 the growth rate is influenced by both Zn and Se desorption. Thus, it appears that it may be easier to control the surface stoichiometry by using a Zn to Se BFR of greater than 1. This generally requires lower growth temperatures.

We have grown ZnSe films at low temperatures (225°C – 300°C) with Zn-to-Se BFRs ranging from 0.5 to 2. Under Se-rich conditions (BFR<1), the films exhibit poor surface morphologies and broad x-ray rocking curves. In contrast, films grown under Zn-rich conditions exhibit mirror-like surfaces. Double-crystal x-ray rocking curves for films 2–3 μm thick typically exhibit FWHMs of ~150 arc sec.

Cl-doped ZnSe films grown under Zn rich conditions exhibit high conductivity. Room temperature carrier concentrations ranging from $1.5 \times 10^{17}\ \text{cm}^{-3}$ to $6.7 \times 10^{18}\ \text{cm}^{-3}$ have been reproducibly obtained by varying the ZnCl_2 oven temperature. Fig. 1 shows the carrier concentration for heavily-doped (C21) and lightly-doped (C35) samples, respectively. The former exhibits degenerate doping characteristics (constant carrier concentration) versus temperature. The carrier concentration of C35, however, is clearly activated over the temperature range from 20 to 300 K. In order to determine the compensation ratio and donor ionization energy, we have calculated the carrier concentration by solving the charge-neutrality equation which, assuming non-degenerate statistics, can be written as [9]

$$\frac{n_0 (N_A + n_0)}{(N_D - N_A - n_0)} = \beta N_c \exp \left(- \frac{E_D}{k_B T} \right) \quad (1)$$

where N_D and N_A are the donor and acceptor concentration,

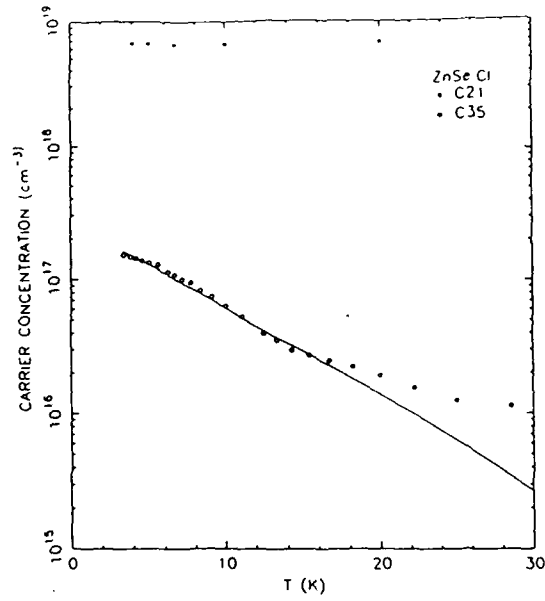


Fig. 1. Temperature dependence of carrier concentration of MBE ZnSe:Cl. The solid curve shows the calculated data.

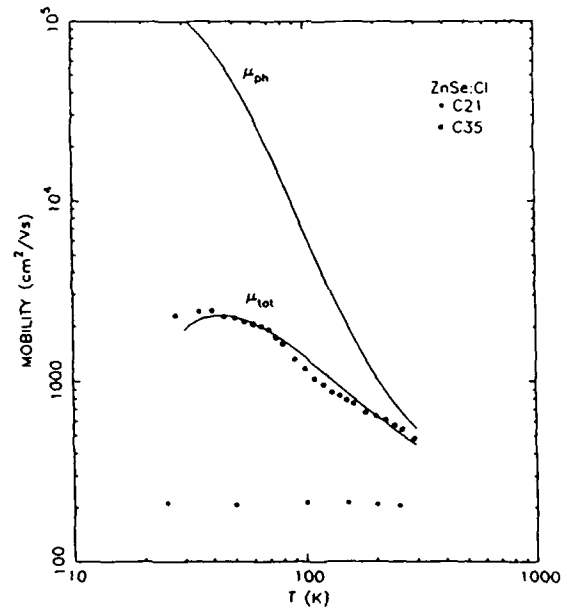


Fig. 2. Temperature dependence of electron mobility of MBE ZnSe:Cl. Solid curves show the calculated data

respectively. The degeneracy factor β is taken to be $1/2$. $N_C = 2(2\pi m_c^* kT/h^2)^{3/2}$ is the density of states of the conduction band. The effective mass for the conduction band m_c^* is taken to be 0.17, and E_D is the ionization energy. The solid curve in Fig. 1 shows the best fit, which is obtained with $E_D = 16.5$ meV, $N_D = 2.3 \times 10^{17}$ cm $^{-3}$, and $N_A = 7.0 \times 10^{15}$ cm $^{-3}$. The ionization energy obtained is lower than the value of 26 meV reported from optical measurements [10]. In addition, below 60K, C35 appears to have an even smaller activation energy. Note, however, that for C35 the Fermi level is about 27 meV below the conduction band minimum at room temperature and that the compensation ratio is only 3%. The low compensation ratio provides clear evidence of the electrical quality of this sample. Therefore, the behavior of the carrier concentration below 60K is attributed to the presence of an unintentional donor.

Plots of Hall mobility versus temperature for samples C21 and C35 are shown in Fig. 2. The mobility of the heavily doped layer C21 is ~ 220 cm 2 /V-s and is independent of temperature. In contrast, the mobility of C35 increases with decreasing temperature to a maximum of 2480 cm 2 /V-s at 40°C. To further analyze these data, the electron mobility of C35 was calculated by numerically solving the Boltzmann equation using the iteration method [11,12]. Four scattering mechanisms were taken into account including polar mode phonon scattering, acoustic mode (deformation-potential coupling), acoustic mode (piezoelectric coupling), and ionized impurity scattering. The results are shown as solid curves in Fig. 2. Curve μ_{ph} is the phonon-scattering-limited electron mobility, while μ_{tot} is obtained when impurity scattering is also included. The impurity concentration N_{imp} for the mobility calculation was taken to be $2N_A + n_0$ [13], where N_A is the acceptor concentration and n_0 is the equilibrium electron concentration. Both n_0 and N_A were obtained from the carrier concentration analysis described above. Note the good agreement between the theoretical calculation and experimental data which supports the low compensation ratio obtained from the carrier concentration analysis.

Fig. 3 shows the 5K PL spectrum obtained for C35. The near-band-edge (NBE) luminescence is shown in the inset. The NBE luminescence consists of a donor bound exciton DBE at 2.7960 eV, an acceptor bound excitons ABE at 2.7911 eV and 2.7825 eV. The fact that the free exciton lines are absent but the DBE line remains narrow (FWHM = 6.2 meV) has the important implication that the Cl atoms are successfully incorporated into the lattice. The two ABE lines, both associated with neutral acceptors, are usually absent in n-type undoped ZnSe epilayers grown by MBE but seem to be present in the Cl-doped samples reported by Ohkawa *et al.* [3]. In our case these two lines are well resolved. The spectrum of C35 also exhibits a very weak emission band at around 2.6 eV, whose peak intensity is about 200 times lower than that of the dominant peak. The deep level emission around 2.2 eV is three orders of magnitude lower than the dominant peak and could hardly be seen.

Fig. 4 shows the room temperature PL spectrum for C35. The spectrum is dominated by a strong near-band-edge (NBE) emission centered at 2.693 eV. This peak energy is consistent with that reported by Ohkawa *et al.* for Cl-doped ZnSe who attribute the PL to donor to valence band recombination [3]. The room temperature spectrum also exhibits weak deep level emission centered at around 2.1 eV. The peak-to-peak ratio between the NBE and deep level

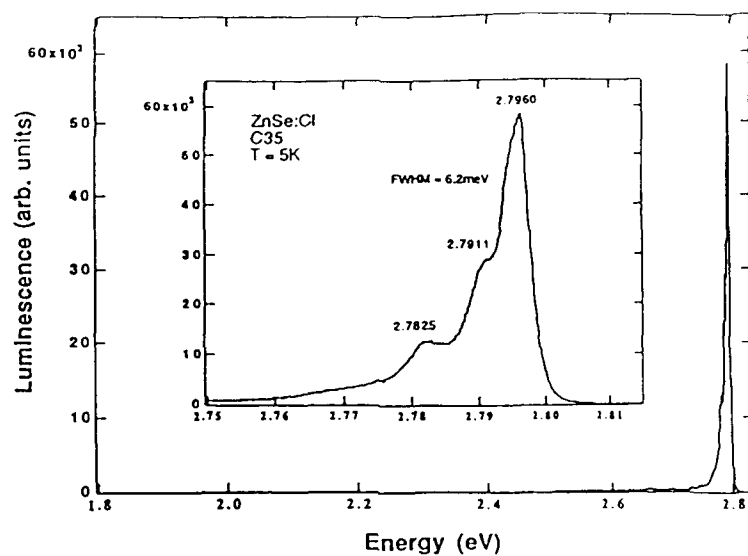


Fig. 3. Photoluminescence spectrum of MBE ZnSe:Cl measured at 5K. The near-band-edge spectrum is shown in the inset.

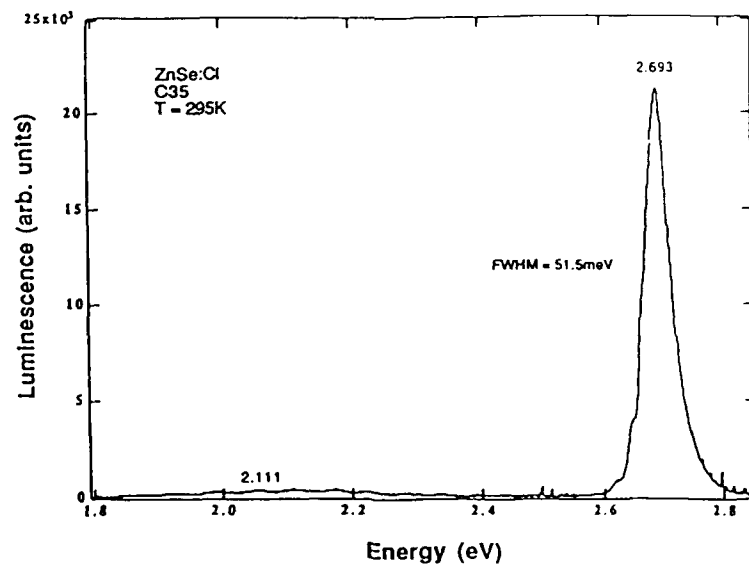


Fig. 4. Photoluminescence spectrum of MBE ZnSe:Cl measured at room temperature.

emission is as high as 46, which is comparable the value reported by Yao for high quality undoped samples [14]. Recently, we have obtained PL spectra comparable in quality to those shown in Figs. 3 and 4 from ZnSe:Cl films grown by MBE at temperatures as low as 225°C. These films also display good electrical properties.

SUMMARY

High quality Cl-doped ZnSe films have been grown by MBE under Zn-rich conditions at low temperatures (225°C). The epilayers exhibit mirror-like surface morphologies, good x-ray rocking curves, low compensation ratios, high electron mobilities, and sharp, bright near-band-edge photoluminescence with minimal deep level emissions. Our data provide further evidence that Cl is very efficient as an n-type donor.

The authors wish to thank J. Matthews and M. Bennet for their assistance in substrate preparation and PL measurements, respectively. This work was supported by DARPA/URI funds under Purdue University subcontract 530-0716.

REFERENCES

1. R.N. Bhargava, *J. Crystal Growth* **86**, 873 (1988).
2. T. Yao, *J. Crystal Growth* **72**, 31 (1985).
3. K. Ohkawa, T. Mitsuyu, and O. Yamazaki, *J. Appl. Phys.* **62**, 3216 (1987).
4. A. Yoshikawa, H. Nomura, S. Yamaga, and H. Kasai *J. Appl. Phys.* **65**, 1223 (1989).
5. K.A. Harris, S. Hwang, D.K. Blanks, J.W. Cook, Jr., N. Otsuka, and J.F. Schetzina, *J. Vac. Sci. Technol. A* **4**, 2061 (1986).
6. J.W. Cook, Jr., D.B. Eason, and K.A. Harris, presented in the 10th Molecular Beam Epitaxy Workshop, Raleigh, North Carolina, September 13-15, 1989.
7. A. Koukitu, H. Nakai, T. Suzuki, and H. Seki, *J. Crystal Growth* **84**, 425 (1987).
8. Z. Zhu, T. Nomura, M. Miyao, and M. Hagino, *J. Crystal Growth* **95**, 529 (1989).
9. J.S. Blakemore, *Solid State Physics*, 2nd ed. (Cambridge University Press, Cambridge, 1985), p.320.
10. E. Kartheuser, R. Evrard, and F. Williams, *Phys. Rev. B* **21**, 648 (1980).
11. D.L. Rode, *Phys. Rev. B* **2**, 4036 (1970).
12. S. Hwang, Ph.D. Thesis, North Carolina State University, 1988.
13. H.H. Woodbury, *Phys. Rev. B* **9**, 5188 (1974).
14. T. Yao, M. Ogura, S. Matsuoka, and T. Morishita, *Appl. Phys. Lett.* **43**, 499 (1983).

PART IV

Thin Films and Heterostructures

SURFACE MORPHOLOGY AND PHOTOLUMINESCENCE SPECTRA OF ZnSe (Na)
AFTER EXCIMER LASER ANNEALING

GUAN-JIUN YI^{*}, G.F. NEUMARK^{*}, Z. LU[#], P.R. NEWBURY[&], C.F. YU[#],
B.J. FITZPATRICK[@], M. SHONE[@], and A. SICIGNANO[@].

^{*}Columbia University, Henry Krumb School of Mines, New York, NY 10027

[#]Columbia University, Dept. of Electrical Engineering

[&]Columbia University, Dept. of Applied Physics; Philips Laboratories Felco.

[@]Philips Laboratories, Briarcliff Manor, NY 10510

ABSTRACT

We have investigated excimer laser annealing of Na doped ZnSe, with emphasis on photoluminescence (PL) characterization as a probe of resultant changes in materials properties. We observed a relative increase, after annealing, of Na on substitutional (acceptor) sites vs. Na on interstitial (donor) sites. Another result was the occurrence of extensive twinning; unfortunately such twinning has complicated the analysis of other changes.

INTRODUCTION

Laser processing has developed into an important technique for impurity incorporation into semiconductors. A particularly attractive feature of this method is that one can achieve non-equilibrium concentrations, i.e. one can exceed the solubility limit [e.g. 1]. This feature is of particular interest for wide-band-gap semiconductors, since it has recently been shown [2] that equilibrium solubilities are very likely to be quite low in such materials.

A material of considerable interest for opto-electronic applications is ZnSe, and it thus appears fruitful to investigate laser processing of this material. There is of course an immediate question in use of such laser processing: can one obtain a temperature high enough for adequate (probably non-equilibrium) impurity incorporation with little or no surface decomposition? This problem would be expected to be particularly severe in a material such as ZnSe, which has a high vapor pressure [3]. It is well known that short pulses tend to minimize decomposition [4], and for this reason we selected excimer lasers. An independent study by Bokhonov et al. [5], on not deliberately doped ZnSe, also used such excimer lasers, and studied some changes in the PL; however, it gave only a few brief results on the PL in the exciton region, and a few comments on the observation of extensive twinning. In the present work we studied ZnSe(Na), and include the changes of PL at longer wavelengths, with particular focus on the donor-acceptor pair (DAP) PL. Both DAP and exciton spectra can be very useful probes of material properties (for a general review on PL, see for ex. [6]).

The present study focused on ZnSe(Na), since the effect on the PL of this dopant has been well established both for the bound exciton spectra [7] and the DAP bands [8]. As regards these DAP bands, it has been shown [8] that Na on the interstitial site (Na_i) gives a characteristic high-energy shoulder on the (more usual) DAP peak of the Group III substitutional donors (where Na on the Zn site - Na_{Zn} - is the acceptor for either donor). This thus provides a "marker" for the Na site.

For convenience, we will discuss the results of the present study in terms of three classes of power levels: 1) "Low" power, where there is no visible change in the surface morphology. 2) "Intermediate" power, with visibly increased twinning and observation of the "Y" band (which occurs at 2.6 eV, and is discussed for instance in [9] and [10]). In this intermediate range, there is no significant change in the spectral shape of the DAP bands. 3) "High" power, where we do observe a change in the shape of the DAP bands, indicative of a higher proportion of Na_{Zn} in the annealed material.

The other changes in this range are qualitatively similar to those in the intermediate range, although often stronger.

EXPERIMENTAL

The samples for the laser annealing consisted of wafers cut from boules grown by the vertical zone method [11]. For the annealing, a Lambda Physik EMG 102 MSC excimer laser was used as energy source; the wavelength was either 308nm (XeCl) or 248nm (KrF), and the duration was typically about 16 nsec. Both single and multiple pulses were used. The annealing was carried out in a chamber filled with nitrogen at 1 atmosphere.

After the annealing, the surface morphology was examined with an optical microscope and/or a scanning electron microscope. The samples were then etched lightly, using a boiling 45% KOH solution for 15 seconds. The etching was done to improve the PL intensity and resolution (which we have noted empirically), but was kept light so as to remove only a minimal amount of the annealed layer. The PL was excited by the UV lines (3638Å and 3551Å) of an Ar⁺ laser, and analyzed with a 0.85 m Spex double monochromator.

The results reported here were taken primarily on wafers from two Na doped ZnSe boules (boule A and B). To check that the dominant impurity was Na - Li is often a contaminant in Na doped ZnSe (e.g. [7]) - we examined the low temperature (6K) exciton spectra for evidence of Li. The results are shown in Fig. 1. Neither boule showed the Li bound exciton peak (which is at 10.5 meV below the free exciton edge, e.g. [7]), indicating little or no Li. Boule A (Fig. 1a) has doublet peaks at 9.1 and 9.9 meV below the free exciton edge. This doublet has been attributed to an $\text{Na}_{\text{Zn}}-\text{Na}_{\text{I}}$ pair [7]. In view of the proximity of the Li exciton peak at 10.5 meV to the 9.9 meV peak, it was checked that we were indeed dealing with the Na structure; this was done by also taking data at a lower temperature (1.6K), and confirming that the doublet did indeed show the thermalization typical of Na [7]. Boule B (Fig. 1b) showed a singlet exciton at about 7.8 meV below the free exciton edge; this has been assigned to Na_{Zn} [7]. The DAP spectrum of boule B is shown in Fig. 2a. A dominant zero-phonon DAP peak close to 2.68 eV is shown; this value is typical for Na_{Zn} as acceptor with group III metals on the Zn site as donors [e.g. 4]. In addition, there is a high energy shoulder on this peak, which has been attributed to Na_{Zn} with Na_{I} as donors [8].

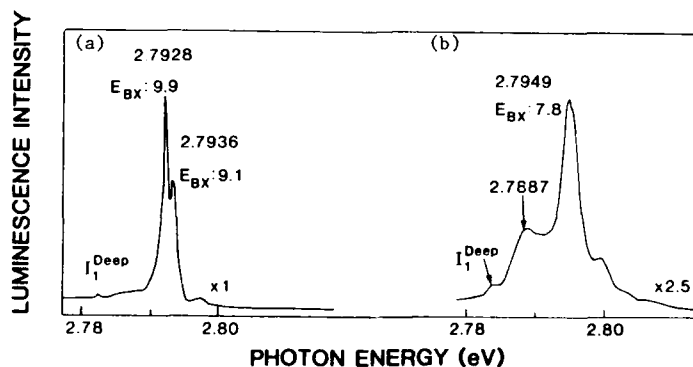
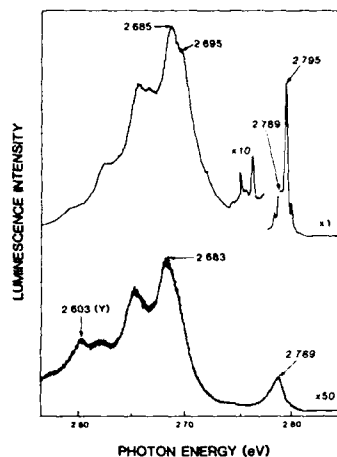


Figure 1: 6K exciton PL spectra of Na doped ZnSe. (a) Boule A, doublet Na bound exciton ($E_{\text{BX}}=9.1$ and 9.9); (b) Boule B, Na exciton with $E_{\text{BX}}=7.8$.

Figure 2: PL spectra (at 6K) of boule B.
(a) Before laser annealing;
(b) Laser annealed by XeCl₂308 nm single pulse, 110 MW/cm².



RESULTS AND DISCUSSION

A very striking result of our excimer laser annealing, with similar results also reported briefly in [5], is the observation of extensive twinning in the ZnSe after annealing in the intermediate and high power ranges. A typical result is shown in Fig. 3a, which shows such an annealed region together with a non-annealed one. The twinning after annealing, with short segments having orientations changing alternatively (shown enlarged in Fig. 3b), is far more extensive than observed prior to the annealing (where there were only a few long, parallel, twin lines). It seems apparent that the increased twinning would be obtained only if the sample is heated at least to the phase transition temperature [12] (1425° C, see [13]), and might require melting. Indeed, Bokhancv et al. assumed that the twinning indicated melting, stating "in the regions which melted and solidified we found ... that periodic structures were formed". In our own work [14] we have concluded, from Auger results showing diffusion of surface oxide, that, at least at the higher power levels, (conservatively, from = 16 MW/cm² up) the material is melted; from these same Auger results we also conclude that, at this power level, the melted layer is at least 0.5 μm thick. As to the

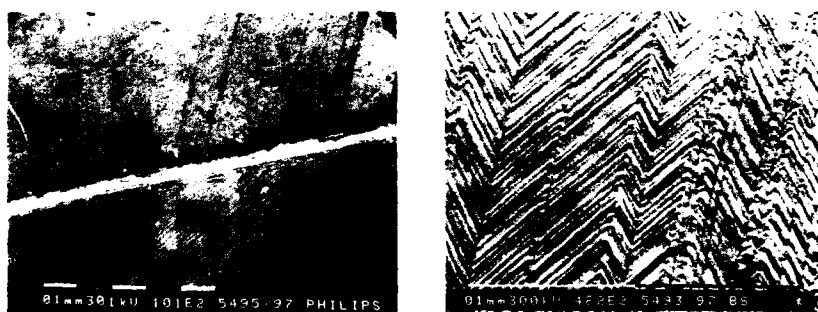


Figure 3: SEM results on the surface morphology of laser annealed ZnSe. The upper part of (a) shows a non-annealed region, the lower part the annealed one; the reoriented twin structure in the lower part of (a) is magnified in (b). The unit of length (the white segment) is 100 μm.

question of surface decomposition, since twinning is so very typical of ZnSe, it seems unlikely that there is appreciable excess Zn or Se.

A summary of our PL results is given in Table I. Similar changes in the exciton lines have also been reported by Bokhonov et al. [5]; in this connection we wish to point out that, based on its spectral position, their primary line (which they call I_1') is in fact the line which is more commonly referred to as I_1^{Deep} [e.g. 15]. Overall, it is obvious that the laser causes various changes. Of course, the matter of primary interest is the basic mechanism(s) causing these changes. Prior to discussing this in terms of the various laser intensity ranges (below) some cautionary notes are in order. Thus, PL changes can of course be due to changes in the properties of the "bulk" material, but alternatively, the surface can also be playing a role. Moreover, internal "interfaces" in the bulk, as caused for instance by twinning, can also affect properties. In terms of more microscopic mechanisms, there can for instance be changes: 1) Due to surface reflection. 2) Due to the formation of surface, interface, and/or "bulk" defect (including dislocation) states, which can introduce non-radiative and/or new radiative paths; as an example, the so-called Y emission band [9] has been associated with dislocations. 3) Due to internal electric fields; it has for instance been suggested [16] that fields associated with surface depletion regions in thin films can give PL quenching, particularly of excitons; since it has been established [17] that twinning can also give internal fields, such a mechanism can also be operative in twinned material. In view of these problems we here comment only briefly on most of our observations (Table I), give some apparent correlations, and give an interpretation primarily for the result of main interest in the present work, i.e. changes in the DAP bands under high laser excitation. We now discuss separately the results in each of the excitation ranges.

In the low excitation range, both the exciton and the DAP PL intensity increases (Table I). We noted no new peaks, nor any changes in the positions of the existing peaks. Since there was no detectable change in the surface morphology, we assume there was no gross bulk re-adjustment; it then follows that the intensity variations are due either to minor surface changes or due to recombination-enhanced defect reactions. Since we observed no changes in the peak positions, it seems unlikely that recombination-enhanced defect reactions (which would be expected to introduce new defects) were playing a role. We thus assume that there were minor surface changes. It is for instance known that it is difficult to remove surface damage by chemical etching, and dry-etching has been shown to improve the PL [18]; mild laser annealing could well be having similar effects.

Table I: Changes of PL spectra in three different power ranges.

	BE Peak Intensity	DAP Intensity	Appearance of Y Band	Appearance of 2.25 eV PL	Elimination of DAP shoulder
Low Power Intensity ($I \leq 3 \text{ MW/cm}^2$)	Increases	Increases	No	No (or minor)	No
Medium Power Intensity ($3 \leq I \leq 20$)	Decreases (no longer detected for most samples)	Decreases	Yes (weak)	Yes	No
High Power Intensity ($I \geq 100 \text{ MW/cm}^2$)	Decreases (no longer detected)	Decreases	Yes (strong)	Yes	Yes

As regards the medium and high excitation ranges, all spectral changes, with the exception of that in the DAP bands, were qualitatively similar. We therefore combine the discussion of these two ranges, except for the high range results on these DAP bands (given below). An interesting spectral change was in the exciton region. Both our boules, as grown, had both Na and I_1^{Deep} exciton lines. After annealing these lines disappeared (Table I) in most samples, and had a much reduced intensity in one. The only remaining spectral feature was a relatively broad peak, at 2.789 to 2.791 eV; this peak was present also prior to annealing, but at a much lower intensity than the Na exciton lines (Fig. 1). This same peak may well be present as a minor feature in various published spectra, but to our knowledge it has not been previously commented on; here we did not study its origin, and we cannot say whether or not it is due to excitons. As to the disappearance of the Na and I_1^{Deep} exciton lines, we cannot establish the cause, with any certainty; however, we wish to point out that internal fields in the twinned regions [17] would tend to dissociate excitons [16]. In terms of changes at lower energies, we noted three in addition to that of the DAP bands (see below). First, the overall PL intensity decreased. We are unable to establish whether this is due to changes in bulk or surface properties, and/or twinning. Second, we noted the appearance of the Y peak (Fig. 2b) subsequent to the annealing; since this peak has been associated with dislocations [9,10], its presence is certainly consistent with the observed heavy twinning. The third change was the appearance of a deep luminescence band, at about 2.25 eV, after the annealing. A band at this energy has been attributed [19] to Cu. Both of the boules we worked with showed the I_1^{Deep} exciton line, which has also been attributed to Cu [15]. Thus some impurity and/or defect site transfer could lead to the formation of the 2.25 eV band; unfortunately, the microscopic centers responsible for either the 2.25 eV band or for I_1^{Deep} do not seem to have been established yet with any certainty, so a detailed mechanism for the present observation cannot be suggested at this time.

A feature of primary interest as regards the present work is that of changes in the DAP peaks observed after annealing at high laser powers. The result for boule B is shown in Fig. 2. Prior to annealing, a high energy shoulder on the main (zero phonon) peak can be clearly distinguished; we attribute this to Na_i [8]. Subsequent to annealing, this shoulder can no longer be observed; moreover, the main peak is shifted to the low energy side. One sample of boule A was annealed under comparable conditions. Prior to the annealing, it showed a strong high energy shoulder. Subsequently, there was no such definite shoulder, but only a broad peak; unfortunately the luminescence intensity was quite low, so it was not possible to evaluate whether or not this peak was a composite. It can thus be seen that the proportion of Na_i was reduced in boule B, and probably also in boule A. This relative change in impurity location is of considerable interest for future work, although it remains to be investigated why comparable changes are not seen at lower power levels (melting - based on the Auger results [14] - was for instance already observed at 16.5 MW/cm²).

As a general further comment, it can be noted that interpretation of the present results is rendered difficult by the occurrence of the heavy twinning. It would thus seem worthwhile to check into means of reducing such twinning. One suggestion would be annealing of material originally without twins (the present boules did, initially, have at least some twinning); perhaps the heavy twinning is "encouraged" by initial twinning. A second possibility might be use of an encapsulating layer.

CONCLUSION

We have shown that excimer laser annealing of ZnSe(Na) can, at least at high power levels, lead to a relative increase in substitutional Na vs.

interstitial Na. This is consistent with prior theoretical predictions [20] on the effect of fast quenching on the relative location of the (amphoteric) alkali dopants in ZnSe. However, such laser annealing leads, in addition, to a quite complex twinning structure. It remains to be determined whether such twinning can be eliminated, and/or what detailed effects result from it.

ACKNOWLEDGEMENT

The authors would like to thank E. Arnold, H. Baumgart, R. Bhargava, S. Colak, T. Marshall, and K. Shahzad (Philips Laboratories) for helpful advice and assistance.

REFERENCES

1. See, for ex., C.W. White, S.R. Wilson, B.R. Appleton, and F.W. Young, Jr., *J. Appl. Phys.* **51**, 738 (1980).
2. G.F. Neumark, *Phys. Rev. Lett.* **62**, 1800 (1989).
3. See, for ex., K.C. Mills, *Thermodynamic Data for Inorganic Sulfides, Selenides, and Tellurides* (Butterworths, London, 1974).
4. S.U. Campisano, G. Foti, E. Rimini, F.H. Eisen, W.F. Tseng, M-A. Nicolet, and J.L. Tandon, *J. Appl. Phys.* **51**, 295 (1980).
5. A.F. Bokhonov, L.N. Tvorcnovich, and G.P. Yablonskii, *Sov. Phys. Sol. State* **30**, 917 (1988).
6. P.J. Dean, *Prog. Cryst. Growth and Charact.* **5**, 89 (1982).
7. G.F. Neumark, B.J. Fitzpatrick, S.P. Herko, and T.F. McGee III, in *Physics of Semiconductors*, edited by O. Engstrom (World Scientific, 1987), p. 975.
8. G.F. Neumark, S.P. Herko, and B.J. Fitzpatrick, in *Proc. 13th. Int. Conf. Defects in Semiconductors*, edited by L.C. Kimerling and J.M. Parsey, Jr. (Metallurgical Soc., 1985), p. 1205.
9. S. Myhajlenko, J.L. Batstone, H.J. Hutchinson, and J.W. Steeds, *J. Phys. C* **17**, 6477 (1984).
10. T. Taguchi, T. Kusao, and A. Hiraki, *J. Cryst. Growth* **72**, 46 (1985).
11. B.J. Fitzpatrick, T.F. McGee III, and P.M. Harnack, *J. Cryst. Growth* **78** 242 (1986); M. Shone, B. Greenberg, and M. Kaczinski, *ibid.*, **86**, 132 (1988).
12. I. Kikuma and M. Furukoshi, *J. Cryst. Growth* **71**, 136 (1985).
13. M.P. Kulakov, V.D. Kulakovskii, I.B. Lavchenko, and A.V. Fadeev, *Sov. Phys. Sol. State* **18**, 526 (1976).
14. G-J. Yi, G.F. Neumark, Z. Lu, C.F. Yu, P.R. Newbury, B.J. Fitzpatrick, M. Shone, and A. Sicignano, *Bull. APS*, **34**, 722 (1989), and to be published.
15. C. Werkhoven, B.J. Fitzpatrick, S.P. Herko, R.N. Bhargava, and P.J. Dean, *Appl. Phys. Lett.* **38**, 540 (1981).
16. P.J. Dean, *Phys. Stat. Sol. (a)* **81**, 625 (1984).
17. G.F. Neumark, *Phys. Rev.* **125**, 838 (1962); B.G. Yacobi and Y. Broda, *Phys. Rev. B* **10**, 665 (1974).
18. K. Ohkawa, T. Karasawa, A. Yoshida, T. Hirao, and T. Mitsuyu, *Appl. Phys. Lett.* **54**, 2553 (1989).
19. G. Jones and J. Woods, *J. Lum.* **9**, 389 (1974).
20. G.F. Neumark, *J. Appl. Phys.* **51**, 3383 (1980).

PLASMA-ASSISTED EPITAXIAL GROWTH OF ZnSe FILMS IN HYDROGEN PLASMA

S. YAMAUCHI AND T. HARIU

Department of Electronic Engineering, Tohoku University
Sendai 980, Japan

ABSTRACT

Plasma-assisted epitaxy (PAE) was applied to the growth of ZnSe films on (100) GaAs for low temperature epitaxial growth in hydrogen plasma. High purity ZnSe films were successfully grown by the control of hydrogen gas flow rate and VI/II supply ratio. Hydrogen-chloride gas and nitrogen gas mixed in pure hydrogen gas plasma around 2% respectively resulted in the growth of highly conductive n-type layers (630Scm^{-1}) and nitrogen-acceptor doped layers (N-acceptor level $\sim 100\text{meV}$), however, the control of VI/II supply ratio is also very important for the efficient N-acceptor doping. The plasma optical emission spectroscopy indicated that Se-N is composed by the reaction of N_2^+ -ion with SeH (or Se) in hydrogen and nitrogen mixed gas plasma with Se supply.

INTRODUCTION

ZnSe has recently been extensively investigated in view of its applications to optoelectronic devices including the heterostructure with GaAs. It has, however, been recognized that the growth of II-VI compound semiconductors with controlled electronic properties is much more difficult than IV and III-V materials due to the strong self-compensation effect by native defects or residual impurities, which are incorporated particularly at high growth temperatures. Thus non-thermal equilibrium growths at low temperatures by molecular beam epitaxy (MBE) (1), metalorganic chemical vapor deposition (MOCVD) (2), atomic layer epitaxy (ALE) (3) and so on have recently been attempted, aiming at the growth of purified ZnSe films and efficient doping.

The purpose of this paper is to describe the plasma-assisted epitaxial growth of ZnSe films in hydrogen plasma, in order to extend the controllability of their electronic property

PAE APPARATUS

The PAE apparatus developed for ZnSe growth is shown in Fig.1. Elemental Zn and Se shots were evaporated from quartz cells by resistive heating and supplied through gas plasma toward (100) GaAs substrates. Hydrogen gas (99.9999% pure gas was purified by palladium diffuser), sometimes mixed with HCl gas (99.95% pure) and N_2 gas (99.9995% pure) for doping was introduced into the chamber and was excited through capacitive coupling by rf power at 13.56MHz. The substrate holder was settled parallel to the applied electric field to avoid the possible bombardment of high energy ions directly accelerated by the field. Optical emission from plasma was detected through a sapphire window at the bottom of the chamber. The detailed growth conditions have been described elsewhere (4).

UNDOPED PAE-ZnSe GROWTH

Typical photoluminescent (PL) spectrum of nominally undoped PAE-ZnSe films of $2.5\mu\text{m}$ thickness grown at 320°C in hydrogen plasma is shown in Fig.2, where the strong emission due to free-exciton (E_x^f) is observed with weak deep level emissions. It is then concluded that the PAE-undoped ZnSe films are of high purity, however, it is to be noted here that the purity

of the ZnSe films is very sensitive to the hydrogen gas flow rate. Figs.3 (a) and (b) respectively show the overall PL spectra and the exciton emissions for the ZnSe films grown with variable hydrogen gas flow rate. As the hydrogen gas flow rate is increased, the exciton emission intensity is increased, the intensity of donor-acceptor (DA) pair emissions due to residual impurities is drastically decreased, and the free-exciton emission dominates over bound exciton emissions. In order to find out the origin of residual donors responsible for I_2 emission (excitons bound to neutral shallow donors), PAE-ZnSe was grown on (100) Ge. The PL spectra shown in Fig.4 indicates that the same I_2 emission dominates in this ZnSe on Ge. Secondary-ion mass spectroscopy shows the intermixing width at the interface of ZnSe/GaAs is very small and also detected Cl inside the ZnSe films. It is then concluded that the residual donor is not Ga diffused from GaAs substrate, but is Cl which most likely comes from the source material. The increase of hydrogen gas flow rate can reduce the incorporation of Cl by producing volatile Cl compounds.

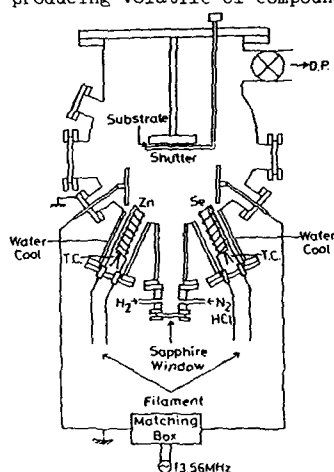


Fig.1 PAE-apparatus for epitaxial ZnSe growth.

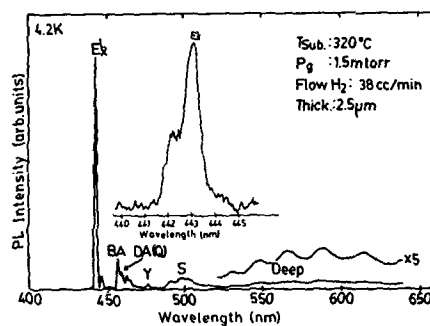


Fig.2 Typical PL spectrum of undoped PAE-ZnSe.

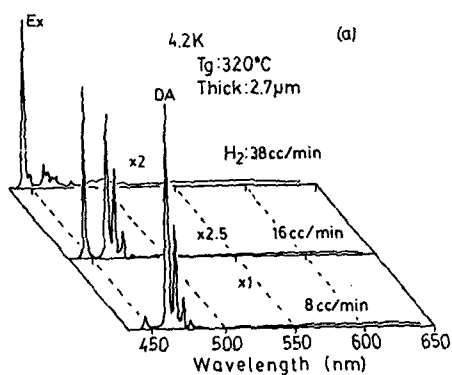
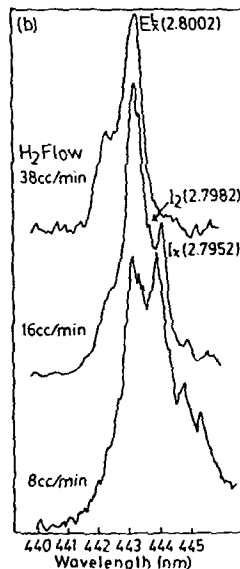


Fig.3 Overall (a) and near bandedge (b) PL spectra of nominally undoped ZnSe growth with variable H_2 gas flow rate.



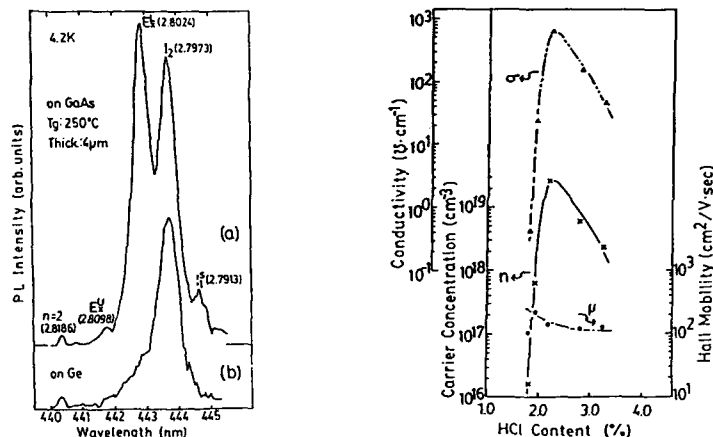


Fig.4 PL spectra near-bandedge of Fig.5 undoped ZnSe growth on (100) GaAs (a) and (100) Ge (b). Electronic properties of Cl-doped ZnSe as a function of fractional HCl gas content in

CL-DOPED PAE-ZnSe GROWTH

Highly-conductive n-type ZnSe films were successfully grown by PAE in a mixed gas plasma of hydrogen and hydrogen-chloride. The detailed growth process has been already described elsewhere (5).

The conductivity, electron concentration and Hall mobility measured by van der Pauw method for layers with 1μm thickness are shown in Fig.5 as a function of fractional content of HCl in hydrogen gas. The highest conductivity of 630Scm^{-1} with electron concentration $2.8 \times 10^{19}\text{cm}^{-3}$ and Hall mobility $140\text{cm}^2/\text{Vs}$, was obtained with about 2.2% HCl in the hydrogen. It is noted here that excessive doping of Cl also reduces the conductivity, probably by increasing Cl-related complex defects as described below.

Fig.6 shows the PL spectra of Cl-doped PAE-ZnSe films grown in the mixed gas plasma with various content of HCl. Donor-acceptor (DA) pair emission shifts to shorter wavelength with the increase of HCl gas content due to the reduced average distance between Cl-donors and undefined acceptors, however, the self-activated (SA) emission which is caused by the association between donors and Zn-vacancies (6) dominates in the highly Cl-doped ZnSe films. It is concluded that SA centres are increasingly produced by excessive Cl and compensate the Cl-donors.

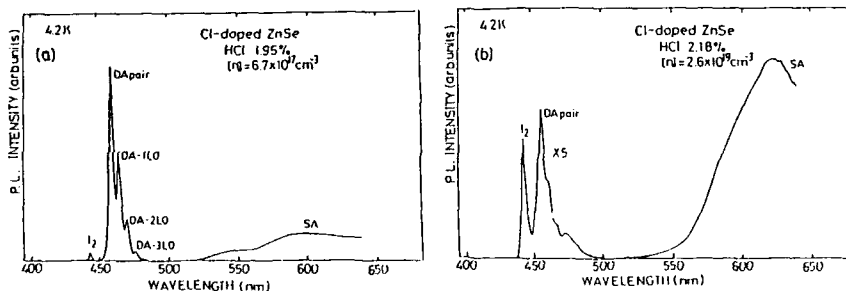


Fig.6 PL spectra of lightly (a) and heavily Cl-doped ZnSe.

N-DOPED PAE-ZnSe GROWTH

PL spectrum of N-doped PAE-ZnSe films grown in H_2+N_2 mixed plasma, shown in Fig.7, are characterized with the exciton emission bound to neutral N-acceptor at 2.791eV (7) and DA pair emission related with N-acceptor at 2.700eV (8). The N-acceptor level was estimated from the band-acceptor (BA) emission to be at 109meV above valence band maximum, in close agreement with that obtained by Stutius (9), but 87meV from the temperature dependence of the BA emission intensity. This difference of two energies can be explained by large lattice relaxation at N-acceptor centres (10).

The doping of nitrogen as an acceptor is very difficult by using N_2 gas due to insufficient chemical reactivity of N_2 , as shown in the growth by MBE (11). Fig.8 shows the advantage of efficient doping by PAE. Fig.8(a) shows the near-bandedge PL spectra for films grown in mixed H_2+N_2 , non-excited gas flow and Fig.8(b) shows the spectra for films grown in H_2+N_2 mixed gas plasma excited by 10W rf power. The DA pair emission related with N-acceptors can be observed in the latter films. These results conclude that the reactive species excited in the mixed gas plasma are useful to dope nitrogen acceptors into ZnSe films.

Optical emission spectroscopy indicated that the intensity ratio of N_2^+ to N_2 emissions in H_2+N_2 mixed gas plasma is greater than the ratio in pure N_2 plasma. It is then suggested that the ionization of N_2 is enhanced by collisional reaction or Penning effect between excited hydrogen atoms or molecules and neutral nitrogen molecules. The emission intensity of N_2^+ ions was not reduced with Zn supply into the H_2+N_2 plasma (Fig.9(a)), but it was decreased with Se supply and a new emission of SeN compound was detected (Fig.9(b)). It should be concluded that SeN produced by the following reaction is responsible for nitrogen doping.

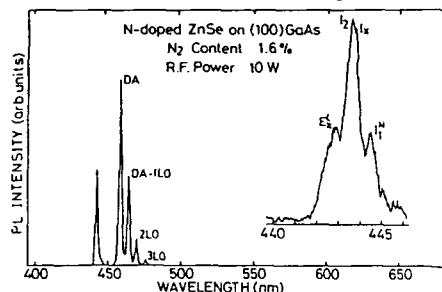
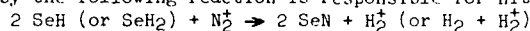
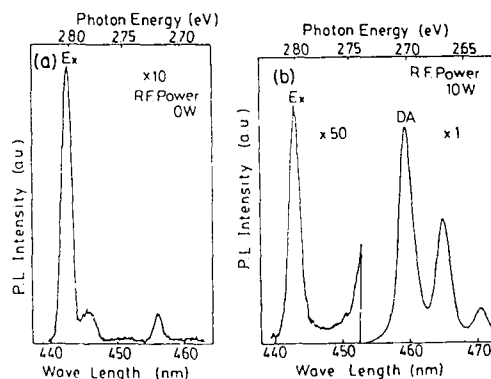


Fig.7
Typical PL spectrum of N-doped
PAE-ZnSe grown in H_2+N_2 mixed
plasma.

Fig.8
Near-bandedge PL spectra of
ZnSe grown in non-excited
 H_2+N_2 mixed gas flow (a) and
 H_2+N_2 mixed gas plasma.



The N-acceptor doping into ZnSe films is also influenced by growth conditions such as Se/Zn supply ratio, N_2 gas content in H_2 gas, applied rf power to excite the plasma and so on. Especially, the supply ratio of Se/Zn must be controlled for the efficient doping as shown in Fig.10. Figs.10 (a) and (b) respectively show the intensity and half-width of DA pair emission in N-doped PAE-ZnSe films as a function of Se/Zn supply ratio. The growth rate doesn't change in this region, where the Se/Zn supply ratio is above 1 (10), because the growth rate is limited by the supply rate of Zn, as in MBE growth of ZnSe films (1). In spite of the growth rate saturation, the maximum intensity of DA pair emission is obtained at a much larger supply ratio around 10. We speculate that this result comes from two competing effects as a function of supply ratio: one is the reduced association between nitrogen and Se-vacancies or interstitial Zn, and the other is the reduction of incorporated nitrogen. The best conditions, indicated so far by PL measurement, are about 10W rf power to excite the plasma with about $2 \times 10^{19} \text{cm}^{-3}$ electron density and $2.5 \times 10^4 \text{K}$ electron temperature, N_2 gas content around 2% in H_2 gas and the supply ratio around 10. The conductivity type of the films have not been determined because of the resistivity higher than $10^3 \Omega \text{cm}$.

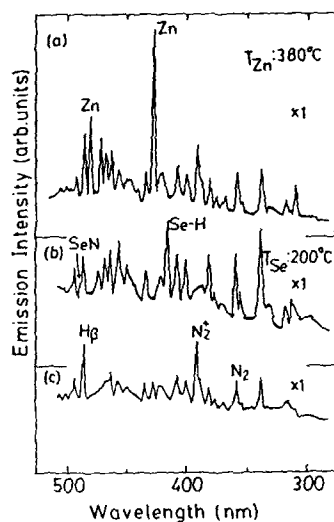


Fig.9 Plasma optical emission spectra of H_2+N_2 mixed plasma with Zn supply (a), with Se supply (b) and without source supply.

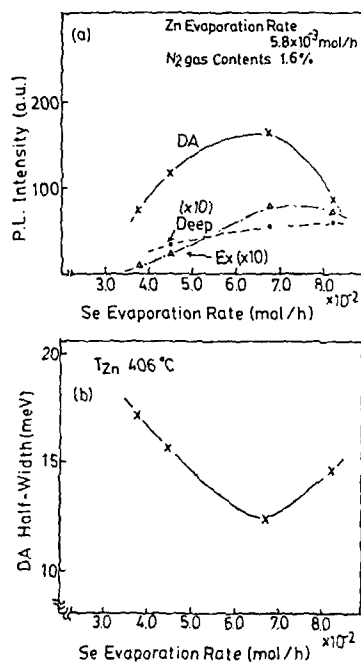


Fig.10 PL intensity (a) and half-width (b) of DA pair emission of N-doped ZnSe as a function of Se/Zn supply.

CONCLUSIONS

ZnSe films on GaAs substrates were grown in H_2 , H_2+HCl and H_2+N_2 plasma by plasma-assisted epitaxy for the growth of high purity, highly conductive and efficient nitrogen-acceptor doped ZnSe films, respectively. The undoped ZnSe films grown in controlled hydrogen gas flow rate and VI/II supply ratio have good photoluminescent properties with strong free-exciton emissions and weak deep-level emissions. The residual donor-impurities in undoped ZnSe films did not come from intermixing at ZnSe/GaAs heterointerface but most likely from the sources. The conductivity of Cl-doped ZnSe films was raised up to $630 S cm^{-1}$ with $2.8 \times 10^{19} cm^{-3}$ electron concentration and $140 cm^2/Vs$ Hall mobility, however, the excess Cl-doping causes the reduction of conductivity by the increase of the density of self-activate centres. The N-acceptor could be efficiently doped into ZnSe films by using of H_2+N_2 mixed gas plasma. SeN composed in the H_2+N_2 mixed gas plasma was detected by plasma optical emission spectroscopy. The supply ratio of Se/Zn should be kept around 10 for the efficient N-doping.

ACKNOWLEDGEMENT

The author wish to thank Professor S. Ono for encouragement and stimulating discussions.

REFERENCES

- (1) T. Yao, Y. Makita and S. Saekawa, Appl. Phys. Lett. 35 (1979) 97.
- (2) W. Stutius, Appl. Phys. Lett. 38 (1981) 352.
- (3) T. Yao, T. Takeda and R. Watanuki, Appl. Phys. Lett. 48 (1986) 1615.
- (4) H. Sato, O. Osada, K. Matsushita, T. Hariu and Y. Shibata, Vacuum 36 (1986) 133.
- (5) S. Yamauchi, T. Hariu and K. Matsushita, Jpn. J. Appl. Phys. 26 (1987) L893.
- (6) S. Sato and K. Igaki, Jpn. J. Appl. Phys. 22 (1983) 68.
- (7) Z. L. Wu, J. L. Merz, C. J. Werkhoven, B. J. Fitzpatrick and R. N. Bhargava, Appl. Phys. Lett. 40 (1982) 345.
- (8) P. J. Dean, W. Stutius, G. F. Neumark, B. J. Fitzpatrick and R. N. Bhargava, Phys. Rev. B 27 (1982) 246.
- (9) W. Stutius, Appl. Phys. Lett. 40 (1982) 246.
- (10) S. Yamauchi and T. Hariu, Appl. Sur. Sci. 33/34 (1988) 862.
- (11) R. N. Park. H. A. Mar and N. M. Salansky, 58 (1985) 1047.

GROWTH OF $\text{ZnS}_x\text{Se}_{1-x}$ BY MBE USING AN ELECTROCHEMICAL SULPHUR SOURCE.

J.M. WALLACE, K.A. PRIOR, B.C. CAVENETT, J.J. HUNTER, S.J.A. ADAMS AND M.J.L.S. HAINES.

Department of Physics, Heriot-Watt University, Edinburgh EH14 4AS, UK.

ABSTRACT

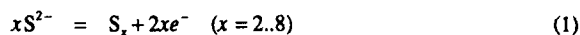
In this paper we describe the use of an electrochemical sulphur cell to grow $\text{ZnS}_x\text{Se}_{1-x}$ alloys on GaAs substrates. The cell uses the ionic transport of Ag ions in Ag_2S to produce a sulphur flux which depends on the applied voltage. The advantages and disadvantages of this type of source will be discussed. We also describe the versatility of the cell for fabricating $\text{ZnS}_x\text{Se}_{1-x}/\text{ZnS}_y\text{Se}_{1-y}$ multilayers as well as more complex profiles.

1 INTRODUCTION

The growth of hetero-epitaxial ZnSe on GaAs substrates by Molecular Beam Epitaxy (MBE) using solid sources is a well established process [1,2], however, the difficulties involved with the addition of sulphur to produce $\text{ZnS}_x\text{Se}_{1-x}$ alloys has resulted in few detailed studies of this alloy system. Sulphur itself is usually considered unsuitable as a source material despite recent work by Kitagawa et al [3] as the vapour pressure is far too high for it to be used in conventional Knudsen cells. This has resulted in a number of different approaches to the problem of sulphur incorporation, generally involving some form of sulphur containing compound. For example, Matsumura et al. [4] have used ZnS as the sulphur source to grow a range of alloy compositions while the Philips group [5] have also used non-elemental solid sources in the form of $\text{ZnS}_x\text{Se}_{1-x}$ ($x \approx 0.5$) polycrystalline charges to fabricate strained layer superlattices. Both these methods have the disadvantage that the (Se + S)/Zn flux ratio cannot be changed to optimize the material properties and the use of alloy charges also results in higher impurity levels in the epitaxial layers introduced during the production of the source material. In gas source MBE sulphur can be introduced into a vacuum system by using compounds such as diethylsulphide (DES) [6] and, although this technique results in the production of good quality material, in general, the growth systems use all gaseous sources. Sulphur can also be produced from a solid state electrochemical cell, which is totally compatible with conventional Knudsen sources. The use of this type of cell to produce fluxes of sulphur molecules S_x ($x = 2 \dots 8$) is well documented [7]. Here we describe the use of such a cell to grow $\text{ZnS}_x\text{Se}_{1-x}$ layers with $x < 0.2$ and discuss its use in the production of more complex structures.

2 ELECTROCHEMICAL SULPHUR CELL.

Figure 1. shows a schematic diagram of the galvanic cell $\text{Ag}/\text{AgI}/\text{Ag}_2\text{S}/\text{Pt}$, used in this work to generate sulphur molecules. When heated to above 200°C to ensure sufficient ionic mobility, application of an EMF to the cell results in the production of sulphur at the positive platinum electrode by the half-cell reaction:



Equilibrium between the various sulphur species S_x has been shown [6] to be described by equation 2.

$$p_{\text{S}_x}(T) = p_{\text{S}_2}^0(T) \exp\left(\frac{2x(E - E^*)F}{RT}\right) \quad (2)$$

where $p_{S_x}^o(T)$ is the pressure of S_x at a cell temperature T over elemental sulphur and $p_{S_x}(T)$ is the pressure within the cell, generated by the application of EMF, E , to the cell. Application to the cell of a voltage E^* results in the production of elemental sulphur at the positive electrode. In this work T in the range $300 - 350^\circ\text{C}$ was used and the corresponding value of E^* is $\sim 245\text{mV}$ [7].

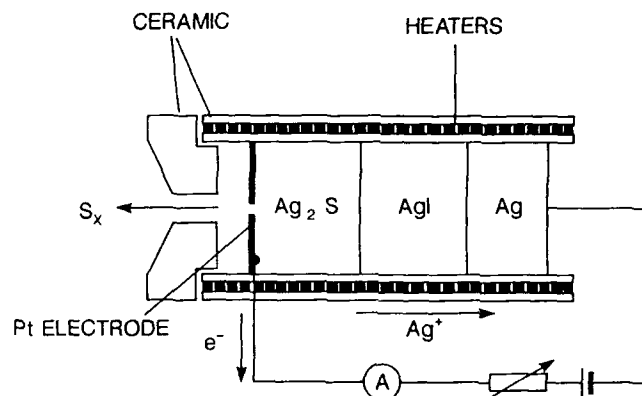


Fig. 1 Schematic diagram of the Electrochemical cell.

Figure 2 shows the pressures of the various sulphur species obtained at 300°C as a function of cell voltage and, although the predominant equilibrium species is S_2 (>95% total flux) for applied cell voltages $E < 200\text{ mV}$, above this voltage the proportion of higher molecular weight species rapidly increases. During growth it is to be expected that the smaller sulphur polymers will incorporate more efficiently as there are fewer kinetic barriers to overcome and thus we have used $E \leq 200\text{mV}$.

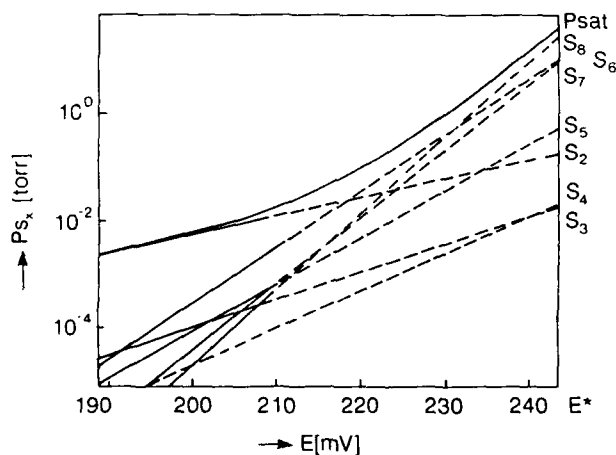


Fig. 2 Partial pressures of the S_x molecules as a function of the EMF, E at 300°C .

Electrochemical sulphur cells have been used as dopant sources for III-V materials and their potential advantages have been summarized elsewhere [8,9]. For our purposes, the main advantage is the ability to control accurately the cell flux by means of the applied voltage, thereby allowing complicated profiles to be easily constructed. An example of this is that the flux from the cell is not limited to only two values (on and off) as is a Knudsen cell. This means that superlattices of the type $\text{ZnS}_x\text{Se}_{1-x}/\text{ZnS}_y\text{Se}_{1-y}$, with $x \neq y \neq 0$ can be grown, including, for example, strain-symmetrized superlattices. While in theory it is possible to produce these structures using a Knudsen cell, the long thermal time constants involved in changing the cell flux and allowing it to stabilize prohibit the growth of any but the simplest structures.

Another type of flux profile which can be produced is a ramp. This is easily produced by changing the cell voltage with time and enables continuously graded buffer layers and wells and/or barriers of varying composition to be produced.

Two key conditions which must be met for the growth of any structures such as those described above are firstly that the response of the cell to any change in the applied cell voltage is fast and secondly that the maximum flux obtainable be sufficient to allow layers with sulphur content 20-30% to be grown.

In the case of low sulphur fluxes used in doping III-V semiconductors, it has been shown [8] that the time constant of the cell for changes in the flux of $\times 100$ is less than 1s. We have found that for the much larger fluxes used in this work the appropriate time constant for a similar $\times 100$ change in flux is of order 10s. While larger than the time for the growth of one monolayer, this is still an improvement of one order of magnitude over the time constant for a Knudsen cell and should not present a great problem for the growth of structures described above. The longer time constant associated with high fluxes is most probably a result of the change in stoichiometry of the Ag_2S which occurs on applying a voltage. This involves a large movement of Ag ions to or from the silver sulphide layer and is therefore determined by the maximum current obtainable from the voltage source.

The other key issue, that of the maximum amount of sulphur obtainable from the cell, is addressed in the following sections.

3 EXPERIMENTAL

ZnSe and $\text{ZnS}_x\text{Se}_{1-x}$ layers were grown in a VG Semicon MB288 kit with conventional Zn and Se K-cells and sulphur produced from a solid state sulphur electrochemical cell manufactured by VG Semicon. Source materials were Se (Osaka Asahi, 6N super grade), Zn (Johnson Matthey 6N) and Ag_2S (Johnson Matthey, Puratronic grade, 5N).

GaAs wafers were degreased and etched in $15:2:2 \text{ H}_2\text{SO}_4:\text{H}_2\text{O}_2:\text{H}_2\text{O}$ before mounting with indium on a sample holder and introducing into the chamber. Following degassing, the samples were heated until a reconstructed RHEED pattern was observed, and then allowed to cool to an indicated growth temperature of 330°C . No attempt was made to improve the surface morphology before growth by treatment with arsenic [10,11].

The photoluminescence (PL) measurements were made using UV argon ion laser excitation (350nm) at approximately 2Wcm^{-2} and recording the spectrum at 4.2K with a double Spex monochromator and photon counting.

All the layers discussed in this paper are around 500\AA in thickness as measured by calibrated source flux rates. Importantly, this ensures that all layers are well below the critical thickness for the generation of misfit dislocations ($\approx 1600\text{\AA}$ for ZnSe on GaAs).

4 RESULTS

Initially a series of pseudomorphic ZnSe layers, were grown to optimize the growth conditions. The growth rate was $0.5\mu\text{m/hr}$ and a typical photoluminescence spectrum is shown in figure 3 where the exciton luminescence is dominated by the $(c' - hh)$ free exciton with a FWHM of 2.3meV . We ascribe the feature at higher energy to the $(c' - lh)$ exciton following Matsumura et al [12] while the emission at 2.800eV corresponds to a donor bound exciton recombination. No deep luminescence bands were observed for the high quality samples and, in fact, the luminescence is comparable to that reported for ZnSe grown on MBE GaAs buffer layers [10].

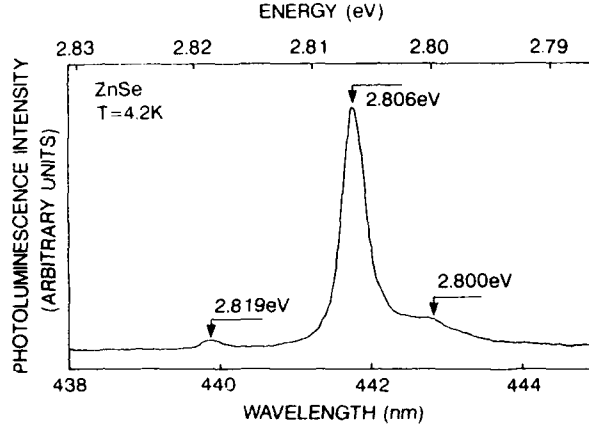


Fig. 3. Photoluminescence of ZnSe epilayer on GaAs.

The initial series of $\text{ZnS}_x\text{Se}_{1-x}$ layers were grown with an unmodified VG Semicon electrochemical sulphur cell, designed for doping, however under typical operating conditions ($T_{\text{cell}} = 350^\circ\text{C}$, $E = 200\text{mV}$) the S_2 flux was insufficient to grow alloy material with $x \geq 0.005$. However, minor modifications to the cell increased the flux by a factor of 10x allowing a greatly increased sulphur incorporation to be achieved. For the maximum sulphur content of the order of $x = 0.2$ it was necessary to reduce the growth rate to $0.05\mu\text{m/hr}$ which is on the limit of practicability for the fabrication of multilayer structures with this composition for barrier layers.

The exciton luminescence was also used to determine the composition of the ternary layers. The advantage of using pseudomorphic layers for this type of measurement is two-fold. Firstly, the lattice strain is well defined and secondly the thermal strain is zero. Also, there are now two self consistent checks on the strain value, namely the light and heavy hole and their splitting. The standard expressions for biaxial strain were used [13] where the electron heavy (light hole) band gap shifts by an amount ΔE_1 (ΔE_2) and

$$\Delta E_1 = E_H + E_U \quad \Delta E_2 = E_H - E_U \quad (3)$$

E_H and E_U are the hydrostatic and uniaxial components of the strain respectively and are given by

$$E_H = 2a \left(\frac{C_{11} - C_{12}}{C_{11}} \right) \epsilon \quad E_U = -b \left(\frac{C_{11} + 2C_{12}}{C_{11}} \right) \epsilon \quad (4)$$

where ϵ , the uniaxial strain is given by

$$\epsilon = \epsilon_{xx} = \epsilon_{yy} = \frac{a_{\text{layer}} - a_{\text{sub}}}{a_{\text{layer}}} \quad (5)$$

where a_{layer} is the unstrained lattice parameter of the epilayer and a_{sub} that of the substrate. The elastic constants, C_{ij} , deformation potentials a, b , lattice parameter, d , and unstrained band gap, E_g were all assumed to vary linearly with composition. These parameter values are given in table 1.

Table 1: Elastic constants C_{11} , C_{12} , lattice parameters d , deformation potentials a, b (from [14]) and the unstrained electronic band gap at 4K, E_g values used to calculate compositional dependence of the ZnS_xSe_{1-x} pseudomorphic band gaps.

		ZnSe	ZnS	GaAs
C_{11}	$\times 10^9 \text{ kgm}^{-2}$	8.26	10.67	
C_{12}	$\times 10^9 \text{ kgm}^{-2}$	4.98	6.66	
d	\AA	5.6686	5.4093	5.6533
a	eV	-5.4	-4.56	
b	eV	-1.2	-0.75	
E_g	eV	2.823	3.84	

Figure 4a shows PL of a ZnS_xSe_{1-x} layer with $x = 0.02$. It is typical for samples with the layer under compression where the main feature is the donor bound exciton I_2 with a high energy shoulder due to the $(e^- - hh)$ free exciton. Another emission occurs at $62 \pm 2 \text{ meV}$ lower energy than the I_2 peak and displays two or more LO phonon replicas which is characteristic of shallow donor - acceptor pair transitions. This emission does not appear in any of the ZnSe layers, and so far is not identified.

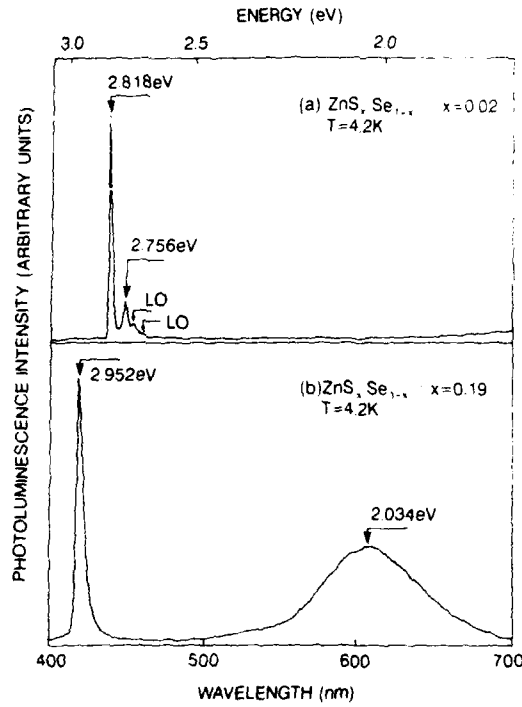


Fig. 4. Photoluminescence of ZnS_xSe_{1-x} on GaAs. (a) $x=0.02$, (b) $x=0.19$

Figure 4b shows the PL of a $\text{ZnS}_x\text{Se}_{1-x}$ layer with the greatest level of sulphur incorporation achieved to date. This layer is under tension and ascribing the main feature to I_2 associated with the $(e^- - \text{h})$ transition gives a sulphur composition of 19% where the very broad FWHM gives an uncertainty of $\pm 2\%$ for this value. The large FWHM could be due to the lack of optimization of the growth conditions as implied by the presence of the SA emission, or perhaps is due to a partial relaxation of the layer. Even if one assumed the layer to be fully relaxed the luminescence energy would still correspond to a composition of 15%.

5 CONCLUSIONS

The results clearly demonstrate that the electrochemical cell is a practical solid state source for MBE, particularly for our current program which involves the characterization of undoped and doped material lattice matched to GaAs and the growth of $\text{ZnS}_x\text{Se}_{1-x}/\text{ZnSe}$ strain symmetrized superlattices. Future developments of the electrochemical cell will improve the lifetime and increase the flux to allow material to be grown with high sulphur concentrations at normal ($\sim 1\mu\text{m/hr}$) growth rates.

6 ACKNOWLEDGEMENTS

We are grateful to the SERC for support of this programme and to VG Semicon for both financial and equipment contributions to the research. We thank Drs. R. Heckingbottom and G.J. Davies of British Telecom Research Laboratories for major equipment support which has made the present programme possible.

7 REFERENCES

1. T. Yao, Japan Annual Reviews in Electronics, Computers and Telecommunications **12**, 111 (1986).
2. R.L. Gunshor and L.A. Kolodziejski, IEEE J. of Quantum Electronics **24**, 1744 (1988).
3. M. Kitagawa, Y. Tomomura, A. Suzuki and S. Nakajima, J. Cryst. Growth **95**, 509 (1989).
4. N. Matsumura, K. Ishikawa, J. Saraie and Y. Yodogawa, J. Cryst. Growth **72**, 41 (1985).
5. D.A. Cammack, R.J. Dalby, H.J. Cornelissen and J. Khurgin, J. Appl. Phys. **62**, 3071 (1987).
6. H. Ando, A. Taïke, M. Konagai and K. Takahashi, J. Appl. Phys. **62**, (1987) 1251.
7. H. Rickert, in Physics of electrolytes - Vol 2, Thermal and Electrode Processes in Solid State Electrolytes, edited by J. Hladik (Academic Press, London, 1972), p. 519.
8. G.J. Davies, D.A. Andrews and R. Heckingbottom, J. Appl. Phys. **52**, 7214 (1981).
9. D. A. Andrews, R. Heckingbottom and G.J. Davies, J. Appl. Phys. **54**, 4421 (1983).
10. L.A. Kolodziejski, R.L. Gunshor, M.R. Melloch, M. Vaziri, C. Choi and N. Otsuka, in Growth of compound semiconductors, SPIE vol. 796, p. 98.
11. M.C. Tamargo, J.L. de Miguel, D.M. Hwang and H.H. Farrell, J. Vac. Sci. Technol. **B6**, 784 (1988).
12. N. Matsumura, M. Tsubokura and J. Saraie, J. Crystal Growth **95**, 525 (1989).
13. K. Shahzad, Phys. Rev. B **38**, 8309 (1988).
14. K. Shahzad, D.J. Olego, C.G. van der Walle, Phys. Rev. B **38**, 1417 (1988).

SELECTIVE AREA DEPOSITION OF PASSIVANTS, INSULATORS, AND EPITAXIAL FILMS OF II-VI COMPOUND SEMICONDUCTORS

D.L. DREIFUS*, Y. LANSARI**, J.W. HAN**, S. HWANG**, J.W. COOK,
JR.**, AND J.F. SCHETZINA**

* Department of Electrical and Computer Engineering, North
Carolina State University, Raleigh NC 27695-7911

** Department of Physics, North Carolina State University, Raleigh
NC 27695

ABSTRACT

II-VI semiconductor surface passivants, insulators, and epitaxial films have been deposited onto selective surface areas by employing a new masking and lift-off technique. The II-VI layers were grown by either conventional or photoassisted molecular beam epitaxy (MBE). CdTe has been selectively deposited onto HgCdTe epitaxial layers as a surface passivant. Selective-area deposition of ZnS has been used in metal-insulator-semiconductor (MIS) structures. Low resistance ohmic contacts to p-type CdTe:As have also been realized through the use of selectively-placed thin films of the semi-metal HgTe followed by a thermal evaporation of In. Epitaxial layers of HgTe, HgCdTe, and HgTe-CdTe superlattices have also been grown in selective areas on CdZnTe substrates, exhibiting specular morphologies and double-crystal x-ray diffraction rocking curves (DCXD) with full widths at half maximum (FWHMs) as narrow as 140 arcseconds.

INTRODUCTION

Selective-area deposition of surface passivants, insulators, and epitaxial films of II-VI semiconductors offers a new approach for the fabrication of a number of devices such as metal-insulator-semiconductor device structures, multicolor detectors, integrated optoelectronic circuits, and waveguide structures.

The performance of Hg-based infrared detectors is often dependent on the type and quality of the surface passivation. Although it is fairly straightforward to complete an epitaxial growth with a passivating layer, once the sample has been removed from the growth system, patterned, and etched, the mesa edges remain exposed. When mesa etching is followed by a blanket deposition of a passivating sulfide or oxide layer, subsequent device fabrication can become difficult if contact vias to the underlying semiconductor are desired. Ideally, it would be desirable to selectively place surface passivation only on sensitive surfaces rather than of blanket depositions that can require additional processing steps and selective etchants in order to obtain electrical contacts. The same requirements hold true for insulators in MIS structures and interlevel metal dielectrics.

Providing that subsequent depositions do not appreciably affect previously grown epitaxial layers, selective-area epitaxy of device structures is perhaps the ideal choice for the integration of the various components for an optoelectronic circuit technology. Frequently, the growth conditions for specialized layers used in optical or electronic devices are grown under a varied set of optimized deposition conditions.

Unfortunately, the selective-area epitaxy of silicon or GaAs requires masking technologies that can withstand elevated deposition temperatures such as SiO_2 or Si masks, which are difficult to fabricate. Additional epitaxial depositions can be detrimental to existing layers due to the elevated growth temperatures. Irvine et. al. have employed optical masks for selective-area growth of CdTe and HgCdTe by photo-induced metal-organic chemical vapor deposition [1], but this technique requires highly specialized crystal growth apparatus. Since the MBE growth temperatures of several of the II-VI semiconducting alloys are sufficiently low to be compatible with photolithography, photoresist becomes a prime candidate for selective-area depositions.

SURFACE PATTERNING

The patterns used in this work are generated from various thicknesses of photoresist that are applied to the substrate surface. In most cases, the substrates are degreased in trichloroethylene (TCE), acetone and methanol for 10 minutes each, and then baked to remove solvents from the surface. AZ1350J and AZ4330 photoresists are applied at a spin speed of 6000 rpm. Bake and exposure times of these layers are experimentally determined. A photoresist profiling scheme, involving a 30 second pre-exposure soak in a 1:2 solution of hexamethyldisilazane and xylene has been devised and used to successfully lift-off 1 μm geometry features. Employing a postbake temperature of 60°C necessitates a baking time in excess of 1 hour in order to increase the photoresist's resiliency to chemical attack. This process mirrors that of the low-temperature device processing technology described elsewhere [2,3], in which the sample is not exposed to temperatures in excess of 60°C, (with the exception of the selective-area epitaxy as described below). Prior to deposition, the native oxide is etched in a 1:1 solution of $\text{HCl}:\text{H}_2\text{O}$ and then the substrate is rinsed in H_2O for 1 minute. As long as the deposition temperature does not exceed 170°C, the photoresist can be removed using solvents.

SELECTIVE-AREA PASSIVATION

CdTe, considered a prime candidate for the surface passivation of HgCdTe due to its close lattice-match, has been selectively deposited in the form of 5 μm wide rings with varying outer diameters between 30 μm and 100 μm , connected to square mesas. A photograph of the selectively deposited CdTe on a CdTe substrate, indicating the fine control of the selective-area linewidth, is shown in Fig. 1. Prior to deposition, a photoresist pattern was imaged on the surface using the low-temperature process described above. The patterned substrate was etched to remove the native oxide, and then loaded into the MBE growth chamber. Several CdTe thin films with thicknesses varying between 600 Å and 1 μm have been successfully deposited and lifted-off in acetone and methanol. CdTe passivating layers have been used in the fabrication of HgCdTe-HgTe-CdZnTe quantum-well modulation-doped field-effect transistors [3] and HgCdTe p-n junction infrared detectors [2], and the passivating properties of these CdTe room temperature MBE depositions on Hg-based alloys are still under investigation.

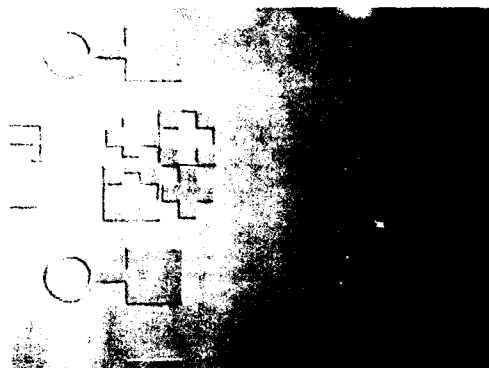


Figure 1. Photograph of selective-area CdTe passivant deposited by molecular beam epitaxy at room temperature. CdTe is 1500 Å thick and the 5 μm-wide rings have diameters in the range between 30 μm and 100 μm.

SELECTIVE-AREA INSULATORS

Thin layers of insulating ZnS, deposited by MBE into the active gate region between the source and drain of a field-effect transistor (FET) structure have been used to successfully fabricate a HgCdTe MISFETs from epitaxial layers of HgCdTe [4]. Thicker layers of insulating ZnS have been employed as an interlevel metal dielectric for advanced multilevel metallization device processing such as CdTe:As-CdTe:In p-n junctions [2]. ZnS has been deposited using a II-VI MBE system with a base pressure of 1×10^{-9} Torr. Then the photoresist pattern and unwanted ZnS are lifted-off in acetone and methanol.

The photograph shown in Fig. 2 illustrates the precise control of the patterned linewidth as well as the ability to selectively place insulators between existing patterned layers. The ZnS T-gate structure is 12 μm wide and 2000 Å thick. From optical microscopy the surface is featureless and there is no evidence of pin-holes that often can be found in thermally evaporated ZnS layers. Further confirmation of the integrity of the insulator is provided by electrical characterization, in which a Au metallization and lift-off provides a gate electrode to the MISFET. From current-voltage measurements on this MIS structure, gate currents of less than 100 nA at 15 V were measured.

Thick layers (in excess of 6000 Å) have also been deposited selectively as an interlevel metal dielectric. In this case, ZnS is deposited over the entire sample with the exception of previous metallization contact pads and future contact areas. Thus, the interlevel dielectric and contact vias to underlying metallization are created simultaneously requiring fewer processing steps. No current is measurable between crossing metallizations at voltages as high as 30 V.

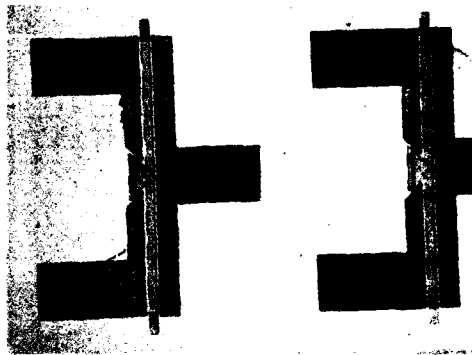


Figure 2. Photograph of selective-area ZnS between the source and drain regions of a field-effect transistor. ZnS is 2800 Å thick, deposited at 60°C by molecular beam epitaxy, and forms a 12 μm wide T-structure.

SELECTIVE-AREA EPITAXY

Epitaxial layers of HgTe, $\text{Hg}_{0.78}\text{Cd}_{0.22}\text{Te}$ and HgTe-CdTe superlattices have been grown onto selective areas of (100) oriented CdZnTe substrates. Prior to epitaxial film growth, chemimechanically polished and etched substrates were photolithographically patterned. The samples were then etched in a 1:1 solution of HCl : H_2O for 30 seconds to remove surface oxides, rinsed, and loaded into a Hg-compatible MBE system. Growth conditions were the same as for non-selective epitaxy as described in Ref. 5, except that no sample preheat at 300°C was performed.

DCXD spectra of the grown epilayers (for a 1 mm² beam cross-section) exhibit structural perfection approaching that of similar unpatterned layers. A summary of the best results are presented in Table I. Each of the listed layers was approximately 1.0 μm thick and grown at a substrate temperature in the range between 140°C and 170°C. The characteristic FWHMs of the layers grown by photoassisted MBE at lower growth temperatures were generally narrower than those of films grown at 170°C. In addition, the lift-off technique was more successful and uniform for the lower temperature growths.

A photograph of selectively-patterned HgCdTe, grown by photoassisted MBE, is shown in Fig. 3 (after lift-off in acetone and methanol). The patterned epitaxial layer exhibited DCXD rocking curves as narrow as 162 arcseconds. The peak x-ray intensity of the epitaxial film was less than half that of the substrate peak because the selective-area HgCdTe patterns comprised only a small fraction of the total surface. Each of the square mesas are 125 μm on a side, while the circular mesas vary in size: 30 μm, 50 μm, 70 μm and 100 μm in diameter. These structures are an appropriate size for infrared detectors operating in the 8 μm to 12 μm spectral region.

The semimetal HgTe has also been grown by conventional MBE at a substrate temperature of 140°C. DCXD rocking curves for 1 μm

Grown Layer	Substrate Material	Growth Temperature	X-Ray FWHM
$\text{Hg}_{0.78}\text{Cd}_{0.22}\text{Te}$	CdZnTe (100)	170°C	162 arcseconds
HgTe-CdTe Superlattice	CdZnTe (100)	150°C	380 arcseconds
HgTe	CdZnTe (100)	140°C	140 arcseconds

Table I. Summary of the structural quality of II-VI semiconductor selective-area epitaxial films as determined from double-crystal x-ray diffraction rocking curves.

thick HgTe layers exhibit FWHMs of 140 arcseconds, demonstrating excellent structural perfection for patterned layers, employing a photosensitive polymer as a mask. In addition, low resistance ohmic contacts to p-type CdTe:As have also been realized through the use of selectively-placed thin films of the semi-metal HgTe followed by the evaporation of indium. This double-layer deposition was successfully lifted-off in the same pattern configuration as shown in Fig. 1. This contact technique was also used in the fabrication of CdTe p-n junctions [2].

Patterning of 10 μm wide lines with 5 μm spacings have been successfully lifted-off as shown in Figs. 4 (a) and (b). These patterns consist of 100 double periods of a CdTe (25 Å) - HgTe (75 Å) superlattice. These structures (b) represent the first NCSU in situ patterned superlattices. These selective area epitaxial superlattices exhibit reasonable x-ray diffraction spectra (with best FWHMs of 380 arcseconds) comparable to other non-patterned HgTe-CdTe superlattices. These structures have potential uses in infrared optical waveguiding and multi-color applications. Selective area epitaxy offers increased versatility for II-VI semiconductor integrated optoelectronics in which a two step

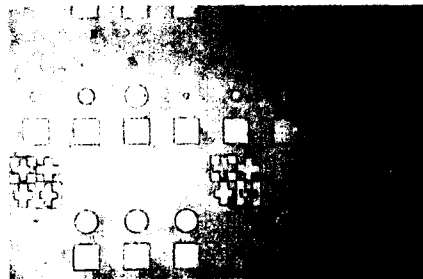
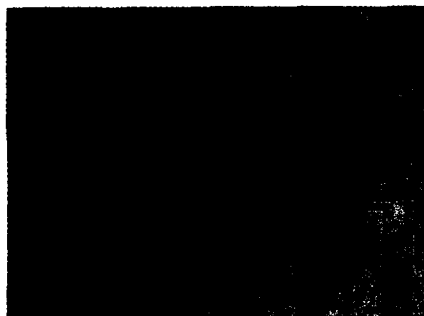
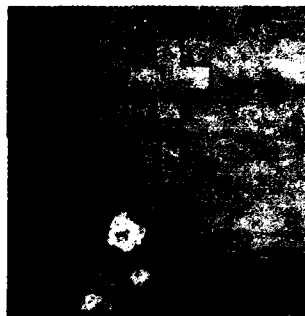


Figure 3. Photograph of selective-area epitaxy of $\text{Hg}_{0.78}\text{Cd}_{0.22}\text{Te}$ grown by photoassisted molecular beam epitaxy at a substrate temperature of 170°C. Square mesa structures are 125 μm x 125 μm while the circular mesas vary in size from 30 μm , 50 μm , 70 μm , and 100 μm in diameter. Total layer thickness is 1.0 μm .



(a)



(b)

Figure 4 (a) and (b). Photographs of selective area HgTe-CdTe superlattice waveguide structures grown on a (100) oriented CdZnTe substrate at 125 °C. The 1 μm -thick superlattice consisted of 100 periods of 25 Å CdTe and 75 Å HgTe. The interdigitated electrodes on the left are 10 μm wide with a 2 μm inter-electrode spacing while the NCSU pattern on the right is only 4 μm in width.

growth process can be used to deposit transistor active regions, followed by the deposition of neighboring detector structures.

The contamination problems that accompany the use of photoresist masks have yet to be determined, but with the trend towards lower growth temperatures they are expected to become less significant.

SUMMARY

Selectively grown II-VI semiconductor surface passivants, insulators and epitaxial films for advanced multilayer device structures would significantly enhance current infrared optoelectronic circuit technologies.

REFERENCES

1. S.J.C. Irvine, H. Hill, J.E. Hails, J.B. Mullin, S.J. Barnett, G.W. Blackmore, and O.D. Dosser, (to be published in J. Vac. Sci. Technol. **A**, 1990).
2. D.L. Dreifus, PhD Thesis, North Carolina State University, 1989.
3. D.L. Dreifus, R.M. Kolbas, B.P. Sneed, and J.F. Schetzina, (to be published in Mat. Res. Soc. Proc. 1989).
4. D.L. Dreifus, R.M. Kolbas, J.W. Han, J.W. Cook, Jr., and J.F. Schetzina, (to be published in J. Vac. Sci. Technol. **A**, 1990).
5. Y. Lansari, Z. Yang, S. Hwang, J.W. Cook, Jr., and J.F. Schetzina, (to be published in Mat. Res. Soc. Proc. 1989).

SPATIAL LIGHT MODULATOR USING A CDS THIN FILM PHOTOCAPACITOR

JOSEPH REICHMAN

Grumman Corporate Research Center, Mail Stop A02-26, Bethpage, N.Y. 11714

ABSTRACT

A brief summary is given of the characterization of an optically addressed Spatial Light Modulator (SLM) that uses a thin film of CdS as the photosensor and a liquid crystal as the electro-optic material. The required high dark impedance of the CdS thin film is achieved by a depletion region created by surface acceptor states. Analysis of the SLM complex impedance as a function of frequency and illumination indicates that the voltage switching is due to the reduction in impedance with illumination caused by the increased capacitance of the CdS thin film. The impedance measurements as well as photoluminescence data were consistent with an acceptor surface state model accounting for the depletion region of the CdS thin film. Additionally the SLM is shown to exhibit photoelectrochemical cell characteristics such as dark rectification, and a photocurrent and photovoltage proportional to the illumination intensity. The SLM performance characteristics of good resolution and sensitivity is attributed to the surface state induced depletion region.

INTRODUCTION

Spatial Light Modulators (SLMs) have numerous applications in a variety of optical computing and image processing systems[1,2]. We have developed a transmissive mode optically addressed SLM that employs a photosensitive layer consisting of a thin film of CdS and a liquid crystal as the electro-optic layer. A schematic cross section of the SLM is shown in Fig.1. The photosensitive layer is a thin film of CdS 2 to 4 microns thick deposited by vacuum evaporation onto an Indium Tin Oxide (ITO) coated

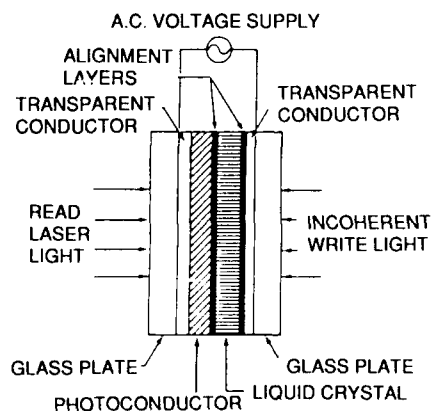


Fig. 1 Grumman Spatial Light Modular (SLM)
Incident laser light is modulated by spatially
varying incoherent write light signal.

glass substrate. The liquid crystal is a cyanobiphenyl which has a positive dielectric anisotropy. It is aligned in a 90 degree twisted nematic configuration by using rubbed polyimide layers on the CdS and ITO surfaces. An AC voltage of 4 to 8 volts rms at 1 to 2 kHz is applied across the ITO electrodes.

When no write light is incident on the photoactive layer, the voltage drop across the liquid crystal is below its switching threshold. Incoming polarized light with photon energy greater than the 2.4 eV bandgap of the CdS is then transmitted with its plane of polarization rotated 90 degrees by the liquid crystal layer. When the CdS is illuminated by write light greater than the band gap energy, its impedance decreases. The voltage drop across the liquid crystal then increases above its threshold value. This results in reorientation of the twist configuration of the liquid crystal molecules. Incoming linearly polarized light in the optically activated region of the device then becomes elliptically polarized. The SLM acts as an amplitude modulator when an analyzer is placed in the output path. With no analyzer, the SLM behaves as a phase modulator.

To switch voltage efficiently during illumination the dark impedance of the CdS thin film should match the liquid crystal impedance. To achieve this high impedance, Schottky barrier[3], MOS[4] or heterojunction[5] structures have been used. This is in contrast to our SLM where the high impedance is obtained by a surface state induced depletion region in a homogeneous thin film.

IMPEDANCE CHARACTERISTICS

To aid in determining the light-activated voltage switching mechanism, the complex impedance of the SLM was measured as a function of frequency with and without illumination. The data and calculated results of an equivalent circuit model of the SLM are given in Fig 2. The equivalent circuit representation of the SLM is given in Fig 3. The liquid crystal layer was modeled as a parallel RC circuit. The resistance and capacitance of the liquid crystal layer was obtained from separate measurements and agreed with calculated values based on its dielectric constants and dimensions [6].

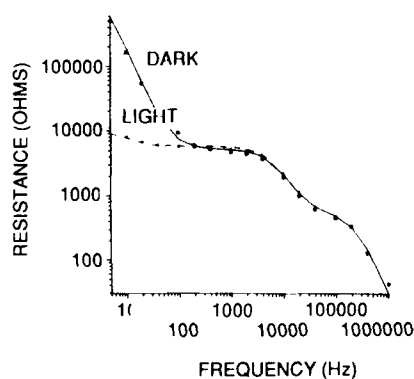


Fig. 2a. Impedance data of SLM and calculated curves using model parameters of Table I (real component).

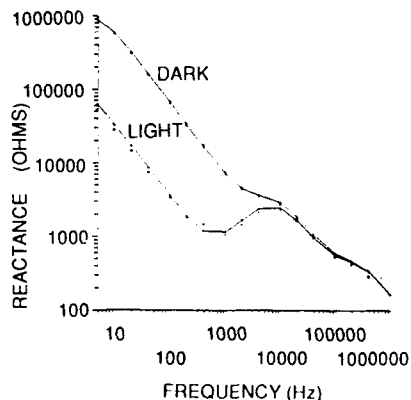
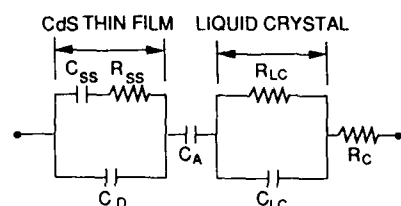


Fig. 2b. Imaginary component.

The CdS thin film depletion region was represented by a surface state impedance model [7]. The surface state capacitance and resistance and the depletion region capacitance are a function of the surface state density, ionized donor density, and band bending voltage. These parameters were determined by using a complex nonlinear least square fitting method [8] and are given in Table 1. The reduction in impedance during illumination is due to the increased capacitance of the depletion region. This results from the generated photovoltage forward biasing the space charge region and an increase in the positive charge density. The latter effect could be due to the capture of photogenerated holes by deep level traps. The switching of voltage to the liquid crystal is thus due to the reduction of the depletion region capacitance during illumination with write light.

PHOTOELECTROCHEMICAL CELL CHARACTERISTICS

The SLM behaves as a photoelectrochemical cell when the current blocking alignment layer is not used. The liquid crystal acts as the electrolyte with oxidation and reduction reactions occurring at the CdS and ITO electrodes respectively. Illumination with white light produces a photovoltage of 0.2 to 0.4 volts. In the dark, the SLM shows rectifying behavior. With illumination, a photocurrent is obtained in reverse bias. At forward bias the currents measured with and without illumination do not differ significantly. The CdS/liquid crystal barrier height appears to be determined by Fermi level pinning due to surface states. This is supported by the observation of similar photovoltage when different liquid crystals were used. The depletion region formed at the CdS surface is most likely due to chemisorption of oxygen. Surface barriers due to surface states created by oxygen chemisorption have been extensively studied [9,10]. These acceptor states capture electrons from the bulk of the semiconductor, thereby creating a depletion region.



C_{SS} = SURFACE STATE CAPACITANCE

R_{SS} = SURFACE STATE RESISTANCE

C_D = DEPLETION REGION CAPACITANCE

C_A = ALIGNMENT LAYER CAPACITANCE

R_{LC} = LAYER
RESISTANCE LIQUID CRYSTAL

C_{LC} = LAYER
CAPACITANCE LIQUID CRYSTAL

R_C = CONTACT RESISTANCE

Table I. Surface state model parameters obtained from best fit to impedance data.

	SURFACE STATE DENSITY	IONIZED DONOR DENSITY	BAND BENDING VOLTAGE
LIGHT	5×10^{10}	10^{15}	0.22
DARK	5×10^{10}	1.6×10^{14}	0.37

Fig. 3. Equivalent circuit model of SLM.

PHOTOLUMINESCENCE

To obtain information concerning the defect structure of the CdS thin films, photoluminescence (PL) measurements were made using the 488 nm line of an Argon ion laser as the excitation source. Room temperature broad band PL was generally observed between 600 and 800 nm. The intensity increased as the temperature was reduced. The intensity correlated with the impedance characteristics of SLMs made from the CdS films. The films showing more intense PL exhibited lower dark impedances resulting in SLMs that were less photosensitive. The lower dark impedances were attributed to smaller depletion widths due to higher donor densities. Since the donor density of CdS is attributed to sulfur vacancies the PL band is attributed to radiative transitions from centers associated with sulfur vacancies. This agrees with previous work relating CdS broadband PL centered at 720nm to sulfur vacancy defects [11,12]. Fig.4 shows the PL spectra for a CdS thin film made by evaporation from the compound and one made by coevaporation using an excess of sulfur. The PL of the film evaporated from the compound is much greater than the coevaporated film indicating a poorer stoichiometry due to sulfur deficiencies.

PERFORMANCE CHARACTERISTICS

The SLM performance parameters of sensitivity and contrast ratio were determined by measuring the transmission of a He-Ne laser as a function of write light intensity using a tungsten halogen light source. An analyzer oriented parallel to the laser polarization axis of was used in the output path. The results are shown in Fig.5 and indicate the SLM is

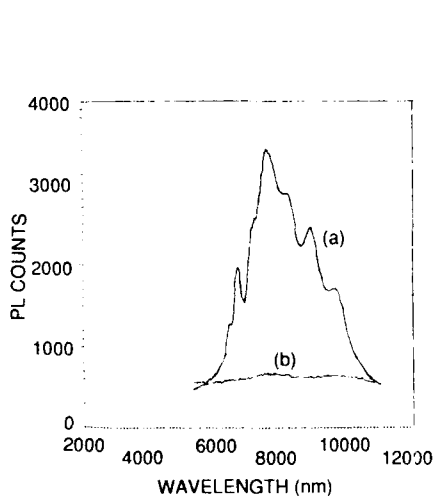


Fig. 4. Photoluminescence spectra of CdS thin films at room temperature.
 (a) Evaporated from compound.
 (b) Evaporated from elements.
 Peaks are due to interference effects.

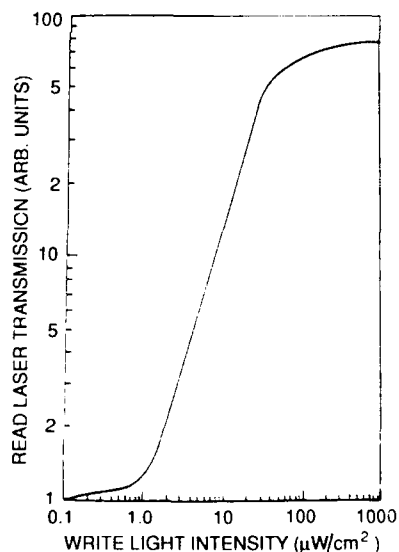


Fig. 5. SLM sensitivity determination where modulation of laser transmission is given as function of write light intensity.

sensitive to write intensities of $1 \mu\text{w}/\text{cm}^2$. At saturation a contrast ratio of 60 to 1 is observed.

A method we have used to determine the resolution of the SLM is to image a resolution chart onto the device and to record it using a He-Ne laser. Fig.6 shows a photograph of the recorded central portion of the resolution chart when the write light is focused on the CdS/liquid crystal interface of the SLM. Group 4 can be clearly seen with elements of group 5 also delineated. This indicates a resolution in the range of 30 to 40 line pairs per mm. When the write signal is incident on the ITO/CdS interface, the resolution is considerably reduced. The resolution appears to be limited by the lateral diffusion of photogenerated carriers which causes image spreading. When the SLM is irradiated with write light incident on the liquid crystal/CdS interface, photogeneration of carriers occurs primarily in the depletion region. There the high electric fields reduces lateral diffusion of photogenerated carriers, thus improving the resolution.

CONCLUSION

We have given a summary of some properties of an optically addressed transmissive SLM that uses a CdS thin film as the photosensitive layer and a liquid crystal as the electro-optic layer. The required high dark impedance is provided by the depletion region at the CdS surface. It is probably formed by acceptor surface states created by adsorption of oxygen. This SLM offers an advantage over existing devices in simplicity of fabrication of the photosensor since special junction forming techniques are not required. Additionally, the transparent nature of the liquid crystal/ CdS interface allows for direct illumination of the depletion region. This results in increased spatial resolution and sensitivity compared to photosensors requiring light blocking layers[4].

ACKNOWLEDGEMENTS

We wish to thank J.DeCarlo, C.Lom, C.Creter, M.Bellucci, and N. Fonneland for carrying out most of the SLM fabrication and characterization. We also thank Dr R. Silberstein for valuable discussions and for help in initiating the impedance and photoluminescence measurements.

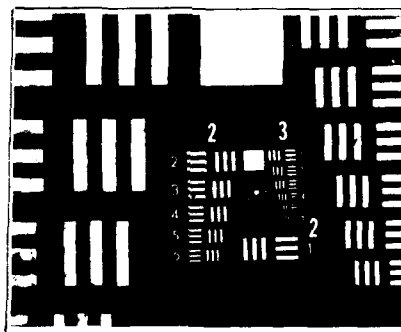


Fig. 6. Resolution capability of SLM demonstrated by photographing He-Ne readout beam for resolution chart input transparency.

REFERENCES

1. F.T.Yu, Optical Information Processing. (John Wiley, New York, 1983).
2. A.A. Sawchuk and T.C.Strand, Proc. IEEE 72, 758 (1984).
3. L. Samuelson, H. Weider, C.R.Guarnieri, J. Chevallier, and A. Onton, Appl. Phys. Lett. 22, 450 (1979).
4. U. Efron, J. Grinberg, P.O. Braatz, M.J. Little, P.G. Reif, and R.N. Schwartz, J. Appl. Phys. 57, 1356 (1985).
5. L. M. Fraas, J. Grinberg, W.P. Bleha, and A.J. Jacobson, J. Appl. Phys. 47, 576 (1976).
6. R.P. Silberstein, J. Reichman, and J. DeCarlo, Bull. Am. Phys. Soc. (March 1985)
7. E.H. Nicollian and J.R. Brews, MOS (Metal Oxide Semiconductor) Physics and Technology (John Wiley, New York, 1982)
8. J. R. Macdonald, Impedance Spectroscopy (John Wiley, New York, 1987)
9. P. Mark, RCA Review, 26, 461 (1965)
10. J. Shapir and A. Many, Surface Science 14, 169 (1968)
11. B.A. Kulp and R.H. Kelley, J.Appl.Phys 31, 1057 (1960)
12. I.J. Ferrer and P. Salvador, J.Appl.Phys. 66, 2568 (1989)

PHOTOLUMINESCENCE PROPERTIES OF GRADED COMPOSITION $\text{Mg}_x\text{Zn}_{1-x}\text{Se}$ CRYSTALS

H. J. Lozykowski, Ohio University; X. D. Jiang, University of Heilongjian, Harbin, PRC; J. L. Merz, University of California, S. Barbara.

ABSTRACT

The photoluminescence properties of $\text{Mg}_x\text{Zn}_{1-x}\text{Se}$ solid solution grown on ZnSe substrate by a closed solid-state diffusion technique have been investigated. The depth profiles of the diffusion region shows distinguished surface layer and thick graded layer. The PL spectra of $\text{Mg}_x\text{Zn}_{1-x}\text{Se}$ side of the sample excited with a wide range of excitation energy shift the edge emission band toward longer wavelengths with decreasing excitation energy. The edge emission spectrum was found to shift toward the shorter wavelength with electric field applied parallel to the compositional gradient of $\text{Mg}_x\text{Zn}_{1-x}\text{Se}$ -ZnSe heterostructure.

INTRODUCTION

Because the direct bandgap, the II-VI compounds are highly efficient for luminescence purposes; ZnSe is a particularly promising candidate for future electroluminescent (EL) devices covering the entire visible spectrum. In order to give good radiative efficiency, however, the material for such devices is often doped with impurities which displace the room temperature emission maximum to a photon energy considerably lower than the bandgap. For many applications it would be desirable to have EL devices with a spectrally narrow emission band, as can be obtained from near-bandgap recombination. However, it seems difficult to make ZnSe crystals which exhibit dominantly such near-bandgap emission. In addition, the availability of a continuous range of emitting wavelengths from such EL devices would be desirable. This might be realized for the violet-UV region of the spectrum in a ternary semiconductor based on ZnSe.

Changing the composition of ZnSe to a $\text{Mg}_x\text{Zn}_{1-x}\text{Se}$ mixed crystal increases the bandgap. Furthermore, the PL characteristics shift dramatically from deep extrinsic emission to ZnSe to that dominated by a narrow near-bandgap emission at all temperatures in the range 2-300 K in $\text{Mg}_x\text{Zn}_{1-x}\text{Se}$ [1].

BANDGAP VARIATION OF $\text{Mg}_x\text{Zn}_{1-x}\text{Se}$

The values of the fundamental bandgap of $\text{Mg}_x\text{Zn}_{1-x}\text{Se}$ ternary alloys ($E_{\text{FGI}-x\text{H}}$) are within the range 2.813 eV (ZnSe) for $x = 0$ and 5.600 eV (MgSe) for $x = 1$ at 80K. The bandgap variation with composition $0 \leq x \leq 1$ is described by equation shown in insert Fig 1 where b is the bowing parameter and ($E_{\text{gMgSe}} - E_{\text{gZnSe}}$) = 2.787 eV at 80K. The bowing parameter, b , can be calculated from the equation:

$$b = \frac{Ze}{8\pi\epsilon_0} \left(\frac{1}{r_F} - \frac{1}{r_G} \right)^2 (r_F + r_G) \exp \left(- \frac{1}{2} s \frac{\sqrt{3}}{4} a \right) \quad (1)$$

where Ze is the charge of the substituting ions, a is the lattice constant of the mid-composition alloy, s is the screening constant ($s = 0.25 \text{ \AA}^{-1}$), and r_F and r_G are the Pauling covalent radii of elements F and G, respectively [2].

The lattice constant of the mid-composition alloy, a , was calculated on the basis of Vegard's law which states that the lattice constant of a solid solution varies linearly with composition. Using $a(\text{ZnSe})_{\text{ZB}} = 5.6676 \text{ \AA}$, $a(\text{MgSe})_{\text{ZB}} = 5.8619 \text{ \AA}$, the last was computed from relation $a_{\text{ZB}} = a_{\text{W}} \sqrt{2}$, [3] and $a(\text{MgSe})_{\text{W}} = 4.145 \text{ \AA}$ [4]. Using covalent radii $r_{\text{Zn}} = 1.225 \text{ \AA}$, $r_{\text{Mg}} = 1.40 \text{ \AA}$ and $a = 5.7647 \text{ \AA}$, we obtain the bowing parameter $b = 0.29$. Figure 1 shows the composition dependence of the bandgap for $\text{Mg}_x\text{Zn}_{1-x}\text{Se}$ alloys at 80K computed using bowing parameter $b = 0.29$. In II-VI compounds consisting of elements AII and BVI of the periodic table the valence band is mainly determined by the local

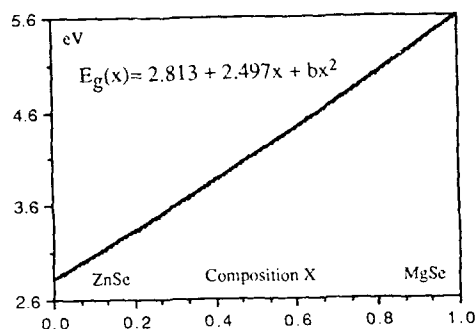


Fig. 1. The bandgap E_g , as a function of composition x .

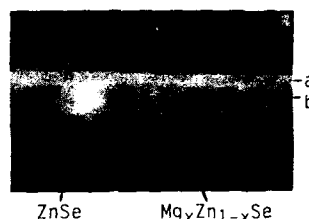


Fig. 2. Luminescence pattern of $\text{ZnSe-Mg}_x\text{Zn}_{1-x}\text{Se}$ obtained under UV excitation.

potential near the anion and the conduction band is determined by the cation region. Therefore, in inhomogeneous mixed crystals such as $\text{Mg}_x\text{Zn}_{1-x}\text{Se}$ we will have a greater composition dependence for the conduction band states than for valence band states.

EXPERIMENTAL

Single crystals of ZnSe were grown from the melt using Merck ZnSe powder of purity 99.999%. The crystals were cut into slices approximately 1 mm thick and oriented in the (111) or (110) directions. A sealed tube technique was employed for diffusion. The diffusion source was metallic Mg placed in an evacuated quartz ampule together with ZnSe crystals. Preparation of crystals, diffusion conditions and all etching procedures used on the material have been described in a previous paper [1]. For the field-dependent photoluminescence the sample was mechanically ground to half its initial thickness after the diffusions. It was then polished and chemically etched. After diffusion the crystals were white-yellow and had an odor of hydrogen selenide. The etching procedure after diffusion removed some part of the heavily doped surface region but also small drops of metal (Mg, Mg + Zn) from the surface. The color of the Mg-doped crystals varied from green to yellow to pink. The composition of the ternary alloys was determined by electron probe microanalyzer (ARL EMX-SM 120,000). The sample surfaces were cleaved to form wafers with orientation (111), or were embedded in epoxy ((110) wafer) and mechanically ground and polished in oil to expose the sample surfaces. These sample surfaces were then degreased with trichloroethylene and placed immediately in the evaporation apparatus. After coating the samples with a thin carbon film they were placed in the microprobe analyzer. An accelerating voltage of 20 KV was used for the electron beam. An Au semi-transparent electrode ~200Å thick was sputtered onto the $\text{Mg}_x\text{Zn}_{1-x}\text{Se}$ surface. The second electrode on the substrate was a brushed In + Hg contact or an indium alloyed contact. Photo-excitation was achieved through the gold semi-transparent electrode. Samples were immersed in either liquid N_2 or in liquid He which could be pumped below the λ point. Photoluminescence measurements were obtained with excitation from a 200 W high-pressure Hg UV lines or from a N_2 -pumped, pulsed tunable dye laser (PAR Model 2100) with spectral linewidth ≤ 0.04 nm and output peak power ≥ 25 KW.

the effect of Mg diffusion is the appearance of peaks at 426.5 and 437.7 nm. For comparison, photoluminescence spectra at 1.4 K for an undoped ZnSe specimen, heat-treated at 1000°C for 48 hours under Zn over pressure is also shown in Figure 3. The very weak I_1 deep line at 445.4 nm with LO phonon replicas and a strong series of edge-emission lines due to the donor-acceptor pair transition in the region 459-485 nm are shown. Although there is a slight shift in energy between the low energy peaks for the diffused and undiffused spectra, we believe that the nature of emission in the region is the same for all three spectra; the shift of the no-phonon line in (c) results from the band-gap shift with temperature. In order to obtain information on the luminescent properties of the $Mg_xZn_{1-x}Se$ -ZnSe graded heterojunctions, we have carried out measurements of photoluminescence spectra at different excitation energies and intensities. Photoluminescence spectra at 77 K for the $Mg_xZn_{1-x}Se$ side of the specimen are shown in Fig 4a is the same as in Fig 3a, excited by the mercury line 365 nm. Fig 4b shows emission using a low power mercury Pen Ray lamp as the excitation source. As can be seen from the figure, the PL spectral distributions under varying excitation intensities are different. At low excitation intensity, the spectrum exhibits only one band in the short wavelength region which occurs at slightly higher energy than in the higher excitation case. The remaining band is edge emission from the ZnSe substrate. Figure 4c and d show photoluminescence spectra for this same crystal excited by different dye laser wavelengths, 404.1 nm and 409.3 nm, respectively. For 404.1 nm excitation a broad emission band can be observed with peaks at 429.0 nm, and 444.0 nm. The emission spectrum excited by wavelength 409.3 nm at 77 K (Figure 4d) shows additionally a new high energy line with a smaller amplitude peak at 410.3 nm. Similar peaks were observed from different crystals and with different excitation wavelengths, but our experimental results are not sufficient to establish the nature of this line. Finally, in order to specify the nature of the observed luminescence transitions, we recorded the photoluminescence spectra at 1.4 K, varying the excitation source. The pulse dye laser with repetition rate 20 pulse/sec was tuned in the wavelength range from 398.2 nm to 439.0 nm with

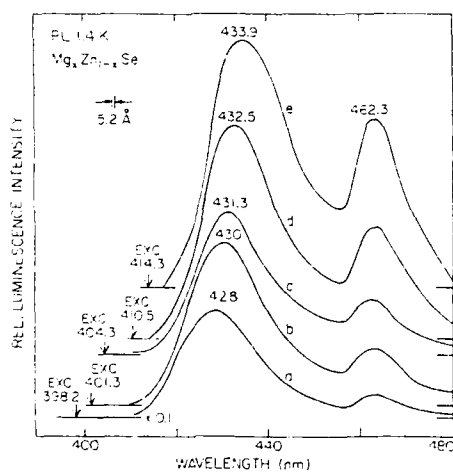


Fig. 5. The PL spectra $Mg_xZn_{1-x}Se$ side excited by different λ at 1.4 K.

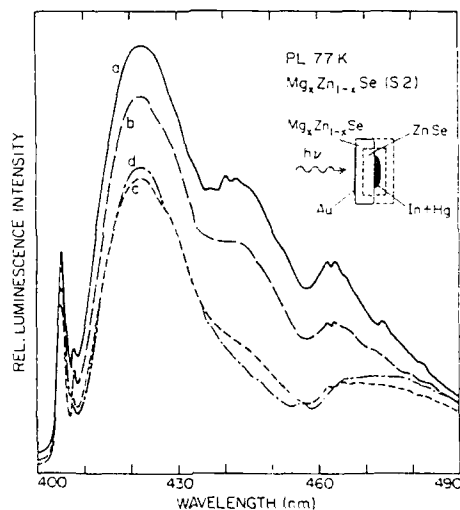


Fig. 6. The PL spectra of $Mg_xZn_{1-x}Se$ crystal (a) no bias, b, c, d, with bias 100V, 130V, 150V.

SCANNING X-RAY MICROPROBE ANALYSIS

The depth profiles were determined by using the scanning X-ray microprobe apparatus. The samples were cut normal to the surface and the 20 KV electron beam with diameter $1.5 \mu\text{m}$ was scanned from the surface into the bulk. The cathodoluminescence observed visually at room temperature changed color from violet at the surface ($\text{Mg}_x\text{Zn}_{1-x}\text{Se}$) to blue in the bulk (ZnSe). The depth profile thus obtained for diffusion at a temperature of 980°C for a period of 48 hours samples (S1), indicate that the solid solution layer can be divided into two regions, one $12\text{--}15 \mu\text{m}$ deep, followed by a transition region with a graded composition to a depth of about $28 \mu\text{m}$. The first region is better approximated by a Gaussian relation which results in a diffusion constant, $D_{\text{Mg}} \sim 8.3 \times 10^{-13} \text{cm}^2 \text{sec}^{-1}$. The depth profile below the surface overlayer is approximated by a simple complementary error function. The diffusion constant obtained in this region is $D_{\text{Mg}} = 4.3 \times 10^{-13} \text{cm}^2 \text{sec}^{-1}$.

Fig 2 shows the luminescence pattern of a crystal cut from a (110)-oriented wafer of ZnSe into which Mg has been diffused at 1000°C . The light region on the photograph corresponds to the $\text{Mg}_x\text{Zn}_{1-x}\text{Se}$ layer, the dark area corresponds to ZnSe. The photoluminescence pattern was obtained under 365 nm ultraviolet excitation at room temperature. The thickness of the luminescent layer is not uniform; the photograph shows a clearly-distinguished thin ($24 \mu\text{m}$) surface layer of one composition (denoted by a in the figure), and another region of varying thickness, from $73\text{--}103 \mu\text{m}$ (denoted by b). The microscopic observation of the luminescence pattern of another sample (S1) after etching shows a $36 \mu\text{m}$ thick graded layer, which is in good agreement with the thickness of the surface layer determined by the scanning X-ray microprobe analyzer.

PHOTOLUMINESCENCE SPECTRA

Fig 3 shows the photoluminescence spectra of two crystals, ZnSe and $\text{Mg}_x\text{Zn}_{1-x}\text{Se}$ (S1), excited with the 365.0 nm Hg line, the sample was cut to half its initial thickness, polished and etched. Curves a and b in Figure 3 shows the emission spectra from the $\text{Mg}_x\text{Zn}_{1-x}\text{Se}$ (S1) and ZnSe sides of the same crystal, respectively, at 77 K . A broad emission band with peaks near 426.5 nm , 437.7 nm and 463.3 nm was observed from the Mg-rich side. The opposite side of this crystal (undiffused ZnSe) showed a spectrum (curve b) with only the low energy peak of the three described above here peaking at 464.5 nm ; the broad band in the short wavelength region is extremely weak. It is clear that

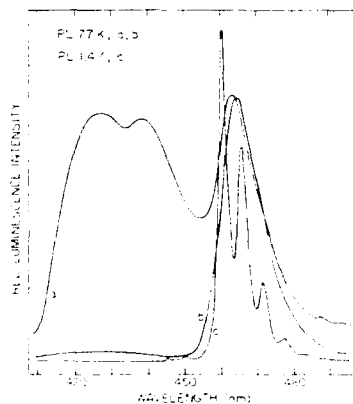


Fig. 3. The PL spectra of (a) $\text{Mg}_x\text{Zn}_{1-x}\text{Se}$ side (b) ZnSe side (c) ZnSe(Rf).

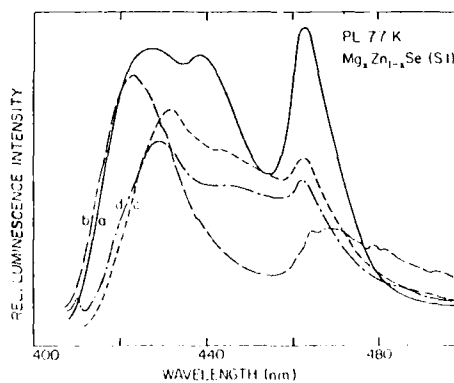


Fig. 4. Luminescence emission spectra of $\text{Mg}_x\text{Zn}_{1-x}\text{Se}$.

halfwidth ≤ 0.04 nm and duration time 2 ns. Figure 5 gives an example of what is obtained. The short wavelengths bands are shifted towards longer wavelengths and the edge emission remains at the same position (462.3-463.3 nm) similar to the spectra taken at 77 K. The tail of the highest energy peak is extended to 410.0 nm when the excitation wavelength is 398.2 nm, as shown in Fig. 5. Note that for 439 nm excitation, little else is seen besides luminescence of bulk ZnSe.

ELECTRIC-FIELD-DEPENDENT LUMINESCENCE SPECTRA

If we irradiate the structure of Fig 6 (insert) through a gold semi-transparent electrode using monochromatic light, the band-to-band transition is excited. The very high absorption coefficient of $\text{Mg}_x\text{Zn}_{1-x}\text{Se}$ at 3650 Å ($\geq 105/\text{cm}$) indicates that only the near surface region is excited. The equations describing the electron and hole currents in graded-band-gap material, assuming space-charge free inhomogeneous semiconductors [5, 6] give the effective field equations which contains, the usual electric field (E) term (determined by the applied voltage), plus terms proportional to the band edge and effective-mass gradients. At thermal equilibrium, with $E = 0$, the ordinary diffusion term and the extra term just balance out in each equation. For the funnel-shape graded band-gap, carriers of both signs will move towards the small gap region (ZnSe), due to the extra diffusion terms which depend on the gradient of the band edges. Fig 6 shows the photoluminescence spectra of $\text{Mg}_x\text{Zn}_{1-x}\text{Se-ZnSe}$ heterostructures with a diffusion-type profile of composition vs depth. The PL was excited by a Hg line (365 nm) through a gold semi-transparent contact at liquid nitrogen temperature (77 K). Curve 6a shows the PL spectrum with no voltage applied to the contacts. This spectrum exhibits three maxima at 423 nm, 422.4 nm and 462.8 nm. Fig 6 b, c, d, shows the PL spectra with different voltages applied across the crystal between the gold electrode and the indium-mercury amalgam electrode. The effect of applying an electric field was to shift the first peak to shorter wavelengths and to reduce the intensities of two longer-wavelength bands when the magnesium-rich end of the crystal (Au contact) is held at a negative potential. Spectra b, c, d, were recorded at the same photo excitation intensity as spectrum a, but with applied voltage of 100V, 130V, and 150V, respectively. The luminescence intensity decreases for all peaks, but does so much faster for peaks in the longer wave-length area of the spectrum (peaks at 442.4 nm and 462.8 nm). At 150 volts the shortest wavelength emissions under an applied electric field increase and shift 7 meV to shorter wavelength as originating from field-enhanced positive hole transport between regions with different band gaps, and the field enhanced diffusion of holes to the surface region, respectively [5-8]. The spectral shift $\Delta(h\nu)$ in the high-field limit for constant gradient dE_g/dx is [8]:

$$\Delta(h\nu) = E \mu_p \tau_p \frac{dE_g}{dx} \quad (2)$$

where μ_p and τ_p are the hole mobility and lifetime. E is the field, and E_g the band gap. Taking $\mu_p = 44$ (cm^2/Vsec), $\tau_p = 2 \times 10^{-9}$ sec [9, 10], an average electrode field $E = 3.6 \times 10^3$ [V/cm], and constant gradient $dE_g/dx = 22$ (eV/cm) we obtain the spectral shift $\Delta(h\nu) = 7$ meV.

CONCLUSION AND DISCUSSION

The bandgap of $\text{Mg}_x\text{Zn}_{1-x}\text{Se}$ was computed as a function of composition using calculated bowing parameter $b = 0.29$ eV. The solid solutions of $\text{Mg}_x\text{Zn}_{1-x}\text{Se}$ were formed by solid-state-diffusion closed tube technique over a wide range of x . The depth profiles of the diffusion region determined by using an X-ray microprobe technique is complex. The transition region profile is approximated by the complementary error function, from which the diffusion constant was estimated to be $4.3 \times 10^{-13} \text{cm}^2 \text{sec}^{-1}$ (at 980°C). The PL spectra excited with a

wide range of excitation energy shifts the shorter wavelength band toward longer wavelengths with decreasing excitation energy, while the edge emission in ZnSe remains at the same position. The nature of the excitation of the edge emission using a wavelength of 365 nm is related to the funnel-shaped graded bandgap. In such structure carriers of both signs created by photoexcitation on the skin of the mixed crystal move towards the small bandgap region because of the extra diffusion terms, which depend on the gradient of the band edges.

The PL spectra of $\text{Mg}_x\text{Zn}_{1-x}\text{Se}$ sample (S1) prepared by magnesium diffusion without zinc overpressure shows a very broad emission band. In contrast with the above results, the sample prepared by diffusing Mg in the presence of excess Zn exhibits narrow band emission obtained with excitation from a Kr + laser (~413 nm), as was described in our previous paper [1]. The observed spectral features in the Mg-doped regions are influenced by the usual broadening from the alloy disorder, as well as a broadening from the gradient in Mg concentration across the excited region of the sample (width 16-30 meV). This means that the bare electronic shape of the edge emission in the $\text{Mg}_x\text{Zn}_{1-x}\text{Se}$ material (obtained by diffusion of Mg + Zn) could be quite sharp, as required, for example for an exciton transition at low temperatures. Further, this peak remains strong in the PL spectrum of $\text{Mg}_x\text{Zn}_{1-x}\text{Se}$ all the way up to room temperature, which is usually not observed for peaks such as exciton transitions related to shallow defect centers.

The broad emission band observed in this paper can be caused by : (a) the higher alloy disorder created by Mg diffusion into the ZnSe crystals without overpressure of Zn, (b) a significant change in bandgap which occurs in the finite thickness of crystal form which light is emitted. The broadening due to the latter effect results from the depth of penetration of excited radiation into the crystal, diffusion of excitons and free carriers to a narrower bandgap region, and reabsorption of light in the graded semiconductor. Finally, the electric field dependent photo-luminescence spectra, which shows a shift toward short wavelength with increasing field and an attenuation of the longer wavelength emission, can be explained on the basis of graded crystal properties. The mechanism involves the transport of minority carriers between regions of different bandgap. The direction of the shift is such that the carriers must be holes recombine nonradiatively. Homogenous $\text{Mg}_x\text{Zn}_{1-x}\text{Se}$ material would be a suitable candidate for the realization narrow band LED's for the violet-UV wavelength range [1].

ACKNOWLEDGEMENTS

The authors wish to thank Dr. W. S. Wise for making accessible the EMX and Dave Pierce of the UCSB Geological Sciences Department for the scanning X-ray microprobe analysis of $\text{Mg}_x\text{Zn}_{1-x}\text{Se}$.

REFERENCES

1. H. J. Lozykowski, P. O. Holtz, and B. Monemar, J. of Electronic Materials, **12**, 653 (1983).
2. R. Hill, J. Phys. C: Solid State Phys., **7**, 521 (1974).
3. W. Giriet, J. K. Furdyne, Semiconductors and semimetals, Vol. 25, (1988).
4. Von H. Mittendorf, Z. Physik, **183**, 113 (1965).
5. L. J. van Ruyven and F. E. Williams, Am. J. Physics., **35**, 705 (1967).
6. T. Gora and F. E. Williams, Phys. Rev., **177**, 1179, (1969).
7. L. J. van Ruyven and F. E. Williams, Solid State Electronics, **10**, 1159 (1967).
8. R. Hill and F. E. Williams, Appl. Phys. Letters, **11**, 269 (1967).
9. J. L. Heaton, G. H. Hammon, and E. B. Goldmer, Appl. Phys. Letters, **20**, (1972).
10. S. Mora, N. Romeo, and L. Tarricone, Solid State Communications, **33**, 1147 (1980).

ATOMIC LAYER EPITAXY OF
WIDE BANDGAP II-VI COMPOUND SEMICONDUCTOR SUPERLATTICES

M.Konagai, Y.Takemura, R.Kimura, N.Teraguchi and K.Takahashi

Tokyo Institute of Technology,
Dept. of Electrical and Electronic Engineering,
2-12-1, Ohokayama, Meguro-ku, Tokyo 152, Japan

ABSTRACT

ZnSe, ZnTe and ZnSe-ZnTe strained-layer superlattices (SLS's) have been successfully grown by atomic layer epitaxy (ALE) using molecular beam epitaxy (MBE-ALE). The ideal ALE growth, i.e., one monolayer per cycle of opening and closing the shutters of the constituent elements, was obtained for ZnSe in the substrate temperature range of 250-350°C. However, for ZnTe, precise control of the Te beam intensity is needed to obtain the ALE growth. Optical properties of the $(\text{ZnSe})_1(\text{ZnTe})_1$ SLS were evaluated by photoluminescence. ZnSe films were also grown by ALE using metalorganic molecular beam epitaxy (MOMBE-ALE). Diethylzinc (DEZn), diethylsulfur (DES) and diethylselenium (DESe) were used as source gases for Zn, S and Se, respectively. The ALE growth of ZnSe was achieved at substrate temperature between 250 and 300°C which is about 150°C lower than that for the conventional MOMBE.

INTRODUCTION

II-VI compound semiconductors, especially strained-layer superlattices (SLS's) consisting of ZnS, ZnSe and ZnTe, are promising for light emitting devices in the visible wavelength region. We have been investigating the properties of ZnSe-ZnTe SLS's prepared by MBE for several years and obtained the following results: (1) The luminescence color changes from blue-green to red by tailoring the structure of the superlattice [1]. (2) The lattice mismatch in the SLS's is accommodated by tetragonal distortion of the crystal lattices of the constituent materials with the thickness below the critical layer thickness [2]. (3) The SLS with modulation doping of ZnTe with Sb and ZnSe with Ga exhibit p- and n-type conductivity, respectively, with a carrier concentration of about $1 \times 10^{14} \text{ cm}^{-3}$ [3]. However, the obtained carrier concentration is still too low for practical device applications. We have clarified factors degrading the SLS quality [4,5]. The factors degrading optical and electrical properties of the SLS's are (1) structural degradation at growth temperature (interdiffusion); (2) thermal diffusion of impurities in the SLS's and (3) poor interface abruptness and uniformity and irregularity in the superlattice period. We have found that the interdiffusion of the constituent materials and the thermal diffusion of impurities were not main factors degrading electrical properties. To solve the third problem, atomic layer epitaxy was employed to grow SLS's [6].

In this paper, we present the detailed ALE growth conditions of ZnSe and ZnTe and growth of ZnSe-ZnTe SLS's. In the ZnSe-ZnTe SLS systems their photoluminescence (PL) peak energies cover the region from blue-green to red. However, to obtain much shorter wavelength, for pure blue color, we have to use S. In MBE, if we use two different kinds of high vapor pressure source materials, especially S and Se, we suffer from elemental cross contamination. Thus, metalorganic molecular beam epitaxy (MOMBE) is found to be a powerful epitaxial growth method for the superlattice systems consisting of ZnS, ZnSe and ZnTe [7]. Preliminary results of MOMBE-ALE growth of ZnS and ZnSe are reported for the first time.

GROWTH AND CHARACTERIZATION OF ZnSe AND ZnTe BY MBE-ALE

Growth system

A conventional MBE system with solid sources was used for ALE growth of ZnSe and ZnTe. Three K-cells contained elemental sources for Zn, Se and Te, and shutter above each cell was manipulated with a stepping motor controlled by a personal computer. The shutters of Zn and chalcogens were alternately opened and closed with an interval of 1 sec.

ALE ZnSe

ZnSe layers were grown on (100)GaAs substrates. The shutter sequence is one of the most important parameters for successful ALE growth. We grew several ZnSe samples by ALE with various durations of Zn supply. Figure 1 shows the ZnSe film thickness as a function of duration of Zn supply for substrate temperature of 250°C. It shows that ideal ALE growth (one monolayer per cycle) is obtained for the Zn supply duration of 4-7 sec. However, at 14 sec, the thickness is much larger than that expected for the ALE growth.

We also investigated the growth rate per cycle as a function of substrate temperature (see Fig. 10). The growth of one monolayer/cycle condition is achieved in the substrate temperature range of 250-350°C. Below 200°C the growth rate decreases rapidly with increasing growth temperature, while above 350°C it decreases gradually due to desorption.

We deposited Zn and Se thin films on glass substrates at room temperature in order to calculate the beam intensity. The calculated number of Zn and Se atoms impinging on the substrate during supply (7 sec for Zn and Se) are $8.3N_s$ and $83N_s$, respectively, where N_s is the surface density of Zn or Se site ($6.22 \times 10^{14} \text{cm}^{-2}$). The calculated number of atoms impinging on the surface per cycle is much larger than the surface density of Zn or Se site. Thus deposition of Zn and Se atoms must automatically stop when deposition of one monolayer is completed. However, as shown in Fig. 1, when the Zn supply duration exceeds 7 sec, the deposition rate rapidly increases, which indicates that excess Zn atoms are not quickly removed from the surface during an interval of 1 sec.

We achieved drastic improvements in the surface flatness and the optical properties of ZnSe films, in contrast to ZnSe films by the conventional MBE. The Nomarski microscope observation shows good morphology without any features for the samples grown at 250 and 300°C. We also observed very fine streaky RHEED patterns for these samples. For the samples grown at substrate temperatures above 400°C or below 200°C, poor surface morphology was observed.

Optical properties of the ALE ZnSe films were studied by PL at 4.2K. The PL spectra of the samples grown at 200 and 250°C are dominated by the donor-bound exciton emission I_2 . However, for substrate temperature above 300°C, a deep-level emission is dominant. The PL spectra of the ALE ZnSe as a function of the Zn supply duration are shown in Fig. 2. The strongest I_2 -line emission is observed for the supply duration of 7 sec. The deep-level emission is suppressed for shorter Zn supply. Although the ALE growth is confirmed, the PL spectrum of the sample grown with the Zn supply duration of 4 sec is dominated by the deep-level emission. The number of Zn atoms impinging on the surface is probably one of key parameters affecting the film quality, even if the ALE growth condition is satisfied.

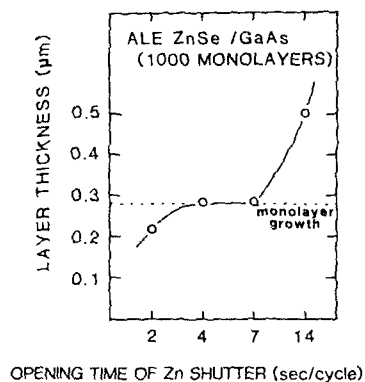


Fig. 1 The dependence of the film thickness of ALE-ZnSe against the Zn supply duration.

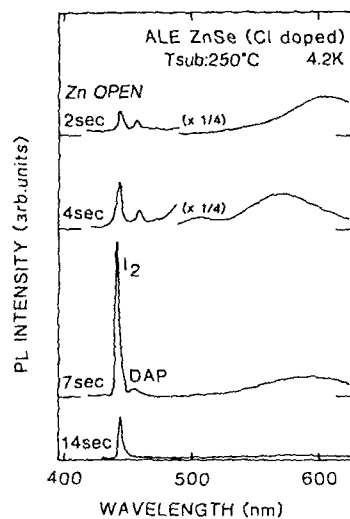


Fig. 2 PL spectra of ALE-ZnSe varying the Zn supply duration.

ALE ZnTe

We also grew ZnTe by MBE-ALE. The ZnTe films were deposited on (100)InP substrates. The shutter sequence was the same as that for the ALE-ZnSe (7 sec of Zn and Te supply and 1 sec of interval). The dependence of the ZnTe layer thickness on growth temperature is shown in Fig. 3 (indicated with circles). The ideal ALE growth is achieved in the substrate temperature range of 240-280°C. The temperature range to obtain a monolayer per cycle is narrower for ZnTe than that for ZnSe, because vapor pressure of ZnTe is about two orders of magnitude higher than that of ZnSe.

The growth rate of ZnTe as a function of the Te beam intensity at growth temperature of 240°C is shown in Fig. 4. The thickness of the ZnTe film is affected by the Te beam intensity, which suggests that deposition of Te atoms does not automatically stop, and that the Te layer thickness exceeds one monolayer for certain beam intensities. This may be due to low vapor pressure of Te, which is three orders of magnitude lower than that of Se.

Surface morphology and RHEED patterns of ZnTe samples grown under various Te beam intensities were studied [8]. The surfaces are very specular for the samples with the thickness below 2800Å (1000 cycles). However, the surface morphology rapidly degrades with hillocks, and RHEED patterns show rings when the deposition rate exceeds one monolayer/cycle. The number of hillocks is varied by the Te beam intensity. The hillocks may be caused by Te precipitates.

Strictly speaking, the growth condition necessary to obtain good crystallinity is not the same as the ideal ALE growth condition for ZnTe. If we adjust the Te beam intensity to achieve the ideal ALE growth (one monolayer per cycle), surface morphology and crystallinity are degraded by hillocks.

In order to obtain high-quality films, we grew ZnTe with the low Te beam intensity. Fig. 3 also shows the growth rate of ALE-ZnTe against substrate temperature for Te supply of 1.9Ns (indicated with squares), which is smaller than that indicated with circles. The dependence of layer thickness on substrate temperature indicated with squares is similar to that for the MBE growth. However, for these samples, good surface morphology could be obtained without hillocks. Especially, the film grown at temperature of 260°C has excellent surface morphology.

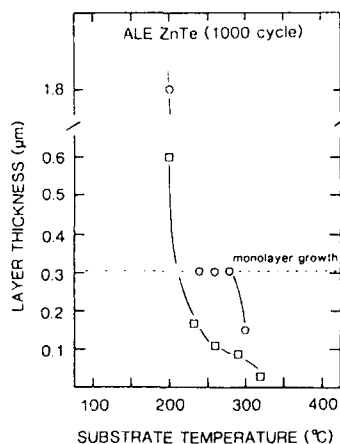


Fig. 3 Film thickness of ALE-ZnTe varying substrate temperatures. The samples indicated with circles and squares were grown under (Zn,Te) supply of (54Ns, 8.7Ns), (11Ns, 1.9Ns), respectively.

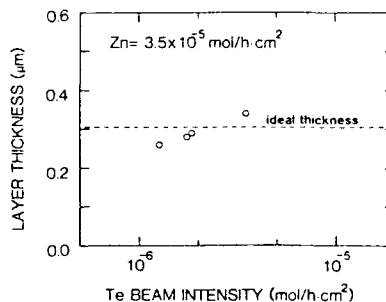


Fig. 4 Film thickness of ALE-ZnTe varying Te beam intensities.

OPTICAL PROPERTIES OF ZnSe-ZnTe STRAINED LAYER SUPERLATTICES

$(\text{ZnSe})_m-(\text{ZnTe})_n$ ($m, n=1-4$) SLS's were grown on InP substrates at 260°C, which is about 60°C lower than that for the conventional MBE. We reported that the PL intensity of the SLS grown by ALE is more than ten times higher than that of the SLS grown by the conventional MBE due to drastic improvements in the abruptness and flatness at the ZnSe-ZnTe interface [6]. In this paper, we report the PL spectra of the $(\text{ZnSe})_1-(\text{ZnTe})_1$ monolayer superlattice.

The PL peak energy of the monolayer superlattice is very sensitive to the layer thickness of ZnTe. If one shutter sequence provides enough atoms to cover one monolayer on the surface, then the ALE growth should be obtained regardless of the beam intensities. But, in our experimental results, the thickness of the ZnTe film was influenced by the Te beam intensity. Figure 5 shows the PL spectra of the $(\text{ZnSe})_1-(\text{ZnTe})_1$ monolayer superlattice grown with various Te beam intensities. As the Te beam intensity increases, the PL peak energy shifts to lower energy, approaching the effective bandgap of the $(\text{ZnSe})_1-(\text{ZnTe})_1$. This indicates that the deposited Te monolayer has poor uniformity over the area for all the Te beam intensities studied in our experiments.

However, the measured SLS thickness agrees with the sum of the thicknesses of ZnSe and ZnTe assuming the ALE growth of each layer. Although detailed structures of these samples have not been evaluated at present, we speculate that the overlaid ZnSe covers "holes" of ZnTe layers created by desorption of Te as shown in Fig. 6.

Figure 7 shows the PL spectra of a 750-period $(\text{ZnSe})_1-(\text{ZnTe})_1$ monolayer superlattice at temperatures from 4.2K to 300K. It should be noted that green-yellow luminescence is observed even at room temperature. Two luminescence peaks are observed between 4.2K and 140K. The peak at higher energy become weak with increasing temperature. By curve-fitting with the sum of two gaussians, the positions of the two peaks observed at 4.2K are 510nm (2.43eV) and 538nm (2.30eV). The two peaks can be associated with S_1 and S_2 bands, which are regarded as the recombinations of excitons trapped at Te atoms and Te_n clusters, respectively [9].

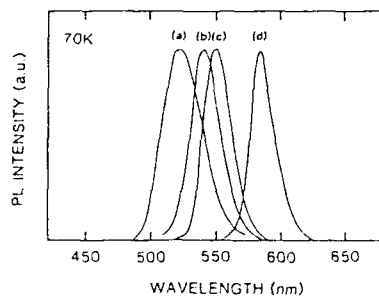


Fig. 5 PL spectra of $(\text{ZnSe})_1-(\text{ZnTe})_1$ monolayer superlattices with various Te beam intensities. (a):(b):(c):(d) = 1:1.5:3.5:4

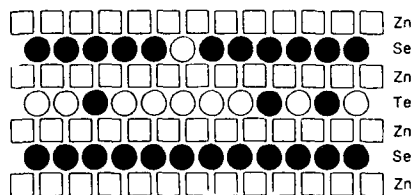


Fig. 6 Speculated $(\text{ZnSe})_1-(\text{ZnTe})_1$ monolayer superlattice structure with "holes" in ZnTe layers.

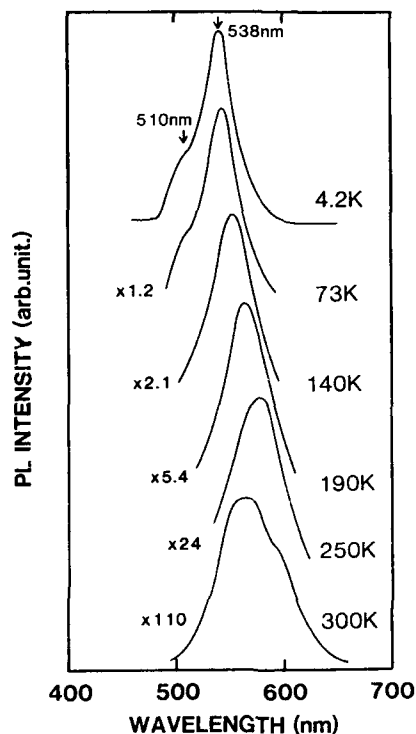


Fig. 7 Temperature dependence of PL spectra of $(\text{ZnSe})_1-(\text{ZnTe})_1$ monolayer superlattice.

GROWTH OF ZnSe AND ZnS BY MOMBE-ALE

The luminescence wavelength of the ZnS-ZnSe SLS covers the short wavelength range (2.7-3.5eV). We studied the optical properties of ZnS-ZnSe SLS system grown by MOMBE [7], and the PL peaks of these SLS's were found to be broad, due to large roughness of the ZnS/ZnSe interface. To improve interface smoothness, the atomic layer epitaxy (ALE) technique was employed.

Growth system

Figure 8 shows a MOMBE growth system used in this work, which consists of two vacuum chambers: a growth chamber and a vent chamber. The source gases flow into the vent chamber before and after the growth and also during intervals. The base pressure of the main chamber is about 2×10^{-8} Torr. Diethylzinc (DEZn), diethylsulfur (DES) and diethylselenium (DESe) were used as source gases for Zn, S and Se, respectively. Hydrogen was used as carrier gas for the metalorganic sources. The pyrolysis of DEZn, DES and DESe was carried out in cracking cells at the outlet of the tube.

ZnSe films were grown on (100)GaAs substrates, while ZnS films were grown on (100)GaP substrates. The cracking temperatures of DEZn, DES and DESe were 750°C, 850°C and 700°C, respectively.

Growth of ZnSe and ZnS by MOMBE-ALE

Figure 9 shows a gas flow sequence during the ALE growth of ZnS and ZnSe. The air valves control the gas flow. Each metalorganic gas flows for 10 sec to deposit one monolayer. The interval time is 2 sec. The number of 1000 cycles was used in all experiments. The substrate temperature was varied between 200 and 450°C. The typical gas flow rates for the ALE growth were 3.3×10^{-4} mol/min (DES and DESe) and 4.9×10^{-5} mol/min (DEZn). These flow rates are 10 times larger than that for the conventional MOMBE growth.

Fig. 10 shows the substrate temperature dependence of the ZnSe film thickness. In this figure, we see a flat region independent of substrate temperature, and the growth rate in the flat region is exactly one monolayer per cycle. From this result, we conclude that the ALE growth can be achieved at substrate temperature from 225 to 300°C, which is about 150°C lower than the optimum substrate temperature in the conventional MOMBE. At substrate temperatures lower than 225°C, the films are thicker than 1000 monolayers. In this temperature range, deposition of Zn atoms on Zn atoms cannot be avoided. While, at growth temperature higher than 300°C, the surface morphology becomes degraded and the film thickness decreases because of Se desorption. These results are very similar to those obtained for the MBE-ALE ZnSe.

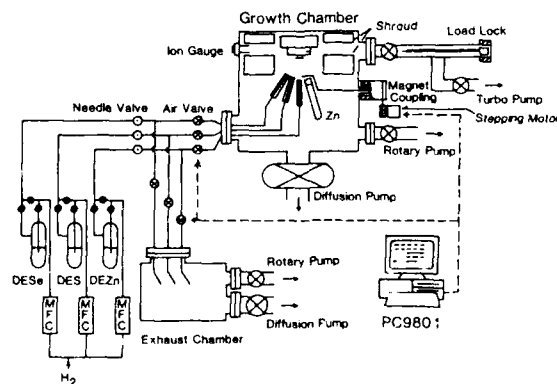


Fig. 8 MOMBE growth system.

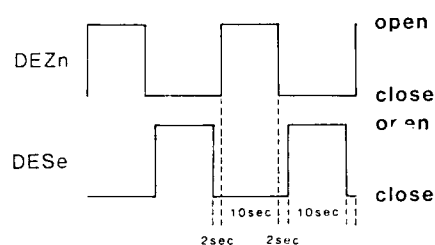


Fig. 9 Gas flow sequence in MOMBE-ALE growth.

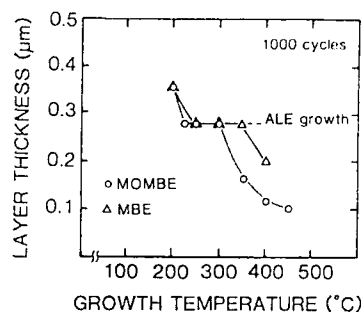


Fig. 10 Film thickness of ZnSe by MBE-ALE and MOMBE-ALE against substrate temperatures.

PL measurements were carried out at 77K for the ZnSe films grown by MOMBE-ALE. However, the excitonic emission intensity is very weak, and the deep-level luminescence (500-750nm) is dominant for all the studied substrate temperature range, as shown in Fig. 11. The sample deposited at 450°C exhibits a strong donor-acceptor pair (DA) emission, probably due to the Ga diffusion from GaAs substrates.

The optical properties of the ALE-ZnSe are very sensitive to the Zn beam intensity. The optimization of the deposition condition is in progress. Another factor that degrades the MOMBE-ALE ZnSe is impurities from gas sources. The number of source gas molecules impinging on the growing surface is about 10 times larger than that for the conventional MOMBE. The decomposition of metalorganic source is also critical to obtain high quality ALE-ZnSe. In the experiments, cracking temperature of DEZn was 750°C, which is not enough high for decomposition of DEZn. Actually, we observed the excitonic emission for the conventional MOMBE ZnSe films grown at higher substrate temperature, and the excitonic emission became strong with increasing substrate temperature for MOMBE-ALE.

We also made ALE growth of ZnS at substrate temperature of 200°C. The typical deposition rate of the conventional MOMBE ZnS is 1000-2000Å/h. The gas flow rate of DES was set to about 4 times larger than that for conventional MOMBE. We obtained epitaxial films with smooth surfaces, but the obtained deposition rate (0.2 monolayer/cycle) was much less than the ideal ALE growth. We speculate that the low deposition rate is due to low cracking efficiency of DES and due to much higher vapor pressure of S than that of Se.

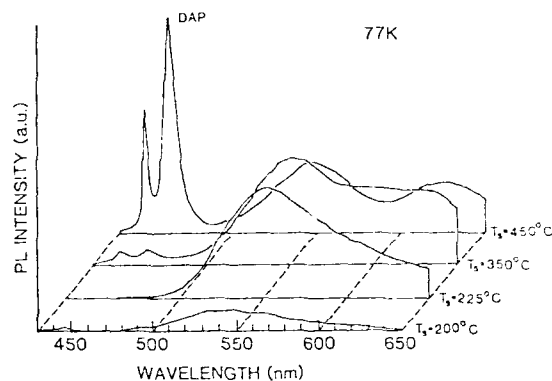


Fig. 11 PL spectra of MOMBE-ALE-ZnSe with various substrate temperature.

CONCLUSIONS

ZnSe and ZnTe films have been grown by MBE-ALE. ideal ALE growth was obtained at the substrate temperature range of 250-350°C. The PL spectra and surface morphology of these films are much superior to those of ZnSe films by the conventional MBE. For ZnTe, high intensity of Te beam is essential to obtain monolayer growth, but surface morphology degrades with hillocks, which may consist of Te precipitates. The PL measurements of the (ZnSe)₁-(ZnTe)₁ monolayer superlattice indicate the poor uniformity of Te monolayers.

We have also grown ZnSe by MOMBE-ALE. ideal ALE growth of ZnSe was obtained, but optimization of the growth condition is in progress to enhance the optical properties. For ZnS, low cracking efficiency of DES gives difficulty realizing monolayer growth.

REFERENCES

- [1] M.Kobayashi, N.Mino, H.Katagiri, R.Kimura, M.Konagai and K.Takahashi, *J.Appl.Phys.* **60** (1986) 773
- [2] M.Kobayashi, M.Konagai, K.Takahashi and K.Urabe, *J.Appl.Phys.* **61** (1987) 1015
- [3] M.Kobayashi, S.Dosho, A.Imai, R.Kimura, M.Konagai and K.Takahashi, *Appl.Phys.Lett.* **51** (1987) 1602
- [4] A.Imai, M.Kobayashi, S.Dosho, M.Konagai and K.Takahashi *J.Appl.Phys.* **64** (1988) 647
- [5] M.Konagai, S.Dosho, Y.Takemura, N.Teraguchi, R.Kimura and K.Takahashi in Growth and optical properties of wide-bandgap II-VI low-dimensional semiconductors, edited by T.C.McGill, C.M.Sotomayor Torres and W.Gebhardt (Plenum Publishing Co., 1989) p.219

- [6] S.Dosho, Y.Takemura, M.Konagai and K.Takahashi
J.Cryst.Growth, 95 (1989) 580
- [7] N.Teraguchi, Y.Takemura, R.Kimura, M.Konagai and K.Takahashi
J.Cryst.Growth, 93 (1988) 720
- [8] S.Dosho, Y.Takemura, M.Konagai and K.Takahashi
J.Appl.Phys. 66 (1989) 2597
- [9] T.Yao, M.Kato, J.J.Davis and H.Tanino
J.Cryst.Growth 86 (1988) 552

GROWTH OF LATTICE-MATCHED ZnSe-ZnS STRAINED-LAYER SUPERLATTICES
ONTO GaAs AS AN ALTERNATIVE TO ZnSSe ALLOYS

H. ONIYAMA, S. YAMAGA AND A. YOSHIKAWA

Department of Electrical and Electronics Engineering, Faculty of
Engineering, Chiba University, 1-33, Yayoi-cho, Chiba 260

ABSTRACT

This paper describes the results of the first attempt to reduce misfit dislocations in epilayers of a wide bandgap II-VI semiconductor on GaAs substrates by utilizing the ZnSe-ZnS strained-layer superlattice (SLS) structure. From a theoretical calculation, SLSs consisting of a 200Å-ZnSe and a 10Å-ZnS layer in one period can be grown as lattice-matched films to GaAs substrates. It has been found from the photoluminescence measurements and electron-beam-induced-current (EBIC) image observations that the generation of misfit dislocations can be markedly reduced, as expected.

Introduction

Zinc selenide is a semiconductor with a direct wide bandgap of 2.67eV at room temperature (R.T.) and is a promising material for the fabrication of blue-light emitting devices. However, several problems must be solved to realize such devices. One of these problems is that caused from the lattice mismatch between ZnSe and substrates. ZnSe epilayers are usually grown on GaAs substrates which have a little lattice mismatch of 0.26 % (at R.T.) with ZnSe, since "substrate-quality" ZnSe bulk crystals can not be obtained at present. Although the lattice mismatch is as small as 0.26% at R.T., it is well known that it causes misfit dislocations which degrade the quality of ZnSe epilayers. For instance, such dislocations create trapping centers and/or deep luminescence centers in ZnSe epilayers. [1] In order to control electrical and optical properties of ZnSe films, the problem arising from the lattice mismatch must be overcome. The way to solve this problem is to lattice-match epilayers to GaAs substrates. Many attempts to grow lattice-matched ZnSSe alloys onto GaAs substrates have been carried out [2], [3], [4].

We propose a new idea to overcome the problem caused from lattice mismatch, utilizing the ZnSe-ZnS superlattice structure as an alternative to ZnSSe alloys. In the case of ZnSe-ZnS superlattices (SLSs), the average lattice constant of the SLSs can be lattice-matched to GaAs when each layer thickness is

appropriate. Because ZnSe has a larger lattice constant and ZnS has a smaller one than does GaAs.

In the present study, lattice-matched ZnSe-ZnS SLs onto GaAs were grown by metalorganic molecular beam epitaxy (MOMBE). Photoluminescence measurements were performed to investigate the strain in the ZnSe layers of the SLs. Furthermore, electron-beam-induced-current (EBIC) image observations were carried out to observe such defects in both the SLs and ZnSe epilayers on GaAs. It has been found from these studies that misfit dislocations can be significantly reduced.

Experiment

ZnSe-ZnS SLs were grown by MOMBE using dimethylzinc (DMZn), H_2Se and H_2S as source materials [5], [6]. The source materials were introduced into the reactor without any carrier or buffer gases. The flow rates of H_2Se and H_2S were controlled by a mass flow controller (MFC), while that of DMZn was controlled by a variable leak valve and monitored by a mass flow meter. The cracking of the source gases was carried out at temperatures of about $900^\circ C$ for DMZn and about $700^\circ C$ for H_2Se . However, H_2S was not cracked in this study, since sulfur corrodes the Ta heater of cracking cells. ZnSe and ZnS layers were alternatively grown by using computer-controlled valves and a shutter placed in the path of gas beams.

ZnSe-ZnS SLs were characterized mainly by X-ray diffraction study and photoluminescence measurements at 18 K. For the EBIC observations, n^+ -GaAs were used as substrates. After the film growth, transparent Au dots were deposited on the surface of both SLs and ZnSe films to form Schottky contacts. The electron beam was injected through the electrodes into the samples at an accelerating voltage of 20 keV.

Results and Discussions

The average lattice constant of SLs (a_{av}^{SLs}), which is parallel to the interface, is calculated from a following equation [7]:

$$a_{av}^{SLs} = a_{ZnSe} [1 - f / (1 + d_{ZnSe} G_{ZnSe} / d_{ZnS} G_{ZnS})],$$

where a_{ZnSe} and a_{ZnS} are the unstrained lattice constants of ZnSe and ZnS, respectively, and f is the lattice mismatch between ZnSe and ZnS. G_{ZnSe} and G_{ZnS} are shear moduli of ZnSe and ZnS, respectively. As is found from this equation, the average lattice constant is determined by the ratio of

$d_{\text{ZnS}}/d_{\text{ZnSe}}$. Substituting the lattice constant of GaAs into the equation, it has been found that the average lattice constant of the SLSs matches to that of GaAs when the ratio becomes 0.05. However each layer thickness must be carefully determined, since the crystallinity of SLSs depends on each layer thickness. So, we have determined each layer thickness as 200 Å for ZnSe layers and 10 Å for ZnS layers, taking into account the critical thicknesses of ZnSe and ZnS films which are each grown on GaAs. When GaAs substrates are used, ZnSe layers in SLSs can be grown coherently onto GaAs up to 1500 Å, which is the critical thickness of the ZnSe films on GaAs. Unlike the case of ZnSe films on GaAs, ZnS critical thickness on GaAs is markedly small, since the lattice mismatch between ZnS and GaAs is as large as 4.4 %. The critical thickness of ZnS films on GaAs substrates can be roughly estimated as follows. When ZnSe is grown on ZnS films, the critical thickness of ZnSe layers is reported to be 13 Å by T. Yokogawa et al. [8]. It is thought natural from their results that the critical thickness of ZnS on ZnSe films must be almost the same, since the stiffness constants of ZnS are nearly equal to those of ZnSe. Moreover, when ZnS films are grown on GaAs substrates of which lattice constant is slightly smaller than that of ZnSe, the critical thickness of ZnS films on GaAs is thought to be a little smaller than 13 Å. Moreover, we have obtained results in which the crystallinity of SLSs becomes poor, when ZnS layers composing SLSs are above about 11 Å. It is thought reasonable that the value of 11 Å is the critical thickness of ZnS on GaAs. Hence, we have determined the thickness of ZnS layers in the SLSs as 10 Å. When the thickness of ZnS layers is 10 Å, that of ZnSe layers are 200 Å, which satisfies the condition where the each layer thickness becomes 0.05. (The structure of SLSs is described as (200,10) here after.)

Figure 1 shows an X-ray diffraction pattern of the (200,10)-SLS which has fifty periods. The period calculated from the result is about 205 Å, which is in fair accord with the value of 210 Å. Satellite peaks up to the 16th order are clearly observed. Moreover, the peaks for $\text{CuK}\alpha_1$ and $\text{K}\alpha_2$ are separated. It has been found from these results that high quality SLSs with extremely flat interface can be grown. It should be noted that, although $a_{\text{av}}^{\text{SLS}}$ is lattice-matched to GaAs as shown later, the 0th peak is observed in a slight lower-angle position compared to the (400) GaAs diffraction peak. This indicates that the average lattice constant normal to the inter-

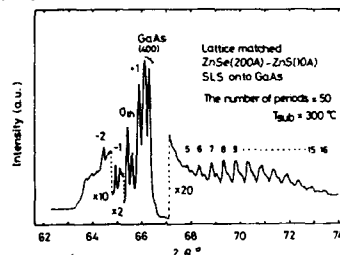


Fig. 1.
X-ray diffraction patterns

face, i.e., $a_{\text{SLS}}^{\text{SLS}}$ is larger than that of GaAs, due to the Poisson effect, where $a_{\text{SLS}}^{\text{SLS}} = (N_{\text{ZnSe}} a_{\text{ZnSe}}^{\text{ZnSe}} + N_{\text{ZnS}} a_{\text{ZnS}}^{\text{ZnS}}) / (N_{\text{ZnSe}} + N_{\text{ZnS}})$. $a_{\text{ZnSe}}^{\text{ZnSe}}$ and $a_{\text{ZnS}}^{\text{ZnS}}$ are lattice constants of ZnSe and ZnS which are normal to the interface, respectively, and N_{ZnSe} and N_{ZnS} are the number of ZnSe and ZnS lattices in one period, respectively.

Figure 2 shows the typical photoluminescence spectra of the SLS grown on GaAs. The total thickness of the SLS is $0.51 \mu\text{m}$. The full width at half maximum of the band edge emission is as narrow as about 9 meV. Moreover, the intensity of deep level emissions for the SLSs is extremely weak. These results indicate that the high quality photoluminescence spectra can be obtained. In this SLS, the carrier confinement is thought to be of lesser effect, since the ZnS barrier layers are much thinner than ZnSe well layers. Hence, it can be thought that the photoluminescent emission does not originate from the recombination of carriers between quantum levels, but emanates solely from the ZnSe layers in the SLS. Furthermore, the reflectance spectrum shown in the inset of figure 2 indicates that the band edge emission was due to recombination of free excitons in ZnSe layers which is strained with the two-dimensional in-plane stress. The excitonic peak was shifted to be shorter in the position of 4416 Å than that of bulk ZnSe crystals. This value is in almost agreement with that of coherently grown ZnSe layers on GaAs, 4417.6 Å [9]. This result suggests that the ZnS layers which are composed of SLS are strained to lattice-match with GaAs.

In order to confirm further whether the SLSs are lattice-matched with GaAs or not, the dependence of excitonic peak position in photoluminescence on the total film thickness has been investigated. The results are shown in figures 3(a) for the SLS and 3(b) for ZnSe films on GaAs. In the case of ZnSe films, the peak position shifts toward the longer-wavelength side as the film thickness increases. It is well known that this is caused by lattice accommodation [10]. In contrast to the case of ZnSe film, no peak shift is observed in case of the SLS on GaAs. This suggests that the

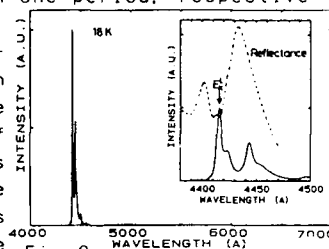


Fig. 2.

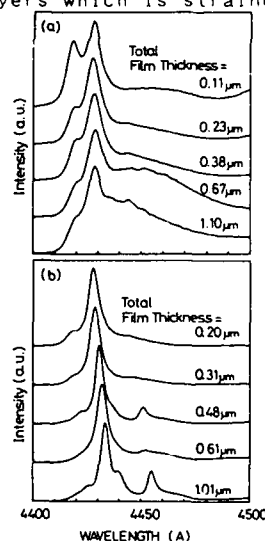


Fig. 3. The total thickness dependence of the excitonic peak position (a) lattice-matched SLS (b) ZnSe film on GaAs.

accommodation process does not exist in the SLs and the SLs are lattice-matched with GaAs substrates. These results can be translated as follows. When only ZnSe films are grown on GaAs, the films are accommodated through the generation of misfit dislocations. However, when thin ZnS layers are incorporated periodically into ZnSe layers, ZnSe films can be uniformly strained to lattice-match with GaAs without forming misfit dislocations. In other words, the SLs can be regarded as the ZnSe films which are grown coherently onto GaAs even up to $1\ \mu\text{m}$ by incorporating periodic thin ZnS layers. Accordingly, the generation of misfit dislocation is thought to be prevented in the SLs.

Finally, electron beam induced current (EBIC) image observations have been performed in order to confirm a reduction of misfit dislocations in the layer.

Figures 4(a) and 4(b) show the EBIC images for a ZnSe film on GaAs and a lattice-matched SLS.

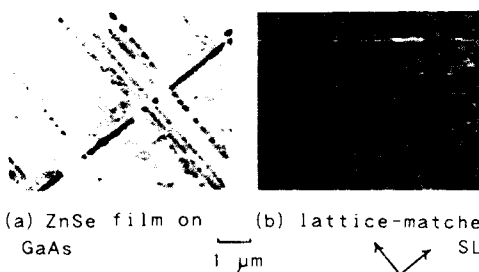


Fig. 4. EBIC images for the SLs, respectively. Each sample is as thin as about 2500 Å. In the ZnSe film, cross-hatched patterns which run along the $\langle 110 \rangle$ direction were observed as shown in figure 4(a). These patterns are the dislocations which can be caused by misfit dislocations[11], suggesting that misfit dislocations are actually generated in ZnSe films on GaAs. On the other hand, these patterns cannot be observed in the case of the SLs. Hence, it has been found from the result that the generation of misfit dislocations is actually reduced in the SLs.

Conclusion

SLs consisting of a 200Å-ZnSe and a 10Å-ZnS layer in one period, which were theoretically estimated to be lattice matched to GaAs, have been grown onto GaAs substrates to eliminate the problem arising from lattice mismatch. It has been found from the total film thickness dependence of the photoluminescent peak position that the SLs can be grown coherently on GaAs. Furthermore, it has been shown from electron beam induced current observations that the generation of misfit dislocations can be remarkably reduced.

Acknowledgement

This work was partly supported by a Grants-in-Aid for Scientific Research, and Scientific Research for Priority Areas, from The Ministry of Education, Science and Culture. The authors would like to express their appreciation to Dowa Mining Co., Ltd. for the supply of GaAs substrates.

References

1. Sz. Fujita, K. Terada, T. Skamoto and Sg. Fujita, J. Cryst. Growth 94, 102 (1989)
2. H. Mitsuhashi, J. Mitsuishi and H. Kukimoto, Jpn. J. Appl. Phys., 24, L864 (1985)
3. N. Matsumura, K. Ishikawa, J. Saraie and Y. Yodogawa, J. Cryst. Growth, 72, 41 (1985)
4. S. Fujita, Y. Matsuda and A. Sasaki, J. Cryst. Growth, 68, 231 (1984)
5. A. Yoshikawa, H. Oniyama, H. Yasuda, S. Yamaga and H. Kasai, J. Cryst. Growth 94, 69 (1988)
6. H. Oniyama, S. Yamaga, A. Yoshikawa and H. Kasai, J. Cryst. Growth 93, 679 (1988)
7. J. W. Matthews and A. E. Blakeslee, J. Cryst. Growth 32, 265 (1975)
8. T. Yokogawa, H. Sato and M. Ogura, Appl. Phys. Lett., 52, 1678 (1988)
9. T. Matsumoto, T. Iijima and T. Ishida, Jpn. J. Appl. Phys., 27, L892 (1988)
10. H. Mitsuhashi, I. Mitsuishi, M. Mizuta and H. Kukimoto, Jpn. J. Appl. Phys., 24, L578 (1985)
11. M. Shinohara, I. Ito, K. Yamada and Y. Imamura, Jpn. J. Appl. Phys., 24, L818 (1985)

U. S. POLYCRYSTALLINE THIN FILM SOLAR CELLS PROGRAM

HARIN S. ULLAL, KENNETH ZWEIBEL, AND RICHARD L. MITCHELL
Solar Energy Research Institute, 1617 Cole Boulevard, Golden, CO 80401, U.S.A.

ABSTRACT

The Polycrystalline Thin Film Solar Cells Program, part of the United States National Photovoltaic Program, performs R&D on copper indium diselenide and cadmium telluride thin films. The objective of the Program is to support research to develop cells and modules that meet the U.S. Department of Energy's long-term goals by achieving high efficiencies (15% - 20%), low-cost (\$50/m²), and long-time reliability (30 years). The importance of work in this area is due to the fact that the polycrystalline thin-film CuInSe₂ and CdTe solar cells and modules have made rapid advances. They have become the leading thin films for PV in terms of efficiency and stability. The U.S. Department of Energy has increased its funding through an initiative through the Solar Energy Research Institute in CuInSe₂ and CdTe with subcontracts to start in Spring 1990.

INTRODUCTION

The Polycrystalline Thin Film Solar Cells Program is part of the United States National Photovoltaic Program. Other areas of research and development included in the national program are the fundamental and supporting research, flat plate thin-films, flat plate crystalline silicon, and concentrator cells [1].

Table I: Polycrystalline Thin Films Program Participants

Research Organization	Objective
ARCO Solar	High efficiency CuInSe ₂ , 900 to 3900 cm ² modules
Boeing Aerospace & Electronics	Evaporated CuGaInSe ₂ cells, 100 cm ² submodules
Institute of Energy Conversion	Evaporated and selenized CuInSe ₂ ; CuTe cells; device modeling
International Solar Electric Technology	E-beam/sputtering Cu,In layers and selenization; 50 cm ² submodules
University of Illinois	Sputtered/evaporated CuInSe ₂ cells
University of Arkansas	Laser-processed Cu/In/Se films made by electroplating or sputtering
California Institute of Technology	Contact investigation of CuInSe ₂ /Mo interface
Solar Energy Research Institute	Growth, characterization and device fabrication of CuInSe ₂
Colorado State University	Characterization and modeling of CdTe and CuInSe ₂ cells
AMETEK	Electrodeposition of n-i-p CdS/CdTe/ZnTe cells and 100 cm ² submodules
Photon Energy	Spraying of 900 to 3900 cm ² CdTe modules
University of South Florida	Close space sublimation of CdTe cells; MOCVD of HgZnTe for n-p cells
Georgia Institute of Technology	MOCVD of CdTe and Cd _{0.9} Zn _{0.1} Te cells

The objective of the Polycrystalline Thin Film Solar Cells Program is to support research to develop cells and modules that meet the U.S. Department of Energy's long-term goals by achieving high efficiencies (15% - 20%), low-cost (\$50/m²), and long-time reliability (30 years). This paper covers the various research aspects of the subcontracts program in the polycrystalline thin film area. Table 1 summarizes the various research activities with the corresponding objectives of each of the subcontracts. The two main materials of interest are copper indium diselenide (CuInSe₂, CIS) and cadmium telluride (CdTe). Specific research areas include fundamentals, modeling, characterization, measurements, device design, solar cell fabrication, module design and development, module processing, and stability of both CuInSe₂ and CdTe [2]. Figure 1 shows the progress of the polycrystalline thin film module technology in the past few years.

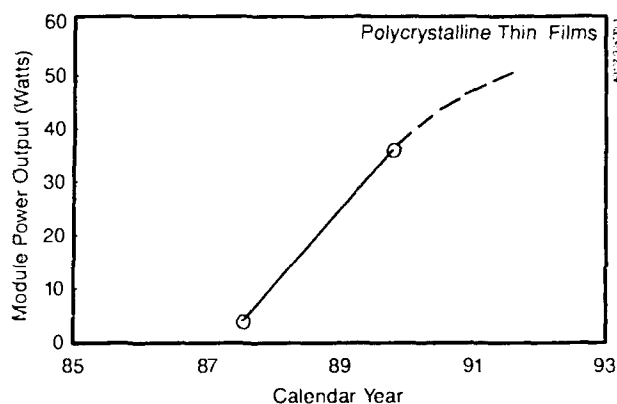


Figure 1 Progress of polycrystalline thin film module power output versus calendar year

COPPER INDIUM DISELENIDE

During the past decade, CuInSe₂ has made significant technical progress and is now considered the leading candidate thin-film photovoltaic material in terms of efficiency and long-term reliability of these devices [3].

Wagner and co-workers at Bell Labs first fabricated 12% efficient CuInSe₂ single crystal cells in 1974 [4]. Single crystals are expensive for practical applications. Nonetheless they demonstrated proof-of-concept for future research in thin-film CuInSe₂ devices for lower cost cells. Grindle et al. at the University of Maine were able to make 5% efficient cells [5] by thermally evaporating CuInSe₂ on low-cost substrates. This was followed by the successful work done by Mickelsen and Chen at Boeing Aerospace which was supported by U.S. DOE funding through the Solar Energy Research Institute (SERI). Boeing was able to make 10% efficient CuInSe₂ cells by coevaporation by 1982 [6].

Several groups followed the pioneering work of Boeing. Among those who initiated research programs were ARCO Solar, Institute of Energy Conversion (University of Delaware), and the Solar Energy Research Institute. All these groups were able to quickly reproduce the Boeing results in solar cell efficiency by making cells in excess of 10% [7,8]. Innovative device design (Fig. 2) first proposed by Choudary et al. [9] and reduced to practice by Potter et al. enhanced the blue response of these CuInSe₂ devices and improved the cell efficiency to 12.5% [10]. Further additions of small quantities of Ga (<10%) improved the reported cell efficiency to 14.1% (active area) for 3.5 cm² area

device. Boeing also improved the cell performance to 12.9% (active area) for a 1 cm^2 device by the addition of 27% Ga in the CuGaInSe_2 cells [11]. The V_{OC} of this device was 555 mV, and was considered a significant improvement.

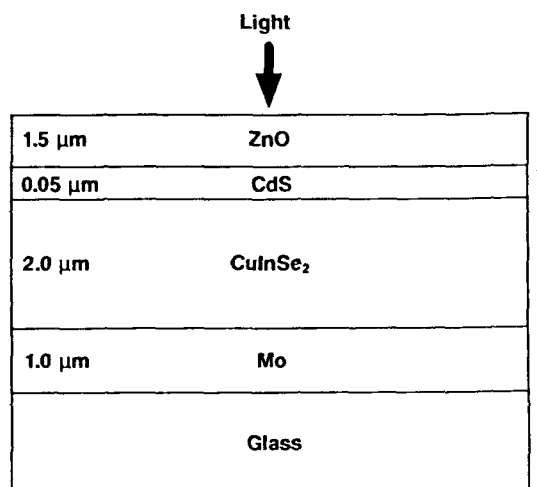


Figure 2 Device structure of a Glass/Mo/CuInSe₂/CdS/ZnO polycrystalline thin film solar cell

International Solar Electric Technology (ISET), a spin-off from ARCO Solar, was also successful in making 10.9% (active area) devices by a low-cost two-stage process [12]. Mo coated on glass is used as a substrate, on which Cu and then In are deposited by E-beam. The Cu-In sandwich is thermally reacted with H_2Se gas, forming high quality CuInSe_2 . To complete the cell fabrication, a thin layer of dip-coated CdS is deposited on the CuInSe_2 to form the heterojunction. Using a similar approach, the Institute of Energy Conversion has demonstrated J_{SC} of 42 mA/cm^2 [13].

During the 1980s, ARCO Solar developed proprietary processes for manufacturing CuInSe_2 modules using a potentially low-cost approach [14,15]. This success in the manufacturability was a significant step for the CuInSe_2 technology and subsequently led to ARCO Solar's scale-up of large-area modules.

Ermer and co-workers reported on the major advances of the performance of large-area CuInSe_2 modules [16]. They reported achieving an 11.1% efficient 1000 cm^2 module, the most efficient at its size among the various thin films. For even larger areas of about 4000 cm^2 , efficiency in excess of 9% with a power output of 35.8 watts (Fig. 3) for unencapsulated modules was also reported. These modules have now been tested at SERI under natural sunlight for 240 days under both load and open-circuit conditions and have been found to be very stable [17].

CADMIUM TELLURIDE

Cadmium telluride (CdTe), normally referred to as the "dark horse" of thin film solar cells, has shown improved performance in the past few years. Based on a bandgap of 1.45 eV, which is an optimum match with the solar spectrum, practical CdTe devices could potentially achieve efficiency up to 18%. Theoretical efficiencies are as high as 27.5% [18%].

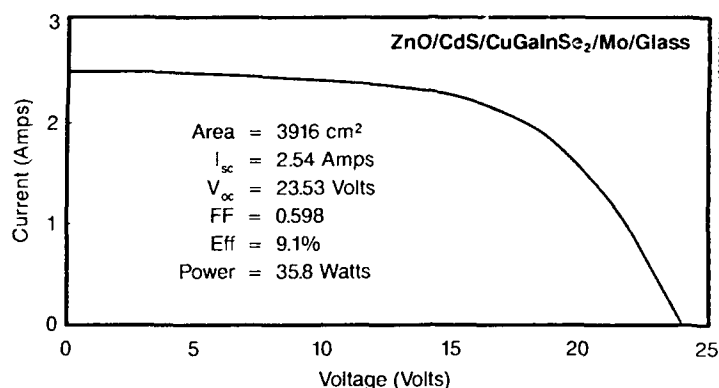


Figure 3 Light I-V characteristics of a large-area 3916 cm² polycrystalline thin film CuInSe₂ module

One of the key problems encountered in fabricating thin-film CdTe devices is its contact stability. To circumvent this problem, a research group at Ametek has developed a novel n-i-p cell design, which is shown in Fig.4. The undoped CdTe acts as an intrinsic layer sandwiched between the n-type CdS and p-type ZnTe layers that induce a drift field across the CdTe. Figure 5 shows the Auger depth profile for this cell structure. One of the key processing steps is a heat-treatment at 400°C for about 20 minutes. This step causes significant change in the morphology [19,20] and is the key to high process yields. During the heat treatment, the polycrystalline grains at the CdS-CdTe interface are believed to coalesce or fuse, thus greatly reducing the density of grain boundary states. Recrystallization occurs over the entire thickness of the CdTe film. Using this cell design, Ametek has fabricated 11% cells by electrodeposition [21]. Ametek has also tested their cells and submodules and have reported stability of their devices for 3000 hours.

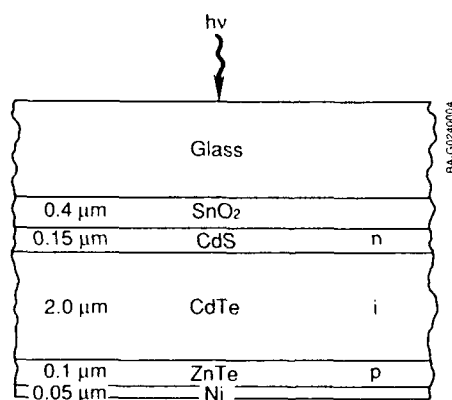


Figure 4 Device structure of a n-i-p n-CdS/i-CdTe/p-ZnTe polycrystalline thin film CdTe solar cell

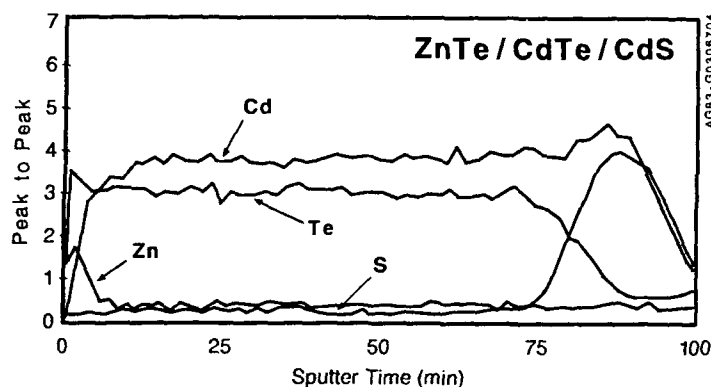


Figure 5 Auger depth profile of a n-i-p n-CdS/i-CdTe/p-ZnTe polycrystalline thin film solar cell

Photon Energy is another successful CdTe group. Their primary focus of research is to fabricate thin film CdTe solar power modules by a potentially low-cost spraying method. To date they have achieved 12.3% efficient small area cells, and 7.3% efficient square-foot module [22]. They have also made prototype four-square-foot CdTe modules for production.

SERI IN HOUSE RESEARCH

Active investigation is underway at the Solar Energy Research Institute to study the materials growth, characterization and device fabrication of thin film CuInSe_2 and related alloy materials. SERI makes state-of-the-art CuInSe_2 devices [23]. Also, extensive support is given to the photovoltaic industry in terms of material characterization such as Auger Electron Spectroscopy, Electron Beam Induced Current, Electron Spectroscopy for Chemical Analysis, Photoluminescence, Scanning Electron Microscopy, Secondary Ion Mass Spectroscopy, Spectroscopic Scanning Tunneling Microscopy, Wavelength Dispersive Spectroscopy, defect chemistry, chemical and heat treatments, stability testing, etc.

CONCLUSIONS

Polycrystalline thin-film CuInSe_2 and CdTe solar cells and modules have made rapid advances and are now the leading thin films for PV in terms of efficiency and stability. They have attained the highest cell efficiencies (14.1% for CuInSe_2 and 12.3% for CdTe), the highest module efficiencies (11.1% for CuInSe_2 and 7.3% for CdTe on a square-foot; 9.1% for 4 square feet for CuInSe_2); the best stabilities (CuInSe_2 240 days without degradation), are made by the lowest cost processes (spraying, electrodeposition, sputtering and selenization). The U.S. Department of Energy has increased its funding through an initiative through the Solar Energy Research Institute in CuInSe_2 and CdTe with subcontracts to start in Spring 1990. The level of federal support for CuInSe_2 and CdTe is doubling to about \$2.4M for each material. Both CuInSe_2 and CdTe are now moving out of the lab and into demonstration projects through the Photovoltaics for Utility Sale Applications (PVUSA) proposals. 20 kW systems of CuInSe_2 supplied by ARCO Solar and 20 KW of CdTe supplied by Photon Energy will be installed in Davis, California, next year for field testing and evaluation.

ACKNOWLEDGMENTS

The authors would like to thank Amy Swartzlander for doing the Auger depth profile analysis. This work was supported by the U.S. Department of Energy under contract # DE-AC02-83CH10093.

REFERENCES

1. Five Year Research Plan, 1987-1991, National Photovoltaic Program, U. S. Department of Energy, DOE/CH10093-7, May 1987
2. H.S. Ullal (Ed.), Proceedings of the Polycrystalline Thin Film Program Meeting, Lakewood, CO, August 16-17, 1989; SERI/CP-211-3550
3. K. Zweibel and H.S. Ullal, in Proceedings of the 24th Intersociety Energy Conversion Engineering Conference, Washington, D.C., August 6-11, 1989, pp. 765
4. S. Wagner, J.L. Shay, P. Migliorato, and H.M. Kasper, Appl. Phys. Letts., **25**, 434 (1974)
5. S.P. Grindle, A.H. Clark, S. Rezaie-Serej, E. Falconer, J. McNeily, L.L. Kazmerski, J. Appl. Phys. **51**, 5464 (1980)
6. R.A. Mickelsen and W.S. Chen, in Proceedings of the 16th IEEE PV Specialists Conference, San Diego, CA, September 27-30, 1982, pp. 781
7. J.D. Meakin, SPIE Photovoltaics, **543**, 1985, pp. 108
8. K. Zweibel and T. Surek, in Proceedings of the 20th Intersociety Energy Conversion Engineering Conference, Miami Beach, FL, August 18-23, 1985, pp. 3398
9. U.V. Choudary, Y.H. Shing, R.R. Potter, J.H. Ermer, and V.K. Kapur, U.S. Patent # 4,611,091, September 9, 1986
10. R.R. Potter, C. Eberspacher, and L.B. Fabick, in Proceedings of the 18th IEEE PV Specialists Conference, Las Vegas, NV, October 21-25, 1985, pp. 1659
11. W.E. Devaney, W.S. Chen, J.M. Stewart, and R.A. Mickelsen, IEEE Trans. on Electron Devices, February 1990, to be published
12. B.M. Basol, V.K. Kapur, and R.C. Kullberg, Solar Cells, to be published
13. R. W. Birkmire, B.E. McCandless, W.N. Shafarman, and R.D. Varrin Jr., in Proceedings of the 9th E.C. Photovoltaic Solar Energy Conference, Freiburg, F.R. Germany, September 25-29, 1989, pp. 134
14. R.B. Love and U.V. Choudary, U.S. Patent # 4,465,575, August 14, 1984
15. J.H. Ermer and R.B. Love, U.S. Patent # 4,798,660, January 17, 1989
16. J. Ermer, C. Fredric, K. Pauls, D. Pier, K. Mitchell, and C. Eberspacher, in Proceedings of the 4th International Photovoltaic Science and Engineering Conference, Sydney, Australia, February 14-17, 1989, pp. 475
17. L. Mrig and S. Rummel, in Outdoor Stability Performance of CIS and CdTe Photovoltaic Modules at SERI, edited by H.S. Ullal, Proceedings of the Polycrystalline Thin Film Program Meeting, Lakewood, CO, August 16-17, 1989, SERI/CP-211-3550
18. J.R. Sites, in Proceedings of the 20th IEEE PV Specialists Conference, Las Vegas, September 26-30, 1988, pp. 1604
19. H.S. Ullal, Electronic Structure of Electrodeposited Thin Film CdTe Solar Cells, May 1988, SERI/TP-211-3361
20. K. Zweibel, H.S. Ullal, and R.L. Mitchell, in Proceedings of the 20th IEEE PV Specialists Conference, Las Vegas, NV, September 26-30, 1988, pp. 1469
21. P.V. Meyers and C.H. Liu, in Proceedings of the 8th E.C. Photovoltaic Solar Energy Conference, Florence, Italy, May 9-13, 1988, pp. 1588
22. S.P. Albright, B. Ackerman, and J.F. Jordan, in IEEE Trans. on Electron Devices, February 1990, to be published
23. R. Noufi and J. Tuttle, in Proceedings of the 9th E.C. Photovoltaic Solar Energy Conference, Freiburg, F.R. Germany, September 25-29, 1989, pp. 283

EXCITONIC PROPERTIES OF ZnSe-ZnS STRAINED-LAYER SUPERLATTICES AND A FIBONACCI SEQUENCE

Tsunemasa TAGUCHI and Yoichi YAMADA

Department of Electrical Engineering, Faculty of Engineering, Osaka University, Suita, Osaka 565, Japan

ABSTRACT

Excitonic properties of ZnSe-ZnS strained-layer quantum wells (SLQWs) with type I band lineups are reviewed on the basis of our recent results of temperature- and strain-dependent photoluminescence and absorption spectra. In order to estimate the conduction and valence band offsets as a function of ZnSe well thickness, we have modified the "model-solid" theory in which the valence bands (heavy-hole band in ZnSe and light-hole band in ZnS) are relatively moved with strains. Temperature and high excitation dependent studies of the $n=1$ heavy-hole excitons suggest a localization of excitons and reveals the important evidence on scatterings of excitons with acoustic and optical phonons. The thermal quenching of the exciton emission is caused by thermal dissociation of quasi-two-dimensional excitons through electrons and holes, from which the activation energy for this dissociation is 4 times larger than $E_{b,30}$ (a binding energy of bulk exciton) of ZnSe. A new superlattice structure with a quasiperiodic crystal which is derived from a finite Fibonacci sequence, has been fabricated by a low-pressure MOCVD method and its photoluminescence properties are for the first time introduced.

1. INTRODUCTION

The most exciting optoelectronics applications for wide bandgap II-VI materials are semiconductor injection emitters and lasers at wavelengths throughout the visible spectrum [1]. These possibilities are now amplified by the rapid progress in the growth of II-VI single and multiple-quantum well (MQW) structures, which can confine electrons and holes in a two-dimensional well, fabricated by MBE [2] and MOCVD [3]. Despite the small amount of effort devoted to these structures in comparison with their equivalents in III-V materials, it has been very recently reported the possibilities of optically-pumped blue laser [4], quantum confined Stark effect [3], waveguide [5] and second-harmonic generator (SHG) [6] from ZnSe-ZnS(Se) and CdZnS-ZnS [7] strained-layer superlattices (SLSs).

In semiconductor strained-layer superlattices, however, the lattice mismatch can be entirely accommodated by elastic layer strain rather than misfit dislocations. The flexibility in the choice of widegap II-VI SLS materials from green (CdS) to violet (ZnS) in the spectral regions, and the interesting effects of nonlinear properties allow SLS materials to exhibit a wide range of photonics devices which are advantageous for SHG and third-harmonic generator (THG) devices [8].

ZnSe-ZnS SLS, exhibiting a type I heterojunction structure, has been most extensively studied using low-temperature excitonic luminescence and absorption measurements to observe the valence band feature of the ZnSe well [3,9]. The lattice mismatch between cubic ZnSe and ZnS is about 4.5 % at RT, so that a critical thickness for each layer along $\langle 100 \rangle$ growth direction, beyond which the layer is expected to deform plastically, is theoretically calculated to be about 100 Å [10]. Therefore, the band structure in the SLS consisting of ZnSe and ZnS appears to be due to reduction in symmetry (D_{2d}) along the axis of the $\langle 100 \rangle$ growth of the quantum well. These properties reflect changes of the band structure, so that excitons are more sensitive to strains.

We have demonstrated that the ZnSe-ZnS superlattice is one of the most

fruitful example for understanding fundamental excitonic properties in the II-VI wide bandgap SLSs [9]. Namely, quasi two-dimensional (2D) excitons are characterized by a large exciton binding energy and large oscillator strength in addition to a strong exciton-LO phonon coupling constant. Theoretical studies of excitons in the II-VI SLSs have recently been started in order to understand a correlation between the 1s exciton binding energy and band offsets for electrons and holes [11].

Since 1987, we have succeeded in growing high-quality ZnSe-ZnS SLSs with MQW showing an excitonic linewidth narrower than the previous one [9] as a result of the optimization of the growth conditions in the low-pressure MOCVD method [12]. We have already pointed out that the exciton localization is the dominant cause for the linewidth broadening. It is therefore desirable to control the interface fluctuation within one monolayer thickness to know the intrinsic excitonic properties.

This paper reviews our recent outstanding results of excitonic properties of ZnSe-ZnS SLSs grown on (100) GaAs and ZnS substrates using the low-pressure MOCVD method. We show the temperature dependence of absorption spectra of the SLS on ZnS substrate without removal of its substrate, and that a large Stokes shift is caused by exciton localization. Our conventional MOCVD system allows to fabricate a new superlattice structure with a finite Fibonacci sequence consisting of ZnSe and ZnS thin layers.

2. STRAINED-LAYER SUPERLATTICE BY LOW-PRESSURE MOCVD

2.1. Conventional sequence

The MOCVD apparatus consists of a main reaction chamber and a sample exchange supplemental chamber with a transfer tube as shown in Fig.1. Special feature is that we employ a halogen lamp capable of heating the substrate up to 600 °C, by infrared (IR) radiation. Two chambers are constructed by all Al materials and each inner wall is coated with TiN films to avoid accidental impurity contamination. Our MOCVD process was described in detail in [12]. Depending upon the times to open the H_2Se and H_2S MFC valves, t_{Se} and t_{S} , various ZnSe and ZnS thickness can be deposited on various substrates such as GaAs, ZnSe and ZnS with [3] or without [9] an appropriate buffer layer. Prior to SLS growth, the substrate was first cleaned by heating at 550°C for 5 to 30 min in Pd-diffused H_2 gas atmosphere after chemical etching. A growth temperature was 350 °C. The growth rate depends upon the operation pressure in the reaction chamber; for example this is estimated to be 0.2 $\mu m/h$ at a constant pressure of 0.3 Torr. We can also control the interval of t , which is time to evacuate residual gases in the chamber in order to improve the

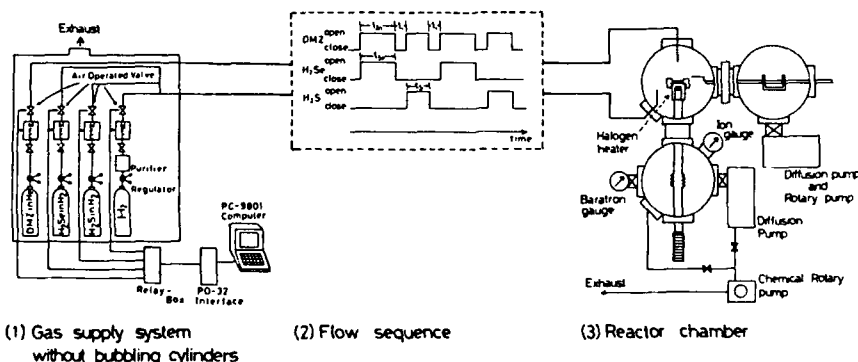


Fig.1. Low-pressure MOCVD apparatus with a load-lock system for growing SLSs.

quality of the SLS films. The thickness of the well and barrier was measured by transmission electron microscopy and also by X-ray diffraction satellite peak positions.

2.2. Fibonacci sequence

Quasi periodic semiconductor superlattices with a Fibonacci sequence [13] were fabricated by ZnSe ($A=25 \text{ \AA}$) and ZnS ($B=35 \text{ \AA}$) films. Fig.2 shows the schematical representation of arrangement of constant ZnSe and ZnS layers in a Fibonacci sequence. The infinite sequence F_1, F_2, \dots is defined recursively by $F_n = F_{n-1} + F_{n-2}$, where F_n is the n -th Fibonacci number. A finite Fibonacci superlattice with the ratio between A and AA is given by the Golden mean $\tau = (1+\sqrt{5})/2$.

Fibonacci superlattice

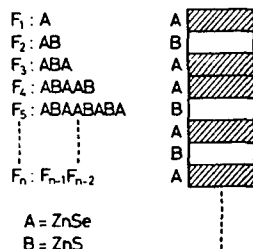


Fig.2. Fibonacci sequence with the widths of $A(\text{ZnSe})=25 \text{ \AA}$ and $B(\text{ZnS})=35 \text{ \AA}$.

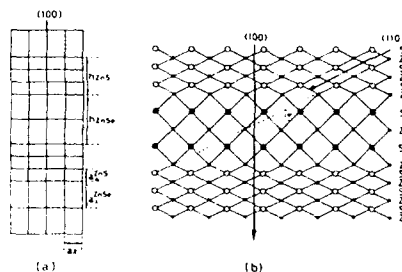


Fig.3. Coherently grown lattice (a) and atom row (b) along $\langle 100 \rangle$ and $\langle 110 \rangle$ directions.

3. INTERFACE OF ZnSe-ZnS SLS

A typical SLS structure is shown schematically in Fig.3(a). The thin SLS layers are alternatively in compression (ZnSe) and tension (ZnS) so that the in-plane lattice constants (a_{11}) of the individual strained-layers are equal. All the lattice mismatch is accommodated by layer strains without the generation of misfit dislocations below the critical thickness about 100 \AA as indicated by 2 MeV TEM plan-view observation [10]. The atomic bonding arrangement is shown in Fig.3(b). A channelling expected along $\langle 100 \rangle$ and $\langle 110 \rangle$ axis indicates that the $\langle 110 \rangle$ channelling shows much higher dechannelling yields than the $\langle 100 \rangle$ case [14]. This suggests that ZnSe can grow in a three-dimensional island growth mode rather than in a layer-by-layer growth mode on ZnS [15].

4. EXCITON PROPERTIES

4.1. Band structure under strains

4.1.1. Uniaxial stress of free exciton of ZnSe

Reflectance spectra of free exciton in bulk ZnSe were measured at 4.2 K under $\langle 100 \rangle$ uniaxial stress with σ and π polarization light. So far, stress-induced change and splitting of exciton line have been observed by Langer et al. [16] under $P \parallel \langle 11\bar{2} \rangle$ and $\langle 111 \rangle$. Under the $\langle 100 \rangle$ uniaxial strain, the crystal symmetry T_d changes to D_{2d} symmetry and as a result the

degeneracy of the valence band is removed. The effect for a uniaxial stress in the $\langle 100 \rangle$ direction is shown in Fig.4. The Γ_8 exciton splits into two components; one E \perp P component shifts to higher energies with increasing stress and the other polarized E \perp P whose energy shifts to lower energies with increasing stress. The E \parallel P component shifts slightly to lower energies with stress.

Fig.5 shows the energy positions of three components and the splitting under σ and π polarizations. These splittings are similar to that predicted by Bailly [17] for the $\langle 100 \rangle$ compressive stress. By extrapolating the σ component to zero splitting, one can obtain the exchange splitting between the Γ_8 and Γ_4 excitons which is nearly zero. Using the $\langle 100 \rangle$ strain Hamiltonian, we can estimate the bandgap deformation constant a and shear deformation potential constant b to be -5.23 and -1.2 eV, respectively.

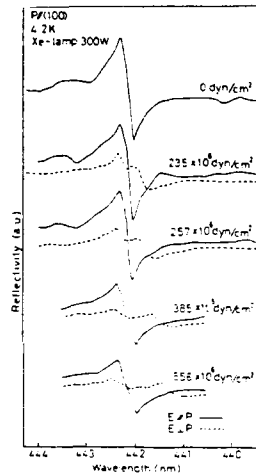


Fig.4. Exciton reflectance spectra at 4.2 K under E \parallel P(π) and E \perp P(σ) polarization.

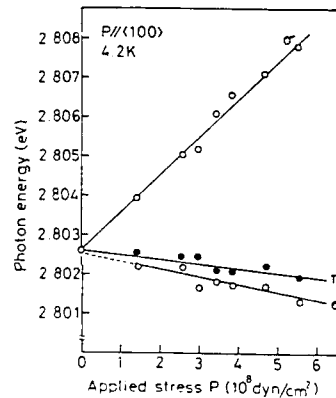


Fig.5. Energy splitting of exciton under σ and π polarization.

4.1.2. Fundamental properties of excitons in SLS and strain

Excitons play a dominant role in determining the optical properties of semiconductor quantum wells [18]. Optical measurements including photoluminescence and absorption are widely adopted for revealing electronic states of these structures. Excitonic behaviour of II-VI superlattices and quantum wells is unique when compared to those of III-V materials because of a large exciton binding energy, large oscillator strength and strong exciton-phonon interaction. In particular, until now, one cannot obtain accurate interpretation of excitons and the energy levels from optical absorption spectra because we always used GaAs substrates which cannot permit to pass visible light at wavelengths from 600 to 400 nm.

In ZnSe-ZnS SLS, ZnSe well layer is considerably under $\langle 100 \rangle$ compressive strain and consequently the valence band consists of heavy-hole $|3/2, 3/2\rangle$ and light-hole $|3/2, 1/2\rangle$ bands. Excitons are presumably created by a Coulombic force [19] between $n=1$ electrons ($E_{n=1}^e$) and $n=1$ heavy-holes or light-holes ($E_{n=1}^h$) in the quantum well. Exciton binding energy E_b^{1s} is estimated from the principal absorption peak position by $E(\hbar\omega) = E_g + E_{n=1}^e + E_{n=1}^h - E_b^{1s}$, where E_g is the apparent bandgap of well layer.

The effective transition strength for the two-dimensional (2D) exciton with $k=0$ is given by [20],

$$F_{2D, 1s} = f_0 E_B^{-1/2} (\mu/M) (r(T)/\Delta(T)) \quad (1)$$

where f_0 is the transition matrix element ($= 2/L^2 a_B$, a_B is a Bohr radius of exciton and L is a well width), $M = m_e^* + m_h^*$, $\mu^{-1} = (m_e^* + m_h^*)^{-1}$, $E_B^{-1/2}$ is the 2D exciton binding energy ($= 2m_e^*/\epsilon^2 \hbar \equiv 4E_{B, 3D}$) and $\Delta(T)$ is the temperature dependent homogeneous linewidth of the exciton.

We assume that the fraction of excitons $r(T)$ with the spectral width $\Delta(T)$ can contribute to recombination, so the fraction $r(T)$ is given by

$$r(T) = 1 - \exp\{-\Delta(T)/kT\} \quad (2)$$

Due to large exciton-LO phonon coupling effect, $\Delta(T)$ is always larger than kT in II-VI SLS. The exciton binding energy $E_B^{-1/2}$ of the 2D case for the 1s ground state has been theoretically treated [19]. Recently, Matsuura [21] has calculated the 1s binding energy of excitons in ZnSe well as a function of well thickness taking into account polaron effect. It has been found that the electron-hole interaction is screened by the high frequency dielectric constant $\epsilon = \epsilon_\infty$. From eqs. (1) and (2), the decay of luminescence is expressed by

$$\tau_{ex, 2D} \propto (E_B^{-1/2})^{-1} (\Delta(T)/r(T)) \quad (3)$$

and since $\Delta(T) \gg kT$ in the present ZnSe-ZnS SLS,

$$\tau_{ex, 2D} \propto (E_B^{-1/2})^{-1} \Delta(T) \quad (3)$$

For instance, in ZnSe (20 Å) and ZnS (50 Å) SLS, $\tau_{ex, 2D}$ was an order of psec at 4.2 K [22].

As already mentioned above, the tetragonal distortion (D_{2d}) is known to shift energy levels and to split band degeneracies. The ZnSe and ZnS layers are subject to a biaxial compressive and tensile strains, respectively, along the $\langle 100 \rangle$ and $\langle 010 \rangle$ directions in the (100) plane. This effect breaks the symmetry of the zincblende structure and splits the degeneracy of the valence band into $|3/2, 1/2\rangle$ and $|3/2, 3/2\rangle$, in addition, the hydrostatic components shift the bandgap to a higher (lower) energy. The schematic band structures near the center of the BZ under biaxial tensile strain for ZnS and compressive strain for ZnSe are shown in Fig.6 for the case along the biaxial stress directions $\langle 100 \rangle$ or $\langle 010 \rangle$. This splitting results in a significant change in the valence band dispersion on the layer plane [23]. ZnSe-ZnS system which has hole confinement in biaxially compressed layers can exhibit

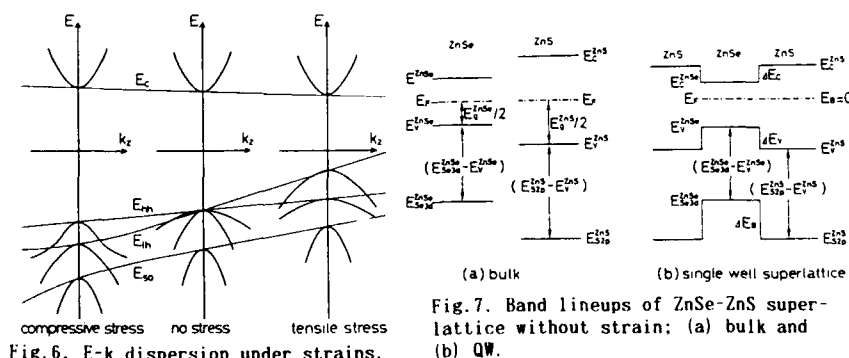


Fig.7. Band lineups of ZnSe-ZnS superlattice without strain: (a) bulk and (b) QW.

2D hole masses near the top of valence band maximum.

Fig.7 shows the energy-band diagrams of the type I superlattice in single quantum-well of ZnSe-ZnS structure without strain and in bulk ZnS and ZnSe crystals before the formation of the heterojunction, taking into account of the equivalent energy position of the Fermi level (E_F) between them. This figure also indicates both the energy difference between E_{v}^{ZnSe} and $E_{s_{3d}}^{ZnSe}$ and the energy difference between E_{v}^{ZnS} and $E_{s_{2p}}^{ZnS}$, assuming the energy position of E_F being located at the middle of the energy bandgap. If the binding energies of S 2p in ZnS and Se 3d in ZnSe in the superlattice are known, ΔE_v is calculated by,

$$\begin{aligned}\Delta E_v &= \Delta B + (E_{s_{3d}}^{ZnSe} - E_{v}^{ZnSe}) - (E_{s_{2p}}^{ZnS} - E_{v}^{ZnS}) \\ &= \Delta B + \text{constant}\end{aligned}\quad (4)$$

where $\Delta B = (E_{s_{2p}} - E_{s_{3d}})$ in the superlattice. Finally, we can get ΔE_c from the relation of $\Delta E_v + \Delta E_c = \Delta E_g$. From our XPS results [14], ΔE_v and ΔE_c are calculated to be 0.73 and 0.25 eV, respectively. These values are in good agreement with the Harrison's LCAO theory (0.82 eV).

If the ZnSe-ZnS SLS approves the free-standing superlattice, the lattice constant $a_{||}$ parallel to the in-plane of the interface depending on strain can be expressed [24],

$$\begin{aligned}a_{||} &= (a_{ZnSe}G_{ZnSeLw} + a_{ZnS}G_{ZnSLb}) / (G_{ZnSeLw} + G_{ZnSLb}) \\ G_i &= 2(c_{11} + 2c_{12})(1 - c_{12}/c_{11})\end{aligned}\quad (5)$$

where i denotes the ZnSe and ZnS, a_i is the lattice constant of the bulk crystal, and c_{11} and c_{12} are the elastic constants. We can express the changes of the bandgap energy of ZnSe well and ZnS barrier in terms of the strain and deformation potential constants listed in Table 1 as follows,

$$E_g^{ZnSe}(L_w) = E_c^{ZnSe} - \{ E_{v,av}^{ZnSe} + \Delta E_{v,2|3/2,3/2} \} \quad (6)$$

$$E_g^{ZnS}(L_b) = E_c^{ZnS} - \{ E_{v,av}^{ZnS} + \Delta E_{v,1|3/2,1/2} \} \quad (7)$$

where E_c is the conduction band and $E_{v,av}$ is the center of gravity of the valence band due to strain. $E_{v,2|3/2,3/2}$ and $E_{v,1|3/2,1/2}$ are heavy-hole and light-hole band, respectively. Fig.8(b) shows the change of the bandgap energy of ZnS barrier and ZnSe well as a function of ZnSe well width. The bandgap of ZnSe well layer increases due to the compressive stress, while

Table 1 Physical parameters used for the calculation of the offsets in ZnSe and ZnS

	ZnSe	ZnS
Lattice constant a (Å)	5.6687	5.4093
Band gap at 4.2 K E_g (eV)	2.822	3.840
Spin-orbital splitting energy Δ_{so} (eV)	0.45	0.072
Exciton binding energy E_b^{1*} (meV)	19	40
Deformation potential constant $a_c - a_v$ (eV)	-5.4	-4.0
b (eV)	-1.2	-0.7
Elastic constant C_{11} (Mbar)	0.826	1.067
C_{12} (Mbar)	0.498	0.666
Offset of the valence band at non strains ΔE_v^0 (eV)	0.82	

that of the ZnS barrier layer decreases due to the tensile stress as was seen in Fig.6.

Recently, Van de Walle [24] has reported a summary of "model-solid" theory for determining the band offsets in strained-heterostructure. We assumed the valence band offset (ΔE_v^0) to the energy difference between the heavy-hole state in ZnSe and the light-hole state in ZnS without strains. In model-solid theory, the conduction and valence band deformation potential are individually obtained. Therefore, the conduction-band offset (ΔE_c) and the valence-band offset (ΔE_v) are expressed as follows,

$$\Delta E_c = E_c^{ZnS} - E_c^{ZnSe} \quad (8)$$

$$\Delta E_v = E_{v, \text{hh}}^{ZnSe} - E_{v, \text{hh}}^{ZnS} + \Delta E_{v, 2}^{ZnSe} \{3/2, 3/2\} - \Delta E_{v, 1}^{ZnS} \{3/2, 1/2\} \quad (9)$$

$$E_c = E_c^0 + a_c (\Delta \Omega / \Omega) \quad (10)$$

$$E_{v, \text{hh}} = E_{v, \text{hh}}^0 + a_v (\Delta \Omega / \Omega) \quad (11)$$

when we used $\Delta E_v^0 = 820$ meV (Harrison's value and is fairly close to the XPS value). $\Delta E_{v, \text{hh}}^0$ is calculated to be 694 meV. Fig.8(a) shows the changes of ΔE_c and ΔE_v as a function of ZnSe well width at a constant barrier layer of 50 Å. From these evidence, it is understood that the conduction band offset is always positive and changes from 60 to 80 meV increasing the well layer width up to 100 Å. This indicates that no type I' conversion can be seen. This is different from the early our expectation [25] because we did not consider the effect of $\Delta E_{v, \text{hh}}$ on strains. However, the type I' which was suggested in Van der Walle's paper [24] is thought to be caused by a choice of the large ΔE_v^0 (=900 meV). If we calculate the ΔE_c using his physical parameters with deformation potential constant and ΔE_v^0 , the ΔE_c is changed from -41.5 to -39.0 meV between 0 and 100 Å well thickness at a constant barrier 50 Å [24,26].

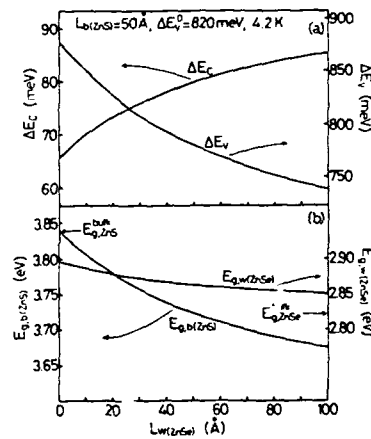


Fig.8. (a) Conduction and valence band offsets and (b) bandgap of ZnSe well and ZnS barrier layers as a function of ZnSe well width.

4.1.3. Exciton luminescence and absorption of SLS on (100) GaAs and ZnS substrates

Fig.9 shows the excitonic luminescence and normal-incidence reflectance spectra obtained at 4.2 K of ZnSe(25Å)-ZnS(35Å) SLS on (100) GaAs substrate with 150 periods. The dashed line is taken under a He-Cd laser (10 mW/cm²) weak excitation and the solid line is taken under a N₂ laser (1 MW/cm²) high excitation. The linewidth of the dashed curve was about 22 meV. The main peak is located at 2.8559 eV and corresponds to the lower polariton branch ($\hbar\omega_L$). The reflectance structure exhibits one distinct minimum ($\hbar\omega_T$) and a sharp maximum ($\hbar\omega_U$). The damping of about 10 meV obtained is considerably larger than in bulk ZnSe (0.4 meV) [27]. This result can be explained by a level broadening due to inhomogeneous strain which reduces the exciton lifetime. The LT splitting is about 20 meV which is much larger than the bulk (~1 meV). This means that the oscillator strength becomes larger.

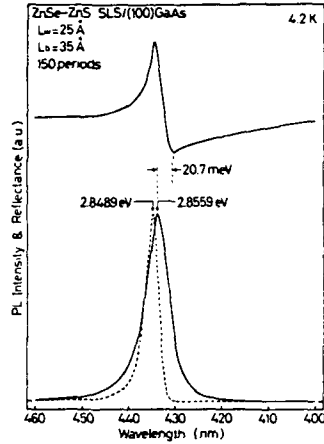


Fig. 9. 4.2K reflectance and luminescence spectra obtained under weak and high excitation conditions.

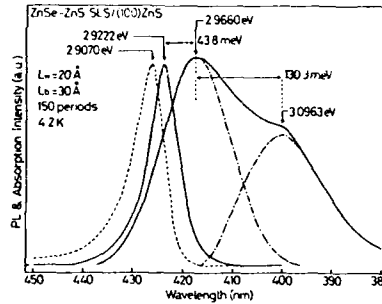


Fig. 10. 4.2K luminescence under weak and high excitation conditions, and absorption spectrum.

We have grown ZnSe-ZnS SLS on (100) ZnS substrate ($\sim 500 \mu\text{m}$ thick) which can allow to penetrate photon energy below 3.5 eV. Fig. 10 shows the exciton luminescence for both excitation conditions, and absorption obtained at 4.2 K of ZnSe(20 Å)-ZnS(30 Å) SLS with 150 periods. The main luminescence peak position is located at 2.9222 eV. The step-wise absorption reflects the 2D character in the density of states due to quantum confinement. Two peaks are resolved assuming a Gaussian lineshape (---) and are located at 2.9660 eV and 3.0963 eV. The energy difference of about 130 meV corresponds to the theoretically estimated energy difference between the heavy-hole and light-hole excitons. Therefore, a Stokes shift is about 44 meV between main PL peak and the $n=1$ heavy-hole exciton absorption peak. The low-energy shoulder of the PL line taken under the weak excitation condition, attributed to excitons trapped at defects, saturates with enhanced excitation density. We attribute the 2.9222 eV emission line to intrinsic recombination from $n=1$ heavy-hole exciton [9].

When the sample temperature is increased from 18 to 300 K, the excitonic absorption peak shifts gradually to lower energy as shown in Fig. 11. The features of free-exciton absorption can be observed even at RT. The Stokes shift results from spectral diffusion of excitons towards the low-energy localized states in the inhomogeneous line. However, the observed Stokes

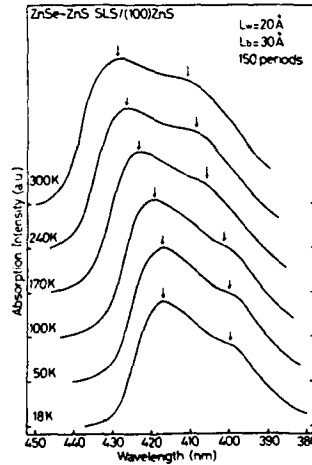


Fig. 11. Temperature dependence of absorption spectra.

shift is also caused by statistical fluctuation of the well layer due to 2 monolayer of the well width. The shift increases to about 50 meV at RT.

4.2. High excitation

We have tentatively proposed that the excitonic line, observed under the weak excitation condition, is related to the localization of excitons as was indicated by an abnormal temperature dependence [9]. But, as shown in Fig.12, the normal temperature dependence of the main excitonic line of a ZnSe-ZnS SLS on a (100)ZnS substrate can be observed [9].

Fig.13(a) and (b) show the temperature dependence of the linewidth and peak position of the exciton emission obtained under the high excitation condition, respectively. In this case, the FWHM is almost constant in the range of 4.2 to about 100 K, but increases more rapidly with temperature above 100 K. The FWHM of the emission line as a function of temperature can be analyzed by the following relation, taking into account the scattering processes with LO and acoustic phonons, and with ionized donor impurities [28]:

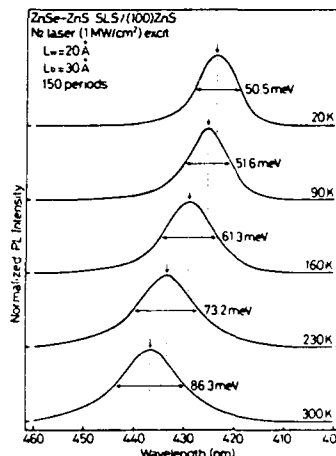


Fig.12. Temperature dependence of excitonic emission of ZnSe-ZnS SLS.

$$\Gamma = \Gamma_0 + \Gamma_A T + \Gamma_L \exp[-\langle E_b \rangle / k_B T] + \Gamma_{LO} / [\exp(\hbar\omega_{LO} / k_B T) - 1] \quad (12)$$

where Γ_0 is the linewidth due to fluctuation of the well layer thickness, Γ_A is a coefficient of the exciton-acoustic phonon interaction, Γ_L is a proportionality factor which accounts for the density of donor centers, $\langle E_b \rangle$ is the binding energy of the donor averaged over all possible positions of the impurities within the well layer, Γ_{LO} is the exciton-LO phonon coupling constant, and $\hbar\omega_{LO}$ is the LO phonon energy (=31.4 meV) in ZnSe.

Putting $\Gamma_0=50.3$ meV, $\Gamma_A=8 \times 10^{-4}$ meV/K, $\Gamma_L=73.7$ meV, $\Gamma_{LO}=35$ meV, and a donor binding energy $\langle E_b \rangle$ of 32.7 meV in eq.(12), the theoretical curve agrees fairly well with the experimental data as shown in Fig.13(a) by the solid curve. It is noticed here that the $\langle E_b \rangle$ is about 1.3 times larger than that of the effective-mass donor binding energy ($E_b=26$ meV). In general, the binding energy of the impurity is reduced by biaxial compressive strain and increased spatial confinement in the well. As a result, E_b is larger than in bulk ZnSe. The emission peak position shifts toward lower photon energy with increasing temperature. Obviously, the variation of its peak energy with temperature reflects the temperature dependence of the ZnSe bandgap [3,9].

As was seen in Fig.13(a), the linewidth becomes homogeneously broader with increasing temperature. Using eq.(3)', we can calculate the fraction of exciton which contributes to recombination and thus the temperature dependence on $\tau_{ex, 2D}$ will be presented as same as $\Delta(T)$.

The appearance of exciton absorption peaks at RT, as shown in Fig.11, suggests that the exciton binding energy is considerably large despite the large exciton-phonon coupling. As mentioned in Ref.[9], the exciton binding energy is 4 times larger than that of three-dimensional bulk excitons (about 19 meV) under the assumption of infinite potential well [21]. Fig.14 shows the temperature dependence of the emission intensity of the excitonic peak

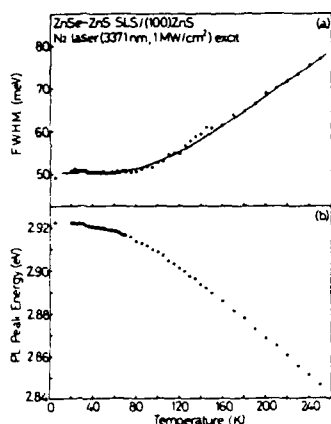


Fig.13. Temperature dependence of FWHM (a) and peak position (b). The solid curve is calculated by eq. (12).

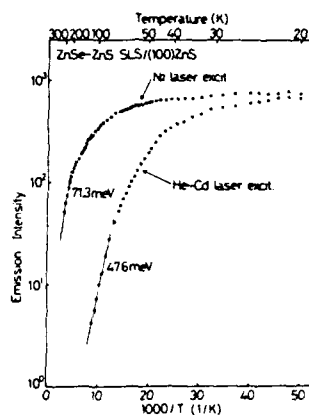


Fig.14. Thermal quenching of excitonic emission line of ZnSe-ZnS SLS.

obtained under the weak and high excitation conditions. The thermal quenching of the emission intensity, under weak excitation condition, starts from 50 K and shows an activation energy of about 48 meV. However, in the case of the high excitation, the thermal quenching starts from about 100 K and the emission intensity is maintained up to 300 K. The activation energy of this quenching is estimated to be 71.3 meV which is approximately 4 times larger than that of the bulk exciton energy E_{ex}^{B} . Thus we suggest from the thermal quenching experiments that the thermal dissociation of 2D electrons and 2D holes results from the n-1 free-excitons in the well.

5. LUMINESCENCE PROPERTIES OF FIBONACCI SEQUENCE

The purpose is to explore excitonic properties in one dimensional quasi periodic superlattice with a modulation following a Fibonacci sequence. This system may expect the Anderson localization [29] of excitons in the quasi

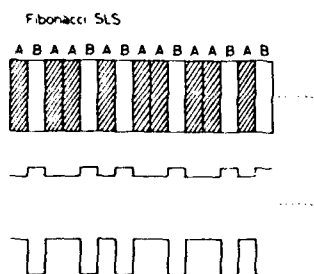


Fig.15. A finite Fibonacci structure and type I band structure with A and 2A potential wells.

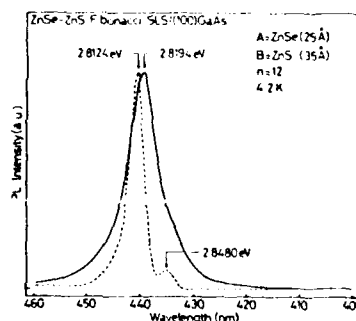


Fig.16. PL spectra of Fibonacci modulated SLS at 4.2 K.

periodic structure. These properties may include large nonlinear susceptibility $\chi^{(3)}$ due to low-dimensionality of excitons [8,29].

The present Fibonacci-modulated SLS of ZnSe-ZnS, already shown in Fig.2, is schematically illustrated with a simple type I band structure in Fig.15. A(=ZnSe) may form the potential well and AA(=2A ZnSe) also form the potential well. We expect that when the well separation increases 2A, exciton states become localized at some site. As a result, the localized states can contribute significantly to photoluminescence and absorption.

Fig.16 shows the PL spectra of a finite Fibonacci superlattice at 4.2 K. We observed two peaks (2.8480 and 2.8124 eV) which may be attributed to the excitonic emission from ZnSe with well A and ZnSe with well 2A, respectively. But, the emission intensity of ZnSe(A) is weaker than that of ZnSe(2A) and the peak positions shift toward higher energy when the N_2 laser excitation (1 MW/cm²) was used. This may indicate a strong localization of excitons in the 2A well [30].

6. CONCLUSIONS

We have introduced the growth and the excitonic characterization of ZnSe-ZnS MQW and Fibonacci-modulated quasiperiodic SLSs by the low-pressure MOCVD method. We have revealed that excitonic luminescence and absorption which originate from the $n=1$ heavy-hole exciton transitions occur in the type I band structure. However, a strong localization appears, so that the control of the well layer fluctuation is very important if we want to fabricate the photonics devices. It is suggested that the thermal quenching experiment indicates the dissociation process of the 2D excitons through electrons and holes.

ACKNOWLEDGEMENTS

One of the authors (T.T.) thanks his former students Y.Asao and S.Hayamizu for their skilful measurements of PL and XPS data. He also acknowledges K.Matsumoto of Nippon Sanso Corp. and M.Hatta of Seitetsu Chemical Ind. for providing DMZn and H₂Se, H₂S gases, and Dr.Y.Masumoto of Tsukuba Univ., Prof.M.Matsuura of Yamaguchi Univ. and Dr.M.Nakayama of Chiba Univ. for the discussion of excitons. This work was partly supported by a Grant-in-Aid for Scientific Research on Priority Areas, New Functionality Materials-Design, Preparation and Control No.1604583 from the Ministry of Education, Science and Culture of Japan.

REFERENCES

- [1] R.N.Bhargava, J. Lumi. 40/41, 24 (1988).
- [2] L.A.Kolodziejski, R.L.Gunshor, N.Otsuka, S.Datta, W.M.Becker and A.V.Nurmikko, IEEE J. Quantum Elect. QE22, 1666 (1986).
- [3] Y.Kawakami and T.Taguchi, J. Vac. Sci. and Technol. B7, 789 (1989).
- [4] I.Suemune, K.Yamada, H.Masato, Y.Kan and M.Yamanishi, Appl. Phys. Lett. 54, 981 (1989).
- [5] T.Yokogawa, M.Ogura and T.Kajiware, Appl. Phys. Lett. 52, 120 (1988).
- [6] T.Yokogawa and T.Narusawa, presented in the 4th Int. Conf. on II-VI Compounds, West Berlin (1989) September, to be published in J.Cryst.Growth
- [7] Y.Endoh and T.Taguchi, This volume.
- [8] T.Hiroshima, E.Hanamura and M.Yamanishi, Phys. Rev. B38, 1241 (1988).
- [9] Y.Yamada and T.Taguchi, presented in the 4th Int. Conf. on II-VI Compounds, West Berlin (1989) September, to be published in J. Cryst. Growth
- [10] Y.Kawakami, T.Taguchi, M.Satoh and A.Hiraki, Nucl. Inst. and Methods B33, 603 (1988).

- [11] H.Hayashi and S.Katayama, Phys. Rev. B39, 8743 (1989).
- [12] Y.Yamada and T.Taguchi, Tech. Rept. Osaka Univ. 39, 211 (1989).
- [13] R.Merlin, K.Bajema, R.Clarke, F.Y.Juang and P.K.Bhattacharya, Phys. Rev. Lett. 55, 1768 (1985).
- [14] T.Taguchi, S.Hayamizu, H.Fujiyasu, M.Satoh, T.Yao and A.Hiraki, Proc. Int. Symp. Hosei Univ.: Application of Ion Beams in Materials Science p.511 (1988).
- [15] B.C.De Cooman, C.B.Carter, G.W.Wicks, T.Tanoue and L.F.Eastman, Thin Solid Films 170, 49 (1989).
- [16] D.W.Langer, R.N.Fuwema, K.Era and T.Koda, Phys. Rev. B2, 4005 (1970).
- [17] P.T.Bailey, Phys. Rev. B1, 588 (1970).
- [18] Y.C.Lee and D.L.Lin, Phys. Rev. B19, 1982 (1979).
- [19] Ji-Wei Wu, Solid St. Commun. 69, 1057 (1989).
- [20] J.Feldmann, G.Peter, E.O.Gobel, P.Dawson, K.Moore, C.Foxon and R.J.Elliott, Phys. Rev. Lett. 59, 2337 (1987).
- [21] M.Matsuura, Phys. Rev. B37, 6977 (1988).
- [22] Y.Masumoto, (private communication).
- [23] H.Kato, N.Iguchi, S.Chika, M.Nakayama and N.Sano, J. Appl. Phys. 59, 588 (1986).
- [24] C.G.Van de Walle, Phys. Rev. B39, 1871 (1989).
- [25] Y.Kawakami, T.Taguchi and A.Hiraki, J. Cryst. Growth 93, 714 (1988).
Our early expectation from the type I to type I' conversion is caused by following the previous model after C.G.Van de Walle and R.M.Martin (Phys. Rev. B34, 5621 (1986)). Figs.5 and 6 are not correct and Fig.5 should be replaced by Fig.8 in the present review.
- [26] K.Shahzad, D.J.Olego and C.G.Van de Walle, Phys. Rev. B38, 1417 (1988).
- [27] H.Venghaus and R.Lambrich, Solid St. Commun. 25, 109 (1978).
- [28] J.Lee, E.S.Koteles and M.O.Vassell, Phys. Rev. B33, 5512 (1986).
- [29] E.Nanamura, Phys. Rev. B38, 1228 (1988).
- [30] Y.Yamada and T.Taguchi, Jap. J. Appl. Phys. (1990) to be published

OPTICAL PROPERTIES OF CdZnS-ZnS STRAINED-LAYER SUPERLATTICES

Yasuyuki Endoh and Tsunemasa Taguchi

Department of Electrical Engineering, Faculty of Engineering, Osaka University, Suita, Osaka 565, JAPAN.

ABSTRACT

The $\text{Cd}_{0.3}\text{Zn}_{0.7}\text{S}$ -ZnS strained-layer superlattices has for the first time been fabricated on (100)GaAs substrates by a low-pressure MOCVD method. Exciton luminescence properties were investigated by the photoluminescence spectroscopies which show that the quantum confinement effect of excitons occurs in the CdZnS alloy layer. Temperature dependence of the exciton properties reveals a dominant scattering process which originates from exciton-phonon interaction ($\hbar\omega_0=68\text{meV}$). Nevertheless, the large exciton binding energy of about 166meV makes it possible to produce the exciton peak at room temperature. The effect of external electric field on the exciton intensity and its peak position is found and is tentatively interpreted in terms of a quantum confined Stark effect.

1. INTRODUCTION

Of available wide bandgap II-VI compounds, it has recently been revealed that quantum well and superlattice structures enhance the exciton effects [1,2] as well as in III-V materials. Among II-VI materials, ZnS and CdS have large exciton binding energies which have been estimated to be 40meV and 28meV [3], respectively. If this alloy, $\text{Cd}_x\text{Zn}_{1-x}\text{S}$ is used to form a superlattice with ZnS, then it acts as a well for electrons and holes, and as a result its electric structure is modified by quantum confinement. However, it is expected that the CdZnS well is considerably under compressive strain, while the ZnS barrier receives tensile strain due to the lattice mismatch between them. Namely this structure exhibits a strained-layer superlattice (SLS) in nature within a certain critical thickness [4,5].

Both quantum confinement effect and biaxial compression will increase the effective energy bandgap of the CdZnS well, so exciton properties are much affected by the band structure changes which remove the degeneracy of the valence band. Furthermore, cubic symmetry of the alloy material will be lost, which makes it possible to create the anisotropy in the susceptibilities. So, the large nonlinear effect of the excitons in the present SLS will appear.

Our objective for investigating exciton properties of the CdZnS-ZnS SLS is as follows: (i) observation of the RT exciton emission, (ii) scattering mechanism and localization of excitons in the alloyed CdZnS well and (iii) quantum confined Stark effect.

We are concerned in this paper with the characteristics of excitons in $\text{Cd}_{0.3}\text{Zn}_{0.7}\text{S}$ -ZnS SLSs grown by low-pressure metalorganic chemical-vapour-deposition (MOCVD). Our discussion will concentrate on the temperature and external electric-field dependence of photoluminescence properties which will be originated from quasi two-dimensional excitons.

2. FABRICATION OF STRAINED-LAYER SUPERLATTICE AND STRUCTURAL PROPERTIES

The CdZnS-ZnS SLSs were grown by all gaseous low-pressure MOCVD method [4,5]. Each layer was alternatively deposited on a Cr-doped semi-insulating

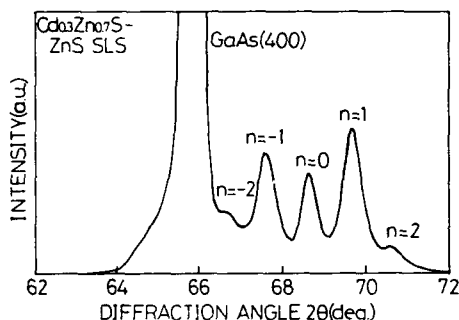


Fig.1 X-ray diffraction satellite spectrum of a $\text{Cd}_{0.3}\text{Zn}_{0.7}\text{S}$ -ZnS SLS on (100)GaAs substrate.

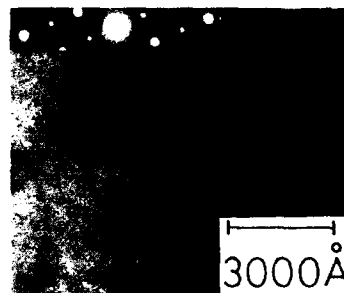


Fig.2 2MeV plane-view TEM bright-field image and electron diffraction pattern.

GaAs substrate. As gas source materials, 1% Dimethylzinc ($(\text{CH}_3)_2\text{Zn}$) and 0.13% Dimethylcadmium ($(\text{CH}_3)_2\text{Cd}$), each of them was diluted with a He gas, were used together with 10% H_2S in H_2 . In the growth of the superlattices, the operation pressure in the reactor was maintained at below 1 Torr.

We have used X-ray diffraction and plane-view high-voltage transmission electron microscope (TEM) to characterize the crystalline structure and the quality of the films.

Fig.1 shows the X-ray diffraction spectrum of a $\text{Cd}_{0.3}\text{Zn}_{0.7}\text{S}$ -ZnS SLS on a (100)GaAs substrate. There appear several clear satellite peaks ($n=\pm 1, 2$) around $n=0$ th peak. A total thickness (L_w+L_b) is calculated to be 124Å, so that the well (L_w) and barrier (L_b) layer thickness are estimated to be about 57Å and 67Å, respectively.

Average lattice constant of this compositional alloy is assumed to be 5.532Å, thus the critical thickness of each layer is estimated to be about 80Å. Fig.2 shows a plane-view TEM bright-field image and electron diffraction pattern observed by a 2MeV electron of a $\text{Cd}_{0.3}\text{Zn}_{0.7}\text{S}$ (57Å)-ZnS(67Å) SLS after removal of the GaAs substrate (where a total layer thickness is approximately 5000Å). No morie fringes can be seen in the (100) epitaxial layer and as a result its coherency-grown SLS layer with (100) orientation can be realized. The electron diffraction pattern appears to be spotty supports the good epitaxial film. It is reasonable to consider that below 80Å thick there appear no structural defects and the strained-layer can be formed as judged from the results of Figs.1 and 2.

Photoluminescence (PL) measurements were performed at 4.2K. The dispersed signal by a 1m Jobin-Yvon single monochromator was lead to the photomultiplier and analyzed by a conventional lock-in detection system. A He-Cd laser (325nm, 10mW/cm²) and a N_2 laser (337.1nm, 1mW/cm²) were used as excitation sources. The temperature

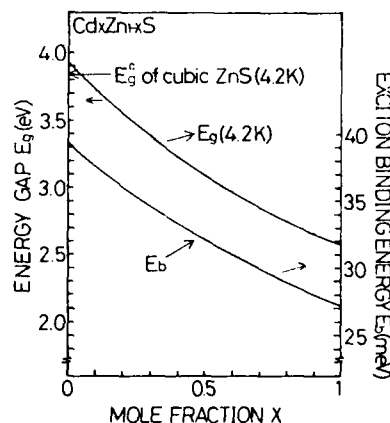


Fig.3 Energy bandgap E_g (4.2K) and exciton binding energy E_b calculated for $\text{Cd}_x\text{Zn}_{1-x}\text{S}$ as a function of x .

dependence of the PL were also measured using a temperature-variable cryostat (4.2K or 19K) up to RT. External electric-field dependence of the PL was measured. For the experiment of the external electric-field effect, Si-doped n^+ -type (100)GaAs substrates ($10^{-3} \Omega \cdot \text{cm}$) were used. The preparation procedures of the sample are as follows: First, to form the ohmic contact to n^+ -type GaAs substrate, Au-Ge film was evaporated on the GaAs substrate and subsequently annealed at 490 °C in H_2 atmosphere for 15min. Second, Au film (the thickness of about 50Å) was evaporated on the surface of the SLS to form the Schottky barrier contact at 10^{-6} Torr. Finally, Cu-wire was fixed on the surfaces of each evaporated film. The external electric-field of about an order of 10^4 V/cm was perpendicularly applied to the (100) growth direction.

3. RESULTS AND DISCUSSION

3.1 Energy gap and exciton binding energy of the CdZnS alloy

It has been well known that ZnS generally forms a mixed texture of cubic and hexagonal structures, while CdS forms a hexagonal structure with exception of a few recent reports [4,5]. When ZnS can alloy with CdS, the apparent band gap energy E_g of this alloy decreases with composition x ($=\text{Cd}$). Using the physical quantities such as each hexagonal band gap and bowing parameter (b), the E_g of the binary compounds [3] is expressed by

$$E_g \text{ Cd}_x\text{Zn}_{1-x}\text{S}(x) = 0.61(1-x)^2 + 0.719(1-x) + 2.582 \quad (\text{eV}) \quad (1)$$

where each band gap of ZnS and CdS at 4.2K is 3.911eV and 2.582eV, respectively, and b is 0.61eV [3]. Fig.3 shows the calculated E_g (4.2K) as a function of x , where the E_g^C means the band gap of the cubic ZnS crystal.

On the other hand, the exciton binding energy can be simply calculated as a function of x using the virtual-crystal approximation (VCA) model for

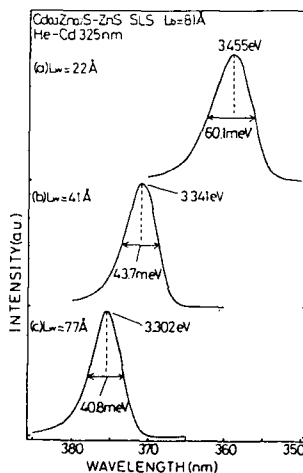


Fig.4 Exciton-emission bands at 4.2K of $\text{Cd}_{0.3}\text{Zn}_{0.7}\text{S-ZnS}$ SLSs as a function of well thickness at a constant barrier of 81Å.

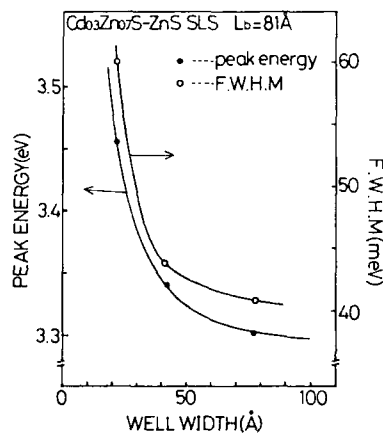


Fig.5 Energy shift of the peak position and linewidth as a function of well thickness.

effective mass and dielectric constant in the alloy crystal [6]. If this model is applicable to estimate the free-exciton energy for the ground-state, the binding energy $E_B(x)$ is presented by following equation,

$$E_B(x) = R \left[\frac{x\mu_A}{\epsilon_A^2} + \frac{(1-x)\mu_B}{\epsilon_B^2} + \frac{x(1-x)}{x\mu_B + (1-x)\mu_A} \left(\frac{\mu_A}{\epsilon_A} - \frac{\mu_B}{\epsilon_B} \right)^2 \right] \quad (2)$$

where $\mu_{A,B}$ is the reduced mass of electrons and holes, $\epsilon_{A,B}$ is the dielectric constant and R is Rydberg constant. For cubic ZnS and CdS crystals, we used $\mu_{ZnS}=0.20$, $\epsilon_{ZnS}=8.32$, $\mu_{CdS}=0.134$ and $\epsilon_{CdS}=8.19$ [1,3]. The calculated results are also plotted in Fig.1. The $E_B(x)$ of $Cd_{0.3}Zn_{0.7}S$ is calculated to be about 35meV and thus the Bohr radius is calculated to be 24Å. The dependence of both E_g and E_B on x indicates a similar behavior.

3.2 PL properties of $Cd_{0.3}Zn_{0.7}S$ -ZnS SLS

Fig.4 shows general spectral changes of the lineshape at 4.2K of a $Cd_{0.3}Zn_{0.7}S$ -ZnS SLS as a function of well (Lw) at a constant barrier thickness (81Å). With decreasing the Lw, the peak position moves toward higher energy, while the linewidth (FWHM) increases dramatically. Fig.5 represents both the peak position and FWHM value as a function of well width. Below 30Å well thickness, the FWHM is significantly increased. Since the well width becomes smaller than the Bohr radius, the localization of excitons will significantly take place. Also, it means that strong quantum confinement relates to the exciton transition. If we assume that this SLS structure belongs to a type I heterojunction, the conduction band offset is relatively larger than that of the valence band. Consequently, the electrons

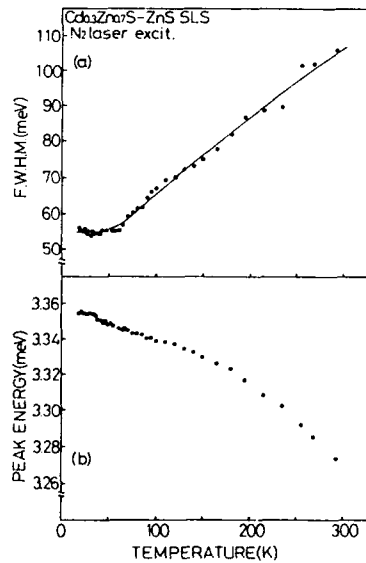


Fig.6 Temperature dependence of linewidth (a) and energy peak position (b) of a $Cd_{0.3}Zn_{0.7}S$ -ZnS SLS (Lw=57Å and Lb=67Å).

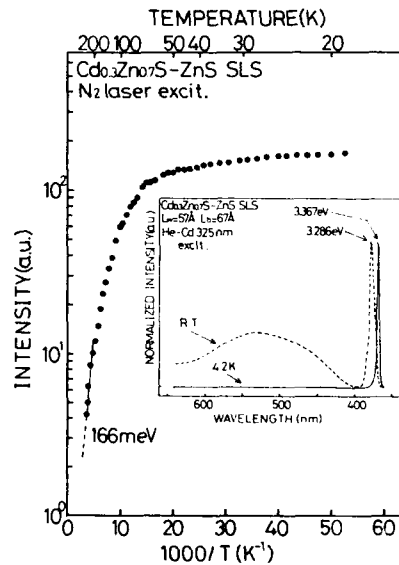


Fig.7 Temperature dependence of luminescence intensity of a $Cd_{0.3}Zn_{0.7}S$ -ZnS SLS and the spectra taken at 4.2K and RT.

are strongly confined in the potential well.

Fig.6(a) and (b) show the temperature dependence of the FWHM and peak position of a $\text{Cd}_{0.3}\text{Zn}_{0.7}\text{S}$ -ZnS SLS ($L_w=57\text{\AA}$, $L_b=67\text{\AA}$ and 100 periods), respectively. The solid curve for the theoretical linewidth broadening of (a) is described using the following equation [2],

$$\Gamma = \Gamma_0 + \Gamma_a T + \Gamma_i \exp(-E_b/k_B T) + \Gamma_{LO} / [\exp(\hbar\omega_{LO}/k_B T) - 1] \quad (3)$$

where Γ_0 is the linewidth at 4.2K, Γ_a is the strength of acoustic phonon-exciton interaction, Γ_i is the coefficient of the fluctuation of excitons trapped at defect sites and E_b is assumed to be an ionization energy of localized center which binds excitons, and Γ_{LO} is the strength of LO phonon-exciton interaction and $\hbar\omega_{LO}$ is about 42meV for $\text{Cd}_{0.3}\text{Zn}_{0.7}\text{S}$ alloy. Using $\Gamma_0=54.8\text{meV}$, $\Gamma_a=5.0 \times 10^{-6} \text{ eV/K}$, $\Gamma_i=66\text{meV}$, $\Gamma_{LO}=68\text{meV}$ and $E_b=18\text{meV}$, we can draw the solid curve which is in good agreement with the experimental points. The peak position moves toward lower energy with increasing temperature and this behavior appears to exhibit the temperature variation of the band gap of the quantum well.

Fig.7 shows the temperature dependence of the exciton emission intensity of the same SLS sample. The activation energy for the thermal quenching is estimated to be about 166meV which is two times larger than that of ZnSe-ZnS SLS [2]. On the basis of our previous assumption [2], this activation energy corresponds to the dissociation energy of excitons through electrons and holes. The 166meV will give the 1s exciton binding energy. In the insert of Fig.7, the spectra obtained at RT and 4.2K under a He-Cd laser excitation condition were displayed.

3.3 Static electric field effect

The spectral change of the PL bands of a $\text{Cd}_{0.3}\text{Zn}_{0.7}\text{S}$ -ZnS SLS ($L_w=77\text{\AA}$,

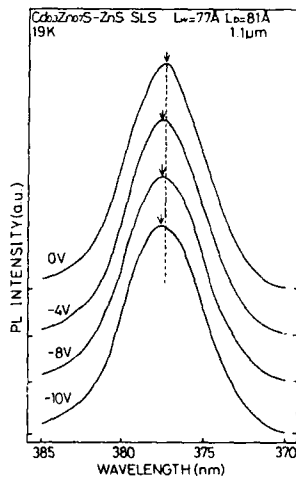


Fig.8 Electric-field dependence of exciton emissions at 19K of a $\text{Cd}_{0.3}\text{Zn}_{0.7}\text{S}$ -ZnS SLS ($L_w=77\text{\AA}$ and $L_b=81\text{\AA}$).

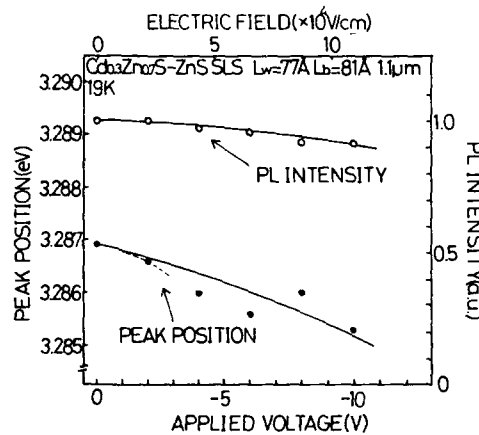


Fig.9 Dependence of the intensity and peak position on electric field.

Lb=81Å and a period of 100 cycles) at 19K is shown in Fig.8 as a function of electric field. With increasing electric field under reverse bias conditions, the band slightly decreases in intensity. Fig.9 shows the static field dependence of the peak position and PL intensity as a function of reverse bias. PL intensity decreases and the peak position shifts toward lower energy side with increasing electric field. We found the energy shift of about 2meV at 10V ($E \sim 10^5$ V/cm). A critical field of exciton ionization due to electric field is estimated to be about 10^4 V/cm [7]. However, the exciton band is not significantly decreased in intensity even over 10^4 V/cm. A slightly decreased luminescence intensity may be caused by the tunnel out of electrons or holes through the well within the barrier. The energy downshift with electric field may be related to a quantum confined Stark effect [8,9].

4. CONCLUSION

The plane-view TEM, electron diffraction pattern and X-ray diffraction measurements indicate that the $\text{Cd}_{0.3}\text{Zn}_{0.7}\text{S-ZnS}$ multiple-quantum well structure consists of the strained-layer superlattice below each 80Å layer thickness. From the well width and temperature dependence, the exciton luminescence shows the strong quantum confinement. We have observed the RT exciton luminescence at 3.286eV and the thermal activation energy of excitons is estimated to be 166meV largest in the present semiconductor SLSs, despite the large LO phonon-exciton interaction ($\Gamma_{LO}=68\text{meV}$). The electric field applied perpendicularly to the (100) direction leads to the decrease in the luminescence intensity and the energy downshift of the peak position, so we suggest that this phenomena may be caused by the quantum confined Stark effect.

ACKNOWLEDGEMENTS

One of the authors (T.T.) acknowledges to K.Matsumoto of Nippon Sanso Ind. and M.Hatta of Seitetsu Chemical Ind. for supplying the DMZn and DMCD gases, and H_2S gas.

REFERENCES

- [1] P.E.Lippens and M.Lannoo, Phys. Rev. 39, 10935 (1989).
- [2] T.Taguchi and Y.Yamada, this volume.
- [3] L.G.Suslina, A.G.Plyukhin, D.L.Fedorov and A.G.Areshkin, Sov. Phys. Semicond. 12, 1331 (1978).
- [4] Y.Endoh, Y.Kawakami, T.Taguchi and A.Hiraki, Ext. Abstracts of the 20th Int. Conf. on Solid State devices and materials, 1988 p407.
- [5] Y.Endoh, Y.Kawakami, T.Taguchi and A.Hiraki, Jpn. J. Appl. Phys. 27, L2199 (1988).
- [6] S.D.Mahanti, Phys. Rev. 10, 1384 (1974).
- [7] M.L.Lebedev and V.G.Lysenko, Sov. Phys. Solid. St. 24, 1721 (1982).
- [8] E.E.Mendez, G.Bastard, L.L.Chang and L.Esaki, Physica 114/118B, 711 (1983).
- [9] J.A.Brum and G.Bastard, Phys. Rev. B31, 3893 (1985).

**PRECISE MEASUREMENTS OF TRANSIENT EXCESS CARRIER
LIFETIMES IN II-VI FILMS AND SUPERLATTICES**

W. O. DOGGETT, MICHAEL W. THELANDER AND J. F. SCHETZINA
North Carolina State University, Physics Department, Raleigh, NC
27695-8202

ABSTRACT

A system has been developed for accurately measuring lifetimes for photo-induced excess current carriers in semiconductors using the transient photoconductivity decay method. The specifications of state-of-the-art equipment, considerations peculiar to the capture of fast transient pulses, and sophisticated statistical data analysis techniques are discussed. Experimental results are presented to demonstrate the capability of the system (a) to measure lifetimes in the 40-ns - 75- μ s range for temperatures varying from 77K to 300K with 10% accuracy for single lifetime decays and 30% accuracy for individual effective lifetimes in a multi-component decay, and (b) to use a 300-ns lifetime photoconductor as a detector to measure nanosecond-time-scale structure of laser pulses. The predominant excess carrier lifetimes of HgCdTe samples grown at NCSU by photoassisted molecular beam epitaxy (PAMBE) ranged from 46 ns at 300K to 341 ns at 77K. CdTe samples and CdMnTe-CdTe superlattices exhibited a multi-component decay with the two longest components having effective lifetimes of 26 μ s and 4 μ s for CdTe and 75 μ s and 10 μ s for CdMnTe-CdTe. These values were relatively insensitive to temperature variation.

TRANSIENT BEHAVIOR OF PHOTO-INDUCED CARRIER CONCENTRATION

The rate of change of the photo-induced current carrier concentration, $\Delta n(t)$, for a semiconductor whose excess carriers are lost only by local recombination in the bulk material with a single lifetime τ is given by [1]

$$\frac{\partial(\Delta n)}{\partial t} = g(t) - \frac{\Delta n(t)}{\tau} \quad (1)$$

The term $g(t) = C_L L(t)$ is the rate of production of carrier concentration and is proportional to the laser intensity $L(t)$. The solution to Eq. (1) is the convolution,

$$\Delta n(t) = \int_0^t g(t') dt' e^{-(t-t')/\tau} \quad (2)$$

At the end of the laser pulse, the concentration is $\Delta n(t_L) \equiv n_0 \Delta_0$ where $n_0 = n(t) - \Delta n(t)$ is the steady-state carrier concentration and $\Delta_0 \approx 10^{-4} - 10^{-2}$. The excess concentration subsequently decays according to

$$\Delta n(t) = n_0 \Delta_0 e^{-t/\tau} \quad (3)$$

in which t in Eq. (3) and below is $t - t_L$ in Eq. (2). The decay is sometimes more complex than a simple exponential form and must be represented by one of the following models.

(a) Decay from different conduction bands or trapping levels [1]

$$\Delta n(t) = n_0(\Delta_1 e^{-t/\tau_1} + \Delta_2 e^{-t/\tau_2} + \dots). \quad (4)$$

(b) Bulk and surface recombination for a finite-thickness sample

$$\Delta n(t) = n_0 \sum_k \Delta_k e^{-(\frac{1}{\tau} + \lambda_k)t} \quad (5)$$

The λ_k are geometry-dependent eigenvalues and Δ_k are the local excitation coefficients for the k^{th} spatial modes in the solution of the continuity equation [1,2].

(c) Bulk and surface recombination for a semi-infinite sample [3]

$$\Delta n(t) = n_0 \Delta_0 \exp[t/\tau(S^2 - 1) \operatorname{erfc}(S\sqrt{t/\tau})], \quad (6)$$

where $S = st/L$, s = surface recombination velocity, L = diffusion length of the minority carriers, and τ = recombination lifetime.

Deviations from the above decay curves can be caused by the following physical factors. An excessive applied electric field can be a problem for p-type samples. Illumination of nonohmic or rectifying contacts can produce a photovoltaic signal. Non-uniform illumination of the sample can cause a departure from an exponential decay. An intense laser pulse can (1) invalidate the assumption of a small-signal level, $\Delta_0 \ll 1$, and (2) change the resistance by increasing the temperature.

THE TRANSIENT PHOTOCONDUCTIVE DECAY METHOD

Figure 1 shows the equivalent circuit for our implementation of the transient photoconductive decay method [1]. A laser pulse produces the carrier concentration $\Delta n(t)$ which causes the following transient change in the conductivity and resistance of the sample,

$$\frac{\sigma(t)}{\sigma_0} = \frac{R_0}{R_s(t)} = 1 + \frac{\Delta n(t)}{n_0}, \quad (7)$$

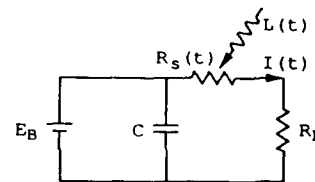


Fig. 1. Equivalent circuit.

in which the subscript 0 denotes steady-state values. The current through the sample is $I(t) = E_B / [R_L + R_s(t)]$. With the assumption that $\Delta n(t)/n_0 \ll 1$, the voltage observed by the oscilloscope is

$$V_L(t) = R_L I(t) = I_0 R_L + I_0 R_L \frac{R_0}{R_0 + R_L} \frac{\Delta n(t)}{n_0}. \quad (8)$$

The shape of the decay curve depends on the model, ranging from a simple or multiple exponential form after the laser pulse to a convolution according to Eqs. (2)-(6) for $\Delta n(t)/n_0$.

DESCRIPTION OF THE EXPERIMENTAL SETUP

The most important consideration in designing this system is the selection of components, circuits, and data acquisition equipment that can capture the true transient behavior of the photo-induced current without distortion. Possible sources of distortion for nanosecond-time-scale signals include: (a) reflections at impedance discontinuities in the signal path from the sample to the oscilloscope; (b) reflections associated with the bias voltage source, or a non-constant voltage source at the sample circuit; (c) inadequate high- and low-frequency response, voltage amplification, or digital accuracy of the oscilloscope; (d) electrical noise generated by the laser supplying the optical pulses or by the bias power supply; and (e) frequency dependent attenuation characteristics of coaxial cables and connectors.

A block diagram of our experimental setup is shown in Fig. 2 and a circuit diagram in Fig. 3. The sample was cooled in a Janis Research Company model 8DT detachable tail dewar. The sample temperature was controlled with a Lakeshore Cryotronics model DRC-91C temperature controller not shown. A Spectra Physics model 171 argon ion laser with a model 344 cavity dumper provided the 10-ns FWHM optical pulses with wavelengths 457.9 - 514.9 nm at a repetition frequency 0 - 4 MHz. A battery powered circuit supplied the dc bias voltage for the sample.

The laser pulse was monitored with a Spectra Physics model 403B ultra-high speed silicon photodiode with a risetime less than 50 ps. The average laser power was measured with a Laser Precision RK-5720 power ratiometer. The signal was captured with a 1-GHz Tektronix 11402 digitizing and sampling oscilloscope.

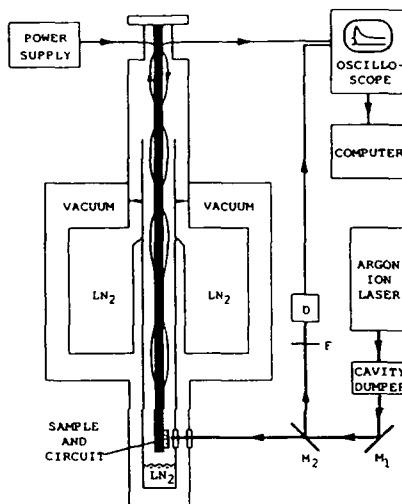


Fig. 2 Block diagram of system showing sample in Janis dewar. Legend: D = photodiode detector, F = attenuation filter, LN₂ = liquid nitrogen, M₁ = mirror, M₂ = partially reflecting mirror.

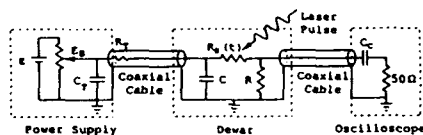


Fig. 3. Circuit diagram for the system. The oscilloscope is shown on AC coupling.

Most signals were recorded with 14-bit accuracy at 5000 points in time with signal averaging set at 1024 scans. Data was down-loaded to a DEC-Pro microcomputer and processed on a VAX 11/750 computer. One of the several electrical circuits successfully used for lifetime measurements is shown in Fig. 3.

DATA ANALYSIS TECHNIQUES

Several linear, iterative linear, and nonlinear least squares procedures were used to fit the data to Eq. (8) for the various models discussed above. One must make decisions on the following factors before fitting a curve: (a) the determination of the baseline--either letting it be a search parameter during the fit or using a fixed average of the data over some appropriate plateau region before or after the decay; (b) the theoretical model--using a single or multiple lifetime or more complex decay, or a convolution model; (c) the region of time for the curve fit--starting (1) at the beginning of the laser pulse, (2) immediately following the end of the laser pulse, or (3) after the early decay of very short effective lifetimes, and ending before or after the transient has decayed into the baseline; and (d) choice of weighting factors for the linear and nonlinear least squares fitting. Some laser pulses have long tails extending 10 - 20 times the FWHM past the peak. For these pulses one must use the convolution, Eq. (2), if the fitting region begins before t_L .

If the lifetime is known, a photoconductor can be used as a detector of the laser pulse with this system even if $\tau \gg t_L$. From Eq. (8), the excess carrier concentration $\Delta n(t)$ is found to be proportional to the voltage, $V_L(t)$, less the baseline, $I_0 R_L$. The laser pulse shape, $L(t)$, can be computed from the $V_L(t)$ data using Eq. (8) for $\Delta n(t)$ in Eq. (1) and numerically differentiating to obtain $L(t) \propto g(t)$. The lifetime τ for use in Eq. (1) can be obtained from the data as shown in Fig. 4.

EXPERIMENTAL RESULTS

A $\text{Hg}_{1-x}\text{Cd}_x\text{Te}$ sample grown at the Santa Barbara Research Center with the liquid phase epitaxy (LPE) method was selected for making extensive tests of the system and for studying the influence of system components and analysis parameters on the computed lifetime. The sample thickness was $5.3 \mu\text{m}$ and the x value was 0.26. Figure 4 shows a semi-logarithmic plot of the data observed at 77K. The spacing between data points was 4 ns and between laser pulses was 244 μs . The average laser power was less than 3 mW and the bias voltage applied to the sample was 1.5 volts.

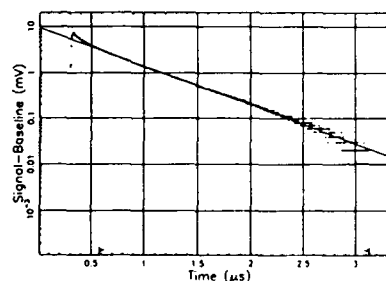


Fig. 4. Decay of photo-induced current for the HgCdTe SBRC sample at 77K and theoretical straight-line curve fit with $\tau = 514 \text{ ns}$.

The straight line is a theoretical fit computed with the nonlinear least squares program which searched for the baseline as well as the lifetime and transient amplitude over a five-lifetime time interval denoted by large tic marks with arrows. The following equation obtained by the program for the fit,

$$V(t) = -475.93 + 5.57 e^{-(t-284)/514}, \quad t > 585 \text{ ns}, \quad (9)$$

with V in mV, and t in ns is in excellent agreement with the data over two orders of magnitude of decay with a single lifetime of 514 ns. The early data lying above the theoretical curve may be due in part to the long tail of the laser pulse and in part to a short lifetime component in the decay.

The excess carrier lifetime for the SBRC sample increased from 298 ns at 300K to a maximum of 754 ns at 225K and then decreased to a minimum of 427 ns at 90K after which it increased to 514 ns at 77K. The accuracy of the lifetimes is 10-15% based on repeated measurements, the length of the fitting region, and the variation of values when analyzed with various fitting routines, weights, and fitting regions.

We next demonstrated the capability of the system to measure the shape of the laser pulse using this sample at 300K as a detector. The rise of the signal (upper points) is shown in Fig. 5 on a greatly expanded time scale. The straight line is a single lifetime fit ($\tau = 298$ ns) extrapolated back from the region of fit. The computed laser shape, shown as the lower curve (with arbitrary intensity units), has the same FWHM, 8.4 ns, as the laser pulse measured directly with a fast photodiode (shown in Fig. 6). Even the fine structure is resolved by the system. These results demonstrate the high frequency and risetime characteristics of the system as well as its accuracy and freedom of noise pickup.

Measurements of a HgCdTe sample grown at North Carolina State University (NCSSU) with the PAMBE method yielded single lifetimes which ranged from 46 ns at 300K to 341 ns at 77K. The thickness of the sample was 2.55 μm and the x value was 0.26.

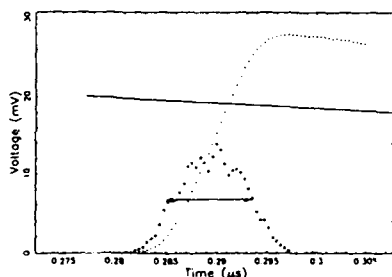


Fig. 5. Initial rise of photo-induced current for the SBRC HgCdTe sample at 300K (upper points) used to calculate the laser pulse shape and the calculated laser pulse shape (lower points). FWHM = 8.4 ns.

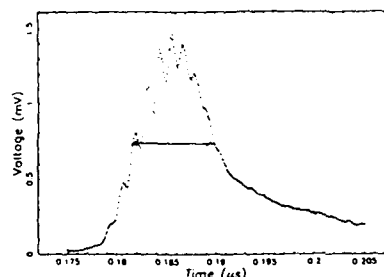


Fig. 6. Laser pulse measured with a fast silicon photodiode. FWHM = 8.4 ns. The modulated fine structure is caused by interference between components of the diffracted beam.

The CdTe samples grown with PAMBE at NCSU [4] exhibited a complex decay that required at least a two-lifetime model for fitting the longer lifetime components. Figure 7 shows a decay analysis for sample 292 at 77K for a two-component fit starting at 2 μ s after the laser pulse. The sample thickness was 5.05 μ m and Hall measurements at 80K, using the Van der Pauw method, showed it to have mobility, $\mu_n = 3.29 \times 10^3$ cm²/V·s with a carrier concentration, $n = 3.22 \times 10^{15}$ cm⁻³. The bias voltage for the sample was 1.0 volt, and laser's repetition rate and average power were 4.1 kHz and 2.4 mW, respectively. Shorter effective lifetime components exist in the decay prior to 2 μ s and are not shown. The upper points are the original data (less the baseline), and the straight line passing through the data is the long lifetime component, $V_1 e^{-t/\tau_1}$. The lower lying points were calculated by subtracting the extrapolated long lifetime component from the earlier data. The straight line through these points is the short lifetime component, $V_2 e^{-t/\tau_2}$. The theoretical curve $V_1 e^{-t/\tau_1} + V_2 e^{-t/\tau_2}$ completely overlays the earlier data points and the τ_1 curve at long times and is not separately discernible. The two longest effective lifetimes were 26 μ s and 4 μ s at 77K, and they did not vary significantly throughout the temperature range to 275K.

Two CdMnTe-CdTe superlattice samples produced by the PAMBE process using modulation doping with indium at NCSU [5,6] were investigated. The decays for these samples were also complex but had somewhat longer lifetimes than those of the CdTe samples. Sample 228 had a well thickness of 75 Å, and a mobility at 80K, $\mu_n = 4.4 \times 10^2$ cm²/V·s with a carrier concentration, $n = 1.01 \times 10^{16}$ cm⁻³. Room temperature values were $\mu_n = 2.55 \times 10^2$ cm²/V·s and $n = 3.15 \times 10^{16}$ cm⁻³. The curve fit for this sample in the region beginning at 2 μ s after the laser pulse required effective lifetimes of approximately 75 μ s and 10 μ s at 77K. These values decreased slightly as the temperature increased to 290K.

SUMMARY

The development and experimental demonstration of a state-of-the-art measurement and analysis system for determining the transient behavior of excess carriers in semiconductors with lifetimes ≈ 20 ns - 100 μ s over the temperature range 77K - 300K using the transient photoconductivity decay method have been described. Excess carrier lifetime results were presented for

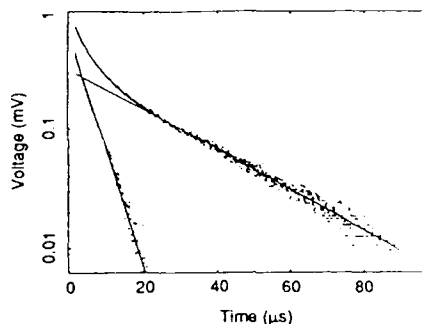


Fig. 7. Decay of photo-induced current for the NCSU CdTe sample 292 at 77K ($\tau_1 = 26 \mu$ s, $\tau_2 = 4 \mu$ s).

some II-VI films and superlattices. Additional measurements are required to extract minority carrier lifetimes from these results for comparison with theory [7]. This paper dealt primarily with a description of our experimental setup and a demonstration of its capability. Comparisons of data with physical parameters and theory will be presented in a later work.

ACKNOWLEDGMENTS

We would like to thank S. Hwang, N. C. Giles, Y. Lansari, D. L. Dreifus, R. L. Harper and J. W. Cook, Jr. for helpful discussions, for providing the grown samples, and for making the Hall measurements. This work was supported by DARPA contracts DAAL03-86-K-0146 and DAAL03-87-K-0153.

REFERENCES

1. John P. McKelvey, Solid State and Semiconductor Physics, (Robert E. Krieger Publishing Company, Malabar, Florida, 1966), Chap. 10.
2. Ronald D. Graft, Frederick F. Carlson, John H. Dinan, Phillip R. Boyd, and Randolph E. Longshore, J. Vac. Sci. Technol. A **1**, 1696 (1983).
3. D. E. Lacklison and P. Capper, Semiconductor Science and Technology **2**, 33 (1987).
4. S. Hwang, R. L. Harper, K. A. Harris, N. C. Giles, R. N. Bicknell, J. W. Cook, Jr., Jan F. Schetzina, and M. Chu, J. Vac. Sci. Tech. A **6**, 2822 (1988).
5. R. L. Harper, S. Hwang, N. C. Giles, R. N. Bicknell, Jan F. Schetzina, Y. L. Lee, and A. K. Randas, J. Vac. Sci. Tech. A **6**, 2628 (1988).
6. D. L. Dreifus, R. M. Kolbas, R. L. Harper, J. R. Tassitino, S. Hwang, and Jan F. Schetzina, Appl. Phys. Lett. **53**, 1279 (1988).
7. Y. Nemirovsky and R. Fastow, Proc. of the 1989 MRS Fall Meeting, Boston, MA (paper E7.1).

PART V

Novel Growth and
Characterization

PHOTOASSISTED MBE OF II-VI SEMICONDUCTOR FILMS AND SUPERLATTICES

N.C. GILES*, R.L. HARPER**, J.W. HAN, AND J.F. SCHETZINA
Dept. of Physics, North Carolina State University, Raleigh, NC
27695-8202

*Present Address: Dept. of Physics, West Virginia University,
Morgantown, WV 26506

**Present Address: Dept. of Physics and Astronomy, Western
Kentucky University, Bowling Green, KY 42101

ABSTRACT

This paper will review recent progress in the growth of II-VI semiconductors at NCSU by photoassisted molecular beam epitaxy, an energy-assisted growth technique in which the substrate is illuminated during the entire growth process. The materials focused on here include undoped and As-doped CdTe, As-doped HgCdTe, and In-doped HgCdTe. These materials were grown as single epilayers, as well as incorporated in other structures including heterojunctions and modulation-doped superlattices. The photo-assist during growth has allowed a substantial reduction in substrate growth temperatures, as well as an enhanced activation of n-type and p-type dopant species. The structural, electrical, and optical properties of the samples will be discussed below.

INTRODUCTION

The family of II-VI semiconductors has long received interest from the electro-optics community owing to their wide range of bandgaps from the ultraviolet (UV) to the infrared (IR). Efforts in recent years at laboratories around the world have focused on the lingering problem of establishing control over n-type and p-type doping in the II-VI's. In 1986, at North Carolina State University (NCSU), a new growth technique called photoassisted molecular beam epitaxy (MBE) was reported to give control over n-type and p-type doping in CdTe [1,2]. The first all thin film in-situ-grown CdTe pn-junction was reported soon after the initial work [3]. Enhanced doping using the photoassisted technique has since been reported in other II-VI semiconductors, including thin films of CdMnTe and CdMnTe-CdTe superlattices [4], and HgCdTe [5]. Reports of devices made from these doped thin films [6-8] show great promise for future applications of II-VI materials.

The intent of this paper is to summarize progress achieved at NCSU using the photoassisted MBE technique. An overview of experimental techniques and materials' properties will be presented. However, for a more detailed explanation of the many growth experiments pursued since 1986, the reader is advised to refer to the publications list in the reference section of the paper, and to companion papers included in this volume. The materials systems that are focused on here include undoped and doped CdTe and HgCdTe. The dopant species which have been employed are As as a p-type dopant, and In as an n-type dopant. The parameters used in the various growth experiments are summarized in the following section. A description of the structural, electrical, and optical properties of selected films and multilayer structures then follows.

EXPERIMENTAL DETAILS

The CdTe and CdTe:As doped films were grown on high quality chemimechanically polished (100) and (111) bulk CdTe substrates. Prior to insertion in the MBE system, the substrates were degreased and rinsed in deionized (DI) water, briefly dipped in a 1:1 mixture of hydrochloric acid and DI water, and given a final rinsing in DI water. (Omission of the HCl dip was investigated for some samples.) Preheat temperatures of between 300 °C and 400 °C were used to drive off the native oxide. Substrate temperatures (T_s) employed ranged from 75 °C to 230 °C.

The illumination source used during the film growth experiments was a Spectra-Physics model 171 argon ion laser with broadband yellow-green optics. The laser beam was coupled into a fiber optic cable inside the growth chamber which directed the light onto the substrate surface. The photon energies associated with the incident photon flux on the growth surface lie in the range from ~2.3-2.7 eV. The laser power density at the substrate during film growth was varied from 50-150 mW/cm². For this range in power densities, substrate heating effects are expected to be negligible. The incident photon flux is about 10^{17} photons/sec-cm². For growth of the undoped CdTe epilayers, two ovens containing high purity polycrystalline CdTe were used. Oven temperatures were adjusted such that typical MBE growth rates of 0.5-2.0 Å/sec were obtained. For growth of CdTe:As layers, an additional oven containing elemental As was employed. Arsenic oven temperatures from 160 °C to 200 °C were used to vary the incorporation rate of the p-type dopant.

Design details for the Hg-compatible MBE systems at NCSU have been reported earlier [9]. MBE source ovens, equipped with computer-controlled shutters and filled with CdTe, Te, and Hg were used in the film growth experiments. For modulation doping, ovens with elemental As or In were employed. The Hg-compatible systems were modified for photoassisted MBE growth experiments by replacing one of the MBE ovens on the main source flange with an ultra-high vacuum Pyrex window. The broadband blue-green output from a Spectra-Physics model 2016 argon ion laser was beam-expanded, collimated, and directed through the window allowing uniform illumination of the substrate surface. Power densities employed ranged from 40-100 mW/cm².

The HgCdTe samples were grown on polished lattice-matched (100) Cd_{0.96}Zn_{0.04}Te substrates. Immediately prior to film growth, the substrates were preheated at 300 °C for 10 minutes in the MBE chamber to drive off residual impurities and to insure a stoichiometric growth surface. A substrate temperature of 170 °C was used throughout the HgCdTe film growth experiments.

The structural quality of the CdTe and HgCdTe samples was assessed using a Blake Industries double-crystal x-ray diffractometer with a Phillips x-ray generator (Cu K α x-rays). This instrument has a rocking curve resolution of 1 arc sec.

Van der Pauw Hall effect measurements were performed on the doped samples over the temperature range 20-300 K to determine carrier type, concentration, and mobility.

The optical properties of the CdTe films were investigated using photoluminescence spectroscopy over the temperature range from 1.6 K to 300 K. The samples were mounted in a Janis Research Products SuperVaritemp optical cryostat. The PL signal was excited using the chopped output from a Spectra-Physics He-Ne

laser focused onto the sample surface giving a power density of ~ 2 W/cm². A SPEX double monochromator with a GaAs photomultiplier tube and lock-in amplifier were used to measure the PL signal.

Selected samples from the series of modulation doped Hg-based structures were analyzed using IR PL spectroscopy at liquid helium temperatures. The PL signal was excited using the chopped output from a Nd:YAG laser focused to a spot on the sample surface to give a power density of ~ 200 W/cm². A SuperVaritemp cryostat with ZnSe infrared windows was employed to cool the samples to 4.2 K. The signal was detected using a Nicolet 60SXR Fourier-Transform-Infrared (FTIR) spectrometer and lock-in amplifier.

PL under high power cw excitation was completed on undoped Hg-based multilayers. The films were chemically removed from the substrates using a selective etching solution consisting of 8 grams K₂Cr₂O₇, 20 ml of nitric acid, and 40 ml of DI. We have used this solution for removal of both CdTe and Cd_{0.96}Zn_{0.04}Te substrates. The multilayered film structures were cleaved with a sharp scalpel to form rectangular parallelepipeds and then pressed into indium. The laser cavities were optically pumped using the 1.064 μ m Nd:YAG laser output (cw). Power densities employed range from 1 to 7 kW/cm² at the sample surface. The PL emission was collected and analyzed using the FTIR spectrometer.

RESULTS AND DISCUSSION

CdTe

Undoped CdTe films grown under illumination are often n-type, as-grown. The conductivity is, however, dependent on substrate preparation, and on the incident illumination power density. The electrical properties of undoped films grown under a power density of ~ 90 mW/cm² were reported earlier [10]. Room temperature carrier concentrations in the range from $2-4 \times 10^{15}$ cm⁻³ and electron mobilities as high as 6600 cm²/V-sec were measured from films grown at T_s = 230 °C (Fig. 1(a)). The donor level responsible for the n-type behavior is believed to be Cl_{Te}, originating from the HCl dip used during the substrate preparation. Indeed, the films grown with the HCl dip omitted were high resistivity, using the same illumination power density during growth.

A study of the PL emission from the n-type undoped films grown under 90 mW/cm² was performed over the temperature range from 1.6-300 K [11]. A typical low temperature spectrum is shown in Fig. 1(b). The bright sharp PL peaks attest to the optical quality of the films grown. The emission at 1.5973 eV is attributed to free exciton (X) recombination. The dominant emission line occurs at 1.5935 eV, and is attributed to superpositions of (D⁰_{Cl,h}) and (D⁰,X) recombinations. The X emission could be well-resolved up to T = 140 K. The PL signal at higher temperatures was found to originate from the 1.5935 eV transition seen at liquid helium temperatures.

Growth experiments using illumination power densities of ~ 150 mW/cm² yielded undoped n-type CdTe films with electron concentrations of over 10^{17} cm⁻³ (see Fig 2). The PL spectrum from one such film is shown in Fig. 3. Note that the PL spectrum is dramatically different from that shown in Fig. 1(b). The dominant PL recombination peak occurs at 1.56 eV in the highly conducting

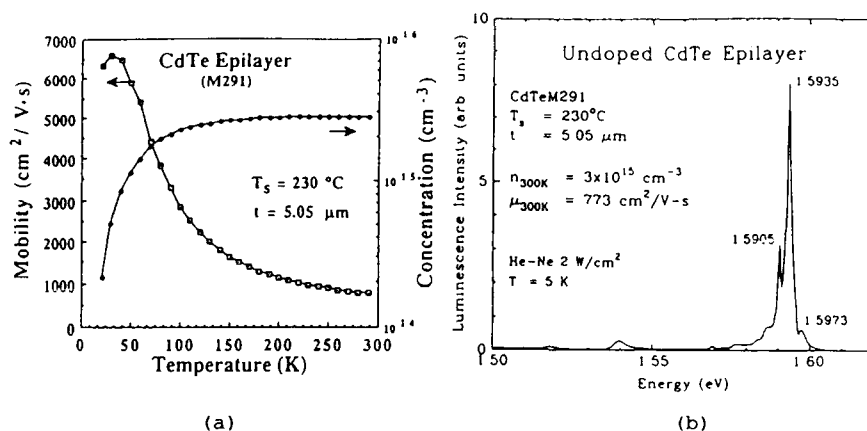


Fig. 1. (a) Carrier concentration and mobility vs. temperature for n-type undoped CdTe film grown under 90 mW/cm² illumination; (b) Low temperature PL spectrum (5 K) showing Cl_{Te} donor-related transition at 1.5935 eV.

n-type films. We do not believe the n-type conductivity is due to residual Cl contamination. We have observed similar spectra from bulk CdTe, which was non-stoichiometric after annealing [12]. We

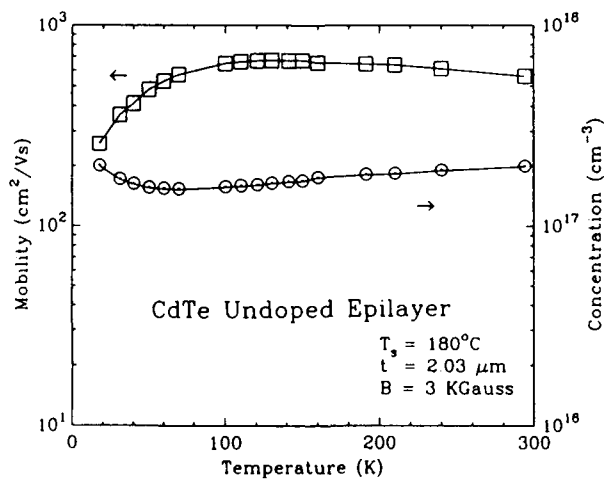


Fig. 2. Plot of carrier concentration and mobility vs. temperature for n-type undoped CdTe film grown under 150 mW/cm² illumination.

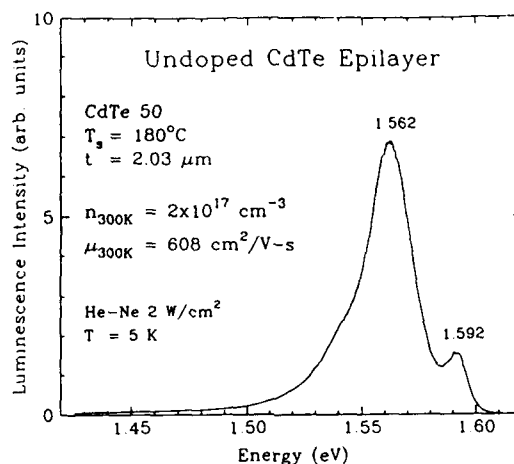


Fig. 3. Low temperature PL spectrum (5 K) from undoped CdTe grown under 150 mW/cm^2 illumination showing main peak at 1.56 eV, giving evidence of non-stoichiometry.

believe a native defect is responsible for the conductivity observed, as explained below.

The effect of incident illumination on the desorption rate of Te_2 from the growth surface of CdTe has been studied using RHEED measurements [13]. An increase in the desorption rate of the Te species was reported, suggesting that the film growth surface would then be non-stoichiometric (Cd-rich). We suggest, then, that the incorporation of residual impurity atoms on Te sites, D_{Te} (such as Cl_{Te}) would then be favored. Under high laser illumination intensity, the number density of the Te vacancies could exceed the concentration of residual donor impurities, while the film growth surface would still be rich in Cd. Both Cd interstitials and Te vacancies act as n-type dopants, and this, we believe, is the reason for the high excess electron concentration observed from films grown under the higher power densities.

A second RHEED study [14] concludes that argon laser light could affect the desorption rates of both the Cd and Te species. This is consistent with PL studies performed on undoped CdTe films grown by photoassisted MBE [15], in which Cd vacancy-donor complex centers ($\text{Cd}_v\text{-D}_{\text{Te}}$, and $\text{D}_{\text{Te}}\text{-Cd}_v\text{-D}_{\text{Te}}$) were observed. The altering of the stoichiometry of the film growth surface is further supported by the report that illumination of the substrate during CdTe film growth is similar to using an additional Cd flux [16]: the Cd/Te ratio is increased in either case.

The photoassisted MBE technique has allowed us to substantially lower the minimum substrate growth temperature T_s at which single crystalline films are obtained. We obtain single-crystal films using $T_s = 100^\circ\text{C}$, which represents a dramatic reduction from the value of 275°C normally employed for homoepitaxial growth of CdTe by conventional MBE (without laser light).

CdTe:As

High quality p-type films have been prepared by photoassisted MBE by doping CdTe with As [17]. Hole concentrations in the 10^{18} cm^{-3} range have been obtained. A lowering of substrate temperature was also investigated with the CdTe:As films. X-ray rocking curves for films grown at 125 °C and 150 °C are shown in Fig. 4.

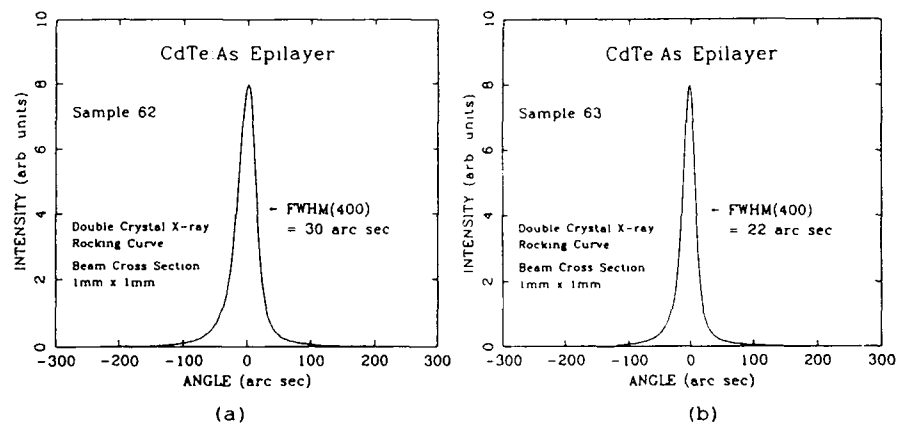


Fig. 4. Double crystal x-ray rocking curves for CdTe:As films grown at (a) 150 °C (#62), and (b) 125 °C (#63).

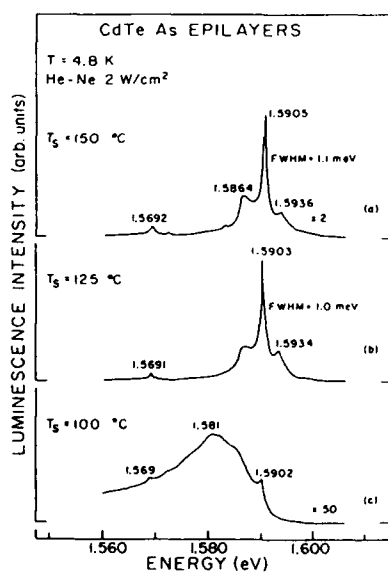


Figure 5. Near-edge PL spectra for CdTe:As films grown at (a) $T_s=150$ °C; (b) $T_s=125$ °C; and (c) $T_s=100$ °C.

The films grown at low T_s exhibit sharp bright excitonic PL emission peaks at low temperature, as shown in Fig. 5. Single-crystal films were grown at $T_s = 100^\circ\text{C}$, however, the optical properties were degraded, as seen in Fig. 5(c).

Modulation-Doped HgCdTe

Photoassisted MBE has been used to grow a series of modulation-doped HgCdTe samples containing doped $\text{Hg}_{0.15}\text{Cd}_{0.85}\text{Te}$ barrier layers [5,18]. Because these barrier layers are ~ 50 Å thick, and well layers are on the order of ~ 1000 Å thick, these structures are essentially δ -doped. Cross-sectional bright-field TEM images [19] of the structures show that a high degree of regularity and structural quality was obtained. Both p-type and n-type structures have been grown, using As and In dopants in the barrier layers, respectively. Double crystal x-ray rocking curves for representative samples are shown in Fig. 6, showing the main

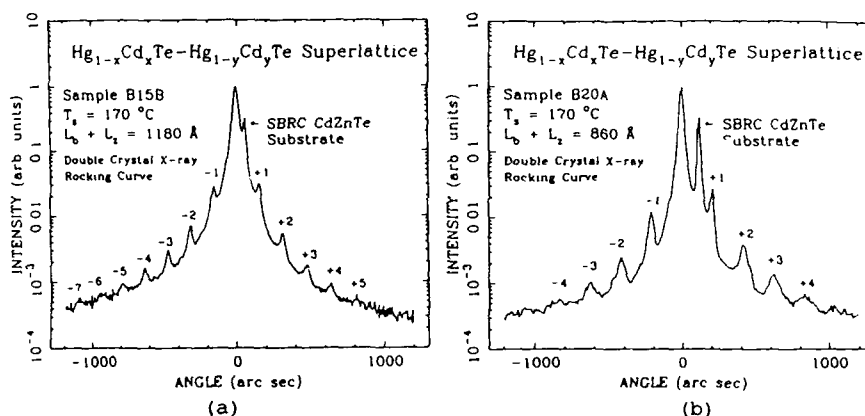


Fig. 6. Double crystal x-ray rocking curves showing several orders of satellites for (a) p-type $\text{Hg}_{0.15}\text{Cd}_{0.85}\text{Te}:\text{As}-\text{Hg}_{0.74}\text{Cd}_{0.26}\text{Te}$; and (b) n-type $\text{Hg}_{0.15}\text{Cd}_{0.85}\text{Te}:\text{In}-\text{Hg}_{0.8}\text{Cd}_{0.2}\text{Te}$ superlattices.

SL diffraction peak and several orders of satellites. Diffraction peak FWHMs in the range ~ 20 - 30 arc sec are measured.

Van der Pauw Hall effect measurements were recorded from 20-300 K. Average hole concentrations ranging from $p=10^{16}$ - 10^{18} cm^{-3} are obtained by varying the dopant even temperature during the various film growth experiments. Electron concentrations in n-type samples range from $n=10^{17}$ - 10^{18} cm^{-3} . Fig. 7 shows the carrier concentration vs. temperature for p-type and n-type samples. The p-type sample has a $\text{Hg}_{1-x}\text{Cd}_x\text{Te}$ well layer for which $x=0.24$. The hole concentration (10^{18} cm^{-3}) is a factor of 5 larger than the maximum solubility of Hg vacancies in HgCdTe for this x -value. This provides evidence that the holes come from the As ions in the barrier layers and are transferred to the wells. Hole freeze-out at low temperatures is not observed in the modulation-doped

structures since there are no acceptor ions present in the smaller band-gap well layers. The hole mobilities are comparable to mobilities in bulk HgCdTe due to the large thickness of the well layers (~ 1000 Å). We also note that the valence band offset (VBO) must be large enough to allow the charge transfer from the As ions in the barrier layers. A lower limit to the VBO for the HgTe/CdTe interface was determined to be 95 meV from 20-300 K [18].

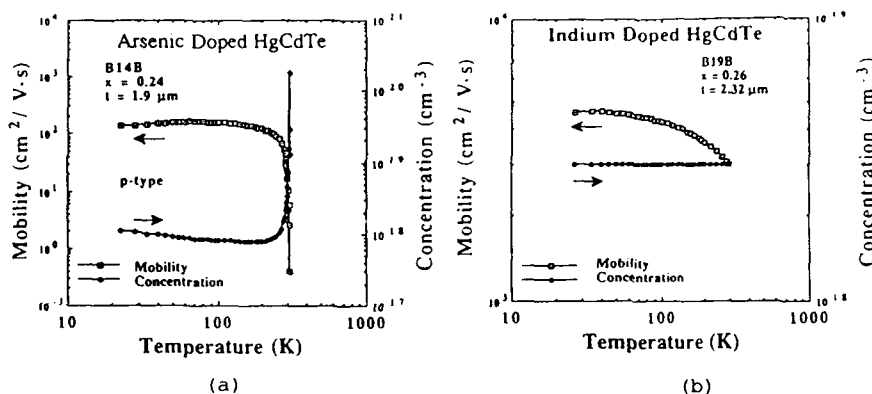


Fig. 7. Hall data for modulation doped HgCdTe superlattices.

Hall data for an n-type sample with well layer x -value of 0.21 is shown in Fig. 7(b). Again, the average carrier concentration is independent of temperature. Since the carrier densities shown in Fig. 7 are determined by assuming a uniform sample, the data implies extremely high doping levels were achieved in the 50 Å thick barrier layers. For our highest doping levels obtained to date, we estimate that As and In ion densities $> 10^{19} \text{ cm}^{-3}$ exist in the barrier layers. High doping levels are expected to produce extremely large band distortions in the vicinity of the heterointerfaces, giving rise to one or more localized (two-dimensional) carrier states. A self-consistent approach to calculating localized hole and electron ground state energies has shown that carriers are tightly bound at these states, thus reducing their mobilities [18].

P-type modulation doped HgCdTe superlattices have also been grown by alternately depositing $\text{Hg}_{0.3}\text{Cd}_{0.7}\text{Te}:\text{As}$ barrier layers with undoped $\text{Hg}_{0.78}\text{Cd}_{0.22}\text{Te}$ well layers. In this way, superlattices consisting of 200 double layers were prepared. The thickness of the $\text{Hg}_{0.3}\text{Cd}_{0.7}\text{Te}:\text{As}$ doping layers was $L_b \sim 50$ Å in each of the superlattices, with the As dopant uniformly distributed (no setback). For the small-band-gap well layers, $\text{Hg}_{0.78}\text{Cd}_{0.22}\text{Te}$ of thickness $L_w = 50\text{-}104$ Å was used in the various superlattice growth experiments. To prepare n-type modulation-doped HgCdTe superlattices, the wide-band-gap $\text{Hg}_{0.3}\text{Cd}_{0.7}\text{Te}$ barrier layers were doped with In rather than As. A summary of measured sample properties appears in companion papers in this volume.

Preliminary growth experiments of n-type modulation-doped heterostructures of HgCdTe which contain an undoped spacer layer have also been completed. These multilayered structures consist

of a ~ 200 Å doping layer of $\text{Hg}_{0.3}\text{Cd}_{0.7}\text{Te}:\text{In}$ onto which is deposited an undoped $\text{Hg}_{0.3}\text{Cd}_{0.7}\text{Te}$ spacer layer followed by a 2000 Å layer of $\text{Hg}_{0.78}\text{Cd}_{0.22}\text{Te}$. The spacer layer thickness was varied from 50–420 Å in the various MBE growth runs. Electron transfer was not observed for the thick spacer layers. N-type conduction was observed for spacer layers < 100 Å. Electron mobilities were fairly temperature-independent. Our results suggest that spacer layers thicknesses of ≤ 100 Å must be employed, if effect charge transfer is to be realized.

P-type and n-type modulation-doped superlattices consisting of 200 double layers of $\text{Hg}_{0.3}\text{Cd}_{0.7}\text{Te}$ - HgTe have also been prepared and studied. Details of that work are also presented elsewhere in this volume.

HgCdTe Lasers

HgCdTe is usually considered as the material of choice for photodetection in the infrared. However, we have observed bright PL from samples grown by photoassisted MBE, even at room temperature. To exploit the light-emitting properties which this material exhibits, we began initial studies to investigate the possibility of using HgCdTe as an IR laser material for the wavelength emission range from 2–5 μm . (This wavelength range includes one of the atmospheric windows.) Theoretical predictions for high-temperature limits of laser oscillation show that HgCdTe is expected to be comparable to InAs-based laser structures [20] from 2–5 μm . For lasing beyond 5 μm , HgCdTe is not expected to compete successfully with the PbSeTe system. For emission at $\lambda < 2$ μm , InGaAsP is often used as a laser material, however, a study of Auger recombination processes favors HgCdTe over this III-V semiconductor even for output at 1.55 μm [21].

Stimulated emission under high power cw optical excitation has been observed from Hg-based quantum well structures grown by photoassisted MBE [22]. Refer to Fig. 8 for a schematic of the laser structure. The active region is a superlattice composed of

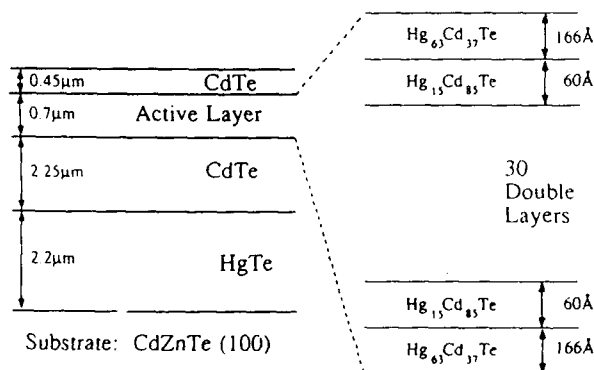


Fig. 8. Schematic of laser double-heterostructure with HgCdTe superlattice active region.

31 quantum wells of $\text{Hg}_{0.63}\text{Cd}_{0.37}\text{Te}$ ($L_z \sim 166\text{\AA}$) alternating with 30 barrier layers of $\text{Hg}_{0.15}\text{Cd}_{0.85}\text{Te}$ ($L_b \sim 60\text{\AA}$). The superlattice is sandwiched between two wide-band-gap HgCdTe layers as shown, thus forming a double-heterostructure. Cavity modes were observed using cw laser power densities as low as 3.4 kW/cm^2 . Under increased optical pumping, many emission modes appear superimposed on the spontaneous PL background. In Fig. 9 is shown the below-threshold PL emission at 5 K from a $65\text{ }\mu\text{m}$ wide cavity centered at about $2.8\text{ }\mu\text{m}$, and a spectrum showing the many cavity modes which result at higher pumping powers.

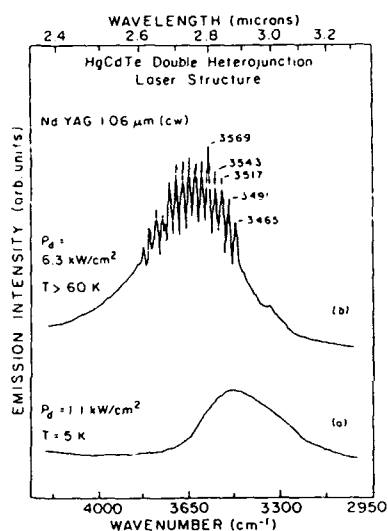


Fig. 9. Stimulated emission from a $65\text{ }\mu\text{m}$ wide cavity: (a) PL emission at 5 K below threshold; (b) Stimulated emission cavity modes superimposed on PL background at $T > 60\text{ K}$.

Considerable sample heating occurred when the laser cavities were illuminated with the cw Nd:YAG output. We made two estimates of the sample temperature increase by considering the temperature-induced shift in the bandgap [22]. Note in Fig. 9, that the observed shift in the PL background emission peak energy from the below-threshold spectrum to the stimulated emission spectrum amounts to 21 meV. One estimate based on the energy bandgap shift of a single epilayer subjected to identical pumping conditions gave an increase of temperature to 50 K. The other estimate used the observed 21 meV shift in the experimental data and related that to a temperature increase of 160 K! Therefore, we have conservatively listed the temperature of the stimulated emission spectrum of Fig. 9(b) as $T > 60\text{ K}$.

The observation of stimulated emission in Hg-based heterostructures of the type described here is especially important since multilayers having this layered structure are also appropriate for fabricating injection lasers by doping the two HgCdTe cladding layers on either side of the active superlattice region n-type and p-type, respectively. Both n-type and p-type doping of HgCdTe by photoassisted MBE has been demonstrated at NCSU. Thus, fabrication of injection lasers may soon be possible. And, if the sample temperature is as high as 160 K, then HgCdTe lasers operating at temperatures at, or above, liquid nitrogen

temperature are indeed possible. We should note that in addition to our results obtained from samples grown with the photo-assist, optically-pumped lasing action in HgCdTe grown by conventional MBE has also been observed [23].

CONCLUSIONS

We have reviewed here recent growth experiments using photo-assisted MBE to control n-type and p-type doping of II-VI semiconductors. The achievements to date include p-type doping of CdTe with As yielding excess hole concentrations in the range of 10^{18} cm^{-3} at room temperature. Single crystal CdTe and CdTe:As can be grown at temperatures as low as 100 °C. This reduction in substrate temperature is especially important when designing a thin-film-structure (such as a superlattice) incorporating layers of CdTe and HgCdTe, since interdiffusion between layers can be substantial at temperatures normally used to grow high quality CdTe. In addition, the growth studies of the undoped CdTe shed some insight on the mechanisms involved in the photo-assisted growth process. The incident illumination is altering the stoichiometry of the growth surface. N-type conductivity in undoped CdTe films can stem from residual donor impurity atoms on Te-sites, or from native defects such as Cd interstitials, or Te vacancies.

Photoassisted MBE has been used to grow modulation-doped HgCdTe structures. The dopant species, either As (p-type) or In (n-type) reside in the wide bandgap barrier layers. High average hole and electron concentrations have been obtained in structures that incorporate no set-back, yielding doping densities as high as 10^{19} cm^{-3} in the thin (~50 Å) δ -doped barrier layers. Substantial distortion of bands near the heterointerfaces are predicted to occur causing formation of localized (two-dimensional) hole and electron states in the p-type and n-type structures.

And, finally, initial HgCdTe IR laser studies have begun. The Hg-based samples are bright emitters of PL. Optically-pumped stimulated emission cavity modes at ~3 μm have been observed from a double heterostructure in which the active region is a superlattice. We are optimistic about the viability and competitiveness of HgCdTe lasers in the emission range from 1.55 μm to 5 μm .

ACKNOWLEDGEMENTS

The authors gratefully acknowledge support from the National Science Foundation (under grant DMR-88-13525), the Navy Research Laboratory (contract N00014-89-J-2024), and General Electric Aerospace Group IR & D funds. We also thank Dr. S. Hwang for the x-ray and Hall effect data shown here.

REFERENCES

1. R.N. Bicknell, N.C. Giles, and J.F. Schetzina, Appl. Phys. Lett. **49**, 1095 (1986).
2. R.N. Bicknell, N.C. Giles, and J.F. Schetzina, Appl. Phys. Lett. **49**, 1735 (1986).
3. R.N. Bicknell, N.C. Giles, J.F. Schetzina, and C. Hitzman, J. Vac. Sci. Technol. **A 5**, 3059 (1987).

4. R.N. Bicknell, N.C. Giles, and J.F. Schetzina, Appl. Phys. Lett. **50**, 691 (1987).
5. Jeong W. Han, S. Hwang, Y. Lansari, R.L. Harper, Z. Yang, N.C. Giles, J.W. Cook, Jr., J.F. Schetzina, and S. Sen, Appl. Phys. Lett. **54**, 63 (1989).
6. D.L. Dreifus, R.M. Kolbas, J.R. Tassitino, R.L. Harper, R.N. Bicknell, and J.F. Schetzina, J. Vac. Sci. Technol. **A 6**, 2722 (1988).
7. D.L. Dreifus, R.M. Kolbas, R.L. Harper, J.R. Tassitino, S. Hwang, and J.F. Schetzina, Appl. Phys. Lett. **53**, 1279 (1988).
8. D.L. Dreifus, R.M. Kolbas, J.W. Han, J.W. Cook, Jr., and J.F. Schetzina, to appear in J. Vac. Sci. Technol. (Proc. of 1989 U.S. Workshop on MCT).
9. J.W. Cook, Jr., K.A. Harris, and J.F. Schetzina, Mater. Res. Soc. Symp. Proc. Vol. **90**, 419 (1987).
10. S. Hwang, R.L. Harper, K.A. Harris, N.C. Giles, R.N. Bicknell, J.W. Cook, Jr., J.F. Schetzina, and M. Chu, J. Vac. Sci. Technol. **A 6**, 2821 (1988).
11. N.C. Giles, K.A. Bowers, R.L. Harper, Jr., S. Hwang, and J.F. Schetzina, to appear in J. Crystal Growth (Proc. of 1989 Int. II-VI Conf.).
12. N.C. Giles, S. Hwang, J.F. Schetzina, S. McDevitt, and C.J. Johnson, J. Appl. Phys. **64**, 2656 (1988).
13. J.D. Benson and C.J. Summers, J. Crystal Growth **86**, 354 (1988).
14. J.M. Arias, S.H. Shin, D.E. Cooper, M. Zandian, J.G. Pasko, E.R. Gertner, R.E. DeWames, and J. Singh, to appear in J. Vac. Sci. Technol. (Proc. of 1989 U.S. Workshop on MCT).
15. W. Ossau, T.A. Kuhn, and R.N. Bicknell-Tassius, to appear in J. Crystal Growth (Proc. of 1989 Int. II-VI Conf.).
16. R.N. Bicknell-Tassius, A. Waag, Y.S. Wu, T.A. Kuhn, and W. Ossau, to appear in J. Crystal Growth (Proc. of 1989 Int. II-VI Conf.).
17. R.L. Harper, Jr., S. Hwang, N.C. Giles, J.F. Schetzina, D.L. Dreifus, and T.H. Myers, Appl. Phys. Lett. **54**, 170 (1989).
18. Jeong W. Han, S. Hwang, Y. Lansari, R.L. Harper, Z. Yang, N.C. Giles, J.W. Cook, Jr., J.F. Schetzina, and S. Sen, J. Vac. Sci. Technol. **A 7**, 305 (1989).
19. J.F. Schetzina, J.W. Han, Y. Lansari, N.C. Giles, Z. Yang, S. Hwang, and J.W. Cook, Jr., to appear in J. Crystal Growth (Proc. of 1989 Int. II-VI Conf.).
20. Y. Horikoshi, in Semiconductors and Semimetals, Vol. **22**, Part C, Chapter 3, ed. W.T. Tsang (Academic Press Inc., 1985) p.93.
21. A. Haug, Semicond. Sci. and Technol. **4**, 803 (1989).
22. N.C. Giles, J.W. Han, J.W. Cook, Jr., and J.F. Schetzina, Appl. Phys. Lett. **55**, 2026 (1989).
23. K.K. Mahavadi, J. Bleuse, X. Chu, and J.P. Faurie, Appl. Phys. Lett. **55**, 1285 (1989).

GROWTH AND INITIAL CHARACTERIZATION OF NOVEL HGTE-BASED II-VI MATERIALS

F.G. Moore*, J.C. Abele** and R.E. Kremer***

*MC - 6832, Naval Research Laboratory, Washington, D.C. 20375

**Department of Physics, Lewis and Clark College, Portland, OR 97219

***Crystal Specialties, Colorado Springs, CO. 80906

ABSTRACT

Hg_{1-x}A_xTe materials where A={Be, Mg, Ba, Sr, Ca} have been synthesized by the vertical Bridgman technique. Hydrostatic density measurements showing segregation are presented and for HgMgTe an effective segregation coefficient is obtained. For HgMgTe a relationship between bandgap E_g and composition x , is developed based on FTIR measurements of cut-on wavelengths. The variation of energy gap with composition is found to be comparable to that of HgMnTe and twice as rapid as that of HgCdTe. Carrier concentration and mobility data from room temperature and 77K Hall measurements are presented for samples annealed in a saturated overpressure of Mercury.

INTRODUCTION

The bulk growth of HgTe-based ternaries (having the general form Hg_{1-x}A_xTe; for example Hg_{1-x}Cd_xTe) is extremely difficult when compared with other semiconducting materials[1]. Standard and modified bulk growth techniques are often limited to boules one to two centimeters in diameter, and thus may never be able to produce large enough samples for some device applications. Still, the equilibrium bulk growth processes, unlike much of the growth based on epitaxy, offers some unique advantages for producing material that may be used to divine more basic information about material properties. Further, the equipment and associated techniques needed to produce novel HgA_xTe materials do not differ substantially from those needed to produce more standard HgTe-based materials.

Of the six possible II(A)-VI HgTe-based ternaries we report the bulk growth of HgBeTe, HgMgTe, HgCaTe, HgSrTe and HgBaTe. Of these growths HgMgTe has been the most extensively studied while a growth of HgBeTe, though completed, has remained completely unstudied for health concerns[2]. Lastly some comparisons are made between the rather novel materials mentioned above and their better known siblings HgCdTe and HgMnTe.

CRYSTAL GROWTH

Growth ampoules were fabricated using standard quartz tubing with a wall thickness of two millimeters. The first-to-freeze end was tapered gradually over approximately 2 cm to form a tip. A ground glass joint was affixed to the upper end of the ampoule just above a pinched region added to facilitate sealing the ampoule after it is charged and evacuated. An ampoule length, measured from the tip to below the pinched region, of nine to ten inches is normally satisfactory for a charge mass of 50-80 grams. Prior to charging the ampoules were thoroughly cleaned and their inner surfaces were deposited with a layer of carbon to guard against adverse, high-temperature interactions between the quartz and the ampoule's charge.

Growth was accomplished in one of two nominally identical Marshall Furnace Company, Model 1138 two-zone furnaces. Modifications had been made to the transport mechanism to provide slower pull rates. The temperature controllers are of the Omega CN-2010 series with two type R (Pt:Pt + 13% Rh) thermocouples used to measure of temperature during growth.

For these novel growths the upper zone temperature was 850° and the lower zone 675°. Both zones were ramped quickly to 700° then raised to 800° over a period of 24 hours. The growth was allowed to synthesize and mix for another 24 hours. The two zones then ramped to their respective growth temperatures over the course of several hours after which the transport system was engaged.

Growth speed and segregation are closely related[3] and there appears to be a tradeoff between radial and longitudinal segregation in HgCdTe[4], and in HgMnTe[5]. For reasons outside the scope of this report it was deemed important to have maximum radial uniformity. This was accomplished by adjusting the pull rate to one millimeter per hour during material growth. Data from the previously cited sources indicates that this growth rate will produce HgCdTe and HgMnTe material with greater radial than longitudinal uniformity. It was hoped that this trend would hold for the more novel materials. Indeed the longitudinal segregation can be advantageous in that it produces samples of varying compositions within a single growth, that can be compared against each other.

DENSITY MEASUREMENTS

Initial characterization of these materials consisted of hydrostatic density measurements[6]. Since the lattice parameter of the ternary is a function of the composition, i.e. $a_0 = a_0(x)$, it follows that the density is also a function of composition. Knowing this functional relationship one can determine the average composition of each section of the ingot on which a density measurement was performed. Since the binaries MgTe, CaTe, SrTe, and BaTe do not occur in the zincblende structure, Vegard's law[7] cannot be applied to generate a relationship between composition and density. However, if the concentration of the minority constituent, for example Mg, is kept low the resulting material may form in a zincblende phase up to some critical concentration[8] below this value an empirical relationship between density and composition can be obtained. For HgMgTe the relationship was extracted from published results[9] and found to be:

$$\rho(x) = 8.063 - 4.826x, \quad (1)$$

where the units of ρ are grams/cm³. For the other novel materials no thorough study has been made to determine $\rho(x)$.

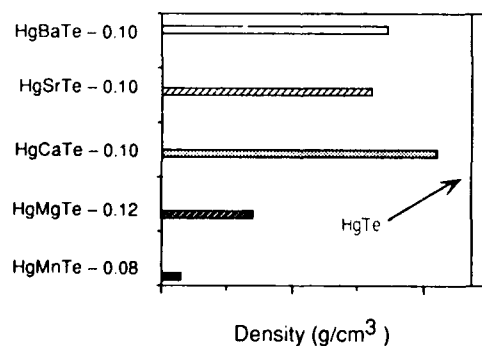


Figure 1: Average measured density of several HgTe-based materials. The density of HgTe is indicated for reference.

Figure 1 shows a bar graph of the average measured densities of the novel HgTe-based materials and for HgTe. The intention of this chart is to demonstrate that the minority constituents (HgATe: A=Mn, Mg, Ca, Sr, Ba), have been incorporated into the growth. For Mg and Mn (the latter for comparison purposes) the density variation with position along the ingot are consistent with a non-unity segregation coefficient. The materials containing Ca, Sr and Ba all showed dramatic fluctuations in density along the ingot indicative of incomplete mixing and/or multiple phases being present. The values obtained for Figure 1 were averaged from outside these regions.

SEGREGATION

For the case of normal freezing Pfann[10] has described the segregation in a growth by:

$$C_s/C_o = K(1-g)^{K-1} \quad (2)$$

where g is the mass-fraction of the melt which has solidified and K is the segregation coefficient. C_s and C_o are, respectively, the concentrations of the solute, for example Mg, in the solid and the nominal concentration of the solute in the growth. A freezing rate which is less than infinite generates a non-equilibrium situation and this equation is no longer strictly valid. In this case the effective segregation coefficient is a function of, at the least composition and growth rate. For HgMgTe it proved possible to generate an effective segregation coefficient for the growth conditions described above. An iterative technique described in the literature was used[11].

From density measurements the concentration of Mg in the solid was determined as a function of g and a relationship was found between $\log(C_s/C_o)$ and $\log(1-g)$. Equation (2) was then cast in the form:

$$\log(C_s/C_o) = \log(K_{eff}) + [K_{eff}-1]\log(1-g). \quad (3)$$

This relationship was then solved iteratively for K_{eff} over the range $0 \leq x \leq 0.09$. Figure 2 shows the results of this iterative technique. Note that K_{eff} is only slightly larger than unity for compositions less than approximately 0.06. That K_{eff} begins to deviate significantly at larger

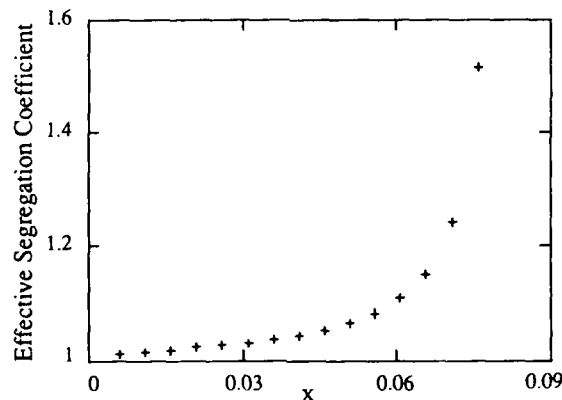


Figure 2: Effective segregation coefficient as a function of composition along the length of the ingot in HgMgTe. Nominal composition was $x=0.12$, and the pull rate was 1mm/hr.

compositions could be an indication that the published reports of critical magnesium composition of 0.2 could be exaggerated, at least for these growth conditions.

INTRINSIC BANDGAP

A key concern about HgCdTe and any of its sibling materials is the issue of intrinsic bandgap variation as a function of composition. This relation is well documented for HgCdTe and HgMnTe, but not well established for HgMgTe. To this end samples of HgMgTe were measured and their composition determined using the above mentioned relationship $p(x)$. The samples were then annealed at a temperature of 300° in an overpressure of mercury. This procedure is necessary to eliminate the dominant as-grown defect, a mercury vacancy which results in p-type material[12] causing very large intra-band absorption and making infrared measurements difficult. The samples were then thinned asymmetrically to avoid "p-core" samples and mounted for easier handling.

A BioRad Digilab FTS-60 fourier transform infrared spectrometer was used to perform the measurement. A glowbar source was used along with an interferometer having a maximum resolution of 0.2 cm^{-1} . A cooled HgCdTe detector was employed for the measurements which were all accomplished at room temperature.

Figure 3 shows the spectra from two samples of HgMgTe and the 1/e-zero intercept transmission cut-on (1/e Zitco). This point has been proposed as a standard value for determining a cut-on wavelength[13]. Using these data points and the known room-temperature intrinsic bandgap for HgTe (HgMgTe where $x=0$) a least squares linear fit was obtained. The intrinsic, room temperature bandgap of HgMgTe is given approximately by:

$$E_g(x) = 3.823x - 0.115, \quad (4)$$

where $E_g(x)$ is in electron volts.

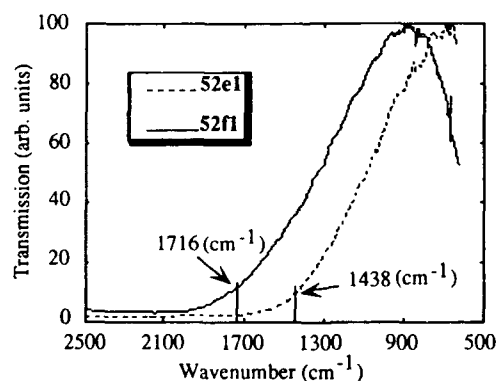


Figure 3: Transmission spectra of two samples from a growth of HgMgTe. The samples were taken from sections approximately one centimeter apart in the ingot. Segregation results is a non-uniform concentration of magnesium, hence the variation in intrinsic gap. The 1/e-Zitco wavenumbers are indicated.

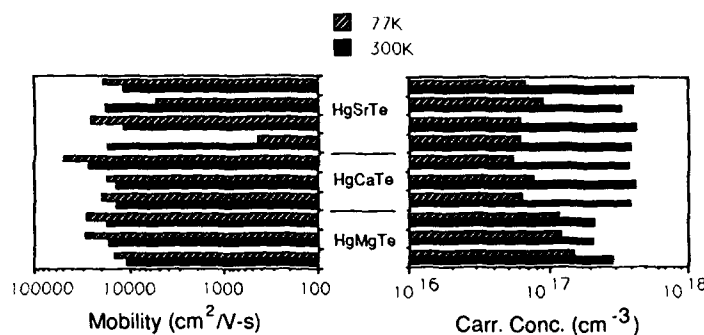


Figure 4: Room temperature and 77K Hall data for several, novel HgTe-based materials.

HALL DATA

Another measure of a material are its Hall carrier concentration and mobility. Figure 4 gives the room temperature and 77K carrier concentration and mobility for several samples of these novel materials. Each of these samples has undergone a post-growth mercury anneal as described above.

The 77K mobilities for the HgMgTe samples are not significantly different from similar data obtained from optimized growths of HgMnTe. However, the corresponding carrier concentrations are an order of magnitude higher. This could be due to the unintentional doping by residual impurities.

Since the growth conditions were not optimized for any of these novel materials more work needs to be done before good comparisons can be made between the materials.

CONCLUSIONS

Of the novel HgTe-based materials that we have grown HgMgTe was the most extensively. An empirical determination of $E_g(x)$ has been made and at room temperature the intrinsic bandgap is found to vary roughly twice as fast as that of HgMnTe, which in turn varies roughly twice as fast as that of HgCdTe. Intrinsic bandgap measurements were attempted for HgSrTe, HgCaTe, and HgBaTe but no transmission could be measured even after an extreme amount of thinning. One possible explanation is that the small amount of calcium, strontium and barium incorporated (as evidenced by density measurements very close to that of HgTe) was insufficient to generate a non-negative gap at room temperature.

Using density measurements we have computed an effective segregation coefficient for HgMgTe as a function of composition. This value is slightly greater than unity for low concentrations of magnesium, but increases rapidly with magnesium concentrations greater than approximately $x=0.06$.

ACKNOWLEDGEMENTS

This paper was prepared while the first author was a National Research Council Postdoctoral Associate. The research was conducted at the Oregon Graduate Center and supported in part by NSF grant #ECS-8402080. We would like to thank Yuan Tang for Hall measurements.

REFERENCES

1. L. Colombo, A.J. Syllaios, R.W. Perlaky and M.J. Brau, *J. Vac. Sci. Technol. A* **3**, 100 (1985).
2. Beryllium: Its Industrial Hygiene Aspects, edited by Herbert E. Stokinger, (Academic Press, 1966).
3. M.R. Tamjidi and R.E. Kremer, *J. Crystal Growth* **55**, 415 (1986).
4. B.E. Bartlett, P. Capper, J.E. Harris and M.J.T. Quelch, *J. Crystal Growth* **46**, 623 (1979).
5. M.R. Tamjidi and R.E. Kremer, *Mater. Lett.* **4**, 90 (1986).
6. O.G. Epanchintsev and Yu. D. Chistyakov, *Zavodskaya Laboratoriya* **33**, 569 (1967).
7. L. Vegard, *Z. Phys.* **5**, 17 (1921).
8. N.G. Gluzman, L.D. Sabirzyanova, I.M. Tsidilkovskil, N.P. Gavaleshko and V.M. Frasunyak, *Sov. Phys. Semicond.* **15**, 957 (1981).
9. V.M. Frasunyak, N.P. Gavaleshko, and I.A. Parenjuk, *Izvestiya Akademii Nauk SSR, Neorganicheskie Materialy*, **18**, 1045, (1982).
10. William G. Pfann, Zone Melting, (John Wiley & Sons Inc. 1958), p. 7ff.
11. P. Capper, C.L. Jones, E.J. Pearce and M.J.T. Quelch, *J. Crystal Growth* **62**, 487, (1983).
12. Theodore C. Harman, *J. Vac. Sci. Technol. A* **5**, 3055, (1987).
13. W.F.H. Micklethwaite, *J. Appl. Phys.* **63**, 2382, (1988).

ELECTRICAL PROPERTIES OF MBE-GROWN HgCdTe

S. HWANG AND J.F. SCHETZINA

Department of Physics, North Carolina State University, Raleigh,
NC 27695-8202

ABSTRACT

A detailed analysis of Hall data obtained at temperatures between 20K and 300K has been made for n-type HgCdTe epilayers prepared by molecular beam epitaxy (MBE). Based on a theoretical calculation for intrinsic concentrations that takes into account the non-parabolicity of the conduction band, the electron concentrations are shown to follow nicely the model for semiconductors in their intrinsic and extrinsic ranges. The scattering mechanisms in these materials are studied through the analysis of electron mobility. Polar mode phonon scattering, acoustic mode via deformation-potential coupling, acoustic mode via piezoelectric coupling, and impurity scattering are included in the mobility calculation. The results indicate that these mechanisms are insufficient to explain the measured mobility.

INTRODUCTION

The compound semiconductor $\text{Hg}_{1-x}\text{Cd}_x\text{Te}$ has attracted a great deal of attention during the past two decades because of its many applications in optoelectronics [1,2]. It has the desirable feature of possessing an approximately linear variation of band gap with composition across the pseudobinary range from CdTe to HgTe, covering the region from 0.8 to beyond 20 μm . The investigations on this material have been aimed at the development of infrared detectors, especially in the 8-12 μm region. In addition, HgCdTe is emerging as a suitable material for applications in fiber-optic communication in the 3-5 μm region, as evidenced by the recent observation of laser action from a HgTe-CdTe superlattice [3].

The development of a HgCdTe technology, however, has been hampered by several problems. Among them is the difficulties encountered in material preparation. HgCdTe is characterized by its native defects that result from the deviation in stoichiometry during crystal growth. These defects are easily ionized and electrically active [4], presenting a serious problem to the electrical properties. Better control of stoichiometry can be achieved by lowering the growth temperature. Several low temperature growth techniques, such as MBE [5,6] and metal-organic chemical vapor deposition (MOCVD) [7], have been used to prepare epitaxial HgCdTe.

The present paper reports the electrical properties of MBE-grown HgCdTe epilayers with $x \sim 0.2$. Electrical characterization is highly sensitive to native defects and provides information pertinent to the concentration of these defects. The samples were grown in an MBE system designed and built at North Carolina State University specifically for the growth of Hg-based materials and multilayers. The details of the system have been described in an earlier paper [6]. The Hall data were measured using standard van der Pauw Hall technique over the temperature range 20-300K with a magnetic field of 3 KG.

INTRINSIC CONCENTRATION

The intrinsic concentration (n_i) of HgCdTe as a function of CdTe mole fraction (x) and temperature is an important parameter in Hall data analysis for narrow gap HgCdTe because it dominates the electrical properties over a wide temperature range. Although empirical expressions for n_i as a function of band gap and temperature have been published by several authors [8,9], it is still necessary to calculate n_i based on the energy band gap since such a calculation also gives the Fermi level (E_F), which is needed in the mobility analysis.

When the conduction band non-parabolicity and degeneracy are taken into account, the electron concentration can be expressed as [10]

$$n = N_c \frac{2}{\pi^{1/2}} \int_0^\infty \frac{y^{1/2} (1+y/\epsilon)^{1/2} (1+2y/\epsilon)}{1+\exp(y-\eta)} dy \quad (1)$$

where $N_c = 2[m_c^* k_B T / 2\pi (\hbar/2\pi)^2]^{3/2}$ is the density of states of the conduction band, $\epsilon = E_g/kT$ is the reduced band gap, and $\eta = E_F/kT$ is the reduced Fermi level. The hole concentration is simply given by

$$p = N_v \exp\left(-\frac{E_v - E_F}{k_B T}\right) \quad (2)$$

where N_v is the density of states of the valence band. To calculate the intrinsic concentration n_i , E_F is first calculated by equating Eqs. (1) and (2) and solving the resultant equation numerically. n_i is then obtained by substituting E_F back into Eq. (1). The expression for E_g is taken from Hansen, Schmit, and Casselman [11]. The integral in Eq. (1), the generalized Fermi-Dirac integral, is calculated using a 16-point Laguerre formula [12]. The above algorithm is suitable for Hall data analysis since it does not involve extensive convergence checking or interpolation. The 16-point formula appears to be sufficient for carrier concentration calculation since a 20-point formula results in a comparable accuracy.

Fig. 1 shows the temperature dependence of calculated intrinsic concentration for five different x values. The results agree well with Hansen and Schmit's data, which are also shown as the solid curves. The slight difference is attributed to the different algorithm used in calculating the generalized Fermi-Dirac integral.

CARRIER CONCENTRATION ANALYSIS

Fig. 2 shows the experimental carrier concentration for MCT82. The sample exhibits intrinsic characteristics as temperature decreases from 300K to -80K. As the temperature further decreases, the carrier concentration saturates and reaches a plateau at very low temperatures. The experimental data are fitted by solving for the electron concentration in the charge neutrality equation

$$n_0^2 + n_0 (N_D^+ - N_A^-) - n_i^2 = 0 \quad (3)$$

where n_0 is the equilibrium electron concentration, and $(N_D^+ - N_A^-)$ is the ionized impurity concentration, which is determined from

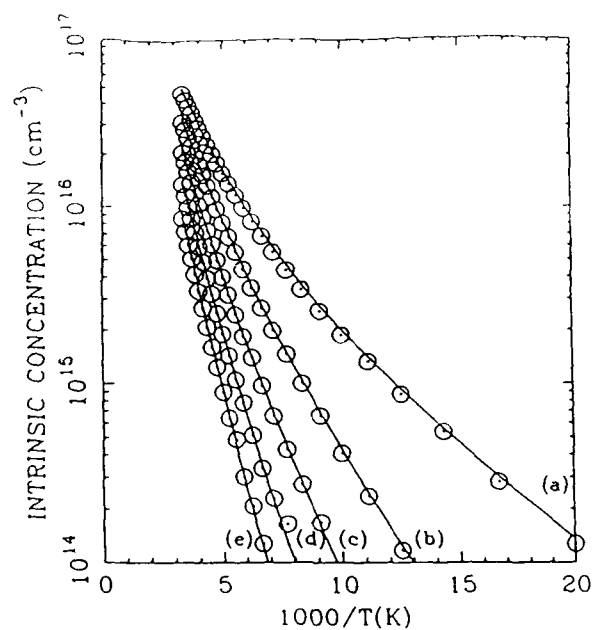


Fig. 1. Temperature dependence of the intrinsic concentration for HgCdTe. x: (a) 0.18, (b) 0.20, (c) 0.22, (d) 0.24, (e) 0.26.

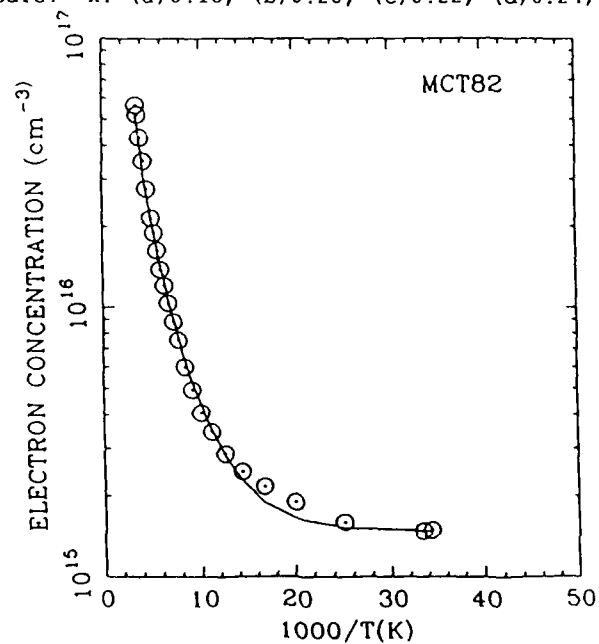


Fig. 2. Temperature dependence of the carrier concentration for MCT82. The solid curve shows the calculated data.

the plateau value of the Hall data. In the fitting process, both the x -value and hole effective mass m_v^* are used as parameters. The best fit is obtained using $x=0.17$, $(N_D^+-N_A^-)=1.5 \times 10^{15} \text{ cm}^{-3}$, and $m_v^*=0.44$. The result is shown in Fig. 2 by the solid curve. A good agreement was obtained between calculated and measured carrier concentration.

Fig. 3 shows the carrier concentration for an In-doped sample (MCT20). In this case, the extrinsic region extends towards high temperatures and the carrier concentration reaches a much higher plateau value at low temperatures. A good agreement was obtained with $x=0.18$, $(N_D^+-N_A^-)=9.5 \times 10^{15} \text{ cm}^{-3}$, and $m_v^*=0.44$.

Based on the above analysis, it appears that Eq. (3) describes the behavior of carrier concentration rather well. It is noticed that, although m_v^* is a fitting parameter, the best fit is always obtained by using $m_v^*=0.44\sim 0.45$. This is consistent with the value derived from magneto-optical measurements [13]. We believe that, in analyzing the carrier concentration data, the generalized Fermi-Dirac integral should not be approximated by the ordinary Fermi integral; otherwise, a much higher value for m_v^* would be necessary [8].

MOBILITY ANALYSIS

To further analyze the Hall data and to understand the scattering mechanisms in HgCdTe, we have completed theoretical calculations for the electron mobility by numerically solving the Boltzmann equation. For the mobility calculation under low electric fields it is sufficient to keep the perturbation of the probability distribution function. The Boltzmann equation thus reduces to [15]

$$S_0(E)\phi(E) - \sum_q \sum_{\pm} S_{q\pm}(E)\phi(E \pm (\hbar/2\pi)\omega_q) = \frac{1}{\gamma'(E)} \quad (4)$$

where ϕ is the perturbation, S_0 is the collision term of the total out-scattering, $S_{q\pm}$ denotes the in-scattering due to phonon emission (+) and absorption (-), and ω_q is the characteristic frequency of the q th phonon mode. The drift mobility is given by

$$\mu_d = \frac{2e}{3m^*k_B T} \langle E\phi \rangle \quad (5)$$

where $\langle E\phi \rangle$ is the Maxwellian average weighted by E .

Four scattering mechanisms are included in the calculation. These consist of polar mode phonon scattering, acoustic mode via deformation-potential coupling, acoustic mode via piezoelectric coupling, and ionized impurity scattering. In calculating the collision terms for polar phonon scattering, it is important that the two-phonon-mode phenomenon be taken into account since both HgTe-like and CdTe-like phonons are observed in HgCdTe [14]. The strength of each phonon is taken to be proportional to its mole fraction, and the characteristic frequencies of longitudinal optical phonons for HgTe and CdTe are taken to be 138 cm^{-1} and 170 cm^{-1} , respectively. To solve Eq. (4) for $\phi(E)$, the energy axis is divided into intervals of length $(\hbar/2\pi)\omega_q$ and $\phi(E)$ is calculated using a modified iteration method [15,16].

Fig. 4 shows two curves obtained using an ionized impurity concentration of $5 \times 10^{15} \text{ cm}^{-3}$ and $9 \times 10^{15} \text{ cm}^{-3}$, respectively, for

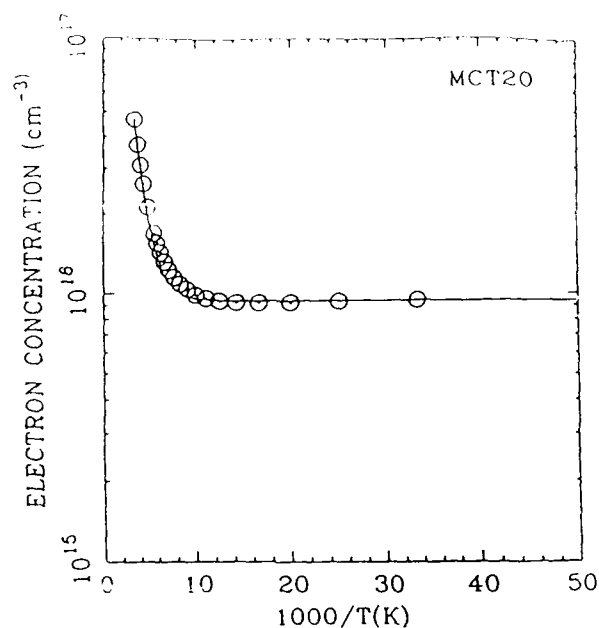


Fig. 3. Temperature dependence of the carrier concentration for MCT20. The solid curve shows the calculated data.

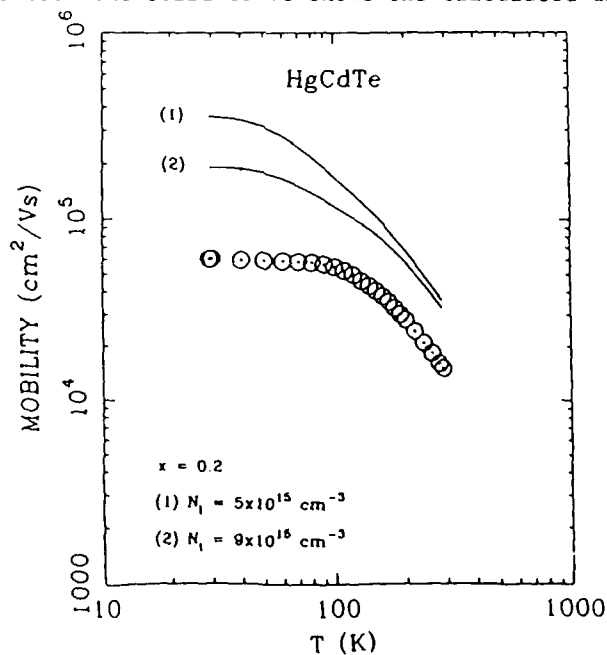


Fig. 4. Temperature dependence of the electron mobility for HgCdTe with $x=0.20$. Circled dots show the Hall mobility of MCT82.

HgCdTe with $x=0.2$. The Hall mobilities of sample MCT82 are also shown for comparison. It is noticed that in the high temperature range the mobility is dominated by phonon scattering with little contribution from impurity scattering. As temperature decreases, impurity scattering becomes dominant and the mobility reaches a plateau at very low temperatures. The measured Hall mobilities are qualitatively in agreement with theoretical results but consistently lower than the calculated values. The results indicate that the four scattering mechanisms included in this study are insufficient to explain the measured mobilities. Scattering by impurity-vacancy complex, micro-twins, and subgrain boundaries, etc. may contribute to the observed reduction in electron mobility.

SUMMARY

Carrier concentration and mobility calculation have been performed to analyze the Hall data of n-type MBE-HgCdTe measured at temperatures between 20K and 300K. The electron concentrations are shown to follow nicely the model for semiconductors in their extrinsic and intrinsic ranges. Polar mode phonon scattering, acoustic mode via deformation-potential coupling, acoustic mode via piezoelectric coupling, and impurity scattering are included for the calculation of electron mobility. The results indicate that these scattering mechanisms are not sufficient to explain the measured mobilities. This work was supported by NRL contract N00014-89-J-2024 and General Electric Aerospace Group IR&D funds.

REFERENCE

1. R. Dornhaus and G. Nimtz, **Narrow Gap Semiconductors**, Vol. 98 in Springer Tracts in Modern Physics (Springer-Verlag, Berlin, 1983).
2. R.F.C. Farrow, J.F. Schetzina, and J.T. Cheung (editors), **Materials for Infrared Detectors and Sources**, Mat. Res. Soc. Symp. Proc. Vol. 90 (Materials Research Society, Pittsburgh, 1987).
3. N.C. Giles, Y. Lansari, J.W. Han, J.W. Cook, Jr., and J.F. Schetzina, presented in the 1989 U.S. Workshop on the Physics and Chemistry of Mercury Cadmium Telluride and Related II-VI Compounds.
4. D.T. Cheung, J. Vac. Sci. Technol. **A 3**, 128 (1985).
5. J.P. Faurie and A. Million, J. Crystal Growth **54**, 582 (1981).
6. K.A. Harris, S. Hwang, D.K. Blanks, J.W. Cook, Jr., J.F. Schetzina, and N. Otsuka, J. Vac. Sci. Technol. **A 4**, 2061 (1986).
7. J. Tunncliffe, S.J.C. Irvine, O.D. Dosser, and J.B. Mullin, J. Crystal Growth **68**, 245 (1984).
8. Y. Nemirovsky and E. Finkman, J. Appl. Phys. **50**, 8107 (1979).
9. G.L. Hansen and J.L. Schmit, J. Appl. Phys. **54**, 1639 (1983).
10. H.B. Bebb and C.R. Ratliff, J. Appl. Phys. **42**, 3189 (1971).
11. G.L. Hansen, J.L. Schmit, and T.N. Casselman, J. Appl. Phys. **53**, 7099 (1982).
12. A.H. Stroud and D. Secrest, **Gaussian Quadrature Formulas** (Prentice Hall, New York, 1966).
13. G.L. Hansen and J.L. Schmit, J. Appl. Phys. **54**, 1639 (1983).
14. J. Baars and F. Sorger, Solid State Commun. **10**, 875 (1972).
15. B.R. Nag, Phys. Stat. Sol. (b) **66**, 719 (1974).
16. S. Hwang, Ph.D. Thesis, North Carolina State University, 1988.

FIRST AND SECOND ORDER RAMAN STUDIES OF COMPOSITION AND STRUCTURAL ORDERING IN $\text{Hg}_{1-x}\text{Cd}_x\text{Te}$

A. COMPAAN* and R. C. BOWMAN, Jr.**

*Department of Physics and Astronomy, The University of Toledo, Toledo, Ohio 43606

**Chemistry and Physics Laboratory, The Aerospace Corporation, Los Angeles, California 90009

ABSTRACT

The effects of alloy fluctuations, defect densities, and short-range clustering on the resonance behavior of first and second order LO and TO Raman scattering are studied in $\text{Hg}_{1-x}\text{Cd}_x\text{Te}$ (MCT). X-values between 0.20 and 0.32 and photon energies from 2.35 to 2.7 eV were used with samples prepared by a wide range of techniques--LPE, MOCVD, MBE, bulk growth, and pulsed laser annealing. We examine the resonance behavior of the HgTe-like TO mode at $\sim 120 \text{ cm}^{-1}$ and the mode at 133 cm^{-1} , which has been identified as originating from the preferential clustering of 3 Hg and 1 Cd about the Te. We find that the intensity of this peak for various bulk and epitaxially grown samples is unusually large only near the E_1 resonance. Pulsed laser annealing with a Nd:YAG-pumped dye laser strongly suppresses this mode in all samples suggesting that extremely rapid epitaxial regrowth may inhibit the 3:1 cluster formation. In addition, the resonance-enhanced LO overtones are suppressed by the pulsed laser anneal.

INTRODUCTION

In $\text{Hg}_{1-x}\text{Cd}_x\text{Te}$ (MCT), as well as several other common anion semiconductor alloys, evidence has been growing recently of the existence of ordered growth, under some conditions, in which each anion is surrounded by the same arrangement of cations. Evidence for such ordering is particularly strong for the case of epitaxially grown III-V semiconductors.¹ For tetrahedrally bonded semiconductors, completely ordered growth is possible only when the cation ratios are either 1:3, 2:2, or 3:1. For other ratios, there may nevertheless be a preferential clustering of cations in these ratios.² That is, the number of anions with nearest neighbors in these ratios may be much larger than that predicted by a statistical distribution. Recently evidence from Raman^{3,4}, infrared⁵, and nuclear magnetic resonance⁶ studies of mercury cadmium telluride has indicated that clustering may be occurring.

In the present work we have studied the effects of differing growth conditions on both first and second order resonance-enhanced Raman scattering. Since phonon frequencies are sensitive to the interatomic forces and to the ion masses, phonon Raman scattering is an effective probe of local structural order. In addition, the intensities of the Raman lines are sensitive to the details of the electronic band structure of the semiconductor, which reflects alloy composition. This intensity dependence is shown most clearly in the resonance enhancements of the various Raman modes as different laser photon energies are used in the region of allowed band-to-band transitions of the semiconductor. Thus the Raman effect is sensitive both to alloy composition and to local structural order.

EXPERIMENTAL

We have used samples prepared by a wide variety of techniques including one grown from the melt ($x = 0.31$), one ($x = 0.28$) prepared by molecular beam epitaxy (MBE) on CdZnTe, one ($x = 0.27$) grown by liquid phase epitaxy (LPE) on CdZnTe, and three grown by organo-metallic chemical vapor deposition (MOCVD) ($x=0.22, 0.24$ and 0.26).

Finally, to examine the extreme case of very rapid crystal growth, we used nanosecond pulsed laser annealing (PLA) on most of these samples.⁴ For Raman scattering the photon energy was varied from 2.35 to 2.7 eV across the E_c critical point in the joint density of electronic states. We present data obtained both before and after PLA.

The laser annealing was performed with a Nd:YAG-pumped dye laser operating at 728 nm with a pulse duration of ~ 8 nsec and an energy density of ~ 0.05 J/cm² (melt threshold ~ 0.02 J/cm²) with the sample held in a pressurized cell with ~ 20 atmospheres of argon.⁴ Raman scattering was performed at liquid nitrogen temperature with the laser beam focused to a line image on the sample to avoid laser heating and surface decomposition. Further details are given in Ref. 4.

The pulsed laser annealing (PLA) technique provides access to an extremely rapid method of recrystallization of the semiconductor surface. Cooling rates exceeding 10^8 K/sec are readily achieved.⁸ This is radically different from the near-equilibrium growth conditions present during bulk growth and LPE. MBE and MOCVD growth occur with substrate temperatures well below the melt temperature; but in contrast with the rapid quench of the PLA process, the MBE and MOCVD growth proceeds slowly enough that significant surface diffusion can occur during growth, and lattice locations can be "optimized." If the formation of clusters has a slight energetic advantage, clustering may be expected to occur in slow, near-equilibrium growth but would be suppressed during the rapid quench that occurs during the pulsed laser annealing process. We believe that the changes in second order spectra and changes in the first order resonance enhancement, which are presented below, are consistent with growth or regrowth-induced changes in the short-range order in the crystals.

ELECTRON-PHONON COUPLING

From $\langle 111 \rangle$ and $\langle 122 \rangle$ surfaces of MCT, both TO and LO modes are dipole-allowed. In general the deformation potential electron-phonon interaction can activate both TO and LO phonon modes. However, in polar semiconductors the LO mode is also activated by electro-optic contributions related to the long-range electric field of the phonon. This Fröhlich coupling usually dominates the electron-phonon coupling near electronic resonances and such is the case for MCT. In addition, however, two related mechanisms may activate LO-phonon Raman scattering in forbidden geometries and polarizations: the intraband Fröhlich interaction, with a wave-vector dependent (q -dependent) matrix element, may produce polarized scattering, and an impurity or disorder-induced Fröhlich mechanism may also produce forbidden scattering.^{9,10,13}

Our studies of samples with $\langle 100 \rangle$ surfaces (from which only LO phonon scattering is allowed), of samples with $\langle 110 \rangle$ surfaces (from which only TO scattering is allowed), and of samples with $\langle 111 \rangle$, and $\langle 122 \rangle$ surfaces indicate that this forbidden, impurity-induced Fröhlich mechanism accounts not only for the LO signals in forbidden configurations (such as the $\langle 110 \rangle$ surface) but also for the LO signals from $\langle 111 \rangle$ and $\langle 122 \rangle$ surfaces. For example little difference is observed in the LO intensities and the resonance behavior from the various surfaces.

Second order LO phonon Raman scattering is generally considered to be produced by an iterated, allowed Fröhlich process and produces overtones of the near-Brillouin-zone-center LO modes. There is no need to invoke a higher order forbidden process to explain the results.

RESULTS

Figure 1 displays first and second order Raman spectra from three as-grown samples for a laser wavelength (496.5 nm) very near the peak of the E_c resonance. Note that the two laser plasma emission lines at 175 cm⁻¹ and 180 cm⁻¹ have been removed from the spectra. Strong similarities are seen in the spectra even though three different growth processes were used—bulk growth, LPE, and MOCVD. As the x -value decreases from 0.31, through 0.27 to 0.22 for traces a to c, some narrowing of the first and second order peaks

is observed as well as changes in the relative peak heights. Our resonance enhancement studies (see below) show that the first-order peak heights change mainly as a result of the decrease in the E_1 critical point energy with decreasing x -value.

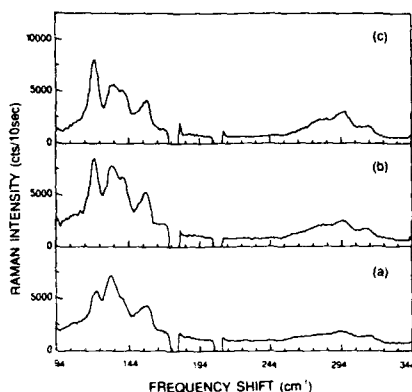


Fig. 1: First and second order Raman spectra obtained from three differently grown samples: a) bulk growth ($x = 0.31$, $\langle 111 \rangle$) b) LPE growth ($x = 0.27$, $\langle 111 \rangle$) and c) MOCVD growth followed by interdiffusion ($x = 0.22$, $\langle 122 \rangle$). Raman excitation at 496.5 nm. Spectrometer resolution 5 cm^{-1} . Laser plasma calibration lines at 176 cm^{-1} and 209 cm^{-1} have been removed from the traces.

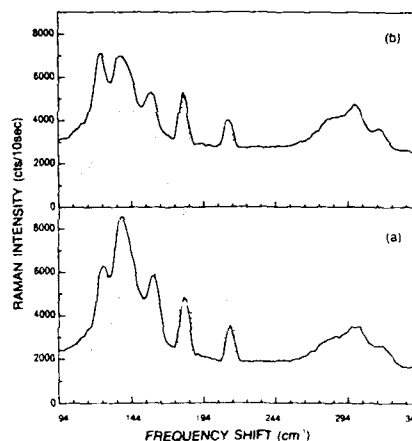


Fig. 2: Raman spectra before (solid line) and after (dotted line) PLA ($\lambda = 728$ nm, 0.05 J/cm^2): a) MOCVD-grown, $x = 0.26$, b) MBE-grown, $x = 0.28$. Raman excitation at 496.5 nm. Spectrometer resolution 7 cm^{-1} .

The second-order spectra in Fig. 1 show three clearly-defined peaks at approximately 280, 296, and 312 cm^{-1} with small shifts due to the x -value differences. These peaks are clearly related to the first-order LO modes at ~ 140 and ~ 156 cm^{-1} as overtones (280 and 312 cm^{-1}) and as an intercombination (296 cm^{-1}). Note that the second order peaks all involve zone-center mode frequencies. This is a consequence of the iterated, allowed Fröhlich process which involves near $q=0$ wavevectors. These second-order peaks confirm the previous identification^{3,4,16} of the peaks near 140 and 156 cm^{-1} as the HgTe-like LO and CdTe-like LO modes respectively. Note that the 133 cm^{-1} mode, identified as a clustering-related peak,^{3,4,16} does not show up in the second order spectra even though it sometimes is the dominant peak in the first-order spectra. Furthermore, the TO peak at ~ 120 cm^{-1} also does not appear clearly in the second order spectra probably because the second order LO modes are more strongly enhanced near resonance.

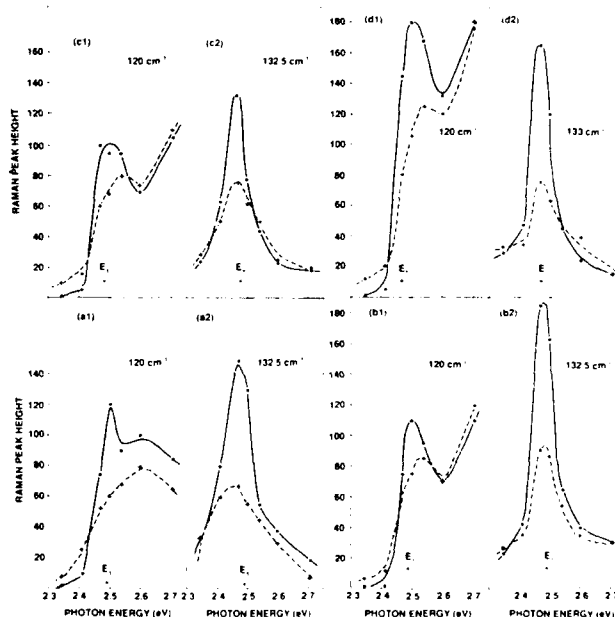
Figure 2 shows the first and second order spectra of two samples before and after pulsed laser annealing at 0.05 J/cm^2 . These two samples are different from any of the three shown in Fig. 1 but the spectra from the as-grown surfaces are quite similar. These spectra were obtained with slightly poorer instrumental resolution (wider slits) in order to facilitate more reliable intensity measurements of the Raman peaks. The spectra obtained after laser annealing show little change in the first-order LO peak heights but a considerable decrease in the peak height of the cluster-related mode at ~ 133 cm^{-1} (more clearly evident after deconvolution)^{4,16} and also for the TO peak at ~ 120 cm^{-1} . The most dramatic change after annealing is the strong decrease in intensity of all three second order LO peaks.

The resonance enhancements of scattering intensities for the four first-order modes were obtained by normalizing each spectrum to the incident laser power and correcting for detection efficiency. To extract individual peak heights in the presence of significant peak

overlap, the spectra were fit by a sum of four equal-width Lorentzian peaks. The best-fit peak amplitudes of the TO mode at $\sim 120 \text{ cm}^{-1}$ and the cluster mode at $\sim 133 \text{ cm}^{-1}$ are shown in Figure 3 as a function of the laser photon energy. These two modes were chosen for display because they are strongly affected by the laser anneal whereas the two LO modes are only slightly changed. The results from four samples are shown, all with x -values near 0.25. These include one sample each grown by LPE and MBE, and two samples grown by MOCVD—one grown as separate layers of CdTe and HgTe and then interdiffused and one grown as the alloy directly.

The resonance enhanced intensity of the cluster mode is strongly reduced by the pulsed laser anneal although clear evidence remains of the resonance near the E_c edge. The TO mode, unlike the cluster mode (or the LO modes), exhibits a gradual rise in intensity through the shortest wavelength used in this study (457.9 nm). The resonance peak near the E_c edge is strongly suppressed after the laser anneal and nearly disappears.

Fig. 3: Intensities of two first-order Raman lines (TO and cluster mode) plotted as a function of the exciting laser photon energy for four different samples: a) LPE-grown $x = 0.27$, b) alloy-grown MOCVD, $x = 0.26$, c) MBE-grown, $x = 0.28$, and d) layer-grown MOCVD and interdiffused, $x = 0.24$. Dots and crosses are from the as-grown and laser-annealed surfaces respectively. Curves are guides to the eye. Arrows indicate estimated E_c position.



Arrows in Fig. 3 indicate the position of the E_c edge obtained from published optical measurements.^{7,14,15} We estimate this position to be uncertain by $\pm 0.03 \text{ eV}$ due to temperature shift extrapolations and to possible errors in x -values in our samples. However, it is clear that the positions of the resonances are unchanged after the pulsed laser anneal. This indicates that any possible macroscopic compositional change in the annealed layer is less than $\sim 2\%$.

DISCUSSION

The suppression of the cluster mode intensity could be a consequence of changes in local structural order induced by the rapid quench of the pulsed laser anneal. Amirtharaj, *et al.*³ have suggested that this mode may be due to clusters in which the Te is surrounded by 3 Hg and 1 Cd. We believe that the resonance intensity behavior shown here, together with the Raman frequencies, are consistent with the interpretation of this mode as arising from the 3:1 clusters. If so, this particular bonding arrangement is apparently energetically preferred and may dominate for x -values near 0.25 and under conditions of near-equilibrium bulk or LPE growth. In addition the lower temperature, but slow, epitaxial growth of the MBE and MOCVD processes appears to facilitate this clustering much like the ordered growth observed in some epitaxially-grown III-V semiconductors.¹

The pulsed laser anneal, however, generates a very rapid thermal quench which can freeze in the statistical arrangements of the high temperature phase. Slight energetic preferences would likely be lost under a rapid quench, and the 3:1 clusters would then appear with the usual statistical probabilities. This would naturally suppress the "cluster" mode intensity in the Raman spectrum. But in addition, this would increase the alloy disorder that might be expected to broaden the critical point energies such as the E₁ edge. Both effects would result in any strongly resonant mode being suppressed more than the less resonant modes.

Very recently Lusson, *et al.*¹³, have studied the behavior of first and second order Raman scattering in HgCdTe ($x = 0.2$) which was implanted with In ions to create damage. Their results show clearly that the second-order peaks are very sensitive to ion-implantation-induced damage. However, they found that the first-order LO peaks did not fall in intensity until much greater levels of implantation-induced damage occurred. These results suggest the important role of the defect-induced Fröhlich mechanism as the dominant process responsible for first-order LO phonon Raman scattering in MCT.

The results presented in this paper, *viz.*, the strong sensitivity to laser annealing of the second-order peaks, the cluster mode, and the TO mode, and the insensitivity of the first-order LO modes to laser anneal, are quite consistent with the implantation-induced damage results of ref. 13. Thus, if the laser anneal increases alloy disorder or point defect densities, the defect-activated forbidden Fröhlich process driving the first-order LO modes is further enhanced and Raman intensities are increased. However, increased disorder or defect densities will also broaden the E₁ edge and thus reduce the resonance enhancement of the phonon lines. These two competing effects explain the absence of substantial intensity changes in the first-order LO modes, whose amplitude arises from a defect-activated Fröhlich process. On the other hand, the second order LO modes are doubly resonant and the cluster-related mode is the most strongly resonant of the first-order modes and thus these modes show a net suppression by disorder broadening of the E₁ electronic states.

Thus the general trends appear to confirm a defect-activated Fröhlich mechanism for the first-order LO phonon modes in MCT. The behavior after the pulsed laser anneal suggests an increase in alloy disorder and a reduction in the amount of clustering of cation ratios around 3:1 although a firm estimate of the amount of clustering is not possible from these Raman data.

ACKNOWLEDGEMENTS

The work at Aerospace Corporation was supported by the Aerospace Sponsored Research Program. We are indebted to D.E. Cooper, J.M. Arias, D.D. Edwall and E.R. Gertner at Rockwell for the MBE-grown and MOCVD-grown samples.

REFERENCES

1. See for example, J.E. Bernard, S.-H. Wei, D.M. Wood, and A. Zunger, *Appl. Phys. Lett.* **52**, 311 (1988); A. Gomyo, T. Suzuki, and S. Iijima, *Phys. Rev. Lett.*, **60**, 2645 (1988); T.S. Kuan, W.I. Wang, and E.L. Wilkie, *Appl. Phys. Lett.*, **51**, 51 (1987).
2. H.W. Verleur and A.S. Barker, *Phys. Rev.* **149**, 715 (1966).
3. P.M. Amirtharaj, K.K. Tiong, P. Parayanthai, F.H. Pollak, and J.K. Furdyna, *J. Vac. Sci. Technol. A* **3**, 226 (1985); P.M. Amirtharaj and F.H. Pollak, *Appl. Phys. Lett.*, **45**, 789 (1984).
4. A. Compaan, B. Aggarwal, R.C. Bowman, Jr., and D. E. Cooper, *SPIE Proceedings* vol. 1055, "Raman Scattering, Luminescence, and Spectroscopic Instrumentation in Technology" p. 67 (1989).
5. L.K. Vodopyanov, S.P. Kozyrev, Yu.A. Aleshchenko, R. Triboulet, and Y. Marfaing, in *Proc. 17th Int. Conf. Phys. of Semiconductors*, 1984, p. 947.
6. D. Zamir, K. Beshah, P. Becla, P.A. Wolff, R.G. Griffin, D. Zax, S. Vega, and N. Yellin, *J. Vac. Sci. Technol. A* **6**, 2612 (1988).
7. D.E. Aspnes & H. Arwin, *J. Vac. Sci. Technol. A* **2**, 1309 (1984); H. Arwin & D.E. Aspnes, *J. Vac. Sci. Technol. A* **2**, 1316 (1984).
8. A. Lietoila and J.F. Gibbons, *J. Appl. Phys.*, **53**, 3207 (1982); A. Compaan, M.C. Lee, and G.J. Trott, *Phys. Rev. B* **32**, 6731 (1985).
9. M. Cardona, in *Light Scattering in Solids II* (Topics in Applied Physics vol. 50) ed by M. Cardona and G. Güntherodt [Springer-Verlag, Berlin, 1982] pp 19-178.
10. J. Menendez, M. Cardona, and L.K. Vodopyanov, *Phys. Rev. B* **31**, 3705 (1985).
11. A. A. Gogolin and E. I. Rashba, *Solid State Commun.* **19**, 1177 (1976).
12. A. Pinczuk and E. Burstein, *Phys. Rev. Lett.* **21**, 1073 (1968).
13. A. Lusson, J. Wagner, and M. Ramsteiner, *Appl. Phys. Lett.* **54**, 1787 (1989).
14. L.E.A. Berlouis, L.M. Peter, M.G. Astles, and R.G. Humphreys, *Appl. Phys. Lett.* **51**, 502 (1987).
15. P. M. Amirtharaj, J. H. Dinan, J. J. Kennedy, P. R. Boyd, and O. J. Glembocki, *J. Vac. Sci. Technol. A* **4**, 2028 (1986); P. M. Amirtharaj, J. J. Kennedy and P. R. Boyd, *J. Vac. Sci. Technol. A* **5**, 3184 (1987).
16. A. Compaan, R.C. Bowman, Jr., & D.E. Cooper, *Semicond. Sci. and Technol.* (in press)

TEMPERATURE-DEPENDENT INFRARED ABSORPTION OF Hg-BASED II-VI SEMICONDUCTOR SUPERLATTICES

Z. Yang, Y. Lansari, J.W. Han, Z. Yu, and J. F. Schetzina,
Department of Physics, North Carolina State University, Raleigh,
NC 27695

ABSTRACT

The optical absorption of a series of HgTe/Cd_{0.85}Hg_{0.15}Te superlattices (SLs) have been measured in the spectral region from 2 to 12 μm at temperatures from 300 K down to 4.2 K. Several subband transitions were identified and their transition energies were compared with theoretical calculations, with the valence band offset ΔE_v between HgTe and CdTe as a fitting parameter. It is found that at a given temperature, a value of $\Delta E_v = 420 \pm 100$ meV fits the results of all the SLs, and ΔE_v does not depend on temperature to within ± 100 meV.

INTRODUCTION

Optical absorption is a strong tool to study the electronic band structure in Hg-based semiconductor superlattices (SLs). Earlier infrared transmission measurements on HgTe/CdTe SLs showed a temperature dependence of the band gap of the SLs, and reasonably good agreement was found between experimental results and theory [1].

We have completed a careful study of the optical absorption of a series of HgTe/Cd_{0.85}Hg_{0.15}Te SLs in the spectral region from 2 to 12 μm and in the temperature region from 4.2 to 300 K. Several inter-subband transitions, namely the first heavy hole subband H1 to the first conduction subband E1 (transition H1E1), the first light hole subband L1 to E1 (transition L1E1), and the second heavy hole subband H2 to the second conduction subband E2 (transition H2E2), have been identified. Theoretical calculations of the subband transition energies and the selection rules were compared with the experimental results, using the valence band offset ΔE_v between HgTe and CdTe as an adjustable parameter.

EXPERIMENTAL DETAILS

Six SLs were grown on (100) CdZnTe substrates. Prior to film growth, the transmission and reflection spectra of the substrates at 300 K were measured. Transmission spectrum of a substrate test piece at various temperatures was also measured. The substrates were found to be transparent in the entire spectral region of interest, with a refraction index of 2.75. Satellite peaks were observed in double-crystal diffraction rocking curves of the SLs, and the periods of the SLs were then determined. The nominal thicknesses of the HgTe and the Cd_{0.85}Hg_{0.15}Te layers within each period were then estimated from the growth rates. As will be seen later, the estimates of the thickness are good to within one monolayer.

The transmission spectra of the SLs were measured at temperatures from 4.2 to 300 K. The reflection spectra at 300 K were also measured. The exact form of the formulas for the

transmission and reflection of a two-layer system was used to obtain the absorption coefficient and the refraction index from the experimental data. The room temperature refraction index was then used to obtain the low temperature absorption curve from the transmission spectra.

RESULTS AND DISCUSSION

Figure 1 shows an absorption spectrum typical of the SLs studied. The spectrum shows step-like features which exist only in superlattice structures. The arrows indicate the predicted energies of particular transitions which are responsible for the sudden rise of the absorption. The H1E1, L1E1 and H2E2 transitions are clearly seen. The identification of these transitions by theory will be discussed later in this paper. Figure 2 shows the absorption and the photoluminescence (PL) of SL A74. It is seen that the PL peak is at the onset of the absorption rise. Figure 3 shows the absorption spectra of SL A20S at several different temperatures. It is seen that when the temperature is increased from 4.2 to 300 K, both the H1E1 and L1E1 transition energies shift to higher energy. The arrows are the transition energies predicted by theory.

The theoretical model used in the analysis has been described in our earlier work [2]. The valence subbands of a $\text{HgTe}/\text{Cd}_{0.85}\text{Hg}_{0.15}\text{Te}$ SL are, in the order of decreasing energy, H1, L1, H2.... The conduction subbands are, in the order of increasing energy, E1, E2.... The selection rules are such that transitions H1E1, L1E1 and H2E2 are allowed, while the remainder of the transitions from the valence subbands to the conduction subbands are forbidden, due to the parities of the envelope functions of the involved subbands.

The PL peak observed is due to band-to-band recombination in the SL, since in small gap semiconductors this is the dominant recombination process [3]. The position of the peak coincides with the energy where the absorption just starts to rise. Such a coincidence has also been seen in other SLs. It is then clear that the energies of the transitions responsible for the steps of the absorption spectra should be at the onset of the absorption steps.

Once the experimental transition energies are determined, they can be compared with theoretical calculations. Besides the valence band offset ΔE_v , the thicknesses of the HgTe and $\text{Cd}_{0.85}\text{Hg}_{0.15}\text{Te}$ layers in each period are also treated as variables, up to one monolayer. It is then found that a single value of ΔE_v at each temperature fits well the transition energies of all the SLs. Table 1 gives a complete summary of results for the six SLs. It is seen that all of the transition energies shift to higher energy as the temperature is increased. The layer thicknesses listed are the nominal estimates. The thicknesses used in the calculations were the nominal ones corrected by the number of monolayers ΔL listed in the table. One monolayer correction means that the layer thickness of HgTe used in the calculations is one monolayer, or 3.24 Å, thinner while that of $\text{Cd}_{0.85}\text{Hg}_{0.15}\text{Te}$ is 3.24 Å thicker than the nominal values. Among the bulk band parameters used, only the band gaps of HgTe and $\text{Cd}_{0.85}\text{Hg}_{0.15}\text{Te}$ change with the temperature. A value of $\Delta E_v = 420$ meV was found to best fit the experimental results. It is seen from the table that the theoretical calculations are in good agreement with the experimental results, except for the H2E2 transitions. This is because the $\mathbf{k}\cdot\mathbf{p}$ model is

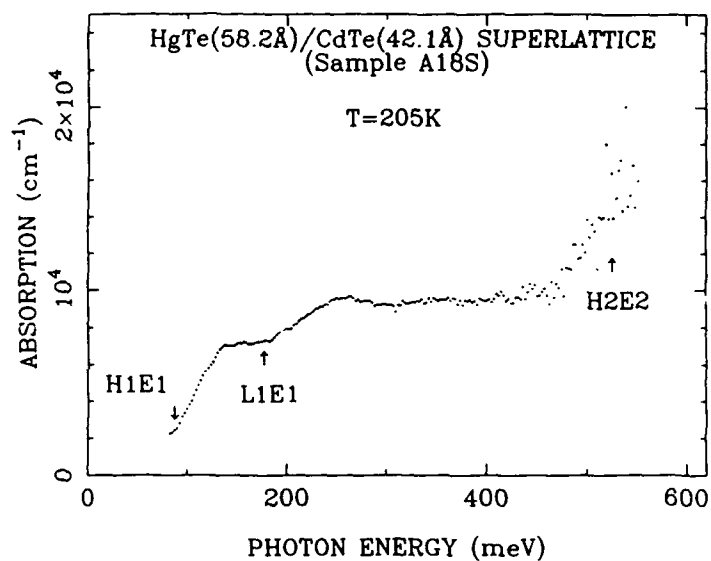


Figure 1. The absorption spectrum of SL A18S at 205 K. The arrows indicate the transition energies predicted by theory.

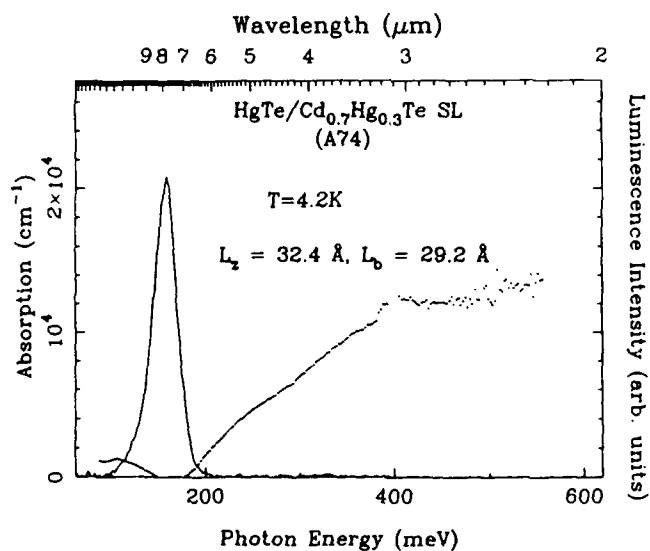


Figure 2. The absorption and photoluminescence (PL) of SL A74 at 4.2 K. The PL peak coincides with the energy where the absorption starts to rise.

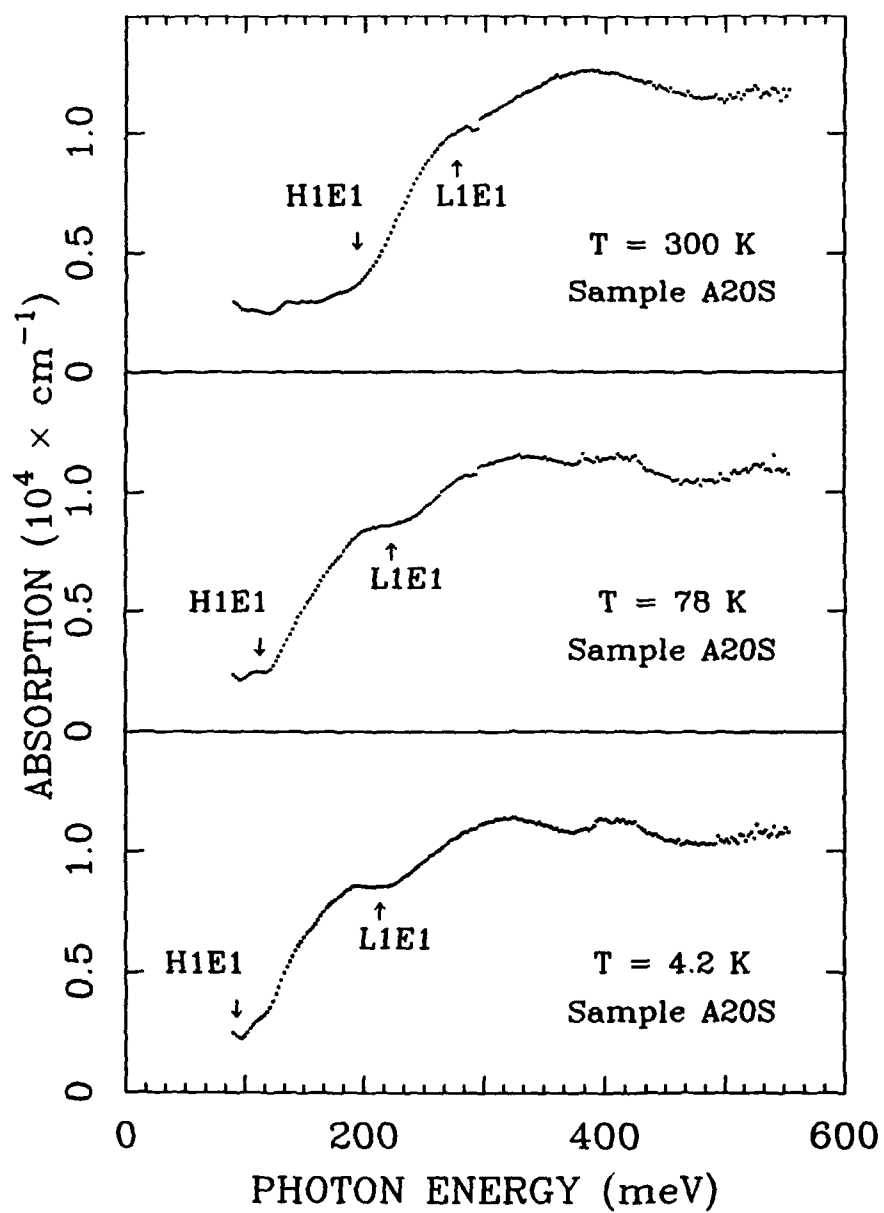


Figure 3. The absorption spectra of SL A20S at several temperatures.

Table 1. The list of nominal layer thicknesses, energies of the observed transitions for the six superlattices. The predicted transition energies and the thickness correction for each superlattice are also listed.

SAMPLE L _z (HgTe) L _b (CdTe) ΔL	T(K)	H1E1 (meV)		L1E1 (meV)		H2E2 (meV)	
		Exp.	Theo.	Exp.	Theo.	Exp.	Theo.
A17S 58.2Å/42.1Å 1	5.0	< 80	35.3	159±20	128.3	424±25	490.5
	58.0	< 80	48.3	165±15	140.5	460±25	500.0
	153.0	90±10	73.0	186±15	163.8	479±25	516.3
	205.0	105±10	87.1	189±15	177.4	483±25	525.6
A18S 58.2Å/42.1Å 1	5.0	< 80	35.3	120±20	128.3	434±25	490.5
	58.0	< 80	48.3	128±15	140.5	431±25	500.0
	99.0	< 80	58.7	145±20	150.3	462±25	506.6
	205.0	83±10	87.1	183±15	177.4	479±25	525.6
A19S 35.6Å/32.4Å 1	4.2	162±20	171.7	- -	275.9	- -	> 650
	78.0	170±30	190.2	- -	294.3	- -	> 650
	300.0	250±20	247.4	- -	351.5	- -	> 650
A20S 45.4Å/38.4Å 1	4.2	100±10	106.4	220±10	209.7	- -	> 650
	78.0	119±10	124.9	238±10	227.9	- -	> 650
	134.0	119±20	140.0	248±10	240.6	- -	> 650
	300.0	190±20	185.5	279±10	287.5	- -	> 650
A21S 54.9Å/42.1Å 1	5.0	< 80	60.9	152±25	159.6	479±25	615.7
	73.0	< 80	79.1	167±20	177.1	493±25	626.1
	137.0	83±10	95.2	186±10	193.0	510±25	630.0
	205.0	91±15	116.5	205±20	211.2	510±25	647.1
A74 32.4Å/29.2Å 0	4.2	160±20	158.8	- -	249.8	- -	> 650
	94.0	170±30	180.0	- -		- -	> 650

not accurate when the energy level is too far away from the bulk band edge, as is the case for the E2 subband. The value of ΔE_v is for the binary HgTe/CdTe heterojunctions. A positive value of ΔE_v means that the valence band of HgTe is above that of CdTe. The value of ΔE_v is assumed to be linearly dependent on the composition of $\text{Cd}_x\text{Hg}_{1-x}\text{Te}$. The energies of the L1E1 transitions are insensitive to the value of ΔE_v . A change of 100 meV in ΔE_v changes the L1E1 transition energy only by 5 meV. The energies of the H1E1 transitions are much more sensitive to ΔE_v , with a change of 5 meV in ΔE_v corresponding to 1 meV change in H1E1 transition energy for a typical SL. Taking into account the errors of the experimental transition energies, we estimate that the uncertainty of ΔE_v determined from the fitting is ± 100 meV. The nominal thicknesses of SLs A17S, A18S and A21S are very close to one another. Their absorption spectra turned out to be also almost identical, although they were grown at different times.

The value of $\Delta E_v = 420 \pm 100$ meV obtained from the fitting exhibits little temperature dependence from 4.2 to 300 K. This is consistent with x-ray photoemission results [4,5] and the recent optical results [6], but is in contradiction with earlier optical results [1,2] and the recent theoretical prediction of its temperature dependence [7].

In summary, we have, for the first time, studied experimentally the optical absorption of $\text{HgTe}/\text{Cd}_{0.85}\text{Hg}_{0.15}\text{Te}$ SLs involving several inter-subband transitions in the temperature range from 4.2 and 300 K. The energies of the observed transitions have been found to shift to higher energy when the temperature is raised. The theoretical results agree very well with the experimental results, if the valence band offset between HgTe and CdTe is 420 meV.

ACKNOWLEDGMENT

This work was supported by NSF grant DMR-88-13525, DARPA contract DAAL03-87-K-0153 and General Electric Aerospace Center.

REFERENCES

- [1] J. Reno, I. K. Sou, J. P. Faurie, J. M. Berroir, Y. Guldner, and J. P. Vieren, *Appl. Phys. Lett.* **49**, 106 (1986)
- [2] Z. Yang and J. K. Furdyna, *Appl. Phys. Lett.* **52**, 498 (1988)
- [3] A. T. Hunter and T. C. McGill, *J. Appl. Phys.* **52**, 5779 (1981)
- [4] S. P. Kowalczyk, J. T. Cheung, E. A. Kraut, and R. W. Grant, *Phys. Rev. Lett.* **56**, 1605 (1986)
- [5] R. Sporken, S. Sivanathan, J. P. Faurie, D. H. Ehlers, J. Fraxedas, L. Ley, J. J. Pireaux and R. Caudano, *J. Vac. Sci. Technol.* **A7**, 427 (1989)
- [6] J. M. Berroir, Y. Guldner, J. P. Vieren, M. Voos, X. Chu, and J. P. Faurie, *Phys. Rev. Lett.* **62**, 2024 (1989)
- [7] K. J. Malloy, and J. A. Van Vechten, *Appl. Phys. Lett.* **54**, 937 (1989)

PROPERTIES OF MODULATION-DOPED HgCdTe SUPERLATTICES

S. HWANG, Z. YANG, Y. LANSARI, J.W. HAN, J.W. COOK, JR.,
N.C. GILES, AND J.F. SCHETZINA
Department of Physics, North Carolina State University, Raleigh,
North Carolina 27695-8202

ABSTRACT

Photoassisted molecular beam epitaxy has been employed to successfully prepare p-type and n-type modulation-doped HgCdTe superlattices. The samples were grown at 170°C. In this paper, we report details of the MBE growth experiments and describe the optical and electrical properties that these new multilayered quantum well structures of HgCdTe possess.

INTRODUCTION

Modulation doping involves the transfer of carriers (holes or electrons) from a substitutionally doped layer (modifier layer) to an adjacent matrix material having a smaller band gap. In 1969, Esaki and Tsu [1] proposed a selectively-doped heterojunction structure for enhanced carrier transport parallel to the hetero-interface. Independently in 1978, Dingle et al. [2], using n-type AlGaAs-GaAs heterostructures, first demonstrated that enhanced carrier transport can, indeed, occur and first evoked the name "modulation doping". Since then, modulation-doped structures composed of III-V semiconductor layers such as GaAs, AlGaAs, and GaInAs have been studied in detail, and the properties that these novel structures possess have subsequently been incorporated into many planar devices [3].

Precise control of the electrical properties of HgCdTe through the addition of substitutional impurities is a fundamental requirement for the fabrication of infrared (IR) detectors based on p-n junctions or p-on-n heterojunctions. The detection of IR radiation is the most important area of application for HgCdTe at present. Boukerche et al. [4] have recently reviewed the problems associated with the use of both Group I elements (Li, Ag, Na) and Group V elements (Sb, As) as potential p-type dopants in HgCdTe. It appears that none of these elements are suitable for use as p-type dopants in MBE-grown HgCdTe.

In an attempt to address this fundamental doping problem we have employed modulation doping techniques coupled with photo-assisted molecular beam epitaxy (MBE) to produce stable p-type alloys of $\text{Hg}_{1-x}\text{Cd}_x\text{Te}$ ($x = 0.18-0.26$) [5]. N-type modulation-doped samples of $\text{Hg}_{1-x}\text{Cd}_x\text{Te}$ ($x = 0.18-0.26$) have also been prepared [6].

In these initial studies, δ -doped $\text{Hg}_{0.15}\text{Cd}_{0.85}\text{Te}$ barrier layers of thickness $L_b \sim 50 \text{ \AA}$ were alternated with $\text{Hg}_{1-x}\text{Cd}_x\text{Te}$ ($x = 0.18-0.26$) well layers of thickness $L_z \sim 1000 \text{ \AA}$. This produced a quantum alloy of HgCdTe, the properties of which are described in [7]. Large doping levels in δ -doped structures are accompanied by a substantial distortion of the band structure in the vicinity of the heterointerfaces which gives rise to one or more localized (2D) carrier states E_{BE} or E_{BHH} [7]. The degree of localization increases with doping density. One way to minimize this type of carrier localization is to employ matrix layer thicknesses that

are small and comparable to the barrier layer thicknesses: $L_b = L_b \sim 30 - 100 \text{ \AA}$. For layer thicknesses of this magnitude, our calculations indicate that there will be little distortion of the inherent superlattice band structure due to the charge transfer process associated with modulation doping. Thus, the carriers introduced by modulation doping will more nearly reflect the properties of the unperturbed superlattice, and transport perpendicular to the layers may be enhanced.

In this paper, we report the growth of these new modulation-doped superlattices of HgCdTe. The structures were prepared by means of photoassisted MBE. Details of the MBE growth experiments are given along with a discussion of the electrical and optical properties that these interesting new HgCdTe quantum structures exhibit.

EXPERIMENTAL DETAILS

Modulation-doped HgCdTe superlattices were grown in a Hg-compatible MBE system designed and built at NCSU. A description of this MBE system together with the techniques that have been developed to grow HgCdTe by both conventional and photoassisted MBE are given in earlier publications [7,8]. In the present work, p-type modulation-doped HgCdTe superlattices were grown by alternately depositing $\text{Hg}_{0.3}\text{Cd}_{0.7}\text{Te}$ barrier layers that were heavily doped with arsenic with undoped $\text{Hg}_{0.78}\text{Cd}_{0.22}\text{Te}$ layers. In this way, superlattices consisting of 200 double layers were prepared. The thickness of the $\text{Hg}_{0.3}\text{Cd}_{0.7}\text{Te:As}$ doping layers was $L_b \sim 50 \text{ \AA}$ in each of the superlattices, with the As dopant uniformly distributed (no setback). For the small-band-gap well layers, $\text{Hg}_{0.78}\text{Cd}_{0.22}\text{Te}$ of thickness $L_w = 50-104 \text{ \AA}$ was used in the various superlattice growth experiments. To prepare n-type modulation-doped HgCdTe superlattices, the wide-band-gap $\text{Hg}_{0.3}\text{Cd}_{0.7}\text{Te}$ barrier layers were doped with indium rather than arsenic.

All of the modulation-doped HgCdTe superlattice samples were grown using lattice-matched (100) $\text{Cd}_{0.96}\text{Zn}_{0.04}\text{Te}$ substrates. The substrates were polished and etched using standard techniques [11]. Immediately prior to film growth, the substrates were preheated at 300°C for 10 minutes in the MBE chamber to drive off residual impurities and to insure a stoichiometric growth surface. A substrate temperature of 170°C was used throughout the film growth experiments.

Electrical characterization experiments consisted of van der Pauw Hall effect measurements performed on each modulation-doped sample over the temperature range $20 - 300 \text{ K}$. Infrared photoluminescence (PL) measurements at 4.2 K were completed for each of the modulation-doped HgCdTe superlattices using a Nicolet 60 SXR Fourier-transform infrared spectrometer (FTIR). In these experiments, the PL signal was excited using the $1.06 \mu\text{m}$ emission from a Nd:YAG laser focussed to a spot on the sample surface to give a power density of approximately 200 W/cm^2 .

MODULATION-DOPED HgCdTe SUPERLATTICES

Figure 1(a) shows plots of Hall mobility and carrier concentration versus temperature for a representative n-type modulation-doped HgCdTe superlattice (B77A) consisting of 200

double layers in which the barrier layer thickness is $L_b = 51.8 \text{ \AA}$ and the well layer thickness is $L_w = 103.7 \text{ \AA}$. These thicknesses are estimates, rounded to the nearest monolayer, that were obtained from the total thickness of the superlattice as measured with a Dektak surface profilometer, the measured x-ray diffraction satellite spacing of the superlattice, and from an analysis of its optical absorption and photoluminescence spectra. Note from the figure that B77A is n-type and exhibits an essentially flat carrier concentration of $3.5 \times 10^{16} \text{ cm}^{-3}$ at temperatures below 200 K. The electron mobility is $7 \times 10^3 \text{ cm}^2/\text{V s}$ at 300 K and increases monotonically to $3 \times 10^4 \text{ cm}^2/\text{V s}$ at 30 K. The photoluminescence spectrum obtained for B77A is shown in Figure 1(b). It consists of a main PL peak centered at 118 meV (10.5 \mu m) having a full-width-at-half-maximum (FWHM) of 30 meV. A high energy shoulder is also seen at $\sim 130 \text{ meV}$. We attribute the observed PL peaks as being associated with transitions between the allowed quantum states of the superlattice, with the principal peak corresponding to the energy released by an electron in going from the $n = 1$ conduction band state to the heavy hole ground state (1H transition), which corresponds to the band gap energy of the superlattice (114 meV at 4.2K).

Figure 2(a) shows plots of Hall mobility and carrier concentration versus temperature for a p-type modulation-doped HgCdTe superlattice (B75A) consisting of 200 double layers in which the barrier layer thickness is $L_b = 51.8 \text{ \AA}$ and the well layer thickness is $L_w = 90.7 \text{ \AA}$. For this superlattice, the Hall coefficient is negative at room temperature due to thermal excitation of carriers, since the electron mobility in HgCdTe is much larger than the hole mobility. The Hall coefficient becomes positive at $\sim 180 \text{ K}$ and at lower temperatures the holes manifest their properties. For B75A, it is seen that the hole mobility increases monotonically as the temperature decreases and reaches a maximum of $\mu_p = 850 \text{ cm}^2/\text{V s}$ at 30 K, the lowest temperature measured. This is an excellent mobility value for $\text{Hg}_{0.78}\text{Cd}_{0.22}\text{Te}$, especially since the quantum confinement shifts the band gap of B75B at 4.2 K to nearly 8 \mu m , corresponding to a bulk alloy of $x \sim 0.26$. Note, in addition, from Figure 2(b) the very bright and narrow (FWHM = 10 meV) PL peak that is observed at 4.2 K. For this superlattice, the low temperature hole concentration is not constant, as would be expected for a modulation-doped structure, suggesting that some of the dopant ions may have diffused across the layer interfaces to provide centers for hole freeze-out at low temperatures. Alternatively, hole freezeout may be due to other impurities (such as Hg deficiencies) in the quantum well layers. It would be premature to speculate further on this point at this time, since only a few superlattices of this type have been grown to date.

Figure 3 shows Hall effect and photoluminescence data for a p-type modulation-doped superlattice B73A for which $L_w = L_b = 51.8 \text{ \AA}$ and $x = 0.22$ for the $\text{Hg}_{1-x}\text{Cd}_x\text{Te}$ well layers. Note that the quantum confinement associated with small L_w is manifested by the large energy shift in the PL peak at 4.2 K to 220 meV (5.6 \mu m), which corresponds to the band gap of an equivalent bulk $\text{Hg}_{1-x}\text{Cd}_x\text{Te}$ alloy having $x = 0.31$. The hole mobility increases with decreasing temperature, as shown in Figure 3(a), and reaches a value of $\mu_p = 200 \text{ cm}^2/\text{V s}$ at 30 K.

ACKNOWLEDGEMENTS

The authors wish to acknowledge J. Matthews, M. Bennet and A. Mohan for their assistance with substrate preparation. Substrates were kindly provided by II-VI, Inc. This work was supported by NSF grant DMR-88-13525, NRL contract N00014-89-J-2024, and General Electric Aerospace Group IR & D funds.

REFERENCES

1. L. Esaki and R. Tsu, IBM Research Note RC-2418 (1969).
2. R. Dingle, H.L. Stormer, A.C. Gossard, and W. Wiegmann, Appl. Phys. Lett. **37**, 805 (1978).
3. "The Technology and Physics of Molecular Beam Epitaxy", edited by E.H.C. Parker, (Plenum Press, New York, 1985).
4. M. Boukerche, P.S. Wijewarnasuriya, S. Sivasanthan, I.K. Sou, Y.J. Kim, K.K. Mahavadi, and J.P. Faurie, J. Vac. Sci. Technol. **A 6**, 2830 (1988).
5. R.N. Bicknell, N.C. Giles, and J.F. Schetzina, Appl. Phys. Lett. **49**, 1095 (1986).
6. J.W. Han, S. Hwang, Y. Lansari, R.L. Harper, Z. Yang, N.C. Giles, J.W. Cook, Jr., S. Sen, and J.F. Schetzina, Appl. Phys. Lett. **54**, 63 (1989).
7. J.W. Han, S. Hwang, Y. Lansari, R.L. Harper, Z. Yang, N.C. Giles, J.W. Cook, Jr., S. Sen, and J.F. Schetzina, J. Vac. Sci. Technol. **A 7**, 305 (1989).
8. K.A. Harris, S. Hwang, D.K. Blanks, J.W. Cook, Jr., N. Otsuka, and J.F. Schetzina, J. Vac. Sci. Technol. **A 4**, 2061 (1986).

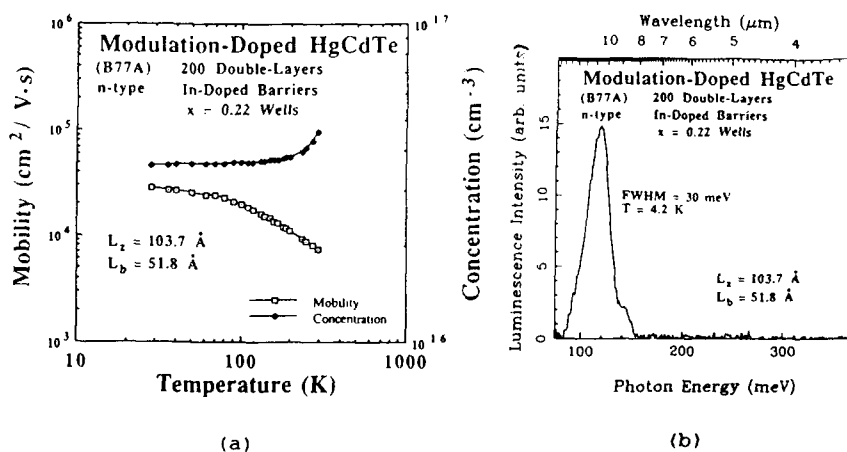


Fig. 1. Hall effect and PL data for n-type superlattice B77A.

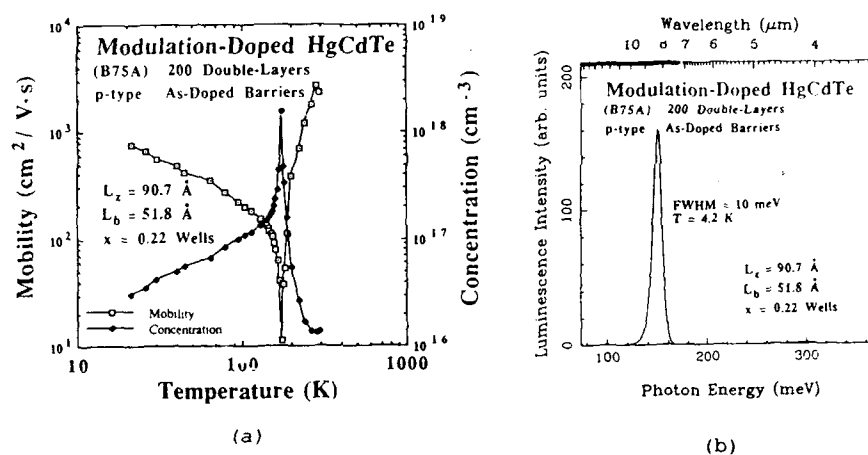


Fig. 2. Hall effect and PL data for p-type superlattice B75A.

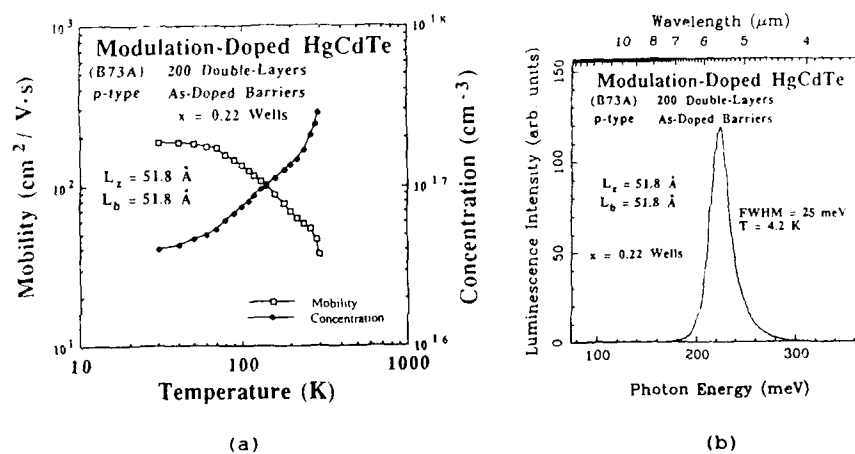


Fig. 3. Hall effect and PL data for p-type superlattice B73A.

PART VI

HgCdTe: Surfaces, Passivants,
and Processing

THE EFFECT OF SURFACE LAYERS IN EPITAXIAL n-TYPE $\text{Hg}_{1-x}\text{Cd}_x\text{Te}$

K.K. PARAT, N.R. TASKAR, I.B. BHAT and S.K. GHANDHI

Electrical, Computer and Systems Engineering Department, Rensselaer Polytechnic
Institute, Troy, New York 12180.

ABSTRACT

The presence of low mobility surface electrons on n- $\text{Hg}_{1-x}\text{Cd}_x\text{Te}$ is generally not apparent in the temperature dependence of the Hall Coefficient (R_H) or the Hall mobility (μ_H) of the layer. However, its influence is clearly seen in the magnetic field (B-field) dependence of R_H . The B-field dependence of R_H can be analyzed to extract the bulk and surface carrier concentrations and their respective mobilities.

This diagnostic technique has been used for evaluating epitaxial $\text{Hg}_{1-x}\text{Cd}_x\text{Te}$ layers grown by organometallic vapor phase epitaxy (OMVPE), which have been converted to n-type by annealing in Hg overpressure. In addition, the effect of anodic sulfide passivation on the B-field dependence of Hall coefficient is also outlined.

Hall-effect analysis in $\text{Hg}_{1-x}\text{Cd}_x\text{Te}$ is often complicated by the presence of surface carriers in addition to the bulk carriers [1-5]. An unpassivated surface of $\text{Hg}_{1-x}\text{Cd}_x\text{Te}$ typically has a sheet layer of surface electrons with a concentration in the range of $3 \times 10^{11}/\text{cm}^2$ to $1 \times 10^{12}/\text{cm}^2$. These surface electrons come about due to the fixed positive charges present in the native oxide of $\text{Hg}_{1-x}\text{Cd}_x\text{Te}$. The mobility of these electrons is usually a factor of 5-10 lower than those of the bulk electrons, while still a factor of 10-20 higher than those of the bulk holes.

The high mobility of the surface electrons compared to the bulk holes makes their presence readily apparent in Hall measurements of p-type $\text{Hg}_{1-x}\text{Cd}_x\text{Te}$, even in cases where the bulk holes far outnumber the surface electrons. As a result, the Hall data on p-type layers including the effect of the surface electrons has been analyzed with great detail [2-5].

The lower mobility of surface electrons compared to the bulk electrons makes them of relatively minor importance in the case of n-type $\text{Hg}_{1-x}\text{Cd}_x\text{Te}$ layers which are either very thick or heavily n-type, such that the surface to bulk ratio is small. In the case of $\text{Hg}_{1-x}\text{Cd}_x\text{Te}$ layers grown by OMVPE, which have been converted to n-type by Hg saturated anneal, we find that this is not the case. Here, the typical layer thickness is around $10 \mu\text{m}$, and the bulk electron concentration is around $5 \times 10^{14}/\text{cm}^3$. For an average surface electron concentration of $5 \times 10^{11}/\text{cm}^2$, the surface and bulk electrons are thus equal in number. This makes Hall measurements of these light n-type layers susceptible to surface effects. The presence of surface electrons causes the measured effective carrier concentration in the layer to be higher than the actual bulk value, and the effective electron mobility to be lower than the bulk value. In addition, the measured values of carrier concentration and mobility depend on the magnetic field at which the Hall measurement is done. However, unless the surface electron concentration is very high compared to the bulk electron concentration, the presence of surface layer is not very apparent in the temperature dependence of the Hall coefficient or mobility of n-type layers.

The Hall effect on layers with multi-carrier conduction has been analyzed in the past [6, 7]. Here the magnetic field dependence of the Hall coefficient, along with the conductivity of the layer, can be used to isolate the various types of carriers. These

techniques have been used to study epitaxial layers of InAs and polycrystalline layers of InSb, where in addition to bulk carriers, surface and interface carriers were observed [8, 9]. More recently such techniques have been employed for studying p-type $\text{Hg}_{1-x}\text{Cd}_x\text{Te}$ layers [3, 4]. In this paper we have applied this technique for evaluating the effects of surface electrons on Hall effect in n-type $\text{Hg}_{1-x}\text{Cd}_x\text{Te}$ layers. The B-field dependence of the Hall coefficient is analyzed in order to separate the bulk and surface carrier concentrations and mobilities. Results of the analysis are verified by subsequently passivating the layers using anodic sulfidization which alters the concentration of the surface carriers without affecting the bulk value.

The data on one particular sample is chosen for the sake of demonstration. The sample described here is a $\text{Hg}_{1-x}\text{Cd}_x\text{Te}$ layer of composition $x = 0.267$. It was grown on a (100) CdTe substrate by the simultaneous pyrolysis of dimethylcadmium, mercury and diisopropyltellurium at 370°C [10]. The as grown layer, which is approximately $4 \times 10^{16}/\text{cm}^3$ p-type due to Hg vacancies, is converted to n-type by annealing under Hg saturated conditions. The n-type conduction in the annealed layer is probably due to the residual donor impurities in the layer. Hall effect measurements were made using the van der Pauw technique [11].

Figure 1 shows the Hall coefficient R_H , and the Hall mobility μ_H of this layer as a function of $1000/T$. A magnetic field strength of 2.4 KG was used for this measurement. The thickness of the layer was $10.6 \mu\text{m}$. Both R_H as well as μ_H shows a "classical" n-type behavior [12]. The carrier concentration shows a slight freeze-out, which is expected in lightly doped n-type $\text{Hg}_{1-x}\text{Cd}_x\text{Te}$ of this composition. The mobility peaks around 30K with a value of $90,000 \text{ cm}^2/\text{Vsec}$, and the measured effective electron concentration in the layer is $7.5 \times 10^{14}/\text{cm}^3$ at this temperature.

With p-type $\text{Hg}_{1-x}\text{Cd}_x\text{Te}$, the presence of surface layers is very obvious in the temperature dependence of R_H and μ_H [2]. However, this is not the case here, where there are no unexpected peaks in the R_H curve and the measured carrier concentration and mobility are also acceptable as the actual bulk values. The presence of two carrier conduction becomes immediately apparent when the Hall effect measurement is carried out as a function of the magnetic field. Figure 2 shows the R_H of this sample measured as a function of B-field at a temperature of 30K. Ignoring the variation in the Hall factor (r_H) with B-field, the R_H is expected to be independent of the B-field if the conduction in the layers is purely due to the bulk electrons. But, in the case of conduction due to carriers with different mobilities, such a variation in R_H with B-field is expected. As the layer is fully extrinsic at 30K, only electrons will be present in the bulk of the sample; and hence the B-field dependence of the R_H has to be due to additional low mobility electrons present at the surface.

The layer was analyzed assuming that there were only two types of carriers present: bulk electrons and surface electrons. It was assumed that they can be characterized by two well-defined mobilities. The good agreement of this model with the experimental results presented here seems to vindicate this assumption. For a layer containing bulk as well as surface carriers, the Hall coefficient R_H is given by:

$$R_H = -\frac{1}{q} \left[\frac{(n\mu^2 + n_s\mu_s^2) + \mu^2\mu_s^2 B^2(n + n_s)}{(n\mu + n_s\mu_s)^2 + \mu^2\mu_s^2 B^2(n + n_s)^2} \right] \quad (1)$$

and the conductivity σ is given by:

$$\sigma = q(n\mu + n_s\mu_s) \quad (2)$$

Here n is the bulk electron concentration, and n_s is the average concentration (sheet carrier concentration N_s , divided by the total thickness of the $\text{Hg}_{1-x}\text{Cd}_x\text{Te}$ layer) of

the surface electrons. μ and μ_s are the corresponding bulk and surface mobilities.

Using computer simulation, the bulk electron concentration in the above sample was calculated to be $4 \times 10^{14}/\text{cm}^3$ with a bulk mobility of $137,000 \text{ cm}^2/\text{Vsec}$ at 30K. The surface electron concentration was calculated to be $6 \times 10^{11}/\text{cm}^2$ with a surface mobility of $23,500 \text{ cm}^2/\text{Vsec}$. The solid curve drawn through the experimental values of R_H in Fig. 2 is the theoretical curve for these values of the bulk and surface parameters. The excellent fit vindicates the assumption that only two types of carriers need to be considered in these layers.

Table 1 shows the result of Hall effect analysis with and without, including the effect of the surface carriers. Here the first column lists the electron concentration and mobility as measured at 30K using a magnetic field strength of 2.4 KG. In the second column the results of the variable B-field analysis, which separates out the bulk carrier and surface carriers, is presented.

To verify that the B-field dependence of R_H was indeed caused by surface effects, and that the bulk parameters extracted using this technique are reliable, the layer was passivated using anodic sulfide [13] and the Hall measurements were repeated. Anodic sulfidization results in a reduced surface carrier concentration; and since it is a low temperature process, the bulk parameters are expected to remain unchanged [4, 13]. Before sulfidization the sample was given 30 seconds etch in 1% Br-methanol, and the sulfidization was carried out in a non-aqueous solution of sodium sulfide in ethylene glycol. After growing about 400 Å of native anodic sulfide, the layer was capped with about 2500 Å of evaporated ZnS. Due to etching and growth of native sulfide the thickness of the $\text{Hg}_{1-x}\text{Cd}_x\text{Te}$ layer was reduced to 9.7 μm from the original value of 10.6 μm .

The R_H of the passivated sample as a function of B-field, as measured at 30K, is shown in Fig. 3. The sample still shows some variation in the R_H with B-field. However, the values of R_H are considerably higher than before, and the total variation is also significantly lower. From the measured values of R_H and σ , the bulk and surface parameters were once again calculated. The bulk electron concentration was evaluated to be $3.9 \times 10^{14}/\text{cm}^3$ with corresponding bulk mobility of $142,000 \text{ cm}^2/\text{Vsec}$. The surface carrier concentration was evaluated to be $1.5 \times 10^{11}/\text{cm}^2$ with a surface mobility of $31,000 \text{ cm}^2/\text{Vsec}$. Table 2 shows the results of the variable B-field analysis before and after passivation. Note that the bulk values are essentially the same. For the sulfidized sample, the surface electron concentration is lower by a factor of 4 compared to the bare sample. There is also some increase in the surface mobility in the sulfidized sample, which is probably due to the reduced concentration of the surface electrons and reduction in the surface scattering as a result of passivation. The R_H vs. B-field characteristic looks very different before and after sulfidization, and yet both yield the same values for the bulk parameters; which proves that the bulk values calculated by this method are correct.

Figure 4 shows the temperature dependence of the R_H and μ_H of the sulfidized layer taken at a B-field of 2.4KG, as in the case of the unpassivated layer (Fig. 1). Due to the reduction in the number of surface electrons, the measured value here become closer to the bulk value as is seen by the increase in the R_H and μ_H . The measured electron concentration and mobility (the effective values) at 30K are $4.9 \times 10^{14}/\text{cm}^3$ and $123,000 \text{ cm}^2/\text{Vsec}$, which are nearer to the bulk values calculated using the variable B-field technique. If the layers were perfectly passivated so that all the surface electrons could be eliminated, these values would have been the same as the bulk values.

In the foregoing discussions it was assumed [3, 4] that the Hall factor r_H did not change with B-field. Theoretical calculations show that at 30K this variation would be

less than 3% in CdTe and less than 10% in HgTe [14]. In the unpassivated sample, the R_H varies by about 30% in the 0 to 6KG range and by about 10% in the passivated sample. The contribution to this from variation in the r_H is unknown at present and has been neglected. But this would certainly be less than 10%.

The variable B-field analysis can only evaluate the effective volume concentrations and mobilities of the two types of carriers, and not their physical location. It is well-known that the bare surface of $Hg_{1-x}Cd_xTe$ usually has surface electrons of the order of $3-10 \times 10^{11}/cm^2$, and that by anodic sulfidization these can be reduced to about $1-2 \times 10^{11}/cm^2$ [4]. In layers investigated in our laboratory, we notice the same trend. Hence, the low mobility electrons have been attributed to the top surface. In addition, the two carrier model gives a near perfect match between the theoretical and experimental values. As a result, we have ignored the presence of any electrons at the epi-substrate interface between $Hg_{1-x}Cd_xTe$ and CdTe which might have mobilities different from those of the bulk and surface electrons.

The results reported here are for an average sample with a bulk carrier concentration of $4 \times 10^{14}/cm^3$, and surface carrier concentration of $6 \times 10^{11}/cm^2$. As is expected, the effect is more severe in layers with lower bulk electron concentrations or higher surface electron concentration. In such cases, ignoring the presence of the surface electrons leads to an overestimation of the bulk doping concentration and an underestimation of the bulk electron mobility.

In conclusion, we have shown that the presence of surface electrons on lightly doped n-type layers of $Hg_{1-x}Cd_xTe$ alters the effective carrier concentration and mobility significantly. The problem can be eliminated by passivating the layer, thus eliminating the surface electrons prior to the Hall measurement. Alternatively, by analyzing the B-field dependence of the R_H , the true bulk electron concentration and mobility can be evaluated. The correctness of the technique was verified by analyzing the Hall-effect of the same bulk layer with different surface carrier concentrations.

ACKNOWLEDGEMENT:

The authors would like to thank J. Barthel for technical assistance on this program and P. Magilligan for manuscript preparation. CdTe substrate material was kindly supplied by C.J. Johnson and S. McDevitt of II-VI, Inc., Saxonburg, PA. Partial funding for this program, from Raytheon Corporation, is hereby acknowledged. This work was sponsored by the Defense Advanced Research Project Agency (Contract No. N-00014-85-K-0151), administered through the Office of Naval Research, Arlington, VA. This support is greatly appreciated.

REFERENCES

1. W. Scott, E.L. Stelzer, and R.J. Hager, J. Appl. Phys. 47, 1408 (1976).
2. L.F. Lou and W.H. Frye, J. Appl. Phys. 56, 2253 (1984).
3. A. Zemel, A. Sher, and D. Eger, J. Appl. Phys. 62, 1861 (1987).
4. M.C. Chen, Appl. Phys. Lett. 51, 1836 (1987).
5. M.C. Chen, J. Appl. Phys. 65, 1571 (1989).
6. A. Neduloha, and K.M. Koch, Z. Phys. 132, 608 (1952).
7. R.L. Petritz, Phys. Rev. 110, 1254 (1958).
8. H.H. Wieder, Appl. Phys. Lett. 25, 206 (1974).
9. A. Zemel and J.R. Sites, Thin Solid Films 41, 297 (1977).
10. S.K. Ghandhi, I.B. Bhat, and H. Fardi, Appl. Phys. Lett. 52, 392 (1988).
11. L.J. van der Pauw, Philips Research Reports 13, 1 (1958).

12. W. Scott, J. Appl. Phys. 43, 1055 (1972).
13. Y. Nemirovsky, L. Burstein, and I. Kidron, J. Appl. Phys. 58, 366 (1985).
14. D.L. Rode, Phys. Stat. Sol. (B) 55, 687 (1973).

TABLE 1

RESULTS OF HALL EFFECT MEASUREMENT AT 30K WITH AND WITHOUT
INCLUDING THE SURFACE EFFECTS

	APPARENT VALUE (B = 2.4KG)	ACTUAL VALUE
$n(/cm^3)$	7.5×10^{14}	4×10^{14}
$\mu(cm^2/V sec.)$	90,000	137,000
$N_S(/cm^2)$	— — —	6×10^{11}
$\mu_S(cm^2/V sec.)$	— — —	23,500

TABLE 2

RESULTS OF THE VARIABLE B-FIELD ANALYSIS AT 30K
BEFORE AND AFTER SURFACE PASSIVATION

	BEFORE SULFIDIZATION	AFTER SULFIDIZATION
$n(/cm^3)$	4×10^{14}	3.9×10^{14}
$\mu(cm^2/V sec.)$	137,000	142,000
$N_S(/cm^2)$	6×10^{11}	1.5×10^{11}
$\mu_S(cm^2/V sec.)$	23,500	31,000

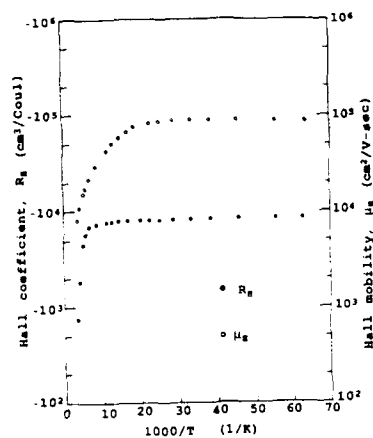


Figure 1. Hall coefficient and Hall mobility vs. $1000/T$ for an n-type $\text{Hg}_{1-x}\text{Cd}_x\text{Te}$ layer. $x = 0.267$, layer thickness = $10.6 \mu\text{m}$. B-field = 2.4KG .

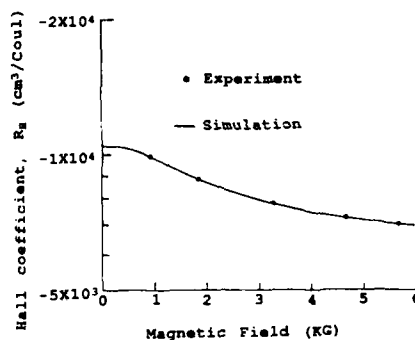


Figure 2. Hall coefficient vs. B-field for the sample of Fig. 1 at 30K . The solid curve is the theoretical fit to the experimental data for two carrier conduction.

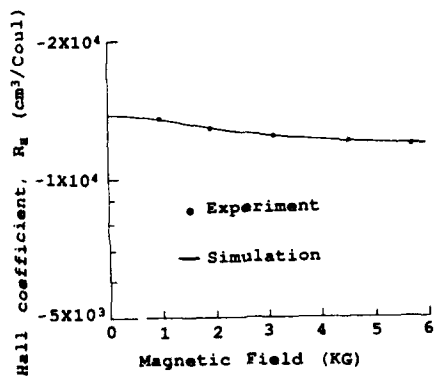


Figure 3. Hall coefficient vs. B-field for the sample of Fig. 2 after surface passivation. The solid curve is the theoretical fit to the experimental data for two carrier conduction.

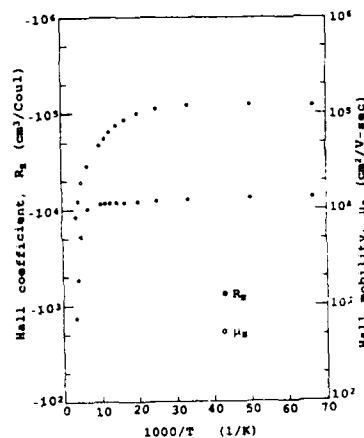


Figure 4. Hall coefficient and Hall mobility vs. $1000/T$ for the sample in Fig. 1 after surface passivation. $x = 0.267$, layer thickness = $9.7 \mu\text{m}$. B-field = 2.4KG .

SURFACE ELECTRONS IN INVERTED LAYERS OF p -HgCdTe

SAMUEL E. SCHACHAM* AND ELIEZER FINKMAN

*NASA Lewis Research Center, Cleveland, OH 44135

Department of Electrical Engineering and Solid State Institute, Technion - Israel Institute of Technology, Haifa 32000, Israel.

*This work was done while this author held a National Research Council - NASA Research Associateship.

ABSTRACT

Anodic oxide passivation of p -type HgCdTe generates an inversion layer. Extremely high Hall mobility data for electrons in this layer indicated the presence of a two-dimensional electron gas. This is verified by use of the Shubnikov-de Haas effect from 1.45-4.15K. Data is extracted utilizing a numerical second derivative of DC measurement. Three sub-bands are detected. Their relative occupancies are in excellent agreement with theory and with experimental results obtained on anodic oxide as accumulation layers of n -type HgCdTe. The effective mass derived is comparable to expected.

INTRODUCTION

The narrow-gap semiconductor HgCdTe is an important infrared detector material. Most photodiodes are implemented on p -type HgCdTe. The performance of these devices is heavily dependent on surface properties. Thus the selection of an appropriate passivation is crucial.

Anodic oxide forms an accumulation layer on n -type material. The two-dimensional sub-bands of this passivation have been thoroughly investigated in recent years. Findings obtained using various magnetoresistance measurements [1-7] are in good agreement with data obtained from other narrow-gap non-parabolic semiconductor systems, in particular on HgTe and HgTe/CdTe superlattices [8-10]. It has been shown both in theory [11,12], as well as experimentally [1,5,6] that narrow-gap non parabolic materials possess common features. One characteristic of accumulation and inversion layers on such materials is a large number of occupied sub-bands, as many as five in HgCdTe [5,6]. Ando [12] has shown that a large change in the band-gap energy has little effect on the relative occupancy of the various sub-bands.

In this work we report the use of the Shubnikov-de Haas (SdH) technique to measure the transport properties of electrons in an inversion layer on p -type $\text{Hg}_{1-x}\text{Cd}_x\text{Te}$. The inversion film was formed by generating an anodic oxide passivation to a low concentration p -type substrate, $N_a - N_d \approx 8 \cdot 10^{14} \text{ cm}^{-3}$, with composition ratio of $x \approx 0.22$. The low acceptor concentration enhanced the Hall data of the inversion layer. An extremely high Hall mobility, higher than measured for electrons in n -type material of similar composition, triggered our speculation that a 2-dimensional electron gas is present [13]. Since previous measurements concentrated on accumulation layers, it seemed intriguing to examine an inversion film, in particular since the theory of Takada et al. [11] was developed for the latter structure (see remark in [7]).

When a magnetic field is applied perpendicular to a surface layer, the translational motion is quantized into Landau levels. Sweep of the field reveals oscillations periodic with inverse magnetic field due to modulation of the density of states at the Fermi level as the Landau levels increase in energy with increasing field. When several sub-bands are occupied, these SdH measurements generate a waveform which is a superposition of the oscillations for each sub-band. The two-dimensionality of the structure can be verified by a vanishing signal as the sample is rotated by 90° .

EXPERIMENTAL WORK

The measurement of DC magnetoresistance on HgCdTe frequently reveals little information. Seiler and Becker [14] introduced an AC technique where the magnetic field is modulated and phase sensitive detection is employed. The second derivative of the amplitude presents clear data of SdH oscillations [2,5,6,8,10]. An alternative method is using a metal-insulator-semiconductor (MIS) structure and modulating the gate voltage [1,7,15]. Since our experimental setup did not provide for modulation of the magnetic field and Hall bar samples were used, we had to develop appropriate numerical methods in order to extract the oscillatory data. Fourier analysis showed no oscillatory pattern following background subtraction. Instead numerical second derivative of the voltage with respect to the field combined with data smoothing was employed. These were obtained by fitting a small number of points to a second degree polynomial. This process eliminates the background and reveals the SdH oscillations.

Figure 1 shows such a plot of the second derivative versus an inverse magnetic field measured at 1.45 K. Several frequencies of oscillations can be observed, corresponding to various sub-band populations and their harmonics. In figure 2 we separated between these frequencies: trace (a), corresponds to 0.31-0.44 T, with a frequency of 3.75 T; trace (b), corresponds to 0.51-0.79 T, with a frequency of 9.7 T and a change of phase (beat) at 0.66 T; trace (c), corresponds to 1.01-1.16 T and shows superposition of the previous frequency with a 30.4 T waveform.

The effect of increasing temperature is presented in figure 3, in which trace 2c is repeated, this time at 4.15 K. There is an obvious decrease of the amplitude of the 30.4 T oscillation, while the reduction in the 9.7 T component is minimal.

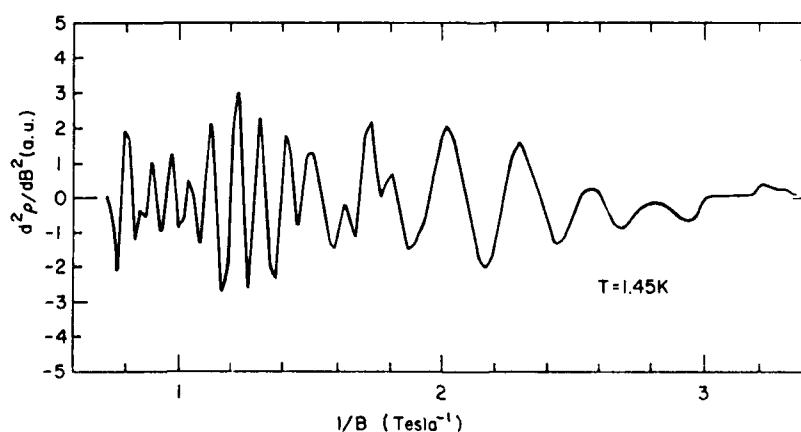


Fig. 1: Numerical second derivative of magnetoresistance measured at 1.45K, showing SdH oscillations of an anodic oxide inversion layer on $p\text{-Hg}_{0.78}\text{Cd}_{0.22}\text{Te}$

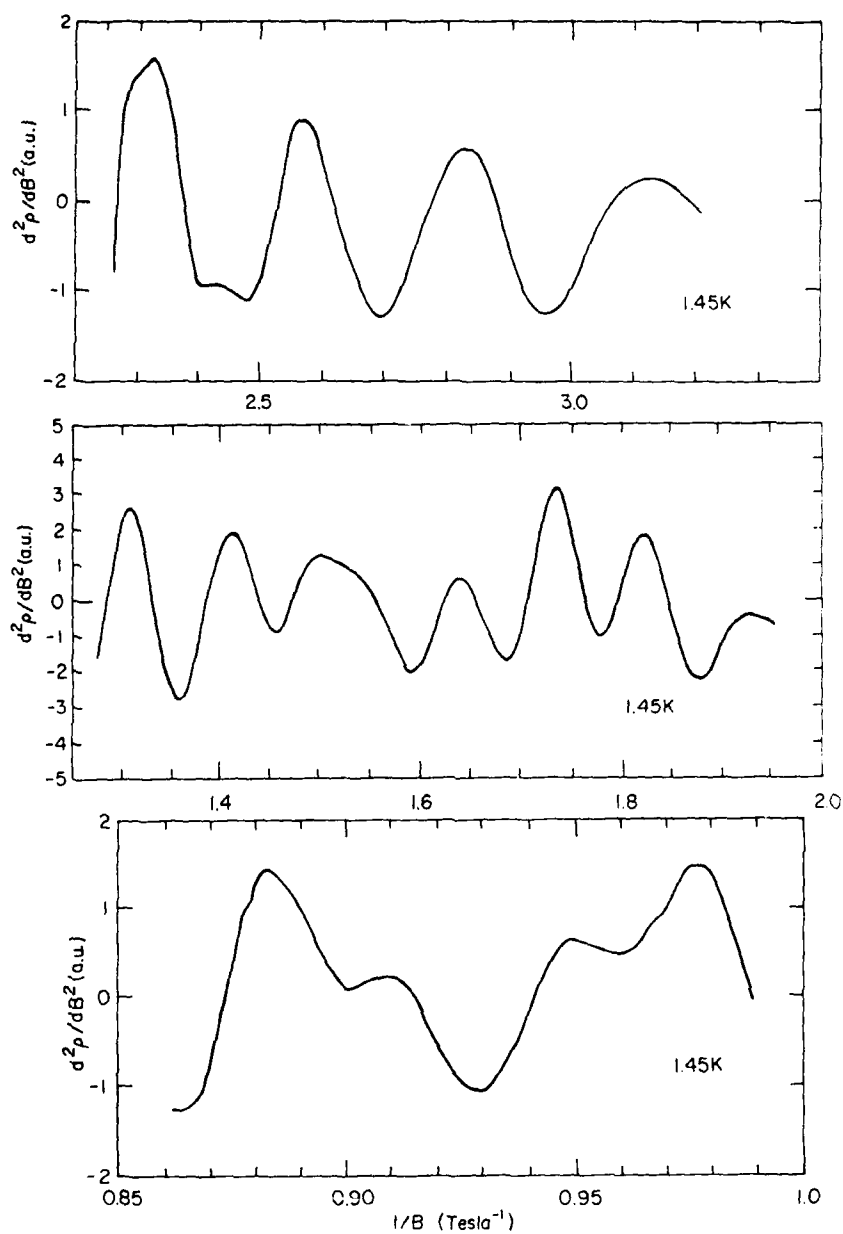


Fig. 2: High resolution data of Fig. 1, revealing 3 oscillation frequencies:
 a. 0.31-0.44T, $F = 3.75$ T.
 b. 0.51-0.79T, $F = 9.7$ T. Note the phase shift at -1.52 $1/T$.
 c. 1.01-1.16T, superposition of $F = 9.7$ T and $F = 30.4$ T.

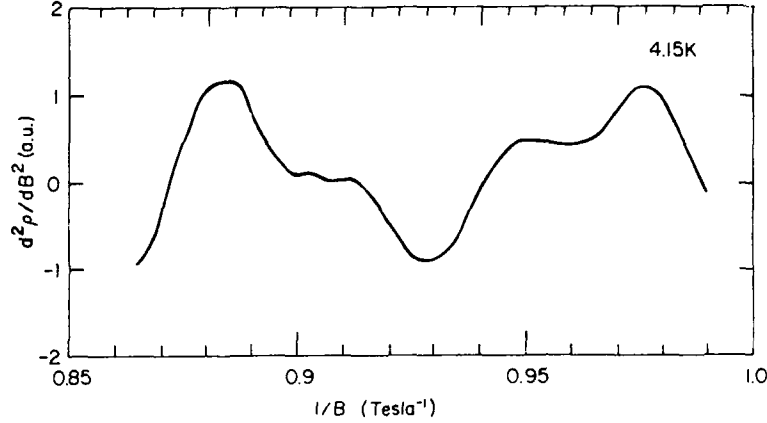


Fig. 3: Same as Fig. 2c, at 4.15, showing substantial decrease of 30.4T component, less of the 9.7 one.

ANALYSIS AND DISCUSSION

The change in the resistivity due to the magnetic field can be expressed as [16]

$$\frac{\Delta\rho}{\rho_0} \propto \sum_n \sum_M T \left[\frac{M \cdot m_r^n}{B} \right]^{1/2} \frac{\exp(-\beta M T_D^n m_r^n / B)}{\sinh(\beta M T m_r^n / B)} \cdot \cos \left[\frac{2\pi M F^n}{B} + \phi^n \right] \quad (1)$$

where T = temperature, B = magnetic field, F = oscillation frequency, ϕ = phase, T_D = Dingle temperature, m_r = effective mass ratio (m^*/m_0), and $\beta = 2\pi^2 k_B m_0 / H B e = 14.7$ T/K. The summation on M is over the harmonic frequencies of a given sub-band n . In order to obtain the occupancy of the various sub-bands, the Fourier transform of the data was obtained using an FFT. Figure 4 shows a transform of the second derivative taken at 4.15 K. Similar spectra were obtained for all other measured temperatures. These results highly resemble the data of Beck and Anderson (Fig. 2, Ref. 7), obtained for an accumulation layer. In addition to the three main frequencies, corresponding to three occupied sub-bands, one can easily observe the second and third harmonics of the 3.75 T line (with the third harmonic more intense than the second).

The effective mass of electrons in the various sub-bands can be derived from the reduction in amplitude with increasing temperatures. This dependence can be summarized as $\chi/\sinh \chi$, where $\chi = \beta T m_r / B$. Unfortunately due to the very small effective mass in HgCdTe and due to the superposition of the various lines, it is hard to obtain precise data in the limited temperature range employed. Figure 5 shows a fit for the amplitude of a peak at 1.05 T (0.95 1/T) which corresponds to the first sub-band, with the largest effective mass. The fitted value is $m^* = 0.033 m_0$. The convex shape of the curve indicates that the argument of the hyperbolic function is indeed small, thus replacing the hyperbolic sine with an exponential function should be done with extreme caution! [9]. The data is summarized in Table I. The uncertainty in the value of the effective masses is large. Moreover, since the ratio of x to its hyperbolic sine approaches rapidly 1 as x approaches 0, the very small effective masses of the second and third subbands renders a ratio which is almost temperature independent, causing a further increase in uncertainty in determination of these values. The accuracy of the derivation may be improved by either a deconvolution of the various frequency components of the waveform, or a simulation this pattern.

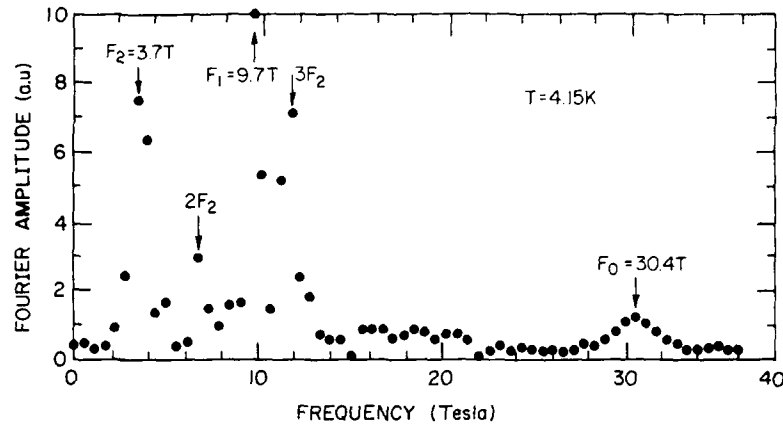


Fig. 4: Fourier transform of SdH oscillations. Clear peaks of 3 fundamental frequencies, due to 3 sub-bands, and harmonics of $F = 3.75$ T.

The sub-band occupancy is given by $N_s^n = \frac{2e}{h} \cdot F^n$. Summing up the concentration of the first three sub-bands, and adding 4% for the higher ones [5], we came up with the ratio of the sub-bands occupancy to total surface concentration N_s^T , presented in Table I.

Table I

n	$F^n(T)$	$N_s^n(cm^{-2})$	N_s^n/N_s^T	m_r^n
1	30.4	$1.47 \cdot 10^{12}$	0.693	0.033 ± 0.008
2	9.7	$4.69 \cdot 10^{11}$	0.221	0.018 ± 0.007
3	3.75	$1.81 \cdot 10^{11}$	0.0855	0.011 ± 0.005

The concentration ratios are in excellent agreement with the theory in [12], the results of Beck and Anderson [7] and the various Singleton, Nicholas and Nasir investigations [1-6]. Taking into consideration the composition ratio ($x = 0.22$), our results indeed fit perfectly with a slight difference between those of $x = 0.2$ and $x = 0.3$ [2]. The discrepancy between these data and that of Zhao et al. [1] was recently explained [5].

The effective masses obtained are on the lower edge of the theory [11] and experimental results [6,7]. However, the large uncertainty in present values necessitates further investigation before any conclusions can be drawn.

The two-dimensionality of the data was verified by rotating the sample by 90° . The numerical analysis renders noise with amplitudes one-order of magnitude smaller than the SdH oscillations, for all temperatures tested. No peaks are present in the Fourier transform.

A change of phase, such as we observed at about 0.66 T, has been previously reported for SdH data on various materials, including HgTe films [8]. The last one was observed only at ~ 1.9 K, and was attributed to strain-effects, rather than to inversion asymmetry, since it was observed at low electron concentration. In this work it is also possible that the beat is a result of the superposition of the two frequencies at 9.7 T (second sub-band) and at 11 T (third harmonic third sub-band).

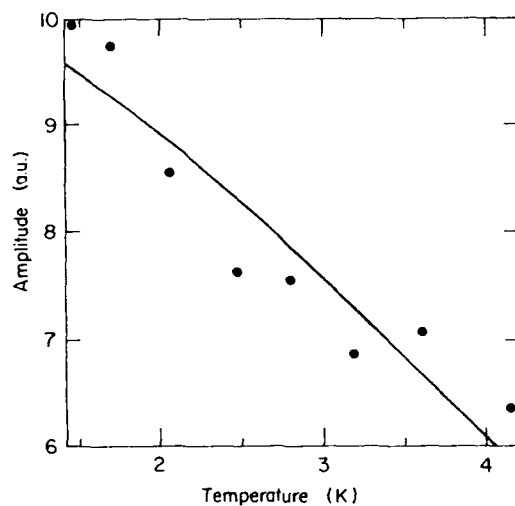


Fig. 5: Measured temperature dependence of peak at 1.05T.
Effective mass derived from theoretical fit $m^* = 0.33m_0$.

CONCLUSIONS

The SdH experimental technique performed on an inversion layer, generated by anodic oxidation of a *p*-HgCdTe, proves the existence of a 2DEG and renders data on three sub-bands. The calculated relative occupancies of these sub-bands agree extremely well with theory and experimental results obtained from accumulation layers on *n*-type materials. The analysis should be extended to achieve better accuracies of the effective mass by both measurements at higher temperatures and by mathematical simulation of the data. This also may render scattering times. Experimental work at higher magnetic fields may reveal additional structures.

The numerical analysis performance in this work has proven that it is possible to compensate for limitations in experimental facilities by appropriate mathematical tools.

REFERENCES

1. W. Zhao, F. Koch, J. Ziegler and H. Maier, Phys. Rev. B 31, 2416 (1985).
2. J. Singleton, R.J. Nicholas, F. Nasir and C.K. Sarkar, J. Phys. C 19, 35 (1986).
3. J. Singleton, F. Nasir and R.J. Nicholas, in Optical Properties of Narrow-Gap Low-Dimensional Structures, Vol. 152 in NATO ASI Series B, edited by C.M.S. Torres, J.C. Portal, J.C. Maan and R.A. Stradling (Plenum, New York, 1987), p. 195.
4. J. Singleton, F. Nasir and R.J. Nicholas, Proc. SPIE 659, 99 (1986).
5. F. Nasir, J. Singleton and R.J. Nicholas, Semicond. Sci. Technol. 3, 654 (1988).
6. R.J. Nicholas, F. Nasir and J. Singleton, J. Cryst. Growth 86, 656 (1988).
7. W.A. Beck and J.R. Anderson, J. Cryst. Growth 72, 437 (1985).

8. R.J. Justice, D.G. Leider, W. Zawadzki, R.J. Koestner, M.G. Goodwin and M.A. Kinch, *J. Vac. Sci. Technol. A* 6, 2779 (1988).
9. L. Ghenim, R.G. Mani and J.R. Anderson, *Phys. Rev. B* 39, 1419 (1989).
10. D.G. Seiler, G.B. Ward, R.J. Justice, R.J. Koestner, M.W. Goodwin, M.A. Kinch and J.R. Meyer, *J. Appl. Phys.* 66, 303 (1989).
11. Y. Takada, K. Arai, N. Uchimura and Y. Vemura, *J. Phys. Soc. Jpn.* 49 1851 (1980).
12. T. Ando, *J. Phys. Soc. Jpn.* 54, 2676 (1985).
13. S.E. Schacham and E. Finkman, to be published in *Opt. Eng.*
14. D.G. Seiler and W.M. Becker, *Phys. Rev.* 183, 784 (1969).
15. J.C. Thuillier and F. Bazenet, *J. Vacuum Sci. Technol.* 16, 1417 (1979).
16. E.N. Adams and T.D. Holstein, *J. Phys. Chem. Solids* 10, 254 (1959).

ELECTRICAL CHARACTERISATION OF P-TYPE $\text{Cd}_x\text{Hg}_{1-x}\text{Te}$ GROWN BY MOVPE

ANNE ROYLE, J S GOUGH, S J C IRVINE AND J B MULLIN

Royal Signals & Radar Establishment, St Andrews Road, Malvern, Worcs WR14 3PS, UK

ABSTRACT

The results of electrical characterisation of a series of MOVPE layers of $\text{Cd}_x\text{Hg}_{1-x}\text{Te}$ (CMT) grown by the interdiffused multilayer process (IMP) are reported. It is shown that the properties of the CMT layers when grown as a "sandwich" between CdTe buffer and cap layers display typical p-type Hall effect curves. These have been modelled and the sensitivity of the fitting parameters are reported. It is shown that there is evidence of complex ("anomalous") two-layer like behaviour in low x material which is not attributable to inversion behaviour.

INTRODUCTION

The assessment of the basic electrical transport properties of epitaxial layers of $\text{Cd}_x\text{Hg}_{1-x}\text{Te}$ by Hall effect measurements can present serious interpretation difficulties. These difficulties arise because surface inversion and interface effects lead to complex "two-layer" R_H curves, often referred to as anomalous. In this paper we report detailed electrical measurements on high quality MOVPE layers in which these effects have been effectively suppressed using controlled growth procedures. The Hall curves have been modelled using a minimum of fitting parameters. The models are sensitive to the choice of alloy composition from which n_i is derived. In the low x range it will be shown that very small changes in n_i can lead to a model which predicts a second low temperature sign change in the Hall coefficient. This effect arises as an intrinsic effect and is not due to inversion phenomena.

ROLE OF INTERFACES/SURFACES

Inversion behaviour involving the creation of n-type carriers in the surface regions of p-type CMT can arise from a variety of causes. In an original study by Mullin and Royle (1) surface oxidation or damage on bulk CMT was identified as an important cause. Subsequently (2) a range of preparation-related phenomena were shown to give rise to inversion-like effects on epitaxial layers. They included impurities on or from substrates, Ga from GaAs for example, capricious growth behaviour resulting in the formation of HgTe or low x CMT, as well as post-growth phenomena involving the effect of Hg in creating n-type surfaces. This latter cause, involving Hg indiffusion during cool-down following the growth of MOVPE layers, has been identified as a common phenomenon. The cool-down conditions which avoid this problem have been modelled by Irvine et al (3). The effects of Hg indiffusion have been avoided by Ghandhi et al (4) and by the authors (3) by using a thin layer, typically $0.1\mu\text{m}$, of CdTe in order to cap the CMT layer. The significantly reduced diffusion in CdTe compared with $\text{Cd}_x\text{Hg}_{1-x}\text{Te}$ can eliminate the problem of Hg converting the surfaces of layers from p to n. The effect of diffusion from the substrate can also be avoided in a similar manner by using a buffer layer of CdTe.

In the present study then the judicious use of CdTe buffers and caps have been used to eliminate extraneous, preparation-related, inversion effects in order to enable the transport properties of pure CMT to be assessed.

MODELLING

The Hall coefficient R_H as a function of $1/T$ and T has been modelled using the standard expression given in equation 1:

$$R_H = \frac{1}{q} \frac{(p - nb^2)}{(p + nb^2)} \quad (1)$$

where p , n , b and q are respectively the hole concentration, the electron concentration, the mobility ratio of electrons to holes and the charge on an electron.

The value of p was obtained from the charge neutrality expression (equation 2)

$$p - n - N_a^- + N_d^+ = 0 \quad (2)$$

by solving equation 2 as a cubic in p where N_a^- and N_d^+ are the ionised donors and acceptors respectively. N_a^- is given by:

$$N_a^- = \frac{P_a \times N_a \text{ (total)}}{p + P_a} \quad (3)$$

$$\text{using } P_a = \frac{N_v}{g} \exp(-E_a/kT): (g=4) \quad (4)$$

$$N_v = \frac{2(2\pi m_h kT)^{3/2}}{n_i^2} \quad (5)$$

$$\text{and } n_i^2 = np \quad (6)$$

where N_v , E_a , m_h and n_i are respectively the density of states in the valence band, the ionisation energy of the acceptor, the hole effective mass ratio (0.55) and the intrinsic number. In order to model R_H it was necessary to input a value of b and choose appropriate values of the five parameters x , b , E_a , N_a and N_d .

The Hall measurements were made over the temperature range 4.2 to 300K at 0.2 Tesla. A series of 18 epitaxial layers were examined, the experimental results being compared against the model. The results and models have been drawn on two scales R_H versus T to define the high temperature range clearly and R_H versus $1/T$ to define the freeze out region. In many cases excellent fits were obtained but in the others, although they were all very good, precise fits were not achieved. The dominant parameters in the high temperature region were x and b and although they are interactive, b was chosen primarily to coincide with R_H maximum and x to give the sign change in R_H at the appropriate temperature.

In the low temperature region N_a and E_a dominate. The choice of N_a is straightforward if there is a well defined exhaustion region. This was rarely the case because this region is only clearly defined for high x and low p -type. Nonetheless adjustment of N_a was made to fit the results. As most results were at fairly high p levels, N_d was not included. It was assumed N_d would be small compared with N_a and SIMS analysis shows that the common donor impurities were either at or below their detection limits of 10^{15} atoms cm^{-3} . The choice of E_a was then made to fit the freeze out region.

EXPERIMENTAL

The epitaxial layers were grown using the IMP process (see 3 and references therein). The growth was carried out at 350°C using Me_2Cd and iPr_2Te . The substrates were CdTe oriented $\sim 3^\circ$ off (100) towards the (110).

The Hall effect measurements were made using the van der Pauw method on $\sim 5\text{mm}$ square cleaved samples from the epitaxial layers using the equipment and procedure described in reference (2). It should be noted that the Hg vacancy (acceptor) concentration in $\text{Cd}_{0.2}\text{Hg}_{0.8}\text{Te}$ layers grown at 350°C would be $\sim 1 \times 10^{17}$ carriers cm^{-3} .

Effect of buffers and caps

Typical Hall curves for three different epitaxial structures are shown in figure 1. The upper curve (J185) shows the results for the first structure for a $7.5\mu\text{m}$ thick epitaxial layer of CMT ($x=0.19$) which was grown without a buffer or a cap. The dotted

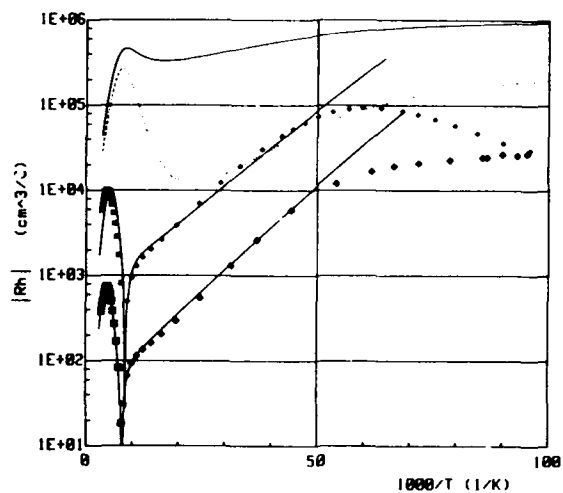


Fig. 1: Results on J185, no cap, no buffer, $x=0.19$ at thicknesses $7.5\mu\text{m}$ full line and $3.5\mu\text{m}$ dotted line with $R_H \times 100$. J203, cap, no buffer, $x=0.198$, small symbols, with $R_H \times 10$. J233 cap and buffer, $x=0.198$, large symbols. J203 fit at $x=0.198$, $b=36$, $E_a=14.5\text{meV}$, $N_a=5.5 \times 10^{16}$ and $R_H \times 10$. J233 fit at $x=0.198$, $b=45$, $E_a=16.5\text{meV}$, $N_a=1.0 \times 10^{17}$. ■ for R_H negative, ♦ for R_H positive

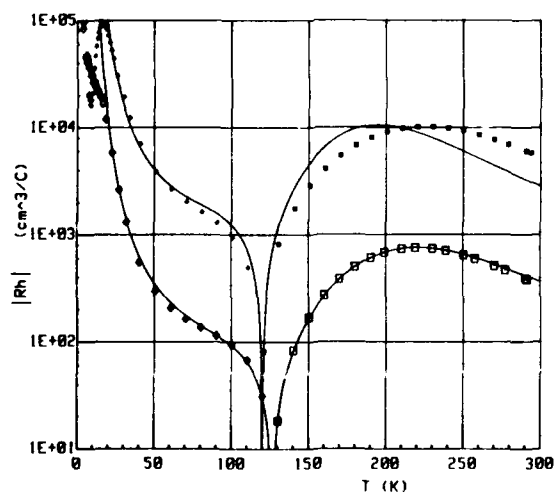


Fig. 2: J203 and J233 same samples and fits as fig 1 but plotted on $R_H \times T$ scale

curve shows the same layer after $3.0\mu\text{m}$ had been removed from the surface. R_H was -ve for both curves throughout the temperature range. The behaviour is typical of a two layer structure (2). It was attributed to the effect of a post-growth anneal occurring in the Hg vapour in the reactor as it cooled from the growth temperature to room temperature.

The second structure for which J203 is an example is characterised by a CMT epitaxial layer onto which was grown a $0.1\mu\text{m}$ cap of CdTe. The results are dramatically different to those of J185. An almost classic p-type* (where the asterix signifies the low temperature R_H characteristic) curve is obtained. However, whereas the height of the peak of R_H and the inversion temperature in the two carrier region could be fitted exactly the fitting around the peak diverged from the experimental points as did the low temperature ($<20\text{K}$) data. This latter turnover (droop) is typical of the presence of minute inversion effects.

However, both exact fitting and the avoidance of droop at low temperatures were achieved in the third category involving a structure of CMT sandwiched between a CdTe buffer and cap. J233 showed a well fitted activation energy of 16.5meV . The line fit diverges from the experimental points around 20K with an indication of a second shallower ionisation level. The model has not taken this into account. This will be considered in a later paper. The divergence of the fitting curves from the experimental data for J203 and J233 shown in figure 1 can be seen more clearly by plotting R_H versus T , as in figure 2. The fit parameters used for these curves are shown in the figure captions.

Sensitivity of fitting parameters

Before discussing the low x material, it is appropriate to note the role of x and n_i on the sensitivity to fitting the data. The equations for deriving n_i are empirical equations in alloy composition (x) and temperature (T). They are derived for a generally limited range of alloy composition. The various equations are in good general agreement but not exact agreement. The variation of n_i with T is shown in figure 3 for Schmit (5) and Hansen and Schmit (6) and Nemirovsky and Finkman (7).

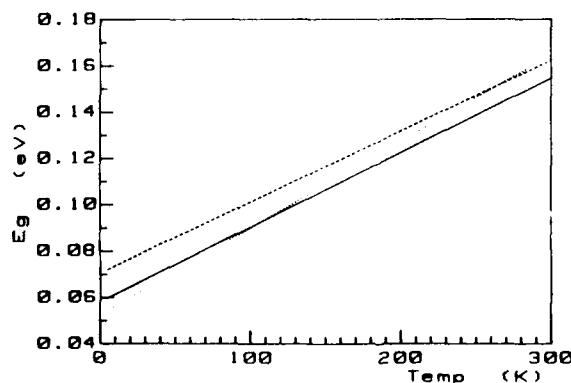


Fig. 3: Plots of the energy gap E_g (eV) versus temperature. The dashed line is ref (5), the full line is ref (6) and the dotted line ref (7)

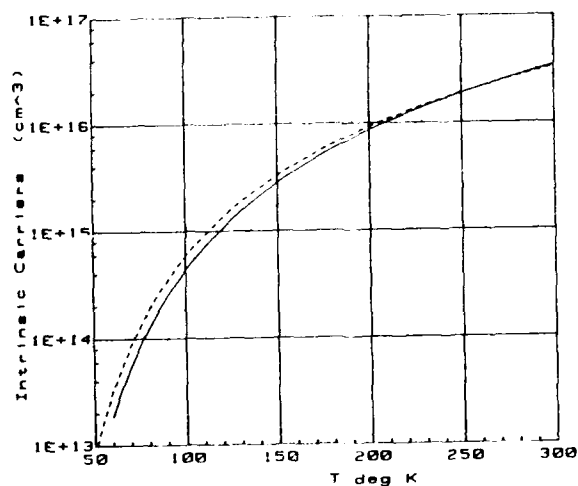


Fig. 4. Plots of intrinsic number n_i ($x=0.2$) versus temperature. The dashed line is ref (7), the full line is ref (6), the dotted lines ref (6), $x=0.19$ and $x=0.21$

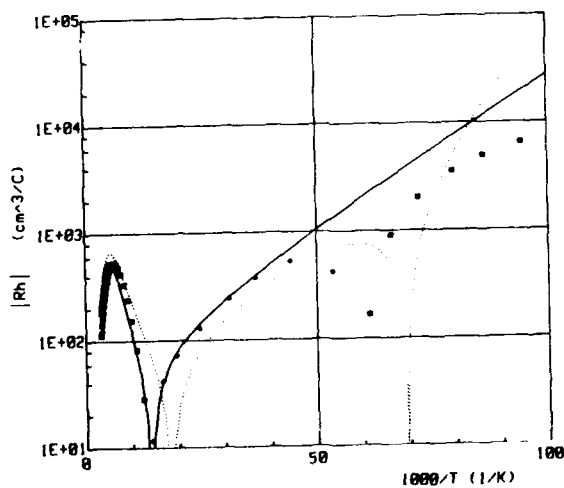


Fig. 5: Results on J235, cap and buffer, ■ for R_H negative, ◆ for R_H positive. The full line is a fit at $x=0.172$, $b=60$, $E_a=9.5\text{meV}$, $N_A=2 \times 10^{17}$, the dotted line models $x=0.171$, $b=70$, $E_a=10\text{meV}$, $N_A=2 \times 10^{17}$ and using a modified n_i using E_σ in ref (8) substituted in ref (6)

A dominant term in the expression for n_i is $\exp(-E_g/2kT)$, E_g being derived as $f(x,T)$ in a similar empirical manner. The overall trend (see figure 4) is towards lower E_g for a given x and for E_g to decrease more rapidly at low temperatures. Consequently the values for n_i are increasing, especially at low temperatures. These higher n_i values at low temperatures could explain the double sign change results seen in low x material discussed in the next section.

Behaviour of low x CMT

In cases of low x and fairly low p CMT the fitting parameters x (n_i) and b can be particularly significant at low temperatures. This behaviour can be seen in figure 5 which shows the Hall data for J235, together with two fitting curves differing only by small changes of the fitting parameters as given in the figure caption.

If n_i is $\sim 10^{15}$ below 50 K then the number of electrons can be comparable with the number of holes (reducing due to freeze out) and if $p < nb^2$ then a second low temperature sign change in R_H , that is from p to n , can occur, as seen in the dotted curve. This sign change, which is frequently seen experimentally in low x material, is not a function of two layer effects but results from the intrinsic fitting parameters. An extrapolation of the effect is that low x and low p -type material will only give rise to Hall coefficients that are negative across the whole temperature range.

CONCLUSIONS

Inversion-like behaviour resulting from surface and interface effects during the measurement of the electrical properties of p -type* CMT can be avoided by the use of CdTe buffers and caps. Using this procedure it should be possible to more accurately determine n_i and assess the various fundamental transport parameters for CMT. Inversion behaviour in low x low p -type CMT may not necessarily be due to interface or surface effects but can be due to intrinsic behaviour.

Acknowledgements: Miss D Jones is thanked for technical assistance with layer growth and Dr A M White for helpful discussions on modelling.

REFERENCES

1. J B Mullin and A Royle, J Phys D: Appl Phys, **17** (1984) L69
2. J B Mullin, A Royle, J Giess, J S Gough and S J C Irvine, J Crystal Growth **77** (1986) 460
3. S J C Irvine, J B Mullin, J Giess, J S Gough and A Royle, J Crystal Growth **93** (1988) 732
4. S K Ghandhi, I B Bhat and H Fardi, Appl Phys Letts **52** (1988) 392
5. J L Schmit, J Appl Phys **41** (1970) 2876
6. G L Hansen and J L Schmit, J Appl Phys **54** (1983) 1639
7. Y Nemirovsky and E Finkman, J Appl Phys **50** (1979) 8107
8. D G Seilier, J R Lowney, C L Littler and M R Loloee, 1989 MCT Workshop on Physics and Chemistry of MCT, J Vacuum Sci and Technol - to be published

SURFACE ROUGHNESS THEORY AND LOW-TEMPERATURE EPITAXY

SRINIVASAN KRISHNAMURTHY*, M.A. BERDING*, A. SHER*, AND A.-B. CHEN**

*SRI International, Menlo Park, CA 94025

**Department of Physics, Auburn University, Auburn, AL 36839.

ABSTRACT

A single-and multilayer growth model is presented. Surface order-disorder transitions are studied with the entropy calculated in the Bragg-William approximation and in the quasi-chemical approximation. A plausible explanation for high-quality growth obtained with energy-assistance is given. The model has been extended to study low-temperature epitaxial growth of HgTe and CdTe on different surfaces. The relevant surface energies are evaluated in a Green's function approach.

INTRODUCTION

The theory of surface order of solids is essential to an understanding of their growth properties. The mechanisms dominating surface order depend on a number of factors, including the crystal orientation, substrate temperature, and growth method. The atoms arriving at a growing surface interact both with the underlying surface and with one another. Their mutual interactions may cause them to undergo an order-disorder transition from a "rough" to a "smooth" (or ordered surface) or from a "rough" to a "superlattice" (SL) surface. In the smooth limit, the newly arriving atoms tend to cluster into islands; in the disordered state, the atoms tend to be randomly distributed [1], and in the SL-ordered state, the atoms and vacancies on the surface form long-ranged ordered patterns. For a half-filled cubic surface, for example, one SL pattern is a checkerboard arrangement of atoms on the available sites. The temperature that characterizes the transition from smooth to rough surface is called *surface roughness transition temperature*, T_c . When the growth temperature T is smaller than T_c , the surface will be smooth. The growth rates and crystal quality are expected to differ in these two limits.

The rough-to-smooth transition occurs when the effective interaction between surface atoms is attractive, while the rough-to-SL transition is a consequence of repulsive surface atom-atom interactions. Because repulsive interactions among surface atoms have not been previously considered to be realistic, this type of order-disorder transition on the surface has not been treated extensively in the literature.

In this paper, we first study the surface roughness for a cubic lattice by obtaining the surface entropy contribution to the change in free energy in a random approximation [also called Bragg-Williams approximation (BWA)], and in the quasichemical approximation (QCA) with pair interactions. Based on the difference between their predictions, we suggest a plausible explanation for better quality growth obtained with energy assistance. The surface roughness model is then extended to study the surfaces of realistic semiconductors—HgTe and CdTe—grown by atomic layer epitaxy (ALE) and by molecular beam epitaxy (MBE). The transition temperatures and surface roughness for growth in various orientations are given.

SURFACE ROUGHNESS THEORY

Because of space limitations, the approach will be discussed in brief; the details can be found in the literature for the single-layer growth model with BWA [1] and for multilayer growth

model with QCA [2]. We begin by considering a monatomic cubic solid grown from a (100)-oriented seed with a smooth crystal surface. The change in enthalpy and entropy are calculated to obtain the change in free energy. The most probable configuration is obtained by minimizing the free energy. The atoms arriving at the surface make one bond each with the layer below and above, and four in-plane surface bonds.

In the multilayer growth model with QCA, we first identify all distinct classes of pairs that contribute to the free energy. Secondly, we write the probability for occurrence of each type of pair. Then, using appropriate factors for indistinguishability of pairs, the entropy for different layers is written with appropriate constraints. The free energy is then minimized to obtain the most probable pair distribution. In this multilayer model, an atomic site in any upper layer is allowed to be occupied, even if the site immediately below it is not occupied. In other words, "over-hangs" are permitted. Although these configurations are energetically less favorable, they contribute to the entropy, and thus should be included in the free energy. In this model, we have four types of pairs: atom-atom, atom-vacancy, vacancy-atom, and vacancy-vacancy. For each layer, there are nine variables (four interlayer pairs, four intralayer pairs, and one layer concentration) and six constraints relating them. The minimization of free energy in two of the remaining three variables can be carried out analytically. The numerical minimization in the remaining one variable is then carried out. The temperature at which the second derivative of the free energy vanishes for the surface coverage of 0.5 gives the transition temperature, T_c .

The calculated layer concentrations in the three-layer growth model are shown in Figure 1 as a function of surface coverage averaged over three layers for three growth temperatures T_1 , T_c , and T_2 ($T_1 < T_c < T_2$) by thick-dashed, dashed, and solid lines, respectively. The index on the curves represent the layer number. At $\bar{x} = 1$, $3N$ atoms have been added to the surface, where N is the number of sites per layer. In this convention, Layer 1 is immediately above the seed surface. We note that at growth temperatures near and above T_c , all three layers grow simultaneously, but with $x_1 > x_2 > x_3$. However, at temperatures below T_c , the upper layers do not grow until the lower layers are nearly full. In this limit, layer-by-layer growth takes place.

At temperatures well below T_c , the atoms arriving at the surface cannot move and imperfect growth results. The quality of the growth can be characterized by the fraction, y_0 , of atom-atom pairs to the total number of pairs in a layer. y_0 has been calculated in the BWA and QCA. Figure 2 shows that less perfect growth occurs in BWA case. However, if there is energy assistance, where photons or ions provide enough energy to permit the atoms to move on the surface, then the QCA entropy is more appropriate and the perfection improves (y_0 increases). The reason for the difference between y_0 in these cases is evident: The BWA entropy is larger, and therefore it emphasizes the drive toward complexity. This results in layers at a given coverage with more imperfections. QCA, where the entropy is smaller, predicts that layers are more nearly perfect.

When the substrate temperature is sufficiently low, the characteristic time constant for surface migration is larger than the the equilibration time for interaction of the surface with beam and gas (thought of as a heat bath). Under these conditions, BWA is more appropriate. However, if the surface mobility is enhanced with an energy assist, the effective time constant for the migration is reduced (so that surface equilibration can take place faster than equilibration with beam or gas bath), then the QCA is more appropriate. This is a plausible explanation for high quality obtained in energy-assisted epitaxial experiments [3,4]. The energy assist in these experiments is sufficient to allow the needed surface mobility.

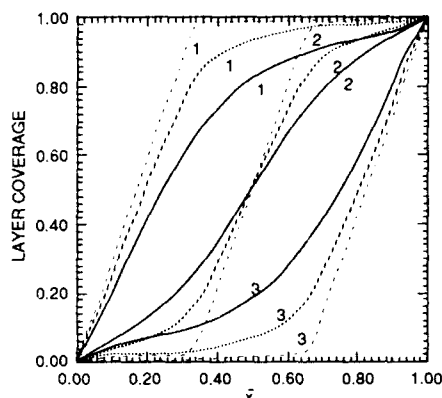


Fig. 1. Layer coverage as a function of average coverage.

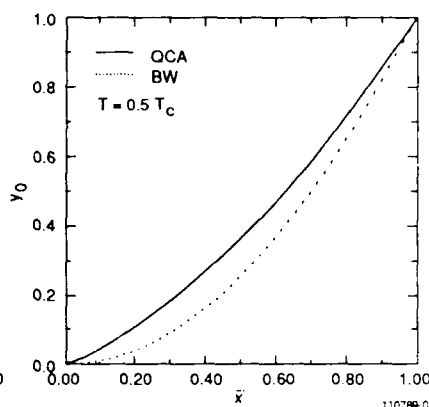


Fig. 2. Variation of y_0 with average coverage

ENERGETICS AND GROWTH MODEL FOR SEMICONDUCTORS

The model described in the previous section has been generalized to the case of diamond and zinc blende lattices. Also, the energies of interaction between pairs on the surface and that between layers has been evaluated, using a Green's function approach. We calculate the energy to remove the atoms from nearly empty surfaces, referred as the *dilute case*, and that to remove the atoms from nearly full surfaces, referred as *concentrated case* [5]. The respective energies are denoted E_d and E_c . The calculations were carried out for the removal of anions and cations from various orientations of Si, GaAs, CdTe, and HgTe. The details of these calculations will be published elsewhere [5]. We report only HgTe and CdTe results here.

In the single-layer growth model, we consider three kinds of pairs: namely, atom-atom, atom-vacancy, and vacancy-vacancy and their respective energies E_{aa} , E_{av} , and E_{vv} . The number of effective bonds an atom makes to the substrate, η_0 , and the number of surface bonds, η_1 , must also be specified. The free energy and the surface-pair populations are obtained from the effective energy E_{eff} , given by $(E_{av} - (E_{aa} + E_{vv})/2)$. Without calculating E_{aa} , E_{av} , or E_{vv} , we can find E_{eff} from the difference of calculated E_c and E_d , and η_1 from Table I. In our convention, a negative E_{eff} indicates an attractive interaction between surface atoms.

In atomic layer epitaxy, grown from a free atom vapor phase, only one type of atom species (anion or cation) is present at a given time, and the growth is necessarily layer by layer. The single-layer model developed in the previous section can be applied to study HgTe and CdTe with the calculated pair energies. QCA is used in the evaluation of surface entropies. When the pair interaction is attractive, the smooth-to-rough transition takes place, as the growth temperature is varied near T_c . However, when the pair interaction is repulsive, the surface is either rough or the atoms are in a SL arrangement with vacancies. Then the order-disorder transition takes place near a different T_c . The preferred ordered SL arrangements are composition-dependent; however, in regions of ordering, the surface will be arranged to maximize the number of atom-vacancy pairs. Calculated values of T_c are given for growth of HgTe and CdTe in (111) and (100) directions in Table I.

Table I. Extraction energies and critical temperatures.

Surface	Atom/ Layer	η_0	η_1	CdTe			HgTe		
				E_d [eV]	E_c [eV]	T_c [K]	E_d [eV]	E_c [eV]	T_c [K]
(111)A	a	1	6	3.9	4.2	710	1.8	3.8	4700
	c	3	6	2.7	0.6	5000*	-0.3	1.1	3300
(111)B	a	3	6	5.2	2.1	7400*	2.8	2.8	0
	c	1	6	2.2	1.3	2100*	-0.2	0.3	1200
(100)	a	2	4	5.0	2.6	5000*	2.4	3.1	1500
	c	2	4	2.1	0.1	4200*	-0.2	1.0	2500

In our calculation, the pair interaction is always attractive in HgTe and the temperatures shown in Table I indicate T_c for the rough-to-smooth transition. However, the pair interaction is repulsive for CdTe, except for the growth of a singly bonded anion layer on the (111)B surface. Temperatures T_c^* denote the rough-SL transition temperatures. Because the T_c values are very large, ALE growth of HgTe occurs mostly in the smooth domain limit and that of CdTe occurs mostly in the SL domain limit.

In layers grown by MBE, both anion and cation atoms impinge on the surface at the same time and both layers can grow simultaneously. The way in which the layer grows depends on the flux rates of the two constituents and their respective sticking coefficients. Hence, an appropriately generalized multilayer model to that described briefly in the previous section is applicable. For simplicity, we assume only double-layer growth. The interlayer pair interaction energies are obtained from E_d and η_0 . The intralayer pair energies for each layer are obtained from E_c , E_d , and η_1 . With the surface entropy obtained in QCA, the free energy is calculated for various values of anion and cation layer coverage. The effect of anti-site defects is not included.

Because of the repulsive intralayer pair energies, CdTe surface is expected to grow in SL domains. Hence, in addition to random distributions considered here, one must consider all ordered configurations for a given concentration. This case is being studied in detail and will not be presented here. However, the interlayer and intralayer pair interactions in HgTe are attractive, so the double-layer growth model applies to this system.

When the minima in the free energy at a given temperature occur near 0 and 1, islands are formed on the surface that are nearly fully occupied and the remainder of the area is nearly empty. As the surface coverage is increased, the islands grow in size with a fixed vacancy concentration until the layer is fully grown. The vacancies fill only at the end of the layer growth; then the formation of the next layer takes place. These events are calculated by examining a sequence of equilibrium arrangements. Realistically, kinetic effects will prevent all vacancies from filling in one layer before the start of the next layer. Thus, we expect that island growth—where the vacancy concentrations are low—is likely to correlate with high-quality material.

Sequential double-layer growth is predicted to be the case for HgTe, for example, in (111)A direction. In this case, at 185°C we predict smooth growth in ALE for both Hg and Te layers, and in either Hg or Te stabilized MBE growth [6] we also predict smooth layer growth. At this same temperature on the (111)B surface in ALE we find smooth growth for the Hg layer, but rough growth for the Te. Moreover, in this particular case, we find Te-stabilized MBE growth to be smooth, and Hg-stabilized MBE growth to be rough. In principle, it is possible to find situations and temperatures where in ALE one layer grows smooth and the other rough, and in MBE the layers grow rough for both stabilizations. This provides a rationale for the sensitivity of material quality to stabilization type, and temperature.

CONCLUSION

We have calculated the excess free energy of the surfaces for addition of several layers of atoms. The surface energies that enter the statistical mechanics are found in a Green's function approach. The entropy calculation employs a surface modification of QCA. While the calculation only finds the equilibrium arrangement of atoms for specified surface coverages, given reasonable speculations about kinetic effects, we can appreciate how energy assist functions, in principle, to improve the quality of epitaxial layers; the phenomenology dominating HgTe growth for different orientations; and reasons to expect differences between the MBE growth habits of CdTe and HgTe.

ACKNOWLEDGMENT

This work was supported in part by NASA under Contract NAS1-18226 and ONR N00014-88-C0096.

REFERENCES

1. K.A. Jackson, D.R. Uhlmann, and J. D. Hunt, *J. Crys. Growth*, **1**, 1 (1967).
2. S. Krishnamurthy, M.A. Berding, A. Sher, and A.-B. Chen, *J. Crys. Growth* (submitted).
3. R.L. Harper, J.W. Han, S. Hwang, Y. Lansari, N.C. Giles, J.W. Cook, and J.F. Schetzina, *J. Vac. Sci. Tech.*, **B7**, 244 (1988).
4. J. Green, *CRC Critical Reviews and Solidstate and Materials Sciences*, **11**, 47 (1984).
5. S. Krishnamurthy, M.A. Berding, A. Sher, and A.-B. Chen, *J. Appl. Phys.* (to be submitted).
6. We define Hg-stabilized growth to be the case where the relative Te and Hg fluxes are such that any exposed surface atoms are Hg; in Te-stabilized growth, the converse is true.

ENHANCED METALLIZATION STABILITY ON MERCURY-CADMIUM-TELLURIDE

A. RAISANEN, G. HAUGSTAD, X. YU, G. CECCONI AND A. FRANCIOSI
Department of Chemical Engineering and Materials Science
University of Minnesota, Minneapolis, MN 55455

ABSTRACT

Synchrotron radiation photoemission studies of ultra-thin Yb diffusion barriers at the interface between Mercury-Cadmium-Telluride semiconductors and Ag overlayers show that the interlayers act as effective diffusion barrier only after thicknesses of 10-15 Å are reached. Studies of interlayer morphology by means of photoemission from physisorbed Xe indicate that effective diffusion barriers are consistent with a model in which a continuous Yb-Te reacted layer is covered by an Yb-rich layer with high alloying enthalpy for Hg.

INTRODUCTION

Mercury-Cadmium-Telluride (MCT) is a pseudobinary semiconducting alloy extensively used in high-performance infrared detectors. Processing of this material is complicated by its low stability, resulting, for example, in Hg loss from the interface region during contact fabrication. Our recent experiments¹⁻³ have demonstrated that thin (3-18 Å) Yb interlayers can be used as effective diffusion barriers at junctions between MCT and reactive metals such as Al¹⁻², In³, and Cr³, with corresponding decrease in atomic interdiffusion, overlayer metal-Te reaction, and associated Hg-depletion of the MCT surface. We have proposed¹⁻³ that the diffusion barrier effect derives from the superior thermodynamic stability of the MCT/Yb reaction products relative to the MCT/overlayer metal reaction products, based on the high Yb-telluride formation enthalpy⁴ and on the calculated^{1-3,5} alloying enthalpies of Hg and Cd in the Yb overlayer.

Unlike the reactive metals we have studied earlier¹⁻³, Ag exhibits reactive behavior on the MCT surface that is dominated by long-range Ag indiffusion into the MCT lattice via Hg vacancies⁶⁻⁷, rather than by a Hg-depleting Ag-Te reaction. The unusual diffusive behavior of Ag on the MCT surface makes MCT/Ag junctions an interesting test case for diffusion barriers. We conducted synchrotron radiation photoemission studies of MCT/Ag junctions in the presence of Yb interlayers of various thicknesses. We observed a non-monotonic coverage dependence of the diffusion barrier effect on Yb thickness. Thin barriers (Yb coverage 3-5 Å) are only partially effective at hindering Ag indiffusion, intermediate thicknesses (8 Å) initially work but fail suddenly at high Ag coverages, while Yb interlayers of 10-15 Å thickness behave as ideal diffusion barriers. To explain the striking non-monotonic Yb coverage-dependence of the diffusion barrier effect, we have conducted studies of the coverage dependence of the interlayer morphology by means of photoemission from physisorbed Xe. To our knowledge this is the first application of this technique to the study of semiconductor metallizations.

EXPERIMENTAL DETAILS

The experiments were conducted using photons from the Aladdin 1 GeV electron storage ring, monochromatized by 3m or 6m toroidal grating monochromators, with overall experimental resolution of 0.15 to 0.25 eV. Single-crystal posts of p-type $\text{Hg}_{0.78}\text{Cd}_{0.22}\text{Te}$ $3 \times 3 \times 10 \text{ mm}^3$ in size were cleaved *in-situ* to expose (110) surfaces. Metal depositions were performed *in-situ* by thermal evaporation from W coils, with metal coverage θ monitored by a quartz thickness monitor. The spectrometer operating pressure was in the low 10^{-11} Torr range, while pressure during metal evaporation remained below 2×10^{-10} Torr. At each metal coverage data were recorded at room temperature, and after cooling at 35K. Exposure to 2L of Xe, corresponding to submonolayer Xe coverages, were performed *in situ*.

RESULTS AND DISCUSSION

In Fig. 1 we present the integrated Te 4d core emission intensity from MCT/Ag junctions as a function of Ag coverage in Å, normalized to the clean-surface Te 4d emission, in the presence of Yb interlayers ranging from 0 Å (no interlayer) to 15 Å. When no interlayer is present (solid circles), the Te 4d intensity decreases slowly with Ag deposition, retaining 80 % of the initial surface intensity even after deposition of 150 Å of Ag. The slow attenuation of the Te 4d signal reflects long-range indiffusion of Ag into the MCT lattice⁶⁻⁷, with relatively little Ag accumulating at the surface. When thin Yb interlayers (3 and 6 Å, shown respectively by solid triangles and squares) are present at the MCT/Ag interface, relatively little difference is observed in the Te 4d intensity coverage dependence relative to the no-interlayer case. Prior to Ag deposition, the Te 4d signal was reduced to about 75 % of the clean-surface value, as a result of Yb deposition; even after deposition of 200 Å Ag, the Te 4d signal retains 70 % of its cleaved-surface intensity. We conclude that in this Yb coverage range the interlayers do not play the role of effective diffusion barriers.

For thicker Yb interlayers (10 and 15 Å, indicated respectively by open triangles and squares), the general trend in Fig. 1 is a nearly exponential decrease in Te 4d signal as a function of Ag coverage. By 100 Å Ag coverage, the Te 4d signal has been reduced below our detection limit. This, together with data for the Ag 4d emission that cannot be presented here due to space limitations¹¹, demonstrates that in this Yb coverage range the interlayer is remarkably effective at reducing Ag indiffusion. Yb interlayers of 8 Å thickness (shown by open circles) induce an intriguing non-monotonic MCT/Ag junction behavior. As indicated in Fig. 1, the Te 4d attenuation rate is initially similar to that observed in the presence of thick Yb interlayers. However, at a Ag coverage of approximately 20 Å, the attenuation rate decreases and becomes similar to that observed in the presence of thin Yb interlayers. This, together with data for the Ag 4d emission intensity, indicate that in this Yb coverage range the Yb interlayer hinders Ag indiffusion at low Ag coverages, but "fails" abruptly at higher coverages.

The effect of Yb interlayers on Ag indiffusion can be understood by making a detailed microscopic examination of the interlayer morphology as a function of Yb coverage. We

accomplished this by the Photoemission of Adsorbed Xenon technique⁸⁻¹⁰, which is used here for the first time to monitor metallization of a semiconductor. The PAX technique exploits the fact that the vacuum level of a Xe film condensed on a metal or semiconductor will align with the vacuum level of the substrate. Since the Xe ionization energy remains constant from substrate to substrate⁹, in photoemission the apparent binding energies of the Xe electronic levels relative to E_f reflects the local work function of the substrate. For a spatially inhomogeneous substrate, differences in the local work function will give rise to multiple Xe features. The apparent binding energy of each feature gives the local work function of the corresponding adsorption site. The relative intensity of the features give the corresponding fractional area, since our studies indicate that the Xe sticking coefficient is constant (within 10%) along the surface.

In Fig. 2 we present photoelectron energy distribution curves (EDC's - solid circles) for the Xe 4d core emission obtained from MCT/Yb junctions formed at room temperature, cooled to 35 K, and exposed to 2L of Xe. Yb coverages are given to the right of the corresponding EDC. Xe physisorption on MCT (0 Å Yb) gives rise to a well-defined Xe 4d core doublet, indicating Xe physisorbed on a homogeneous semiconductor surface. Physisorption on MCT/Yb interfaces yields two Xe 4d doublets at all Yb coverages below 7 Å, while only a single Xe 4d doublet is observed for Yb coverages above 7 Å. A least squares fit of each Xe 4d component in terms of a Lorentzian function convoluted with a Gaussian function was performed to deconvolve the two Xe doublets. The results are the Xe 4d I (substrate-induced) and 4d II (overlayer-induced) doublets shown in Fig. 2 (dotted and dashed line, respectively). These measurements clearly indicate that at all Yb coverages < 7 Å, regions of the bare MCT surface are available for Xe physisorption. At coverages > 7 Å, only a metallic film of low work function relative to MCT is exposed to Xe¹¹. We therefore conclude that islands are present at all Yb coverages < 7 Å, and that the islands have coalesced with the formation of a continuous layer at a Yb coverage of 7 ± 1 Å.

The PAX measurements described above allow us to construct a detailed microscopic picture of the effect of Yb interlayers on Ag indiffusion. We can also use the apparent binding energy of the Xe 4d II doublet to probe the overlayer work function, and therefore its composition¹¹. We saw in Fig. 1 that thin (3-6 Å) Yb interlayers had little effect on Ag indiffusion, as indicated by the persistence of the Te 4d signal at high Ag coverage. For thin Yb interlayers (< 7 Å), the interlayer is composed of islands of nonmetallic, high work function Yb-Te reaction products¹¹, separated by regions of bare MCT. Upon Ag deposition, the bare MCT regions will offer no barrier to Ag indiffusion, while the islands will hinder Ag indiffusion. Although we observe some increase in the Ag concentration at the surface due to Ag atoms collecting on the islands¹¹, the Te 4d coverage-dependence in Fig. 1 is consistent with minimal reduction in Ag indiffusion.

Fig. 1 indicates that for the 8 Å Yb interlayer, Ag indiffusion is substantially reduced relative to the no interlayer case for Ag coverages < 20 Å, while at higher Ag coverages little effect on Ag indiffusion is observed. The Ag 4d emission intensity displays a sudden decrease at a Ag coverage of 20 Å¹¹, consistent with an onset of Ag indiffusion at this coverage. Fig. 2 indicates that, at this Yb coverage, the interlayer consists of a continuous Yb-Te layer; measurements of the work function and core emission indicate that this layer has little or no metallic Yb on top¹¹ and

Fig.1. Integrated Te 4d core emission intensity ($h\nu = 110$ eV) from MCT/Ag junctions with various Yb interlayer thicknesses, normalized to the clean surface Te 4d intensity.

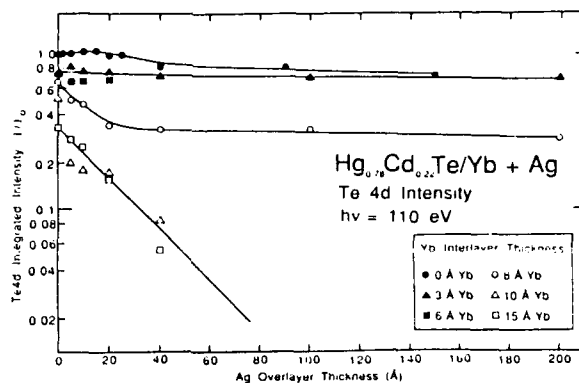
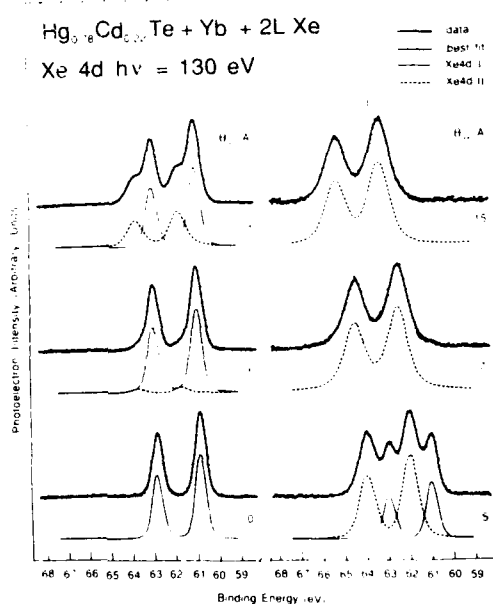


Fig.2. Xe 4d emission from MCT/Yb junctions formed at room temperature, cooled to 35 K, and exposed to 2 L Xe. Solid circles represent the experimental data, while the solid line through the points represents the best fit of the data in terms of two Gaussian-broadened Lorentzian lineshapes. The two individual Xe 4d contributions are also shown (dotted and dashed lines) displaced slightly below the experimental points. The vertical bars represent the apparent binding energy of the Xe $4d_{5/2}$ levels for Xe physisorbed on polycrystalline Yb.



that relatively small amounts of Ag are able to diffuse into the Yb-Te layer. Therefore, we propose that the "failure" of the 8 Å Yb interlayer for Ag coverages greater than 20 Å is related to Ag alloying with the reacted Yb-Te layer; at a Ag coverage of 20 Å, the solubility limit is reached, and metallic Ag precipitates out at the interface where it is free to diffuse into the MCT lattice.

The results for the thick (10-15 Å) Yb interlayer regime indicate substantial reduction of Ag indiffusion at all Ag coverages explored, as shown by the exponential decrease in Te 4d signal with Ag coverage. Our PAX measurements indicate that the interlayer morphology in this regime consists of a continuous Yb-Te layer covered by a metallic Yb-rich low work function layer¹¹. Correspondingly, we find that in this Yb coverage range the Yb interlayers act as effective diffusion barriers against Ag. We propose that the success of Yb interlayers in hindering Ag indiffusion derives from the formation of a continuous Yb-Te layer, which blocks the diffusion pathways for Ag into the MCT lattice, as well as the formation of a metallic Yb-rich layer at the surface, which may act to chemically trap Ag at the interface due to the large enthalpy of alloying for Ag in Yb (-88 kJ/mol Ag).

ACKNOWLEDGEMENTS

This work was supported by the Office of Naval Research under grant N00014-89-J-1407 and by the Center for Interfacial Engineering at the University of Minnesota. We thank the entire staff of the Synchrotron Radiation Center of the University of Wisconsin-Madison, supported by the National Science Foundation, for their cheerful support.

REFERENCES

1. A. Franciosi, A. Raisanen, A. Wall, S. Chang, P. Philip, N. Troullier, and D.J. Peterman, Appl. Phys. Lett. 52, 1490 (1988).
2. A. Raisanen, A. Wall, S. Chang, P. Philip, N. Troullier, A. Franciosi, and D. J. Peterman, J. Vac. Sci. Technol. A6, 2741 (1988).
3. A. Raisanen, D. J. Peterman, A. Wall, S. Chang, G. Haugstad, X. Yu, and A. Franciosi, Solid State Commun. 71, 585 (1989).
4. K.C. Mills, Thermodynamic Data for Inorganic Sulphides, Selenides, and Tellurides, (Butterworths, London, 1974).
5. A.R. Miedema, P.F. de Chatel, and F.R. de Boer, Physica B100, 1 (1980).
6. D.J. Friedman, G.P. Carey, C.K. Shih, I. Lindau, W.E. Spicer, and J.A. Wilson, Appl. Phys. Lett. 48, 44 (1986).
7. D.J. Friedman, G.P. Carey, C.K. Shih, I. Lindau, W.E. Spicer, and J.A. Wilson, J. Vac. Sci. Technol. A4, 1977 (1986).
8. K. Wandelt, J. Vac. Sci. Technol. A2, 802 (1984).

9. I.T. Steinberger and K. Wandelt, Phys. Rev. Lett. 58, 2494 (1987).
10. M. Onellion and J.L. Erskine, Phys. Rev. B36, 4495 (1987).
11. A. Raisanen, G. Haugstad, X. Yu, G. Ceccone, and A. Franciosi, J. Vac. Sci. Technol. A (submitted)

GROWTH OF HIGH QUALITY LWIR FILMS BY LIQUID PHASE EPITAXY

Dipankar Chandra

Texas Instruments Incorporated, Dallas, Texas 75265

ABSTRACT

Growth of long wavelength infra-red mercury cadmium telluride films by liquid phase epitaxy has usually yielded films of inferior electrical properties as evidenced by Hall mobilities lower than theoretical values by factors of 5 or more at 77°K. In addition the Hall behavior over the entire temperature range did not follow classical patterns. A systematic series of investigations was conducted to improve the electrical performance of these films by four methods: i) growth of HgCdZnTe films, where a portion of the cadmium was replaced by zinc, ii) growth at temperatures $> 550^{\circ}\text{C}$, iii) growth at a slow rate on a CdZnTe substrate following 'cleaning' in the melt of the substrate surface and iv) doping the film by controlled levels of indium. The first method did not lead to any improvements in the Hall behavior. In addition, the films grown displayed varying dislocation densities. The second method led to a small but definite increase in the yield of non-anomalous or classical films (5%). The third method yielded films with classical or non-anomalous Hall behavior about 20% of the time. The last method consistently led to films with classical Hall behavior. This was accomplished with indium doping levels at $1.5 \times 10^{14}/\text{cm}^3$. Preliminary data indicate that it will be possible to go to still lower doping levels while maintaining classical Hall behavior. The improvement in electrical properties of these epilayers can be attributed to the reduction or elimination of type inhomogeneities known to degrade Hall mobilities in films grown by liquid phase epitaxy.

INTRODUCTION

An extensive series of investigations has been in progress at Texas Instruments to grow high quality thin films of mercury cadmium telluride. A prime objective of the present investigations was to understand the mechanisms limiting LWIR LPE quality prior to the initiation of the present investigations. A wide survey of the data base revealed the following:

- i) a large majority of the n-type epilayers (converted to n-type by post-growth stoichiometric adjustment anneal) displayed Hall mobilities > 5 times lower than theoretically predicted values for the respective cutoffs; a small fraction (5-10%) did display Hall mobilities within 50% of the theoretical mobilities,
- ii) all films however displayed 'anomalous' Hall behavior when the measurements were carried out as functions of temperatures [1].

Hence all epilayers displayed deviations from classical behavior, the latter being by far the most important deviation. Two important related observations are: a) the 'anomalous' behavior is not a 'skin' effect; progressive removal of the surface did not remove the anomalous behavior, b) it also could not be related to possible 'absorption' of impurities by the 'misfit' dislocation band near the epi-substrate interface, removal of the substrate and the misfit band and placing the Hall contacts on the backside of the film did not remove the anomalous behavior [2]. The anomalous behavior appears to exist throughout the bulk of the epilayer. The observed behavior, therefore, is consistent with the model where a three dimensional network of

interconnected p-type regions was assumed within a n-type matrix [1]. This model requires the least number of unlikely assumptions.

The Hall behavior of the LPE thin films therefore was different from the observations made on 'bulk' samples grown by the solid state recrystallization technique. For the latter, a 'classical' variation of Hall mobility with temperature was observed with a significant yield when the post-growth annealing treatments were appropriate [3].

EXPERIMENTAL PROCEDURES

The films were grown by liquid phase epitaxy on lattice matched CdZnTe substrates from tellurium rich melts following the dipping method [4]. Various average growth rates were employed. It was possible to alter the average growth rate by employing either one or both of the following techniques:

- i) changing the temperature 'cool-down' rate during actual growth,
- ii) changing the temperature profile imposed on the melt. The latter was accomplished by installing a small 'compensating' heating coil over the existing heating elements of the furnace. The shape of the temperature profile could be changed by large degrees by altering the power input into the compensating coil. For growth to occur, the temperature gradient needed to be positive (colder above). For negative temperature gradients (hotter above), not only no growth was recorded, but a slow dissolution of the substrate (etchback) started. Hence it was possible, not only to control the growth rate with a degree of precision using this method, but also to 'etchback' the substrate even at temperatures nominally below the liquidus! Detailed description and analysis of this procedure will be discussed elsewhere [5].

The average growth rate was observed to be the single most important parameter controlling the degree of melt inclusions in the films grown. Onset of constitutional supercooling at growth rates above a 'critical' rate, leading to a breakdown of the melt-solid interface, was the primary cause of inclusion incorporation. Note that substrate misorientations exceeding 0.5° will lead to poor surface, which might worsen the problem of melt inclusions. The following separate series of investigations were performed:

- 1) Growth of HgCdZnTe: Elemental zinc was added to the melt. Segregation coefficients controlling zinc uptake by the films were determined from the present series of investigations and have been reported elsewhere [6].
- 2) The films were grown between two widely separated temperature regimes: i) between 450 and 500°C and ii) between 540 and 590°C. For the latter group of experiments, the Hg reservoir needed to be maintained at or above the normal (atmospheric) boiling point of mercury. Heavy refluxing of mercury took place during these studies; these experiments pushed the operating temperature limits of the dipping reactors.
- 3) Slow growth following heavy etchback: Etchback of the substrates was performed by dipping the substrate in the melt at temperatures 25–30°C above the liquidus for varying lengths of time. Following the etchback, the melt was reequilibrated and the epigrowth performed by equilibrium cooling.
- 4) Extrinsic Doping: This method was used to eliminate the p-type micro-inclusions [1] without necessarily eliminating the inhomogeneous distribution of the impurities themselves. Both indium and gallium have been used. The doping was

performed by first doping the melt.

RESULTS AND DISCUSSIONS

A. Undoped Films:

The growth and treatment procedures developed permitted control over a wide range of microstructural properties.

Hall behavior: These were measured for a large number of samples. A wide variation in the 77°K Hall behavior was observed. The Hall mobility at 77°K varied between 1×10^4 and $1.8 \times 10^5 \text{ cm}^2/\text{V} \times \text{sec}$ (Figure 1). No measurable correlation could be established between growth parameters and the Hall behavior observed. Post growth annealing at temperatures as low as 200°C did not appear to influence this behavior. The only measurable correlation possible to be established was the relationship between incompletely annealed and completely annealed films. In a number of instances, the films switched completely from n-type to p-type on completion of annealing. Completion of annealing for the LPE films refers to the completion of annihilation of tellurium precipitates by the in-diffusing mercury, similar to the mechanism observed for bulk mercury cadmium telluride [7].

In attempts to establish some correlation between microstructural properties, growth parameters and electrical results, Hall data were obtained over the entire temperature range. Immediately, two groups of films were observed. The overwhelming majority consisted of films where the variation of mobility with temperature was not 'classical'. In general the mobility reached a maximum value around 77°K and decreased with decreasing temperature. The height of the maximum or the 'peak' varied from film to film. Two examples of this behavior are given in Figure 1, in agreement with the general behavior referred to and modelled by Chen et. al [1]. These films can be classified as 'anomalous' films. The Hall behavior can be interpreted as arising from an interconnected network of p-type regions existing in a n-type matrix (Figure 5 in Ref. [1]). The relative volume of the p-type regions will be significant in determining the magnitudes of the mobility values, though the general shape will all be similar to the examples shown (Figure 1). An inhomogeneity in type across the film therefore is responsible for this type of behavior. Note that since the effect arises from a 'three dimensional' network, and not a skin, no amount of surface removal and/or surface preparation will eliminate the inhomogeneity. This has been confirmed during the present investigations. Differential Hall measurements, that is repeated removal of surface did not lead to any change in the basic shape displayed in Figure 1, though the magnitudes of mobility values within the respective segments varied. These results add to the earlier data referred to above.

A small minority of films however displayed 'classical' behavior (Figure 1). Homogeneity in type therefore was achieved for these instances.

To decrease the yield of these 'anomalous' films two separate avenues were explored: i) variation in growth parameters, ii) addition of substituents or dopants.

Variation in growth parameters: The parameters which were varied were i) growth rate, ii) etchback time of the substrate prior to growth, iii) film thickness and iv) temperature of growth.

Growth rate: As discussed above, the average growth rate alone appeared to control the degree of melt inclusions. Figure 2 shows the number of melt inclusions as a function of average growth rate. Below a 'critical' rate the density of melt inclusions appeared to be virtually zero. Elimination of melt inclusions virtually

eliminated the incidence of p-type films, but still did not lead to the growth of films which displayed 'classical' behavior following stoichiometric adjustment anneal.

Etchback time: The etchback time of the substrate in the melt immediately prior to growth appeared to significantly affect the electrical behavior. Increasing the etchback time increased the yield of near-classical or classical films, but it reached a plateau between 15 and 25% for etchback times higher than 120 seconds (Figure 3). Etchbacks higher than 350 seconds began to degrade the surface quality even with rotation.

Film Thickness: A distinct correlation between Hall behavior and film thickness was not observed.

Growth temperature: The yield of classical or near-classical films displayed small but definite increase on raising the growth temperature from 480 to 550°C. Combining the high growth temperature with heavy etchback increased the yield of near-classical films to 25-30%. However, growth at these temperatures degraded the surface quality due to rapid Hg droplet formation either just prior to insertion of the substrates into the melt or immediately after removal from the melt following growth.

B. Doped Films:

Addition of dopants: Drastic increases in yield of classical films was observed when a substrate etchback of approximately 120 seconds was combined with the use of either indium or gallium as a dopant. Figure 4 demonstrates the increase in yield with indium doping, more than 80% of the films converting to classical hall behavior with indium doping levels at $< 5 \times 10^{14}/\text{cm}^3$. Approximately half of the films yielded classical Hall behavior with indium doping levels at $2 \times 10^{14}/\text{cm}^3$. Recent data indicate that a significant yield of classical films will be obtained even with lower indium doping levels, at approximate $1 \times 10^{14}/\text{cm}^3$. The segregation coefficient controlling indium incorporation from the melt was measured during the present investigations and shown in Figure 5. With increasing indium concentration, the segregation coefficient appeared to approach unity.

CONCLUSION

The Liquid Phase Epitaxy process has been studied and modified to yield high quality films reproducibly and routinely. This was possible both with and without using an extrinsic dopant. The yield was close to 100% for the former, even for doping levels lower than $5 \times 10^{14}/\text{cm}^3$.

References

1. M.C. Chen, S.G. Parker, and D.F. Weirauch, J. Appl. Phys. 58, 3150 (1985).
2. S.G. Parker (private communication); D. Chandra (unpublished data).
3. J.H. Tregilgas (private communication).
4. C.F. Wan, D.F. Weirauch, R. Korenstein, E.G. Bylander, and C.A. Castro, J. Electron. Mater. 15, 151 (1986).
5. D. Chandra (unpublished data).
6. D. Chandra, IRIS Materials Specialty Group, June, 1986.
7. H.F. Schaake, J.H. Tregilgas, J.D. Beck, M.A. Kinch and B.E. Gnade, J. Vac. Sci. Technol. A3, 143 (1985).

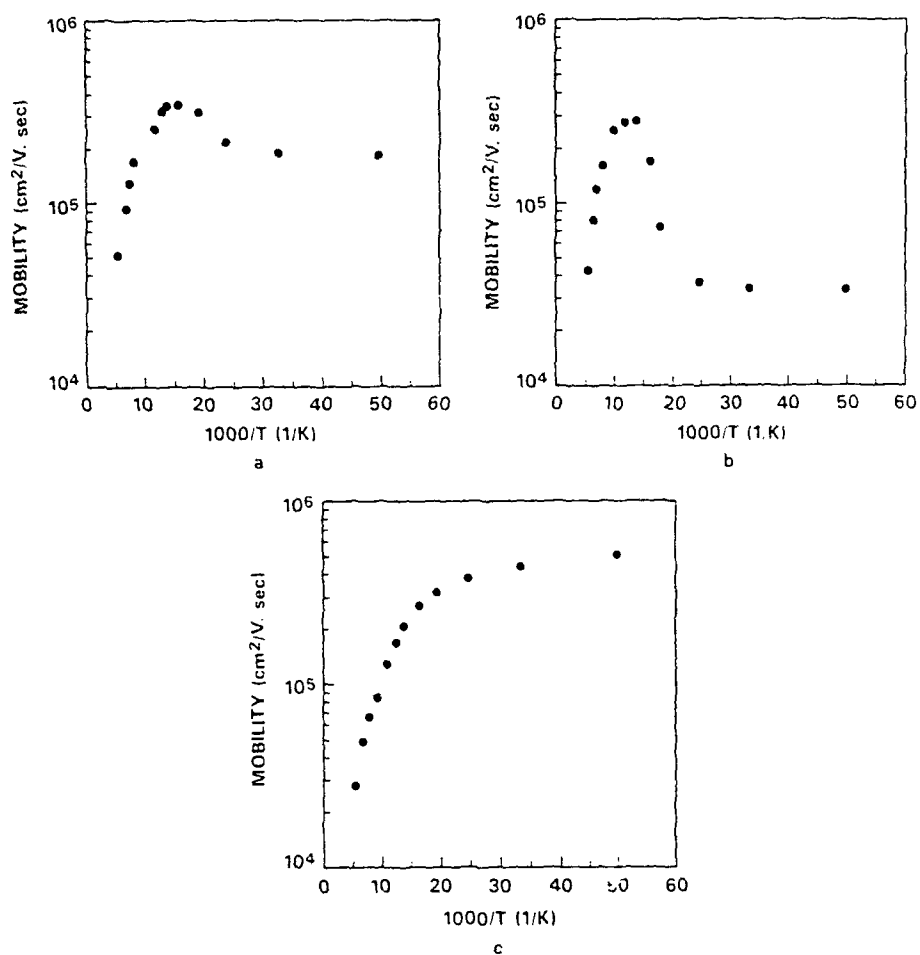


Figure 1. a) Anomalous behavior commonly observed in films grown by liquid phase epitaxy.
 b) Anomalous behavior sometimes observed in films grown by liquid phase epitaxy,
 c) Classical Hall behavior.

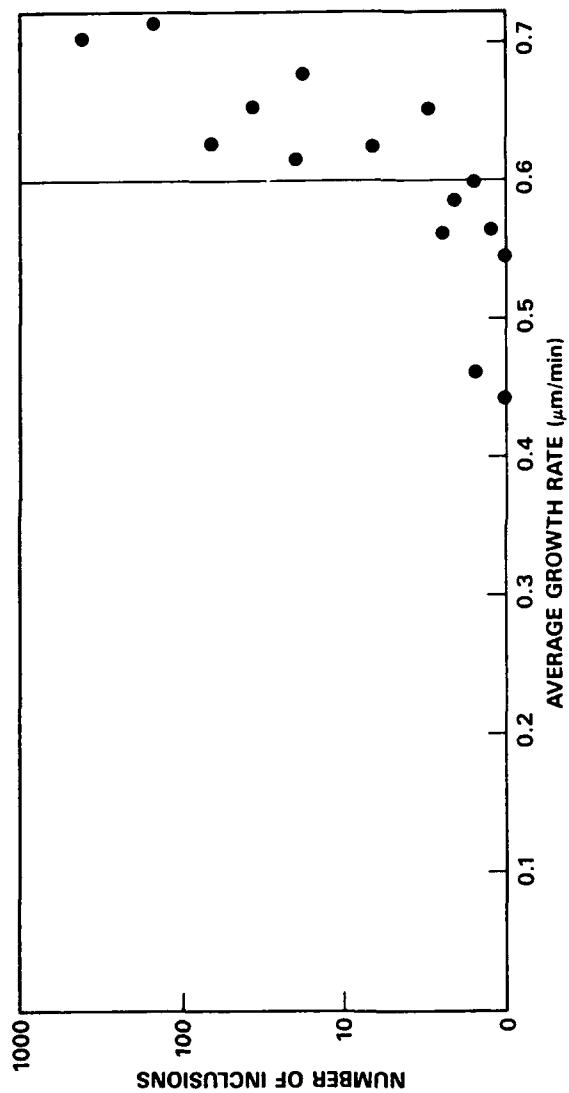


Figure 2. Number of melt inclusions in LPE films as a function of the average film growth rate.

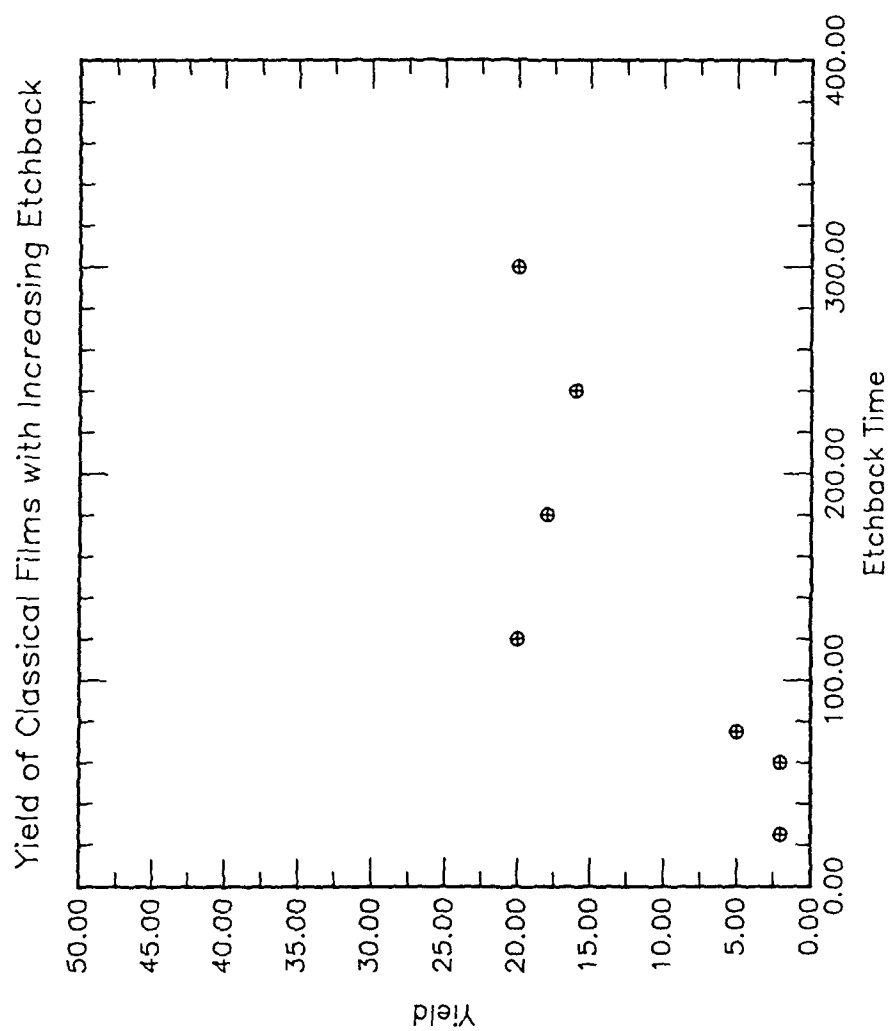


Figure 3. Yield of 'Classical' Films with increasing etchback.

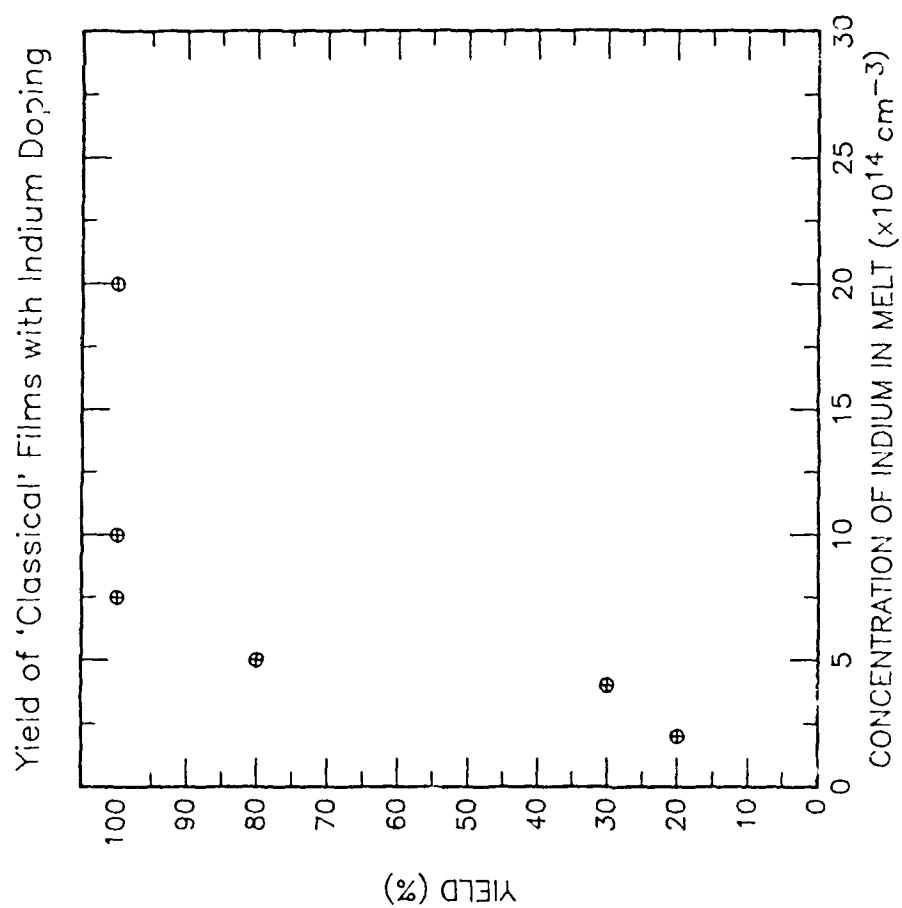


Figure 4. Yield of 'Classical' Films with increasing indium doping.

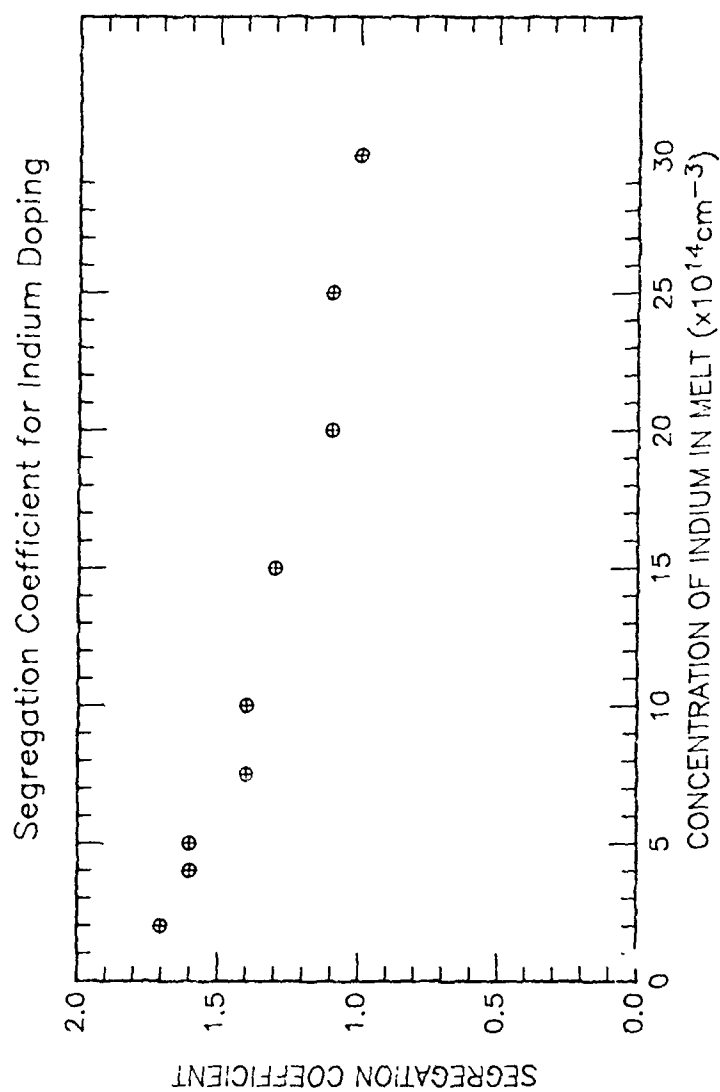


Figure 5. Segregation Coefficient controlling indium doping of Mercury Cadmium Telluride epilayers grown from tellurium-rich melts.

EFFECTS OF DEFECTS ON METAL-INSULATOR-SEMICONDUCTOR PROPERTIES OF HgCdTe FILMS GROWN BY LIQUID PHASE EPITAXY

Dipankar Chandra* and Michael W. Goodwin*

*Infrared Devices Laboratory, Texas Instruments, Incorporated; Dallas,
Texas

ABSTRACT

A comprehensive study of all materials parameters influencing metal-insulator-semiconductor (MIS) properties of n-type HgCdTe films grown by liquid phase epitaxy from tellurium rich melts was conducted. When the epitaxy process was optimized to grow films free of inclusions and terracing, the first indications of the MIS properties to be expected could be obtained from the temperature dependence of the Hall electron mobility.

Films displaying an anomalous dependence of the Hall mobility on temperature yielded non-classical low frequency MIS properties with little or no measurable 'dark' storage times ($< 2 \times 10^{-6}$ second). The MIS performance of these films appeared relatively independent of other materials parameters; remaining, for example, virtually unaffected by the film dislocation density changing between 5×10^4 and $2 \times 10^6/\text{cm}^2$.

Films displaying a classical dependence of the Hall mobility on temperature yielded drastically improved classical high frequency MIS properties. For these films, the MIS performance appeared almost exclusively dependent on dislocation density levels as long as the donor density remained lower than $1 \times 10^{15}/\text{cm}^3$. The dark storage time of classical films increased continuously with decreasing dislocation density levels, rising to $100 \mu\text{sec}$ for a dislocation density level of $1 \times 10^5/\text{cm}^2$ for materials with a 77°K cutoff wavelength of $10.5 \mu\text{m}$. A simple monotonic relationship could be established between the MIS performance parameters and the dislocation density over the entire measurement span: from 5×10^4 to $2.5 \times 10^6/\text{cm}^2$.

INTRODUCTION

An extensive series of investigations has been in progress at Texas Instruments to grow epitaxial thin films of mercury cadmium telluride using liquid phase epitaxy. The prime objective is to produce films which will fulfill MIS photocapacitor performance requirements within the LWIR range ($8\text{--}12 \mu\text{m}$ at 77°K). It is therefore essential to establish the materials obstacles limiting device performance, with particular emphasis placed on prioritizing these factors. The thrust can then be concentrated towards solving the most important limitation. Once this is achieved, it can then be redirected towards a solution of the next most important problem and so on.

MATERIALS ISSUES

The only information available from device physics of relevance to materials growth scientists has been the desired upper limits in carrier concentrations for n-type and p-type materials respectively [1]. To this could be added the data base

collected from bulk materials establishing the importance of dislocation density levels. Prior to the initiation of the present investigations, net donor densities in films grown by liquid phase epitaxy were comparable to the magnitudes observed in bulk materials. Nevertheless, MIS properties of these films were almost exclusively very poor, the large majority displaying low frequency behavior at 2 MHz. The dislocation density levels in these films were generally high, in the $10^6/\text{cm}^2$ range. This alone however would not explain the poor MIS data observed, since bulk materials with comparable defect density levels displayed MIS performance parameters, which while inferior to bulk containing low dislocation density levels, were still superior to materials grown by LPE [2].

Hence the materials obstacles confronting films grown by LPE in fused silica dipping reactor appear to be considerably more complex and severe. An examination of the various parameters measured establishes the following salient features for LWIR LPE:

1. Hall mobility; a significant fraction of films grown by LPE displayed mobilities > 5 times lower than theoretically predicted values for respective cutoffs at 77°K. Other films (5–10%) did display Hall mobilities within 50% of theoretically predicted values. All films however displayed 'anomalous' Hall behavior when the measurements were carried out as functions of temperature. Anomalous Hall behavior has also been reported by workers at other laboratories on LPE films [3,4,5].
2. The dislocation density levels generally stayed within the high 10^5 to low $10^6/\text{cm}^2$ range. It slowly decreased with increasing distance from the epi/substrate interface.
3. Melt inclusions: A relatively small fraction of the films contained melt inclusions. These generally were the thicker films, with thicknesses exceeding $75\mu\text{m}$. An important factor contributing to melt inclusions is the growth rate. High growth rates lead to constitutional supercooling, which in turn may lead to a breakdown of the planarity of the melt-solid interface, leading to 'entrapment' of melts. This will be discussed in more details elsewhere [6].
4. Terracing: The degree of terracing appeared to vary significantly from run to run. Severe terracing was almost invariably related to a severe melt inclusion problem. In addition to growth rates as discussed above, terracing can be influenced by pretreatment of the substrate, substrate holder design etc. [7].

In all this the importance of the substrate quality cannot be overestimated. It will influence all of the above, in most instances being the single most important influence. For example, in conformity with observations by other workers [8], films grown on substrates where the growth face is misoriented by more than 0.5° from the (111) B face contained a high degree of terracing and frequently melt inclusions. Furthermore, in as grown films, a general correlation has been observed between the dislocation density within the 'bulk' of the film and the substrate dislocation density [6], also in agreement with observations reported by some workers [9].

APPROACH AND EXPERIMENTAL PROCEDURES

To isolate the most important materials obstacle among the various problems outlined above, it was decided to concentrate on materials where as many of the above aspects have been optimized as possible. For example, only properly oriented substrates were employed following screening. A significant reduction in the sub-

strate dislocation density was possible following the replacement of CdTe substrates with CdZnTe substrates [10]. A detailed description of the instrumental aspects of the dipping liquid phase epitaxy process itself from tellurium rich melts has been provided elsewhere [11,12].

The degree of melt inclusions was drastically eliminated by reducing the growth rate, by eliminating constitutional supercooling. A systematic decrease in the growth rate was achieved by employing both a lower 'cooldown' rate as well as by progressively altering the temperature profile imposed on the melt using a novel heating element design. These have been referred to in the preceding publication [13], and will be discussed in more details in a forthcoming publication [6]. Limiting substrate misorientation to $< 0.5^\circ$ and decreasing the average growth rate below a 'critical' value [13] permitted the growth of even thick films ($> 100\mu\text{m}$ thick) free of melt pockets. Note that the 'critical' rate depended on the imposed temperature gradient and will vary from reactor to reactor. This was particularly important for LWIR films ($x < 0.23$). Due to reasons not completely understood, for MWIR films, inclusion free growth was possible even at higher growth rates.

Establishment of procedures permitting growth of films without melt inclusions increased the relative importance of substrate impurity levels drastically. Two aspects are relevant here: impurity at the substrate surface or near surface regions and impurity levels within the bulk of the substrate.

Surface and Near surface impurity levels: Accumulation of impurity levels at the substrate surface was confirmed both directly and indirectly, though the reasons for this deposition remain unclear. The direct method involved SIMS profiling of impurity levels as a function of depth within the film and the substrate (Figure 1), where relatively drastic increases in impurity levels were observed at the film-substrate interface [10]. Note that the impurity species examined by Weirauch were silicon, potassium, sodium, aluminum, lithium, chromium, carbon and chlorine. Since other species were not studied, the total extent of contamination introduced into the film from an 'impure' substrate surface remains unclear. This observation is consistent with the Hall data collected on such films during the present investigation. These data indicate a high incidence of p-type films, n-type films with high carrier concentrations and low mobility n-type films.

This accumulation is observed when film deposition is allowed to be initiated on the substrate not subjected to any 'cleaning' immediately prior to growth. A radically altered condition develops when the substrate is 'cleaned' in the nutrient melt held at a temperature above the liquidus, immediately prior to growth. A significant if remarkable change in the Hall data is observed. The incidence of p-type films drastically decreases, the incidence of high mobility at 77°K increases. Furthermore, as referred in the preceding publication [13], during the present investigations it was observed that the yield of films displaying a classical dependence of Hall mobility on temperature increased, almost continuously with increasing severity of the 'cleaning' or the 'etchback' procedure. Note that the increased 'severity' of the etchback procedure refers only to increased time of immersion of the substrate in the nutrient melt immediately prior to growth. A general consistency is observed between these Hall results and Weirauch's SIMS data. For the latter, the 'hump' in the impurity level near the substrate-epi interface is drastically reduced for films grown on etched-back substrates (Figure 2).

The introduction of etchbacks exceeding 120 seconds permitted a significant yield

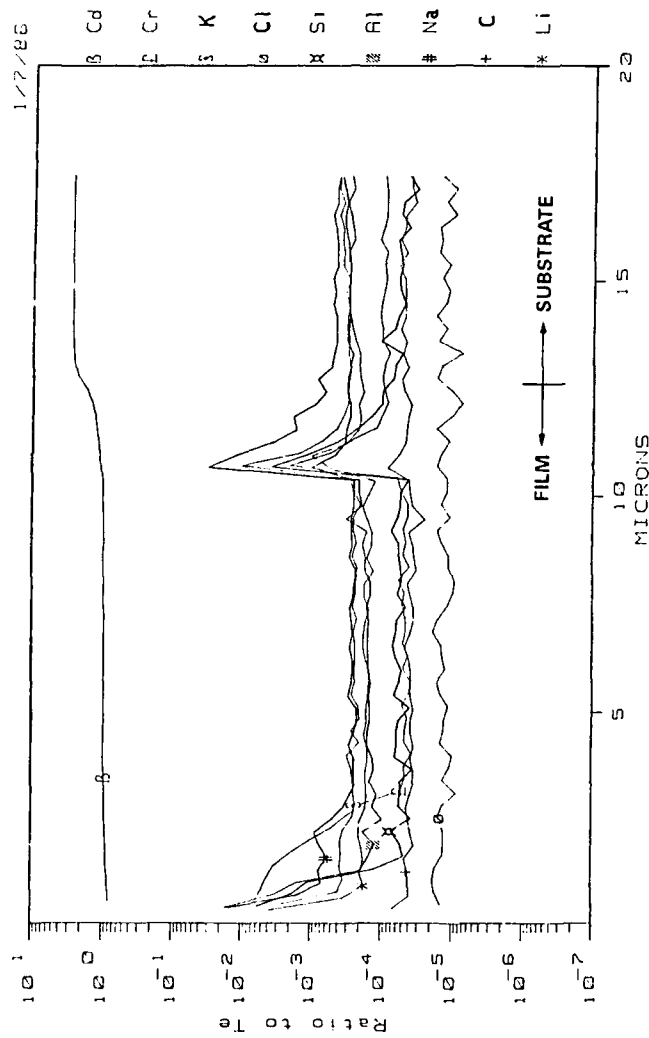


Figure 1. SIMS (Secondary Ion Mass Spectrometry) measurement of impurity variations within a LPE film and the substrate [10]. The ratios indicated do not represent stoichiometric proportions. The actual levels are likely to be orders of magnitude different from the levels indicated by these ratios. Note that the substrate-epi interface is approximately at a depth of 13 μm , whereas the 'hump' as described in the text is located at a depth of 11 μm .

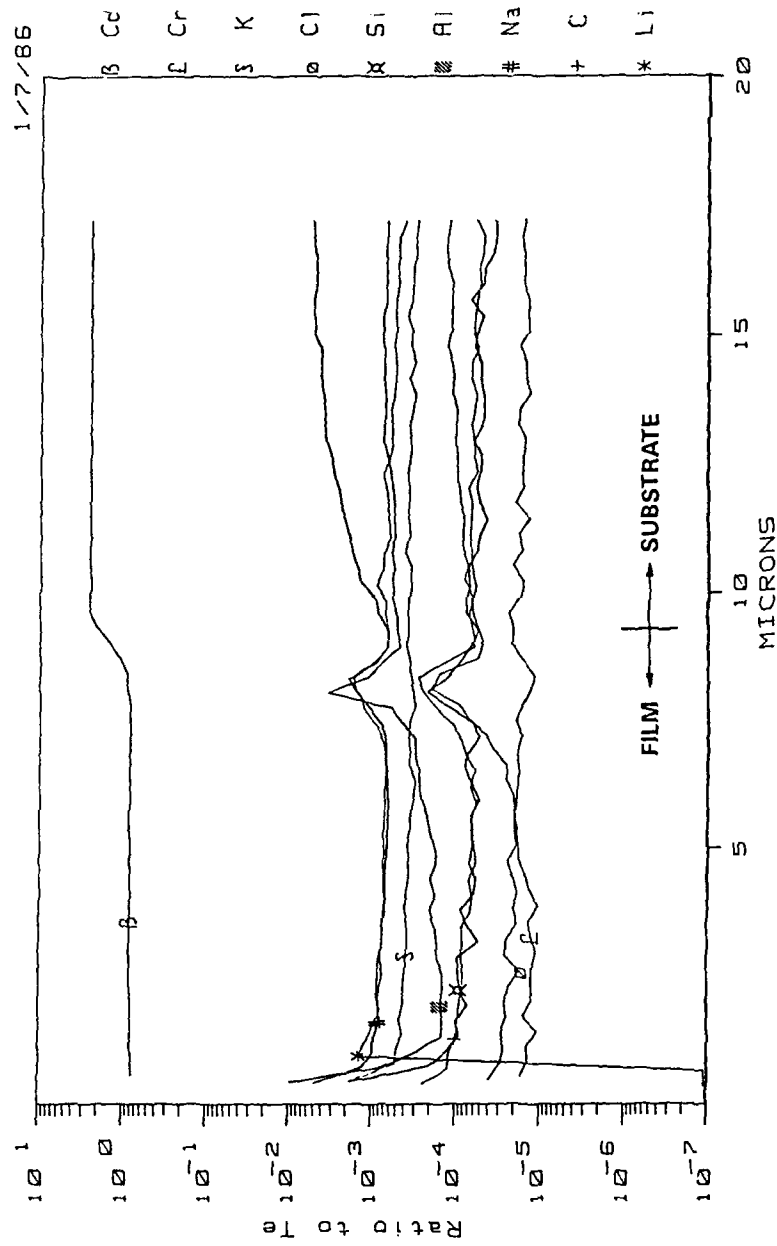


Figure 2. SIMS measurement of impurity variations within a LPE film and the substrate, where the substrate was subjected to a significant etchback immediately prior to growth of the epilayer. The substrate-epi interface is at a depth of 9 μm .

of films displaying classical or non-anomalous dependence of Hall mobility on temperatures. As is evident, a type of saturation phenomenon is observed when the etchback times are extended to considerably longer than 120 seconds [13]; no further increase in yield of classical films is observed. Since increasing length of etchback progressively degrades the surface quality of the growth face which in turn leads to the growth of films with increasing degrees of terracing leading to melt inclusions, etchback times significantly longer than 120 seconds were not employed. Note that the highest yield of classical films did not exceed approximately 20%. Hence between 70-80% of films still displayed either an anomalous dependence of Hall mobility on temperature or an outright p-type behavior. The latter (p-type behavior) occurred about 15% of the times.

DISLOCATION DENSITY MEASUREMENTS

The dislocation density distribution in these films varied widely. A consistent behavior was established during the present investigations by rapidly cooling the film following growth: the dislocation densities within the 'bulk' of the films immediately after growth and prior to any heat treatments generally followed the substrate dislocation density (Figure 3). Following the stoichiometric adjustment anneal however, the dislocation density increased by degrees ranging between 300 and 1000% (Figure 3). This mechanism has been studied earlier in bulk materials and has been traced to the formation of HgTe when excess tellurium is annihilated by the advancing mercury front [12]. During the present investigations, a dislocation multiplication reduction (DMR) annealing procedure for thin epitaxial films was developed. It will be discussed elsewhere [14]. Interposition of this anneal process prior to the stoichiometric adjustment anneal virtually eliminated the degree of dislocation multiplication. The dislocation density within the 'bulk' of the epifilm (i.e. in regions removed from the 'misfit' dislocation band) again tracked the substrate dislocation density levels approximately (Figure 3).

RESULTS AND DISCUSSIONS

These films, both with and without prior DMR anneal, were henceforth subjected to MIS characterization. The MIS devices on these films were fabricated at Texas Instruments. A general description of the methods followed and the general device physics have been discussed extensively by Kinch [1]. The details of the device performance and physics will therefore not be discussed in this space; only the performance parameters relevant to understanding the materials issues will be referred to. For these films, the dislocation densities varied widely, since some were subjected to DMR and some were not. The DMR treatment only permitted the dislocation densities in the films to follow the substrate dislocation density, as discussed above. When the 'dark' storage times were plotted vs. the dislocation density (Figure 4), immediately two groups of films were apparent. The first group contained films which displayed classical or non-anomalous dependence of the Hall mobility on temperature, whereas the second group consisted of films which showed an anomalous dependence of the Hall mobility on temperature. Films displaying a non-anomalous dependence of the Hall mobility on temperature show 'dark' storage times strongly dependent on dislocation density values (Figure 4). The higher the dislocation densities, the lower the storage times. No such strong dependence is noticeable for films

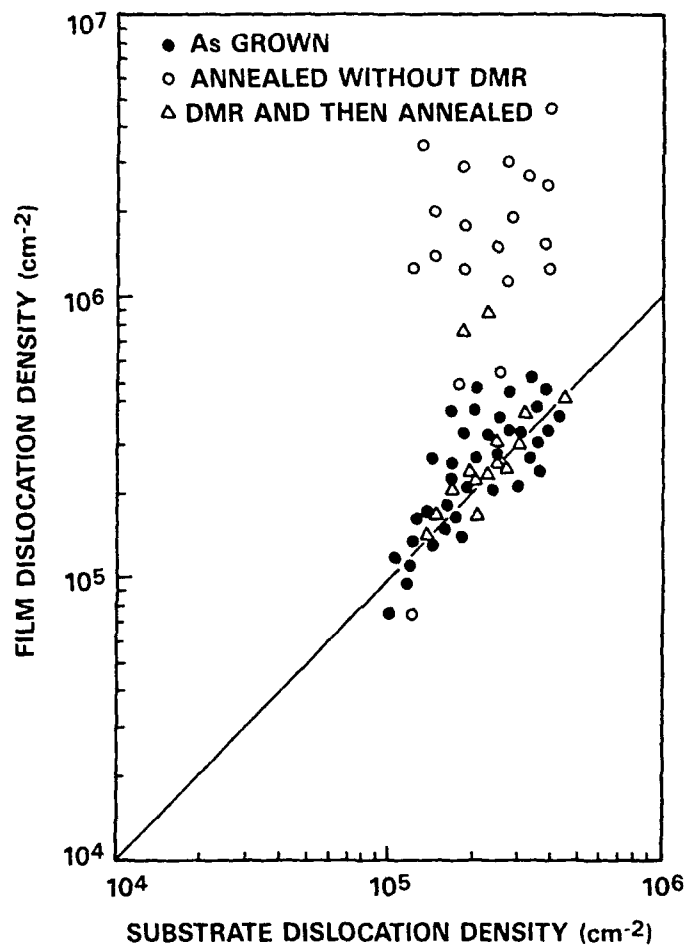


Figure 3. Dependence of the dislocation density within the 'bulk' of the epifilm (in regions well removed from the substrate-epi interface) on the substrate dislocation density. The respective symbols in the figure signify different heat treatments as indicated in the figure and described in the text.

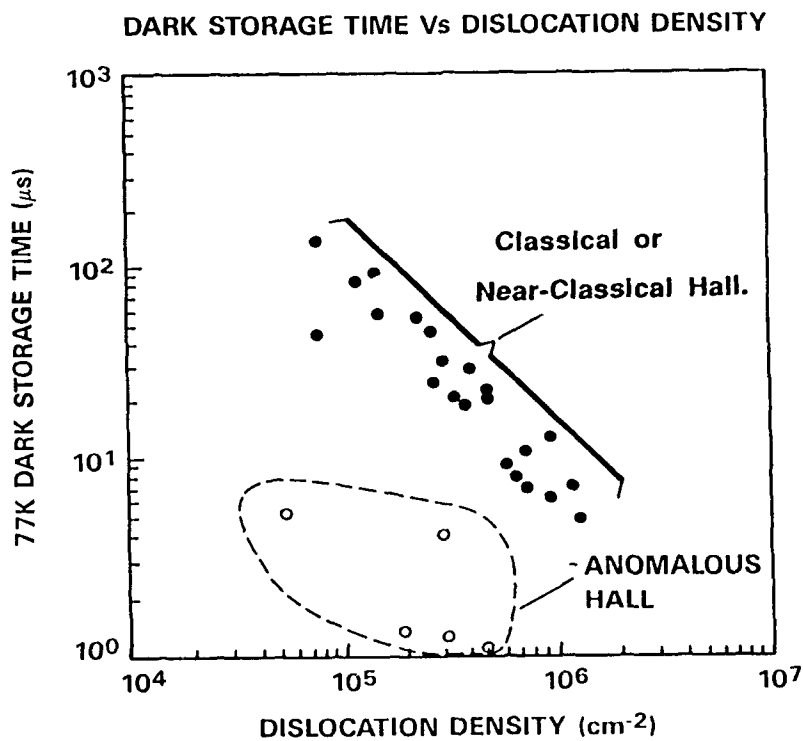


Figure 4. Dependence of the 'dark' storage time of devices built on LWIR LPE films on the film dislocation density. The respective symbols in the figure signify different Hall behavior as indicated in the figure and described in the text. The MIS spectral response measured cutoffs for all data points range between 10.0 and 10.5 μm at 77 K.

displaying an anomalous dependence of the Hall mobility on temperature (Figure 4), even though here too the performance as measured by the storage time generally degrades with increasing dislocation density. The storage times are drastically inferior for films showing the anomalous dependence. Note that for the classical or non-anomalous films, the storage times decrease with increasing dislocation densities approximately linearly, with values rising to $> 100 \mu\text{sec}$ for dislocation densities at or below $10^5/\text{cm}^2$. The cutoffs at 77°K for all the films shown fall between 10.0 and $10.5 \mu\text{m}$.

These results indicate the significantly stronger influence of the Hall behavior on MIS device performance when compared to the effect of the dislocation densities. The dislocation density becomes performance limiting once the classical Hall behavior is reached.

CONCLUDING REMARKS

Clear and unambiguous establishment of the greater importance of obtaining classical Hall behavior over lowering of dislocation density levels in attaining superior MIS device performance as measured by the dark storage times was achieved by following the data obtained from a random selection of classical and anomalous films with varying dislocation densities. For the first time a materials variable was uniquely identified as the key parameter to be fulfilled to achieve desired MIS performance for n-type LWIR LPE. A method to systematically and reproducibly solve this problem will be described elsewhere [6].

References

1. M.A. Kinch, in *Semiconductors and Semimetals*, Vol. 18, "Mercury Cadmium Telluride," ed. by R.K. Willardson and A.C. Beer (1981).
2. L. Colombo and A.J. Syllaios, IRIS Detector Specialty Group, July, 1982.
3. M.C. Chen, S.G. Parker, and D.F. Weirauch, *J. Appl. Phys.* 58, 3150 (1985).
4. L.F. Lou and W.H. Frye, *J. Appl. Phys.* 56, 2253 (1984).
5. B. Pelliciani and G. Baret, *J. Appl. Phys.* 62, 3986 (1987).
6. D. Chandra (unpublished data), to be submitted for publication.
7. S.G. Parker, D.F. Weirauch and D. Chandra, *J. Crystal Growth* 86, 173 (1988).
8. C.F. Wan, D.F. Weirauch, R. Korenstein, E.G. Bylander, and C.A. Castro, *J. Electron. Mater.* 15, 151 (1986).
9. H. Takigawa, M. Yoshikawa, and T. Maekawa, *J. Cryst. Growth* 86, 446 (1988).
10. D.F. Weirauch (private communication).
11. D. Chandra and M.W. Goodwin, IRIS Materials Specialty Group, June, 1988.
12. H.F. Schaake, J.H. Tregilgas, J.D. Beck, M.A. Kinch and B.E. Gnade, *J. Vac. Sci. Technol.* A3, 143 (1985).
13. D. Chandra, *Proceedings of the Materials Research Society Fall Meeting*, Boston, Massachusetts (1989).
14. D. Chandra and J.H. Tregilgas (unpublished data), to be submitted for publication.

LOW TEMPERATURE DEVICE PROCESSING TECHNOLOGY FOR II-VI SEMICONDUCTORS

D.L. DREIFUS*, R.M. KOLBAS*, B.P. SNEED**, AND J.F. SCHETZINA**

* Department of Electrical and Computer Engineering, North Carolina State University, Raleigh NC 27695-7911

** Department of Physics, North Carolina State University, Raleigh, NC 27695-8202

ABSTRACT

Low temperature (<60°C) processing technologies that avoid potentially damaging processing steps have been developed for devices fabricated from II-VI semiconductor epitaxial layers grown by photoassisted molecular beam epitaxy (MBE). These low temperature technologies include: 1) photolithography (1 μm geometries), 2) calibrated etchants (rates as low as 30 Å/s), 3) a metallization lift-off process employing a photoresist profiler, 4) an interlevel metal dielectric, and 5) an insulator technology for metal-insulator-semiconductor (MIS) structures. A number of first demonstration devices including field-effect transistors and p-n junctions have been fabricated from II-VI epitaxial layers grown by photoassisted MBE and processed using the technology described here. In this paper, two advanced device structures, processed at <60°C, will be presented: 1) CdTe:As-CdTe:In p-n junction detectors, grown *in situ* by photoassisted MBE, and 2) HgCdTe-HgTe-CdZnTe quantum-well modulation-doped field-effect transistors (MODFETs).

INTRODUCTION

Controlling the conductivity of Hg-based alloys by the deliberate creation of defects (through ion implantation or thermal annealing) has been employed to fabricate p-n junctions [1] and metal-insulator-semiconductor field-effect transistors (MISFETs) [2]. These techniques are adequate for devices formed in bulk or thick epitaxial layers, but are inappropriate or self-defeating when applied to thin films and multilayer heterostructures. With the advent of controlled substitutional doping of many II-VI semiconductors, new processing techniques are needed to preserve (not destroy) the as-grown characteristics to make possible advanced device structures for optoelectronic circuits.

Unfortunately, the II-VI materials are too soft and temperature-sensitive to use traditional Si or GaAs device processing techniques, since processing-induced crystal damage, Hg vacancies, or Hg-interdiffusion can appreciably alter the characteristics of thin multilayers. In addition, basic information concerning etching, surface passivation, ohmic contacts, and design rules are unavailable in the open literature either because they have not been developed or are considered proprietary.

The thrust of this work is the development and demonstration of a processing technology that uses low-temperatures (<60°C) and minimizes crystal damage or variations in the as-grown material characteristics. CdTe metal-semiconductor field-effect transistors (MESFETs) [3], HgCdTe MISFETs [4], and CdMnTe Schottky diodes and MESFETs [5] have already been demonstrated using these low-temperature processing techniques.

II-VI SEMICONDUCTOR DEVICE PROCESSING TECHNOLOGY

A successful II-VI semiconductor device processing technology requires wafer handling schemes, reduced-temperature photolithography, controlled chemical etching, metallization lift-off processes, and an insulator technology for MIS structures and interlevel metal dielectrics.

To address the issue of wafer softness a series of Teflon supports and stainless steel holders were devised to mount and transfer wafers. This avoids the use of tweezers and minimizes the chance that a sample can become inverted (epitaxial layer side down), which can adversely affect the ability to fabricate functioning devices. These techniques have dramatically reduced accidental processing induced damage.

Traditionally, the maximum processing temperature for Hg-based alloys is around 100°C. However, based on Hg diffusion studies [6] this temperature is inappropriate for devices requiring multilevel masking sequences. This can involve several hours of processing at elevated temperatures, leading to significant Hg interdiffusion at heterointerfaces (and thus variation in the bound state energies of quantum confined structures). In this work an upper limit on the processing temperature of 60°C was selected to be compatible with 1) the minimum hard-baking temperature of the photoresist and 2) reduced Hg-interdiffusion and vacancy generation.

Photoresist exposure times, bake times, and spin speeds for the reproducible photolithographic transfer of patterns at a maximum temperature of 60°C are as follows. Initially, the sample is degreased in trichloroethylene, acetone, and methanol at room temperature for 10 minutes in each solution. The sample is baked at 60°C for 60 minutes, AZ 1350J photoresist is applied at a spin speed in excess of 6000 rpm, and exposure and develop times (using a 1:1 AZ Developer : H₂O) solution are experimentally optimized for the various photoresist thicknesses. A profiling scheme involving a 30 second pre-exposure soak in a 1:2 solution of hexamethyldisilazane and xylene has been devised and used to successfully lift-off 1 μm geometry features. Employing a postbake temperature of 60°C necessitates a baking time in excess of 1 hour in order to increase the photoresists' resiliency to chemical attack. The photoresist pattern on top of the etched mesa structures is preserved with a negligible amount of shrinkage in the etched pattern.

Controlled etching is required for device processing. We have focused on wet chemical etching since plasma and ion beam etching are unsuitable due to the potential damage that they can cause. A measure of success in calibrating various etchants compatible with the 60°C photolithographic process has been realized. These include nonselective etchants consisting of bromine and ethylene-glycol, and selective etchants based on potassium dichromate and nitric acid. Although the etching rates of these solutions are somewhat unstable as a function of time, they can be used to achieve reproducible etch rates as low as 30 Å/s. For example, MODFETs require a complicated processing sequence that involves the selective etching of unwanted surface layers in order to facilitate ohmic contacts to the two dimensional (2D) electron gas. An etchant consisting of 4 gm K₂Cr₂O₇ : 10 ml HNO₃ : 20 ml H₂O has been successfully employed to remove CdTe from HgCdTe or HgTe (100:1 for HgTe:CdTe). HgTe thin films can now be employed as stop-etch layers and have been

successfully used to remove CdTe substrates for optically pumped HgCdTe laser structures. [7]

Ohmic contacts and Schottky barrier rectifying contacts have been successfully made to n-type and p-type II-VI semiconductors. The sample temperature during metallization is carefully monitored and is not permitted to exceed 60°C. Low-resistance ohmic contacts to n-type CdTe, CdMnTe, HgTe, and HgCdTe have been accomplished using In (exhibiting contact resistances in the range between 0.5 Ω to 10 Ω for a 100 μm square metal pad). In order to obtain ohmic contact to p-type CdTe:As, a multilevel metallization was developed, consisting of three consecutive electron-beam evaporations of Ni (75 Å), Cu (250 Å), and Au (2500 Å). Unfortunately, this ohmic contact scheme required a 20 minute anneal at 200°C in a nitrogen ambient. An alternate approach has been the MBE deposition of HgTe followed by a thermal evaporation of In. These unannealed contacts exhibited linear current-voltage characteristics similar to the Ni-Cu-Au contacts, and have been used successfully to obtain device results for CdTe p-n junctions. Au has been employed for p-type ohmic contact to HgCdTe and Schottky barrier diode gates on n-type CdTe:In and CdMnTe:In.

An insulator technology is required to fabricate MIS structures, to prevent junction shorting in p-n junction detectors when running metal interconnects off mesa structures, and for multilevel metallizations. Several insulator technologies such as a remote plasma deposition of SiO₂, spin-on glass, and thermal evaporations of ZnS were investigated. The best results, however, were obtained for room temperature MBE depositions of ZnS. Since the insulator deposition is performed at room temperature, photoresist masking becomes a viable choice for the pre-patterning of the deposited insulator. Using the same lift-off profiling scheme as was developed for metallization definition, selective area depositions of ZnS have been accomplished. Prior to each ZnS deposition, the surface is etched for 15 seconds in a 1:1 solution of HCl:H₂O to improve the surface adhesion. This technique has been used successfully in the fabrication of HgCdTe MISFETs [5], and a photograph of processed devices is shown in Fig. 1. These clearly defined patterns (5 μm gate lengths) illustrate the control of the patterned linewidth achievable employing the low-temperature processing technology. The entire surface, except for the In ohmic contact pads, has been coated with MBE-deposited ZnS.

DEVICE RESULTS

CdTe:In-CdTe:As double layer p-n junctions were grown *in situ* by photoassisted MBE. (100) oriented, polished, and etched CdTe semi-insulating substrates were used onto which a 1 μm buffer layer of semi-insulating CdTe was deposited by conventional MBE. The photoassisted MBE deposition of a 2 μm thick layer of n-type CdTe:In followed by another 2 μm thick layer consisting of p-type CdTe:As was performed at 180°C. Carrier concentrations and mobilities, based on previous single layer growths, have been estimated to be in the range of $1 \times 10^{17} \text{ cm}^{-3}$ (for both layers), and 500 $\text{cm}^2/\text{V}\cdot\text{s}$ (n-type) and 80 $\text{cm}^2/\text{V}\cdot\text{s}$ (p-type) respectively.

Fabrication of the device structures began with two 2 μm deep mesa isolation etches to form columns of p-type material on top of the n-type mesas. An etch consisting of a 1:1 solution of HCl:H₂O solution was performed prior to a thermal evaporation of In to form ohmic contacts to the n-type CdTe:In. Next, a 4800 Å thick

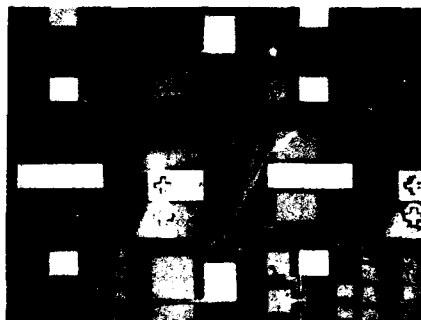
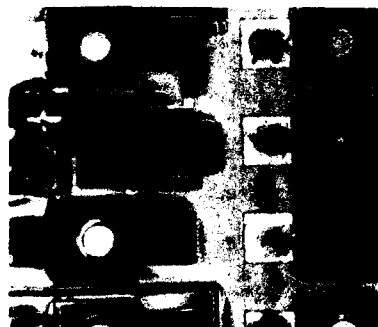


Figure 1. Photograph of processed HgCdTe MISFETs. Ohmic contact to n-type material was performed using In, while Au was employed as the gate contact. Transistor gate length by gate width include $5\text{ }\mu\text{m} \times 25\text{ }\mu\text{m}$, $5\text{ }\mu\text{m} \times 50\text{ }\mu\text{m}$, $5\text{ }\mu\text{m} \times 200\text{ }\mu\text{m}$, and $100\text{ }\mu\text{m} \times 200\text{ }\mu\text{m}$ area structures. An MBE deposition of ZnS (2800 Å) was used as the gate insulator.

selective-area MBE ZnS deposition was performed leaving the In contact pads and the centers of the p-type semiconductor columns exposed. A 2500 Å thick HgTe layer was deposited at room temperature using a Hg-compatible MBE system, followed by a thermal evaporation of 3000 Å of In, and subsequently lifted-off in acetone. A photograph and schematic cross-section of the processed device structure is shown in Fig. 2.

Current-voltage measurements of the CdTe p-n junction detector structure are shown in Fig. 3, exhibiting reverse break-down voltages in excess of 20 V. By subtracting a series resistance from these characteristics, a junction ideality factor



SCHEMATIC CROSS-SECTION OF PROCESSED CdTe P-N JUNCTION

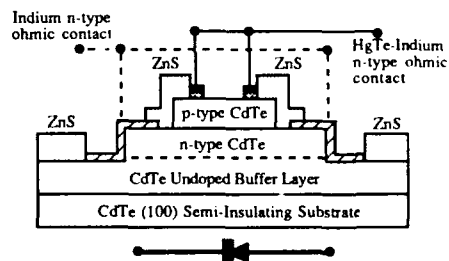


Figure 2. Photograph and schematic cross-section of processed CdTe p-n junction detectors. Ohmic contact to n-type material was performed using In, while Ni-Cu-Au was employed as the p-type contact. The open rings are $5\text{ }\mu\text{m}$ thick and vary in diameter between $30\text{ }\mu\text{m}$ and $100\text{ }\mu\text{m}$. ZnS (4800 Å) was used as an interlevel metal dielectric.

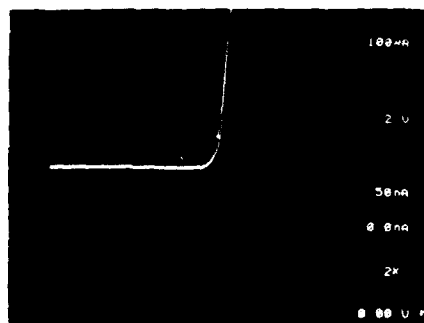


Figure 3. Current-Voltage characteristics of a CdTe:As-CdTe:In p-n junction. Ohmic contact to the n-type CdTe was obtained using In while a combination of MBE-deposited HgTe and In was used for the p-type ohmic contact. Reverse breakdown voltages were in excess of 20 V (<100 nA of reverse bias current).

in the range between 4 and 8 can be determined. It had been speculated that p-n junctions could not be grown using both In and As in the same MBE growth chamber because of a dopant memory effect observed for indium. This first demonstration of p-on-n layers demonstrates that these structures can be grown by photo-assisted MBE and that detector structures can be successfully fabricated in CdTe using the low temperature processing technology.

Modulation-doped quantum well structures containing the semimetal HgTe have been successfully grown by MBE [8]. Epitaxial structures were grown in order to study the behavior of HgTe quantum wells and then later used in the device fabrication. The potential well is composed of 150 Å of HgTe sandwiched between the CdZnTe substrate and a 100 Å $\text{Hg}_{0.15}\text{Cd}_{0.85}\text{Te}$ cap layer. These epitaxial layers were grown at a substrate temperature of 150°C and exhibited characteristics of a 2D electron gas with approximate electron densities of $1.0 \times 10^{12} \text{ cm}^{-2}$ and low-temperature electron mobilities of 9000 $\text{cm}^2/\text{V}\cdot\text{s}$.

MODFET device fabrication proceeded with a 3000 Å mesa etch. Subsequently, a semi-insulating CdTe surface passivation layer was deposited at room temperature by MBE. Prior to an ohmic contact metallization using indium, the CdTe cap and surface passivation layers were selectively removed in a $\text{K}_2\text{Cr}_2\text{O}_7$ and HNO_3 solution. 2000 Å of In was deposited by thermal evaporation and the excess metal was removed by the lift-off technique. Finally, a 2500 Å thick layer of Au was deposited by electron-beam evaporation.

A schematic cross-section of the processed device structure and the drain-to-source current-voltage characteristics for a 100 μm gate length by 200 μm gate width device structure are shown in Fig. 4. Unfortunately, these devices did not achieve pinch-off, but a rough calculation of the room temperature transconductance yielded approximately 4.0 mS/mm . The inability of this device to achieve pinched-off is probably due to the formation of an inversion layer at the HgCdTe-CdTe interface. These results are promising and indicate that many of the advanced III-V multilayer device structures such as quantum-well MODFETs may now be fabricated from II-VI semiconductor epitaxial layers.

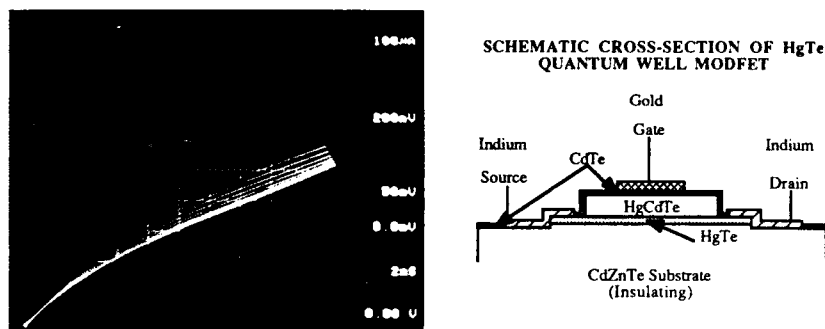


Figure 4. Drain-to-Source current-voltage characteristics and schematic cross-section of the processed device for a 100 μm gate length by 200 μm gate width HgCdTe-HgTe-CdZnTe quantum well modulation-doped field-effect transistor. (Gate voltage steps = -50 mV, vertical scale = 100 $\mu\text{A}/\text{div}$, horizontal scale = 200 mV/div).

SUMMARY

The low-temperature device fabrication methods explored in this research work have been developed to take full advantage of the the as-grown electrical and optical properties of heterojunction and superlattice device layers. Using the low-temperature techniques, the first demonstrations of advanced metals device structures such as CdTe p-n junctions, grown *in situ* by photoassisted MBE, and HgTe quantum-well MODFETs are reported.

ACKNOWLEDGEMENTS

The authors would like to thank John Tassitino for his assistance in the development of the processing technology. This work was supported by NSF grant DMR-88-13525, and by General Electric Aerospace Group IR&D funds.

REFERENCES

1. M.B. Reine, A.K. Sood, and T.J. Tredwell in **Semiconductors and Semimetals**, R.K. Willardson and A.C. Beer, eds., (Academic Press, New York, 1981).
2. See for example: Y. Nemirovsky, S. Margalit, and I. Kidron, *Appl. Phys. Lett.* **36**, 466 (1980).
3. D.L. Dreifus, R.M. Kolbas, K.A. Harris, R.N. Bicknell, N.C. Giles and J.F. Schetzina, *Appl. Phys. Lett.* **51**, 931 (1987).
4. D.L. Dreifus, R.M. Kolbas, J.W. Han, J.W. Cook, Jr., and J.F. Schetzina, *J. Vac. Sci. Technol.* **A**, to be published.
5. D.L. Dreifus, R.M. Kolbas, R.L. Harper, J.R. Tassitino, S. Hwang, and J.F. Schetzina, *Appl. Phys. Lett.* **53**, 1279 (1988).
6. D.L. Dreifus, PhD Thesis, North Carolina State University, 1989.
7. N.C. Giles, Y. Lansari, J.W. Han, J.W. Cook, Jr., and J.F. Schetzina, *J. Vac. Sci. Technol.* **A**, to be published.
8. Y. Lansari, Z. Yang, S. Hwang, J.W. Cook, Jr., and J.F. Schetzina, to be published in *Mater. Res. Soc. Proc.*

PART VII

HgCdTe: Epitaxial Growth

RECENT PROGRESS IN THE OMVPE GROWTH OF HgCdTe

SORAB K. GHANDHI

Electrical, Computer and Systems Engineering Department, Rensselaer Polytechnic Institute, Troy, New York 12180

ABSTRACT

The last two years has seen rapid development in the growth of mercury cadmium telluride material for use in far infrared detectors. This paper will briefly review the progress before this period, and will focus on recent developments in these materials.

The emphasis will be on the direct alloy growth of HgCdTe material by organometallic vapor phase epitaxy (OMVPE).

TECHNICAL

The epitaxial growth of $\text{Hg}_{1-x}\text{Cd}_x\text{Te}$ (MCT) has received considerable attention during the past several years, because of its potential for producing active layers of higher electrical quality than those grown by bulk methods. Several methods have been reported for the growth of these layers; of these, organometallic vapor phase epitaxy (OMVPE) has emerged as the most promising candidate [1-8] for the commercialization of this material. To this end, a major effort is underway at the present time.

Compositional Uniformity:

The driving force for these developments is the need for focal plane array detectors, operating in the 10.6 μm range. Here, the main requirements are layers of 10-15 μm thickness, with an x value around 0.2. A high degree of compositional uniformity (± 0.005) is required for x (the Cd-fraction), and devices as large as 1 cm \times 1 cm are envisioned. This composition uniformity is relatively easy to obtain in mass transport limited systems such as AlGaAs and InGaAs. In these systems, OMVPE has a unique advantage since source reactants can be mixed prior to entry into the reactor. As a result, compositional uniformity over the substrate is achieved under all flow conditions and independent reactor details or layer thickness.

The situation with HgCdTe is, unfortunately, more complex, since growth is limited by surface kinetics. One approach around this problem is to grow the binaries, HgTe and CdTe, in a sequential manner, and then homogenize them in a final heat treatment. This method, known as the Interdiffused Multilayer Process (IMP), can be used [9, 10] to readily achieve the compositional uniformity goal. However, it involves an interdiffusion process which requires a rather high temperature, which offsets the advantage of low temperature growth. In addition, the crystallinity of interdiffused HgCdTe layers has been shown to be poorer than that of alloy grown HgCdTe, as determined by double-crystal x-ray diffraction [11]. This has been attributed to defects generated due to the lattice mismatch between HgTe and CdTe, and to incomplete diffusion.

Additional problems with the IMP process come about because of the large differences in incorporation rate for dopants in HgTe and CdTe. Together with the fact that diffusion rates of the preferred dopants are extremely slow compared to the homogenization rate, this leads to striations in doping rather than uniformly doped layers. It is for these reasons that we have adopted the conventional approach of direct

alloy growth.

In our own work we have used a vertical reactor, operated at 380 Torr. Here, we have achieved a uniformity of $x = 0.2 \pm 0.002$ over a 1 cm \times 1 cm area, using a stationary susceptor [12, 13]. More recently, using a rotating susceptor, we have improved the compositional uniformity to $x = 0.2 \pm 0.001$ over a 1" diameter. The eventual goal of our work in this area, to extend the uniformity to a 2" diameter substrate, should be met in the reasonably near future.

Annealing:

HgCdTe is a semiconductor material in which defects are electronically active. Conventional devices use this property to obtain both p- and n-doped layers for diode fabrication. Typically, controlled annealing in a Hg-overpressure is used to set the level of $[V_{Hg}]$, which is p-type. Controlled damage, by ion implantation, is used to produce a region which is n-type. While this combination of processes has resulted in useful devices, the exploitation of advanced HgCdTe structures will demand the controlled use of extrinsic dopants of both impurity types. A necessary pre-condition for extrinsic doping is the need for fully annealing the grown layers so as to eliminate (or minimize) the residual background concentration due to Hg-vacancies. This annealing is carried out by heat treatment in a sealed quartz ampoule in which excess Hg is present.

HgCdTe layers usually have a high mobility n-type layer on their surface, resulting from charge states in the native surface oxide. The presence of such a surface layer on lightly doped p-type $Hg_{1-x}Cd_xTe$ is readily apparent, since it gives rise to anomalous behavior in the Hall Coefficient vs. Temperature data. This behavior, which has been analyzed in great detail [14, 15], is a consequence of the fact that these inversion layer electrons have surface mobilities which are a factor of 10 to 20 times higher than those of the bulk holes. Their concentrations lie in the range of 3×10^{11} to $1 \times 10^{12}/cm^2$, depending on the nature of the surface and its treatments.

The annealing behavior of bulk HgCdTe is well understood, unlike that for OMVPE grown material. For the latter, extremely long times (21 days) and high temperatures were reported [16], with full anneal to n-type occurring in only isolated cases.

We have made an extensive study of annealing of OMVPE grown material over the last two years. For our work, layers were sealed in ampoules which were evacuated to 10^{-7} Torr using a turbo-molecular pump equipped with a liquid nitrogen trap. All annealings were carried out with the sample kept 2°C warmer than the Hg reservoir, to avoid Hg from condensing on them. The annealed samples were characterized without any further surface treatment. For some samples which exhibit anomalous p-type behavior, the surface was passivated by anodic sulfidization [17] and Hall data were taken once again.

Figure 1 shows the Hall coefficient (R_H) and the conductivity (σ) for a 6.7 μm thick as grown $Hg_{1-x}Cd_xTe$ layer with a 0.5 μm thick undoped CdTe cap layer and an alloy composition of 0.228. The data were taken at a magnetic field of 2.1 kG. The solid curve shown here is a computer simulation which gives a least square fit to the experimental data. The best fit corresponded to $(N_A - N_D)$ of $3.61 \times 10^{16}/cm^3$, a hole ionization energy of 6.2 meV, and a low temperature hole mobility (μ_{po}) of 840 cm^2/Vs . Because of the high doping due to Hg vacancies, it was not necessary to consider the presence of any inversion layer in order to obtain this fit.

Figure 2 shows R_H for a sample annealed at 230°C for nine hours, taken at 2.1 kG. This sample had an x value of 0.208 and a thickness of 12 μm . This combination of temperature and time should be sufficient to anneal bulk $Hg_{1-x}Cd_xTe$ up

TABLE I. DATA FOR FULLY ANNEALED SAMPLES

x	Thickness (μm)	Annealing Conditions	$(N_D - N_A)$ (cm^{-3})	$\mu_n(30K)$ (cm^2/Vs)
0.205	8.2	290°C/15 hr. +220°C/13 hr.	5.4×10^{14}	334,000
0.220	5.8	290°C/15 hr. +220°C/13 hr.	6.2×10^{14}	210,000
0.226	5.8	290°C/15 hr. +220°C/13 hr.	3.3×10^{14}	120,000
0.226	5.8	270°C/14 hr. +220°C/12 hr.	3.5×10^{14}	190,000

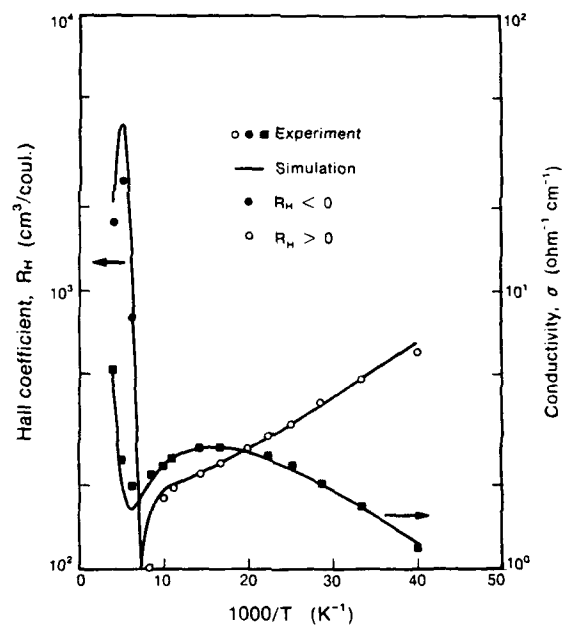


Figure 1. Hall coefficient and conductivity for an unannealed HgCdTe epilayer.

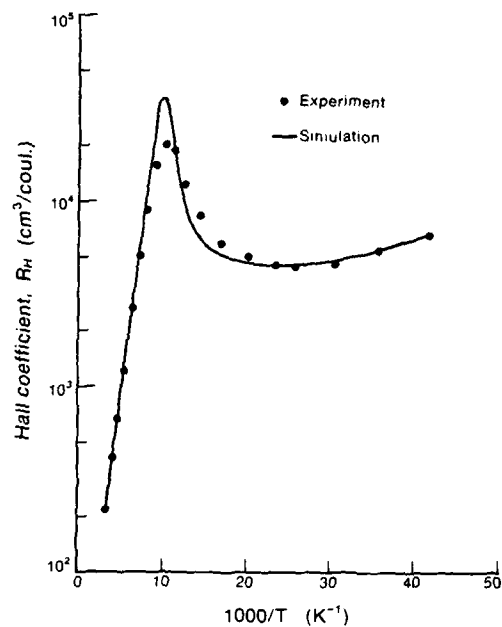


Figure 2. Hall coefficient for a partially annealed layer.

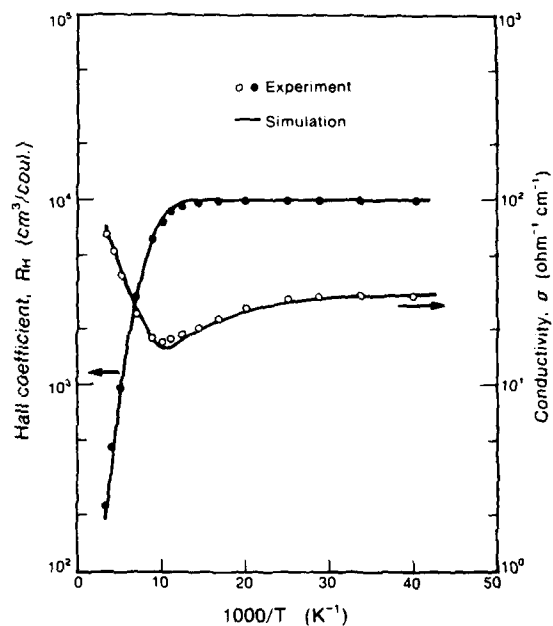


Figure 3. Hall coefficient and conductivity for a fully annealed layer.

to a depth of 15 μm . Even though significant reduction of hole concentration is observed here, the complete conversion of the epilayer is not achieved. This curve was fitted to a computer model which assumes a p-type epilayer with n-type surface inversion. Parameters providing the best fit (represented by the solid curves) are N_A of $1.65 \times 10^{15}/\text{cm}^3$, N_D of $4 \times 10^{15}/\text{cm}^3$, E_A of 7.0 meV and a low temperature hole mobility (μ_{po}) of $1620 \text{ cm}^2/\text{Vs}$ for the bulk layer. The inversion layer carrier concentration was $2.2 \times 10^{11}/\text{cm}^2$, with a low temperature surface electron mobility (μ_{so}) of $7000 \text{ cm}^2/\text{Vs}$. Note that the theoretical fit to the experimental data points is not very good in the region where R_H begins to fall with decreasing temperature. This is due to some degree of nonuniformity in the hole concentration through the layer.

Figure 3 shows R_H and σ versus $1000/T$ for a sample annealed with 290°C for 15 hours, followed by a 220°C anneal for 13 hours. The layer was $8.2 \mu\text{m}$ thick, with $x = 0.205$. The data were taken at 1.1 kG. It is seen from the shape of the R_H curve, as well as the high mobility value, that this is an n-type layer. However, it is possible that the measured electron concentration and mobility may be different from the actual bulk values, due to the presence of the surface electrons. The measurement of R_H as a function of B field allows the effect of these carriers to be separated [18].

Table 1 lists the results of Hall data on this and several other annealed samples, which show complete conversion to n-type. Samples were annealed at 220°C following the initial high temperature anneal. At 220°C , the equilibrium concentration of Hg vacancies is expected to be in the 10^{12} - $10^{13}/\text{cm}^3$ range [19]. Hence, the compensation due to the Hg vacancies is expected to be negligible, so that the net donor concentration N_D approximates the free electron concentration ($N_D - N_A$). These residual donor impurities are probably associated with process related issues such as chemical contamination from the system and bubblers, as well as inherent defects in $\text{Hg}_{1-x}\text{Cd}_x\text{Te}$ due to lattice and thermal expansion coefficient mismatch between the epilayer and the substrate. The number of such donor impurities is seen to be in the range of $3\text{-}6 \times 10^{14}/\text{cc}$ in these layers.

In summary, full annealing of HgCdTe layers is now routinely achievable, using a two-temperature anneal process. However, the difference between the annealing characteristics of OMVPE grown and bulk layers is not understood at the present time. We propose that this can be explained by considering the role of Te precipitates in the annealing process. Interstitial Hg is expected to react readily with these precipitates [20], the reaction rate being limited by the mass transport of the Hg to the Te precipitate, which act as a sink for this Hg. During the annealing process, the diffusion length of interstitial Hg is comparable to the spacing between the Te precipitates, resulting in an overall reduction of $[I_{Hg}]$ in the lattice. This would cause a higher concentration of vacancies to exist in the lattice as long as the Te precipitates are present. Once the Te precipitates are all annihilated, $[I_{Hg}]$ can rise, and $[V_{Hg}]$ can drop, to their equilibrium values. A higher annealing temperature enhances the in-diffusion of Hg, and increases the rate of annihilation of the Te precipitates. This, followed by a low temperature anneal, will reduce the Hg vacancies and convert the layer to n-type.

Doping:

As mentioned earlier, doping of HgCdTe devices is commonly achieved by the use of ion damage for n^+ -regions, and controlled annealing to produce V_{Hg} , which are p-type. Extrinsic p-doping with As and Sb has been achieved with LPE by low temperature annealing in a Hg-rich ambient [21].

Extrinsic n-type doping of OMVPE grown HgCdTe material has been shown to be relatively straightforward [22] with indium as the dopant of choice. P-type doping

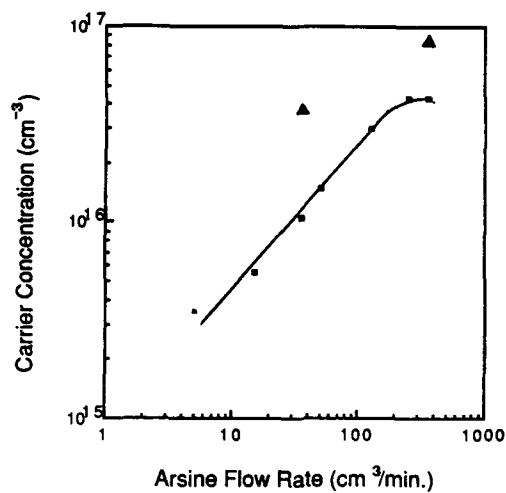


Figure 4. Net acceptor concentration as a function of arsine flow: (■) GaAs substrate; (▲) CdTe substrate.

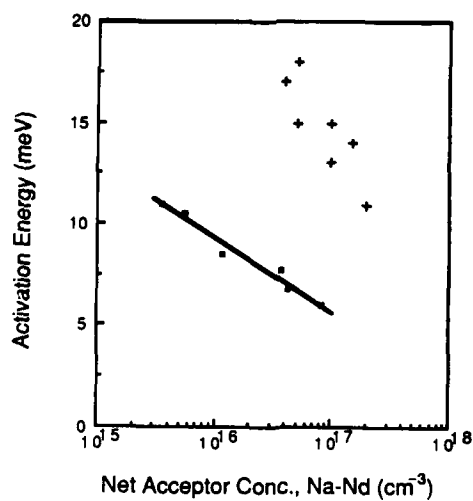


Figure 5. (■) Activation energies of arsenic in HgCdTe. The energy of Hg vacancies is also shown (+) for comparison.

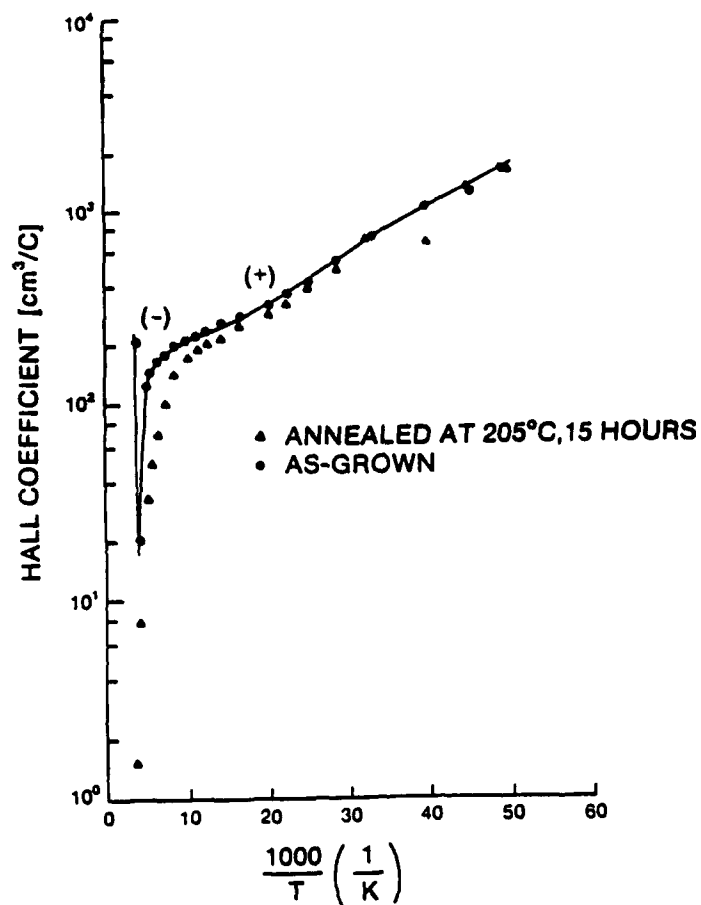


Figure 6. Hall coefficient as a function of reciprocal temperature for an as-grown and an annealed HgCdTe layer doped with As. The Cd composition of both the layers was 0.31.

is considerably more difficult. In principle, both group V elements (which are incorporated on the Te sublattice), and the group I elements (which incorporate on the metal sublattice), act as p-type dopants [23]. Group V elements are preferred because they are much slower diffusing species and hence can be used to form stable device structures.

We have demonstrated [24, 25] that it is possible to achieve extrinsic p-type doping of HgCdTe during growth by OMVPE. Arsine gas in hydrogen was used as the dopant source. Figure 4 shows the net acceptor concentration as a function of arsine flow rate. The measured doping concentration increased from 3.5×10^{15} to $4.3 \times 10^{16} \text{ cm}^{-3}$ as the arsine flow was increased from 5 to 250 sccm, with all the other parameters held constant. The mobility of these films was in the range 400-600 cm^2/Vs , which is comparable to that of bulk p-type films using Hg-vacancy doping.

Arsenic incorporation in these layers has been confirmed by SIMS measurements [26]. Moreover, the activation energy of the arsenic acceptor has been measured on a series of p-doped samples, as shown in Fig. 5. Also shown are values of the Hg-vacancy acceptor [27]. Note that the ionization energy obtained for arsenic is consistently a factor of 2 lower than that for Hg acceptors. The same order of difference in the ionization energy between Hg vacancies and external impurities has been observed in bulk and LPE doped films.

A major advantage of extrinsic doping is that it is considerably more stable with temperature than p-doping using V_{Hg} . This is shown in Fig. 6 where data for an as-grown arsenic doped layer is compared to that for a similar layer which was subjected to a 205°C heat treatment for 15 hours. The similarity of these curves clearly establishes the stability of extrinsic doping in HgCdTe. Moreover, it shows that modern devices, using regions of controlled doping, can now be made with this semiconductor.

Low Temperature Growth:

HgCdTe is highly susceptible to thermally induced defects at growth temperatures. As a result, significant improvements can be made by reducing the growth temperature. In recent years, much research has aimed at low temperature growth by OMVPE, using laser assisted and other forms of stimulated growth, in addition to the use of less stable Te precursors [28-30]. Of all these methods, growth by using Te alkyls, which are more readily cracked, is the most promising one since it results in material with a minimum of damage.

Historically, progress in the OMVPE growth of HgCdTe has steadily aimed at the exploration of new chemicals for reducing the growth temperature. Initially, diethyltelluride was used with growth at around 415°C or higher temperatures. Growth with alternative chemicals such as diisopropyltelluride (DIPT) has allowed reduction of the growth temperature to around 370°C, with a corresponding improvement in the resulting crystal quality. At the present time, this alkyl is available in high purity, and is routinely used for HgCdTe growth. Other Te precursors such as ditertiarybutyltelluride [31] and diallyltelluride [32] have been used to grow HgTe at low temperatures (250-350°C). A disadvantage of these chemicals is their low vapor pressure, which necessitates the use of heated bubblers and lines to transport a sufficient amount of Te to the reactor.

Recently, methylallyltelluride (MATe) has been used to grow HgTe at about 320°C, using dimethylmercury [33]. This Te source has a relatively high vapor pressure (6.2 Torr at 20°C) so that it can be transported readily to the reaction zone. In our recent work [34] we have shown that HgTe and HgCdTe can be grown over the 240-320°C range using this Te alkyl. Growth at 320°C resulted in featureless surfaces. Material quality of layers grown at 320°C is demonstrated in Fig. 7 by the very nar-

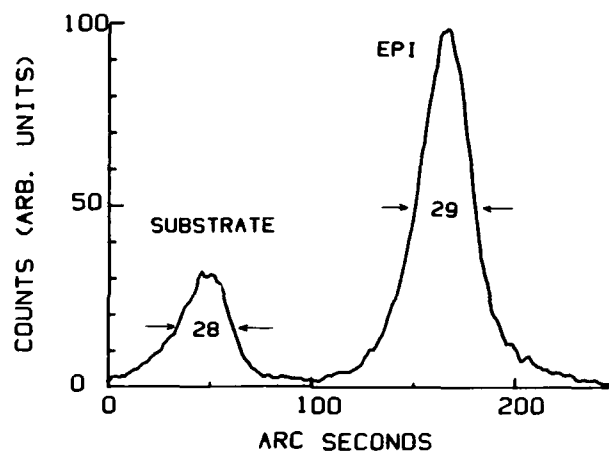


Figure 7. X-ray diffraction rocking curve for a HgTe layer on a CdTeZn substrate.

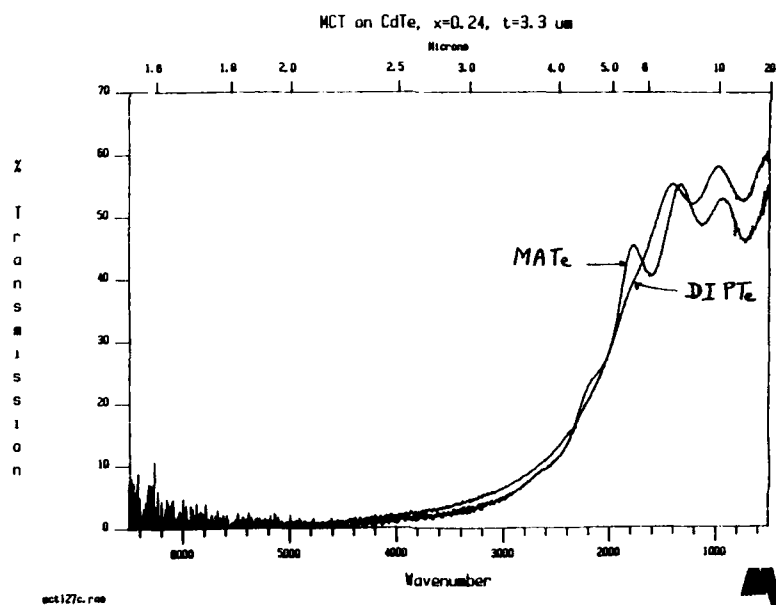


Figure 8. FTIR spectrum for HgCdTe layers grown using MATE and DIPTe.

row full width at half maximum (FWHM) of x-ray diffraction (29 arc secs), which is comparable to that of the substrates used in our study.

HgCdTe layers were also grown at 320°C, using DMCD, MATe and Hg. Figure 8 shows the FTIR spectrum for two layers grown on CdTe substrates. The excellent epilayer substrate interface is demonstrated by the sharp interference fringes present, even for a thin layer (3.3 μm), when grown using MATe. For layers grown with DIPTe at higher temperatures, these fringes are less sharp due to interdiffusion effects. X-ray rocking curves, taken on HgCdTe layers and grown on CdZnTe substrates, show the FWHM of this 3.5 μm epilayer to be 70 arc secs. Comparable values have been obtained for 6 μm thick layers grown with DIPTe at 370°C.

In summary, we have shown that MATe can be used to grow HgTe and HgCdTe layers of excellent crystalline quality. The electrical quality of these layers is not, however, as good as that obtained with well established Te sources such as DIPTe. This is probably due to residual contaminants in this newly developed chemical.

CONCLUSIONS

This paper has reviewed the significant progress which has been made in the alloy growth of HgCdTe by Organometallic Vapor Phase Epitaxy during the last two years. Progress has been made in the areas of compositional uniformity, annealing, extrinsic n- and p-type doping, and low temperature growth. Commercial exploitation of OMVPE grown material can now be considered for the first time. Significant issues, on which much further work needs to be done, are the control of Te precipitates, the measurement and improvement of lifetime, and the growth of hillock-free layers of high quality HgCdTe on GaAs substrates. Selective epitaxy, growth on silicon substrates, and surface passivation of OMVPE grown material are additional research issues for this important material.

ACKNOWLEDGEMENT

I would like to thank P. Magilligan for manuscript preparation. Many of the results reported here are the work of N.R. Taskar, K.K. Parat, Dr. H. Ehsani and Prof. I.B. Bhat at Rensselaer Polytechnic Institute, combined with the technical support of J. Barthel. Their efforts are also acknowledged here. I am grateful to C.J. Johnson and S. McDevitt of II-VI, Inc. for kindly providing CdTe and CdTeSe substrate materials, and to Dr. G. Miller of the American Cyanamid Co. for making the methylallyltelluride available to us. This work was sponsored by the Defense Advanced Research Projects Agency (Contract No.: N-00014-85-K-1051) administered through the Office of Naval Research, Arlington, VA and through a grant from the Raytheon Corp.. This support is hereby acknowledged.

REFERENCES

1. S.J.C. Irvine and J.B. Mullin, *J. Cryst. Growth*, 55, 107 (1981).
2. W.E. Hoke, P.J. Lemonias and R. Traczewski, *Appl. Phys. Lett.*, 45, 1092 (1984).
3. J.L. Schmit, *J. Vac. Sci. Technol.*, A3, 89 (1985).
4. S.J.C. Irvine, J. Tunicliffe and J.B. Mullin, *J. Cryst. Growth*, 65, 479 (1983).
5. W.E. Hoke and R. Traczewski, *J. Appl. Phys.*, 54, 5087 (1983).
6. S.K. Ghandhi and I. Bhat, *Appl. Phys. Lett.*, 44, 779 (1984).
7. P.M. Raccach, J.W. Garland, Z. Zhang, V. Lee, S. Ugur, S. Mioc, S.K. Ghandhi and I. Bhat, *J. Appl. Phys.*, 57, 2014 (1985).
8. I.B. Bhat and S.K. Ghandhi, *J. Cryst. Growth*, 75, 241 (1986).
9. J. Tunicliffe, S.J.C. Irvine, O.D. Dosser and J.B. Mullin, *J. Cryst. Growth*, 68, 245 (1984).

10. M.J. Bevan and K.T. Woodhouse, *J. Cryst. Growth*, 68, 254 (1984).
11. D.D. Edwall, E.R. Gertner and L.O. Bubulac, *J. Cryst. Growth*, 86, 240 (1988).
12. I.B. Bhat, H. Fardi, S.K. Ghandhi and C.J. Johnson, *J. Vac. Sci. Tech.*, A6(4), 2800 (1988).
13. S.K. Ghandhi, H. Fardi and I.B. Bhat, *Appl. Phys. Lett.*, 52, 392 (1988).
14. W. Scott, E.L. Stelzer and R.J. Hager, *J. Appl. Phys.*, 47, 1408 (1976).
15. M.C. Chen, *Appl. Phys. Lett.*, 51, 1836 (1987).
16. M.J. Hyliands, J. Thompson, M.J. Bevan, K.T. Woodhouse and V. Vincent, *J. Vac. Sci. Technol.*, A4, 27 (1986).
17. Y. Nemirovsky, L. Burstein and I. Kidron, *J. Appl. Phys.*, 58, 366 (1985).
18. K.K. Parat, N.R. Taskar, I.B. Bhat, S.K. Ghandhi, *J. Cryst. Growth* (submitted).
19. H.R. Vydyanath and C.H. Hiner, *J. Appl. Phys.*, 65, 3080 (1989).
20. H.F. Schaaake, J.H. Tregilgas, J.D. Beck, M.A. Kinch, and B.E. Gnade, *J. Vac. Sci. Tech.*, 3A, 143 (1985).
21. H.R. Vydyanath, J.A. Ellsworth and C.M. Devaney, *J. Electron. Mater.*, 16, 13 (1987).
22. J.S. Whiteley, P. Koppel, V.L. Conger and K.E. Owens, *J. Vac. Sci. Technol.*, A6(4), 2804 (1988).
23. P. Capper, *J. Cryst. Growth*, 57, 280 (1982).
24. S.K. Ghandhi, N.R. Taskar, K.K. Parat, D. Terry, H. Ehsani and I.B. Bhat, *Appl. Phys. Lett.*, 43, 1641 (1988).
25. N.R. Taskar, I.B. Bhat, K.K. Parat, D. Terry, H. Ehsani and S.K. Ghandhi, *J. Vac. Sci. Technol.*, A7, 281 (1989).
26. Courtesy of G. Scilla, IBM, T.J. Watson Research Center, Yorktown Heights, NY.
27. P. Capper, J.J.G. Gosney, C.L. Jones, I. Kenworthy and J.A. Roberts, *J. Cryst. Growth*, 71, 57 (1985).
28. L.S. Lichtmann, J.D. Parsons and E.H. Cirlin, *J. Cryst. Growth*, 86, 217 (1988).
29. D.W. Kisker, M.L. Steigerwald, T.-Y. Kometani and K.S. Jeffers, *Appl. Phys. Lett.*, 50, 1681 (1987).
30. W.E. Hoke and P.J. Lemonias, *Appl. Phys. Lett.*, 46, 398 (1985).
31. W.E. Hoke and P.J. Lemonias, *Appl. Phys. Lett.*, 48, 1669 (1986).
32. R. Korenstein, W.E. Hoke, P.J. Lemonias, K.T. Higa and D.C. Harris, *J. Appl. Phys.*, 62, 4929 (1987).
33. J.D. Parsons and L.S. Lichtmann, *J. Cryst. Growth*, 86, 222 (1988).
34. S.K. Ghandhi, I.B. Bhat, H. Ehsani, D. Nucciarone and G. Miller, *Appl. Phys. Lett.*, 55, 137 (1989).

VAPOUR PRESSURE MEASUREMENTS ON ORGANOTELLURIUM PRECURSORS FOR MOVPE

J.E. HAILS, S.J.C. IRVINE AND J.B. MULLIN

Royal Signals & Radar Establishment, St Andrews Road, Malvern, Worcs, WR14 3PS, UK

ABSTRACT

Before an organometallic compound can be used as an MOVPE precursor, certain basic properties need to be known and one of the most important of these is vapour pressure. A technique for the measurement of vapour pressures using an MOVPE system designed for precursor assessment is described. Results on the assessment of di-*iso*-propyl-telluride, di-*n*-propyl-telluride, di-allyl-telluride, methyl-allyl-telluride and di-*t*-butyl-telluride are presented.

INTRODUCTION

A well accepted objective for improved material quality in the MOVPE growth of the infra-red detector material (Hg,Cd)Te is deposition at lower temperatures. This will lead to reduction and control of the equilibrium mercury vacancy concentration, allowing greater control of the electrical properties. Lowering the growth temperature would also reduce the interdiffusion between substrates and epitaxial layers, thus enabling more complex structures to be grown. There are two ways in which the growth temperature can be lowered, both of which will require the use of tellurium precursors other than the commonly available $\text{Pr}^{\text{I}}_2\text{Te}$ and Et_2Te . Firstly by the use of precursors which are thermally less stable than those currently limited to 410°C by Et_2Te or 350°C by $\text{Pr}^{\text{I}}_2\text{Te}$, this essentially means a less stable tellurium precursor. Secondly photolytic growth can also provide a way of growing (Hg,Cd)Te at lower temperatures[1].

Before a new organometallic compound can sensibly be used as an MOVPE precursor, certain basic chemical and physical properties need to be known about it and one of the most important of these is vapour pressure in the range of temperature typically used for bubblers, 0–30°C. Ideally the volatility should be above 1 Torr at 20°C and the precursor be thermally stable at these temperatures. Several tellurium precursors have been tried recently, but vapour pressures recorded in the literature are limited to single temperature measurements (Table 1, reference 2). Even the commonly used $\text{Pr}^{\text{I}}_2\text{Te}$ is only recorded as 5.6 Torr at 30°C [3,4]. In order to remedy this situation, vapour pressure measurements over the range of temperatures 0–30°C on a number of possible tellurium precursors have been measured and are presented here.

EXPERIMENTAL

All the vapour pressure measurements which are discussed here have been carried out using an MOVPE system specifically designed to investigate organotellurium compounds for suitability as MOVPE precursors[2]. The section of the system used in measuring vapour pressures, shown schematically in Fig. 1, is located between the gas handling section and the MOVPE reactor. The pipework shown in the diagram was held at 40°C throughout.

Prior to collection of a sample for vapour pressure measurement, the reactor and the section in Fig. 1 up to valves A and B were evacuated to 9×10^{-7} Torr at the Penning gauge on the pumping system and checked for leaks using helium and a mass spectrometer. The pressure transducer, an MKS Baratron, was zeroed at this point. In order to obtain a background reading, valve C was closed and the change in pressure recorded. This had to be below 0.012 Torr over 1000 seconds before the experiment proceeded further.

A sample of the organometallic compound under investigation was collected by passing palladium diffused hydrogen through the required bubbler and then through the vapour pressure cell (valve A closed, valves B and C open) held at liquid nitrogen temperature to condense out the precursor. When sufficient compound had been collected, the gas flow was stopped, valves A and B closed and the reactor section of the system evacuated, still with the silica cell in liquid nitrogen. After about 5 minutes the cell was isolated and allowed to warm up. From this point onwards the sample was kept dark to avoid photoinduced decomposition. The sample

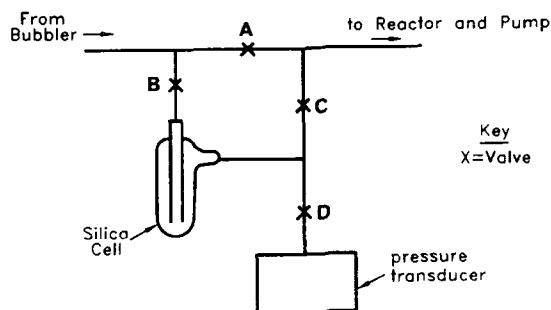


Fig. 1 Schematic illustration of apparatus used for vapour pressure measurements.

was "conditioned" by 3-4 cycles of pumping for 10 seconds (valve C open) and around 1 minute recovery while the cell was held at 0°C. For each individual measurement valve C to the pump was opened for 5 seconds and the recovery of the pressure recorded over a period of 1000 seconds. The background was subtracted to ideally give curves as in Fig. 2. The vapour pressure was read off the flat portion of the plot. The background subtraction was particularly important for less volatile compounds such as $\text{Pr}^{\text{II}}_2\text{Te}$. This method of pumping on the sample for 5 seconds and monitoring the recovery of the pressure is similar to that described in reference 5, but differs in that a sample is removed from the bubbler in our experiments. This has the advantage that any involatile decomposition products are left behind in the bubbler when removing a sample and any volatile products are removed during "conditioning". The vapour pressure equations were calculated from a series of pressure measurements at different temperatures working from 0 to 30°C and back down to 0°C again.

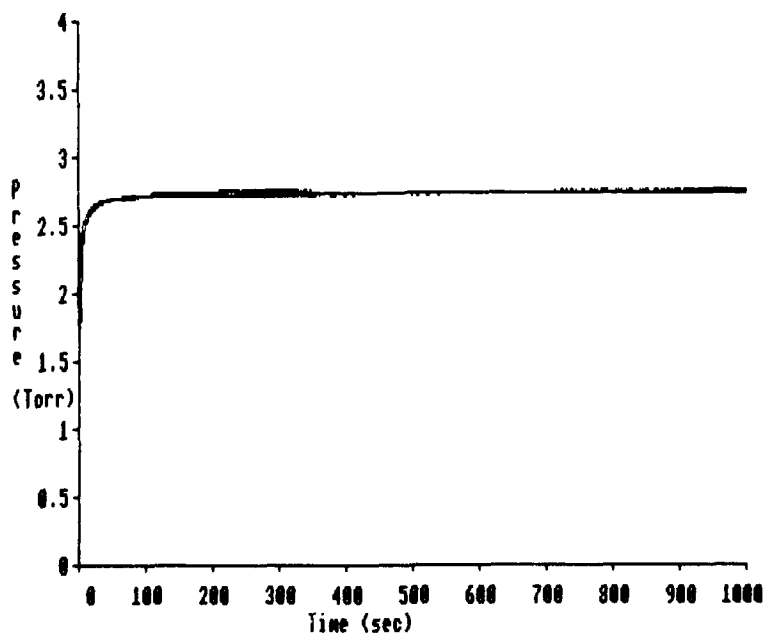


Fig. 2 Three pressure versus time curves at 21°C for PrI_2Te .

Measurements at 0°C and at a temperature around 20°C were repeated several times to check for consistency and possible decomposition. The $(\text{allyl})_2\text{Te}$ and Bu_2Te were obtained from St. Andrews University, Pr^i_2Te from Epichem Ltd, the Pr^n_2Te from Alfa Products and the Me-allyl-Te from American Cyanamid Company.

RESULTS AND DISCUSSION

Fig. 2 shows three pressure versus time curves for Pr^i_2Te obtained at 21°C and illustrates its reproducibility. A similar series was obtained at 0°C. The Arrhenius plot of $\log P(\text{Torr})$ against reciprocal temperature is illustrated in Fig. 3. The 25 points lie close to the least squares fit line giving confidence in the reliability of the technique. The only published data on the vapour pressure of Pr^i_2Te is 5.6 Torr at 30°C [3,4]. The comparable value obtained from the equation here is 4.65 Torr at 30°C.

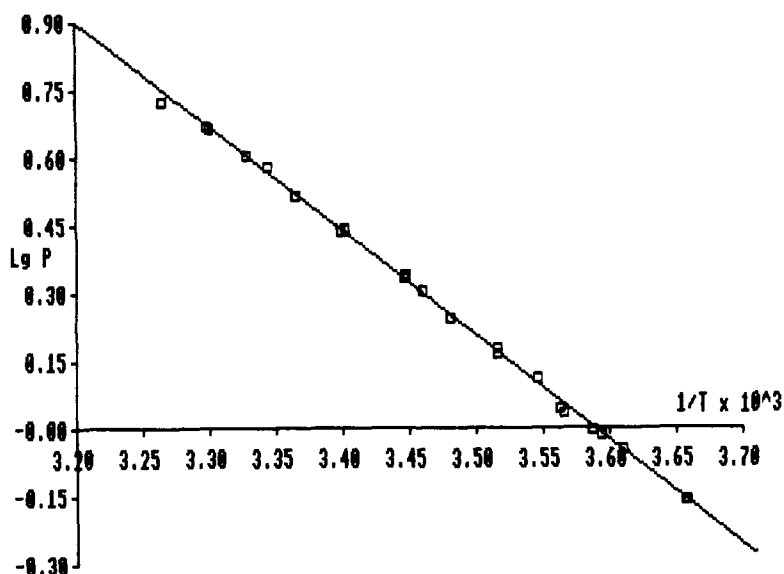


Fig. 3 Arrhenius plot for Pr^i_2Te . Vapour pressure is given by $\text{Lg } P(\text{Torr}) = 8.288 - 2309/T$.

Pr^n_2Te is much less volatile than Pr^i_2Te , but the pressure measurements were very consistent. The Arrhenius plot is shown in Fig. 4. The published vapour pressure point for Pr^n_2Te [4] is 2.0 Torr at 30°C while the extrapolation of our vapour pressure equation is 1.62 Torr at 30°C. At 20°C the vapour pressure is 0.82 Torr which falls below the criteria of 1 Torr at 20°C for suitability as an MOVPE precursor for $(\text{Hg}, \text{Cd})\text{Te}$. It is unlikely that a sufficiently high growth rate could be achieved with Pr^n_2Te .

Methyl-allyl telluride has recently been used as an MOVPE precursor [6,7]. It, too, gave reproducible pressure versus time plots of the type illustrated in Fig. 2. Its Arrhenius plot is reproduced in Fig. 5. On returning to 0°C, the points obtained were close to, but not exactly the same as, those obtained at the start of the series of measurements, probably indicating slight decomposition of the sample during measurement. Its vapour pressure at 20°C is 4.48 Torr and at 30°C is 7.92 Torr, making it the most volatile of the precursors discussed here. The vapour pressure equation given in the Cyanamid literature is $\text{Lg } P = 7.718 - [2028/T]$ which corresponds to 6.3 Torr at 20°C and 10.6 Torr at 30°C. These values are somewhat higher than those presented here. Gandhi et al [6] report that HgTe can be grown using liquid Hg and methyl-allyl telluride in the range 250–320°C and this together with its volatility makes it a tellurium compound worthy of further investigation as an MOVPE precursor.

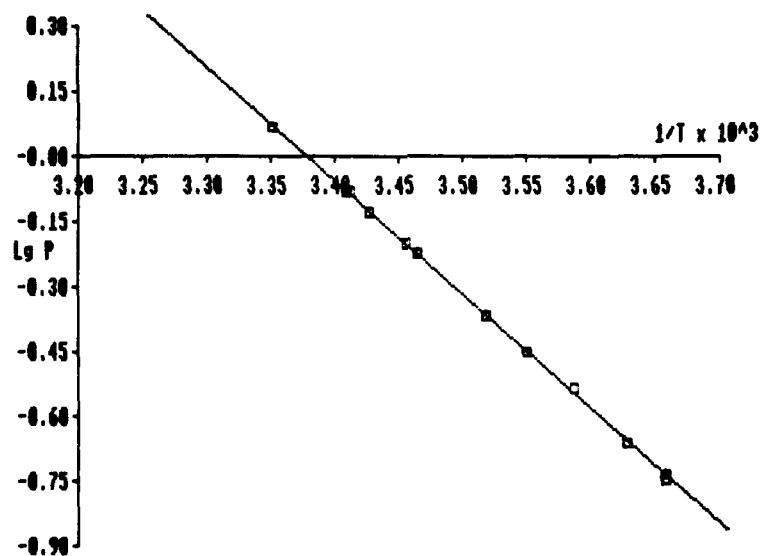


Fig. 4 Arrhenius plot for $\text{Pr}^{\text{III}}\text{Te}$. Vapour pressure is given by $\text{Lg}P(\text{Torr}) = 8.857 - 2620/T$.

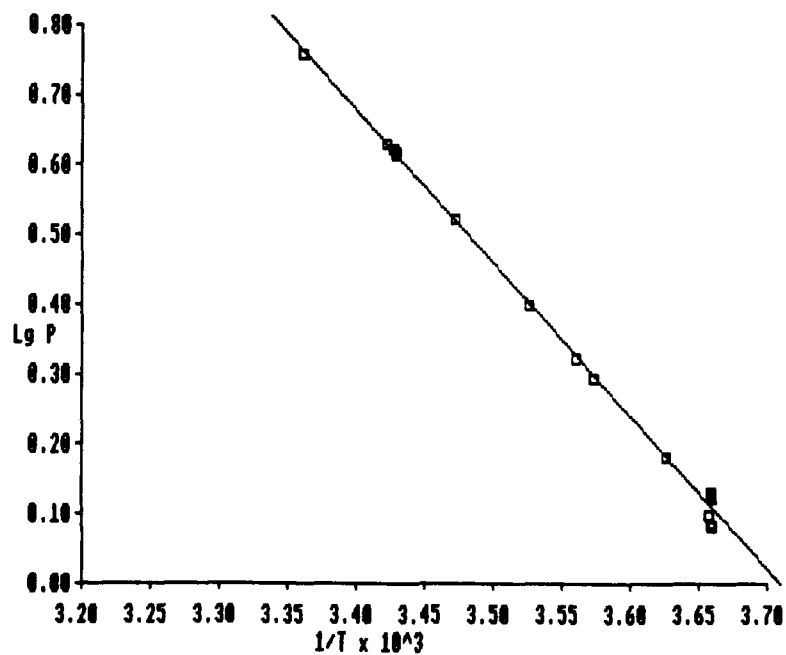


Fig. 5 Arrhenius plot for Me-allyltelluride. Vapour pressure given by $\text{Lg}P(\text{Torr}) = 8.146 - 2196/T$.

Attempts at establishing the vapour pressure equation of $(\text{allyl})_2\text{Te}$ did not prove so successful. Repeated pressure versus time plots were not reproducible as illustrated in Fig. 6,

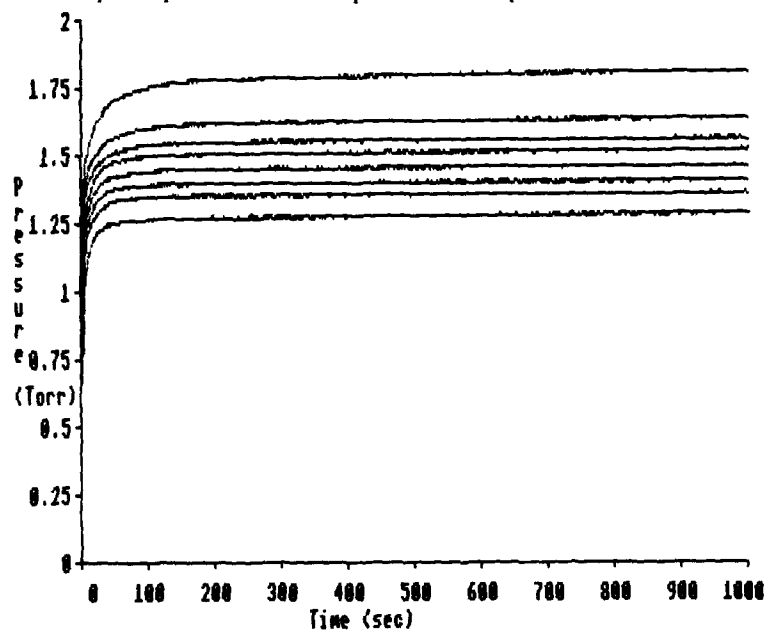


Fig. 6 Pressure versus time curves at 19°C for diallyltelluride.

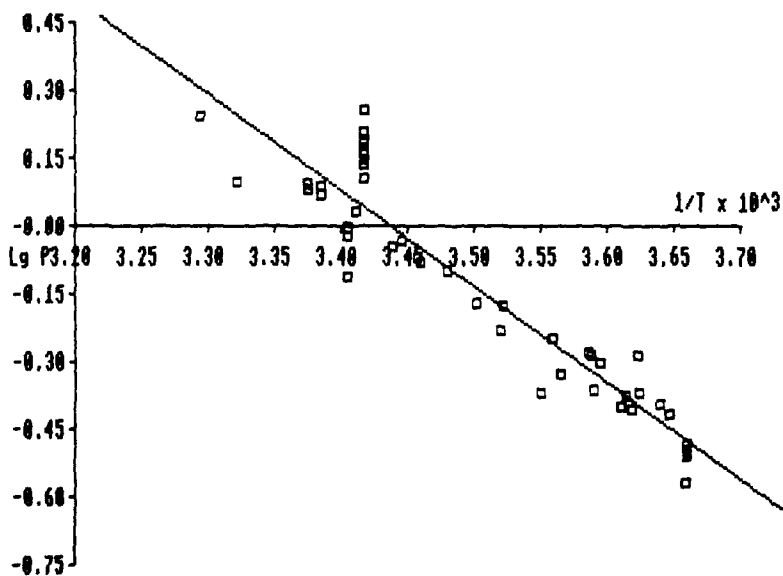


Fig. 7 $\text{Lg}P$ versus $1/T$ plot for diallyltelluride. Equation of line is $\text{Lg}P(\text{Torr})=7.308-2125/T$.

which shows plots obtained at 19°C. Successive plots always gave a lower pressure than those obtained previously. In addition, the plots were not flat, the pressure always slowly rising. At the end of the series of measurements the $(\text{allyl})_2\text{Te}$ was removed leaving the inside of the silica cell with a black coating, presumably of tellurium, where it had been in contact with $(\text{allyl})_2\text{Te}$. Not surprisingly, this behaviour did not give a good straight line Arrhenius plot (Fig. 7). The conclusion from these observations is that the $(\text{allyl})_2\text{Te}$ is thermally unstable in the range 0–30°C and was slowly decomposing while measurements were being made. The decomposition is probably of the form:



The volatile product is responsible for the slow rise in the pressure versus time plots, but would be removed during the next 5 second pumping cycle. From initial Gas Chromatograph Mass Spectrometry work, it would appear that this volatile product is 1,5-hexadiene, boiling point 59°C. The involatile product, tellurium or possibly diallylditelluride, would not be removed from the cell during the measurements and its concentration would steadily increase. Following Raoult's law this build up of an involatile product would lead to a progressive lowering of the vapour pressure at a given temperature. This is what is observed. Given this thermal instability and its involatility $(\text{allyl})_2\text{Te}$ is not an improvement on existing precursors.

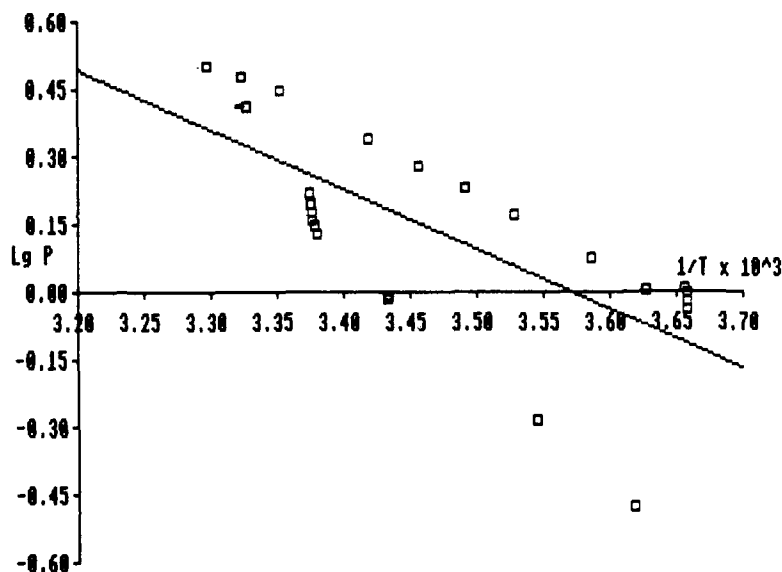


Fig. 8 LgP versus $1/T$ plot for Bu^t_2Te . Equation of line is $\text{LgP}(\text{Torr}) = 4.727 - 1323/T$.

Measurements on Bu^t_2Te were even less successful as Fig. 8 illustrates. The vapour pressure measurements were not reproducible for heating and cooling with the latter lying below the former. The line in Fig. 8 is the best least squares fit through the points, but in reality has no practical use. We believe the Bu^t_2Te is decomposing as measurements are made on it, but in contrast to $(\text{allyl})_2\text{Te}$ no deposit of tellurium was observed. Further work remains to be done to explain this behaviour, but Bu^t_2Te is unlikely to prove a suitable MOVPE precursor for alloy growth.

CONCLUSIONS

A method for measuring vapour pressures of organometallics likely to be used as MOVPE precursors has been described. The method also gives information on the stability of the compounds at around room temperature. The vapour pressure equations for $\text{Pr}^{\text{I}}_2\text{Te}$, $\text{Pr}^{\text{II}}_2\text{Te}$ and methylallyltelluride have been determined.

ACKNOWLEDGEMENTS

The authors wish to thank Professor D. Cole-Hamilton and Dr. E. McQueen of St. Andrews University for supply of $(\text{allyl})_2\text{Te}$ and $\text{Bu}^{\text{t}}_2\text{Te}$ and Drs. I. Girling and D Stern of G.E.C., Hirst Laboratories for GCMS work on $(\text{allyl})_2\text{Te}$.

Copyright © HMSO, London 1989

REFERENCES

1. S.J.C. Irvine, J. Giess, J.B. Mullin, G.W. Blackmore and O.D. Dosser. *J. Vac. Sci. Technol.* **B3**(5), 1450, (1985).
2. J.E. Halls, S.J.C. Irvine, J.B. Mullin, D.V. Shenai-Khatkhate and D. Cole-Hamilton, *Mat. Res. Soc. Symp. Proc.* **131**, 75 (1989).
3. J. Thompson, P. Mackett and L.M. Smith, *Materials Letters* **5** (3), 72 (1987).
4. W.E. Hoke and P.J. Lemonias, *Appl. Phys. Lett.* **46** (4), 398, (1985).
5. O. Kayser, H. Heinecke, A. Brauers, H. Lüth and P. Balk, *Chemtronics*, **3**, 90 (1988).
6. S.K. Ghandhi, I.B. Bhat and H. Ehsani, *Appl. Phys. Lett.*, **55**(2), 137 (1989).
7. J.D. Parsons and L.S. Lichtmann, *J. Crystal Growth*, **86**, 222 (1988).

**STRUCTURAL AND ELECTRICAL PROPERTIES OF
HETEROEPITAXIAL HgCdTe/CdZnTe/GaAs/Si**

S.M. JOHNSON, W.L. AHLGREN, M. H. KALISHER, J. B. JAMES, AND W. J. HAMILTON,
JR.
Santa Barbara Research Center, 75 Coromar Dr., Goleta, CA 93117

ABSTRACT

The structural and electrical properties of heteroepitaxial HgCdTe/CdZnTe/GaAs/Si were evaluated using high-resolution x-ray diffraction techniques and Hall-effect measurements as a function of temperature. Significant tilting of the layers was found for both {100} and {111} CdZnTe layers grown on misoriented {100}GaAs/Si substrates, consistent with the interpretation of a low-angle tilt boundary being formed at the interface to relieve the large lattice mismatch between the layers. The GaAs layer is in a state of biaxial tension before and after the growth of the CdZnTe layers. The x-ray FWHM of HgCdTe layers grown by LPE on these substrates was found to be reduced from that of the MOCVD-grown CdZnTe buffer layer due to both an annealing effect during LPE growth and to the increased distance of layer surface from the defective CdZnTe/GaAs interface. Hall-effect mobility for {100}HgCdTe layers was nearly identical to that of layers grown on bulk CdZnTe substrates. High-quality heterojunction infrared detectors have been fabricated using these materials.

INTRODUCTION

HgCdTe grown by liquid-phase epitaxy (LPE) on lattice-matched single-crystal CdZnTe substrates is currently the best-established technology for the fabrication of second-generation infrared focal-plane arrays [1,2]. Although this technology currently uses bulk CdZnTe substrates with areas as large as 20 cm², there is strong interest in substituting a Si-based alternative substrate for the bulk substrate for improvements in size, strength, cost, and reliability of hybrid focal-plane arrays and for the development of advanced monolithic arrays. The alternative substrate employed in this work is heteroepitaxial CdZnTe/GaAs/Si grown by metalorganic chemical vapor deposition (MOCVD).

Epitaxial growth of CdTe on GaAs/Si composite wafers has been demonstrated previously using congruent vacuum evaporation from a CdTe source [3-6] and using MOCVD for the growth of CdTe [7-9] and the alloy CdZnTe [10,11]. HgCdTe was then grown on these substrates using close-spaced vapor-phase epitaxy [3-6] and MOCVD [8] for undoped material and using LPE [12] and MOCVD [9] for growth of doped HgCdTe. The motivation for this work is to evaluate the structural properties of Cd_{1-y}Zn_yTe/GaAs/Si (nominal y=0.04) grown by conventional pyrolytic MOCVD [11] and the structural and electrical properties of controllably doped HgCdTe grown by LPE on these substrates.

X-RAY ANALYSIS OF GaAs/Si AND CdZnTe/GaAs/Si

X-ray rocking curve measurements were made utilizing a novel, compact Si four-crystal monochromator to produce CuK α_1 x-rays. Lattice tilt and strain measurements were made using a high-resolution diffractometer that incorporates a Ge four-crystal monochromator and has an optically encoded angular readout of the diffractometer axis for precise angular measurements [13]. Layer tilt was determined from symmetric x-ray reflections by measuring the peak separation between the substrate and the layer twice for the same reflection but using a different geometry where the second measurement has a reversed pathway for the incident beam [14]; the incident beam direction is always normal to the tilt axis of the diffracting planes so that the true tilt angle is measured. The perpendicular and parallel strain in the layer ($\Delta a_1/a_s$) is determined from symmetric and asymmetric x-ray reflections of the substrate and layer by a procedure described in detail elsewhere [15].

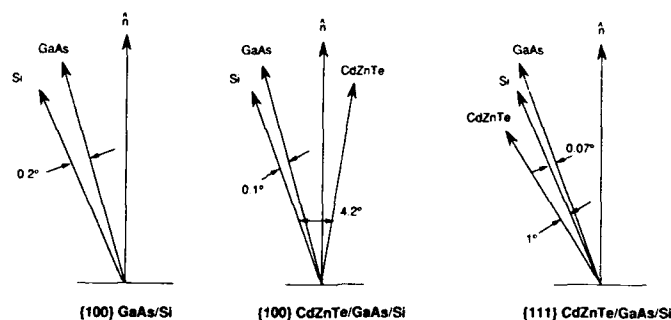


Fig. 1. Schematic showing layer tilts relative to Si (100) which is tilted 3-4° off normal toward the nearest $\langle 111 \rangle$.

The starting substrates were GaAs/Si wafers, which consisted of a GaAs layer 2.5 μm thick grown on (100)Si tilted about a $\langle 011 \rangle$ tilt axis 3-4° toward the nearest $\langle 111 \rangle$; typical (400) rocking-curve full-width at half-maximum (FWHM) values for these GaAs/Si substrates are 150-200 arc-sec. Either (100)- or (111)-oriented CdZnTe layers could be obtained in the MOCVD growth depending on the growth conditions [10,11]. For (100) heteroepitaxy, the layer $\langle 011 \rangle$ is parallel to the substrate $\langle 011 \rangle$ and is the tilt axis. For (111)CdZnTe/(100)GaAs/Si the layer $\langle 112 \rangle$ is parallel to the substrate $\langle 011 \rangle$; these directions were found to be coincident with the tilt axes of the layer and substrate, respectively.

Figures 1a, b, c show a schematic representation of the relative layer tilts for multilayer structures of (100)GaAs/Si, (100)CdZnTe/(100)GaAs/Si, and (111)CdZnTe/(100)GaAs/Si, respectively, where the tilt angles are measured with respect to the Si (400). Figure 1a shows that the thin GaAs layer is tilted back toward the surface normal by 0.2° in the starting substrate; subsequent growth of a (100)CdZnTe layer decreases this tilt to about 0.1°, while growth of a (111)CdZnTe layer decreases this to about 0.07°. Figure 1b shows that the (100)CdZnTe layer is substantially tilted, by 4.2°, from the Si back toward the substrate surface normal, while Figure 1c shows that the (111)CdZnTe layer is tilted about 1° from the Si farther away from the substrate surface normal. Large layer tilts are consistent with previous observations for CdZnTe layers grown on bulk GaAs substrates and are attributed to the interaction of closely spaced misfit dislocations that arrange to form a tilt boundary [16]. The smaller tilt of the (111) layer may be related to the fact that the lattice mismatch along the coincident $\langle 112 \rangle / \langle 011 \rangle$ tilt axis for the layer and substrate is small ($\approx 0.7\%$) [17], so that fewer dislocations are needed to make up the mismatch at this interface.

Table I summarizes the tilt measurements and the perpendicular and parallel strain measured with respect to the Si substrate for the layers discussed above. For (100)GaAs and CdZnTe layers, the symmetric (400) and asymmetric (511) reflections were used for strain analysis. For the (111)CdZnTe layer the lattice constant was measured using the Bond technique from symmetric (333) and asymmetric (513) reflections and then used to calculate the strain. Table I shows that the as-grown GaAs/Si substrate is

Table I. Summary of heteroepitaxial layer tilt and strain measurements.

Layer/Substrate	GaAs Tilt (deg)	GaAs $\Delta a_{\text{perp}}/a_s$ ($\times 10^{-2}$)	GaAs $\Delta a_{\text{para}}/a_s$ ($\times 10^{-2}$)	CdTe Tilt (deg)	CdTe $\Delta a_{\text{perp}}/a_s$ ($\times 10^{-2}$)	CdTe $\Delta a_{\text{para}}/a_s$ ($\times 10^{-2}$)	a_{perp} (Å)
(100)GaAs/Si	-0.213	3.962	4.202	-	-	-	5.6461
(100)CdZnTe/(100)3°GaAs/Si	-0.121	3.596	4.347	-4.166	19.289	19.288	6.4785
(111)CdZnTe/(100)3°GaAs/Si	-0.066	3.957	4.244	0.968	19.307	19.356	6.4795

Table II. Summary of twin density measurements.

Layer/Substrate	X-ray {333} FWHM (arc-sec)	Relative Twin Volume Density
{111}CdZnTe/(100)GaAs	256	0.96
{111}CdZnTe/{111}2°GaAs	205	0.86
{111}CdZnTe/{100}3°GaAs/Si	230	0.12
{111}HgCdTe/CdZnTe/{100}3°GaAs/Si	119	0.0

tetragonally distorted and in a state of biaxial tension ($\Delta a_{para}/a_s > \Delta a_{perp}/a_s$). The perpendicular lattice constant of the GaAs layer is 5.646Å, which is in excellent agreement with measurements reported for 2µm thick layers of GaAs/Si grown by MBE [18]. Subsequent growth of a {100}CdZnTe layer causes further tetragonal distortion of the GaAs layer while growth of a {111}CdZnTe layer leaves the GaAs in essentially the same state of strain.

Table I shows that there is no tetragonal distortion in the {100} CdZnTe layer and that the {111}CdZnTe layer has only a very slight distortion. These layers are thus virtually incoherent with the substrate, and the lattice mismatch is accommodated by misfit dislocations at the interface, consistent with the interpretation of a tilt boundary at this interface. This interpretation is also consistent with a recent high-resolution TEM study of this same {100} multilayer structure [19]. Table I also shows that the lattice constant of both CdZnTe layers is slightly less than the bulk CdTe lattice constant of 6.481Å, and indicates their alloy compositions are $y < 0.01$, rather than the nominal $y = 0.04$.

A disadvantage of using {111} is that VPE-grown layers of CdTe and CdZnTe are usually heavily twinned, with the {111} twin planes lying parallel to the growth interface. This type of twinning can be detected by using asymmetric {422} x-ray reflections; an untwinned crystal will have three such reflections (three-fold symmetry) accessible from a {111} surface while a twinned crystal will have six such reflections (six-fold symmetry) [20]. As a relative measure of twin "density" we have taken the ratio of {422} x-ray rocking curve intensities measured in the direction of a {422} and rotated 180° from that position; this twin volume "density ratio" is thus zero in an untwinned crystal and unity for a layer having 50% of its volume rotated 180° about the <111> surface normal.

Table II summarizes these measurements made on the {111}CdZnTe layer described above together with {111} layers grown on bulk {111}GaAs tilted 2° toward the nearest <123> and {100}GaAs all in the same MOCVD growth run [11]. Table II shows that the {333} FWHM of each of these layers is similar (200-250 arc-sec, independent of the GaAs crystal quality (bulk GaAs is 15-20 arc-sec versus 150-200 arc-sec for GaAs/Si)). Table II also shows that the twin volume density in the CdZnTe grown on GaAs/Si is very low in comparison with that of the layers grown on the bulk substrates. These results illustrate that the GaAs/Si substrate misorientation can help to suppress twinning under certain growth conditions. Table II also shows that an LPE HgCdTe layer grown on a sister {111}CdZnTe/{100}GaAs/Si substrate from this same MOCVD run was untwinned. This implies that the twins in the CdZnTe layer were not close to the layer surface where they would have propagated into the LPE layer, as we observed when heavily twinned substrates were used for LPE growth.

LPE HgCdTe ON CdZnTe/GaAs/Si

To evaluate the quality of the CdZnTe/GaAs/Si substrates, In-doped [21], n-type, $Hg_{0.72}Cd_{0.28}Te$ layers were grown simultaneously on CdZnTe/GaAs/Si and {111}A CdZnTe bulk substrates using "infinite-melt" vertical LPE [1,2] from a Hg-rich solution. Figures 2a,b show optical micrographs of the surface morphology of a {100}CdZnTe/{100}GaAs/Si substrate and an LPE-grown HgCdTe layer grown on a similar substrate, respectively. Figure 2a shows a surface facet on the {100}CdZnTe surface that is found to be elongated in the

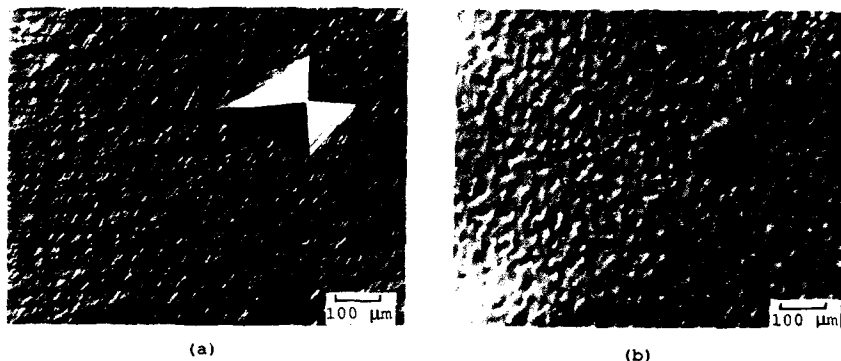


Fig. 2. Optical micrographs showing surface morphology of
a) $\{100\}$ CdZnTe/GaAs/Si substrate and b) LPE-grown HgCdTe on a
similar substrate; (Si $\{100\}$ tilted towards LHS of micrograph).

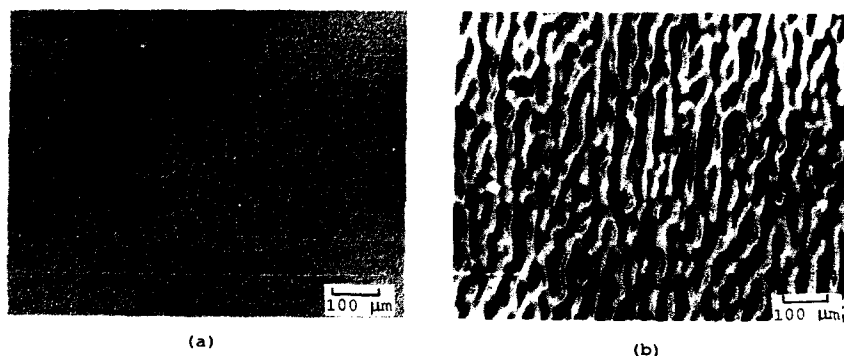


Fig. 3. Optical micrographs showing surface morphology of
a) $\{111\}$ CdZnTe/GaAs/Si substrate and b) LPE-grown HgCdTe on a
similar substrate; (Si $\{100\}$ tilted towards LHS of micrograph).

direction of the Si substrate tilt. After an LPE HgCdTe layer is grown, the tops of such facets are flattened; however, their height above the surface is still approximately 5 μm . These defects on the $\{100\}$ surface have been directly correlated with a local increase in detector leakage current [12], and growth conditions must be found to eliminate them.

Figures 3a,b show optical micrographs of the surface morphology of a $\{111\}$ CdZnTe/ $\{100\}$ GaAs/Si substrate and an LPE-grown HgCdTe layer grown on a similar substrate, respectively. Figure 3a shows that the $\{111\}$ CdZnTe surface morphology is smooth, while the LPE-grown HgCdTe morphology is wavy, which is characteristic of growth on misoriented $\{111\}$ CdZnTe substrates. Although this HgCdTe surface is not specular, it does not have the growth facets that are typical of the $\{100\}$ surface (Figure 2b); it may be better for fabricating detectors.

We have found that the x-ray rocking-curve width of the LPE-grown HgCdTe layer is better than that of the CdZnTe/GaAs/Si substrate. This has also been recently reported by other workers for an MOCVD-grown HgCdTe/CdTe/GaAs structure [22]. Figure 4 shows a plot of the FWHM of the HgCdTe layer versus that of the CdZnTe/GaAs/Si substrate obtained using symmetric x-ray reflections. Figure 4 shows that the FWHM of the HgCdTe layer is typically reduced from that of the initial CdZnTe buffer layer. To see if this effect was due to annealing during the LPE growth, a $\{100\}$ CdZnTe/GaAs/Si substrate

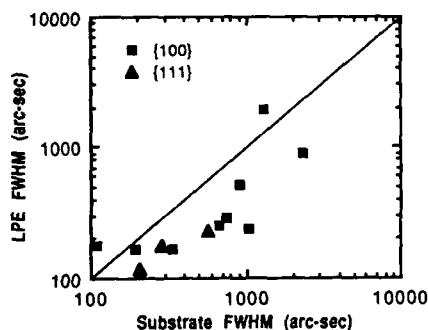


Fig. 4. X-ray rocking curve FWHM of LPE-grown HgCdTe layer versus that of CdZnTe/GaAs/Si substrate.

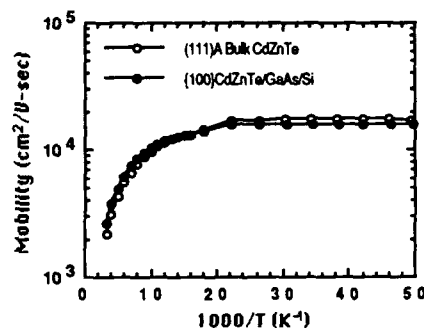


Fig. 5. Hall mobility versus temperature for In-doped $\text{Hg}_{0.72}\text{Cd}_{0.28}\text{Te}$ layers grown simultaneously by LPE on bulk CdZnTe and (100)CdZnTe/GaAs/Si.

was annealed in the LPE melt without exposing the surface, to simulate the growth conditions without growing the HgCdTe layer. The as-grown substrate {400} FWHM was 390 arc-sec, and following anneal it reduced to 265 arc-sec. Additionally, high-resolution TEM studies have shown that the dislocation density in the CdZnTe is reduced significantly within about 2 μm of the CdZnTe/GaAs interface due to dislocation annihilation by intersection with others as the growth continues [19]. An improvement in rocking-curve width is then seen as the distance from this interface increases, relative to a fixed sampling depth of the x-rays, by growing an additional layer of HgCdTe.

Figure 5 shows that the Hall mobility versus temperature (field = 10 kG), measured after a Hg-overpressure anneal, is nearly identical for In-doped $\text{Hg}_{0.72}\text{Cd}_{0.28}\text{Te}$ layers grown simultaneously by LPE on (100)CdZnTe/GaAs/Si and (111)A CdZnTe bulk substrates. These same results were also obtained for LPE HgCdTe layers grown on (100) CdZnTe bulk substrates. The 77K carrier concentration for these layers is $4 \times 10^{15} \text{ cm}^{-3}$. We have not yet evaluated the electrical properties of recently grown HgCdTe layers on (111)CdZnTe/GaAs/Si.

High-quality p-on-n heterojunction infrared detectors have been fabricated using controllably doped HgCdTe grown by LPE on the (100)CdZnTe/GaAs/Si substrates and used to demonstrate the first 128×128 focal plane array fabricated on these materials [12]. Detectors with a cutoff wavelength of 6.0 μm and a resistance-area product (R_0A_j) average of $6.0 \times 10^4 \text{ ohm-cm}^2$ at 80K for 16,189 detectors in the array were achieved. For operating temperatures above $\sim 120\text{K}$ these were comparable in performance to detectors co-fabricated on standard lattice-matched bulk CdZnTe substrates [12].

CONCLUSIONS

The structural and electrical properties of heteroepitaxial HgCdTe/CdZnTe/GaAs/Si were evaluated using high-resolution x-ray diffraction techniques and Hall-effect measurements as a function of temperature. Significant tilting of the layers was found for both (100) and (111) CdZnTe layers grown on misoriented (100)GaAs/Si substrates, consistent with the interpretation of a low-angle tilt boundary being formed at the interface to relieve the large lattice mismatch between the layers. The GaAs layer is in a state of biaxial tension before and after the growth of the CdZnTe layers. The x-ray FWHM of HgCdTe layers grown by LPE on these substrates was found to be reduced from that of the MOCVD-grown CdZnTe buffer layer due to both an annealing effect during LPE growth and to the increased distance of layer surface from the defective CdZnTe/GaAs interface. Hall-effect mobility for (100)HgCdTe layers was nearly identical to that of layers grown on bulk CdZnTe substrates. High-quality heterojunction infrared detectors have been fabricated using these materials.

ACKNOWLEDGMENTS

The authors thank K.T. Miller for his help with the high-resolution x-ray measurements and M.E. Boyd for the Hall-effect measurements and appreciate the critical review of this manuscript by R.P. Ruth.

REFERENCES

1. T. Tung, M.H. Kalisher, A.P. Stevens, and P.E. Herning, in Materials for Infrared Detectors and Sources, edited by R.F.C. Farrow, J.F. Schetzina, and J.T. Cheung (Mater. Res. Soc. Vol 90, Pittsburgh, PA, 1987), p. 321.
2. T. Tung, J. Cryst. Growth **86**, 161 (1988).
3. K. Zanio, R. Bean, K. Hay, R. Fischer, and H. Moroc in Heteroepitaxy on Silicon, edited by J.C.C. Fan and J.M. Poate (Mater. Res. Soc. Vol 67, Pittsburgh, PA, 1986), p. 141.
4. R. Kay, R. Bean, K. Zanio, C. Ito, and D. McIntyre, Appl. Phys. Lett. **51**, 2211 (1987).
5. K.R. Zanio and R.C. Bean, Proc. SPIE **930**, 44 (1988).
6. R. Bean, K. Zanio, and J. Ziegler, J. Vac. Sci. Technol. **A7**(2), 343 (1989).
7. A. Nouhi, G. Radhakrishnan, J. Katz, and K. Koliwad, Appl. Phys. Lett. **52**, 2028 (1988).
8. N.W. Cody, U. Sudarsan, and R. Solanki, J. Appl. Phys **66**, 449 (1989).
9. D.D. Edwall, J. Bajaj, and E.R. Gertner, 1989 U.S. Workshop on Physics and Chemistry of HgCdTe and related II-VI Compounds submitted to J. Vac. Sci. Technol. **A**. (1990).
10. W.L. Ahlgren, S.M. Johnson, E.J. Smith, R.P. Ruth, B.C. Johnston, M.H. Kalisher, C.A. Cockrum, T.W. James, D.L. Arney, C.K. Ziegler, and W. Lick, J. Vac. Sci. Technol. **A7**(2), 331 (1989).
11. W.L. Ahlgren, S.M. Johnson, W.J. Hamilton, A. Szilagy, G.S. Tompa, C.K. Ziegler, and W.J. Lick, these proceedings.
12. S.M. Johnson, M.H. Kalisher, W.L. Ahlgren, J.B. James, and C.A. Cockrum, submitted to Appl. Phys. Lett.
13. K.T. Miller, Hughes Research Laboratories, unpublished.
14. W.J. Bartels and W. Nijman, J. Cryst. Growth **44**, 518 (1978).
15. T. Vreeland, Jr., A. Dommann, C.-J. Tsai, and M.-A. Nicolet, in Thin Films: Stresses and Mechanical Properties, edited by J.C. Bravman, W.D. Nix, D.M. Barnett, and D.A. Smith (Mater. Res. Soc. Vol 130, Pittsburgh, PA 1989) p. 3.
16. S.M. Johnson, W.L. Ahlgren, M.T. Smith, B.C. Johnston, and S. Sen, in Advances in Materials, Processing, and Devices in III-V Compound Semiconductors, edited by D.K. Sadana, L. Eastman, and R. Dupuis (Mater. Res. Soc. Vol. 144, Pittsburgh, PA 1989), p. 121.
17. G. Cohen-Solal, F. Bailly, and M. Barbe, Appl. Phys. Lett. **49**, 1519 (1986).
18. T. Yao, Y. Okada, H. Kawanmi, S. Matsui, A. Imagawa, and K. Ishida, in Heteroepitaxy on Silicon II, edited by J.C.C. Fan, J.M. Phillips, and B.-Y. Tsaur (Mater. Res. Soc. Vol. 91, Pittsburgh, PA 1987), p. 63.
19. H.-J. Kleebe, W.J. Hamilton, W.L. Ahlgren, S.M. Johnson, and M. Ruhle, these proceedings.
20. M. Oron, A. Raizman, H. Shtrikman, and G. Cinader, Appl. Phys. Lett. **52**, 1059 (1988).
21. M.H. Kalisher, J. Cryst. Growth **70**, 365 (1984).
22. A.M. Keir, A. Graham, S.J. Barnett, J. Gless, M.G. Astles, S.J.C. Irvine, Fourth Intl. Conf. on II-VI Compounds, Berlin, Sept. 1989.

Properties of HgTe:ZnTe Strained Layer Superlattices Grown by MOVPE

J.T. Mullins, P.A. Clifton, P.D. Brown, D.O. Hall and A.W. Brinkman.

Applied Physics Group, S.E.A.S. University of Durham, South Road,
Durham DH1 3LE, U.K.

Abstract

HgTe:ZnTe superlattices have been grown by thermal MOVPE at temperatures down to 325°C. At this temperature, interdiffusion is sufficiently low to make superlattice periods as low as 45Å practicable. The results of theoretical calculations of the electronic structure of these materials are also reported. These show that the electronic structure may be significantly different to that found for the HgTe:CdTe system due to the large biaxial compression present in the HgTe well layers.

Introduction

HgTe:ZnTe strained layer superlattices have been proposed as an alternative to $\text{Hg}_{1-x}\text{Cd}_x\text{Te}$ for long wavelength infra-red devices^[1]. In contrast to the more widely studied HgTe:CdTe superlattice system^[2], interdiffusion coefficients are expected to be about an order of magnitude lower. This makes them suitable for growth by thermal Metal Organic Vapour Phase Epitaxy (MOVPE) at currently attainable temperatures. In a previous paper^[3] we reported the development of a process for the growth of HgTe:ZnTe superlattices by thermal MOVPE. In that work, growth was carried out at 395°C using di-methyl zinc (DMZ), di-ethyl telluride (DET), and elemental mercury and some interdiffusion was observed.

Here we report growth at the reduced temperature of 325°C which has been made possible by the substitution of di-isopropyl telluride (DIPT) for DET as the tellurium precursor. Transmission electron (T.E.) microscopy has been used to characterise the resulting structures and provide information on the total thickness and hence period of the superlattices. EDX was used to determine the composition and hence to provide an estimate of the relative well and barrier thicknesses. Infra-red transmission measurements were performed at room temperature and for one superlattice indicated an energy gap of 0.2 eV.

Also reported are the results of some theoretical calculations of the electronic structure of these materials. The HgTe wells may be under considerable biaxial compression due to the 5.2% mismatch between HgTe and ZnTe. This is in contrast to the case of HgTe:CdTe superlattices where the wells are under a small biaxial tension. This change in the sense of the strain can lead to significant differences in the electronic structure of the two systems.

Structure and Interdiffusion

A T.E. micrograph of a HgTe:ZnTe superlattice with a period of $\approx 115\text{\AA}$ grown on {100} GaAs at 395°C using DET is shown in Fig.1(a). Fringe contrast can be observed for approximately 20 periods at the top of the layer. By assuming that the lower portion of

the layer had interdiffused, and from a knowledge of the growth time and superlattice period, it was possible to estimate a value of $\sim 1 \times 10^{-15} \text{ cm}^2 \text{ s}^{-1}$ for the interdiffusion coefficient between HgTe and ZnTe at 395°C ^[3]. This value of the interdiffusion coefficient is one order of magnitude lower than that found for the interdiffusion of CdTe and HgTe during the development of the interdiffused multilayer process^[4] for the growth of $\text{Hg}_{1-x}\text{Cd}_x\text{Te}$ which was determined under essentially similar conditions of temperature, mercury vapour pressure and annealing time. It is also at least two orders of magnitude lower than that expected from the HgTe:ZnTe diffusion couple experiments of Granger and co-workers^[5]. Their work was performed in vacuum while the superlattice growth reported here took place under one atmosphere of hydrogen with a mercury partial pressure of 20 Torr. Mercury vacancies are known to control the interdiffusion and it may be that the lower interdiffusion coefficient found for the superlattice growth is due to the presence of a lower concentration of mercury vacancies.

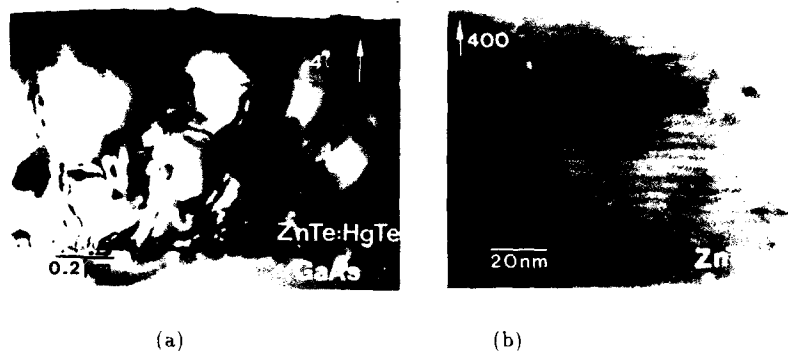


Fig.1. T.E. micrographs of HgTe:ZnTe superlattices grown at (a) 395°C and (b) 325°C

Fig.1(b) shows a T.E. micrograph of part of an 80 period HgTe:ZnTe superlattice grown on {100} GaAs with a ZnTe buffer at 325°C using DIPT. For this sample the period was $\approx 45\text{\AA}$ with approximately equal well and barrier thicknesses. In contrast to growth at 395°C , and despite a growth time 30% longer than for the sample discussed above which was grown at the higher temperature, clear fringe contrast was observed throughout the layer. When the extremely short period is considered this result clearly demonstrates the feasibility of growing HgTe:ZnTe superlattices by thermal MOVPE at this temperature.

Optical Properties

One 40 period HgTe:ZnTe superlattice grown at 395°C with a period of $\approx 200\text{\AA}$ comprising $\approx 70\text{\AA}$ of HgTe and $\approx 130\text{\AA}$ of ZnTe exhibited strong optical absorption at $\sim 6\mu\text{m}$.^[3] In this case consideration of the interdiffusion coefficient discussed in the previous section suggested some interdiffusion would have taken place although even near the substrate/superlattice interface this would not have been complete as the period was greater and fewer periods were grown than for the sample considered previously.

Graphs of the optical absorption coefficient, α , versus photon energy, $h\nu$, and $(\alpha h\nu)^2$ versus $h\nu$ for this sample are shown in Figs. 2(a) and 2(b) respectively. The absorption coefficient has an exponential dependence on photon energy up to values of $\sim 1 \times 10^3 \text{ cm}^{-1}$. This may be fitted to the empirical expression of Urbach^[8]

$$\alpha = \alpha_0 \exp(B(h\nu - \epsilon))$$

where ϵ is a constant. B is the gradient of the logarithmic portion of the absorption curve and in this case is equal to 34 eV^{-1} . For larger values of α up to the maximum of 4×10^3 the dependence is parabolic. Extrapolating this parabolic region to $(\alpha h\nu)^2 = 0$ yields a value of 0.2 eV for the energy gap of the superlattice.

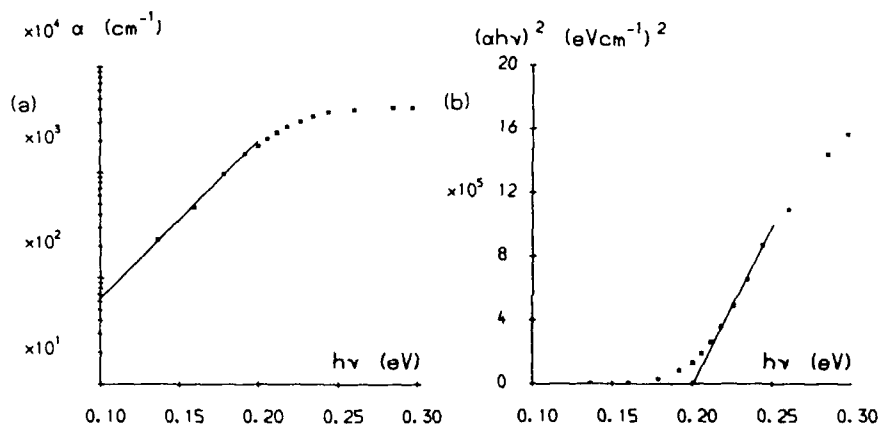


Fig.2 (a) optical absorption coefficient versus $h\nu$ and (b) $(\alpha h\nu)^2$ versus $h\nu$ for a 40 period HgTe:ZnTe superlattice grown at 395°C .

The energy levels in HgTe:ZnTe superlattices were calculated using the Kronig-Penney model as reformulated for superlattices by Hung-Sik Cho et al^[7]. In the calculations the superlattices were assumed to be free standing and fully strained. The strain in the constituent binary layers was calculated from simple elasticity theory. The effect of this strain on the energy levels was incorporated using deformation potentials as given by Wu and McGill^[9] for HgTe and by Gil et al^[9] for ZnTe. Conduction band effective masses of $0.01m_0$ and $0.116m_0$ were used for HgTe and ZnTe respectively while the heavy hole mass was taken to be $0.7m_0$ in both cases. The valence band offset ($E_{v,av}(\text{HgTe}) - E_{v,av}(\text{ZnTe})$) where $E_{v,av}$ is the average energy of the light and heavy Γ_8 bands) was taken to be 250 meV as determined by Hsu et al^[10].

Here we consider a superlattice composed of 130\AA ZnTe barriers and 70\AA HgTe wells as estimated for the superlattice above. The band lineups of the binary constituents are shown in Fig.3(a). Both the Γ_8 valence-like bands and the Γ_6 conduction-like band in the HgTe lie above the ZnTe valence bands. When the HgTe is placed under a biaxial

stress corresponding to the 6.176 Å in-plane lattice constant calculated for the superlattice (Fig.3(b)), the energy gap is increased (made less negative) slightly and the light and heavy Γ_8 bands are split by the uniaxial component of the strain. In this diagram $E_{v,av}$ is represented by the dotted line. This splitting is the most significant effect the strain has on the electronic structure. In contrast to the HgTe:CdTe case, the heavy hole like Γ_8 state moves up in energy while the light hole state moves down. This difference is due to the HgTe wells being under biaxial compression rather than biaxial tension as is the case for HgTe:CdTe superlattices. When the superlattice is formed, quantum confinement moves the Γ_6 band up in energy by 190 meV leading to a conventional positive energy gap between the Γ_6 conduction band and the Γ_8 heavy hole valence band. The superlattice is type II for light holes with the Γ_8 light hole band lying 230 meV below the heavy hole band and so this band is not expected to contribute to the electrical or optical properties.

The above analysis predicts a direct energy gap for the superlattice of 90 meV while experimental value was 200 meV. This discrepancy may be explained by the effects of interface non-ideality and strain relief in the real structure and uncertainty in the input parameters for the theoretical model. In particular this model is very sensitive to the exact value taken for the HgTe electron effective mass. However the essential features of the electronic structure of this system can be seen.

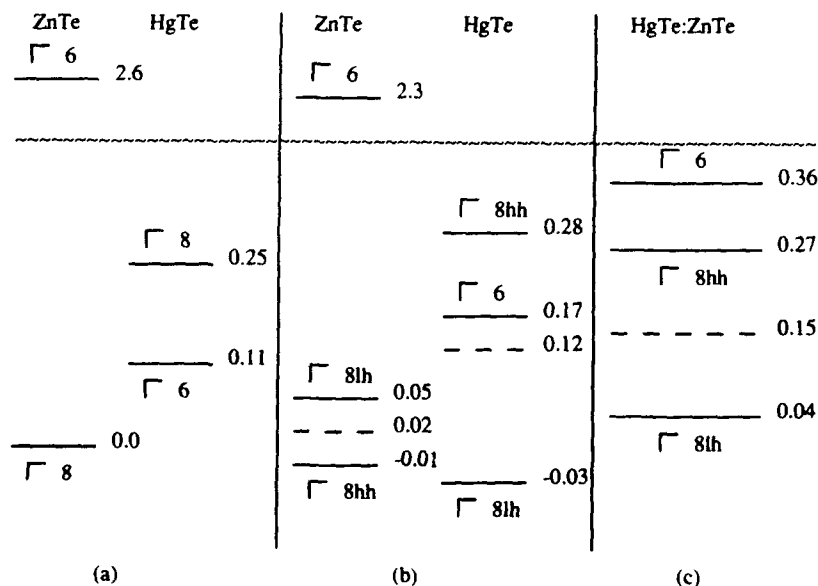


Fig.3. Energy levels in the HgTe:ZnTe system at 300 K. (eV)
(a) Bulk compounds (b) strained bulk compounds (c) superlattice

Conclusions

The growth of HgTe:ZnTe superlattices by thermal MOVPE has been demonstrated. For growth at 325°C interdiffusion does not present a problem as evidenced by the growth of a superlattice with a period of $\approx 45\text{\AA}$. Infra-red absorption measurements have shown strong optical absorption at wavelengths commensurate with the formation of a superlattice rather than a ternary alloy.

The electronic structure of HgTe:ZnTe superlattices has been calculated using a modified Kronig-Penney model. It has been shown that splitting of the Γ_8 bands is the most significant effect of the strain in this system and that in contrast to the HgTe:CdTe superlattice system, the light hole Γ_8 band is moved down in energy and does not contribute to the electrical or optical properties.

REFERENCES

1. J.P. Faurie, S. Sivananthan, X. Chu and P.A. Wijewarnasuriya, Appl. Phys. Letters **48** 785 (1986).
2. J.P. Faurie, IEEE Journal of Quantum Electronics **QE-22** 1656 (1986).
3. P.A. Clifton, J.T. Mullins, P.D. Brown, N. Lovergine, A.W. Brinkman and J. Woods, (proceedings of the 9th International Conference on Crystal Growth, (1989) to be published in J. Crystal Growth)
4. J. Tunncliffe, S.J.C. Irvine, O.D. Dosser and J.B. Mullin, J. Crystal Growth **68**, 245 (1984)
5. R. Granger, C. Pobla, S. Rolland and R. Triboulet, (proceedings of the 4th International Conference on II-VI Compounds (1989), to be published in J. Crystal Growth)
6. F. Urbach, Phys.Rev **92** 1324 (1953).
7. N. Hung-Sik Cho and P.R. Pracnal, Phys. Rev. B **36** 3237 (1987).
8. G.Y. Wu, and T.C. McGill, Appl. Phys. Letters **47** 634 (1985).
9. B. Gil, D.J. Dunstan, J. Calatayud, H. Mathieu and J.P. Faurie, Phys. Rev. B **40** 5522 (1989).
10. C. Hsu, Tran Minh Duc and J.P. Faurie, J. Vac. Sci. Technol. B **5** 1229 (1987).

MBE GROWTH AND CHARACTERIZATION OF SMALL BAND GAP HgTe-HgCdTe SUPERLATTICES.

Y. LANSARI, Z. YANG, S. HWANG, J.W. COOK, Jr, and J.F. SCHETZINA,
Department of Physics, North Carolina State University, Raleigh,
NC 27695-8202.

ABSTRACT

A series of modulation-doped small-band-gap HgTe-Hg_{1-x}Cd_xTe superlattices (SLs) have been grown by photoassisted MBE. N-type or p-type conductivity was obtained in the modulation-doped samples by incorporating either In or As dopant atoms in the barrier layers, respectively. The electrical and optical properties that these new multilayered quantum well structures display will be discussed.

INTRODUCTION

In recent years, important advances in the growth and characterization of undoped HgTe-CdTe SLs have been achieved [1,2,3]. However, the problem of *in-situ* doping of these SLs has only recently been addressed [4]. Since the well layers consist of HgTe, a negative-band-gap semimetallic material, it is possible to engineer a semiconducting structure having a band gap in the long wavelength infrared (LWIR) region of the wavelength spectrum. In fact, by choosing appropriate barrier layer L_b and well layer L_w thicknesses, superlattices can now be prepared reproducibly that exhibit either semiconducting or semimetallic properties.

Here, we report the properties of a series of modulation-doped HgTe-Hg_{1-x}Cd_xTe superlattices grown by photoassisted MBE in which the Hg_{1-x}Cd_xTe barrier layers were doped either p-type or n-type by using In or As as the dopant species, respectively.

EXPERIMENTAL DETAILS

All of the modulation-doped superlattices (SLs) were grown in a Hg-compatible MBE system, designed and built at North Carolina State University that is described in an earlier publication [5]. The modulation-doped SLs were deposited onto high structural quality, chemimechanically polished (100) CdZnTe (4% Zn) substrates. Prior to their loading into the MBE system, the substrates were degreased and etched in a 1:1 HCl and DI water solution to remove the native oxide. The substrates were then preheated at a temperature of 300 °C while in the MBE growth chamber. All of the modulation-doped SLs were grown at 140 °C using photoassisted MBE. In the photoassisted MBE process, the beam-expanded, broad-band output (458-514 nm) from a Spectra-Physics model 2016-05 argon-ion laser was used to uniformly illuminate the substrates during film growth. Power densities of 40 mW/cm² were employed, resulting in negligible substrate heating from the laser beam. The Hg flux, with equivalent beam pressure of $\sim 1.5 \times 10^{-4}$ Torr, was maintained constant throughout each growth. The CdTe barrier layers, therefore, are grown under a Hg flux. Because of this overpressure of Hg, the barrier layers are actually Hg_{1-x}Cd_xTe, where the x-value depends on the growth

conditions. The CdTe and Te fluxes were such that the growth rates obtained for HgCdTe and HgTe were in the range of 1 Å/s and 3 Å/s, respectively.

In the modulation doped samples, In and As were used as the n-type and p-type dopants, respectively. The dopants were incorporated uniformly in the barrier layers (no setback), and the temperatures of the In and As ovens were varied from run to run, resulting in a range of doping levels obtained for the series of SLs. Each of the superlattices consisted of 200 double layers of HgTe-Hg_{1-x}Cd_xTe.

The individual layer thicknesses for each SL were determined by using DEKTAK total thickness measurements, the angular separation of x-ray satellite peaks relative to the main diffraction peak, and the growth rates of HgTe and HgCdTe determined using calibration layers grown under the same conditions. HgTe well layer thicknesses L_z between 23-81 Å and Hg_{1-x}Cd_xTe barrier layer thicknesses L_b from 26-52 Å were thus obtained.

Double-crystal x-ray rocking curve measurements were performed on all the SLs included in this study. The full-width-at-half-maximum (FWHM) of the main (400) diffraction peak was used as a measure of structural quality. FWHM values as low as 28 arcsec (small L_b) and as high as 300 arcsec (large L_b) were measured. Electrical characterization of the SLs consisted of standard van der Pauw Hall measurements over the temperature range between 30-300 K. Optical absorption coefficients for selected SLs were determined by measuring their transmittance and reflectance at room temperature. Details of these experiments are given in an earlier paper [6].

RESULTS AND DISCUSSION

N-type and p-type modulation-doped SLs were successfully grown for a range of single layer thicknesses ($L_b = 26-52$ Å, $L_z = 23-81$ Å) and doping levels (4×10^{14} - 1×10^{17} cm⁻³ at low temperatures). Figure 1 shows Hall data for four In-doped superlattices, respectively. These four SLs were grown under identical conditions, except that the In dopant oven temperature was increased sequentially by 25°C from one growth to the next. The effects of doping are clearly manifested by the Hall effect data. The electron concentration for A66B, prepared using an In oven temperature of 400°C, decreases monotonically with decreasing temperature reaching a value of $\sim 1.0 \times 10^{16}$ cm⁻³ at 30 K. The mobility exceeds 10^5 cm²/V s at temperatures below 80 K. For A67B ($T_{In} = 425^\circ\text{C}$), the carrier concentration decreases with decreasing temperature and then begins to plateau at about 1.5×10^{16} cm⁻³ at temperatures below 50 K. The electron mobility reaches a maximum in excess of 10^5 cm²/V s at 70 K and then decreases at lower temperatures. The maximum in the mobility occurs because the band gap of this SL approaches zero at about this temperature. In the zero gap state, both the electron and hole mobilities become very large because the effective mass of both types of carriers becomes small [7]. At lower temperatures, A67B becomes semimetallic, the carrier effective masses become larger and, thus, the mobility decreases.

This decrease in mobility at low temperatures associated with the negative-band-gap state is even more pronounced in the Hall data for A68A, grown using an In oven temperature of 450°C. Note, also, that the low temperature carrier concentration reaches a

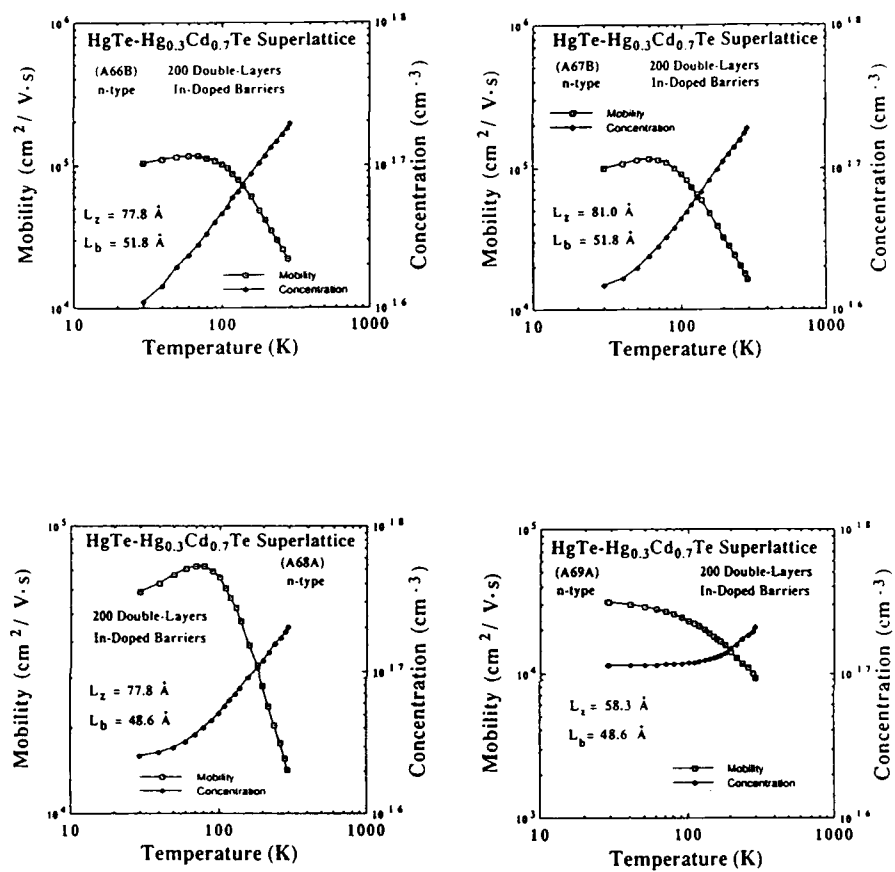


Fig.1. Hall effect data for n-type superlattices A66B, A67B, A68A and A69A.

plateau at about $2.5 \times 10^{16} \text{ cm}^{-3}$. SL A69A ($T_{In} = 475^\circ\text{C}$) has a well thickness of 58.3 Å and a barrier thickness of 48.6 Å, corresponding to a band gap $E_g = 19.5 \text{ meV}$ at 77 K. From the figure, it is clearly seen that modulation doping has been successfully achieved for this semiconducting SL. The electron concentration is constant and equal to $1.1 \times 10^{17} \text{ cm}^{-3}$ at temperatures below ~100 K. The electron mobility increases with decreasing temperature and reaches a maximum of $32,000 \text{ cm}^2/\text{V s}$ at 30 K.

Optical absorption coefficients versus photon energy for SLs A66B-A69A are shown in Figure 2. Each spectrum shows sharp steps which are a manifestation of the 2D quantum nature of these structures. Note, in particular, for the three SLs (A66B, A67B, and A68B) which undergo a transition from the semiconducting to semimetallic state at low temperatures the occurrence of a step beginning at about 110-115 meV. This corresponds to the light hole (H1) to conduction band (E1) transition and thus is a measure of the light and heavy hole energy splitting in the valence band due to quantum confinement. Its occurrence at this energy is consistent with a large valence band offset (about 360 meV for the HgTe-CdTe binary interface). Note also that for the semiconducting SL A69A the onset of absorption occurs at about 100 meV and the H1-E1 transition is barely discernable at about 210 meV.

Figure 3 shows Hall data for two p-type modulation-doped SLs. A74 is a p-type sample for which $L_z = 25.9 \text{ Å}$ and $L_b = 35.6 \text{ Å}$. These layer thicknesses correspond to a band gap $E_g = 171 \text{ meV}$ at 77 K. In this case, the Hall coefficient becomes positive at ~285 K. At temperatures below ~180 K, the hole concentration is constant and equal to $\sim 7 \times 10^{16} \text{ cm}^{-3}$. The hole mobility is approximately $250 \text{ cm}^2/\text{V s}$ over this temperature range, which is reasonable for a $\sim 7 \text{ μm}$ band gap structure. Corresponding Hall data for A76 is also shown. In this case the Hall coefficient becomes positive at about 180 K. Note that for this SL the low temperature mobility approaches $10^4 \text{ cm}^2/\text{V s}$ while the hole concentration decreases to less than 10^{16} cm^{-3} . The decrease in hole concentration at low temperatures implies that impurities capable of inducing hole freeze-out are present in the well layers. This is most likely As atoms due to the very small barrier layer thicknesses employed.

SUMMARY

We have found that it is possible to prepare n-type modulation-doped HgTe-Hg_{0.3}Cd_{0.7}Te superlattices reproducibly, with desired carrier concentrations determined by an appropriate choice of the In dopant oven temperature. We have prepared n-type structures having various band gaps by simply changing the well layer thickness L_z , including modulation-doped near-zero gap and even negative band gap structures. P-type structures have only been prepared for superlattices having layer thicknesses which place them in the semiconducting regime. Zero band gap and negative band gap (semimetallic) structures are always n-type, even when large densities of As dopant atoms are added to the barrier layers of such structures. The reason for this is presently unclear. It may be related simply to the growth parameters employed at NCSU, or there may be new physics to be understood about the transfer of holes to states in the valence

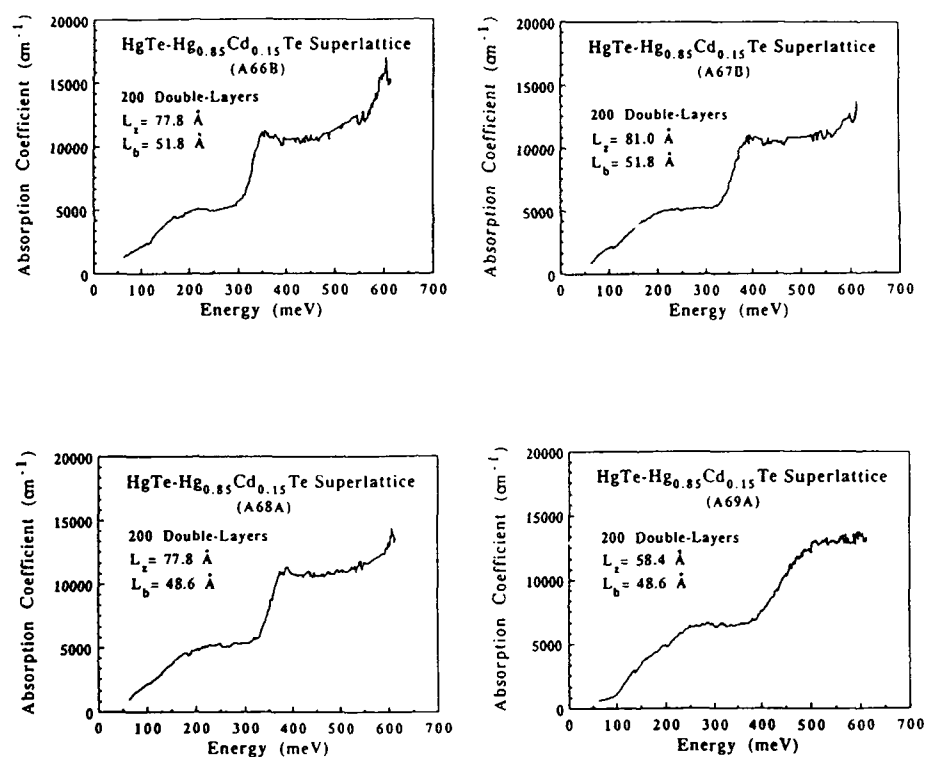


Fig.2. Optical absorption data for superlattices A66B, A67B, A68A and A69A.

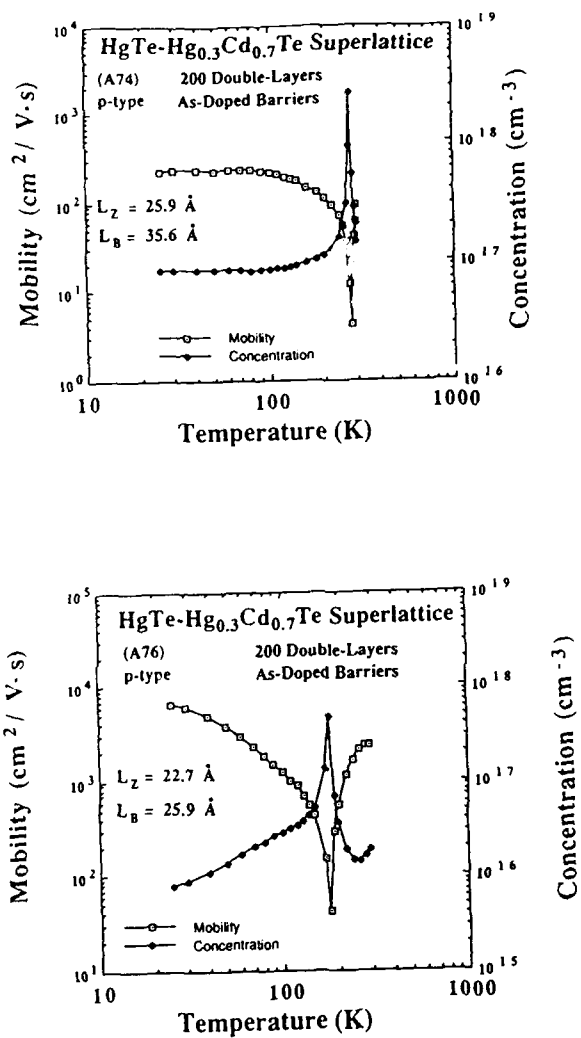


Fig.3. Hall effect data for p-type superlattices A74 and A76.

band that may lie above corresponding electron states in the conduction band in the zero band gap and negative band gap regimes. Additional superlattice growth experiments and new characterization experiments are needed to clarify this point.

ACKNOWLEDGEMENTS

The assistance of J. Matthews and A. Mohan with substrate preparation, and A. Sowers with optical measurements is gratefully acknowledged. This work was supported by NSF grant DMR-88-13525, DARPA contract DAAL03-87-K-0153 and General Electric Aero-space Group IR & D funds.

REFERENCES

1. J.N. Schulman, Yia-chung Chang, Phys. Rev. **B 33**, 2594 (1986).
2. C. Mailhot, D.L. Smith, Phys. Rev. **B 35**, 1242 (1987).
3. M.W. Goodwin, M.A. Kinch and R.J. Koestner, J. Vac. Sci. Technol. **A 6**, 2631 (1988).
4. M.L. Wroge, D.J. Peterman, B.J. Feldman, B.J. Morris, D.J. Leopold and J.G. Broerman, J. Vac. Sci. Technol. **A 7**, 435 (1989).
5. J.W. Cook, Jr., K.A. Harris, and J.F. Schetzina, Mat. Res. Soc. Symp. Proc., **90**, 419 (1987).
6. Y. Lansari, J.W. Han, S. Hwang, L.S. Kim, J.W. Cook, Jr., J.F. Schetzina, J.N. Schulman, N. Otsuka, J. Vac. Sci. Technol. **B 7**, 241 (1989).
7. J.R. Meyer, C.A. Hoffman, F.J. Bartoli, J.W. Han, J.W. Cook, Jr., J.F. Schetzina, X. Chu, J.P. Faurie, J.N. Schulman, Phys. Rev. **B 38**, 2204 (1988).

ON THE FIELD EMISSION FROM HgTe-CdTe SUPERLATTICES WITH GRADED STRUCTURES UNDER MAGNETIC QUANTIZATION

KAMAKHYA P. GHATAK* AND SAMBHU N BISWAS*

*Department of Electronics Engineering, University of Jadavpur,
Calcutta-700032, India

**Department of Electronics and Telecommunication Engineering, Bengal
Engineering College, Shibpur, Howrah-711103, West Bengal, India

ABSTRACT

In this paper, we studied the magneto-field emission from HgTe/CdTe superlattices with graded structure and compared the same with the bulk specimens of the constituent materials. It is found that the field emitted current density increases both with electron concentration and magnetic field in an oscillatory manner. The field emission in HgTe/CdTe SL is greater than that of the same from constituent materials the theoretical results are in agreement with the experimental observation as reported elsewhere.

INTRODUCTION

With the advent of MBE [1], MOCVD [2] and other experimental techniques, it has become possible to fabricate superlattices (SLs) of small-gap semiconductors, many of which are currently under study due to their interesting physical properties. The SL finds wide applications in many device structures, such as photodetectors [3], transistors [4], light emitters [5] etc. Among the various types of SLs, HgTe/CdTe SLs have raised a great deal of attention since 1979 when they were first suggested as a promising new materials for longwave length infrared detectors and other electro-optic applications [6]. Interest in Hg based SLs has further been increased which has revealed new properties with potential device applications [7]. The features arise from the unique zero-band gap material HgTe [8] and the direct band gap semiconductor CdTe which can be described by three band Kane model [9]. The aforementioned SLs have been proposed with the assumption of zero interface thickness. Since an intermediate potential region exists for the electrons, the influence of the finite thickness of the interface on the electron dispersion law becomes very important since the electron energy spectrum controls all the electronic properties. Though considerable work has already been done, nevertheless it appears from the literature that the field emission under magnetic quantization from HgTe/CdTe SL with graded structures has yet to be investigated. We wish to note that at the field strength of the order of 10^9 V/m, potential barriers at the surfaces of metals, alloys and semiconductors usually become very thin and result in field emission of the electrons due to tunnel effect [10]. In the present paper we shall study the magneto field emission from HgTe/CdTe SL with graded structures and compare the same with the bulk specimens of constituting materials.

THEORETICAL BACKGROUND

The dispersion relation of conduction electrons in bulk specimens of HgTe/CdTe SL are given by [8,9],

$$E = (\hbar^2 k^2 / 2m_1^*) + (3 e^2 k / 128 \epsilon_s) \quad (1)$$

$$\text{and } E = \frac{\hbar^2 k^2}{2m_2^*} \cdot G(E, E_{g2}, \Delta_2) \quad (2)$$

where E is the energy as measured from the edge of the conduction band in the absence of any quantization, \hbar is Planck's constant, m_1^* and ϵ_s are the effective band-edge electron mass and the permittivity of HgTe, m_2^* , E_{g2} and Δ_2 are the effective band-edge electron mass, band-gap and spin-orbit splitting of CdTe respectively. The magneto-electron energy spectrum in HgTe/CdTe SL with graded structure can be written as

$$K_z = [A(E, n)]^{1/2} \quad (3)$$

where $A(E, n) = [p(E, n) - 2e B l_0 \frac{1}{\hbar} (n + \frac{1}{2})] p(E, n) = \sqrt{\cos^{-1} \{ \psi(E, n) \} }^2$
 $\psi(E, n) = \sqrt{2 \cosh \{ \beta(E, n) \} \cos \{ \gamma(E, n) \} + \epsilon(E, n) \sinh \{ \beta(E, n) \} \sin \{ \gamma(E, n) \} + \Delta_0 \sqrt{(K_0^2(E, n) Q^{-1}(E, n) - 3Q(E, n)) \cosh \{ \beta(E, n) \} \sin \{ \gamma(E, n) \} + (3K_0^2(E, n) - Q(E, n) K_0^{-1}(E, n)) \sinh \{ \beta(E, n) \} \cos \{ \gamma(E, n) \} + \Delta_0 \sqrt{2 K_0^2(E, n) - Q^2(E, n)} \cosh \{ \beta(E, n) \} \cos \{ \gamma(E, n) \} + (1/12) \cdot (5K_0^2(E, n) \cdot Q^{-1}(E, n) + 5Q^3(E, n) K_0^{-1}(E, n) - 34Q(E, n) K_0(E, n) \sinh \{ \beta(E, n) \} \sin \{ \gamma(E, n) \})} \sqrt{\epsilon(E, n) = \sqrt{Q^{-1}(E, n) K_0(E, n) - K_0^{-1}(E, n) \cdot Q(E, n)}}$
 $Q(E, n) = \sqrt{K_0(E, n) (a_0 - \Delta_0)}$, $K_0(E, n) = \sqrt{\frac{2E \hbar^2 m_1^*}{\hbar^2} G(E - V_0, \alpha_2, \Delta_2) + \frac{2eB}{\hbar} (n + \frac{1}{2})} \sqrt{\frac{1}{2}}$, $E' = V_0 - E$, V_0 is the potential barrier encountered by the electron, $\alpha_2 = 1/E_{g2}$, B is the quantizing magnetic field along z -direction, n is Landau quantum number, e is electron charge, $Q(E, n) = \sqrt{\frac{m_1^*}{\hbar^4} \left\{ \frac{-3e^2}{128 \epsilon_s} + \left\{ \left(\frac{-3e^2}{128 \epsilon_s} \right)^2 + \frac{2E \hbar^2}{m_1^*} \right\}^{\frac{1}{2}} \right\}^2 - \frac{2eB}{\hbar} (n + \frac{1}{2}) \sqrt{\frac{1}{2}}}$, $l_0 (= a_0 + b_0)$ is the period length, Δ_0 is the interface width and a_0 and b_0 are the widths of the barrier and well respectively. The use of (3) leads to the expression of field emitted current density and the electron concentration respectively as

$$J = K_1 \sum_{n=0}^{n_{\max}} \ln t(\eta, \lambda_0) \exp(-\phi) \quad (4)$$

$$\text{and } n_0 = c_0 \sum_{n=0}^{n_{\max}} \sqrt{\psi_1 + \psi_2} \quad (5)$$

where $K_1 = e^2 B k_B T / 4 \pi \hbar^2$, k_B is Boltzmann constant, T is temperature, $t(\eta, \lambda_0) = \sqrt{1 + \exp(2\eta)} + 2 \exp(\eta) \cos(\lambda_0) \sqrt{}$, $\eta = (E_F - E_n)/k_B T$, E_F is the Fermi energy in the present case, E_n is obtained from the quality $A(E_n, n) = 0$, $\lambda_0 = \Gamma/k_B T$, $\Gamma = T/k_B T_D$, T_D is Dingle temperature, $\phi = \sqrt{A(E, n) \sqrt{3/2} / 4 \cdot 3e F_A'(\bar{E}, n)}$, $\bar{E} = \phi_0 + e_F - E_n$, ϕ_0 is the work-function, F_z is the electric field along z -axis, prime denotes the differentiation w.r.t. E_F , ψ_{real} part of $\sqrt{A(E, n)}$, $E_0 = E_F + i\Gamma$, $i = \sqrt{-1}$, $\psi_2 = \sum_{T=1}^T \phi(T) \cdot 2 \cdot (k_B T)^{2T}$

$(1-2^{1-2r}) \frac{d^{2r}}{d\epsilon_F^{2r}} \zeta(2r)$, r is the set of real positive integers, $C_0 = eB/\pi \hbar^2 n_0$ and $\zeta(2r)$ is zeta function.

The magneto-dispersion law of the bulk specimens can be expressed as

$$\hbar^2 k_z^2 / 2m_j^* + (n + \frac{1}{2}) \hbar \omega_{oj} \pm g_j \frac{\mu}{2} B = \epsilon_j(\epsilon) \quad (6)$$

which $j = 1$ and 2 , $\omega_{oj} = eB/\hbar m_j^*$, g_j are the magnitudes of the band edge g -factors for HgTe and CdTe respectively, μ is Bohr magneton $\epsilon_j(\epsilon) = \sqrt{4 A_0}^{-1} \sqrt{-B_0 + \sqrt{B_0^2 + 4 A_0 \epsilon^2}}$, $A_0 = \hbar^2 / 2m_1^*$, $B_0 = 3e^2 / 128 \epsilon_s$ and $\epsilon_2(\epsilon) = \epsilon G(\epsilon, E_{g2}, A_2)$. The basic expressions of (4) and (5) remain same where $\phi = 4 \sqrt{2m_j^*} \{p(\epsilon)\}^{3/2} / 3\hbar e F_s p'(\epsilon)$, $p(\epsilon) = [\epsilon_j(\epsilon) - (n + \frac{1}{2}) \hbar \omega_{oj} \pm \frac{1}{2} g_j \mu B]$, $\psi_1 = \text{Real part of } \sqrt{p(\epsilon_0)}$ and $C_0 = eB/\pi \hbar^2 n_0$.

Under the conditions $E_s \rightarrow 0$ and $E_{g2} \rightarrow 0$, (6) assume the well known form

$$\hbar^2 k_z^2 / 2m_j^* + (n + \frac{1}{2}) \hbar \omega_{oj} \pm \frac{1}{2} g_j \mu B = \epsilon \quad (7)$$

Under the conditions $B \gg 0$ and $T \gg 0$ we get

$$J = (e^3 F_s^2 / 8 \pi \hbar \phi_0) \exp \left[- \frac{4(2m_1^*)^{1/2}}{(3\pi e F_s)} \phi_0 \right]^{3/2} \quad (8)$$

which is the well-known Fowler-Nordheim formula, [11].

RESULTS & DISCUSSION

Using equations (4) and (5) and taking the parameters $\sqrt{12} m_1^* = 0.025 m_0$, $\epsilon_s = 20 \epsilon_0$, $m_2^* = 0.043 m_0$, $A_2 = .9 \text{ eV}$, $E_{g2} = .73 \text{ eV}$, $\Gamma = 4.2 \text{ k}$, $\Gamma_D = 3 \text{ K}$, $\Delta_0 = 5 \text{ \AA}$, $a_0 = 50 \text{ \AA}$, $b_0 = 40 \text{ \AA}$ and $B = 2 \text{ Tesla}$ we have plotted the field emitted current density from HgTe/CdTe SL as a function of n_0 as shown in plot a of fig. 1. The simplified cases for $\Delta_0 = 0$, HgTe, CdTe and parabolic energy bands are shown in the plots b, c, d and e of fig. 1 respectively. The circular plots exhibit the experimental results as given elsewhere [13]. In fig. 2 we have plotted all the above cases as functions of B corresponding to an electron concentration of 10^{23} m^{-3} .

It appears from Fig. 1 that the current density increases with increasing electron concentration in an oscillatory manner and the SL structure exhibits the greatest value of the current density as compared to that of bulk specimens of the constituent materials for a given value of n_0 . It appears from fig. 2 that the current density oscillates with B and the appearance of the humps in both the figures are due to SdH effect. Finally we should note that though the influence of image face and many-body effects have not

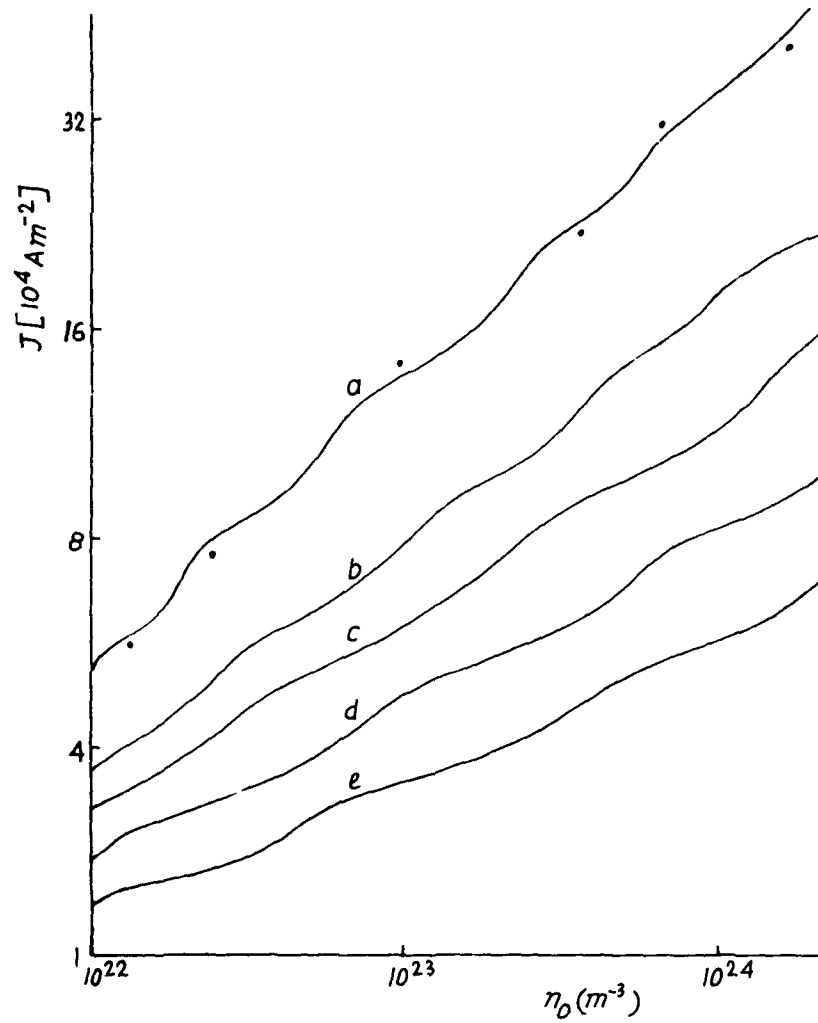


Fig. 1 Plot a shows the doping dependence of the magneto-field emitted current density from HgTe/CdTe SL with graded structures. The plots, b, c, d and e exhibit the same dependence for $\Delta_0 = 0$, HgTe, CdTe and parabolic energy bands respectively.

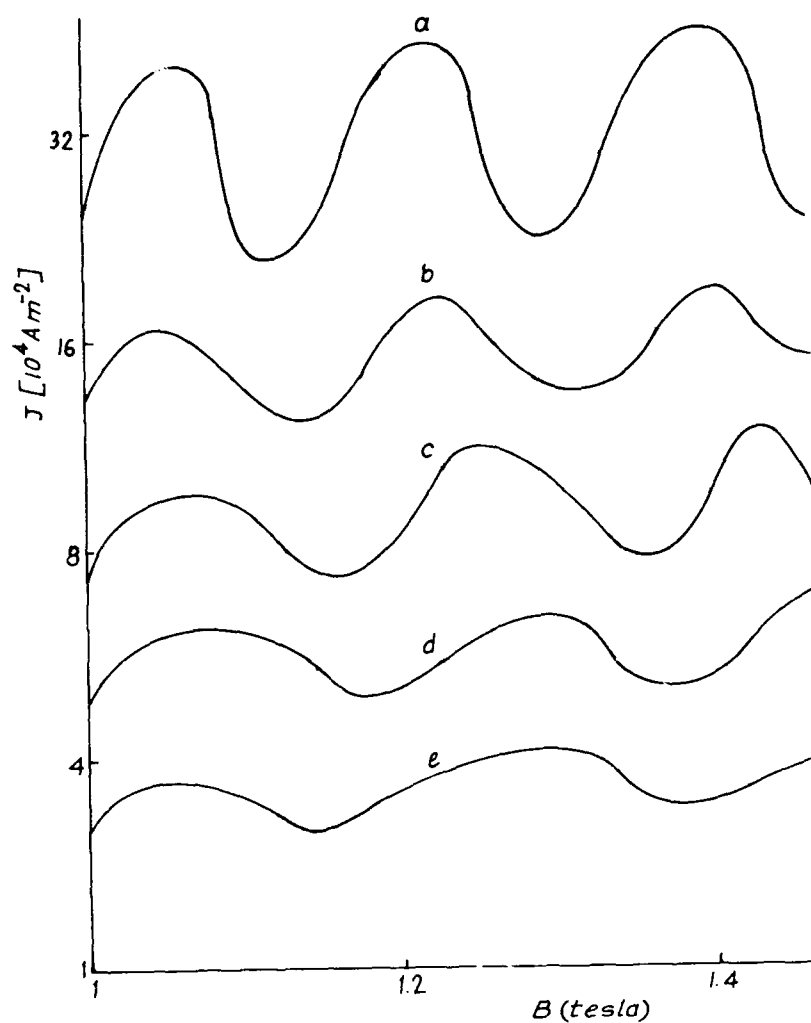


Fig. 2 Plot a shows the magnetic field dependence of the magneto-field emitted current density from HgTe/CdTe SL with graded structures. The plots b, c, d and e exhibit the same dependence for $\Delta_0 = 0$, HgTe, CdTe and parabolic energy bands respectively.

been considered in this simplified analysis, our theoretical formation is in agreement with the experimental observation as reported elsewhere and we have obtained the famous Fowler-Nordheim formula from our results which is also an indirect test of our simple analysis.

References

1. J. Dibert, P.M. Petroff, G.J. Delan, S.J. Pearton, A.L. Gossard and J.H. English, Appl. Phys. Letts. 49, 1275 (1986).
2. P.M. Petroff, A.C. Gossard and W. Weighmann, Appl. Phys. Letts. 45, 420 (1984).
3. F. Capasso, K. Mohammed, A.Y. Chu, R. Halland A.L. Hutchinson, Appl. Phys. Letts. 47, 420 (1985).
4. M. Hieblum, D.C. Thomas, C.M. Knoedler and M.I. Mathan, Appl. Phys. Letts. 47, 1105 (1985).
5. K. Floog and G.H. Dohler, Adv. Phys. 32, 285 (1983).
6. B.A. Wilson, IEEEQE-24, 1963 (1988).
7. G. Bastard, E.E. Mendez, L.L. Chang and L. Esaki, Phys. Rev. 28B, 3241 (1983).
8. V.A. Yokololav, Sov. Phys. Semicond. 13, 692 (1979).
9. B.R. Nag, Electron Transport in compound semiconductors, Springer-Verlag, Berlin, Heidelberg, N.Y., 1980.
10. D.A.B. Miller, D.S. Chemla and T.C. Damen, Phys. Rev. 32B, 1043 (1985), J. Bono and R.H. Good, Surface Science 134, 272 (1983).
11. R.H. Fowler and L.W. Nordheim, Proc. Roy. Soc. A119, 173 (1928), D.K. Roy, Quantum Mechanical Tunnelling and its applications, World Scientific, Singapore, 1988, p. 201.
12. M. Newberger, Electronic Materials, 2, Plenum data corporation, N.Y. 1971.
13. B.L. Belmont and A. Chuiko, Sov. J. Exp. and Theo. Phys. 103, 1120 (1989).

MBE GROWTH AND CHARACTERIZATION OF LWIR HgCdTe

M.B. LEE, J. DECARLO, D. DIMARZIO, and M. KESSELMAN
Grumman Corporate Research Center, Bethpage, NY 11714-3580

ABSTRACT

We have grown high-mobility LWIR HgCdTe thin films on CdTe substrates, using molecular beam epitaxy (MBE). The structural, optical, and electrical properties of these epilayers were determined by SEM, DCRC, FTIR, and Hall effect measurements. For films of 10 to 11 μm thick and composition X value ranging from 0.152 to 0.172, the highest mobility observed was $7.5 \times 10^5 \text{ cm}^2/\text{V}\cdot\text{sec}$, and the FWHMs of the rocking curves were 75 to 110 arcsec. We also have carried out the temperature-dependent EXAFS study of HgCdTe.

INTRODUCTION

In spite of recent advances in the growth of other materials with long wavelength infrared (LWIR) detection potential [1,2], HgCdTe remains the most promising detector material for the spectral range of 8-12 μm . Molecular beam epitaxy (MBE) is a growth technique in which all important growth parameters can be precisely controlled. Therefore, it is ideally suited for the growth of LWIR HgCdTe, for which optimal deposition conditions must be carefully maintained for long growth periods.

In this paper, we describe the experimental conditions for MBE growth and the procedures used for epilayer characterization. The structural, optical, and electrical properties are summarized. Finally, the quality of these epilayers is compared with other published results.

EXPERIMENTAL TECHNIQUES

The HgCdTe epilayers were deposited in a RIBER 2300 MBE system on 1 cm x 1 cm CdTe (100) substrates purchased from II-VI Corporation. Double crystal rocking curve (DCRC) measurements of the substrates indicated that the FWHM of the (400) reflection spot was about 50 arcsec.

The substrates were degreased and etched with 1.5 % bromine/methanol solution for 90 sec prior to mounting in the growth chamber. Within the growth chamber, the substrates were first annealed at 320°C for 90 min. A CdTe buffer layer, 0.5 μm thick, was grown on each substrate before the depositing of HgCdTe. HgCdTe epilayer deposition was carried out at 200°C, and the substrate temperature was maintained throughout the growth period to within 0.2°C. IR transmission data were taken with a Mattson Cygnus 100 FTIR spectrometer, which uses a special wafer-scanning software. The Van der Pauw technique was used to measure the electrical properties of the epilayers. Indium micro-ball cold wire bonding was used for electrical connection to the sample.

The electrical transport properties were measured over a temperature range of 10 to 270 K and in a magnetic field from 1000 to 8000 Gauss. EXAFS experiments were carried out at the National Synchrotron Light Source (NSLS) of Brookhaven National Laboratory over temperatures ranging from 10 K to 300 K.

RESULTS

Table I summarizes the growth conditions for three LWIR HgCdTe epilayers that will be discussed in this paper. The growth conditions for all three samples were identical except for Hg flux, which was deliberately varied to study its influence on bandgap.

The epilayer's thickness was measured directly using a Tencor Instruments model Alpha 2000 surface profiler, which has ultimate resolution of 40 Å.

A SEM photo of sample MCT27 is shown in Fig. 1; characteristic pyramidal hillock structures are clearly observed. Samples MCT28 and MCT29 also exhibit these hillock structures. Similar features have been observed for MBE growth of HgCdTe along the (100) orientation and have been previously reported [3,4].

Surface density of these defects for the epilayers is listed in Table II. The values in Table II are comparable to previous work [4] that reported the hillock structure density ranging from 10^4 to $10^5/\text{cm}^2$ on HgCdTe films grown on CdZnTe substrates.

Table I Epilayer Growth Conditions

EPIPLAYER	TEMP, °C	Hg FLUX, ARB. UNIT	THICKNESS μm
MCT27	200	1	11
MCT28	200	0.96	11
MCT29	200	0.93	10

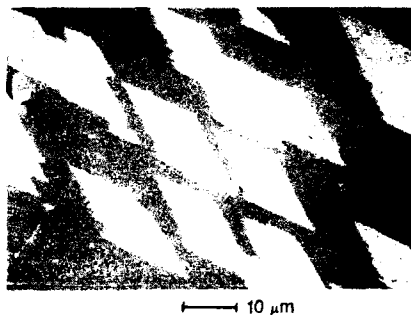


Fig. 1 SEM picture of MCT 27 showing pyramidal hillock structures.

Table II Characterization Result Summary

EPIPLAYER	X	DCRC, ARCSEC	HILLOCK DENSITY, cm^{-2}	MOBILITY, $\text{cm}^2/\text{V-SEC}$	CARRIER CONC, cm^{-3}
MCT27	0.153	75	7.6×10^4	9.2×10^4	2×10^{15}
MCT28	0.160	110	1.0×10^5	7.5×10^5	4.8×10^{15}
MCT29	0.172	100	7.7×10^4	6.0×10^5	3.4×10^{15}

Figure 2 shows the FTIR transmission spectrum measured near the center of one of the three epilayers. The spectrum exhibits a sharp onset of transmission in the LWIR spectral range, indicating good compositional uniformity along the growth direction. The FTIR spectra of the other two samples also exhibit a sharp transmission onset. From these spectra, the epilayer bandgap is assumed to be the energy corresponding to an absorption coefficient of 500 cm^{-1} .

Composition X value is then determined from the bandgap by applying the equation used by Hansen et al. [5].

The FTIR spectrometer also was used to obtain wafer-scanning IR transmission profiles by measuring the spectrum at 1.0 mm intervals across the samples. The spot size was slightly less than 1 mm in diameter. Due to the dimensions and the geometry of the present sample mount, the scanning profile is limited to a circular area about 5 mm in diameter. Figure 3 is an example of an IR transmission profile. As indicated in the figure, the X value of the epilayer is uniform to within 0.003 for up to 2.5 mm from the center of the wafer.

Figure 4 shows the double crystal rocking curve measurement result for sample MCT 27. The FWHM of the (400) reflected beam is about 75 arcsec; for samples MCT 28 and MCT 29, it is 110 arcsec and 100 arcsec, respectively.

The electrical properties of the three epilayers measured at 20 K also are summarized in Table II. All are n-type and show high mobility at 20 K.

Hall effect measurements also were carried out over a wide range of temperature and magnetic field. Figure 5 shows the variation of mobility and carrier concentration for MCT 29 from 10 K to 270 K at a magnetic field of 8000 G. Hall measurements of MCT 29 over the same temperature range but at lower magnetic fields gave results nearly identical. The electrical measurements for MCT27 and MCT28 indicate high-quality n-type material.

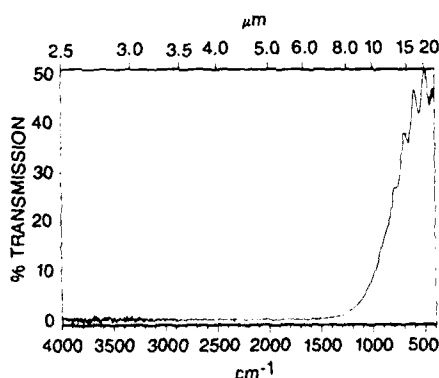


Fig. 2 FTIR transmission spectrum of MCT28.

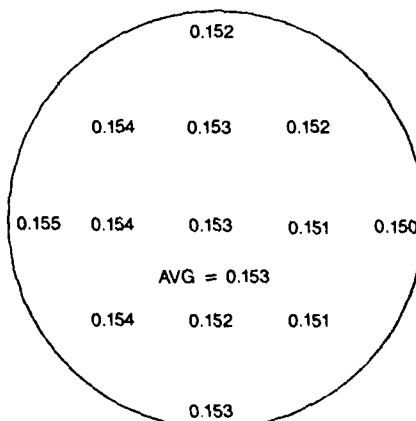


Fig. 3 Composition profile of MCT27.

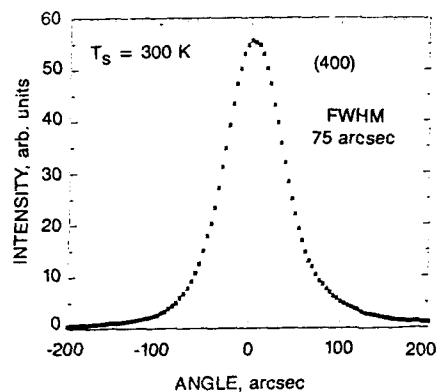


Fig. 4 Double crystal X-ray rocking curve for MCT27.

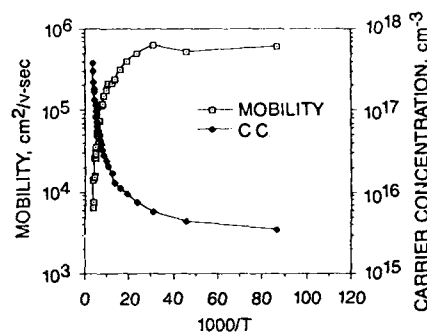


Fig. 5 Electron concentration and mobility vs temperature of MCT28 measured at 8000 Gauss.

DISCUSSION

As shown in Fig. 1, our epilayers exhibit pyramidal hillock structures. Most of these structures are similar in size, which increases with the thickness of an epilayer. These features are consistent with those observed in previous studies [4]. The origin of these structures also has been discussed elsewhere [3,4].

As shown by Fig. 2, the samples we studied exhibit an onset of IR transmission that is sharper than for LWIR HgCdTe recently described [6]. If we define the wavelength at which IR transmission intensities are reduced to 25 % of maximum as the cutoff wavelength, then the cutoff wavelengths for samples MCT27, MCT28, and MCT29 are 11.7 μm , 9.6 μm , and 9.3 μm , respectively.

The compositional uniformity of our epilayers is as good as some of the latest published results [6,7], although the area covered by our IR scanning profile is not as large.

Significantly, however, we have shown that the cutoff wavelength for LWIR HgCdTe can be fine-tuned simply by varying the Hg flux. Furthermore, this was accomplished while maintaining the sharpness of the transmission onset.

The DCRC results for our epilayers are comparable to some of the published results [6,8], but clearly inferior to the best published DCRC results [9,10,11]. Since the FWHM of our CdTe substrates was at least 50 arcsec, the peak width for our epilayers might be limited in part by the quality of our substrates.

The mobilities we observe, especially for MCT28 and MCT29, are comparable to the best published mobility data for n-type, undoped HgCdTe to date [11]. Furthermore, all three samples show well-behaved electrical properties for a wide range of temperature and magnetic field.

In an attempt to further characterize our material, we have recently measured the extended x-ray absorption fine structure (EXAFS) of Hg, using the L_{III} absorption edge in HgCdTe thin film as well as HgTe (x=0). EXAFS has already proven to be a powerful tool for determining the local structure in ternary semiconductor compounds [12].

EXAFS was measured for each sample as a function of temperature from 13 K to 300 K.

Figure 6 shows the radial distribution function (Fourier transform of the EXAFS data) of consecutive atomic shells surrounding the Hg atoms in sample MCT28. At 300 K, only the first (nearest neighbor) Hg-Te shell is observed, while at 13 K the Hg-Hg, Cd second shell and the Hg-Te third shell appear. The large peaks in Fig. 6 agree with theoretical predictions for a zincblende lattice. The difference in the Debye-Waller disorder parameter, $\Delta\sigma^2$, for the Hg-Te first shell between 300 K and 13 K is 0.00728 \AA^2 . This indicates that a significant amount of thermal disorder exists in this material at room temperature ($\Delta\sigma^2$ of Pt is 0.00299 \AA^2 [13]).

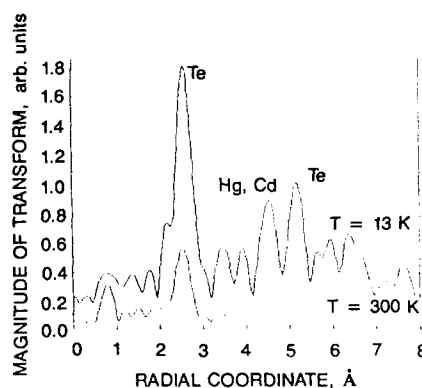


Fig. 6 Hg edge EXAFS spectrum of MCT28 taken at 300 K and 13 K.

There is also a significant degree of anharmonicity in the interatomic potential at 300 K as derived from bond length analysis. For the HgTe (x=0) thin film, the bond length change with temperature is insignificant, consistent with the thermal expansion, but for the three MCT epilayers there is an apparent decrease in the average first shell Hg-Te bond length of about $0.03 \pm 0.01 \text{ \AA}$ from 300 K to 13 K. The first shell Hg-Te bond length at 300 K was found not to change significantly as the composition X varied from X = 0 to X = 0.17.

A detailed analysis of the EXAFS data, including a temperature-dependent analysis of the Debye-Waller parameter to separate thermal from static disorder, determination of the relative bond strengths, and a full account of the relative bond length changes in these materials, will be presented in a future publication [14].

CONCLUSION

We described procedures for MBE growth of LWIR HgCdTe with cutoff wavelengths ranging from 9.3 μm to 11.9 μm and thicknesses of 10 to 11 μm . Comprehensive characterization of these epilayers shows that they are compositionally uniform, are of good crystal quality, and possess excellent electrical properties.

ACKNOWLEDGMENTS

The authors wish to express their sincere gratitude to Dr. M. Brown for guidance, advice, and encouragement, Dr. F. Szofran of NASA/Huntsville for providing us with his FTIR scanning program, Dr. S.M. Heald of Brookhaven National Laboratory for his assistance in EXAFS data acquisition and analysis, Dr. D. J. Larson, Jr., for his help in initial DCRC measurements, Dr. L. Casagrande for his contribution in EXAFS data acquisition, C. Creter for SEM characterization, and G. Vilardi of R.P.I. for his assistance in Hall effect measurements.

REFERENCES

1. S.R. Kurtz, L.R. Dawson, R.M. Bierfeld, I.J. Fritz, and T.E. Zipperian, *Appl. Phys. Lett.* **53**, 1961 (1988) and references within.
2. B.F. Levine, C.G. Bethea, G. Hasnain, J. Walker, and R.J. Malik, *SPIE* vol. 930, **114** (1988) and references within.
3. R. J. Koestner and H.F. Schaake, *J. Vac. Sci. Technol.* **A 6** (4), 2834 (1988).
4. A. Million, L. DiCioccio, J.P. Gailliard, and J. Piaguet, *J. Vac. Sci. Technol.* **A 6** (4), 2813 (1988).
5. G.L. Hansen, J. L. Schmit, and T.N. Casselman, *J. Appl. Phys.* **53**, 7099 (1982).
6. Ishwatra B. Bhat, Hamid Fardi, and Sorab K. Ghandhi, *J. Vac. Sci. Technol.* **A 6** (4), 2800 (1988).
7. D. Lange, S. Sivananthan, X. Chu, and J.P. Faurie, *Appl. Phys. Lett.* **52** (12), 978 (1988).
8. J.M. Arias, S.H. Shin and E. Gertner, *J. of Crystal Growth* **86**, 362 (1988).
9. R.J. Koestner, H.-Y. Liu, and H. F. Schaake, *J. Vac. Sci. Technol.* **A 7** (2), 517 (1989).
10. S. Sivananthan, M.D. Lange, G. Monfroy, and J. P. Faurie, *J. Vac. Sci. Technol.* **B 6** (2), 788 (1988).
11. T.H. Myers, R.W. Yanka, K. A. Harris, A.R. Reisinger, J. Hans, S. Hwang, Z. Yang, N. C. Giles, J. W. Cook, Jr., J. F. Schetzina, R.W. Green, and S. McDewitt, *J. Vac. Sci. Technol.* **A 7** (2), 300 (1989).
12. B.A. Bunker, *J. Vac. Sci. Technol.* **A 5** (5), 3003 (1987).
13. S.M. Heald and J.M. Tranquada, in *Physical Methods of Chemistry*, edited by B.W. Rossiter and I.F. Hamilton (John Wiley & Sons, N.Y.) Vol. 05, to be published.
14. D. DiMarzio, M. Lee, and J. DeCarlo, in preparation.

PART VIII

Hg-Based Superlattices

FREE-CARRIER INDUCED OPTICAL NONLINEARITIES IN NARROW BANDGAP SEMICONDUCTORS

D. Walrod^(a), S. Y. Auyang and P. A. Wolff^(b)
Francis Bitter National Magnet Laboratory
Massachusetts Institute of Technology
Cambridge, MA 02139

ABSTRACT

Free-carrier induced third-order optical nonlinearities can be both large and fast in narrow-gap semiconductors. We have studied a variety of mechanisms in bulk semiconductors and heterostructures using CO₂ lasers and found third-order susceptibilities as large as 2×10^{-3} esu with picosecond relaxation times. These mechanisms saturate at much higher intensities than do slower mechanisms and hence induce huge modulations of the dielectric function. In addition, most of these processes are nonresonant so they do not require the exact matching of material parameters and are relatively insensitive to temperature.

1 INTRODUCTION

The first observation of a third-order nonlinearity caused by a free-carrier process in semiconductors was made by Patel *et al.*¹ These modest nonlinearities in *n*-InSb, *n*-GaAs and *n*-InAs were explained by Wolff and Pearson as resulting from the nonparabolicity of the conduction band.² The nonlinearity was very fast, relaxation times in the picosecond range, but fairly weak. Hence, for many years, it was believed that fast processes such as these were intrinsically weak. Our studies have shown that this is not the case. There are several free-carrier processes which are both fast and moderately large. We have observed $\chi^{(3)}$ of 2×10^{-3} esu with picosecond relaxation times in Hg_{0.84}Cd_{0.16}Te epilayers with a near-zero bandgap. Similar nonlinearities have been found in other II-VI epilayers.

The major free-carrier processes that we have investigated rely on a modulation of the free-carrier dielectric function. In narrow bandgap semiconductors, the important mechanisms are

1. Nonparabolicity of the energy bands.
2. Excitation of interband transitions.
3. Excitation of intervalence band transitions.
4. Energy dependence of carrier scattering.

These mechanisms have been observed in both bulk and epitaxially grown semiconductors. Enhanced nonparabolicity due to superlattice structure has also been observed in various narrow gap superlattices.³

Free-carrier nonlinearities have a number of features that are very desirable for device applications. Most processes have very fast relaxation times, so they are well suited to devices where speed is critical. They also do not tend to saturate at high power. Since most of the processes are non-resonant, there are not stringent requirements placed on material parameters and they are fairly insensitive to temperature changes.

Table 1. Figures of Merit for Third-Order Optical Nonlinearities in Semiconductors

Medium	Nonlinear Mechanism	T(K)	$\chi^{(3)}$ (esu)	α (cm ⁻¹)	τ (sec)	$\chi^{(3)}/\alpha\tau$
Hg _{0.84} Cd _{0.16} Te	interband ⁴	80	2×10^{-8}	3000	5×10^{-12}	9×10^4
HgTe	interband ⁵	300	2×10^{-4}	3400	5×10^{-12}	9×10^3
n-InSb	nonparabolicity ¹⁰	2	2×10^{-7}	2	4×10^{-12}	3×10^4
p-Hg _{0.78} Cd _{0.22} Te	intervalence ⁶	300	8×10^{-6}	48	2×10^{-13}	8×10^5
p-GaAs	intervalence ⁷	300	1×10^{-6}	5000	5×10^{-13}	4×10^2
n-Si:P	impurity ²⁵	300	3×10^{-7}	700	1×10^{-12}	4×10^2
Hg _{0.77} Cd _{0.23} Se:Fe	impurity ²³	80	1×10^{-6}	90	8×10^{-13}	2×10^4
InSb ^a	band filling ¹⁷	80	3×10^{-1}	70	4×10^{-7}	1×10^4
Hg _{0.78} Cd _{0.22} Te	band filling ²¹	80	6	24	3×10^{-6}	8×10^4
p-Hg _{0.78} Cd _{0.22} Te	band filling ²⁰	80	5×10^{-2}	8	3×10^{-8}	2×10^5
Ge	valence electron ¹¹	300	1×10^{-10}	0.01	1×10^{-14}	1×10^6
GaAs/GaAlAs ^b	free exciton ⁸	300	4×10^{-2}	12000	2×10^{-8}	170

^a $\lambda = 5.4 \mu\text{m}$ ^b $\lambda = 0.84 \mu\text{m}$

2 THIRD ORDER FREE-CARRIER INDUCED NONLINEARITIES

Free-carrier nonlinearities are caused by a modulation of the free-carrier dielectric function

$$\epsilon = - \sum_j \frac{4\pi N_j e^2}{m_j^* \omega^2} \left(1 - \frac{iv_j}{\omega} \right). \quad (1)$$

This modulation can be accomplished by changing the occupation of states and by promoting carriers to states with different effective masses or scattering rates.

We will use the following plane-wave expansion for the total electric field driving the dielectric function,

$$E(x, t) = \frac{1}{2} \text{Re} \sum_j [E_j \exp(-i\omega_j t) + \text{c.c.}]. \quad (2)$$

Under this convention, the intensity is given by $I = cn_0 |E|^2 / 8\pi$

So that we can treat nondegenerate four-wave mixing, we will assume that the incident light consists of two different frequencies ω_1 and ω_2 . Hence, the laser can modulate the dielectric at the difference frequency. This can be utilized to measure the relaxation time of the nonlinear process.

The i th component of the nonlinear polarization is given by

$$P_i^{(3)} = 3\chi^{(3)}(E_1 \cdot E_2^*)E_i = \left(\frac{\delta\epsilon}{4\pi} \right) E_i. \quad (3)$$

The factor 3 in the definition of $P^{(3)}$ arises from the requirement that the polarization be invariant to spatial symmetry operations⁹. Now, let us take X to be any parameter in the dielectric function that can be modulated by the incident electric fields. X can either be modulated directly, or indirectly through carrier heating. This leads to a modulation of ϵ of the form

$$\delta\epsilon = (\partial\epsilon/\partial X)\delta X = 12\pi\chi^{(3)}E_1 \cdot E_2^*. \quad (4)$$

For the case of direct modulation, a simple kinetic equation can be used to describe the steady state response of X for dissipative nonlinearities. We will concentrate primarily on nonlinearities where dissipation is important because they tend to have $\chi^{(3)}$'s that are much larger than those where dissipation is small. When the difference frequency $\Delta\omega \approx \omega$, the ratio of the dissipative to the nondissipative effect is of the order of the ratio of the energy to momentum relaxation times τ_T/τ_m .¹⁰ The equation of motion for the parameter X is

$$\frac{\partial \delta X}{\partial t} + \frac{\delta X}{\tau} = \frac{\xi c n_0 \alpha}{8\pi} E_1 \cdot E_2^* \exp(-i\Delta\omega t), \quad (5)$$

where α is the absorption coefficient responsible for the modulation of X , ξ is the efficiency of the process, and τ is the relaxation time of the nonlinear mechanism. If we assume X to be modulated at the difference frequency $\Delta\omega = \omega_1 - \omega_2$, then we immediately obtain an expression for $\chi^{(3)}$

$$\chi^{(3)} = -\frac{\xi c n_0 \alpha \tau}{96\pi^2(1-i\Delta\omega\tau)} \left(\frac{\partial \epsilon}{\partial X} \right). \quad (6)$$

The parameter X can also be modulated by laser induced fluctuations in the carrier energy. In most cases it is proper to identify the carriers with a temperature because the rate of energy flow from the carrier to the lattice is quite small compared to the carrier-carrier collision rate. Hence, we will assume that the carriers have an equilibrium temperature of T and the lattice has an equilibrium temperature of T_L . This then allows us to write the following kinetic equation for carriers being heated by the incident lasers

$$\left(\frac{\partial T}{\partial t} + \frac{T - T_L}{\tau_T} \right) \left(\frac{\partial \delta W}{\partial T} \right) = \frac{c n_0 \alpha}{8\pi} E_1 \cdot E_2^* \exp(-i\Delta\omega t), \quad (7)$$

where $(\partial \delta W / \partial T) = C_V$, the specific heat of the carriers, and τ_T is the thermalization time. Since the carrier temperature is modulated at $\Delta\omega$ we obtain this equation for $\chi^{(3)}$

$$\chi^{(3)} = -\frac{\xi c n_0 \alpha \tau}{96\pi^2(1-i\Delta\omega\tau)} \left(\frac{\partial \epsilon}{\partial X} \right) \left(\frac{1}{C_V} \frac{\partial X}{\partial T} \right). \quad (8)$$

Some important points should be made about these basic equations for the third-order nonlinear susceptibility. From Eq. (1) and Eqs. (7-8) we see that $\chi^{(3)}$ is inversely proportional to the effective mass m^* . Hence narrow band gap semiconductors, with their small effective masses, generally have fairly large third-order susceptibilities. Also, note that $\chi^{(3)}$ is proportional to α and τ . This means that materials with large absorptions and long relaxation times tend also to have large nonlinearities. What makes the free-carrier mechanisms that we have studied so interesting, is that we have observed large $\chi^{(3)}$'s with fairly small absorption and picosecond relaxation times.

The $(1-i\Delta\omega\tau)$ in the denominator shows that all mechanisms will exhibit some dispersion in $\chi^{(3)}$ as a function of $\Delta\omega$. The relaxation time of the nonlinear mechanism can be determined by taking advantage of this dispersion and measuring the four-wave signal as a function of $\Delta\omega$. It is clear from Eq. (8) that the four-wave signal will experience a roll-off when $\Delta\omega\tau \approx 1$. For $\Delta\omega\tau \gg 1$ the carriers are driven in a "sloshing" mode. The carriers are perturbed in velocity space by the incident electric field. In this nondissipative mode, the carriers and the field interchange energy without loss. It is this mode that Patel, et al observed¹ and Wolff and Pearson described². This was thought to be the only mode until Yuen¹⁰ discovered a large dispersion of $\chi^{(3)}$ in $\Delta\omega$ in n -InSb.

When $\Delta\omega\tau \ll 1$, the electrons enter a new, dissipative mode. This "breathing mode" results because there is now an irreversible flow of energy from the electric field to the carriers to the lattice. Both modes contribute to the nonlinearity, but the "sloshing" mode dominates for $\Delta\omega\tau \gg 1$ and the "breathing" mode dominates for $\Delta\omega\tau \ll 1$.

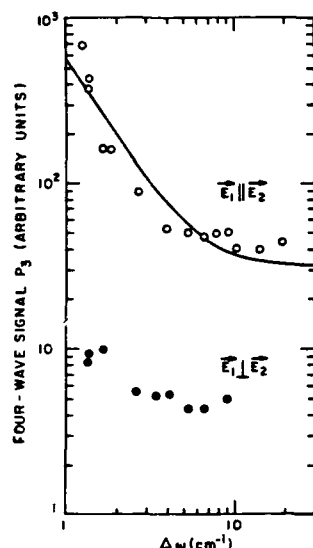


Figure 1. Four-wave mixing signal in $n\text{-Hg}_{0.74}\text{Cd}_{0.26}\text{Te}$ at 2K as a function of the difference frequency for two polarization configurations. The nonlinear mechanism is conduction band nonparabolicity.

The electric field of the lasers interact with the carriers through $\mathbf{p} \cdot \mathbf{A}$ term in the Hamiltonian. So, for a dissipative process at finite $\Delta\omega$, it is required that $\mathbf{E}_1 \cdot \mathbf{E}_2 \neq 0$. This is because when the fields are perpendicular, there is no cross term of the form $\mathbf{E}_1 \cdot \mathbf{E}_2 e^{-i\Delta\omega t}$. Hence, there will be no modulation of the carriers at the difference frequency and consequently the dissipative effects described in Eqs. (5) - (8) will disappear. Nondissipative processes such as those observed by Patel *et al.*¹ will still be observable, however the magnitude of the signal will be decreased by a factor of nine.

3 EXPERIMENTAL SETUP

We are able to perform both non-degenerate and degenerate four-wave mixing experiments. Figure 2 gives a schematic of the experimental setup. The laser source is a pair of line tunable, synchronously Q-switched CO_2 lasers. The pulse length is 120 nsec and they are capable of producing intensities at the sample of 1 MW/cm². When the lasers are operating at two different frequencies ω_1 and ω_2 , the minimum difference frequency $\Delta\omega$ is 1.38 cm⁻¹. This is limited by the spacing of the CO_2 lines. The light from the lasers can be polarized parallel or perpendicular to each other. Also, by using a polarizer, the laser polarization can be rotated to any arbitrary angle. This technique is used in studies of superlattices. The four-wave signal is at $\omega_3 = 2\omega_1 - \omega_2$ and it is separated from the pump beams by a double-pass spectrometer. A Cu:Ge detector is then used to observe the signal.

In the non-degenerate configuration, a piece of optical grade Ge is used as a reference. This allows us to obtain absolute values for $\chi^{(3)}$. Unfortunately, there is some uncertainty regarding the value of $\chi^{(3)}$ for intrinsic Ge. Values of 1.0×10^{-10} esu¹¹ and 2.5×10^{-11} esu¹² have been reported. We use the larger value as a reference because it is the most widely quoted and is much closer to the theoretical value of 8.1×10^{-11} esu.¹³ The four-wave signal is referenced to the Ge by using¹¹

Table 2. Relaxation Times Measured by Nondegenerate Four-Wave Mixing Experiments Compared to Theoretical Predictions

Nonlinear Mechanism	Medium	τ_{exp} (psec)	τ_{th} (psec)
Light to heavy hole transitions by optical phonon emission	$p\text{-GaAs}^a$	0.09	0.13
	$p\text{-GaAs}^a$	0.23	0.20
	$p\text{-GaAs}^a$	0.46	0.52
	$p\text{-Ge}^a$	0.70	1.7
Thermal Relaxation	$n\text{-InSb}^b$	3	-
	$n\text{-GaAs}$	0.7	-
	$n\text{-Si:P}^c$	1	-
	$n\text{-HgCdSe:Fe}^d$	0.7	-

^a Reference 7

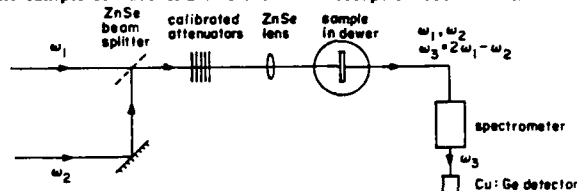
^b Reference 10

^c Reference 25

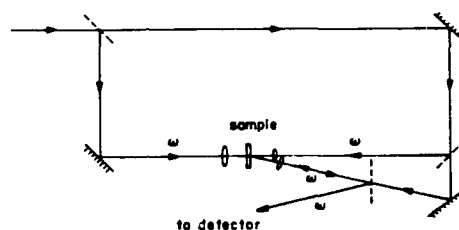
^d Reference 23

$$I = \frac{256\pi^4}{c^4 n_0^4} [3\chi^{(3)}]^2 I_1^2 I_2^2 T_R^4 e^{-\alpha L} \left(\frac{1 - e^{-\alpha L}}{\alpha L} \right)^2 L^2. \quad (9)$$

where I_1 and I_2 are the laser intensities, L is the thickness of the nonlinear medium, T_R is the transmission at the sample surface and α is the total absorption coefficient.



(a)



(b)

Figure 2. Schematic of experimental setup: (a) nondegenerate four-wave mixing, (b) degenerate four-wave mixing

The degenerate configuration is useful for studying samples that have relaxation times so slow that $\Delta\omega\tau > 1$ even for $\Delta\omega = 1.38 \text{ cm}^{-1}$. The probe beam makes an angle of approximately 5° with respect to the two counterpropagating pump beams and is about 20 times weaker. The four-wave signal reflected along the direction of the probe beam is separated with a beam splitter. The Ge reference cannot be used in this case because the different thickness of the Ge and the sample make comparisons unreliable. Instead, the magnitude of the four-wave signal is referenced to the reflected intensity when the sample is replaced by a mirror. This reflectivity is given by¹⁴

$$R = \frac{256\pi^4\omega^2}{c^4 n_0^4} [6\chi^{(3)}]^2 I_1 I_2 L^2 T_R^4 \frac{e^{-\alpha L}}{(1 + \alpha L/2)^2}. \quad (10)$$

Proper sample preparation is very important. The bulk samples are polished on both sides and the light is incident normal to the crystal surface. If Fabry-Perot interference proves to be a problem, the back side of the sample is roughened to minimize reflections.

4 NONLINEAR PROCESSES

A ENERGY BAND NONPARABOLICITY

One of the best known free-carrier optical nonlinearities is that produced by the nonparabolicity of the energy bands.^{1,10,16} As the carriers are heated by the incident laser radiation, their effective masses change. This leads to a modulation of the dielectric function resulting in an optical nonlinearity.

In the two-band model, the effective mass of the electrons can be approximated by¹⁶

$$\frac{1}{m^*} = \frac{1}{m_0(1 + p^2/m_0^2 E_g)} \quad (11)$$

The third order nonlinear susceptibility is then given by

$$\chi_{\text{app}}^{(3)} = -\frac{cn_0 e^2 \alpha_f \tau_T}{12\pi m_0^2 \omega^2 E_g (1 - i\Delta\omega\tau_T)} \left[\frac{E_g^2}{E_g^2 - (\hbar\omega)^2} \right]^2 \frac{1 + 8E_f/5E_g}{(1 + 4E_f/E_g)^{5/2}} \quad (12)$$

where E_f is the Fermi energy and $\alpha_f = 4\pi Ne^2/m_0^2 \omega^2 cn_0 \tau_T$ is the free carrier absorption coefficient. The second term on the right hand side of Eq. (12) results from resonant enhancement as the laser frequency approaches the band gap.

The third term in Eq. (12) comes from averaging over the carrier velocity distribution. The carriers near the Fermi energy have a larger contribution to the nonlinear process and the average effective mass is quite different from the band-edge value. This effect is important in heavily doped semiconductors.

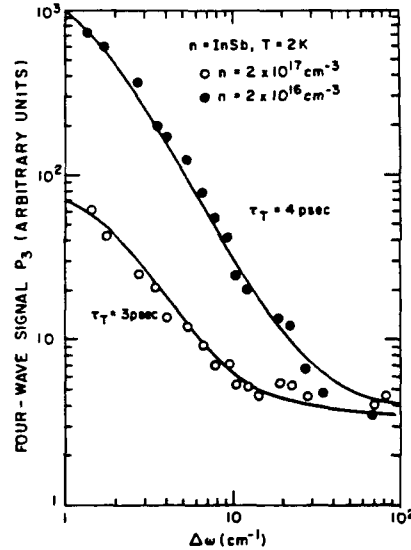


Figure 3. Four-wave mixing signal versus $\Delta\omega$ due to nonparabolicity in the conduction band of n -InSb. The solid curves were generated from Eq.(12) using measured relaxation times

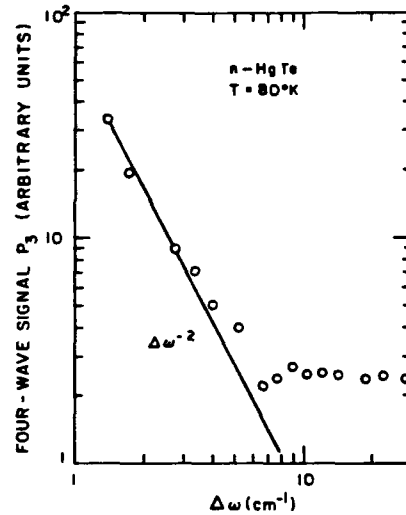


Figure 4. Four-wave mixing signal versus $\Delta\omega$ due to interband transitions in HgTe at 80K. The increase in the four-wave signal at small $\Delta\omega$ is due to thermal population modulation, while the tailing off of the signal at large $\Delta\omega$ is due to direct interband recombination.

We have observed optical nonlinearity due to band nonparabolicity in bulk n -type GaAs, GaSb, HgCdTe, HgMnTe as well as InSb/InAlSb and GaAs/GaAlAs superlattices at temperatures from 2K to 300K. In all our experiments, the relaxation times were on the order of a few picoseconds. This is much shorter than the relaxation times reported using low power transport measurements in InSb. The difference is caused by the fact that in our experiments the electrons

are heated by the laser to 20K to 30K even when immersed in liquid helium. When the electrons are hot, they can relax by the more efficient process of optical phonon emission. Hence the relaxation time is very short.

B INTERBAND TRANSITIONS

In narrow gap semiconductors, optical nonlinearities arising from interband transitions can be driven either directly by the absorption, or indirectly by the modulation of the carrier temperature.

The direct modulation of the carrier populations, commonly known as band filling^{17,18,19,20,21}, is the only important mechanism in materials where the band gap is large compared to the carrier temperature. The nonlinear susceptibility follows immediately from Eq (8).

$$\chi^{(3)} = -\frac{cn_0 e^2 \alpha_i \tau_R}{24\pi\hbar\omega^3 m^* (1 - i\Delta\omega\tau_R)}, \quad (13)$$

where α_i is the interband absorption coefficient and τ_R is the interband recombination time. Band filling effects have been observed in InAs, InSb¹⁷ and HgCdTe.²¹

If the band gap is only somewhat larger than the carrier temperature, then population fluctuations can be driven by the laser heating of the carriers. From Eq (8) we see that

$$\chi^{(3)} = -\frac{cn_0 \alpha \tau_T}{24\pi m^* \omega^2 (1 - i\Delta\omega\tau_T)} \frac{1}{C_v} \frac{\partial N_0}{\partial T}, \quad (14)$$

where α is the total absorption, including both interband and free carrier.

We have observed optical nonlinearities due to both direct and indirect carrier population modulation. Their relative strengths depend on the interband recombination time and the thermal relaxation time.

The variation with signal of the four-wave power in HgTe at 80K (Figure 4) shows the existence of these two processes. At small $\Delta\omega$, the signal increases as $1/(\Delta\omega)^2$. This is caused by the thermally modulated population fluctuations. A degenerate four-wave mixing experiment has allowed us to estimate the momentum relaxation time for this process to be about 5 psec. As $\Delta\omega$ increases, the four-wave signal becomes constant. This indicates the existence of another faster but weaker nonlinear process. We have attributed this to direct interband transitions with a relaxation time of about 0.3 psec.

In superlattices, one could also utilize intersubband transitions to drive optical nonlinearities.⁶ These transitions would be formally very similar to the interband transitions mentioned previously. While intersubband induced nonlinearities have not yet been observed, it is predicted that they should have very large $\chi^{(3)}$'s.

C INTERVALENCE BAND TRANSITIONS

The carrier population distribution can be modulated by intervalence absorption which promotes holes from the heavy-hole to the light-hole band. In this mechanism, the laser is directly modulating the heavy hole N_h and light hole N_l populations such that $\delta N_l = -\delta N_h$. This immediately gives from Eq. (6)

$$\chi^{(3)} = \frac{cn_0 e^2 \alpha_{lh} \tau_{lh}}{24\hbar\omega^2 (1 - i\Delta\omega\tau_{lh})} \left(\frac{1}{m_h} - \frac{1}{m_l} \right), \quad (15)$$

where α_{lh} is the intervalence band absorption and τ_{lh} is the relaxation time from the light to the heavy hole band.

This mechanism has been observed in *p*-type GaAs, Ge and HgCdTe and the measured values for $\chi^{(3)}$ agree well with Eq. (15).

D CARRIER SCATTERING

All of the above mentioned mechanisms are based on the modulation of the real part of the dielectric function. However, if the carrier scattering rate has an energy dependence, then it also can be the basis for a nonlinearity. This mechanism was first proposed by Kaw²², who suggested a case where the scattering rate changes abruptly with energy. We have observed two different mechanisms which are based on impurity levels.

The first mechanism is based on the presence of resonant scattering levels in HgCdSe doped with Fe²⁺.²³ By choosing the proper composition, the impurity levels can be made to lie inside the conduction band.²⁴ We have observed a large optical nonlinearity in a HgCdSe sample with the Fe²⁺ state 73 meV above the conduction-band edge. This nonlinearity was absent in a similar sample where the Fe²⁺ state was located inside the band gap.

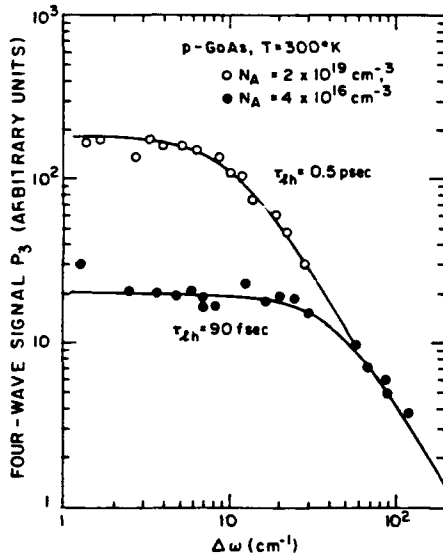


Figure 5. Four-wave signal versus $\Delta\omega$ due to intervalence band transitions in p-GaAs. The solid curves were generated from Eq.(15) using measured relaxation times

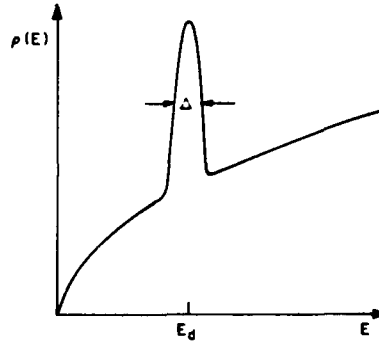


Figure 6. Electronic density of states in a system with a resonant scattering level at $E = E_d$.

A peak in the density of states (Figure 6) is created by the existence of an impurity level inside the conduction band. The electrons experience a huge increase in scattering when they are near E_d . The lasers can create a temperature modulation that drives the electrons in and out of this range. This then causes a modulation in the dielectric function.

Using the Anderson model to calculate the conductivity in the presence of a resonant scattering level, we arrive at

$$\chi_{\text{total}}^{(3)} = i \frac{2cn_0 e^2 \alpha_f \tau_f E_0 \Delta^2}{27\pi^2 m^* \hbar \omega^3 (1 + i\Delta\omega\tau_f)} \left(\frac{E_f + \hbar\omega}{E_f} \right) \left(\frac{\rho(E_f + \hbar\omega)}{\rho(E_f)} \right) \left(\frac{E_d - E_f}{[(E_d - E_f)^2 + \Delta^2]^2} \right). \quad (16)$$

where E_d is the location of the impurity level above the conduction-band edge, Δ is its width and $\rho(E)$ is the band density of states of energy E . We can obtain a theoretical value for $\chi^{(3)}$ by fitting the theoretical absorption with the measured absorption. This gives us $\Delta = 12\text{ meV}$ and $\chi^{(3)} = 6 \times 10^{-7}$ esu. This agrees well with the measured value of 1×10^{-6} esu in the $\text{Hg}_{0.77}\text{Cd}_{0.23}\text{Se:Fe}$ sample.

The second nonlinear mechanism based on the modulation of carrier scattering was observed in $n\text{-Si:P}$. Si is normally regarded as a very linear material. However, as the doping density was increased through the metal-insulator transition, we observed a peak in the optical nonlinear susceptibility per carrier.²⁶ The variation of $\chi^{(3)}$ per carrier with doping density is nearly quadratic. This is consistent with a scattering mechanism where there is an excitation of an electron from a localized state (i.e. one strongly influenced by the impurity) to a delocalized state (i.e. one weakly influenced by the impurity).

5 HETEROSTRUCTURE EFFECTS

All of the above data is from bulk semiconductors and uniformly grown epilayers. As such, the magnitude of the effects are limited by the natural material characteristics. Superlattices allow more freedom to design the crystal band structure in such a way as to maximize nonlinearities. The mechanisms at work in a superlattice are essentially the same as those discussed in Section 4. The only new mechanism is intersubband transitions. Intersubband transitions are of the same character as the interband transitions. The only modification needed is that in Eq. (13) α must now refer to the intersubband absorption and τ is the intersubband recombination time. The real difference lies in the fact that we can to some extent tailor the crystal bandstructure to suit our needs.

Currently, we are exploring the enhancement of several different nonlinear processes in narrow band gap superlattices. An enhancement in the nonparabolicity nonlinearity has been observed in an InSb/InAlSb and a HgTe/HgCdTe superlattice.

We also report here for the first time an enhancement of the nonlinearity in thin, n -type epilayers. In n -type GaAs and InSb epilayers we have observed a $\chi^{(3)}$ 10 to 50 times larger than that found in bulk samples of comparable doping levels.

A ENHANCEMENT OF NONPARABOLICITY

The nonparabolicity of the energy bands in superlattices can be increased over that found in the constituent bulk materials. The coupling between the light and the carriers is given by the matrix element $\mathbf{p} \cdot \mathbf{A}$ where \mathbf{A} is the vector potential of the light and \mathbf{p} is the momentum of the electron. Clearly, any enhancement due to the superlattice modification of the band structure will only be observed for light polarized in the superlattice growth direction. Light polarized parallel to the superlattice layers will only probe the bulk bands of the various layers.²⁶ Hence, to observe the enhancements in $\chi^{(3)}$ due to the superlattice structure, a technique different from that used for bulk samples must be used.

In order to observe the effects of superlattice structure, the incident light must have a substantial polarization component along the growth direction. One method that we have used to achieve this is end firing. With end firing, the light is brought in along the edge of the superlattice. This technique allows all of the light to be polarized along the growth direction and potentially gives very long interaction lengths. It is also quite convenient to rotate the polarization and thereby compare the superlattice structure to the bulk structure. Unfortunately, since it is difficult to cleave a sample much narrower than 1 mm, this configuration will not work if the absorption coefficient of the superlattice is much larger than about 10 cm^{-1} .

In order to calculate the enhancement in $\chi^{(3)}$, one must take into account the anisotropy of both the nonlinear mechanism and the absorption. For the case where nonparabolicity is the dominant mechanism

$$\chi^{(3)} = \frac{d}{dT} \left(\frac{1}{m} \right) \Delta T, \quad (17)$$

where ΔT is the laser-induced carrier temperature modulation.²⁷ In the superlattice,

$$\Delta T \sim (\alpha_x \cos^2 \theta + \alpha_y \sin^2 \theta), \quad (18)$$

where θ is the polarization angle and α_i is the absorption coefficient for i-polarized light. This gives us the four-wave power as a function of θ

$$P(\omega_s, \theta) \sim \left\{ \left[\frac{d}{dT} \left(\frac{1}{m_z} \right) (\alpha_z \cos^2 \theta + \alpha_x \sin^2 \theta) \cos \theta \right]^2 + \left[\frac{d}{dT} \left(\frac{1}{m_z} \right) (\alpha_z \cos^2 \theta + \alpha_x \sin^2 \theta) \sin \theta \right]^2 \right\}. \quad (19)$$

Fitting this to the data showing four-wave power as a function of θ allows us to estimate the enhancement of both $\chi^{(3)}$ and α due to subband structures in the growth direction. We find that the enhanced $\chi^{(3)}$ is approximately 8.5×10^{-6} , or 7.7 times the bulk value, and that α_z about 3.8 times α_x .

The absorption of the superlattice was small enough that we were able to observe the anisotropy of $\chi^{(3)}$ by using the end firing technique. Figure 7 shows the variation of $\chi^{(3)}$ with angle θ , where $\theta = 0$ means that the incident light is completely polarized along the superlattice growth direction.

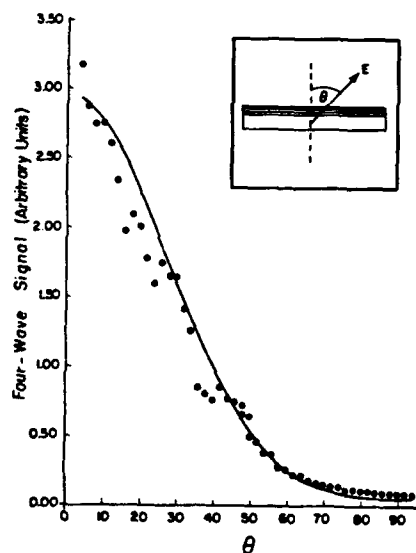


Fig. 7. Four-wave signal vs. polarization angle for the InAlSb superlattice. 0 is normal to the plane of the superlattice. The signal is normalized to account for the loss from the linear polarizer used to rotate the polarization. The theoretical result from (19) also is plotted.

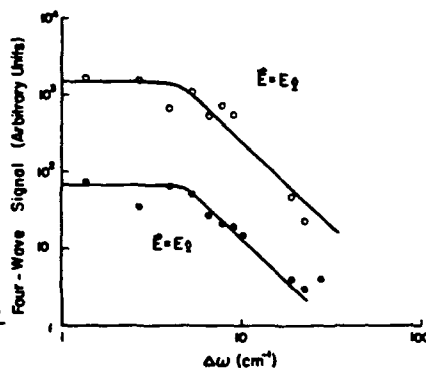


Fig. 8. Four-wave signal vs. difference frequency for the InAlSb superlattice with polarization normal and parallel to the plane of the superlattice.

The AlInSb/InSb superlattice we studied consists of 50 periods, each with 45 Å of InSb and 60 Å of $\text{Al}_{0.08}\text{In}_{0.92}\text{Sb}$. The sample is not intentionally doped, but contained on the order of $10^{16}/\text{cc}$ thermally excited carriers.

In order to definitively determine the nonlinear mechanism responsible for the enhancement, we measured the four-wave signal for the two orthogonal polarizations. We observed a well defined roll-off at $\Delta\omega=10\text{ cm}^{-1}$, corresponding to an energy relaxation time of 0.5 ps for the nonparabolicity mechanism in the bulk direction. The polarization of the light was then switched to the superlattice growth direction which displayed a roll-off nearly identical to that found for the bulk direction (see Figure 8). The similarity of the relaxation times for the two different polarizations strongly suggests that the enhanced nonlinear signal is caused by the greater nonparabolicity of the subbands in the superlattice direction and possibly by greater absorption in the superlattice direction.

Similar enhancements in the nonparabolicity have also been observed in HgTe/HgCdTe superlattices.

B EPILAYER ENHANCEMENT

We have measured the value for $\chi^{(3)}$ in *n*-GaAs and *n*-InSb epilayer and found an enhancement of 20 to 50 times over that found in the bulk. In these cases, it appears that the thickness of the nonlinear medium affects the nonlinear signal. The figure of merit for these samples is among the highest we have ever observed. The measured values of $\chi^{(3)} = 4 \times 10^{-6}$ esu $\alpha = 30\text{ cm}^{-1}$ and $\tau = 1\text{ psec}$ give a figure of merit of $\chi^{(3)}/\alpha\tau = 1 \times 10^5$. This compares very favorably with the other figures we have observed in the processes shown in Table I.

In GaAs we have measured this for a series of doping levels, and found that the enhancement seems to peak at $n_D \approx 2 \times 10^{18}\text{ cm}^{-3}$. A similar though somewhat smaller enhancement has also been observed in InSb epilayers.

ACKNOWLEDGEMENTS

This research was supported by the National Science Foundation (grant EET-8718417), the Naval Research Laboratory (contract N00014-87-K-2031) and the U.S. Office of Naval Research (contract N00014-86-K-0760). The Francis Bitter National Magnet Laboratory is supported by the National Science Foundation.

(a) Also with the Department of Physics, Massachusetts Institute of Technology.

(b) Current address: NEC Research Institute, 4 Independence Way, Princeton, NJ 08540.

REFERENCES

1. C.K.N. Patel, R.E. Slusher and P.A. Fleury, Phys. Rev. Lett. 17, 1011 (1966).
2. P.A. Wolff and G.A. Pearson, Phys. Rev. Lett. 17, 1015 (1966).
3. D. Walrod, S.Y. Auyang, P.A. Wolff, Appl. Rev. Lett. (to be published Jan. 1990).
4. S.Y. Auyang, P.A. Wolff, K.A. Harris, J.W. Cook, Jr. and J.F. Schetzina, J. Vac. Sci. Technol. A6, 2693 (1988).
5. P.A. Wolff, S.Y. Yuen, K.A. Harris, J.W. Cook, Jr. and J.F. Schetzina, Appl. Phys. Lett. 50, 1858 (1987).
6. S.Y. Yuen, Appl. Phys. Lett. 43, 479 (1983).
7. S.Y. Yuen, P.A. Wolff and R. Ram-Mohan, Solid State Commun. 56, 485 (1985).
8. D.A.B. Miller, D.S. Chemla, D.J. Eilenberger, P.W. Smith, A.G. Gossard and W. Wiegmann, Appl. Phys. Lett. 42, 925 (1983).
9. P.D. Maker and R.W. Terhune, Phys. Rev. 137, A801 (1965).
10. S.Y. Yuen and P.A. Wolff, Appl. Phys. Lett. 40, 457 (1982).
11. J.J. Wynn and G.D. Boyd, Appl. Phys. Lett. 12, 191 (1968); J.J. Wynn, Phys. Rev. 178, 1295 (1969).

12. D.E. Watkins, C.R. Phipps, Jr., and S.J. Thomas, *Opt. Lett.* **5**, 248 (1980).
13. S.S. Jha and N. Bloembergen, *Phys. Rev.* **171**, 891 (1968).
14. A. Yariv and D.M. Pepper, *Opt. Lett.* **1**, 16 (1977).
15. M.A. Khan, P.W. Kruse and J.F. Ready, *Opt. Lett.* **5**, 261 (1980).
16. E.O. Kane, *J. Phys. Chem. Solids* **1**, 249 (1957).
17. D.A.B. Miller, C.T. Seaton, M.E. Prise and S.D. Smith, *Phys. Rev. Lett.* **47**, 197 (1981).
18. D.A.B. Miller, S.D. Smith and A.M. Johnston, *Appl. Phys. Lett.* **35**, 658 (1979).
19. M.A. Khan, R.L.H. Bennet and P.W. Kruse, *Opt. Lett.* **6**, 560 (1981).
20. S.Y. Yuen and P. Becla, *Opt. Lett.* **8**, 356 (1983).
21. A. Miller, G. Parry and R. Daley, *IEEE J. Quantum Electron.* **QE-20**, 710 (1984).
22. P. Kaw, *Phys. Rev. Lett.* **21**, 539 (1968).
23. P.A. Wolff, S.Y. Auyang, R.R. Galazka and A. Mycielski, *J. Vac. Sci. Technol.*, **A6**, 2696 (1988).
24. A. Mycielski, P. Dzwonkowski, B. Kowalski, B.A. Orlowski, M. Dobrowolska, M. Arciszewska, W. Dobrowolski and J.M. Baranowski, *J. Phys. C* **19**, 3605 (1986).
25. P.A. Wolff, S.Y. Yuen and G.A. Thomas, *Solid State Commun.* **60**, 645 (1985).
26. G. Bastard, *Phys. Rev.* **25**, 7584 (1982).
27. S.Y. Auyang and P.A. Wolff, *J. Opt. Soc. Am. B*, Vol. **6**, No. **4**, 595 (1989).

NARROW-GAP NONLINEAR OPTICAL MATERIALS

E. R. YOUNGDALE, C. A. HOFFMAN, J. R. MEYER, AND F. J. BARTOLI
Naval Research Laboratory, Washington, D.C. 20375

J. W. HAN, J. W. COOK JR., AND J. F. SCHETZINA
North Carolina State University, Raleigh, NC

A. MARTINEZ
Naval Surface Weapons Center, Silver Spring, MD

ABSTRACT

We report an experimental study of the nonlinear optical properties of HgTe-CdTe superlattices grown by MBE and $\text{Pb}_{1-x}\text{Sn}_x\text{Se}$ grown by hot wall epitaxy. Nondegenerate four-wave mixing has been employed to measure third-order nonlinear susceptibilities at $10.6\text{ }\mu\text{m}$ as a function of temperature, laser intensity, and difference frequency. The nonlinearity is believed to be due to modulation of the free carrier temperature and density by the optical beams. The HgTe-CdTe results are compared to theoretical calculations based on free carrier contributions to the susceptibility, and the agreement with experiment is quite good. In $1\text{-}\mu\text{m}$ -thick $\text{Pb}_{1-x}\text{Sn}_x\text{Se}$ layers, multiple internal reflections of the light within the sample is found to enhance the nonlinear signal by an order of magnitude.

INTRODUCTION

It has recently been demonstrated that semimetallic Hg-based semiconductors such as HgTe,[1] $\text{Hg}_{0.16}\text{Cd}_{0.84}\text{Te}$ [2] and HgTe-CdTe superlattices[3] have highly attractive nonlinear optical properties which combine the advantages of large $\chi^{(3)}$, picosecond response, and high saturation threshold. Here we report an experimental and theoretical investigation of semiconducting HgTe-CdTe superlattices with energy gaps between 35 and 80 meV. We also discuss the first study of carrier-generation nonlinearities in $\text{Pb}_{1-x}\text{Sn}_x\text{Se}$ alloy layers. Besides having large nonlinear optical coefficients, growth of that material on BaF_2 substrates is demonstrated to lead to the opportunity for significant Fabry-Perot enhancement of the nonlinear response.

THEORETICAL

The magnitude of the four-wave signal P_3 is related to the third-order nonlinear susceptibility $\chi^{(3)}$ by the relation

$$P_3(\omega_3) \sim \left| \chi^{(3)}(\Delta\omega) \right|^2 P_1^2 P_2 \quad (1)$$

where P_1 and P_2 represent the intensities of the beams at frequencies ω_1 and ω_2 , respectively, $\omega_3 = 2\omega_1 - \omega_2$ is the frequency of the four-wave signal, and $\Delta\omega \equiv \omega_1 - \omega_2$ is the difference frequency. Optical nonlinearities result from a modulation at the difference frequency of the free-carrier contribution to the dielectric constant. The $\chi^{(3)}$ associated with modulation of the free carrier density may be written[1, 3]

$$\chi^{(3)} = \frac{\eta c e^2 f \alpha}{24 \pi m_n \hbar \omega^3} \sum_k \frac{Q_k \tau_k}{(1 + i \Delta\omega \tau_k)}, \quad (2)$$

Sample	d_W/d_B (Å/Å)	t (μm)	E_g^0 (meV)	T (K)	τ (ps)	$\chi_{\text{exp}}^{(3)}$ (esu)	$\chi_{\text{theory}}^{(3)}$ (esu)
<u>HgTe-CdTe Superlattices</u>							
BMCCT16	78/29	2.1	0	300	> 3	4.1×10^{-5}	3.4×10^{-5}
BMCCT18	61/39	2.0	35	8	1.4	1.2×10^{-5}	1.5×10^{-5}
BMCCT17	58/45	2.0	54	8	0.8	8.7×10^{-6}	7.5×10^{-6}
BMCCT21	55/49	2.1	80	8	1.1	7.5×10^{-6}	5.4×10^{-6}
<u>Pb_{1-x}Sn_xSe</u>							
89-44-I	$x = 0.20$	1.0	≈ -50	300	> 3	2.2×10^{-4}	

where η is the index of refraction, c is the speed of light, f is a resonant enhancement factor,[1] α is the absorption coefficient, and m_n is the electron effective mass (hole contributions are usually much smaller). The summation is over carrier generation mechanisms, and τ_k is the relaxation time for a given process. For example, in the case of photoexcitation across the forbidden gap τ would be the excess carrier recombination time, while for intrinsic electron generation due to optical heating of the free carrier plasma τ is the energy relaxation time. In analyzing the data for HgTe-CdTe superlattices, it has been assumed that the dominant mechanism is carrier heating as it is in semimetallic Hg-based materials studied previously.[1, 2, 3] Equation (2) has then been used in conjunction with a detailed modeling of the electron density and free carrier specific heat as functions of the laser intensity and carrier temperature,[3] where experimental magneto-transport results on the same superlattices[4] have been incorporated. A detailed description of the theory will be provided elsewhere.

EXPERIMENTAL

Nonlinear optical coefficients have been determined for a series of HgTe-CdTe superlattices grown by molecular beam epitaxy (MBE) on [100] CdTe substrates. The well and barrier thicknesses listed in Table 1 are such that the low-temperature energy gaps varied between 0 to 80 meV at $T = 0$ K. Measurements have also been performed on a Pb_{0.80}Sn_{0.20}Se alloy layer grown by hot wall epitaxy (HWE) on a [111] BaF₂ substrate. Total film thicknesses for each sample are listed in Table 1. The electrical properties for the superlattices are documented in detail elsewhere,[4] and the Pb_{1-x}Sn_xSe sample was p -type with $p \approx 7 \times 10^{17} \text{ cm}^{-3}$ and $\mu_p \approx 3 \times 10^4 \text{ cm}^2/\text{Vs}$ at low temperatures.

The experimental arrangement for the nonlinear optical measurements has been described elsewhere.[3] The sample was excited using two synchronously Q-switched CO₂ lasers, which were grating-tuned to frequencies ω_1 and ω_2 . The excitation generated a nonlinear optical signal at the mixing frequencies $\omega_3 = 2\omega_1 - \omega_2$ and $\omega_4 = 2\omega_2 - \omega_1$, and a 0.85-m double monochromator was used to discriminate the mixing signal from the transmitted pump beams. The intensity of the mixing signal was measured using a Hg_{1-x}Cd_xTe detector at 77 K.

The magnitude of $\chi^{(3)}$ can be determined by comparing the the signal from the sample to that from a piece of optical-grade germanium ($\chi^{(3)} \approx 1.0 \times 10^{-10} \text{ esu}$ [5]), and making the appropriate corrections for sample thickness, index of refraction, optical

absorption, and surface reflection losses. When measurements were made on Hg-based samples, the back surface of the substrate was roughened in order to minimize the effects of multiple internal reflections. This technique is effective because the reflectivity at the sample/substrate boundary is fairly low due to the similar indices of refraction of the two materials. In the case of the $\text{Pb}_{1-x}\text{Sn}_x\text{Se}$, however, only a small fraction of the light is actually reflected from the back surface due to the relatively low index of refraction of the BaF_2 substrate. The $\text{Pb}_{1-x}\text{Sn}_x\text{Se}$ itself has a large index of refraction (≈ 5.2 [6]), meaning that both the front surface and the interface with the substrate have high reflectivities. Furthermore, the round-trip optical path length for light within the $1\text{-}\mu\text{m}$ -thick sample is $10.4\text{ }\mu\text{m}$, which is quite close to the laser wavelength of $10.6\text{ }\mu\text{m}$. There should thus be constructive interference of the internally-reflected light, i.e., the internal electromagnetic fields are strongly amplified by the effective presence of a Fabry-Perot etalon cavity. In the Appendix, we briefly summarize the derivation of the expected correction factor by which the apparent value of $\chi^{(3)}$ obtained from the experiment should be larger than the actual value obtained after correction for etalon effects. Results for $\chi^{(3)}$ reported below will refer to the actual value after correction.

We take the absorption coefficient for the $\text{Pb}_{1-x}\text{Sn}_x\text{Se}$ sample to be 3400 cm^{-1} which is based on the measured transmission at 300 K. Using this value and the index of refraction cited above, the etalon enhancement factor of $\chi^{(3)}$ at $10.6\text{ }\mu\text{m}$ is estimated to be ≈ 3.6 . From Eq. (1) we see that the nonlinear optical signal is amplified by $(3.6)^2$, more than an order of magnitude over what it would have been had there been no etalon effect. (The apparent $\chi^{(3)}$ is larger than the actual $\chi^{(3)}$ because we are at the transmission peak of the etalon. At a transmission minimum the apparent $\chi^{(3)}$ would be smaller than the actual $\chi^{(3)}$).

RESULTS

Figure 1 shows the dependence of the third-order nonlinear susceptibility on temperature for two different samples, HgTe-CdTe superlattice BMCCT21 and the $\text{Pb}_{1-x}\text{Sn}_x\text{Se}$ alloy layer. The dramatic decrease of the superlattice $\chi^{(3)}$ above $T \approx 65\text{ K}$ is clearly due to the temperature shift of the energy gap. A theoretical calculation of the band structure for the appropriate well and barrier thicknesses[4] yields that $\hbar\omega < E_g$ for $T > 140\text{ K}$, which is in good agreement with the experimental temperature beyond which the nonlinear signal becomes too weak to be detectable. For $\text{Pb}_{1-x}\text{Sn}_x\text{Se}$, the $\chi^{(3)}$ shown is the actual value obtained following the correction for etalon enhancement. Since the energy gap in $\text{Pb}_{0.8}\text{Sn}_{0.2}\text{Se}$ is no greater than 100 meV for any $T < 300\text{ K}$,[7] it is not surprising that the temperature dependence is much weaker for that sample.

Figure 2 shows $\chi^{(3)}$ as a function of laser power within the material for the same two samples. The nonlinearity for HgTe-CdTe at an initial temperature of 8 K saturates somewhat due to laser heating of the sample, i.e., the lattice temperature increases to the point where the laser light is no longer strongly absorbed (see Fig. 1). The curve represents the results of a calculation which has no adjustable parameters, since input electronic properties have been obtained from magneto-transport measurements on the same superlattice.[4] The agreement between theory and experiment is seen to be remarkably good. The nonlinearity for $\text{Pb}_{0.8}\text{Sn}_{0.2}\text{Se}$ at 300 K also saturates somewhat, possibly because of a similar shift of the energy gap due to laser heating (at 300 K , a relatively modest temperature shift would move the gap beyond the photon energy). However, for that material a more detailed analysis is required to verify the interpretation.

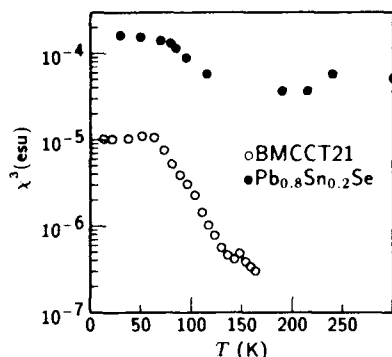


Figure 1 (above). $\chi^{(3)}(\Delta\omega = 1.8 \text{ cm}^{-1})$ vs sample temperature for HgTe-CdTe superlattice BMCCT21 ($E_g^0 = 80 \text{ meV}$) and the $\text{Pb}_{1-x}\text{Sn}_x\text{Se}$ alloy layer.

Figure 2 (above right). $\chi^{(3)}(\Delta\omega = 1.8 \text{ cm}^{-1})$ vs laser intensity for the same two samples. The points are experimental and the curve is theoretical.

Figure 3 (right). $\chi^{(3)}$ vs $\Delta\omega$ for the same two samples. The laser powers were 1 MW/cm^2 for the HgTe-CdTe and 200 kW/cm^2 for the $\text{Pb}_{1-x}\text{Sn}_x\text{Se}$. The points are experimental and the curves represent fits to Eq. (2).

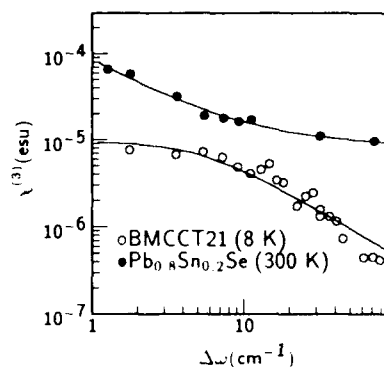
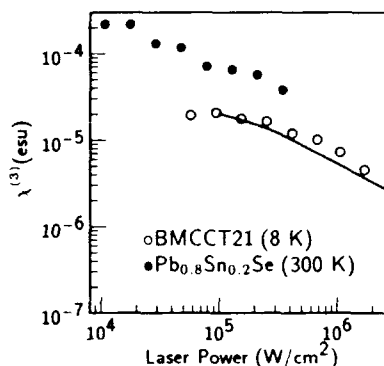


Figure 3 shows the dependence of $\chi^{(3)}$ on $\Delta\omega$ for the same two samples. For the HgTe-CdTe superlattice, $\chi^{(3)}$ is inversely proportional to $\Delta\omega$ at large $\Delta\omega$ but becomes constant at small $\Delta\omega$. The solid curve shows a fit to Eq. (2), which yields a relaxation time of 1.1 ps. By contrast, the data for the $\text{Pb}_{1-x}\text{Sn}_x\text{Se}$ sample is nearly constant at large $\Delta\omega$ but shows a $1/\Delta\omega$ dependence at smaller $\Delta\omega$. This apparently indicates the presence of two different nonlinear mechanisms which have different relaxation times [see Eq. (2)]. A fit to the data yields $\tau_1 < 70 \text{ fs}$ and $\tau_2 > 3 \text{ ps}$. Until a more complete study has been carried out, we defer speculation concerning the identity of these mechanisms.

Table 1 summarizes the nonlinear optical coefficients of four different HgTe-CdTe superlattices with a range of energy gaps as well as results for the $\text{Pb}_{1-x}\text{Sn}_x\text{Se}$ alloy layer. For the HgTe-CdTe, $\chi^{(3)}$ monotonically decreases with increasing energy gap. The theoretical calculation accurately reproduces this trend, which is due primarily to the inverse dependence of $\chi^{(3)}$ on electron effective mass [see Eq. (2)]. The nonlinearity for $\text{Pb}_{1-x}\text{Sn}_x\text{Se}$ exceeds those of the superlattices, and is in fact among the highest reported for fast processes in narrow-gap semiconductors.[2] Etalon enhancement effects further increase the achievable nonlinear optical signal over the base level one predicts using the "actual" $\chi^{(3)}$ from the Table.

CONCLUSIONS

In summary, nonlinear optical coefficients have been determined from non-degenerate four wave mixing measurements on a series of HgTe-CdTe superlattices as well as a $\text{Pb}_{1-x}\text{Sn}_x\text{Se}$ alloy layer. The superlattice results are accurately reproduced by a theory which contains no adjustable parameters. Although the nonlinearity for finite-gap samples are found to saturate at high laser powers, $\chi^{(3)}$'s in zero-gap samples show no evidence for saturation at powers up to 2 MW/cm^2 . [3] The results for $\text{Pb}_{1-x}\text{Sn}_x\text{Se}$ are significant in that the magnitude of the nonlinearity is quite high. There is evidence for two nonlinear optical mechanisms, one much faster than the other, and etalon enhancement further increases the nonlinear response. These results demonstrate that free carrier nonlinear optical processes in narrow-gap IV-VI materials should be investigated further.

This research was supported by SDIO/IST and managed by NRL.

APPENDIX

Calculation of the actual $\chi^{(3)}$ in an etalon is a two step process: we calculate an apparent $\chi^{(3)}$ by assuming that the reflected light plays no role in the nonlinear optical generation, and then a correction factor is determined to account for the etalon effects. The correction term itself consists of two factors, a correction for the electric field strength of each pump beam, and a correction for the nonlinear beam.

The correction factor for the pump field strength can be found by summing an infinite series corresponding to each pass of the beam. One obtains[8]

$$F_1 = \frac{1}{1 - r_1 r_2 e^{(-\alpha_1 + 2ik_1)L}} \quad (3)$$

where $r_j = \sqrt{R_j}$, R_j is the reflectivity for surface j , α_i and k_i are the absorption coefficient and propagation constant at frequency ω_i , and L is the sample thickness. Note that this term becomes unity in the limit of no internal reflection, since reflection losses at the surfaces and absorption losses due to the first pass through the sample have already been taken into account in the calculation for the apparent $\chi^{(3)}$.

The correction factor for the nonlinear beam can be found by breaking the field at frequency ω_3 into two components, a beam traveling from left to right (\vec{E}_{3r}) and a beam traveling from right to left (\vec{E}_{3l}). For definiteness, we take the incident pump beams to be traveling rightward. The equations obeyed by these field intensities are as follows:

$$\vec{E}_{3r}(\vec{r}, L) = \vec{E}_{3r}(\vec{r}, 0)e^{-\alpha_3 L/2} e^{ik_3 L} + K \vec{E}_{1r}^2(\vec{r}, 0) \vec{E}_{2r}^*(\vec{r}, 0) \quad (4)$$

$$\vec{E}_{3l}(\vec{r}, 0) = \vec{E}_{3l}(\vec{r}, L)e^{-\alpha_3 L/2} e^{ik_3 L} + K \vec{E}_{1l}^2(\vec{r}, L) \vec{E}_{2l}^*(\vec{r}, L) \quad (5)$$

$$\vec{E}_{3l}(\vec{r}, L) = r_2 \vec{E}_{3r}(\vec{r}, L) \quad (6)$$

$$\vec{E}_{3r}(\vec{r}, 0) = r_1 \vec{E}_{3l}(\vec{r}, 0), \quad (7)$$

where K is the nonlinear optical gain including absorption losses due to a single pass. The leftward and rightward pump beam fields must satisfy the relation

$$\vec{E}_{1l}^2(\vec{r}, L) \vec{E}_{2l}^*(\vec{r}, L) = \vec{E}_{1r}^2(\vec{r}, 0) \vec{E}_{2r}^*(\vec{r}, 0) (r_2)^3 e^{-(2\alpha_1 + \alpha_2)L/2} e^{ik_3 n_3 L} \quad (8)$$

since there must be one pass through the sample and a reflection before there is a leftward pump beam. Equations (4-8) can be solved for electric field of the nonlinear beam just

before it exits the sample,

$$\vec{E}_3(\vec{r}, L) = K \vec{E}_1^2(\vec{r}, 0) \vec{E}_2^*(\vec{r}, 0) \left\{ \frac{1 + r_1 r_2^3 e^{(-\alpha_3/2 - \alpha_1 - \alpha_2/2 + 2ik_3 n_3)L}}{1 - r_1 r_2 e^{(-\alpha_3 + 2ik_3 n_3)L}} \right\} \quad (9)$$

If there are no multiple internal reflections [$r_1 r_2 e^{-\alpha_3 L} \rightarrow 0$], then the term in brackets becomes unity and we obtain the required result for the electric field of the nonlinear beam corresponding to the apparent $\chi^{(3)}$: $\vec{E}_3(\vec{r}, L) = K \vec{E}_1^2(\vec{r}, 0) \vec{E}_2^*(\vec{r}, 0)$. The correction factor for the nonlinear beam is thus the bracketed term in Eq. (9), and the total correction factor is given by

$$C_\chi = F_1^2 F_2 \times \left\{ \frac{1 + r_1 r_2^3 e^{(-\alpha_3/2 - \alpha_1 - \alpha_2/2 + 2ik_3 n_3)L}}{1 - r_1 r_2 e^{(-\alpha_3 + 2ik_3 n_3)L}} \right\} \quad (10)$$

REFERENCES

1. P. A. Wolff, S. Y. Yuen, K. A. Harris, Jr., J. W. Cook, and J. F. Schetzina. Appl. Phys. Lett. **50**, 1858, (1987).
2. S. Y. Auyang, P. A. Wolff, K. A. Harris, Jr., J. W. Cook, and J. F. Schetzina. J. Vac. Sci. Technol. A. **6**, 2693, (1988).
3. E. R. Youngdale, C. A. Hoffman, J. R. Meyer, F. J. Bartoli, X. Chu, J. P. Faurie, J. W. Han, J. W. Cook, Jr., and J. F. Schetzina. J. Vac. Sci. Technol. A. **7**, 365, (1989).
4. C. A. Hoffman, J. R. Meyer, F. J. Bartoli, J. W. Han, J. W. Cook, Jr., J. F. Schetzina, and J. N. Schulman, Phys. Rev. B **39**, 5208 (1989).
5. J. J. Wynne. Phys. Rev. **178**, 1295, (1969).
6. Y. Shani, R. Rosman, and A. Katzir. IEEE Jour. Quantum Electronics. **QE-21**(1), 51, (1985).
7. G. Nimtz and B. Schlicht. Springer Tracts in Modern Physics. **98**, 1, (1983).
8. M. Born and E. Wolf, *Principles of Optics*, 2nd edition, (MacMillan, New York, 1964), Section 7.6.

TRANSPORT PROPERTIES OF NARROW GAP II-VI SUPERLATTICES

C. A. HOFFMAN, J. R. MEYER, AND F. J. BARTOLI
 Naval Research Laboratory, Washington, D. C. 20375

ABSTRACT

The present understanding of the carrier transport properties in Hg-based superlattices such as the HgTe-CdTe system is reviewed. Novel features in the calculated superlattice band structures and their implications for macroscopic transport properties are discussed. Nearly all of the main experimental results are qualitatively consistent with a large valence band offset, but are difficult to explain if the offset is small. The valence band offset controversy thus appears to have been largely resolved.

INTRODUCTION

Impressive advances have been made in the fabrication of narrow-gap II-VI heterostructures since the first successful MBE growth of a HgTe-CdTe superlattice in 1982.[1] Significant strides have been made experimentally and theoretically toward the development of a fundamental understanding of their properties.[2, 3] It is now apparent that the band structures of these superlattices exhibit unique features that are distinct from those found in either Hg-based alloys or in wide-gap superlattices. These have led to the observation of a number of novel phenomena.

Only two years ago there was no clear picture of the relation between the predictions of band structure theory and the results of experimental studies. Several intriguing observations, such as extremely high superlattice hole mobilities,[4] were unexplained except for the vague suggestion that they may be related to some special property of the Type-III interface states. Early magneto-optical investigations[5] reported a valence band offset Δ of 40 meV, in sharp disagreement with x-ray photoemission experiments[6, 7] which yielded $\Delta \approx 350$ meV. Several *a priori* calculations also tended to support a larger value for Δ . [8] It will be seen in the following sections that most of the principle experimental results can now be understood qualitatively in terms of theoretical dispersion relations which are sensitive to Δ . It will be argued that the long-standing controversy concerning the valence band offset has effectively been resolved in favor of a large value.

The unique nature of narrow gap HgTe-CdTe superlattice band structures makes them attractive for a variety of electronic and electro-optical applications. Indeed, promising infrared applications of these superlattices were discussed theoretically as early as 1979.[9] However, to assess the ultimate potential, a thorough understanding of their fundamental properties is required. In this paper, we review recent advances in the understanding of HgTe-CdTe and related superlattices. Section 2 summarizes theoretical results for the superlattice band structure, including its strong dependence on valence band offset. In Section 3, recent magneto-transport data are reviewed and correlated with the predictions of band structure theory.

BAND STRUCTURE THEORY

Theoretical investigations of the HgTe-CdTe superlattice band structure have been discussed in previous reviews.[2, 3] Many of the treatments include strain effects.[10]

which are significant despite the close lattice match between HgTe and CdTe. Magnetic fields parallel to the growth direction are also easily incorporated when the $k \cdot p$ approach is used.[11-14] In general the results appear to be relatively independent of the method employed, as long as the formalism is sufficiently detailed. For example, it has been explicitly demonstrated that the transfer-matrix $k \cdot p$ algorithm of Ram-Mohan et al.[11] generates band structures which are in good qualitative and quantitative agreement with those obtained from the multi-band tight-binding calculation of Schulman and Chang.[12] Nonetheless, even though adequate formalisms have been available for several years, many of the most significant implications of the theory had not been fully appreciated until recently.

In summarizing the primary results of the calculations, we first briefly outline how the energies of the dominant bands vary with superlattice parameters, such as well and barrier thickness, strain, and valence band offset.[13] It is well known that if the well thickness d_W is relatively thin, quantum confinement causes there to be a sizable energy gap E_g between the lowest-order electron-like band, E1, and the lowest-order hole-like bands HH1 and LH1. Here we temporarily set the valence band offset and strain to zero, so that there is nothing to lift the degeneracy of the two hole bands at the zone center. This band structure is quite similar to that of semiconducting $\text{Hg}_{1-x}\text{Cd}_x\text{Te}$ ($x \geq 0.16$), except for the additional presence of a series of zone-folded heavy hole bands, HH2, HH3, etc. If we next increase d_W and weaken the quantum confinement, E_g shrinks until at some point E1 meets HH1 and LH1 at the Γ -point. For still larger d_W the energy gap becomes negative and the two light-carrier bands invert, with LH1 becoming a conduction band and E1 a valence band as in semimetallic $\text{Hg}_{1-x}\text{Cd}_x\text{Te}$ ($x \leq 0.16$). However, in this region E1 continues to respond to reductions in the quantum confinement by moving down like an electron band rather than up like a hole band. Similarly, even though LH1 is now a conduction band it is unaffected by quantum confinement as long as there is no valence band offset. We also note that as in $\text{Hg}_{1-x}\text{Cd}_x\text{Te}$, the in-plane effective masses for both E1 and the lighter of the two hole bands is approximately proportional to $|E_g|$. The effect of tuning d_W in the superlattice is thus seen to be quite analogous to that of varying the composition x in the $\text{Hg}_{1-x}\text{Cd}_x\text{Te}$ alloy system, even though the physical mechanisms are often different in the two cases.

We next introduce strain and a valence band offset, whose effects are superimposed on the variation with d_W discussed above. For a well thickness such that there is a small positive energy gap, Fig. 1 shows the results of leaving the valence band offset small ($\Delta = 40$ meV) but including strain. Because the lattice constant of CdTe is 0.3% larger than that of HgTe, strain in the superlattice has the effect of moving the LH1 band to higher energies with respect to the HH1 band.[10] Figure 1 also illustrates an important aspect of the mass anisotropy of the two hole bands.[10] Whereas E1 has a light effective mass both in the plane (k_x) and in the growth direction (k_z), LH1 has a light mass only in the growth direction, i.e., $m_{Lx} \gg m_{Lz}$. Conversely HH1, which is nearly dispersionless in the growth direction, has an in-plane mass which mirrors that of the electrons ($m_{hx} \approx m_{ex} \ll m_{hz}$). This complementarity between light (heavy) mass along one axis vs heavy (light) mass in the transverse direction occurs not only in superlattices but in any zincblende or diamond structure semiconductor with a uniaxial perturbation.[14] Clearly, any measurable property which depends on the effective mass of free holes along either axis will be extremely sensitive to whether LH1 or HH1 is the

uppermost valence band.

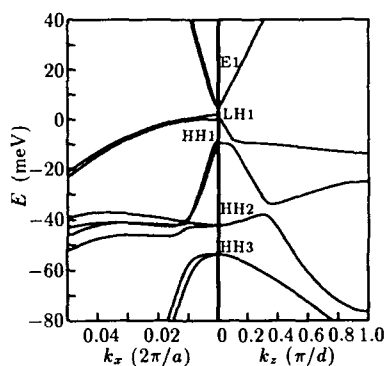


Figure 1. In-plane and growth-direction dispersion relations for a [100] HgTe-Hg_{0.13}Cd_{0.87}Te superlattice with $\Lambda = 40$ meV and including strain ($d_W = 84$ Å, $d_B = 29$ Å).[15]

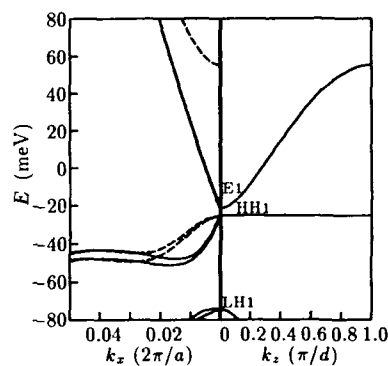


Figure 2. Superlattice in-plane and growth-direction dispersion relations for $\Lambda = 350$ meV and including strain ($d_W = 61$ Å, $d_B = 29$ Å).[15] The dashed curves are in-plane dispersion for $k_z = \pi/d$.

The ordering of the two hole bands can be reversed by increasing the hole quantum confinement, i.e., by assuming a large valence band offset. Because quantum confinement has much more effect on light-carrier bands, LH1 moves below HH1 whenever $\Lambda > 150$ meV, although an offset of ≈ 200 meV is required before there is enough separation for the light in-plane mass of HH1 to become evident.[13] Figure 2 shows that when the XPS value[6, 7] of $\Lambda = 350$ meV is employed, HH1 dominates near the zone center and as was discussed above, $m_{hx} \approx m_{ex} \ll m_{hz}$. It is also apparent from a comparison of the solid ($k_z = 0$) and dashed ($k_z = \pi/d$) curves that the in-plane dispersion for HH1 has a very strong dependence on growth-direction wavevector. This is because $m_{hx} \propto E_g$, and E_g is seen to be a rapidly-varying function of k_z . Since the valence band maximum extends along the entire k_z axis, the consequence is that holes with a wide range of in-plane masses coexist within the superlattice, a phenomenon which has been designated "mass-broadening".[16] In the example shown in Fig. 2, $m_{hx}^0 \approx 0.0015m_0$ while $m_{hx}^{\pi/d} \approx 0.04$, i.e., the hole masses vary by a factor of 27. Thus the low-temperature hole mobility should be intrinsically broadened and not describable in terms of a single type of hole with sharply-defined mobility. Note also in Fig. 2 the extreme nonparabolicity of the in-plane dispersion for HH1. At $k_z = 0$ (solid curve), m_{hx} varies from $\approx 0.0015m_0$ near the valence band maximum to essentially infinite (or electron-like) only 22 meV lower in the band. One should expect that such a dramatic variation of the free hole effective mass with energy should be reflected in the experimental properties.

The band structure shown in Fig. 2 is for a small positive energy gap. The effect of further decreasing the electron quantum confinement is that E_g at $k_z = 0$ becomes zero or negative, i.e., E1 crosses below HH1. Once the confinement has been reduced sufficiently for the bands to cross, the superlattice converts from a semiconductor to a semimetal. Although $E_g < 0$ at the zone center, there is some $k_z = k_{zc}$ for which the energy gap is nearly zero and the in-plane electron and hole masses are extremely small.

Both electrons and holes can exhibit strong mass broadening in this regime. The extent of the semimetallic region is directly related to the k_z dispersion of the E1 band, i.e., it depends strongly on d_B . If the quantum confinement is decreased further, E1 eventually falls completely below HH1 and a net "negative energy gap" opens up,[17, 18] i.e. the superlattice again becomes a semiconductor.[19] For small valence band offsets there is no extended semimetallic region, so that no semiconductor-semimetal-semiconductor double transition is predicted.

Summarizing, a central result of the theory is that the identity of the dominant hole band depends on whether the valence band offset is large or small. If it is large as in Fig. 2, HH1 is the highest hole sub-band and the growth direction hole mass is extremely heavy while the in-plane electron and hole masses at the zone center are mirror-images of one another. The in-plane dispersion of HH1 is extremely nonparabolic and mass-broadening should occur. Furthermore, it is predicted that a second semiconducting regime may exist in the region of large well thicknesses. On the other hand, if the offset is small as in Fig. 1, LH1 dominates and the growth-direction electron and hole masses are comparable while the hole mass in the plane should be much heavier than that of the electrons. Strong nonparabolicity, mass-broadening, and the semiconductor-semimetal-semiconductor double transition are not predicted for small offsets. Obviously, such significant differences should have numerous consequences on the observable experimental properties.

RECENT EXPERIMENTAL RESULTS

In this section, we summarize some recent experimental magneto-transport results, which have contributed substantially to our understanding of the superlattice band structure and electronic properties. We will see that the experiments are far more consistent with the theoretical predictions of the preceding section when a large valence band offset is assumed.

Recent magneto-transport studies have demonstrated numerous qualitative correlations between the experimental results and specific features in the theoretical band structures. From a mixed conduction analysis of Hall and conductivity data as a function of magnetic field, Hoffman et al. obtained electron and hole densities and mobilities vs temperature (4.2 to 300 K) for a large number of HgTe-CdTe and $\text{Hg}_{1-x}\text{Zn}_x\text{Te}$ -CdTe superlattices.[20,21,24-26] Since many of the samples had zero or relatively narrow energy gaps, intrinsic electrons were often observable over a broad temperature range. The temperature dependence of n_i could therefore be used to obtain an accurate non-optical characterization of E_g . [17, 20] If $n_i(T)$ is normalized to $T^{3/2}$ and plotted vs. T^{-1} on a semilog scale, to a first approximation the slope of the line obtained is proportional to the zero-temperature extrapolation of the gap, E_g^0 . Figure 3 illustrates this for five HgTe-CdTe superlattices with varying well thicknesses. As theory predicts, the superlattices are semiconducting whenever the wells are relatively thin. With increasing d_W , E_g^0 decreases until near $d_W \approx 75 \text{ \AA}$, they enter a semimetallic regime where $n_i \propto T^{3/2}$. A large number of samples with a wide range of well thicknesses have been found to have $E_g^0 \approx 0$. However, recent data (filled circles) indicate a significant energy gap (16 meV) in a sample with $d_W = 128 \text{ \AA}$ and relatively wide barriers ($d_B = 89 \text{ \AA}$). [21] This verifies the theoretical prediction discussed in the preceding section, of a second semiconducting region at large well thicknesses. No extended semimetallic regime or semiconductor-semimetal-semiconductor double transition would be expected to occur if the valence band offset is small. Furthermore, experimental energy gaps obtained in this manner for

a series of HgTe-CdTe samples with a wide range of d_W were found to agree much better with theoretical gaps calculated assuming a large Λ (350 meV).[17]

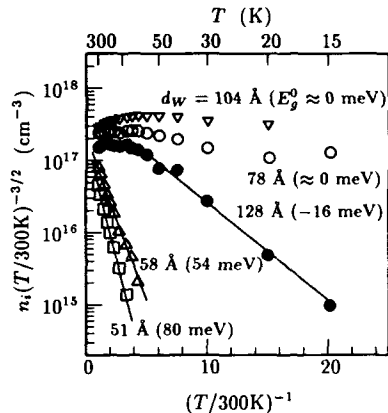


Figure 3. Experimental intrinsic carrier densities (normalized by $T^{3/2}$) vs inverse temperature for five HgTe-CdTe superlattices.[21]. Well thicknesses and energy gaps derived from the slopes of the straight-line fits are indicated.

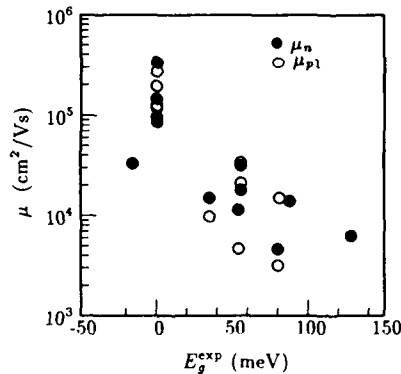


Figure 4. Low-temperature electron and hole mobilities vs experimental energy gap. Data from fourteen HgTe-CdTe and $\text{Hg}_{1-x}\text{Zn}_x\text{Te}$ -CdTe superlattices are represented. The negative-gap data point is for the thick-well sample whose $n_i(T)$ is given by the filled circles in Fig. 3.

One of the more dramatic findings of the early experimental work on Hg-based superlattices was the observation by Faurie et al.[4] of low-temperature hole mobilities that are much higher than any seen in $\text{Hg}_{1-x}\text{Cd}_x\text{Te}$ alloys.[22] Recent measurements on zero-gap superlattices have yielded $\mu_p > 2 \times 10^5 \text{ cm}^2/\text{Vs}$,[16] the highest ever for a II-VI semiconductor. Until recently these results were largely unexplained. Figure 4 illustrates low-temperature electron and hole mobilities as a function of energy gap for fourteen different HgTe-CdTe[16, 17, 21, 23] and $\text{Hg}_{1-x}\text{Zn}_x\text{Te}$ -CdTe[16, 24] superlattices. In general, there is seen to be a strong inverse dependence of both μ_n and μ_p on $|E_g|$, with semimetallic samples clearly having the highest mobilities. Furthermore, $\mu_n \approx \mu_p$ in all samples for which a comparison could be made, implying a near equality of the electron and hole effective masses. These observations are entirely consistent with the calculated band structures as long as one employs a large valence band offset, since HH1 is then the dominant valence band and $m_{hx} \approx m_{ex} \propto |E_g|$ (see Fig. 2). However, the data are difficult to explain if a small Λ is assumed, because LH1 is uppermost and $m_{hx} \gg m_{ex}$ in that case (see Fig. 1).

The temperature dependence of the transport properties also provides useful information. Figure 5 gives experimental mobilities for electrons and two types of holes in a semimetallic HgTe-CdTe superlattice.[17] For nearly all p -type samples with zero energy gap, it was found that one could not account for the low-temperature Hall and conductivity data as a function of magnetic field if only a single species of high-mobility hole was assumed to be present. In fact, that observation is consistent with the band structure analysis discussed in the preceding section, since strong mass-broadening of the hole

population is predicted whenever a large valence band offset is employed. The two-hole fit shown in Fig. 5 may therefore be viewed as a simplified approximation to a continuous distribution of hole mobilities, where the values of μ_{p1} and μ_{p2} roughly indicate the range of mobilities being spanned. Mass broadening for electrons in semimetallic samples has also recently been observed.[21] Figure 5 further illustrates that while $\mu_{p1} \approx \mu_n$ at low temperatures, μ_{p1} decreases much more abruptly when T is increased above 30 K. This result, which appears to be general for p -type Hg-based superlattices with small energy gaps, is probably related to the theoretical prediction that the in-plane dispersion for HH1 is extremely nonparabolic[17] (see Fig. 2). With increasing T the holes will populate higher-energy states which have a much larger effective mass, hence a lower mobility. Again, it is difficult to account for the data when a small offset is assumed, since both mass-broadening and strong nonparabolicity are then absent (see Fig. 1).

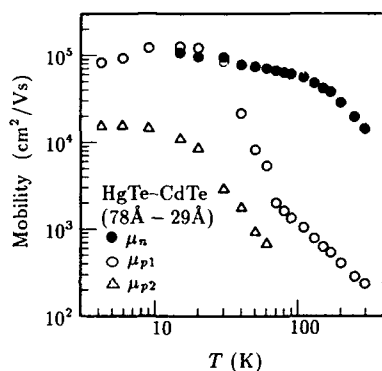


Figure 5. Experimental electron and hole mobilities vs temperature for a p -type HgTe-CdTe superlattice.[17] At low T the fits yield $p_1 \approx 1.2 \times 10^{13} \text{ cm}^{-3}$ and $p_2 \approx 3 \times 10^{15} \text{ cm}^{-3}$.

Reno et al.[25] measured the hole mobility in a series of $\text{Hg}_{1-x}\text{Cd}_x\text{Te-CdTe}$ superlattices with well compositions x spanning the range 0 to 0.27. They observed a relatively abrupt drop in the hole mobility when x was increased from 0.08 to 0.16, and attributed it to a disappearance of symmetry-induced interface states at the transition from Type-III to Type-I superlattices. Meyer et al.[13] suggested that the mobility drop is instead related to a shift of HH1 holes from very light-mass states near the Γ -point to states with much heavier mass farther out in the zone ($k_x \approx 0.03$), which coincidentally is predicted to occur at some x near that corresponding to the Type-III to Type-I transition. While theory clearly predicts the existence of these quasi-interface states, there is no conclusive evidence that any of the dramatic effects observed in the transport or magneto-optical properties result from the Type-III to Type-I transition.

The experimental results discussed above overwhelmingly support a large valence band offset. This conclusion is confirmed by magneto-optical and optical experiments. For example, Perez et al.[26] have reported hole cyclotron resonance in a p -type HgTe-CdTe superlattice with E_g^0 very near zero. From measurements in Faraday and Voigt geometries, the hole effective mass ratio was determined to be $m_{h\perp}/m_{h\parallel} \approx 280$. As discussed in the previous section, the large ratio is fully consistent with a large valence band offset (Fig. 2) but is difficult to explain if the offset is small (Fig. 1). Furthermore, the two resonances observed in the Faraday geometry and their magnetic field dependences are correctly predicted by Landau-level calculations[27] if a large Δ is assumed. (Johnson et al.[18] have recently shown that early magneto-optical investigations,[5] which argued

for a small offset, could also be understood assuming a large Λ .)

Recent infrared absorption spectra on HgTe-CdTe superlattices of particularly high quality also strongly support a large Λ . Their spectra exhibit not only the broad steps which correspond to transitions between the various heavy hole and electron sub-bands, but also a weaker feature due to LH1 to E1 transitions.[28] The valence band offset must be at least as large as the observed separation of the two peaks.

DISCUSSION

In the previous sections it was seen that there is a good qualitative correlation between theory and experiment for HgTe-CdTe superlattices. Unfortunately, a quantitative comparison with experiment is not yet possible, since a suitable formalism for the macroscopic transport properties in narrow-gap superlattices does not exist. The theory for macroscopic superlattice properties, must be completely reformulated to incorporate the unique features found in narrow gap superlattice band structures. Here we briefly outline just a few of the many issues which must be addressed in the development of such a theory.

Due to extreme nonparabolicity in the band structure, it is necessary to develop a formalism which treats arbitrary in-plane and perpendicular dispersion relations. Similarly, since the electrons tend to have perpendicular masses (m_z) which are of the same order of magnitude as their in-plane masses (m_x), the transport should be considered as anisotropic in three-dimensions rather than two-dimensional. As was discussed in the previous section, the theory must also account for k_z -degeneracy "mass-broadening" in the valence and conduction bands. The dominant scattering mechanisms at low temperatures have not yet been positively identified. Besides ionized-impurity and possibly interface-roughness scattering, electron-hole scattering should be important in narrow and zero-gap samples. In contrast to the case of zero-gap bulk materials, electron-hole events will strongly affect transport of both electrons and holes. The interface nature of electron and light hole states may play a role in some instances, and the treatment of screening by very light and extremely nonparabolic carriers may require special care. Dielectric enhancement in the zero-gap regime due to virtual band-to-band transitions[29] must be reformulated for the superlattice case.

As should be clear from this partial list of considerations, the unique features of narrow-gap superlattices will require the development of a comprehensively new theoretical transport formalism. Minor modification of existing theories developed for narrow-gap alloys or III-V superlattices will not be adequate. When available, such a theory will allow more detailed predictions of how the unusual aspects of narrow-gap superlattice band structures affect the macroscopic properties. It will naturally also be necessary to develop new approaches to such phenomena as nonlinear optical properties, energy-relaxation mechanisms, optical and magneto-optical transitions, recombination in indirect zero-gap materials, etc.

CONCLUSIONS

In this review we have attempted to summarize the current understanding of transport properties in Hg-based superlattices. Theory shows that the free hole properties should be highly sensitive to whether the uppermost valence band is HH1 or LH1. While LH1 dominates for small valence band offsets, HH1 dominates whenever Λ is greater than

approximately 200 meV. For large offsets, theory predicts roughly equal in plane electron and hole masses which are approximately proportional to the energy gap, extremely non-parabolic hole bands, a very large hole effective mass in the growth direction, strongly mass-broadened holes and electrons in narrow-gap and zero-gap structures, and a double semiconductor-semimetal-semiconductor transition which occurs as the well width is varied. By assuming a large Λ , we can account for a broad range of experimental data in lowest order by considering only the straightforward consequences of the theoretical dispersion relations. However, the reported experimental observations would be difficult to explain if Λ were small, since LH1 would then be the dominant valence band and the predicted band edge properties would be very different.

It should be noted that detailed quantitative theories for free carrier magneto-transport, optical and magneto-optical transitions, carrier recombination etc., which depend on distinctive features of the Hg-based superlattice band structure, have not yet been developed. Future work should focus on placing the broad qualitative observations discussed above on a more rigorous theoretical footing.

REFERENCES

1. J. P. Faurie, A. Million, and J. Piagnet, *Appl. Phys. Lett.* 41, 713 (1982).
2. J.-P. Faurie, *IEEE J. Quant. Electron.* QE-22, 1656 (1986).
3. J. R. Meyer, C. A. Hoffman, and F. J. Bartoli, *Semicond. Sci. Technol.* (in press).
4. J. P. Faurie, M. Boukerche, S. Sivananthan, J. Reno, and C. Hsu, *Superlatt. and Microstruct.* 1, 237 (1985).
5. Y. Guldner, G. Bastard, J. P. Vieren, M. Voos, J. P. Faurie, and A. Million, *Phys. Rev. Lett.* 51, 907 (1983).
6. S. P. Kowalczyk, J. T. Cheung, E. A. Kraut, and R. W. Grant, *Phys. Rev. Lett.* 56, 1605 (1986).
7. T. M. Duc, C. Hsu, and J. P. Faurie, *Phys. Rev. Lett.* 58, 1127 (1987).
8. J. Tersoff, *Phys. Rev. Lett.* 56, 2755 (1986); A. Munoz, J. Sanchez-Dehesa, and F. Flores, *Phys. Rev. B* 35, 6468 (1987); S.-H. Wei and A. Zunger, *Phys. Rev. Lett.* 59, 144 (1987); N. E. Christensen, *Phys. Rev. B* 37, 4528 (1988); W. R. L. Lambrecht and B. Segall, *Phys. Rev. Lett.* 61, 1764 (1988).
9. J. N. Schulman and T. C. McGill, *Appl. Phys. Lett.* 34, 663 (1979).
10. G. Y. Wu and T. C. McGill, *Appl. Phys. Lett.* 47, 634 (1985).
11. L. R. Ram-Mohan, K. H. Yoo, and R. L. Aggarwal, *Phys. Rev. B* 38, 6151 (1988).
12. J. N. Schulman and Y.-C. Chang, *Phys. Rev. B* 33, 2594 (1986).
13. J. R. Meyer, F. J. Bartoli, C. A. Hoffman, and J. N. Schulman, *Phys. Rev. B* 38, 12457 (1988).
14. G. E. Pikus and G. L. Bir, *Fiz. Tverd. Tela* 1, 1642 (1959) [*Sov. Phys. Solid State* 1, 1502 (1959)].
15. J. R. Meyer, C. A. Hoffman, F. J. Bartoli, and J. N. Schulman, *J. Vac. Sci. Technol. A* 7, 404 (1989).
16. J. R. Meyer, C. A. Hoffman, F. J. Bartoli, J. W. Han, J. W. Cook, Jr., J. F. Schetzina, X. Chu, J. P. Faurie, and J. N. Schulman, *Phys. Rev. B* 38, 2204 (1988).
17. C. A. Hoffman, J. R. Meyer, F. J. Bartoli, J. W. Han, J. W. Cook, Jr., J. F. Schetzina, and J. N. Schulman, *Phys. Rev. B* 39, 5208 (1989).
18. N. F. Johnson, P. M. Hui, and H. Ehrenreich, *Phys. Rev. Lett.* 61, 1993 (1988).
19. Although the direct energy gap is always negative for sufficiently thick wells, the valence band maximum can occur at $k_z > 0$ when d_W is large, and under some circumstances the superlattice may remain semimetallic for all well thicknesses.

20. M. W. Goodwin, M. A. Kinch, R. J. Koestner, M. C. Chen, D. G. Seiler, and R. J. Justice, *J. Vac. Sci. Technol. A* 5, 3110 (1987).
21. C. A. Hoffman, J. R. Meyer, F. J. Bartoli, J. W. Han, J. W. Cook, Jr., and J. F. Schetzina, *Phys. Rev. B* 40, 3867 (1989).
22. J. R. Meyer, F. J. Bartoli, and C. A. Hoffman, *J. Vac. Sci. Technol. A* 5, 3035 (1987).
23. C. A. Hoffman, J. R. Meyer, R. J. Wagner, F. J. Bartoli, X. Chu, J. P. Faurie, L. R. Ram-Mohan, and H. Xie, *J. Vac. Sci. Technol.* (in press).
24. C. A. Hoffman, J. R. Meyer, F. J. Bartoli, X. Chu, and J. P. Faurie, 19th Int. Conf. Phys. Semicond. (Warsaw, 1988), ed. W. Zawadzki, (Polish Academy of Sciences, Warsaw, 1988), p. 467.
25. J. Reno, I. K. Sou, P. S. Wijewarnasuriya, and J. P. Faurie, *Appl. Phys. Lett.* 48, 1069 (1986).
26. J. M. Perez, R. J. Wagner, J. R. Meyer, J. W. Han, J. W. Cook, Jr., and J. F. Schetzina, *Phys. Rev. Lett.* 61, 2261 (1988).
27. J. R. Meyer, R. J. Wagner, F. J. Bartoli, C. A. Hoffman, and L. R. Ram-Mohan, *Phys. Rev. B* 40, 1388 (1989).
28. J. N. Schulman, O. K. Wu, E. A. Patten, J. W. Han, Y. Lansari, L. S. Kim, J. W. Cook, Jr., and J. F. Schetzina, *Appl. Phys. Lett.* 53, 2420 (1988).
29. J. G. Broerman, *Phys. Rev. B* 1, 4568 (1970).

HgTe-CdTe MULTIPLE QUANTUM WELLS

C. A. HOFFMAN, D. J. ARNOLD, J. R. MEYER, AND F. J. BARTOLI
Naval Research Laboratory, Washington, D. C. 20375

Y. LANSARI, J. W. COOK, JR., AND J. F. SCHETZINA
North Carolina State University, Raleigh, NC 27695

J. N. SCHULMAN
Hughes Research Laboratories, Malibu CA 90265

ABSTRACT

We report a detailed magneto-transport investigation of HgTe-CdTe multiple quantum wells. The data yield the first experimental confirmation of a theoretically-predicted "negative-gap" semiconducting region in wide-well Hg-based heterostructures. Gaps of up to 19 meV are observed.

INTRODUCTION

It is well known that in the low-temperature limit, the $\text{Hg}_{1-x}\text{Cd}_x\text{Te}$ alloy system is semiconducting for compositions $x > 0.16$ and semimetallic for $x < 0.16$. It has recently been demonstrated experimentally[1] that HgTe-CdTe superlattices are somewhat analogous in that as the well thickness d_W is decreased, there is a point at which the material undergoes a semiconductor to semimetal transition. Whereas samples with thin quantum wells are semiconducting, superlattices with $d_W > 78 \text{ \AA}$ (and up to 130 \AA) are found to have energy gaps of zero to within the experimental uncertainty.[1, 2] The observation of a semimetallic regime is easily understood theoretically[1] in terms of a crossing of the E1 energy band, which has strong dispersion in the growth direction (k_z), and HH1, which is nearly dispersionless in k_z . At well widths for which the two bands cross, both the conduction band minimum and the valence band maximum lie at the same energy along different portions of HH1. Electrons occupy the region of the Brillouin zone between $k_z = 0$ and the crossing point (k_{zc}) while holes occupy the region between k_{zc} and π/d . However, it has recently been argued theoretically[3] that in contrast to the $\text{Hg}_{1-x}\text{Cd}_x\text{Te}$ alloy, HgTe-CdTe superlattices should display a second transition back to the semiconducting state whenever the well thickness becomes so large that the bands no longer cross, i.e., E1 lies completely below HH1. We also point out that the band crossing responsible for the semimetallic behavior occurs only when the E1 band has a strong dispersion in the growth direction. It follows that HgTe-CdTe multiple quantum wells (whose barriers are too thick to allow significant interactions between neighboring wells) should display no extended semimetallic regime. Instead, as the well thickness is increased the material should pass directly between a positive-gap semiconducting state and a negative-gap semiconducting state.

In the present work, we have carried out a detailed experimental magneto-transport investigation of HgTe-CdTe multiple quantum wells with relatively large well widths. Energy gaps for each sample have been determined from an analysis of the temperature dependence of the intrinsic carrier density. As a consequence, we are able to report the first experimental verification of the negative-gap semiconducting regime which is predicted to occur at large well thicknesses.

QUANTUM WELL BAND STRUCTURES FOR WIDE WELLS

Recent publications have treated at some length the systematics of HgTe-CdTe superlattice band structures in the positive-gap semiconducting and semimetallic regimes.[1, 4] However, the wide-well (negative-gap semiconducting) regime has not previously been discussed in any detail. We therefore briefly summarize some of the primary considerations.

Theoretical band structures were obtained numerically using the multiband tight-binding theory developed by Schulman and Chang.[5] A valence band offset of 350 meV was employed, and strain was ignored since the present multiple quantum wells were grown on lattice-matched substrates. Figures 1 and 2 illustrate results for the in-plane (k_x) and growth-direction (k_z) dispersion relations of multiple quantum wells with two different well thicknesses, 81 Å and 128 Å. In both cases the barrier thickness of 89 Å is wide enough that there is no significant dispersion in k_z . The theory predicts that E_g is positive (E_1 lies above HH1) only when $d_W < 78$ Å, thus there is a small negative gap of 5 meV at $d_W = 81$ Å (Fig. 1). In this regime the energy gap is direct and both electrons and holes have very small in-plane effective masses near the band extrema. However, due to the side-maximum at $k_x \approx 0.035$, holes with energies only 15 meV below the band edge have a much larger mass and a much higher density of states.

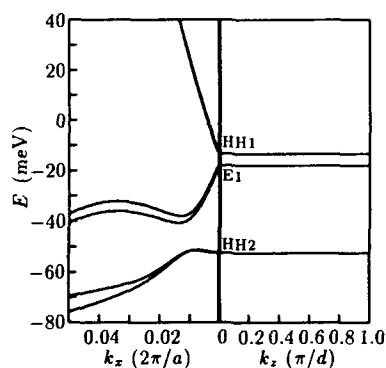


Figure 1. In-plane and growth-direction dispersion relations for a [100] HgTe-Hg_{0.15}Cd_{0.85}Te multiple quantum well ($d_W = 81$ Å, $d_B = 89$ Å). A valence band offset of 350 meV has been assumed.

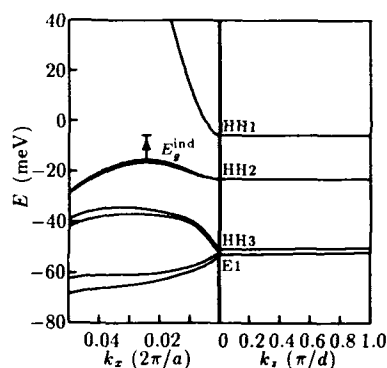


Figure 2. In-plane and growth-direction dispersion relations for a multiple quantum well with $d_W = 128$ Å, $d_B = 89$ Å). The indirect energy gap is indicated.

When the well thickness is increased to 128 Å (Fig. 2), E_1 lies below not only HH1 but also HH2 and HH3. In this regime HH1 is the conduction band and HH2 is the valence band. Note that while the negative energy gap increases with d_W as long as E_1 is the valence band, it begins to decrease again as soon as E_1 passes below HH2. This is because reducing the quantum confinement by increasing d_W has the effect of moving the hole bands closer together, hence decreasing the gap between HH1 and HH2. We also find that the valence-band maximum is now at $k_x \approx 0.025$, i.e., the gap is indirect. In this example, $E_g^{\text{ind}} \approx 9.5$ meV (see the arrow in the figure) while $E_g^{\text{dir}} \approx 17$ meV. The

in-plane mass for electrons has increased from $.0019m_0$ in Fig. 1 to $0.017m_0$ in Fig. 2 (it is roughly proportional to the separation between HH1 and E1). Furthermore, the hole mass in Fig. 2 is much larger than the electron mass, in contrast to their near equality in Fig. 1. These implications of the theoretically-derived band structures will be considered when the experimental data is interpreted below.

MBE GROWTH AND EXPERIMENTAL

Six 100-period HgTe-Hg_{0.15}Cd_{0.85}Te multiple quantum wells were grown in an MBE system which has been described previously.[6] Deposition was directly onto a lattice-matched [100] Cd_{1-x}Zn_xTe substrate with no buffer layer. The well and barrier thicknesses listed in Table 1 were accurately determined from x-ray satellite peaks in conjunction with growth-rate data.[1] Note that the barrier thicknesses of 89-109 Å are large enough to prevent any significant tunneling between neighboring wells. Thus all bands in these structures are predicted to be nearly dispersionless in k_z , in contrast to most previous studies involving superlattices with much thinner barriers (≤ 60 Å).

Table 1 - Sample Characteristics

#	d_w (Å)	d_B (Å)	n_0 [p_0] (cm^{-3})	μ_n^{max} (cm^2/Vs)	$\mu_n^{300\text{K}}$ (cm^2/Vs)	$ E_g^{\text{exp}} $ (meV)	E_g^{theo}	
							Dir.	Ind.
1	68	97	1.8×10^{16}	5.6×10^4	1.2×10^4	≈ 0	+17	
2	83	99	2.5×10^{15}	4.8×10^4	1.1×10^4	8	-8	-19
3	96	99	$[2.3 \times 10^{15}]$	4.3×10^4	1.4×10^4	11	-19	-15
4	112	109	1.4×10^{15}	5.1×10^4	2.5×10^4	9	-19	-12
5	128	89	≈ 0	5.7×10^4	2.4×10^4	19	-17	-10
6	160	102	$[1.7 \times 10^{15}]$	3.9×10^4	2.7×10^4	9	-12	-7

Van der Pauw Hall and conductivity measurements were performed on each sample as a function of magnetic field (0-70 kG) and temperature (4.2-300 K). A mixed-conduction analysis was then employed to extract the electron and hole densities and mobilities as a function of temperature. In contrast to some previous studies of HgTe-CdTe heterostructures, the data showed no evidence for the presence of charge-transfer electrons or holes.[7, 8] Furthermore, in contrast to previous studies of thin-barrier HgTe-CdTe superlattices, the fits did not yield multiple electron or multiple hole species due to "mass-broadening".[1, 9] Table 1 gives the electron or hole concentration in the low-temperature limit (n_0 or p_0), along with the maximum electron mobility (which generally occurred at intermediate temperatures), and the electron mobility at 300 K.

RESULTS

With increasing temperature, the electron and hole densities are observed to increase in a manner consistent with the thermal generation of intrinsic carriers. In previous studies of Hg-based superlattices, analysis of the temperature dependence of n_i has been found to provide a valuable method for determining the energy gap.[1] However, the lowest-order analysis is slightly different in the cases of a superlattice, which may be thought of as an anisotropic three-dimensional material, and a multiple quantum well.

which has no k_z dispersion and thus contains quasi-two-dimensional electron and hole gases in each well. Whereas the earlier treatment[1] had used the conventional 3D "law of mass action" result

$$n_i^{3D} \approx 2 \left(\frac{k_B T}{2\pi\hbar^2} \right)^{3/2} (m_n^{ds} m_p^{ds})^{3/4} e^{-\gamma/2k_B} e^{-E_g^0/2k_B T}, \quad (1)$$

here we will use the 2D analog for the intrinsic density per well,

$$n_i^{2D} \approx \left(\frac{k_B T}{\pi\hbar^2} \right) (m_n^{ds} m_p^{ds})^{1/2} e^{-\gamma/2k_B} e^{-E_g^0/2k_B T}. \quad (2)$$

In both expressions, E_g^0 is the zero-temperature extrapolation of the energy gap, γ is the temperature coefficient of $E_g(T)$, and m_n^{ds} and m_p^{ds} are the density-of-states electron and hole effective masses. Since the 3D and 2D results have the same exponential dependences on T^{-1} , the key difference between the two expressions is the proportionality to $T^{D/2}$, where D is the dimensionality.

We see from Eq. (2) that if n_i^{2D} is normalized to T and plotted vs T^{-1} on a semilog scale, the slope of the curve should be proportional to E_g^0 . For three of the multiple quantum wells, such plots of the experimental intrinsic densities are illustrated in Fig. 3.[10] Results for the sample with the thinnest wells (68 Å) indicate that the low-temperature gap is near zero. This compares with a theoretical value in Table 1 of +17 meV (theory predicts that the zero-gap point should occur when $d_W \approx 76$ Å). When d_W is increased, data for all of the other multiple quantum wells show clear evidence for the opening of a negative E_g . For example, the slope shown in the figure for Sample 6 (160 Å) gives a gap of 9 meV. The most dramatic case is Sample 5 (128 Å), for which the intrinsic density freezes out by three orders of magnitude when T is lowered from 60 K to 15 K. For that sample, the data from the figure yield $E_g^0 \approx 19$ meV.[11] At low temperatures (e.g., 15 K), n_i is largest in the 68 Å sample because its direct gap is much smaller than the indirect gaps in the other two samples. However, with increasing T , $k_B T$ becomes comparable to the gaps of the thicker well samples and the much larger density of states at the indirect valence band maximum becomes the dominant factor. Although the increase of the slope for the 68 Å sample at higher T is probably due to the contribution of the indirect maximum, that sample has the largest E_g^{ind} and therefore the lowest intrinsic density at high T . A further consideration at higher T is that when d_W is large, the sub-band spacings for HH2, HH3, etc. are much smaller and higher-order bands contribute increasingly to the available density of states. This probably accounts for the larger $n_i(300\text{K})$ in Sample 6 than in Sample 5. Comparison of the experimental and theoretical energy gaps listed in Table 1 shows quite good agreement with respect to the general magnitudes of $|E_g|$. For the five negative-gap samples, theory gives values between 7 and 15 meV while the data yield 8 to 19 meV. However, the experimental dependence on d_W is not very systematic. It is unclear whether this is due to an insensitivity of the data to relatively small changes in E_g , or whether some other factor which has not been accounted for is having a higher-order effect on the experimental results (e.g., band bending due to unintentional modulation doping).

Shown in Fig. 4 are electron and hole mobilities as a function of temperature for the sample with the thickest wells ($d_W = 160$ Å). We note first that $\mu_n(T)$ does not decrease significantly with increasing temperature until $T > 200$ K, i.e., a positive slope persists well into the regime where phonon events have become the dominant scattering mechanism. For the series of six multiple quantum wells, there is a nearly monotonic increase

with d_W of the temperature at which the electron mobility has its maximum. This qualitative observation is easily understood in terms of the theoretical band structures and the relation between in-plane effective mass and the E1-HH1 energy gap: $m_x(T) \propto |E_g(T)|$. Since $E_g(T=0) \leq 0$ in the present samples and since $dE_g/dT > 0$, there will be some intermediate temperature at which the gap passes through zero and the mass has its minimum value. While this occurs in the low temperature limit for Sample 1 ($d_W = 68$ Å), the minimum mass in Sample 6 (160 Å) is not predicted to occur until $T \approx 220$ K. The ambient-temperature electron mobilities listed in Table 1 are seen to increase with increasing d_W . This is consistent with the theoretical prediction that at higher temperatures the positive E_g monotonically decreases with increasing d_W . We conclude that in wide-well HgTe-CdTe heterostructures, the main qualitative features of the temperature-dependent electron mobility are dominated by the strong variation of the band structure with T rather than by the details of the scattering mechanisms.

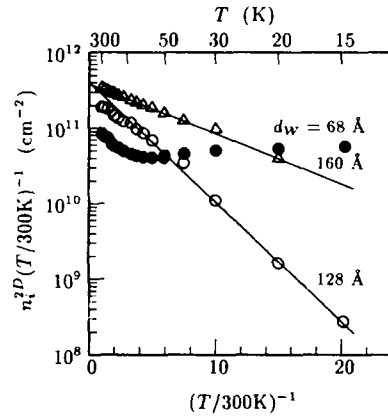


Figure 3. Experimental 2D intrinsic carrier densities per well (normalized by T) vs inverse temperature for three HgTe-CdTe multiple quantum wells. Well thicknesses for each sample are indicated.

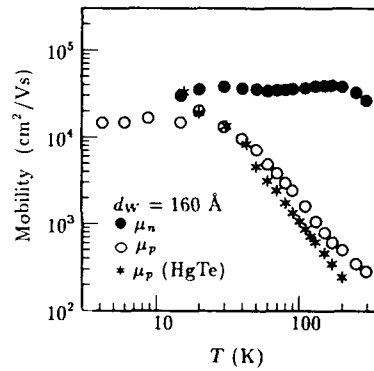


Figure 4. Experimental electron and hole mobilities vs temperature for a HgTe-CdTe multiple quantum well. Hole mobilities for HgTe[12, 13] are shown for comparison.

Whereas the band structure calculations predict a very light effective mass for holes in the thin-well regime (see Fig. 1), theory also predicted that for thicker wells the mass at the indirect valence band maximum is roughly equal to that of the heavy holes in HgTe (see Fig. 2). It is therefore noteworthy that the low-temperature mobility ratio μ_n/μ_p in Fig. 4 is only about a factor of 2 even though the mass ratio m_p/m_n should be greater than 10. For comparison, Fig. 4 also gives temperature-dependent mobilities for holes in HgTe.[12, 13] We find that μ_p in the multiple quantum well and in HgTe are quite similar, which is not surprising since the effective masses and scattering mechanisms are probably comparable. On the other hand, while the electron mass in Sample 6 is predicted to be slightly smaller than that in HgTe[14] ($\approx 0.02m_0$ vs $0.028m_0$), the electron mobility in the figure is nearly an order of magnitude lower than that in comparably-doped HgTe.[12, 13] This may imply the presence of an additional scattering mechanism in the multiple quantum well. One possibility is interface roughness scattering, which is expected to have much more effect on the electrons than holes due to a strong inverse

dependence on effective mass.[15]

CONCLUSIONS

We have carried out a detailed magneto-transport investigation of HgTe-CdTe multiple quantum wells. The results provide the first experimental confirmation of the negative-gap semiconducting regime which had been theoretically predicted[1, 3] to occur in HgTe-CdTe heterostructures with wide quantum wells. As the well width is increased from 68 Å to 160 Å, the energy gap is observed to increase from 0 to as much as 19 meV. We thus have the counter-intuitive finding that in some regions, the energy gap increases with decreasing quantum confinement. The present data on multiple quantum wells contrast previous results for superlattices, which have been found to be semimetallic for a broad range of d_w between 78 and 130 Å. We also find that for the range of well thicknesses studied, the temperature at which the electron mobility has its peak is more sensitive to the band structure than to the details of the scattering mechanisms. Due to the negative temperature coefficient of the effective mass, μ_n in thick-well samples increases with T well into the region where phonon scattering dominates the momentum relaxation.

REFERENCES

1. C. A. Hoffman, J. R. Meyer, F. J. Bartoli, J. W. Han, J. W. Cook, Jr., J. F. Schetzina, and J. N. Schulman, Phys. Rev. B 39, 5208 (1989).
2. C. A. Hoffman, J. R. Meyer, F. J. Bartoli, X. Chu, and J. P. Faurie, 19th Int. Conf. Phys. Semicond. (Warsaw, 1988), ed. W. Zawadzki, (Polish Academy of Sciences, Warsaw, 1988), p. 467.
3. N. F. Johnson, P. M. Hui, and H. Ehrenreich, Phys. Rev. Lett. 61, 1993 (1988).
4. J. R. Meyer, F. J. Bartoli, C. A. Hoffman, and J. N. Schulman, Phys. Rev. B 38, 12457 (1988).
5. J. N. Schulman and Y.-C. Chang, Phys. Rev. B 33, 2594 (1986).
6. K. A. Harris, S. Hwang, Y. Lansari, J. W. Cook, Jr., J. F. Schetzina, and M. Chu, J. Vac. Sci. Technol. A 5, 3085 (1987).
7. J. M. Berroir, Y. Guldner, J. P. Vieren, M. Voos, X. Chu, and J. P. Faurie, Phys. Rev. Lett. 62, 2024 (1989).
8. C. A. Hoffman, J. R. Meyer, R. J. Wagner, F. J. Bartoli, X. Chu, J. P. Faurie, L. R. Ram-Mohan, and H. Xie, J. Vac. Sci. Technol. (in press).
9. C. A. Hoffman, J. R. Meyer, F. J. Bartoli, J. W. Han, J. W. Cook, Jr., and J. F. Schetzina, Phys. Rev. B 40, 3867 (1989).
10. For comparison with past results, the equivalent n_i^{3D} may be obtained from the relation $n_i^{3D} \leftarrow n_i^{2D}/d_w$.
11. In a previous paper (Ref. 9), a fit to the 3D intrinsic density expression yielded the slightly smaller value of 16 meV.
12. Z. Dziuba and J. Wrobel, phys. stat. sol. b 100, 379 (1980).
13. J. R. Meyer, C. A. Hoffman, F. J. Bartoli, J. M. Perez, J. E. Furneaux, R. J. Wagner, R. J. Koestner, and M. W. Goodwin, J. Vac. Sci. Technol. A 6, 2775 (1988).
14. Y. Guldner, C. Rigaux, M. Grynberg, and A. Mycielski, Phys. Rev. B 8, 3875 (1973).
15. H. Sakaki, T. Noda, K. Hirakawa, M. Tanaka, and T. Matsusue, Appl. Phys. Lett. 51, 1934 (1987).

QUANTUM-CONFINED STARK EFFECT IN II-VI SEMICONDUCTOR COUPLED QUANTUM WELLS

Z. Yang, and J. F. Schetzina, Department of Physics, North Carolina State University, Raleigh, NC 27695

ABSTRACT

The Quantum-Confined Stark Effect in II-VI semiconductor coupled quantum wells is studied theoretically. It is found that because of the difference in localization of the wavefunctions of the heavy hole and the electron subbands involved, large band gap shifts can be induced by an external electric field for quantum wells with zero-field band gaps in the spectrum region from 0.4 μm to 12 μm . Several potential device applications based on this effect are proposed.

INTRODUCTION

The Quantum-Confined Stark Effect (QCSE) in III-V semiconductor quantum wells (QWs) has been studied extensively in recent years, and various device applications based on the effect have been demonstrated [1-3]. The effect in Hg-based narrow gap II-VI semiconductor QWs was recently studied theoretically, and large band gap shifts were predicted in coupled QW structures [4,5]. In this paper we extend our previous work [5] to II-VI semiconductor QWs with zero-field band gaps ranging from 0.4 μm to 12 μm . Novel device applications are also proposed.

QUALITATIVE ANALYSIS

A typical coupled QW structure chosen for study is shown in Fig. 1(a). In the structure two $\text{Hg}_{1-x}\text{Cd}_x\text{Te}$ well layers are separated by a thin $\text{Hg}_{1-y}\text{Cd}_y\text{Te}$ ($y > x$) wider-band-gap barrier layer, and the three layers are sandwiched between two thick CdTe barrier layers. The structure can be repeated many times to form thick samples. The two wells separated by the thin low barrier within each structure are coupled while, because of the thick CdTe barriers, each structure is isolated from one another.

The QCSE in the coupled wells can be qualitatively analyzed in the following way: With proper x and y values and layer thicknesses, the electronic subbands in the structure are such that the first two heavy hole subbands, H_1 and H_2 , are above the valence band edge of the low barrier and therefore their wavefunctions are mostly localized in the left-side well and in the right-side well respectively. The first conduction subband E_1 lies above the low barrier conduction band edge with its wavefunction thus extending over both the wells and the low barrier region. The light hole subband L_1 is below the valence band edge of the low barrier and its wavefunction also spreads over the entire structure. Its contribution to the QCSE is thus very limited. When an external electric field is applied perpendicular to the well layers in the direction shown in Fig. 1(b) (defined as positive bias), an additional potential $V(z)$ exists, where z is the coordinate along the field direction. If the center point of the structure is chosen as $z = 0$ and $V(0) = 0$,

$V(z)$ is then positive when $z < 0$ and negative when $z > 0$. The first order perturbation to the energy of a particular subband is

$$\Delta E = \int |\Psi(z)|^2 V(z) dz,$$

where $\Psi(z)$ is the envelope wavefunction of the subband. It is readily seen that the level H1 will increase in energy while E1 remains unchanged as the field strength increases, if the two wells are of the same thickness. Level H2 will decrease in energy. The band gap of the structure, determined now by the energy difference between E1 and H1, will then decrease. When the field direction is reversed (negative bias) H2 will increase in energy while H1 will decrease in energy, in exactly the same way as for positive bias, since the structure is symmetric. The band gap of the structure, now determined by the energy difference between E1 and H2, again decreases as the field strength increases. Therefore, for a symmetric coupled-well structure the applied electric field induces a RED shift in the band gap of the QW structure.

Suppose now the left-side well layer is thicker than the right-side one, as is shown in Fig. 2. At zero field, level H1 is above level H2. The field will induce either a RED shift or a BLUE shift, depending on the direction of the field. If the field direction is the same as in Fig. 2(b) then, since the band gap is determined by the energy difference between E1 and H1 as long as H1 is above H2, and H1 decreases in energy faster than E1 does when the field strength increases, the band gap will BLUE shift. The band gap will RED shift after H2 is above H1. Under positive bias, H1 increases in energy and the band gap RED shifts when the field strength increases.

RESULTS

The theoretical model used in this work to calculate the subbands of QWs in the presence of an external electric field has been presented in detail in our previous work [4,5]. Room temperature bulk band parameters of $\text{Hg}_{1-x}\text{Cd}_x\text{Te}$ alloy are used and strain effects are neglected. The valence band offset between HgTe and CdTe is taken as 360 meV and a linear dependence of the offset on the composition is assumed.

Figure 3(a) shows the calculated band gap E_g versus applied electric field E for a symmetric QW structure with both the wells comprised of a 42.12 Å HgTe layer. The low barrier is a 35.64 Å $\text{Hg}_{0.8}\text{Cd}_{0.2}\text{Te}$ layer. The thick high barriers are $\text{Cd}_{0.85}\text{Hg}_{0.15}\text{Te}$ layers. The zero-field band gap of the structure is 118 meV, or 10.5 μm . The band gap decreases almost linearly to 86 meV when the field strength increases to 100 KV/cm. Such a high field is attainable in Hg-based QWs, as has been demonstrated in Ref. 6. The band gap changes in the same way as the field is reversed, since the structure is symmetric.

By using higher x -values for the well and the low barrier, QWs with zero-field band gaps at shorter wavelengths can be obtained. An example is shown in Fig. 3(b). Both wells are made of a 58.32 Å $\text{Hg}_{0.8}\text{Cd}_{0.2}\text{Te}$ layer, separated by a 32.4 Å $\text{Hg}_{0.6}\text{Cd}_{0.4}\text{Te}$ barrier. The zero-field band gap is 305 meV, or 4.05 μm . The gap reduces to 250 meV when the field strength is 100 KV/cm.

Figure 4 shows the change in band gap E_g as a function of the applied field E , which is pointing in the same direction as in

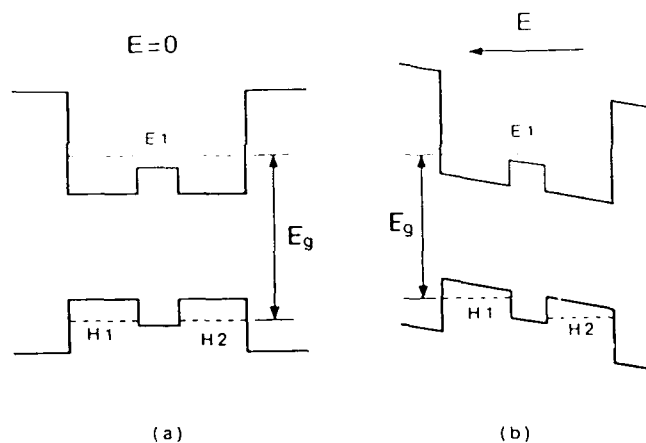


Figure 1. Schematic diagram of a symmetric coupled quantum well structure. The thick lines are the potential the electrons see and the dashed lines are the subband levels. (a) No applied field. (b) Under positive bias.

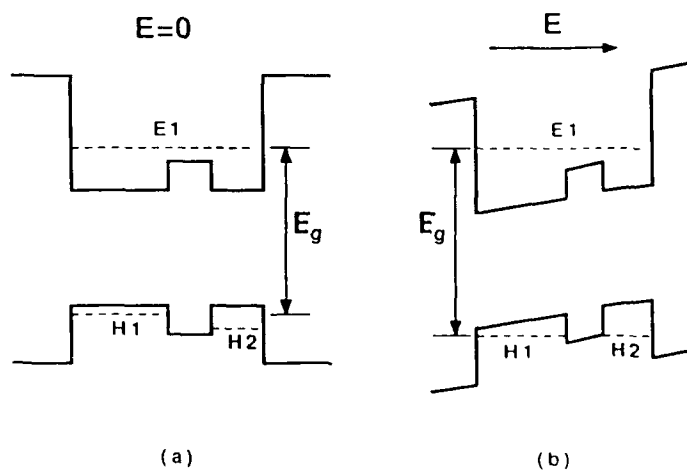


Figure 2. Schematic diagram of an asymmetric coupled quantum well structure. The thick lines are the potential the electrons see and the dashed lines are the subband levels. (a) No applied field. (b) Under negative bias.

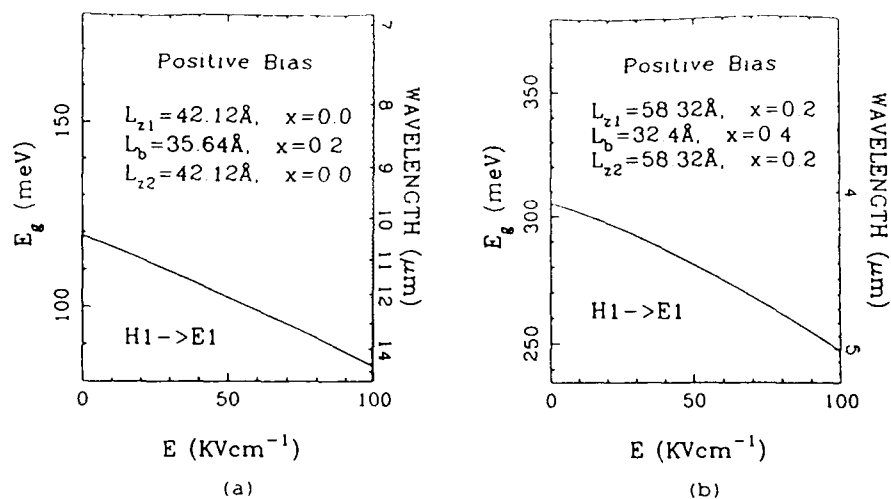


Figure 3. The band gap E_g of symmetric structures versus the applied electric field E . The gaps RED shift when the field is applied. (a) The zero-field band gap of the structure is 118 meV, or 10.5 μm . (b) The zero-field band gap is 305 meV, or 4.05 μm .

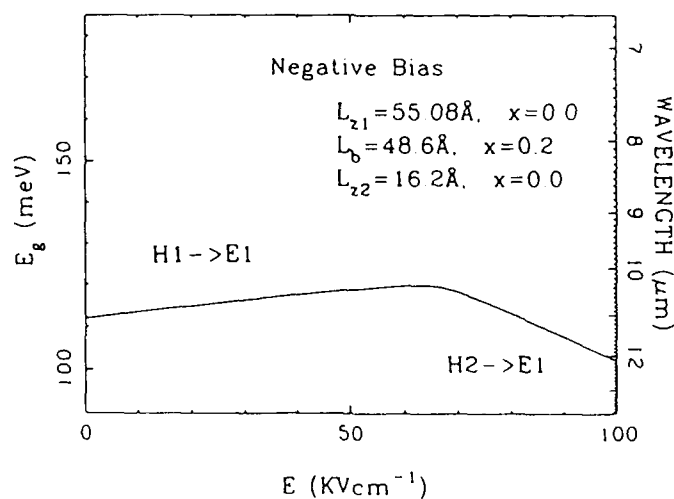


Figure 4. The band gap E_g of an asymmetric structure versus the applied electric field E . The structure is under negative bias. The band gap BLUE shifts until the field strength reaches 65 KV/cm.

Fig. 2(b) for an asymmetric QW structure. The left-side well is a 55.08 Å HgTe layer and the right-side well is a 16.2 Å HgTe layer, with a 48.6 Å $\text{Hg}_{0.8}\text{Cd}_{0.2}\text{Te}$ barrier in-between. The band gap BLUE shifts up to 7 meV when the field strength reaches 65 KV/cm. Level H2 is then above H1 when the field strength further increases, and the band gap red shifts rapidly.

Structures with even larger band gaps can be obtained by using even higher x -values and large band gap shifts continue to exist. Finally for the structures with band gaps in the visible light region, we propose to use $\text{ZnS}_x\text{Te}_{1-x}/\text{ZnSe}$ coupled QWs. With an x -value of 0.7, the two semiconductors are nearly lattice-matched. If a linear dependence of the band parameters of the $\text{ZnS}_x\text{Te}_{1-x}$ alloy on the composition is assumed, then the conduction band edge in $\text{ZnS}_{0.7}\text{Te}_{0.3}$ will be about 250 meV above that in ZnSe, while its valence band edge will be about 300 meV below that in ZnSe. The $\text{ZnS}_{0.3}\text{Te}_{0.7}/\text{ZnSe}$ can then be used to form a type-I QW, with ZnSe being the well and $\text{ZnS}_{0.7}\text{Te}_{0.3}$ being the barrier. $\text{ZnS}_x\text{Te}_{1-x}$ with an x -value slightly lower than 0.7 can be used as the low barrier in the coupled well structure. Large band gap shift with the electric field is expected.

APPLICATIONS

One potential application of the QCSE in II-VI QWs is for high speed electrooptic modulators in the important infrared spectral regions from 8 to 12 μm and from 3 to 5 μm , and in the visible region near 4000 Å. A light beam with photon energy slightly below the zero-field band gap of a coupled QW structure will pass through it with little loss. When a bias is applied to the structure, the band gap shifts to lower energy and the incident light will be absorbed. The intensity of the transmitted light is therefore controlled by the bias voltage. The switching speed of such a device is mainly limited by the RC time constant of the bias circuit, as has been demonstrated in III-V QWs [2].

Another application is the self-electro-optic device (SEED) [3]. QWs with band gaps that can be BLUE shifted are needed, since in narrow gap II-VI QWs there is no excitonic feature near the band edge absorption. The device circuit includes a constant voltage source, a coupled QW and a series resistor. When there is no incident light, there is a certain voltage drop across the series resistor. The remaining source voltage is across the QW and its band gap is blue shifted. A monochromatic light beam with photon energy slightly below the shifted band gap is incident on the QW. When the light intensity is low, little photo-current is generated and the QW is transparent to the light. However, when the intensity is high, additional photo-current is generated, and the voltage drop across the series resistor increases, and the bias on the QW decreases. The reduction of the bias then shifts the band gap to lower energy, which in turn increases the light absorption and therefore increases the photo-current, which in turn further reduces the bias. Such a positive feed-back process will quickly shift the band gap from above the photon energy to below the photon energy, until a flat absorption region is reached. The QW is then opaque to the incident light.

A third application is a non-linear optical device, where a high power laser beam provides the electric field for a symmetric QW structure. The beam should be incident at an angle relative to the QW layers so that there is a finite component of the electric

field perpendicular to the QW layers, or the beam could be coupled in so that it propagates parallel to the layers, with its polarization being perpendicular to the layers. The oscillating electric field induces a red shift of the band gap and therefore alters the optical properties of the structure. Such a non-linear optical process is expected to be very fast, since no band filling or thermal redistribution of the electrons is needed in order to induce the process.

In summary, we have demonstrated theoretically that in II-VI semiconductor coupled quantum well structures large band gap shifts can be induced by an external electric field applied perpendicular to the QW layers. The zero-field band gap of the structure can be chosen to be anywhere from 0.4 μm to 10 μm . These QCSE structure can be used as electro-optic modulators, self-electro-optic devices, and ultrafast non-linear optical devices.

ACKNOWLEDGMENT

This work was supported by NSF through grant DMR-88-13525 and NRL contract N00014-89-5-2024

REFERENCES

- [1] D. A. Miller, D. S. Chemla, A. C. Gossard, W. Wiegmann et al. *Phys. Rev. Lett.* **53**, 2173 (1984)
- [2] T. H. Wood, E. C. Carr, C. A. Burrus, R. S. Tucker, T-H. Chiu, and W-T. Tsang, *Electron. Lett.* **23**, 10 (1987)
- [3] D. A. Miller, D. S. Chemla, A. C. Gossard, et al. *Appl. Phys. Lett.* **45**, 13 (1984)
- [4] Z. Yang, and J. K. Furdyna, *J. Appl. Phys.* **64**, 5248 (1988)
- [5] Z. Yang, J. F. Schetzina, and J. K. Furdyna, *J. Vac. Sci. Technol.* **A7**, 360 (1989)
- [6] M. A. Reed, R. J. Koestner, and M. W. Goodwin, *Appl. Phys. Lett.* **49**, 1293 (1986)
- [7] Hiroshi Fujiyasu and Koji Mochizuki, *J. Appl. Phys.* **57**, 2690 (1985)
- [8] Khalid Shahzad, Diego J. Olego, and Chris G. Van de Walle, *Phys. Rev.* **B38**, 1417 (1988)

PART IX

Dilute Magnetic Semiconductors

RECENT DEVELOPMENTS IN II-VI DILUTED MAGNETIC SEMICONDUCTORS

N. SAMARTH AND J. K. FURDYNA

Department of Physics, University of Notre Dame, Notre Dame, IN 46556.

ABSTRACT

Much of the work in diluted magnetic semiconductors (DMS) in past years has focused on the $A_{1-x}^{II}Mn_xB^{VI}$ alloys such as $Cd_{1-x}Mn_xTe$. Recently, there has been an increasing accent on DMS alloys containing the transition metal ions Fe^{2+} and Co^{2+} . We review here the properties of these new materials and compare them with the $A_{1-x}^{II}Mn_xB^{VI}$ alloys. We also examine the novel opportunities afforded by the molecular beam epitaxy of epilayers and heterostructures containing the "metastable" zinc-blende phase of $Cd_{1-x}Mn_xSe$.

INTRODUCTION

The term "diluted magnetic semiconductor" (DMS) was originally coined to describe alloys such as $Cd_{1-x}Mn_xTe$ in which Mn^{2+} ions are randomly substituted for the group II atoms in a II-VI semiconductor [1]. However, this nomenclature has grown to include diverse systems derived from other semiconductors (such as IV-VI's) and incorporating other magnetic ions (such as Co^{2+} , Fe^{2+} and Eu^{2+}) [2]. Moreover, the non-equilibrium technique of molecular beam epitaxy (MBE) has enabled the growth of DMS materials not readily accessible to bulk growth, such as zinc-blende phases of $MnSe$ [3], $MnTe$ [4], $FeSe$ [5] and $Cd_{1-x}Mn_xSe$ [6], as well as a new class of DMS alloys derived from III-V semiconductors [7]. In this paper, we review the properties of some of the new II-VI materials, beginning with the $A_{1-x}^{II}Fe_xB^{VI}$ alloys. We then discuss the new $A_{1-x}^{II}Co_xB^{VI}$ alloys ($Zn_{1-x}Co_xSe$, $Zn_{1-x}Co_xS$ and $Cd_{1-x}Co_xSe$), followed by a look at the opportunities provided by the epitaxial growth of zinc-blende $Cd_{1-x}Mn_xSe$, and conclude with a look at future prospects.

 $A_{1-x}^{II}Fe_xB^{VI}$ DMS ALLOYS

As shown in Table I, the $A_{1-x}^{II}Fe_xB^{VI}$ alloys grown to date include both wide-gap materials ($Zn_{1-x}Fe_xSe$ [8,9] and $Cd_{1-x}Fe_xSe$ [10]), as well as narrow-gap alloys ($Hg_{1-x}Fe_xSe$ [11, 12] and $Hg_{1-x}Fe_xTe$ [13]). The alloy $Hg_{1-x}Fe_xSe$ is of great interest due to the unique relationship between the Fe^{2+} level and the bottom of the conduction band of $HgSe$. Since the properties of this alloy have been extensively reviewed elsewhere [11, 12], we shall omit this material in the present review.

The ground state of Fe^{2+} is a non-degenerate A1 orbital singlet that has no permanent magnetic moment. At high temperatures, there is sufficient contribution from excited states with a finite moment so as to give paramagnetic behavior with $S \approx 2.1$ [10]. The values of the nearest-neighbor d-d exchange integral J as deduced from the Curie-Weiss behavior of the high temperature static susceptibility are comparable to those in the corresponding $A_{1-x}^{II}Mn_xB^{VI}$ alloys -- see Table I. At low temperatures, the non-magnetic ground state of Fe^{2+} results in Van Vleck paramagnetism, as opposed to the Brillouin paramagnetic behavior of the $A_{1-x}^{II}Mn_xB^{VI}$ alloys. This was first demonstrated in studies of $Hg_{1-x}Fe_xTe$ [13], and also later inferred from studies of $Cd_{1-x}Fe_xSe$ [10] and $Zn_{1-x}Fe_xSe$ [8,9].

TABLE I. Crystal structure, composition range and exchange constants of $A_{1-x}^{II}T_xB^{VI}$ ($T = \text{Co}^{2+}, \text{Fe}^{2+}$) alloys.

Alloy	Crystal Structure	Composition Range	$J_{dd}(\text{K})$	$N_0\alpha$	$N_0(\alpha-\beta)$
$\text{Zn}_{1-x}\text{Co}_x\text{S}$	zinc blende	$0 < x \leq 0.12$	-47 ± 6	----	----
$\text{Zn}_{1-x}\text{Co}_x\text{Se}$	zinc blende	$0 < x \leq 0.06$	-54 ± 8	----	2.42
$\text{Zn}_{1-x}\text{Fe}_x\text{Se}$	zinc blende	$0 < x \leq 0.30$	-22	----	1.56
$\text{Cd}_{1-x}\text{Co}_x\text{Se}$	wurtzite	$0 < x \leq 0.22$	37 ± 5	0.32	----
$\text{Cd}_{1-x}\text{Fe}_x\text{Se}$	wurtzite	$0 < x \leq 0.15$	-19	0.23	2.13
$\text{Hg}_{1-x}\text{Fe}_x\text{Se}$	zinc blende	$0 < x \leq 0.15$	-18	----	----
$\text{Hg}_{1-x}\text{Fe}_x\text{Te}$	zinc blende	$0 < x \leq 0.12$	----	----	----

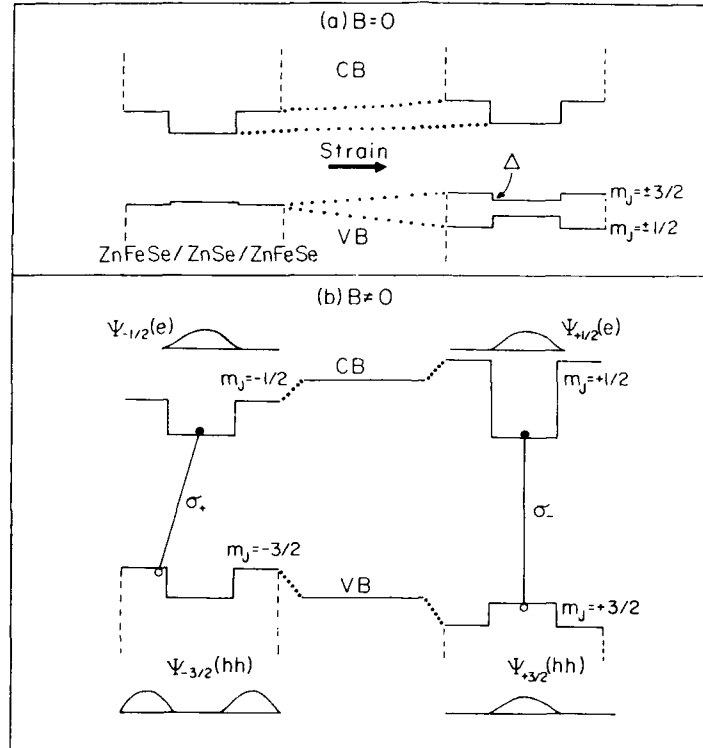


Fig. 1. Band diagrams for a $\text{Zn}_{1-x}\text{Fe}_x\text{Se}/\text{ZnSe}/\text{Zn}_{1-x}\text{Fe}_x\text{Se}$ single quantum well structure. (a) In zero magnetic field, the effect of strain removes the degeneracy between heavy hole and light hole states. (b) In the presence of a magnetic field, there is a spin splitting of the conduction band and the heavy hole valence band. Transitions excited by σ^+ and σ^- polarizations of incident light are indicated, as well as the general shapes of the single particle wavefunctions. [14]

The growth of $\text{Zn}_{1-x}\text{Fe}_x\text{Se}$ by MBE is of particular interest both because of the wide alloy composition range ($0 \leq x \leq 1$) [5] and because of the unusual properties of $\text{ZnSe}/\text{Zn}_{1-x}\text{Fe}_x\text{Se}$ quantum well structures [14]. Magneto-reflectivity studies of pseudomorphic $\text{ZnSe}/\text{Zn}_{1-x}\text{Fe}_x\text{Se}$ ($x = 0.1$) single quantum wells grown on (100) GaAs reveal a novel situation in which the confining valence band potential in a magnetic field is determined mainly by the magnetic-field-induced spin splitting. As shown in Fig. 1, in zero magnetic field the heavy and light hole states are split as a result of strain. The application of a magnetic field removes the degeneracy between the heavy hole $m_j = 3/2$ and $m_j = -3/2$ states, raising the energy of the former while lowering the energy of the latter. At high enough magnetic fields, the spin splitting results in a novel spin-dependent confinement: heavy holes in the $m_j = 3/2$ state are confined to the ZnSe well (type I behavior), while simultaneously, holes in the $m_j = -3/2$ state are confined to the $\text{Zn}_{1-x}\text{Fe}_x\text{Se}$ barrier (type-II behavior). This band alignment is dramatically manifested in an asymmetric Zeeman shift of the reflectivity signatures associated with the spin-split heavy-hole states. Since holes in the $m_j = -3/2$ state are confined to the $\text{Zn}_{1-x}\text{Fe}_x\text{Se}$ region, the associated optical transition (excited by light polarized in the σ^+ sense) experiences a very large sp-d exchange-related Zeeman shift. However, the $m_j = 3/2$ holes are confined to the non-magnetic ZnSe layer and hence the associated reflectivity feature (excited by σ^- polarization) shows a relatively small shift. The magneto-reflectivity experiments allow an accurate and elegant determination of the valence band offset between ZnSe and $\text{Zn}_{0.9}\text{Fe}_{0.1}\text{Se}$. It is estimated that the valence band offset is only 1.5 meV, which is about 1.5% of the total unstrained band offset. By comparison, the spin-splitting in $\text{Zn}_{0.9}\text{Mn}_{0.1}\text{Se}$ at a field of 10 kG is almost a factor of 10 larger (about 13 meV), hence permitting the spin-segregation effects just described.

$\text{A}_{1-x}^{II}\text{Co}_x\text{B}^{\text{VI}}$ DMS ALLOYS

The $\text{A}_{1-x}^{II}\text{Co}_x\text{B}^{\text{VI}}$ alloys have been prepared by chemical vapor transport [15], sintering [16] and by MBE [17]. As indicated by Table I, the incorporation of Co^{2+} into a II-VI host lattice is not easily accomplished, resulting in a limited alloy composition range. Apparently, even the non-equilibrium technique of MBE cannot overcome this difficulty [17].

The atomic ground state of Co^{2+} ($3d^7$) in a tetrahedral environment is an orbital singlet ($^4\text{A}_2$) with a spin $S = 3/2$. Consequently, the $\text{A}_{1-x}^{II}\text{Co}_x\text{B}^{\text{VI}}$ alloys, like the $\text{A}_{1-x}^{II}\text{Mn}_x\text{B}^{\text{VI}}$ alloys, are Brillouin paramagnets. However, due to spin-orbit mixing of the $^4\text{A}_2$ ground state with the next excited state triplet ($^4\text{T}_2$), the Co^{2+} ion acquires a significant orbital angular momentum component, leading to a Lande g-factor larger than the spin-only value for Mn^{2+} ($g = 2$). For instance, the g-factor measured in $\text{Zn}_{1-x}\text{Co}_x\text{Se}$ and $\text{Cd}_{1-x}\text{Co}_x\text{Se}$ is 2.27 [18] and 2.32 [19], respectively. Another striking difference between the Mn- and Co-based alloys lies in the values of both the sp-d and d-d exchange constants, which are much larger in the latter class. Since these two types of exchange are at the root of the unique magnetic and magneto-optical properties of DMS alloys, the experimental determination of the associated exchange integrals is extremely important, and we now address this issue.

Static susceptibility measurements have been employed to deduce the nearest-neighbor Co-Co exchange integral J in $\text{Zn}_{1-x}\text{Co}_x\text{Se}$ ($x \leq 0.05$) and $\text{Zn}_{1-x}\text{Co}_x\text{S}$ ($x \leq 0.145$) single crystals grown by chemical vapor transport [15]. The d-d exchange integral calculated from the Curie-Weiss temperature has values of $J = 47 \pm 6\text{K}$ and $-54 \pm 8\text{K}$ for the sulfide and the selenide, respectively. These values are at least three times larger than the d-d exchange in the corresponding Mn alloys. Furthermore, the $\text{A}_{1-x}^{II}\text{Co}_x\text{B}^{\text{VI}}$ alloys do not seem to follow the chemical trends found in the $\text{A}_{1-x}^{II}\text{Mn}_x\text{B}^{\text{VI}}$ alloys: the exchange integral in $\text{Zn}_{1-x}\text{Co}_x\text{Se}$ is larger than in $\text{Zn}_{1-x}\text{Co}_x\text{S}$, unlike the corresponding Mn-based alloys. Since a detailed theoretical calculation of the exchange in the $\text{A}_{1-x}^{II}\text{Co}_x\text{B}^{\text{VI}}$ alloys is not yet available, the reason for this change in trends is not understood.

Another method of measuring the d-d exchange integral is by means of inelastic neutron scattering, and this technique has been successfully used for single crystal as well as polycrystalline sintered samples of $\text{Zn}_{1-x}\text{Co}_x\text{S}$ [16]. Essentially, the inelastic neutron scattering

technique directly probes the energy spectrum of a pair of magnetic ions. The three excited states for a $\text{Co}^{2+}\text{-Co}^{2+}$ pair are $2J$, $6J$ and $12J$ for a total spin of $S_T = 1, 2$ and 3 , respectively. The neutron energy loss in an inelastic scattering process is equal to the difference between two neighboring levels, with the selection rule $\Delta S_T = 0, \pm 1$. At very low temperatures, practically all the pairs are in the lowest energy state $S_T = 0$. Hence, only one transition ($S_T = 0$ to $S_T = 1$) corresponding $E = 2J$ is seen. At higher temperatures, the $S_T = 1$ to $S_T = 2$ transition becomes possible, giving rise to an additional peak at $E = 4J$. The observation of such peaks (shown in Fig. 2) hence allows the very direct and precise determination of $J = 47.5 \pm 0.6\text{K}$ for $\text{Zn}_{1-x}\text{Co}_x\text{S}$.

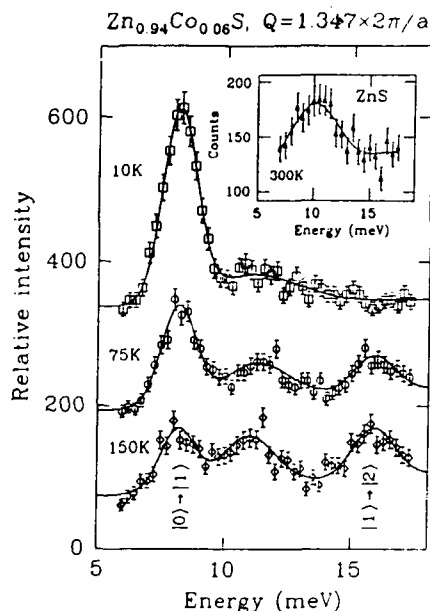


Figure 2. Inelastic neutron scattering spectra obtained from triple axis spectrometer measurements on $\text{Zn}_{0.94}\text{Mn}_{0.06}\text{S}$ at various temperatures, showing the decrease of the intensity of the $0 \rightarrow 1$ transition ($E = 2J$), and the emergence of the $1 \rightarrow 2$ peak ($E = 4J$) with increasing temperature. As shown in the inset, the maximum emerging at $E = 11\text{ meV}$ is also seen in the data from pure ZnS , indicating that this effect arises from phonon scattering.

We find that single-phase zinc-blende $\text{Cd}_{1-x}\text{Mn}_x\text{Se}$ can be grown directly on (100) GaAs, as well as on buffer layers of ZnSe and ZnTe grown on (100) GaAs.

We have also examined the growth of the following modulated structures: $\text{ZnSe}/\text{Cd}_{1-x}\text{Mn}_x\text{Se}$ [6] and $\text{ZnTe}/\text{Cd}_{1-x}\text{Mn}_x\text{Se}$. These two systems are extremely attractive because they provide deep magnetic quantum wells situated between non-magnetic barriers.

The sp-d exchange integral in $\text{Zn}_{1-x}\text{Co}_x\text{Se}$ has been determined from magneto-reflectivity experiments performed on epilayers grown on (100) GaAs [18]. These experiments, which measure the excitonic spin-splitting in a magnetic field, yield the parameter $N_0(\alpha - \beta) = 2.42 \pm 0.04\text{ meV}$, where α and β describe the exchange between the Co ions and valence band and between the Co ions and conduction band, respectively. This is almost twice as large as in $\text{Zn}_{1-x}\text{Mn}_x\text{Se}$. The sp-d exchange in $\text{Cd}_{1-x}\text{Co}_x\text{Se}$ has been deduced by observing spin-flip Raman scattering from electrons bound to donors [19]. By measuring the Raman shift of such a spin-flip resonance as a function of magnetic field, it is possible to deduce the value of the sp-d exchange integral α and this is found to have a value of around 320 meV . (For comparison, $N_0\alpha = 261\text{ meV}$ for $\text{Cd}_{1-x}\text{Mn}_x\text{Se}$.)

CUBIC $\text{Cd}_{1-x}\text{Mn}_x\text{Se}$: EPITAXIAL LAYERS AND MODULATED STRUCTURES

It is well known that, in the bulk, $\text{Cd}_{1-x}\text{Mn}_x\text{Se}$ -- like CdSe -- crystallizes exclusively in the hexagonal wurtzite phase [1]. However, epitaxial growth of CdSe [20] and $\text{Cd}_{1-x}\text{Mn}_x\text{Se}$ [6] by MBE on (100) zinc-blende substrates can produce single-phase zinc-blende epilayers. The isolation of this phase is aided by at least two factors. First, at the low growth temperatures (around 200°C) employed in the MBE process, the zinc-blende phase is likely to be more stable than the wurtzite [21]. Second, the symmetry of the (100) face is incompatible with that required for the coherent nucleation of a hexagonal structure.

This offers the possibility of observing dramatic magnetic-field-induced effects due to the sp-d exchange, particularly when the Mn concentration is in the vicinity of $x = 0.1$. Further, since $\text{Cd}_{1-x}\text{Mn}_x\text{Se}$ can be easily doped n-type, such structures are potential candidates for studying confinement and localization effects on phenomena such as the bound magnetic polaron and spin-flip Raman scattering from donor-bound electrons. We discuss here the opportunities provided by the growth of such heterostructures, and also examine the difficulties encountered so far.

$\text{Cd}_{1-x}\text{Mn}_x\text{Se}$ Epilayers on (100) GaAs

The stabilization of single-phase zinc-blende epilayers of $\text{Cd}_{1-x}\text{Mn}_x\text{Se}$ on (100) GaAs is possible for a wide composition range ($0 \leq x \leq 0.8$) [6]. The lattice mismatch between the $\text{Cd}_{1-x}\text{Mn}_x\text{Se}$ epilayers and GaAs varies from around 7% to 4% for this composition range. (We recall that bulk-growth of single-phase wurtzite $\text{Cd}_{1-x}\text{Mn}_x\text{Se}$ is limited to $x < 0.5$ [1].) The single-phase zinc-blende structure of these epilayers is clearly indicated by both transmission electron microscopy (TEM), as well as x-ray diffraction. Further, the epilayers show clear Raman phonon spectra characteristic of cubic symmetry, as shown in Fig. 3 [22]. It is likely that very thin epilayers of composition larger than $x = 0.8$ can also be stabilized, for instance in $\text{ZnTe}/\text{Cd}_{1-x}\text{Mn}_x\text{Se}$ superlattices, and this possibility is currently being investigated.

After examining the epitaxy of $\text{Cd}_{1-x}\text{Mn}_x\text{Se}/(100)$ GaAs using a wide variety of growth conditions, we have concluded that the epilayers -- at least those grown so far -- tend to contain a large number of structural defects. This is indicated by broad double crystal rocking curves (with full width at half maximum (FWHM) typically around 1800 arc-seconds) and broad photoluminescence (PL) spectra dominated by mid-gap defect states. TEM observations indicate that the predominant structural defects are stacking faults that occur in the [111] direction [23]. The stacking fault density as seen in TEM cross-sectional views of orthogonal [110] faces is highly asymmetric, suggesting that they arise due to unequal propagation rates of different [111] growth fronts.

The most dramatic experimental phenomenon exhibited by $\text{Cd}_{1-x}\text{Mn}_x\text{Se}$ epilayers occurs in neutron diffraction experiments [24]. We have found clear evidence for a second-order antiferromagnetic phase transition in $\text{Cd}_{1-x}\text{Mn}_x\text{Se}$ epilayers for $x \geq 0.70$. This is deduced from the appearance of diffraction peaks corresponding to long-range type-III antiferromagnetic order

(AFM-III, see Fig. 4) at temperatures below a well-defined Neel temperature (in the vicinity of 56 K). The correlation lengths deduced from these experiments are around 300 Å. (We believe that the extent of the AFM-III ordering in

$\text{Cd}_{1-x}\text{Mn}_x\text{Se}$ epilayers is limited only by the presence of crystalline defects such as stacking faults.) These correlation lengths are in marked contrast with studies of bulk-grown single-crystal DMS alloys of comparable Mn concentration ($\text{Cd}_{0.3}\text{Mn}_{0.7}\text{Te}$ and $\text{Zn}_{0.32}\text{Mn}_{0.68}\text{Te}$), where the AFM-III correlations increase gradually with decreasing temperature, eventually reaching saturation values of at most 70 Å. Experimental studies of

magnetic ordering in $\text{A}_{1-x}^{\text{II}}\text{Mn}_x\text{B}^{\text{VI}}$ alloys in the composition range $x > 0.6$ are of fundamental importance to the understanding of randomly diluted, fully frustrated Heisenberg vector antiferromagnets [25]. Consequently, efforts aimed at improving the crystalline quality of $\text{Cd}_{1-x}\text{Mn}_x\text{Se}$ epilayers in this composition range are continuing.

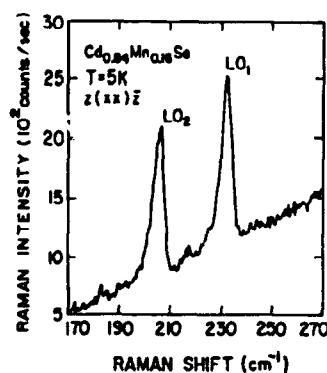


Figure 3. Raman spectrum of a zinc-blende $\text{Cd}_{0.84}\text{Mn}_{0.16}\text{Se}$ epilayer at $T = 5$ K. The spectrum was recorded in the backscattering geometry $z(xx)z$ with an incident wavelength of 6328 Å [22].

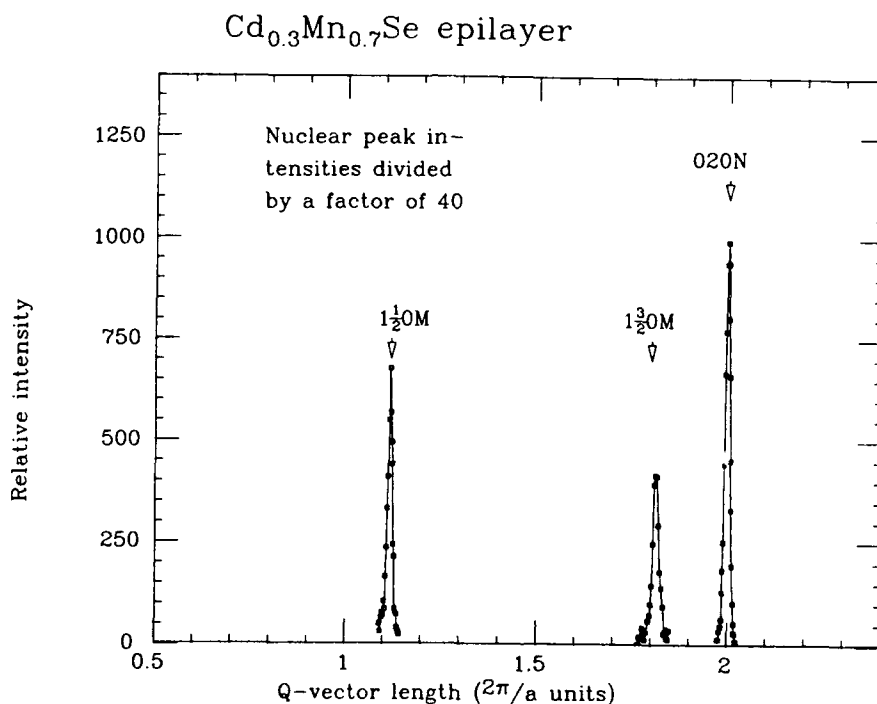


Fig. 4. Neutron diffraction spectrum at $T = 5\text{K}$ from a $2\text{ }\mu\text{m}$ thick epilayer of $\text{Cd}_{0.25}\text{Mn}_{0.75}\text{Se}$ grown on (100) GaAs, showing the (0,2,0) nuclear peak and the (1,1/2,0) and (1,3/2,0) magnetic peaks corresponding to AFM-III order. The scans were carried out for the longitudinal direction, and the peaks are plotted as a function of the magnitude of the Q-vector. Note that the widths of the magnetic and nuclear peaks are about the same. The correlation length estimated from the width of the magnetic peaks is $380 \pm 80\text{ }\text{\AA}$.

ZnSe/Cd_{1-x}Mn_xSe Heterostructures

Although $\text{Cd}_{1-x}\text{Mn}_x\text{Se}$ has about the same lattice mismatch with ZnSe as with GaAs, one might expect better nucleation of $\text{Cd}_{1-x}\text{Mn}_x\text{Se}$ on an epitaxially grown ZnSe buffer. Surprisingly, this is not the case, and a three-dimensional nucleation is observed. Consequently, ZnSe/ $\text{Cd}_{1-x}\text{Mn}_x\text{Se}$ quantum well structures have atomically rough interfaces -- clearly indicated by TEM observations -- and characteristically show broad (FWHM $\sim 50\text{ meV}$) PL peaks [6]. Despite these imperfections, ZnSe/ $\text{Cd}_{1-x}\text{Mn}_x\text{Se}$ superlattices exhibit a spectacular spin-flip Raman spectrum, in which the resonances associated with transitions within the Zeeman-split Mn^{2+} manifold ("Raman-EPR") are highly enhanced. This allows the unprecedented observation of seven orders of spin-flip resonances, as shown in Fig. 5 [22]. The reason for this large enhancement is not completely understood, but is quite intriguing, especially given the structural imperfections in this system.

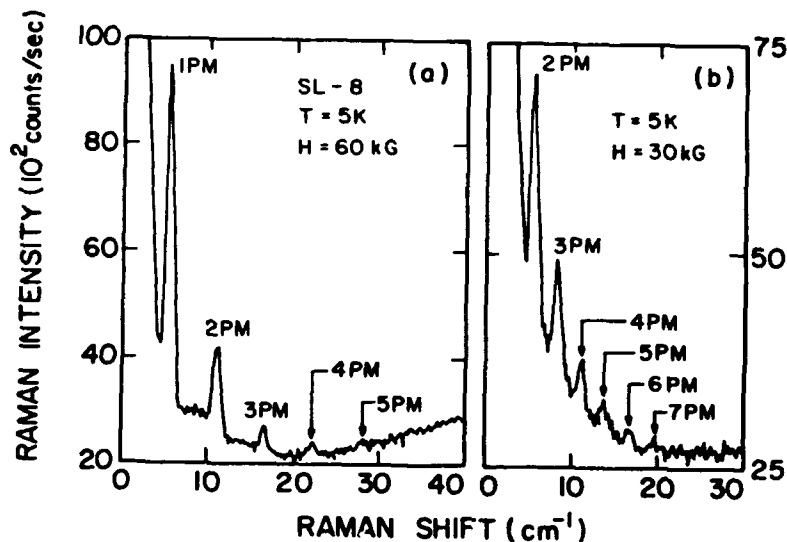


Fig. 5. Raman-EPR spectrum of a ZnSe/Cd_{0.9}Mn_{0.1}Se superlattice at $T = 5$ K. The spin-flip resonances labeled n PM ($n = 1, 2, \dots, 7$) have Raman shifts in a magnetic field H given by $\hbar\omega_{PM} = ng\mu_B H$, with $g = 2$ for Mn^{2+} . The spectrum is obtained in the crossed polarization configuration $z(yx)\bar{z}$, with the magnetic field along x and incident wavelength of 6764 \AA [22].

ZnTe/Cd_{1-x}Mn_xSe Heterostructures

In contrast to the growth of Cd_{1-x}Mn_xSe on ZnSe, RHEED observations indicate a smooth two-dimensional nucleation of Cd_{1-x}Mn_xSe on ZnTe. As a consequence, Cd_{1-x}Mn_xSe/ZnTe heterostructures can be expected to much better interface quality than Cd_{1-x}Mn_xSe/ZnSe. In this system of heterostructures, the lattice mismatch ranges from around 0.2% for CdSe/ZnTe to around 4% for MnSe/ZnTe. RHEED observations further show that the growth of Cd_{1-x}Mn_xSe layers on ZnTe proceeds reasonably well for thicknesses less than under about 2000 Å. Beyond this limit, RHEED indicates the rapid formation of structural defects. The microscopic nature of these defects is currently being studied by TEM. It appears that ZnTe/Cd_{1-x}Mn_xSe superlattices with a small number of periods (10-20) can be grown with sharp interfaces and few defects as long as the Cd_{1-x}Mn_xSe layer thicknesses are kept small (for instance, see Fig. 6) [26].

Such ZnTe/Cd_{1-x}Mn_xSe superlattices offer an unusual system of band configurations. Theoretical estimates [27] of the valence band offset of CdSe/ZnTe predict a type-II alignment, since the valence band of ZnTe ($E_g = 2.3$ eV) is about 350 meV above that of CdSe ($E_g = 1.67$ eV for cubic epilayers [20]). Consequently, we expect ZnTe/Cd_{1-x}Mn_xSe to also form a type-II superlattice for small x , with holes confined to the ZnTe layers and electrons in the magnetic Cd_{1-x}Mn_xSe layers. With increasing Mn concentration, the energy gap of Cd_{1-x}Mn_xSe increases, while the valence band is expected to remain relatively stationary. Consequently, beyond some value of x , the band alignment of ZnTe and Cd_{1-x}Mn_xSe will transform to a type-I configuration, with both holes and electrons confined to the ZnTe layers. We are currently performing optical measurements of ZnTe/Cd_{1-x}Mn_xSe superlattices ($x = 0, 0.3, 1$) to test these ideas.

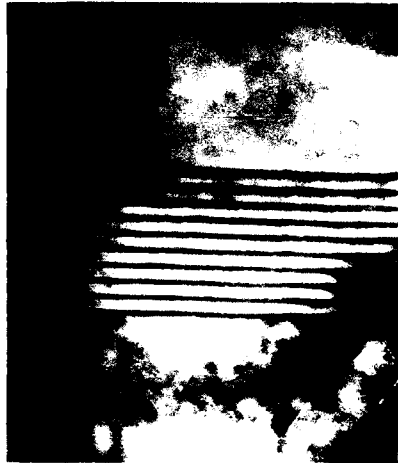


Fig. 6. TEM image of a 10-period $\text{ZnTe}/\text{Cd}_{0.70}\text{Mn}_{0.30}\text{Se}$ multiple quantum well structure, with 20 Å layers of $\text{Cd}_{0.70}\text{Mn}_{0.30}\text{Se}$ and 26 Å layers of ZnTe . The buffer and cap layers are ZnTe , and the entire structure is grown on a (100) GaAs substrate [26].

FUTURE PROSPECTS

We have tried to illustrate the rich variety of new problems that are being generated by the latest additions to the family of II-VI DMS alloys. The novel spin-dependent type-I/type-II behavior observed in $\text{ZnSe}/\text{Zn}_{1-x}\text{Fe}_x\text{Se}$ single quantum well structures has provided the first demonstration of magnetic-field-sensitive confinement effects. Further studies of such structures, such as the magneto-transport properties of modulation-doped $\text{ZnSe}/\text{Zn}_{1-x}\text{Fe}_x\text{Se}$ superlattices, can be expected to produce fascinating physical phenomena. The Co-based alloys with very strong sp-d and d-d exchange interactions are very attractive for their magneto-optical and magnetic properties. It is hoped that the epitaxial growth of modulated structures involving these alloys will be further pursued. Finally, the recent introduction of a system of heterostructures involving ZnTe and zinc-blende $\text{Cd}_{1-x}\text{Mn}_x\text{Se}$ promises a rich variety of band line-ups. It is hoped that the structural quality of these heterostructures will soon be optimized so that systematic investigations of the magnetic and optical properties can be undertaken.

ACKNOWLEDGEMENTS

We thank R. G. Alonso, U. Debska, T. Giebultowicz, W. Girit, P. Klosowski, Y. R. Lee, A. Lewicki, H. Luo, N. Otsuka, S. B. Qadri, A. K. Ramdas, and A. Twardowski for their contributions to various aspects of this work. The authors wish to acknowledge the support of NSF Grant No. DMR-8520866 and DARPA-ONR Grant No. N00014-86-K-0760.

REFERENCES

1. For a recent review containing an extensive bibliography, see J. K. Furdyna, *J. Appl. Phys.* **64**, R 29 (1988).
2. For reviews of other DMS alloys such as $\text{Pb}_{1-x}\text{Eu}_x\text{Te}$ and $(\text{Cd}_{1-x}\text{Mn}_x)_3\text{As}_2$, see *Diluted Magnetic (Semimagnetic) Semiconductors*, edited by R. L. Aggarwal, J. K. Furdyna, and S. von Molnar (Vol. 89, Materials Research Society Symposia Proceedings, Pittsburgh, PA, 1987).
3. L. A. Kolodziejski, R. L. Gunshor, N. Otsuka, B. P. Gu, Y. Hefetz, and A. V. Nurmikko, *Appl. Phys. Lett.* **48**, 1482 (1986).
4. S. Durbin, M. Kobayashi, Qiang Fu, N. Pelekanos, R. L. Gunshor, and A. V. Nurmikko, *Appl. Phys. Lett.* (in press).
5. B. T. Jonker, J. J. Krebs, S. B. Qadri, G. A. Prinz, F. A. Volkening, and N. C. Koon, *J. Appl. Phys.* **63**, 3303 (1988).
6. N. Samarth, H. Luo, J. K. Furdyna, S. B. Qadri, Y. R. Lee, R. G. Alonso, E. K. Suh, A. K. Ramdas, and N. Otsuka, *Proceedings of Fourth International Conference*

on *Modulated Semiconductor Structures*, Surface Science (to be published).

7. H. Munekata, H. Ohno, S. Von Molnar, A. Segmuller, L. L. Chang, and L. Esaki, *Phys. Rev. Lett.* **63**, 1849 (1989).
8. B. T. Jonker, J. J. Krebs, S. B. Qadri, and G. A. Prinz, *Appl. Phys. Lett.* **50**, 848 (1987).
9. A. Twardowski, M. von Ortenberg and M. Demianiuk, *J. Cryst. Growth* **72**, 401 (1985).
10. A. Lewicki, J. Spalek and A. Mycielski, *J. Phys. C* **20**, 2005 (1987).
11. A. Mycielski, in *Diluted Magnetic (Semimagnetic) Semiconductors*, edited by R. L. Aggarwal, J. K. Furdyna, and S. von Molnar (Vol. 89, Materials Research Society Symposia Proceedings, Pittsburgh, PA, 1987), p. 159.
12. R. Reifenberger and J. Kossut, *J. Vac. Sci. Technol.* **A5**, 2995 (1987).
13. Y. Guldner, C. Rigaux, M. Menant, D. P. Mullin and J. K. Furdyna, *Solid State Commun.* **33**, 133 (1980).
14. X. Liu, A. Petrou, J. Warnock, B. T. Jonker, G. A. Prinz and J. J. Krebs, *Phys. Rev. Lett.* (in press).
15. A. Lewicki, A. I. Schindler, J. K. Furdyna and W. Giriat, *Phys. Rev. B* **40**, 2379 (1989).
16. T. Giebultowicz, P. Klosowski, J. J. Rhyne, T. J. Udovic, J. K. Furdyna and W. Giriat, *Phys. Rev. B* (in press).
17. B. T. Jonker, J. J. Krebs and G. A. Prinz, *Appl. Phys. Lett.* **53**, 450 (1988).
18. X. Liu, A. Petrou, B. T. Jonker, G. A. Prinz, J. J. Krebs and J. Warnock,
19. D. U. Bartholomew, E. K. Suh, A. K. Ramdas, S. Rodriguez, U. Debska, and J. K. Furdyna, *Phys. Rev. B* **39**, 5865 (1989).
20. N. Samarth, H. Luo, J. K. Furdyna, S. B. Qadri, Y. R. Lee, A. K. Ramdas and N. Otsuka, *Appl. Phys. Lett.* (1989)
21. N. Kh. Abrikosov, V. F. Bankina, L. V. Poretskaya, L. E. Shelimova, and E. V. Skudnova, *Semiconducting II-VI, IV-VI, and V-VI Compounds*, Plenum Press, New York (1969), p. 3.
22. R. G. Alonso, E. K. Suh, A. K. Ramdas, N. Samarth, H. Luo, J. K. Furdyna, *Phys. Rev. B* **40**, 3720 (1989).
23. D. Li and N. Otsuka (private communication).
24. T. Giebultowicz, P. Klosowski, N. Samarth, H. Luo, J. K. Furdyna and J. J. Rhyne, *Proceedings of Materials Research Society*, December 1989.
25. C. Henley, *Phys. Rev. Lett.* **62**, 2056 (1989).
26. N. Samarth, H. Luo, J. K. Furdyna, A. Mahalingam, and N. Otsuka (unpublished).
27. W. Harrison and W. Tersoff, *J. Vac. Sci. Technol.* **B 4**, 1068 (1986).

TEM STUDY OF DEFECTS IN CdTe/CdMnTe SUPERLATTICES ON (100) InSb

S.J. DIAMOND AND J.W. STEEDS

Bristol University, Department of Physics, Tyndall Ave., Bristol BS8 1TL, UK

D. ASHENFORD AND B. LUNN

Hull University Department of Engineering and Computing, Cottingham Rd., Hull, UK

ABSTRACT

CdTe/Cd_{1-x}Mn_xTe superlattices with well/barrier thicknesses ranging from 20Å to 300Å were examined via plan and cross section TEM in analytical instruments capable of EDX and CL. Misfit dislocations, inclined dislocations and stacking faults were observed with a net density of around 10⁸cm⁻².

It was observed that the dislocations originated near the substrate/epilayer interface and that stacking faults appeared preferentially on the pair of {111}B (tellurium terminated) planes in the growth direction rather than on the {111}A planes.

It is suggested that this is due to a difference in mobility between α and β dislocations originating at or near the substrate.

INTRODUCTION

II-VI semiconductors are becoming important as their large band-gaps are suited to optoelectronic devices such as solid state lasers and optical detectors. Furthermore, dilute magnetic semiconductors (DMS) such as CdMnTe offer additional applications as the interaction between their electronic and magnetic properties produces large magneto-optical effects such as magnetically tunable band gaps [1]. Molecular beam epitaxy (MBE) growth techniques allow high quality epilayers to be grown, including quantum well and superlattice structures which exploit two dimensional confinement effects for band gap tailoring purposes, and have been found to be strong photo-emitters.

This study involves CdTe/Cd_{1-x}Mn_xTe superlattice structures grown on (100) InSb at Hull University. Values of x were near to 0.2 and quantum well thicknesses varied between 20 and 300Å. InSb was chosen as the substrate material for its good lattice matching with both CdTe (approximately 0.02% mismatch at 25°C) and Cd_{1-x}Mn_xTe (approximately 0.45% at 25°C for $x=0.2$). Furthermore high quality InSb is available which is suited to low temperature MBE growth [2], reducing the interdiffusion of layers.

Samples of the CdTe/CdMnTe system have been examined in both cross section and plan view transmission electron microscopy (TEM), with both orientations revealing extensive detail. A typical sample consists of a (100) InSb substrate on which a 1000Å CdTe buffer layer is grown, followed by a 2000Å CdMnTe isolating layer. This CdTe buffer layer has been found to be critical to layer quality [2]. Superlattices comprising of wells and barriers of equal thickness, between 20 and 300Å for different samples, with an overall thickness of about 1500Å are then grown on this base. A second 2000Å CdMnTe capping layer is finally grown to allow manganese composition determination by photoluminescence (PL).

The (100) p-type InSb substrates were chemically cleaned and surface oxide was removed in vacuo using argon ion milling and growth temperature thermal anneal cycles until C(8x2) surface reconstruction was observed using *in situ* RHEED. The superlattices were grown in a VG Semicon V80H MBE system using high purity CdTe and Mn sources. Layers were grown at a rate of 0.5 microns per hour on substrates at a temperature between 200 and 250°C.

Cross section samples were produced by mechanical polishing and iodine reactive ion milling to reduce the ion beam damage associated with argon-thinned II-VI materials [3]. Plan section samples were produced by mechanical polishing followed by chemical jet etching with a 0.5% bromine-methanol solution. Samples were examined in Philips EM430 and EM400 machines (300KeV and 120KeV respectively) capable of energy dispersive X-ray (EDX) analysis and microscopic cathodoluminescence (CL).

RESULTS

Figure 1 shows a typical cross section, consisting of two {110} oriented samples separated by a thin layer of glue. As the CdTe system is non-centrosymmetric, the two $\langle 110 \rangle$ type directions in the growth plane are not equivalent. The [110] direction defines the intercept of the pair of {111}B planes advancing in the growth direction and [110] the intercept of advancing {111}A planes. Cross sections were prepared with two orthogonal halves to show both orientations. It can readily be seen that the defect structure in the two directions is different.

In both halves of the cross section the interfaces between InSb and CdTe are seen to be decorated with dark regions which EDX analysis showed to be iodine rich particles resulting from specimen preparation. Both halves of the sample also show a number of $a/2\langle 110 \rangle$ dislocations running through the epilayers. These often bend over at internal interface planes to produce misfit dislocation (MD) segments. The most common MD lie between the 1000Å CdTe and 2000Å CdMnTe layers nearest the substrate. MD segments within the superlattice itself were rarely seen in samples with individual layer thicknesses below 150Å. Very few dislocations were observed in the InSb substrate, most seeming to originate at the InSb surface. It should be noted that as the two halves of the cross section were not exactly orthogonal the {220} diffraction condition for the two halves has a differing deviation parameter, giving one side better dislocation contrast than the other.

Only in the upper half, however, can planar defects be seen lying on the two edge on {111} type planes. The majority of these defects were single layer stacking faults (SF) rather than micro-twins (as demonstrated by the absence of extra twin spots in selected area diffraction patterns). The stacking faults generally appeared to originate at the substrate interface although as some SFs may have originated outside the plane of the cross section this conclusion is somewhat tentative at the moment.

Figure 2 shows a substrate-epilayer interface region in more detail. Although there is little contrast between the 1000Å and 2000Å thick layers the position of the first CdTe/CdMnTe interface was deduced from the known layer thicknesses. It can be seen that there are a number of short dislocations running along this interface (arrowed) and also at the interface between the 2000Å CdMnTe layer and the start of the superlattice. It can also be seen that there are a number of small black/white contrast spots which are taken to be small precipitates. These spots are seen most at the first CdTe/CdMnTe interface. Within the superlattice similar precipitates seem to lie preferentially at interface sites rather than within layers.

Figure 3 shows a typical plan-section. The details observed in such sections correspond well with those from the cross-sections. For example dislocation segments are seen running up through the foil with straight (misfit) sections running along both orthogonal $\langle 110 \rangle$ directions (note that the {220} diffraction condition of fig.2 only shows one set of these MDs). The misfit dislocations can be seen as created from inclined dislocations which bend over to run in the (100) plane for a while before continuing up through the foil. This is shown by the fact that the dislocations at either end of the misfit segments run in different directions, one part running down to the substrate and the other continuing up to the surface, forming "s" shapes around the MDs. Again stacking faults are clearly shown to lie in preference on one pair of {111} planes (no SFs show up in the orthogonal reflection). Stacking faults were seen to lie on both {111} planes of the preferred pair. Stereographic imaging showed that few of the threading dislocations lay on their {111} slip planes.

In order to determine the character of the habit planes of the stacking faults, crystal polarity was determined by convergent beam electron diffraction using the method of Spellward and Preston [4]. This approach compares the asymmetry in convergent beam discs down $\langle 110 \rangle$ with that in computer simulations. Good matching with theoretical simulations was found for both plan and cross-section samples. Both cases gave the result that the stacking faults lay on {111}B type (tellurium) terminated planes. It should be mentioned that the small number of micro-twins that were observed in certain samples also lay preferentially on these planes.

Microscopic CL was carried out on a number of samples at liquid helium



Fig. 1

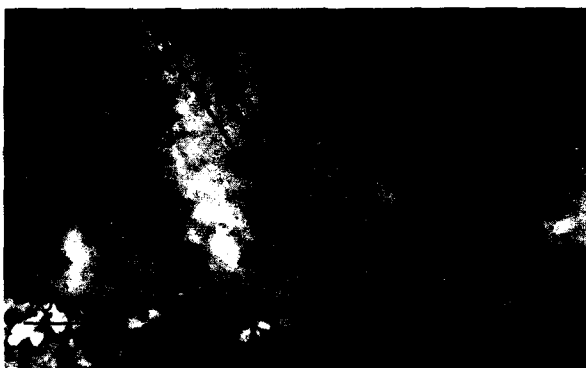


Fig. 2



Fig. 3

recombination rates but plan section band-gap to deep level intensity ratios indicated good quality material. The high level of dislocations, however, acted to reduce CL intensity and to complicate excitonic emission spectra. Lower dislocation densities would be necessary to separate the various effects which are evidently occurring.

DISCUSSION

The strains in this system ($< 0.5\%$) are sufficient for misfit dislocations to be energetically favourable for quite thin layers. As the mismatch between CdTe and $\text{Cd}_{0.8}\text{Mn}_{0.2}\text{Te}$ is much greater than that between CdTe and InSb, MDs within the epilayer, particularly between the thick layers, are likely to be more important than those at the substrate/buffer layer interface. Using the Mathews model [5] the critical thickness for CdTe on CdMnTe (the thickness at which the strain energy relieved by a misfit dislocation exceeds the dislocation energy) is approximately 170Å at 25°C but falls to about 70Å at the growth temperature. These values, however, relate to the growth of a thin layer onto bulk material. In the case of superlattices where both layers are strained about an average lattice constant the critical thickness rises to about 1000Å. The model considers the generation of misfit dislocations by the glide of existing dislocations. To introduce dislocations into a perfect layer, however, requires the dislocation nucleation energy to be overcome and consideration of likely nucleation mechanisms suggests that homogenous generation of misfit dislocations is unlikely in systems with strain below about 2% [5]. In the absence of such a mechanism for generating dislocation half loops, and given the low density of substrate dislocations it appears that dislocations are produced at inhomogenous regions within the layers. This is hardly surprising as InSb surface preparation is known to be problematical, with a tendency to leave indium rich sites which might act as dislocation nucleation points [6]. Furthermore, the observations suggesting micro-precipitates within the samples provides a second possible dislocation source. This conclusion is supported by the fact that the majority of dislocations appear to originate at the substrate/buffer layer interface.

A mechanism where dislocations originate at or near the substrate and propagate through the epilayer until they reach a level at which the strain is sufficient to cause them to glide to generate MD segments is consistent with our observation. Both cross-section views and the "s" shape in plan view of dislocations involving MD segments indicate that the dislocations originate at the substrate region rather than gliding in from the surface. It may also be deduced that the dislocation glide occurs early on during growth because dislocations rising to the surface are not restricted to their slip planes. It follows that after gliding to form MDs the dislocations propagating into the rest of the layer are free to climb as well as glide. Further, the critical thickness calculations show that MDs are more likely to be produced at the growth temperature and within the current surface layer rather than within the body of the superlattice itself. The plausibility of these thickness calculations is supported by the fact that MD segments were only seen within the superlattice for layer thicknesses greater than 100Å, in good agreement with theory.

The most likely cause of the stacking faults found in the epilayers is the commonly seen dissociation of a perfect $a/2\langle 110 \rangle$ dislocation into $a/6\langle 211 \rangle$ Shockley partials with the generation of such a stacking fault. It is also possible that stacking fault irregularities may occur in the early stages of island growth as previously reported in the case of GaP [7]. Both mechanisms offer explanation for the preferred occurrence of stacking faults on one pair of $\{111\}$ planes.

In the first case, misfit dislocations lying at a certain interface will always be oriented such that all dislocations running in one $\langle 110 \rangle$ direction will be so called α dislocations and all those in the perpendicular direction will be β dislocations. This conclusion follows from the fact that the extra half set of planes associated with the dislocations must always lie on the same side of the interface so as to relieve strain. It is most likely that there will be a difference in the mobility of the α and β dislocations making one more likely to dissociate than the other. Hence the faults originating at a given interface will be more likely to lie on the pair of $\{111\}$ planes common to the preferred $\langle 110 \rangle$. Since the majority of MDs occurred at the interface between the buffer

would show a preferred direction. The 2000Å CdMnTe was grown under tension and it was seen that dislocations running in the $[110]$ direction dissociate on the $\{111\}$ B planes. This direction corresponds to α dislocations with the extra half planes terminated on tellurium atoms. It would follow that the α dislocations dissociate preferentially.

Alternatively it is possible that such stacking faults are grown into the material by misordered layer deposition. Such behaviour has been observed in GaP [7] where in the early stages of growth islands form with facets which lie predominantly on one pair of the advancing $\{111\}$ planes due to differences in surface energy. Misordered deposition on these surfaces then gives stacking faults or twins in a preferred direction.

Both of these models give plausible explanation for the preferred orientation of stacking faults and also for that of the smaller number of micro-twins seen in some samples. In the second mechanism reversal of layer order during growth may clearly give rise to twins. In the first case it is possible to envisage twin formation by the successive production of stacking faults on adjacent planes since a twin is identical to a series of stacking faults. Examination of layers terminated before island coalescence occurred should distinguish between the two mechanisms.

SUMMARY

In the series of samples examined the dislocation densities observed are fairly high (10^8 - 10^{10})/cm². The dislocations appear to originate at the substrate/buffer interface or at precipitates within the epilayers. These dislocations are distorted to form misfit sections in agreement with the model proposed by Mathews. The formation of stacking faults on a preferred pair of $\{111\}$ planes is thought to result from the difference in mobility between α and β type dislocations, although an alternative explanation is advanced based on faceted islands in the early stages of growth.

ACKNOWLEDGEMENTS

Thanks to SERC for funding and to B.Lunn and D.Ashencroft of Hull University for provision of samples.

REFERENCES

- [1] J.Furdyna J.Appl.Phys. **64** (4) pp 229-264 (1988)
- [2] G.Williams, A.Cullis, C.Whitehouse, D.Ashenford and B.Lunn Appl.Phys.Lett. **55** (13) pp 1303-1305 (1989)
- [3] N.Chew and A.Cullis Ultramicroscopy **23** pp175-198 (1987)
- [4] P.Spellward and A.Preston Inst.Phys.Conf.Ser. **93** (2) pp 29-30 (1988)
- [5] J.Mathews, J.Blakeslee and S.Madir Thin Solid Films **33** pp225 (1976)
- [6] D.Ashenford, D.Johnston, B.Lunn and C.Scott J.Phys.Condens.Matter **1** pp SB51-54 (1989)
- [7] F.Ernst and P.Pirouz J.Appl.Phys. **64** (9) pp 4526-4530 (1989)

Ga AND In AUTODOPING OF $\text{Cd}_{1-x}\text{Mn}_x\text{Te}$ EPITAXIAL LAYERS GROWN ON GaAs AND InSb SUBSTRATES

J.J. DUBOWSKI*, J.M. WROBEL**, S. ROLFE*, J.A. JACKMAN*, J.H. MAZUR** AND J. NOAD#

* Division of Physics, NRC, 100 Sussex Dr., Ottawa, Ont., Canada K1A 0R6

** Department of Physics, University of Missouri, Kansas City, MO 641110, USA

* Metals Technology Laboratories, CANMET, Ottawa, Ont., Canada K1A 0G1

** Materials Science Department, University of Southern California, Los Angeles, USA

Communication Research Centre, Ottawa, Ont., Canada K2H 8S2

ABSTRACT

A study of Ga and In outdiffusion into $\text{Cd}_{1-x}\text{Mn}_x\text{Te}$ ($0 \leq x \leq .70$) epitaxial layers grown on (111)GaAs and (001)InSb was carried out. The layers were grown by pulsed laser evaporation and epitaxy on substrates held at temperatures below 310 °C. The structural quality of the layers was examined using x-ray diffraction and transmission electron microscopy. A tendency toward precipitation of Ga at the near surface region of (111)CdMnTe grown on (111)GaAs, usually less than 300 nm wide, has been observed with secondary ion mass spectroscopy. Similar results were observed for the migration behaviour of In in (001)CdTe grown on (001)InSb. The ion imaging revealed that both In and Ga accumulate near the surface at localized spots, up to about 10 μm in diameter. The concentration of the spots is in the range of $10^4 - 10^6 \text{ cm}^{-2}$. The Ga- and In-rich channels sometimes extend over the whole sample. Annealing at temperatures as low as 400 °C for 2 h significantly increases the concentration of the Ga spots and the average concentration of Ga in the films to above 10^{16} cm^{-3} . Low-temperature photoluminescence data obtained for annealed samples do not indicate any structural deterioration typical for heavily doped Bridgman grown samples. A sharp neutral-donor bound-exciton transition (D^0, X) is observed for samples with $0 < x < .10$.

INTRODUCTION

A continuing interest has been observed in the application of GaAs and InSb substrates for epitaxial growth of CdTe, HgCdTe and CdMnTe. Relatively mature technologies of CdTe, and HgCdTe on GaAs and InSb promise potential applications of these structures in IR detection^{1,2} and high-speed MIS devices³. Epitaxial layers of CdMnTe are of particular interest due to their potential application in devices based on magneto-optical effects⁴ and as an alternative to CdTe substrate used in HgCdTe IR detectors. Performance of such devices will depend upon the ability to control the unintentional doping that takes place as CdTe or CdMnTe are grown on GaAs and InSb. Significant migration of Ga^{5,6} and In^{7,8} into epitaxial layers of CdTe grown on GaAs and InSb has been reported. Recently, we found⁹ that accumulation of Ga in localized spots takes place near the surface region of CdTe grown on GaAs. The presence of Ga was verified in such a case with low-temperature photoluminescence (PL)¹⁰ and electrolyte electroreflectance¹¹ measurements.

In this paper, we describe the use of secondary ion mass spectroscopy (SIMS) and low-temperature PL to study Ga diffusion in (111)CdMnTe grown on (111)GaAs. Preliminary results of In diffusion in (001)CdTe grown on (001)InSb are also presented.

EXPERIMENTAL DETAILS

The epitaxial layers of (111) $\text{Cd}_{1-x}\text{Mn}_x\text{Te}$ ($0 \leq x \leq .70$) and (001)CdTe were grown by pulsed laser evaporation and epitaxy (PLEE)^{12,13} on the B-face of (111)GaAs and on (001)InSb, respectively.

The (111) $\text{Cd}_{1-x}\text{Mn}_x\text{Te}$ layers were grown on substrates held at a fixed temperature in the range of 210 - 310 °C. The basic properties of the layers were studied using scanning electron microscopy, reflection high-energy electron diffraction and low-temperature PL, and these results were published elsewhere¹³. A single crystal x-ray diffractometer study was carried

out for the samples 0.8 - 1.3 μm thick. (111) K_β reflections with full widths at half maximum (FWHM) between 0.10 deg and 0.046 deg were observed for the layers. For comparison, the same reflection observed for (111)GaAs substrate was 0.038 deg. An example of an x-ray diffraction spectrum obtained for a 1.0 μm thick $\text{Cd}_{0.92}\text{Mn}_{0.08}\text{Te}$ layer grown on (111)GaAs is shown in Fig. 1. It can be seen that the spectrum is characterized by well resolved (111) K_{α_1} and K_{α_2} reflections from both the layer and the substrate. Aside from (111) K_α and K_β no other reflections were observed in the studied samples indicating the absence of non-cubic structures or orientations other than (111) in the layers.

A group of (001)CdTe samples grown by PLE on (001)InSb was used to study the outdiffusion of In. The substrates were degreased in standard solvents, and then etched in-situ with 1000 eV Ne-ions of density $\sim 10^{-6} \text{ A/cm}^2$. The substrates were kept at 300 $^\circ\text{C}$ during ion etching and as a result of this treatment a reconstructed (001)InSb-[4x2] surface was obtained. The growth, at a fixed temperature in the 190 - 290 $^\circ\text{C}$ range, produced (001)CdTe. Most often, a reconstructed (001)CdTe-[2x1] surface was recorded with RHEED. A detailed study of the structural properties and low-temperature PL measurements for these samples is currently being carried out.

The SIMS measurements were carried out using a Cameca IMS 4f system. An O_2^+ ion beam operating at 1.5 keV (impact energy per ion) was used for sputtering the samples at a rate of $\sim 60 \text{ nm/min}$. The primary beam was scanned over an area of $250 \mu\text{m} \times 250 \mu\text{m}$. The size of the analyzed area was $150 \mu\text{m}$ in diameter for ion imaging. For in-depth profiling the size of the analyzed area was $62 \mu\text{m}$ in diameter. The Ga^{69} mass was used for tracing the presence of Ga. In some cases, additional measurements of the ratio of the SIMS signal for Ga^{69} and Ga^{71} were taken to verify the results. This ratio was always constant. The concentration of Ga in the layers was estimated on the basis of the known concentration of dopants in Ga implanted CdTe. The SIMS detection limit for Ga in this experiment was estimated as $5 \times 10^{15} \text{ cm}^{-3}$. Some measurements were carried out also for samples annealed at 400 $^\circ\text{C}$ under a saturated pressure of Cd vapour. The In^{115} mass was used for tracing In. The detection limit for In was $\sim 10^{15} \text{ cm}^{-3}$. An In doped bulk CdTe sample was used to determine the detection limit for In. A complementary study of both as-grown and annealed at 600 $^\circ\text{C}$ bulk In-doped CdTe was also carried out.

Transmission electron microscopy observations were performed using a JEOL 200CX electron microscope operated at 200 kV. The cross-sections were prepared by Ar ion milling using a cold stage to reduce ion damage.

RESULTS AND DISCUSSION

A SIMS Ga ion imaging study revealed that migration of Ga from the GaAs substrate into the layers is a strongly nonuniform process. Islands of Ga-rich material, against a relatively uniform Ga background, were always seen at the surface of investigated specimens. The diameter of an individual island ranged from 2 μm to 10 μm and their concentration was in the range of $10^4 - 10^6 \text{ cm}^{-2}$. This result is similar to our earlier findings concerning outdiffusion of Ga in CdTe grown on (001)GaAs⁹. An example of Ga ion images observed at different depths of a 1.82 μm thick (111) $\text{Cd}_{0.92}\text{Mn}_{0.08}\text{Te}$ layer which was grown on the (111)GaAs substrate is

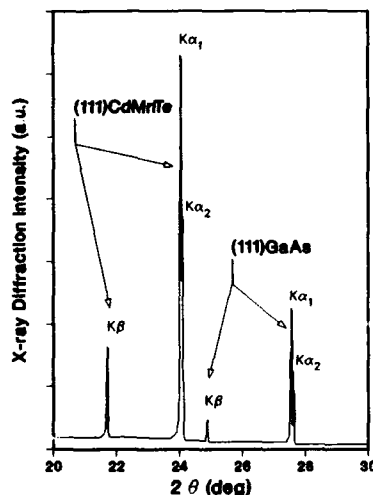


Figure 1 X-ray diffraction spectrum for a 1.0 μm thick (111) $\text{Cd}_{0.92}\text{Mn}_{0.08}\text{Te}$ layer grown by PLE on a (111)GaAs substrate.

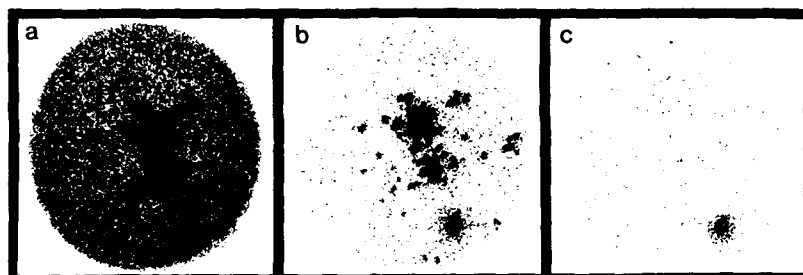


Figure 2 The Ga ion image of a $1.82 \mu\text{m}$ thick $(111)\text{Cd}_{1-x}\text{Mn}_x\text{Te}$ layer. As-grown surface (a), and surface after sputtering of a layer $\sim 0.07 \mu\text{m}$ thick (b), and $\sim 0.8 \mu\text{m}$ thick (c).

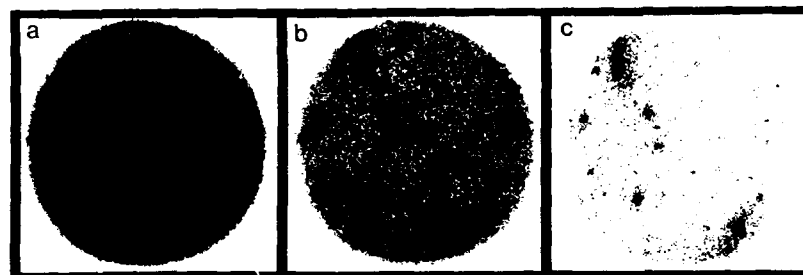


Figure 3 The Ga ion image of the sample from Fig. 2 after annealing at 400°C . As-produced surface (a), and surface after sputtering of a layer $\sim 0.15 \mu\text{m}$ thick (b), and $\sim 1.1 \mu\text{m}$ thick (c).

shown in Fig. 2. The islands of Ga-rich material are seen at the near surface region. The islands extend into the sample to a depth of more than $0.07 \mu\text{m}$. Some of the Ga islands, such as the one observed in Fig. 2c, persist over the whole depth of the specimen. A dramatic increase in the concentration and the size of Ga islands was observed in annealed samples. Fig. 3 shows the effect of annealing in saturated Cd vapours at 400°C for 2 hours for the same sample as in Fig. 2. A more intense Ga background when compared to an as-grown sample can be seen even at a depth of $0.15 \mu\text{m}$. The concentration of Ga islands that propagate throughout the layer is also significantly increased. Thus, a relatively low-temperature annealing induces a significant increase in migration of Ga into $\text{Cd}_{1-x}\text{Mn}_x\text{Te}$ epitaxial layers grown on GaAs substrates. In this study, we did not observe any influence of the chemical composition of the layers on the level of Ga migration.

For all the investigated samples, the SIMS Ga and In depth profiles showed a rapid decrease of Ga and In concentrations near the GaAs and InSb substrate, respectively. Such a decrease, usually to below $5 \times 10^{15} \text{ cm}^{-3}$, took place within $0.3 - 0.4 \mu\text{m}$ from the $\text{Cd}_{1-x}\text{Mn}_x\text{Te}/\text{GaAs}$ and CdTe/InSb interfaces. We note, however, that because of a nonuniform distribution of Ga and In in the films, the SIMS concentration can only be treated as an approximate value which is averaged over the analyzed area of $62 \mu\text{m}$ in diameter. A substantial increase in intensity of SIMS Ga and In signals was observed near the surface of the analyzed samples. A transition region, where the near surface concentration of Ga and In increased from the SIMS detection limit to $\sim 10^{18} - 10^{19} \text{ cm}^{-3}$, usually had a width of less than $0.2 \mu\text{m}$. An example of a Ga depth profile, in the sample for which the Ga ion images were presented in Fig. 2, is shown by curve 1 in Fig. 4. It can be seen that the concentration of Ga changes near the surface region by approximately one order down to the detection limit within a depth of less than $0.01 \mu\text{m}$. The fact that the Ga-rich spots for this sample were still observed at a distance greater than $0.07 \mu\text{m}$ implies that, sometimes, it may be difficult to reach any definite conclusion about the presence of Ga (In) in $\text{Cd}_{1-x}\text{Mn}_x\text{Te}$ films grown on GaAs (InSb) if observation is limited to the SIMS depth profile alone. A Ga depth profile

obtained after annealing of this sample at 400 °C is depicted by curve 2 in Fig. 4. Evidence of temperature induced Ga 'percolation' toward the surface is clearly demonstrated. The broadening of the CdMnTe/GaAs interface is very minimal, whereas the average concentration of Ga in the layer is now higher than 10^{16} cm^{-3} . A drastic increase of some 3 orders of magnitude in the average Ga concentration near the surface corroborates with the results of the Ga image observed in Fig. 3.

Low-temperature PL measurements were carried out on $(111)\text{Cd}_{1-x}\text{Mn}_x\text{Te}$ samples as-grown and annealed at 400 °C for 2 hours. For samples with $x < 0.10$, the neutral-acceptor bound-exciton recombination, which is known in the literature¹⁴ as the L2 transition, dominated the PL spectra of as-grown samples¹³. The FWHM for this transition was in the range of 9.5 - 12 meV. We did not detect any features in the PL spectra that could be directly related to the presence of Ga in these films. A weak shoulder that was sometimes observed on the high-energy side of L2 transition could originate from the neutral-donor bound-exciton transition (D^0X). However, the position of this transition overlapped with an expected position of a free exciton and it was difficult to obtain an unambiguous conclusion. A dramatic change in PL spectra was observed in annealed samples. An example of the PL spectra obtained for an as-grown and an annealed $\text{Cd}_{0.92}\text{Mn}_{0.08}\text{Te}$ layers, for which the SIMS results are presented in Fig. 3 and 4 (curve 2), is shown in Fig. 5. The intensity of the main PL peak in an annealed sample is about 2 orders of magnitude greater than the intensity of the L2 transition observed for this sample before annealing (the same excitation conditions and temperature were used in both cases). The position of the new peak is shifted toward a higher energy by 4 meV when compared to the position of the L2 before annealing. It seems reasonable to link this new peak with a donor, probably neutral-donor bound-exciton (D^0X) transition since, as a result of annealing, the sample became strongly Ga-doped ($n_{\text{Ga}} > 10^{16} \text{ cm}^{-3}$). The FWHM of this transition is 6 meV which approaches bulk-like behaviour for a donor-bound exciton line. It is worthwhile noting that for most of the annealed samples the FWHM of the D^0X transition was in the range of 6 - 8 meV. We take this as a measure of the quality of the crystal structure of the material produced with PLEE. The weak feature with a maximum at 743 nm, that can be seen in Fig. 5, is believed to be related to a free-electron neutral-acceptor (eA^0) transition¹⁵. From these results, we conclude, that complementary to the study of Ga and In doped bulk $\text{Cd}_{1-x}\text{Mn}_x\text{Te}$, the annealing of the $\text{Cd}_{1-x}\text{Mn}_x\text{Te}$ layers grown on GaAs and InSb substrates provides a useful tool for the study of the behaviour of Ga and In impurities in these materials. Further PL investigation of as-grown and annealed PLEE samples is in progress.

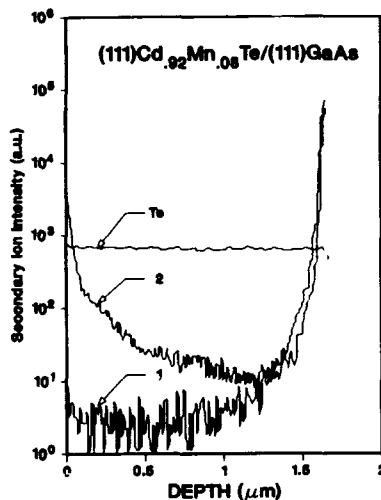


Figure 4 The SIMS Ga profile for the sample from Fig. 2 (curve 1) and from Fig. 3 (curve 2).

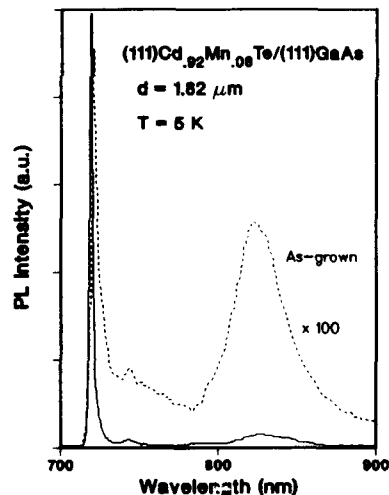


Figure 5 PL spectra from an as-grown (solid line) and an annealed at 400 °C for 2 h (dashed line) $(111)\text{Cd}_{0.92}\text{Mn}_{0.08}\text{Te}$ layers.

An In ion imaging carried out for (001)CdTe grown on (001)InSb revealed qualitatively the same features as those observed in the case of Ga outdiffusion. A significant accumulation of In took place at the surface and near the surface region of CdTe. The size and concentration of In islands were of the same order as those of Ga islands. However, a tendency toward agglomeration of the In islands was less evident. Typically, the In-rich spots disappeared within 0.1 - 0.2 μm . This depth was usually greater than the distance from the surface at which the measured In concentration decreased below the SIMS detection limit. We also observed an increase in the concentration of In near the surface of In-doped and annealed bulk CdTe, similar to the effect of Ga surface accumulation in Ga-doped bulk CdTe⁹. The lateral distribution of In was strongly nonuniform. The In-rich islands of 2 - 3 μm in diameter were observed at distances of up to - 0.2 - 0.3 μm from the surface.

Transmission electron microscopy observations of the specimens grown on the B-face of (111)GaAs revealed a considerable number of twins with coherent twin boundaries parallel to the substrate surface. Twins of a few μm in length were observed. The coherent twin boundaries were atomically flat, although some of their segment were separated by ledges of one to several (111) interplanar distances in height, indicating that growth had proceeded via a ledge mechanism. These macroscopic ledges correspond to incoherent twin boundaries. Stacking faults, misfit dislocations and threading dislocations were also found in the films grown on (111)GaAs. The substrate-thin film interface was found to undulate locally with an amplitude of up to 10 nm. The undulations most probably resulted from a predeposition substrate surface treatment. Layers grown on (001)InSb contained only a few microtwins that originated in thin film, with very few microtwins originating at the interface. The interface between the substrate and the film was found to be planar. Threading dislocations, originating at the (001)CdTe/(001)InSb interface, were also observed. Examples of TEM micrographs indicating the existence of threading dislocations in (111)CdTe grown on B-face of (111)GaAs and in (001)CdTe grown on(001)InSb are shown in Fig. 6.

The mechanism responsible for the nonuniform accumulation of In or Ga at the surface of CdTe is unclear at this stage, but it seems reasonable to relate this mechanism to defects such as threading dislocations and incoherent twin boundaries that are found in the investigated layers with TEM. A pipe diffusion and a grain boundary diffusion appear to be feasible processes that could lead to the formation of the surface Ga (In) islands. A pipe diffusion is strongly related to the concentration of dislocations as has been observed, for example, in In-implanted Si¹⁶. Since low-angle grain boundaries and high concentration of dislocations (above 10^5 cm^{-2}) are commonly observed in bulk CdTe, similar diffusion

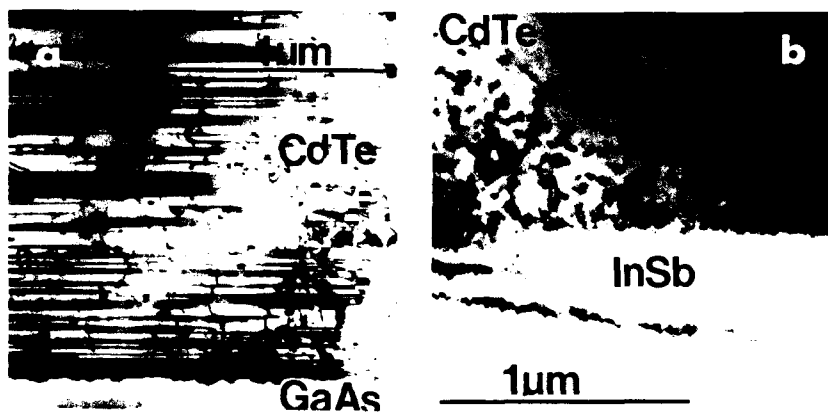


Figure 6 Bright field TEM images of the structure of CdTe films grown on (a) B-face of (111)GaAs, (b) (001)InSb. Note the presence of threading dislocations.

mechanisms appear to be responsible for surface precipitation of Ga (In) in annealed bulk CdTe which was originally uniformly doped with Ga (In).

CONCLUSIONS

This SIMS and PL study of Ga incorporation in $(111)\text{Cd}_{1-x}\text{Mn}_x\text{Te}$ films grown on $(111)\text{GaAs}$ and of In incorporation in $(001)\text{CdTe}$ grown on $(001)\text{InSb}$ shows that: (1) There is a substantial migration of Ga (In) toward the surface of an epitaxial layer. This process is laterally strongly nonuniform. The islands of Ga-rich (In-rich) material, on a relatively uniform Ga (In) background, are always seen at the surface of an investigated specimen. (2) The size of an individual Ga (In) island ranges from $2\text{ }\mu\text{m}$ to $10\text{ }\mu\text{m}$. Islands or their agglomerates, in concentrations of up to 10^6 cm^{-2} , were observed at the surface region of epitaxial layers. (3) The concentration of Ga (In) in the as-grown films, aside from the interface and near the surface region, is usually below the detection limit, i.e. $5 \times 10^{15}\text{ cm}^{-3}$. (4) Pipe diffusion appears to be the process responsible for the nonuniform distribution of Ga (In) near the surface of $\text{Cd}_{1-x}\text{Mn}_x\text{Te}$ epitaxial layers grown on GaAs (InSb). (5) Annealing of $(111)\text{Cd}_{1-x}\text{Mn}_x\text{Te}/(111)\text{GaAs}$ samples produces a strongly Ga-doped material with $n_{\text{Ga}} > 10^{16}\text{ cm}^{-3}$. A strong donor related transition (D^0, X) with $\text{FWHM} = 6 - 9\text{ meV}$ is observed in such samples. (6) We believe that annealing induced Ga and In doping of $\text{Cd}_{1-x}\text{Mn}_x\text{Te}$ epitaxial layers grown on GaAs and InSb substrates may serve as a useful tool in the study of the behaviour of donor-like impurities in these materials.

ACKNOWLEDGMENTS

The authors are indebted to A.P. Roth for providing the use of the PL system. The authors also wish to thank J.K. Furdyna for much helpful discussion. TEM work was performed in the National Center for Electron Microscopy at Lawrence Berkeley Laboratory and supported by the U.S. Department of Energy under contract No. DE-AC03-76SF00098.

REFERENCES

1. E.R. Gertner, S.H. Shin, D.D. Edwall, L.O. Bubulac, D.S. Lo, and W.E. Tennant, *Appl. Phys. Lett.* **46**, 851 (1985).
2. M.D. Lange, S. Siranathan, X. Chu, and J.P. Faurie, *Appl. Phys. Lett.* **52**, 978 (1988).
3. R.F.C. Farrow, in: 'The Chemical Physics of Solid Surfaces and Heterogeneous Catalysis', Edited by D.A. King and D.P. Woodruff, Elsevier Sci. Pub. B.V., 1988, vol. 5, ch. 9.
4. J.K. Furdyna, *J. Appl. Phys.* **64**, R29, (1988).
5. J. Giess, J.S. Gough, S.J.C. Irvine, G.W. Blackmore, J.B. Mullin, and A. Royle, *J. Cryst. Growth* **72**, 120 (1985).
6. R. Kay, R. Bean, and K. Zanio, *Appl. Phys. Lett.* **51**, 2211 (1987).
7. G.M. Williams, C.R. Whitehouse, N.G. Chew, G.W. Blackmore, and A.G. Cullis, *J. Vac. Sci. Technol.* **B3**, 705 (1985).
8. J.M. Ballingall, D.J. Leopold, and D.J. Peterman, *Appl. Phys. Lett.* **47**, 262 (1985).
9. J.J. Dubowski, J.M. Wrobel, J.A. Jackman, and P. Becla, *Mat. Res. Soc. Symp. Proc.* **131**, 143 (1989).
10. J.M. Wrobel, J.J. Dubowski, and P. Becla, *J. Vac. Sci. Technol.* **A7**, 338 (1989).
11. M. Kallergi, J.L. Aubel, S. Sundaram, J.M. Wrobel, J.J. Dubowski, and P. Becla, submitted to *J. Appl. Phys.*
12. J.M. Wrobel and J.J. Dubowski, *Appl. Phys. Lett.* **55**, 469 (1989).
13. J.J. Dubowski, presented at the Fourth International Conference on II - VI Compounds, Berlin (West), 1989 (to be published in *J. Cryst. Growth*).
14. A. Golnik, J. Ginter, and J.A. Gaj, *J. Phys. C* **16**, 6073 (1983).
15. M. Bugajski, P. Becla, P.A. Wolff, D. Heiman, and L.R. Ram-Mohan, *Phys. Rev.* **B38**, 10512, (1988).
16. S. Yu. Shiryayev, A. Nylandsted, and N. Safronov, *J. Appl. Phys.* **65**, 4220 (1989).

**PHOTOLUMINESCENCE STUDIES OF DILUTED MAGNETIC
SEMICONDUCTORS UNDER HYDROSTATIC PRESSURE: $\text{Cd}_{1-x}\text{Mn}_x\text{Te}$**

MANEESHA PRAKASH*, MEERA CHANDRASEKHAR*, H.R. CHANDRASEKHAR*, I.
MIOTKOWSKI[‡], AND A.K. RAMDAS[‡]

* Department of Physics, University of Missouri, Columbia, MO 65211

[‡] Department of Physics, Purdue University, W. Lafayette, IN 47907

ABSTRACT

We present a photoluminescence study of the excitons and electron-to-acceptor ($e\text{-}A^0$) transitions in $\text{Cd}_{1-x}\text{Mn}_x\text{Te}$ ($x = 0.05$ and 0.15) under hydrostatic pressure at 15K. We investigate the changing magnetic and Coulombic binding energies of the $e\text{-}A^0$ transition under pressure. We find that the $e\text{-}A^0$ binding energy *increases* with pressure for $x = 0.15$ where the magnetic term due to the acceptor bound magnetic polaron is large, while it *decreases* for $x = 0.05$. We also obtain the pressure coefficients of the excitonic and acceptor related transitions.

INTRODUCTION

The diluted magnetic semiconductors (DMS) display novel spin dependent phenomena arising from the sizeable $sp\text{-}d$ exchange interactions. Among these novel phenomena are bound magnetic polarons (BMP), which are ferromagnetic spin clusters caused by the exchange interaction between the spin on the magnetic ion and a carrier spin localized at an impurity¹. The model Hamiltonian for the BMP is²

$$H = \frac{p^2}{2m^*} - \frac{e^2}{\epsilon_0 r} - J \sum_j [(\mathbf{s} \cdot \mathbf{S}_j) \delta(\mathbf{r} - \mathbf{R}_j)] \quad (1)$$

where m^* is the effective mass, ϵ_0 is the static dielectric constant, \mathbf{s} and \mathbf{S} are the spins, and \mathbf{r} and \mathbf{R} are the position vectors of the carrier and the magnetic Mn^{2+} ion, respectively. The strength of the exchange interaction JN_0 is about 1 eV for holes, allowing large acceptor BMP effects to be observed in the photoluminescence spectra. The formation of BMPs gives rise to an additional binding energy in the acceptor related transitions, due to the third term in Eq. (1).

The magnetic part of the binding energy is temperature dependent, unlike Coulomb binding energies. At low temperature, the spins are aligned, producing large binding energies. As the temperature is increased, thermal fluctuations decrease the degree of spin alignment, and hence the binding energy. The BMP binding energies also depend on the concentration of magnetic ions. For small Mn concentrations ($x < 0.1$), the response is essentially paramagnetic, and the BMP binding energy increases with x . For $x > 0.1$, the antiferromagnetic coupling between nearest neighbor Mn^{2+} ions lowers the effective $s\text{-}d$ interaction, causing the binding energy to saturate beyond $x \sim 0.25$.

The effects of x and temperature have been studied in the prototype DMS, $\text{Cd}_{1-x}\text{Mn}_x\text{Te}$ using different acceptor related transitions. Acceptor BMP effects have been observed both in

the neutral acceptor bound exciton³, A^0X , and the electron to neutral acceptor, $e-A^0$ transitions⁴. For the A^0X one faces a complicated three body problem in interpreting the data. The $e-A^0$, however, is relatively simpler to interpret. Bugajski et. al⁴ have studied P-doped $Cd_{1-x}Mn_xTe$, and find that the $e-A^0$ shifts to lower energies relative to the band gap with increasing x ($0 < x < 0.35$), indicating an increase in the magnetic part of the binding energy. The binding energy also has a sizeable temperature dependence which is composition dependent, decreasing with increasing temperature. The Coulomb part of the bare acceptor energy is not expected to vary significantly with either x or temperature, since the changes in the effective mass and dielectric function are not large. Thus the additional binding energy is almost totally magnetic.

Our present experiments study the effect of hydrostatic pressure on the energies of the excitons and the $e-A^0$ transitions. We study two samples, one with $x=0.05$, in the paramagnetic regime, and another with $x = 0.15$, where the antiferromagnetic coupling between nearest neighbor Mn^{2+} spins begins to play a role. We find that the $e-A^0$ binding energies decrease with pressure for $x = 0.05$, where the Coulombic effects are relatively large compared to the magnetic effects, while they increase for $x = 0.15$ where the magnetic effects are large. In addition, we obtain the pressure coefficients of the excitonic and acceptor related transitions.

Our low temperature measurements have allowed us to study both the magnetic and bandgap effects. Previous measurements of $Cd_{1-x}Mn_xTe$ under hydrostatic pressure were mainly 300K studies of the change in the bandgap and the Mn^{2+} intraionic transitions⁵.

EXPERIMENT

$Cd_{1-x}Mn_xTe$ crystals were grown using the vertical Bridgman technique. They were doped with Sb to levels of $\sim 10^{17} \text{ cm}^{-3}$. Photoluminescence (PL) was excited using 0.2 to 10 mW of 5145\AA radiation from an argon ion laser. Measurements were conducted at 15K in a diamond anvil cell, using argon as the pressure transmitting medium. Other experimental details are published elsewhere⁶.

RESULTS AND DISCUSSION

Photoluminescence spectra at ambient pressure are shown by the solid lines in Figs. 1 and 2 for $x = 0.05$ and 0.15 , respectively. The sharp peak at the highest energy is identified as the bound exciton, A^0X . The weak peak at slightly lower energies, 1.648 eV (1.806 eV) in Fig. 1 (Fig. 2) has been attributed⁷ to a magnetically localized free exciton (self trapped magnetic polaron), designated as L1 in these papers. At lower energies is the $e-A^0$ peak. The energy separation between A^0X and $e-A^0$ increases from 46 to 83 meV upon increasing x from 0.05 to 0.15 (at ambient pressure), larger than the separation of 35 meV for CdTe. The additional energy (over the Coulombic CdTe value) is due to the binding energy of the BMP. An increase in temperature from 15 to 100K shows that the separation between A^0X and $e-A^0$ decreases, consistent with the lowering of the magnetic part of the binding energy of $e-A^0$ with temperature.

The application of hydrostatic pressure increases the band gap. In most semiconductors, the excitons follow the band gap closely. In Fig. 3, we plot the energies of the four peaks observed in the $x = 0.05$ sample: A^0X , L1, $e-A^0$, and a phonon replica of $e-A^0$ (not shown in Fig. 1).

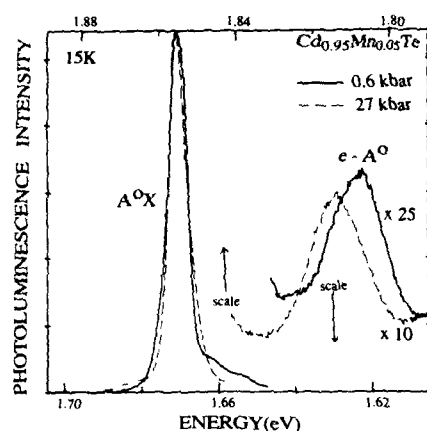


Fig. 1. PL spectra of $\text{Cd}_{0.95}\text{Mn}_{0.05}\text{Te}$ at 0.6 (solid line, bottom energy scale) and 27 kbar (dashed line, top energy scale). The spectra are shifted so that the energies of the A^0X excitons coincide.

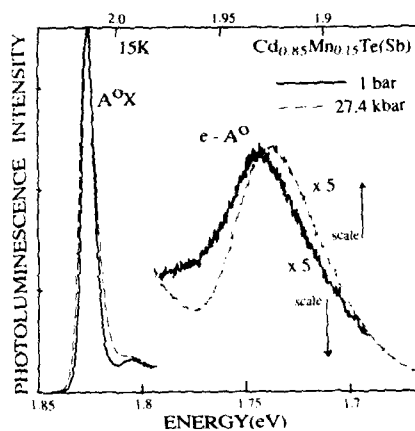


Fig. 2. PL spectra of $\text{Cd}_{0.85}\text{Mn}_{0.15}\text{Te}(\text{Sb})$ at 1 bar (solid line, bottom energy scale) and 27.4 kbar (dashed line, top energy scale). Note the increasing separation between A^0X and e-A^0 , in contrast to Fig. 1.

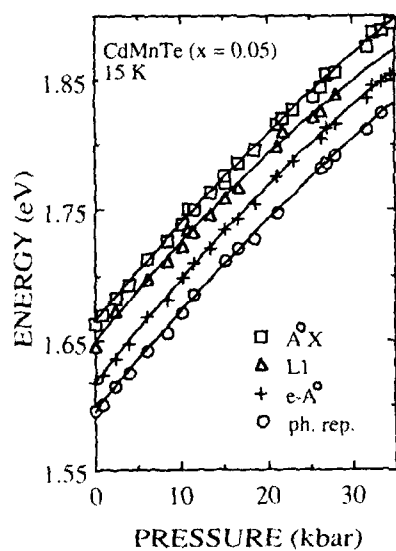


Fig. 3. The energies of A^0X , L1 , e-A^0 , and its phonon replica as a function of pressure for $\text{Cd}_{0.95}\text{Mn}_{0.05}\text{Te}$ at 15K. The solid lines are fits to Eq. (2).

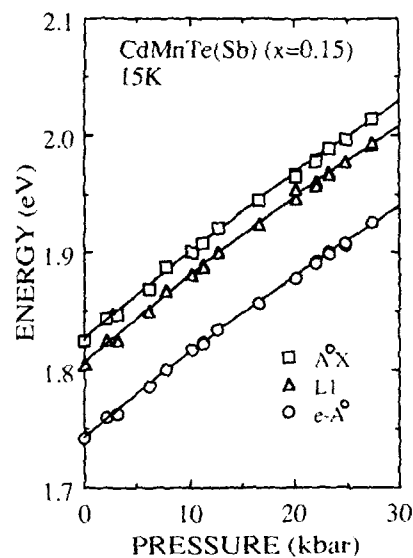


Fig. 4. The energies of the A^0X , L1 , and e-A^0 transitions as a function of pressure for $\text{Cd}_{0.85}\text{Mn}_{0.15}\text{Te}(\text{Sb})$ at 15K. The solid lines are fits to Eq. (2).

The energies increase sublinearly with pressure. The first three peaks listed above are also observed for $x = 0.15$, and their pressure dependence is shown in Fig. 4. Owing to larger alloy broadening, the phonon replica of the $e-A^0$ peak could not be observed in this sample. It was found that the relative intensities of the A^0X and $e-A^0$ varied considerably with incident laser power (for $x = 0.15$). The $e-A^0$ was relatively stronger for low incident intensities, and optimal powers of 0.25 and 2mW were used. The spectra shown in Fig. 2 were obtained with 0.25 mW of laser power. One can also see in Fig. 2 that the $e-A^0$ rides on a decreasing background. It was necessary to subtract the decreasing background to obtain reliable values of the peak energy for $e-A^0$. The energies plotted in Fig. 4 are obtained after background subtraction.

Data were obtained upto ~35 kbar, beyond which a phase transition to the NaCl structure⁸ occurs, and no luminescence is observable.

Pressure coefficients were obtained (Table I) by fitting the energies E as a function of pressure P (in kbar) to the expression

$$E(P) = E(0) + \alpha P + \beta P^2 \quad (2)$$

Table I. Pressure coefficients of the PL peaks in $Cd_{1-x}Mn_xTe$ at 15K.

x	Identification	E(0) (eV)	α (meV/kbar)	β (meV/kbar ²)
This work (15K):				
0.05	A^0X	1.663 ± 0.001	7.91 ± 0.17	-0.036 ± 0.005
	L1	1.648 ± 0.002	8.17 ± 0.3	-0.05 ± 0.01
	$e-A^0$	1.616 ± 0.001	8.44 ± 0.14	-0.044 ± 0.004
	Phonon replica	1.595 ± 0.001	8.01 ± 0.2	-0.035 ± 0.005
0.15	A^0X	1.826 ± 0.001	7.66 ± 0.2	-0.032 ± 0.007
	L1	1.806 ± 0.002	7.92 ± 0.3	-0.041 ± 0.009
	$e-A^0$	1.742 ± 0.001	7.53 ± 0.2	-0.033 ± 0.006
Previous work (300K, Wei Shan et. al., Ref.5):				
0.0	Band gap	1.483	8.3	-0.04
0.1	Band gap	1.618	7.7	-0.039

While absorption measurements for exactly the same compositions and temperature are not available, there is good agreement between the pressure coefficients for the band gap and the A^0X for compositions that are fairly close. There is also a slight decrease in α with x .

More interesting are the differences in α for the A^0X and the $e-A^0$ transitions. For $x = 0.05$, $\alpha(A^0X)$ is smaller than $\alpha(e-A^0)$, indicating a *decreasing* separation between the two. This can be appreciated better in Fig. 1, where the spectra for 0.6 and 27 kbar are plotted so that the exciton positions coincide. The $e-A^0$ peak is clearly seen to be closer to A^0X at the higher pressure. The energy difference between the peaks is plotted in Fig. 5, and is seen to decrease monotonically with pressure from 47 to 40 meV.

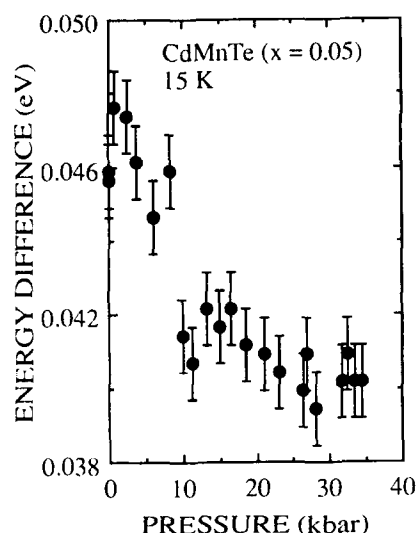


Fig. 5. The energy separation between A^0X and $e-A^0$ as a function of pressure for $Cd_{0.95}Mn_{0.05}Te$ at 15K.

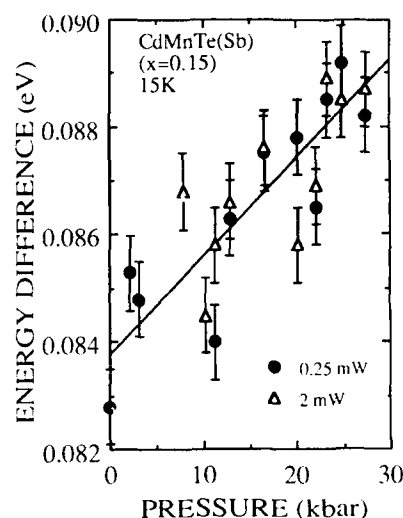


Fig. 6. The energy separation between A^0X and $e-A^0$ as a function of pressure for $Cd_{0.85}Mn_{0.15}Te$ at 15K. The solid line is a guide to the eye.

In contrast, an examination of the pressure coefficients for the $x = 0.15$ sample, shows that $\alpha(A^0X)$ is *larger* than $\alpha(e-A^0)$, implying an *increasing* separation under pressure, borne out by the spectra in Fig. 2, and by the increasing separation as a function of pressure in Fig. 6. Though the pressure coefficients of A^0X and $e-A^0$ appear very close, within their experimental uncertainties, their energy separations, obtained in the same spectrum and at exactly the same pressure, are less sensitive to the statistical errors that are present in the α 's. The trend of *increasing* binding energies with pressure is then evident.

The binding energy of $e-A^0$ consists of Coulombic and magnetic parts, both of which could, in principle, change with pressure. Strictly speaking, the binding energy of $e-A^0$ is measured relative to the band gap³, and is 56 meV (94 meV) for $x = 0.05$ ($x = 0.15$) at 15K⁹. In our discussions here, we assume that changes in the $e-A^0$ binding energy are reflected in the separation between A^0X and $e-A^0$, and that the relatively smaller A^0X binding energy (10 meV for $x = 0.05$) does not change much under pressure.

The BMP binding energy has contributions² from the kinetic, Coulomb and magnetic terms in the Hamiltonian (Eq. (1)). The effect of pressure on all three terms requires a full calculation of the acceptor BMP binding energies, and is quite complex. Our measurements on CdTe¹⁰ show that the (purely Coulombic) separation does not change much with pressure. It appears then, that the acceptor BMP binding energy changes due to the combined effects of the decreasing lattice constant on the dielectric function, effective mass, and possibly the exchange

integrals. It is also possible that antiferromagnetic coupling for $x = 0.15$ plays a role. A detailed calculation is currently in progress.

ACKNOWLEDGEMENTS

The work at the University of Missouri was supported by U.S. Army Research Office under grant number DAAL03-86-K0083 and the U.S.D.O.E. under grant number DE-FG02-89ER45402. The work at Purdue University was supported by the National Science Foundation grant number DMR-85-20866.

REFERENCES

- ¹ For a review, see P.A. Wolff, *Semiconductors and Semimetals*, Vol 25, ed. J.K. Furdyna and J. Kossut, (Academic Press, NY, 1988), p. 413.
- ² L.R. Ram-Mohan and P.A. Wolff, *Phys. Rev. B* **38**, 1330 (1988), and references therein.
- ³ A. Golnik, J. Gaj, M. Nawrocki, R. Planel, and C. Benoit à la Guillaume, *Proc. of the XV Intl. Conf. Phys. of Semiconductors, Kyoto*, J. Phys. Soc. Japan, Suppl. **A 49**, 819 (1980).
- ⁴ M. Bugajski, P. Becla, P.A. Wolff, D. Heiman, and L.R. Ram-Mohan, *Phys. Rev. B* **38**, 10512 (1988).
- ⁵ G.A. Babonas, R.A. Bendoryus, and A.Yu. Shileika, *Sov. Phys. -Semicond.* **5**, 392 (1971); G. Ambrazevicius, G.A. Babonas, S. Marcinkevicius, V.D. Prochukhan, and V.Yu. Rud, *Solid State Commun.*, **49**, 651 (1984); Wei Shan, S.C. Chen, and H.R. Zhu, *Solid State Commun.* **55**, 475 (1985). References to other DMS compounds studied under pressure are listed by W.M. Becker, *Semiconductors and Semimetals*, Vol 25, ed. J.K. Furdyna and J. Kossut, (Academic Press, NY, 1988), p.35.
- ⁶ U. Venkateswaran and M. Chandrasekhar, *Phys. Rev. B* **31**, 1219 (1985).
- ⁷ A. Golnik, J. Ginter, and J. Gaj, *J. Phys. C, Solid State Phys.* **16**, 6073 (1983); D. Heiman, P. Becla, R. Kershaw, D. Ridgley, K. Dwight, A. Wold, and R.R. Galazka, *Phys. Rev. B* **34**, 3961 (1986).
- ⁸ S.B. Qadri, E.F. Skelton, A.W. Webb, E.R. Carpenter, M.W. Schaefer, and J.K. Furdyna, *Phys. Rev. B* **35**, 6868 (1987).
- ⁹ The $e-A^{\circ}$ binding energies are calculated by adding the binding energy of $A^{\circ}X$, 10 (11) meV to the separation between $A^{\circ}X$ and $e-A^{\circ}$. The $A^{\circ}X$ binding energy has a Coulombic part that contributes 7 meV (obtained for CdTe), and 3 (4) meV magnetic part at 15K for $x = 0.05$ (0.15). These values were obtained from Ref. 3.
- ¹⁰ M. Prakash, M. Chandrasekhar, H.R. Chandrasekhar, I. Miotkowski and A.K. Ramdas, unpublished.

OBSERVATION OF Mn^{2+} TRIPLET CLUSTERS AND NON-NEAREST-NEIGHBOR EXCHANGE EFFECT IN $(Cd,Mn)Te$

XIAOMEI WANG*, D. HEIMAN, S. FONER* AND P. BECLA

Massachusetts Institute of Technology, Francis Bitter National Magnet Laboratory, Cambridge, MA 02139

* Also Department of Physics

Introduction

Dilute magnetic semiconductors (DMS), such as $Cd_{1-x}Mn_xTe$, are excellent hosts for the study of disordered magnetic systems. In these diluted random alloys, neighboring magnetic ions form clusters through short range spin exchange interactions. A number of experiments [1-8] have been devoted to the investigation of the nearest-neighbor (NN) coupled magnetic ion pairs, by measuring the quantized total spin in a field. In $(Cd,Mn)Te$, the obtained NN exchange constant J_1 is -6.1 K [7,8]. However, to understand full range of magnetic and optical phenomena in DMS, it is important to explore the behavior of clusters larger than pairs and interactions beyond NN.

In this report, we summarize the recent results of high-field magnetization measurements using a Faraday rotation technique on $(Cd,Mn)Te$ up to 60T at liquid helium temperature [9]. We provide quantitative evidence of magnetic ion triplets, and of the saturation of magnetic ion pairs. Quantitative agreement with the experimental results is obtained from a NN cluster model. Effects of further-neighbor interactions are observed in the form of an experimental bias field Δ . We found a linear relationship between Δ and magnetization M for ion pairs, independent of manganese concentration x for $x \leq 0.1$. From this relation, we deduce the next-nearest-neighbor (NNN) exchange constant $J_2/k_B = -1.1$ K. For detailed discussions, see reference 9.

Magnetic Ion Triplet Clusters

In the nearest-neighbor interaction model [10], for low magnetic ion concentration ($x \leq 0.1$), small clusters such as singlets, pairs and triplets (open and closed) dominate the magnetic ion population. The magnetization of these small clusters can be obtained exactly from general thermal ensemble theory. At $T=0$ K, each type of clusters show a series of equal-step like magnetization increases with magnetic field. The onset field of the ladder and the number of steps are different for different cluster types. Pairs have five steps starting at ~ 10 T, while open triplets have seven steps starting at ~ 30 T. At $T=4$ K these equal-step ladders are broadened into linear trends and the structure of $M(B)$ is simplified. Thus we expect an increase in the slope dM/dB due to the contribution from open triplets. In the range of interest, larger clusters have no effect in the slope change as indicated by the self-consistent calculation [9] using the Weiss molecular-field model.

Fig.1 displays the measured and calculated magnetization derivative dM/dB versus field B at $T \sim 4$ K. In the range of 15T to 60T, the magnetization versus B is composed of three different linear regimes. At approximately 30T, we observed a slope increase due to the onset of open triplets. The

decrease of slope at ~ 50 T is attributed to the saturation of pairs. The amount of increase and decrease in the slope is proportional to the number of open triplet clusters and pairs respectively. Quantitative comparison with the calculated probabilities [10] assuming random distribution is given in Ref.9.

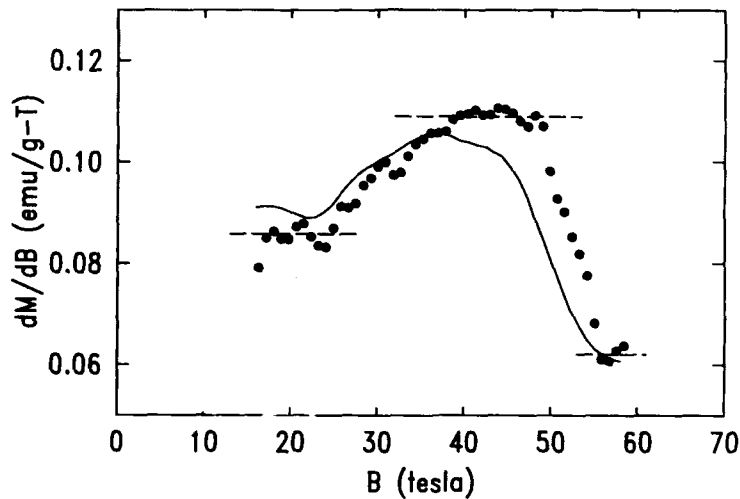


Fig.1 Comparison of experimental and theoretical derivative of magnetization M as a function of applied magnetic field B in the range 15T to 60T at $T \sim 4$ K for $\text{Cd}_{1-x}\text{Mn}_x\text{Te}$, $x=0.095$. (after Ref.9)

Effect of Non-Nearest-Neighbor Interactions

In DMS materials, the effective field experienced by a given (NN) cluster differs from the external field by a bias field--average exchange field due to further-neighbor interactions. For pairs the bias field at the n th step is defined as $\Delta_n^p \equiv B_n^p(\text{meas.}) - B_n^p(\text{NNcalc.})$, where B_n is the step field. Since the magnetization M is a measure of total spin alignment, we expect that Δ is proportional to M . Fig.2 is a collection of all available data on Δ for $\text{Cd}_{1-x}\text{Mn}_x\text{Te}$ plotted versus M . These include the data obtained at different steps of the same sample. Despite the difference in manganese

concentrations (which varies from 0.033 to 0.095), a *single* linear relation between Δ and the total magnetization M for pairs is observed,

$$\Delta = cM. \quad (1)$$

The constant c is directly related to the non-nearest-neighbor exchange energies.

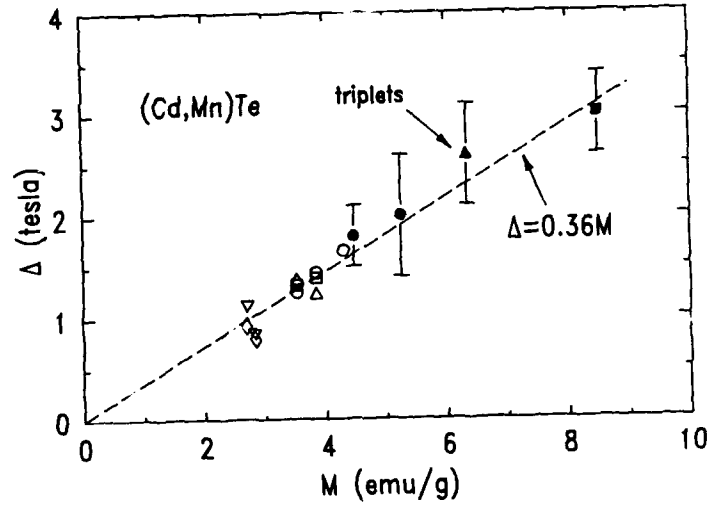


Fig.2 Magnetization dependence of the bias field Δ for pairs and triplets for various x and T . For pairs: $x=0.033$ at $T=1.3K$ (\diamond) and $T=1.28K$ (∇) (Ref.7); $x=0.047$ at $T=1.3K$ (\triangle) and $T=0.47K$ (\square) (Ref.3), and $T=1.4K$ (\circ) (Ref.8); $x=0.095$ at $T=0.6K$ (\bullet) and $T=4K$ (\blacksquare) (this work). For triplets: $x=0.095$ at $T=4K$ (\blacktriangle) (this work). Typical error bars are shown here. The data include those obtained at different steps of the same sample. (after Ref.9)

In the mean-field theory[4,9], assuming that on average, the two spins in a pair have equivalent paramagnetic environments, the bias field may be written as

$$\begin{aligned} \Delta &= \sum_{r \geq 2} N_r J_r \frac{x \langle S_z \rangle}{g \mu_B} \\ &= - \sum_{r \geq 2} N_r J_r \left(\frac{M}{(g \mu_B)^2 (A/W)} \right), \end{aligned} \quad (2)$$

where N_r is the number of r th neighbors for pairs and J_r is the r th neighbor exchange constant. A is Avogadro's number, $g=2$, and W is the formula molecular weight for $Cd_{1-x}Mn_xTe$. Combining Eqs.(1) and (2), we obtain

$$c = - \left(\frac{W}{(g \mu_B)^2 A} \right) \sum_{r \geq 2} N_r J_r. \quad (3)$$

Note that c is independent of temperature T , and weakly dependent on x through W . This is consistent with experimental observation. To estimate J_2 , the form $J_{(r,2)} = J_2 [\sqrt{2}/r]^2$ [11] is assumed. We find $J_2/k_B = -1.1 \pm 0.2K$ for interactions up to 4th neighbors are included. This value is comparable to the approximately estimated values [4,12,13].

In summary, we provide *quantitative evidence* of triplet ion clusters in DMS. Mn^{2+} pair saturation is observed at $\sim 52T$. Quantitative agreement between our experiment and calculations using the nearest-neighbor cluster model is obtained. The linear dependence of the bias field on the total magnetization derived here is consistent with the mean-field model. These results give important information on interactions beyond nearest-neighbors.

This work was supported by the National Science Foundation Grant No. DMR8807419, and DARPA-N00014-86-0760. The Francis Bitter National Magnet Laboratory is supported by the National Science Foundation.

References

1. Y. Shapira, S. Foner, D.H. Ridgley, K. Dwight and A. Wold, *Phys. Rev.* **B30**, 4021 (1984).
2. R.L. Aggarwal, S.N. Jasperson, Y. Shapira, S. Foner, T. Sakakibara, T. Goto, N. Miura, K. Dwight and A. Wold, *Proc. 17th Intern. Conf. on Phys. of Semicon.*, p. 1419 (Springer, New York 1985).
3. Y. Shapira and N.F. Oliveria Jr., *Phys. Rev.* **B35**, 6888 (1987).
4. B.E. Larson, K.C. Hass and R.L. Aggarwal, *Phys. Rev.* **B33**, 1718 (1986).
5. R.R. Galazka, W. Dobrowolski, J.P. Lascaray, M. Nawrocki, A. Bruno, J.M. Broto, and J.C. Ousset, *J. Magn. Magn. Mat.* **72**, 174 (1988) and references therein.
6. N. Yamada, S. Takeyama, T. Sakakibara, T. Goto, and N. Miura, *Phys. Rev.* **B34**, 4121 (1986) and references therein.
7. E.D. Isaacs, D. Heiman, P. Becla, Y. Shapira, R. Kershaw, K. Dwight and A. Wold, *Phys. Rev.* **B38**, 8412 (1988).
8. S. Foner, Y. Shapira, D. Heiman, P. Becla, R. Kershaw, K. Dwight and A. Wold, *Phys. Rev.* **B39**, 11793 (1989), and references therein.
9. Xiaomei Wang, D. Heiman, S. Foner, P. Becla, *Phys. Rev.* **B41**, 1135, (1990)
10. R.E. Behringer, *J. Chem. Phys.* **29**, 537 (1958).
11. W.J.M. de Jonge, A. Twardowski, C.J.M. Denissen, and H.J.M. Swagten. *Mat. Res. Soc. Symp. Proc.* Vol. **89**, 153 (1987).
12. M. Escorne and A. Mauger, *Phys. Rev.* **B25**, 4674, (1982).
13. T.M. Giebultowicz and T.M. Holden, *Semiconductors and Semimetals*, Vol.25, 125, 1988

IN-SITU STUDIES OF SEMIMAGNETIC HETEROJUNCTION PARAMETERS

XIAOHUA YU, N. TROULLIER, A. RAISANEN, G. HAUGSTAD, AND A. FRANCIOSI

Dept. of Chemical Engineering and Materials Science, University of Minnesota, Minneapolis, MN 55455

ABSTRACT

We have conducted a systematic study of Ge-Cd_{1-x}Mn_xTe heterostructures prepared in situ by deposition of polycrystalline Ge onto atomically clean Cd_{1-x}Mn_xTe (110) surfaces. We examined by means of high resolution synchrotron radiation photoemission the valence band offset ΔE_v as a function of the substrate composition x ($x=0$, 0.35, and 0.60) and bandgap E_g ($E_g=1.47$, 1.93, and 2.13 eV). We find $\Delta E_v=0.84\pm0.10$ eV in all cases, and no dependence of ΔE_v on the substrate bandgap within experimental uncertainty. This finding indicates that within the range of validity of the transitivity rule, Cd_{1-x}Mn_xTe-Cd_{1-y}Mn_yTe heterojunctions may actually follow the common anion rule.

INTRODUCTION

Semimagnetic semiconductors are usually ternary alloys in which some of the cations in a II-VI semiconductor lattice have been replaced by magnetic atoms such as Mn or Fe. The resulting materials exhibit new magneto-optical and magnetotransport properties, such as giant Landau splitting, giant electronic g -factor and large magnetoresistance[1,2]. Consequently, heterostructures formed by these materials would exhibit magnetically tunable superlattice optical and transport properties which could open the way to novel device applications[3]. However little information is available about crucial heterojunction parameters of these materials, including the valence band offset ΔE_v , which is one of the most important parameters for any device design[4].

In this paper we present a first synchrotron radiation photoemission study of the electronic properties of the semimagnetic semiconductor heterojunction Ge-Cd_{1-x}Mn_xTe(110). We measured the valence band offsets ΔE_v for different substrate compositions ($x=0$, 0.35, and 0.6) and bandgaps ($E_g=1.47$, 1.93, and 2.13 eV) using both conventional methods and a new method which exploits spectra for Ge and Cd_{1-x}Mn_xTe to generate a composite valence band edge, and a least squares fitting procedure to fit the experimental spectra for the Ge-Cd_{1-x}Mn_xTe(110) interface to the composite valence band obtained a priori. The two procedures obtain remarkable consistent results only if a proper lineshape analysis of the Ge core level is performed as a function of coverage. Failure to do so yields incorrect estimates of band bending and therefore erroneous values of ΔE_v from the conventional procedure. The new procedure is instead immune from these problems. The main conclusion of this work is that the valence band offsets are identical (0.84 ± 0.10 eV), within experimental uncertainty, for all

of the heterojunctions examined, so that, if the transitivity rule applies to such systems, $\text{Cd}_{1-x}\text{Mn}_x\text{Te}-\text{Cd}_{1-y}\text{Mn}_y\text{Te}$ will follow the common anion rule.

EXPERIMENTAL DETAILS

Single crystals of $\text{Cd}_{1-x}\text{Mn}_x\text{Te}$ alloys were grown at Purdue University and characterized through X-ray diffraction and X-ray microprobe analysis. Atomically clean (110) surfaces were obtained by cleaving the samples in situ in a photoelectron spectrometer at an operating pressure of 5×10^{-11} Torr. Heterojunctions were prepared at room temperature by Ge sublimation from a W basket at pressure of 5×10^{-10} Torr with coverage monitored by a quartz thickness monitor. Angle integrated photoelectron energy distribution curves (EDC's) were obtained in the $45 \leq h\nu \leq 110$ eV range using a 3m toroidal grating monochromator, radiation from the 1 GeV Aladdin electron storage ring at the Synchrotron Radiation Center of the University of Wisconsin-Madison, and a commercial hemispherical electron energy analyzer. The overall energy resolution was 0.2 - 0.3 eV. More details on the experimental procedures employed can be found in Ref.5-6.

RESULTS AND DISCUSSION

EDC's for the leading edge of the valence band emission from $\text{Ge}-\text{Cd}_{1-x}\text{Mn}_x\text{Te}(110)$ interfaces ($x=0, 0.35$, and 0.6) at a Ge coverage of 5 \AA are shown in Fig.1 (solid circles). The spectra have been normalized to the main emission feature and are shown in arbitrary units. The binding energy scale is referred to the substrate valence band maximum E_v , estimated through a linear extrapolation of the leading edge of the substrate valence band[7]. All of the spectra in Fig.1 exhibit similar structure. The main feature corresponds in all cases to a Te-derived density of states (DOS) feature, and the well defined shoulder on the low binding energy side derives from the Ge valence band emission. Valence band discontinuities much larger than the experimental energy resolution have been measured directly in the past[5] by simply linearly extrapolating the leading edge of the substrate and overlayer-related valence band features in EDC's similar to those displayed in Fig.1. Unfortunately, by this method we could not obtain quantitatively consistent results throughout the Ge coverage range explored. Values of ΔE_v as low as 0.42 eV and as high as 0.67 eV were obtained for Ge coverage between 1 and 5 \AA . Since the coverage-dependence of the substrate and overlayer emission intensity indicates[8] that negligible interdiffusion takes place across the interface during room-temperature formation of these heterojunctions, the experimental valence band emission in Fig.1 (solid circles) should reflect a simple superposition of a Ge-type valence band emission with a $\text{Cd}_{1-x}\text{Mn}_x\text{Te}$ type of valence band, shifted relative to each other by the valence band offset ΔE_v . We therefore used EDC's for the valence band emission prior to Ge deposition, and for the Ge-covered surface at the highest coverage explored (20 \AA) to obtain a "composite" valence band that could be compared with the experimental valence band EDC's for $\text{Ge}-\text{Cd}_{1-x}\text{Mn}_x\text{Te}$ in the Ge

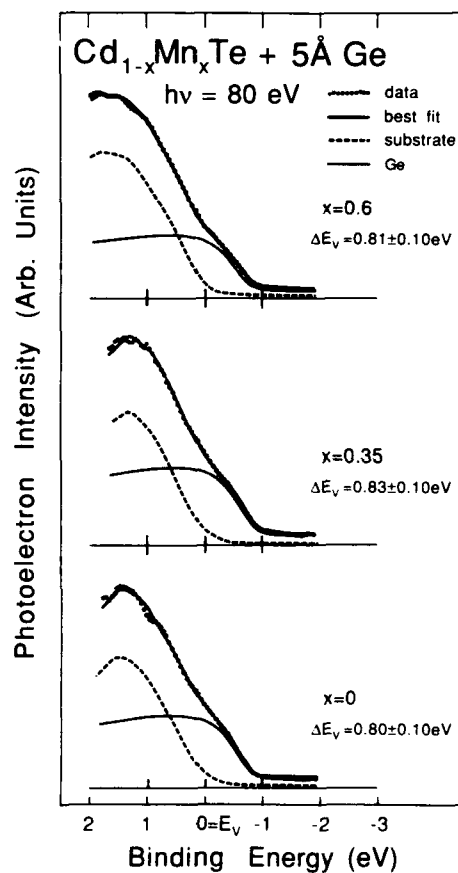


Figure 1. Valence band EDC's at $h\nu=80\text{eV}$ for 5\AA Ge on $\text{Cd}_{1-x}\text{Mn}_x\text{Te}(110)$ with $x=0, 0.35$, and 0.6 (solid circles). Best fit of the overall lineshape (solid line) were obtained through a least squares procedure described in the text. Two components correspond to substrate VB emission (dashed line) and overlayer VB emission (dotted line). The distance in energy between the two components gives rise to ΔE_v .

coverage range from 1 to 5Å. Positions and intensities of the two EDC's comprised in the composite valence band were used as fitting parameters, and were determined through a non-linear least squares fitting procedure. The best fits are shown in Fig.1. (solid lines) superimposed to the experimental EDC's (solid circles). We also give the individual Ge-type (dotted line) and substrate-type (dashed line) valence band spectra corresponding to the best fit. Comparing the linearly extrapolated value of the valence band maximum for these two spectra we obtained for ΔE_v values of $0.80 \pm 0.10 \text{ eV}$, $0.83 \pm 0.10 \text{ eV}$, and $0.81 \pm 0.10 \text{ eV}$, respectively, for $\text{Ge-Cd}_{1-x}\text{Mn}_x\text{Te}$ heterojunctions with $x=0$, 0.35, and 0.6. We note that most of the experimental uncertainty on each single value of ΔE_v derives from the linear extrapolation criterion to determine E_v . On the variation of ΔE_v with x the uncertainty is actually smaller, since it derives primarily from the least squares fitting procedure, and would not be affected by a systematic error in the determination of E_v for one or the other of the two semiconductors. We estimate the uncertainty on the variation of ΔE_v in the series to at most 0.05 eV. The validity of our method is supported by the fact that it yields quantitatively consistent values of ΔE_v in the whole Ge coverage between 1 and 5Å, and by the value of $\Delta E_v = 0.85 \pm 0.10 \text{ eV}$ reported by Katnani and Margaritondo for $\text{Ge-CdTe}(110)$ [7].

A more conventional method to obtain ΔE_v exploits the zero-coverage and high coverage limits of the linearly extrapolated position of the valence band maximum. The difference of the two positions reflects, in principle, ΔE_v and the variation in overlayer and substrate band bending in the coverage range examined. If the band bending can be estimated from the coverage dependence of the substrate and overlayer core binding energies [9], then one can extract the value of ΔE_v . Recently this very successful method came under some criticism [10], since high resolution core level photoemission studies during Ge heterojunction formation with a number of III-V semiconductors repeatedly showed lineshape changes due to interface chemistry which greatly complicated the task of extracting the band bending variation. We decided to compare the ΔE_v value obtained with our valence band fitting method with the result of the conventional method. In the present high resolution results we observed no detectable coverage dependence of the Te 4d lineshape, and we used the apparent Te 4d binding energy to monitor the substrate band bending. We observed instead lineshape changes for the Ge 3d core levels. A superposition of two 3d doublets could be used to obtain a good fit of the overall lineshape in the intermediate Ge coverage range (1-5Å). The coverage-dependence of the two doublets clearly identify the high binding energy doublet as due to Ge atoms involved in a chemically-induced local interface dipole and the low binding energy doublet as due to the growing elemental Ge overlayers. We used the energy position of this second Ge 3d contribution to estimate the band bending variation within the Ge overlayer. The values of ΔE_v derived from the two methods are summarized in table I. All of the values are consistent within experimental uncertainty, and we conclude that the valence band offset is $0.84 \pm 0.10 \text{ eV}$ for all of the heterojunctions examined, and that the valence band offset change in the series is less than $\pm 0.05 \text{ eV}$.

Table I. Valence band offsets ΔE_v for $\text{Ge-Cd}_{1-x}\text{Mn}_x\text{Te}$ determined from two different methods discussed in the text.

interface	$\Delta E_v(\text{eV})^a$	$\Delta E_v(\text{eV})^a$
	VB fitting	core levels
Ge-CdTe	0.80	0.80
Ge- $\text{Cd}_{0.65}\text{Mn}_{0.35}\text{Te}$	0.83	0.85
Ge- $\text{Cd}_{0.4}\text{Mn}_{0.6}\text{Te}$	0.81	0.86

a

Uncertainty of each numerical value of ΔE_v is 0.10eV, but uncertainty on the change in ΔE_v in the $\text{Cd}_{1-x}\text{Mn}_x\text{Te}$ series is only 0.05eV (see text).

The transitivity rule[4,9] would allow us in principle to determine the value of ΔE_v for a hypothetical $\text{Cd}_{1-x}\text{Mn}_x\text{Te-Cd}_{1-y}\text{Mn}_y\text{Te}$ heterojunction from the known value of the valence band offset for heterojunctions of the two semiconductors with a common third semiconductor. From the results of table I one would then conclude that a valence band offset of $0.00 \pm 0.05\text{eV}$ is expected, i.e. that the $\text{Cd}_{1-x}\text{Mn}_x\text{Te-Cd}_{1-y}\text{Mn}_y\text{Te}$ system would follow the much maligned common anion rule[9]. We should add, however, a word of caution: to date, the transitivity rule has been found to hold only within a substantial experimental uncertainty ($\pm 0.15\text{eV}$).

CONCLUSIONS

We have employed two different analysis methods to study the valence band offset at heterojunctions between Ge and semimagnetic $\text{Cd}_{1-x}\text{Mn}_x\text{Te}$ semiconductors as a function of x . In particular, we have proposed a new simple least squares fitting procedure to obtain values of the valence band offset with an accuracy of 0.05eV in the change of this parameter in the heterojunction series. We found the valence band offset for $\text{Ge-Cd}_{1-x}\text{Mn}_x\text{Te}$ to be independent of substrate composition and bandgap. We conclude that within the range of validity of the transitivity rule, $\text{Cd}_{1-x}\text{Mn}_x\text{Te-Cd}_{1-y}\text{Mn}_y\text{Te}$ heterojunctions may follow the common anion rule.

ACKNOWLEDGEMENTS

This work was supported in part by the Army Research Office under grant No. DAAL03-90-G-0001 and by the Center for Interfacial Engineering of the University of Minnesota. We thank J.K. Furdyna for providing us with the bulk sample used in this study. Finally, we thank the whole staff of the Synchrotron Radiation Center of the University of Wisconsin-Madison,

supported by the National Science Foundation, for their cheerful support.

REFERENCES

1. G. Bastard, C. Rigaux, Y. Guldner, J. Mycielski, and A. Mycielski, J. Phys. (Paris) **39**, 87 (1978); T. Dietl, Solid State Sci. **24**, 334 (1981).
2. R. Reifengerger and D.A. Schwarzkopf, Phys. Rev. Lett. **50**, 907 (1983).
3. M. von Ortenberg, Phys. Rev. Lett. **49**, 1041 (1982).
4. H. Kroemer, in Molecular Beam Epitaxy and Heterostructures, edited by L.L. Chang and K. Ploog, NATO ASI Series, (Martinus Nijhoff, Dordrecht, 1985), and references therein.
5. A. Wall, S. Chang, P. Phillip, C. Caprile, A. Franciosi, R. Reifengerger, and F. Pool, J. Vac. Sci. Technol. **A4**, 2051 (1987).
6. A. Franciosi, in Diluted Magnetic (Semimagnetic) Semiconductors, R.L. Aggarwal, J.K. Furdyna, and S. von Molnar eds., Materials Research Society, Pittsburgh, Pennsylvania, 1987, p.175.
7. A.D. Katnani and G. Margaritondo, Phys. Rev. B **28**, 1944 (1983).
8. Xiaohua Yu and A. Franciosi, (to be published).
9. G. Margaritondo, in Heterojunction Band Discontinuities: Physics and Device Applications, edited by F. Capasso and G. Margaritondo (Elsevier Science Publishers B.V., 1987).
10. C.M. Aldao, I.M. Vitomirov, F. Xu, and J.H. Weaver, Phys. Rev. B **40**, 3711 (1989).

PULSED LASER EVAPORATION AND EPITAXY GROWTH OF $\text{Cd}_{1-x}\text{Mn}_x\text{Te}$

X.L. Zheng, C.A. Huber*, P. Becla, M. Shih, and D. Heiman

Francis Bitter National Magnet Laboratory, Massachusetts Institute of Technology, Cambridge, MA, 02139

ABSTRACT

Epitaxial layers of $\text{Cd}_{1-x}\text{Mn}_x\text{Te}$ have been grown on CdTe (100) substrates by evaporating a target with a $1.06\text{ }\mu\text{m}$ pulsed laser. The high - quality materials were characterized by photoluminescence spectroscopy (PL) and energy dispersive analysis of x-ray (EDAX). We find that the incorporation of the Mn in the epitaxial layer is about two - thirds of the concentration in the target. A comparison is made to the epitaxial layers grown on CdTe (111) and GaAs (100) substrates.

Diluted magnetic semiconductors, like $\text{Cd}_{1-x}\text{Mn}_x\text{Te}$, form a novel class of semiconductor materials. Epitaxial growth of these materials has recently become feasible. $\text{Cd}_{1-x}\text{Mn}_x\text{Te}$ epitaxial layers have been grown by molecular beam epitaxy (MBE)^{1,2}, metalorganic chemical vapor deposition (MOCVD)³, atomic layer epitaxy (ALE)⁴, and pulsed laser evaporation and epitaxy (PLEE)^{5,6}.

The PLEE technique has some advantages over the MBE technique for fabricating layered semiconductors and microstructures.^{7,8} Instead of using an effusion (Knudsen) cell as a molecular beam source, PLEE uses suitable solid targets that are heated locally to a few thousand degrees $^{\circ}\text{C}$ with a pulsed laser beam to produce an atomic-beam source. One unique characteristic provided by this technique is that composition changes can be made during the epitaxial layer growth by directing the laser beam to different targets using a computer controlled mirror. This can be employed to layer different materials in superlattices and quantum wells. In addition, since a single laser shot produces only about one tenth of a monolayer, materials from different targets can be evaporated and directed to the substrate during the deposition of a single monolayer. Therefore one can anticipate that single monolayer growth with any reasonable composition can be obtained, and that an ordered material like Cd_3MnTe_4 might be grown by this technique⁹.

A pulsed Nd: YAG laser operated at $1.06\text{ }\mu\text{m}$, repetition rate of 10 Hz and pulse duration of 0.1 ms, is used in the growth. In general the growth rate depends on the laser power, beam diameter, target material, and the distance between target and substrate. We obtain a growth rate between $2\text{ \AA}/\text{sec}$ and $4\text{ \AA}/\text{sec}$ using an average power of 0.8 W (80 mJ/pulse), beam diameter of 0.5 mm, and target to substrate distance of 7 cm. The energy density per pulse is $30\text{ J}/\text{cm}^2$. To ensure a uniform evaporation of the targets, the laser beam is scanned across the rotating targets. The former is accomplished by a computer-controlled stepping motor attached to a reflecting mirror. An ultra-high-vacuum chamber is used with a base pressure of 1×10^{-8} torr. The growth rate is monitored by a quartz - crystal thickness monitor and the substrate growth temperature is

typically 300 °C. Optical characterization of the as-grown epitaxial layers is carried out by photoluminescence (PL) spectroscopy at liquid helium temperature using an alignment-free fiber optics apparatus.¹⁰

Epitaxial layers of CdTe and $\text{Cd}_{1-x}\text{Mn}_x\text{Te}$ were grown on CdTe substrates with two different substrate orientations, (100) and (111B). Usually no substrate etching is used after the original chemical polishing by the vendor. After rinsing in methanol, the substrates were mounted on tantalum discs by using indium solder, and then degassed by heating to 350 °C for 5 minutes in the chamber prior to the growth.

One conclusion from our experiments is that (100)-oriented substrates of CdTe give higher quality epitaxial layers for the growth of CdTe and $\text{Cd}_{1-x}\text{Mn}_x\text{Te}$, compared to the (111B) oriented substrates. The PL intensity is at least 20 times stronger for the epitaxial layers grown on (100) oriented substrates than those grown on (111B)-oriented substrates. This has been verified within a reasonable range of the growth rate and growth temperature.

We also found another interesting result when comparing the Mn concentration in the $\text{Cd}_{1-x}\text{Mn}_x\text{Te}$ epitaxial layer to that in the target: less Mn incorporates when CdTe substrates are used, but excess Mn incorporates when GaAs substrates are used. The latter has also been observed recently by other authors, and was compensated by using an over-pressure of Cd introduced during the growth in order to maintain the stoichiometry.^{5,6}

Both PL and EDAX were used to determine the Mn concentration. Comparison of PL spectra from a $\text{Cd}_{1-x}\text{Mn}_x\text{Te}$ target and from the epitaxial layer grown from the same target material clearly shows this Mn deficiency in the layer (see Fig.1). Three types of transitions can be identified in the spectrum of the target shown in the Fig.1(a): a donor-bound-exciton transition (D^0X) at 1705 meV; an acceptor-bound-exciton transition (A^0X) at 1692 meV; and a broad and weak transition centered at about 1647 meV, which is related to donor-acceptor-pair transition (DAP) and/or band-acceptor transition (eA^0). To determine the Mn concentration, we use a formula for the acceptor-bound-exciton transition energy (or L1 transition energy)¹¹

$$E_{\text{L1}}(x) = 1588.8 + 1440x \text{ meV} \quad (\text{for } 0 < x < 0.1 \text{ at } T=4\text{K}),$$

and obtain a Mn concentration $x=0.071$. Next we examine the $\text{Cd}_{1-x}\text{Mn}_x\text{Te}$ epitaxial layer. In Fig. 1(b) there is a small additional peak at 1590 meV, and is identified as a bound-exciton transition from the CdTe substrate. Since this epitaxial layer has a thickness of 1.5 μm , the exciting photons with 1.96 eV are mostly absorbed in this layer (absorption length $\alpha^{-1} = 0.4 \mu\text{m}$). The excitons are created in the layer and then some migrate to the substrate when they recombine. We have confirmed this exciton migration by performing PL with higher photon energy (2.6 eV) and still observed a similar CdTe-related-transition peak, while in this case the photons are totally absorbed in the layer (absorption length $\alpha^{-1} = 0.13 \mu\text{m}$). Now, the (A^0X) transition has moved to 1653 meV and the (DAP / eA^0) transition has moved to about 1610 meV. In the same way, we can determine the Mn concentration in the epitaxial layer as $x=0.044$, which is 38% less than in the original target material. Another indication from the PL spectra is that there are more acceptors in the epitaxial layer than in the target, since the (D^0X) transition is

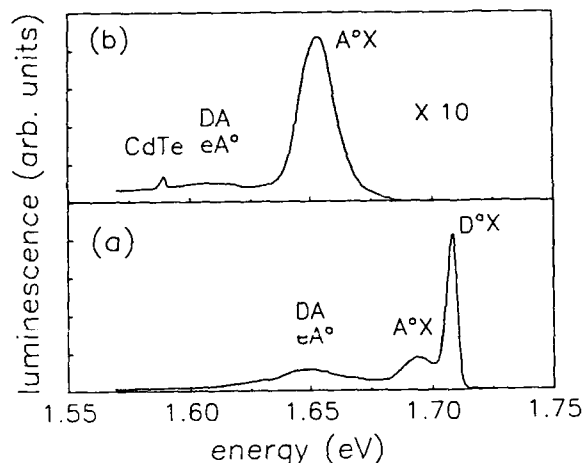


Fig. 1 PL spectra from: (a) $\text{Cd}_{1-x}\text{Mn}_x\text{Te}$, $x=0.071$, target; and (b) $\text{Cd}_{1-x}\text{Mn}_x\text{Te}$, $x=0.044$, epitaxial layer grown on CdTe (100) substrate from the same target material as shown in (a). The sample temperature is 4.2 K. The exciting photon energy is 1.96 eV and the light intensity on the sample is 0.1W/cm^2 .

absent in the epitaxial layer. Also the relative amplitude of the (A°X) transition to the ($\text{DAP} / \text{eA}^\circ$) transition is several times larger in the epitaxial layer. The excess acceptors are probably related to additional Cd vacancies in the epitaxial layer.

The above results for the $\text{Cd}_{1-x}\text{Mn}_x\text{Te}$ epitaxial layer composition based on PL spectra are confirmed by the EDAX data shown in Table I, which is from another set of target and epitaxial layer samples with higher Mn concentration. The Mn concentration in the target is $x=0.28$, but is only $x=0.17$ in the epitaxial layer grown on a CdTe (111) substrate. Again, the loss is 39%. This Mn deficiency is consistent with the PL results from the sample with low Mn concentration as described above. In contrast, Table I shows that the $\text{Cd}_{1-x}\text{Mn}_x\text{Te}$ epitaxial layer grown on a GaAs substrate has a Mn concentration higher than the target. No PL data was

Table I. EDAX data from a $\text{Cd}_{1-x}\text{Mn}_x\text{Te}$ target and the epitaxial layers grown from this target, using various substrates.

Material	Concentration(%)			x- value
	Mn	Cd	Te	
target	13.9	35.9	50.2	0.28
epilayer on (111B)CdTe	8.5	37.5	53.9	0.17
epilayer on (100)GaAs	16.7	32.4	50.9	0.33
Spot,epilayer on (100)GaAs	35.3	15.2	49.5	0.71

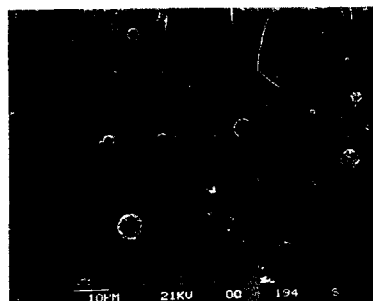


Fig. 2 SEM micrograph of an layer of $\text{Cd}_{1-x}\text{Mn}_x\text{Te}$, grown on a GaAs (100) substrate.

obtained to confirm this, probably due to the poor surface morphology and the gallium-related defects. Many spots of 1 - 10 μm diameter were observed on the layer grown on GaAs substrate. The Mn concentration was found to be as high as 0.70 on these spots. An SEM micrograph of this layer is shown in Fig.2. The EDAX analysis of the same sample revealed the presence of significant amounts of gallium in the layer. Smaller amounts of gallium in the layer has been reported previously¹².

In summary, we have grown high-quality epitaxial layers of $\text{Cd}_{1-x}\text{Mn}_x\text{Te}$ on CdTe (100) substrates by PLEE technique. PL and EDAX data indicate that about two-thirds of the Mn in the target is incorporated in the epitaxial layers, for targets with $x=0.07$ and 0.28. On the other hand, epitaxial layers grown on GaAs substrates show higher Mn concentration than the targets, in addition to the very high Mn concentration spots. We also find that the use of CdTe (100) substrates results in a high-quality epitaxial layer than CdTe (111) substrates.

We thank J.T.Cheung for many invaluable conversations on the construction and operation of apparatus, L.A.Kolodziejski for expert advice, and J.Perkins for his help. This work is partially supported by grants NSF-DMR-8807419 and NSF-DMR-8813164.

Reference

- * Permanent address: Department of Physics, University of Puerto Rico, Rio Piedras, Puerto Rico 00931.
- 1. L.A.Kolodziejski, T.Sakamoto, R.L.Gunshor, and S.Datta, Appl. Phys. Lett. **44**, 799 (1984).
- 2. R.N.Bicknell, R.W.Yanks, N.C.Giles-Taylor, D.K.Blanks, E.L.Buckland, and J.F.Schetzina, Appl. Phys. Lett. **45**, 93 (1985).
- 3. A. Nouhi and R.J.Stirn, Appl. Phys. Lett. **51**, 2251 (1987).
- 4. M.A.Herman, O.Jylha, and M.Pessa, J. Cryst. Growth **66**, 480 (1984).
- 5. J.M.Wrobel and J.J.Dubowski, Appl. Phys. Lett. **55**, 469 (1989).
- 6. J.J.Dubowski, J. Cryst. Growth (to be published).
- 7. J.T.Cheung, M.Khoshnevisan, and T.Magee, Appl. Phys. Lett. **43**, 462 (1983).
- 8. J.J.Dubowski, Chemtronics, **3**, 66 (1988).

9. D.Heiman, E.D.Isaacs, P.Becla, and S.Foner, in Diluted Magnetic (Semimagnetic) Semiconductor, edited by R.L.Agarwal, J.K.Furdyna and S.von Molnar (Mater. Res. Soc. Proc. 89, Pittsburgh, PA, 1987) p.21.
10. D.Heiman, X.L.Zheng, S.Sprunt, B.B.Goldberg, and E.D.Isaacs, SPIE, 1055, 96 (1989).
11. D.Heiman, P.Becla, R.Kershaw, D.Rideley, K.Dwight, A.Wold, and R.R.Galazka, Phys. Rev. B34, 3961 (1986).
12. J.J.Dubowski, J.M.Wrobel, S.Rolfe, J.A.Jackman, J.H.Mazur, and J.Noad, this proceeding.

PHOTOLUMINESCENCE OF ZnSe EPILAYERS ON GaAs UNDER HYDROSTATIC PRESSURE

JUDAH A. TUCHMAN, ZHIFENG SUI, IRVING P. HERMAN, R. L. GUNSHOR,*
L. A. KOLODZIEJSKI,** D. A. CAMMAC*** and M. SHONE***

Department of Applied Physics, Columbia University, New York, NY 10027

*School of Electrical Engineering, Purdue University, West Lafayette, IN 47907

**Department of Electrical Engineering, Massachusetts Institute of Technology,
Cambridge, MA 02139

***North American Philips Corporation, Briarcliff Manor, NY 10510

ABSTRACT

The near bandgap photoluminescence of ZnSe epilayers grown on GaAs substrates is measured for pressures up to ~25 kbar using a diamond anvil cell at $T = 9$ K.

The bandgap changes with pressure, dE/dp , for pseudomorphic and nonpseudomorphic films are obtained, and are compared with results for bulk crystalline ZnSe.

INTRODUCTION

Commensurate growth of ZnSe on GaAs has been achieved for thicknesses up to $\sim 0.15 \mu\text{m}$ [1-3]. Elastic strain due to the lattice mismatch (0.25% at room temperature) is accommodated until the critical thickness is obtained. For larger thicknesses misfit dislocations lower the total energy of the system and incommensurate growth ensues. Previous studies have demonstrated the relation of this strain to epilayer thickness, with its concomitant effect on the density of misfit dislocations [2,4]. Moreover, photoluminescence (PL) studies have demonstrated the effect of this strain on band-edge emission [4-6].

The presence of biaxial strain in very thin films is also expected to alter the effect of applied hydrostatic pressure (p) on the band-edge photoluminescence relative to its effect on the PL from bulk material. Previous reports have determined dE/dp , the change in bandgap energy with pressure, to be in the range 6.0 – 7.5 meV/kbar for bulk ZnSe at room temperature down to 77 K [7-9]. The current study determines dE/dp for ZnSe epilayers of contrasting thickness, grown by MBE on GaAs, and compares these values with the bulk crystalline value, which is also measured here. All measurements are made at 9 K.

EXPERIMENTAL PROCEDURE

Photoluminescence measurements were made on 0.1 and 2.1 μm -thick ZnSe epilayers grown on GaAs by MBE and on bulk ZnSe grown by zone melting. The "thin" epilayer was commensurately grown, while the "thick" layer was thicker than the critical thickness for commensurate growth. Experiments were conducted at a temperature of $T = 9\text{ K}$ and at pressures up to $\sim 25\text{ kbar}$. The GaAs substrate was initially $\sim 300\text{ }\mu\text{m}$ thick, and was thinned down to $\sim 50\text{ }\mu\text{m}$ by mechanical polishing.

High pressure measurements were made in a gasketed Merrill-Bassett diamond anvil cell (DAC) [10,11], contained within a closed cycle refrigerator (9 K). The ZnSe sample was loaded with ruby chips in a liquid argon bath within the DAC to obtain near-hydrostatic pressure conditions at low temperature [12]. ZnSe and ruby photoluminescence were excited using the 4067 \AA line from a krypton ion laser, and were detected using a 0.85 m double spectrometer and a cooled PMT. Photon counting electronics were interfaced to an IBM AT for A/D data conversion, storage, and analysis.

The pressure in the DAC was determined using the calibration scale for ruby fluorescence vs. pressure [13]. This was in turn calibrated using the 6929.468 \AA line from a neon discharge lamp, together with the 6965.430 \AA line from an argon lamp. The pressure determination is accurate to $< 0.15\text{ kbar}$, and energy measurements for the ZnSe photoluminescence are accurate to $< 0.6\text{ meV}$. The resultant uncertainty in the values of dE/dp is less than 0.21 meV/kbar .

RESULTS

Near band-edge PL spectra are shown for the three samples at ambient pressure (1 bar) and $T = 9\text{ K}$, as the lower spectra in each of the three parts of Figure 1. For the bulk crystalline sample in Fig. 1a, the dominant feature at 2.7973 eV (I_{20}) is associated with a neutral bound donor exciton, attributed to either an In or Ga impurity. A neutral bound acceptor accounts for the exciton feature at 2.7924 eV (I_1). The feature at 2.7829 eV (I_1^{DEEP}) is due to a deep level acceptor, commonly attributed to Cu. The phonon replica, $I_1^{\text{DEEP-LO}}$, is found 31.6 meV lower in energy than I_1^{DEEP} . Finally, the two weak features higher in energy than I_{20} , are due to the excited state ($n=2$) of a donor bound exciton at 2.8014 eV (I_{2D}) and the free exciton transition at 2.8039 eV (FE).

Identification of the PL peaks is less certain for the epilayers. For the "thick" film in Fig. 1b, the ambient pressure peak at 2.8009 eV (FE) is attributed to the ground state free exciton peak. The red shift from the bulk value may be due to a slight tensile strain [3]. The peak at 2.7958 eV (I_{20}) is associated with an exciton bound to a neutral donor and

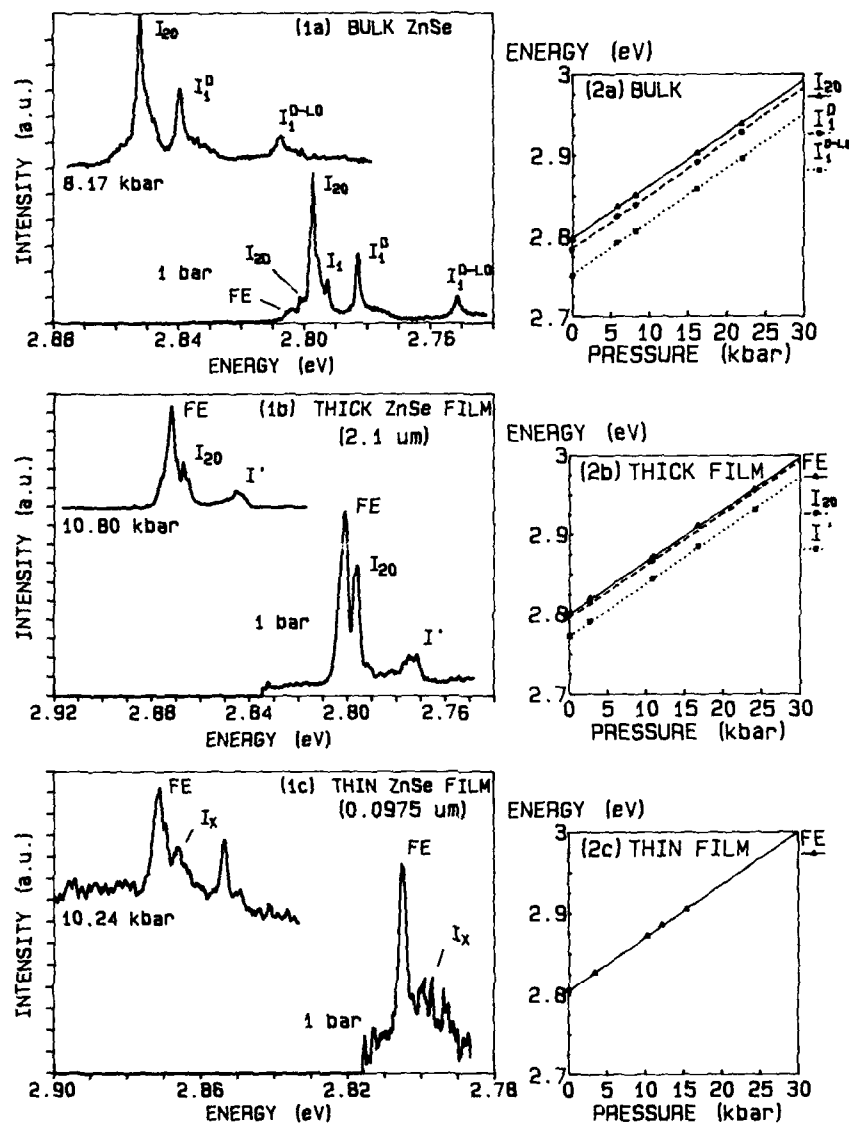


Figure 1. Photoluminescence spectra at $T = 9$ K.

Figure 2. Plots of energy vs. pressure for the various exciton peaks.

the peak at 2.7728 meV (I') is as yet unidentified. For the "thin" film in Fig. 1c, one large peak is obtained. This corresponds to the ground state free exciton transition with energy 2.8055 eV (FE). The blue shift from the bulk value corresponds to an in-plane compressive strain due to a lattice mismatch at 9 K of $\sim 0.23\%$. A very small peak is found near 2.7998 eV (I_x), which is usually attributed to a neutral bound exciton.

The photoluminescence is monitored with increasing pressure for all three samples. A representative plot for each sample at a higher pressure is provided by the upper spectra in the three parts of Figure 1. For the "thick" epilayer, the I_{20} peak intensity decreases with increasing pressure and disappears altogether at approximately 16 kbar. At approximately the same pressure, a new feature begins to grow at 2.9170 eV, which is 6.4 meV higher in energy than the FE peak. As pressure is increased the exciton energies I_{20} , I_1^{DEEP} , and $I_1^{\text{DEEP-LO}}$ are monitored for bulk ZnSe, the FE, $I_{20}^{\text{Cl,In,Ga}}$, and I' peaks are monitored for the "thick" sample, and the free exciton transition (FE) is monitored for the "thin" sample. The resultant plots of energy vs. pressure are shown in Figure 2. Least square lines are plotted for these data, yielding values for dE/dp . For bulk crystalline ZnSe, a value of $dE/dp = 6.64 \pm 0.12$ meV/kbar is obtained for the dominant I_{20} peak, with $dE/dp = 6.59 \pm 0.12$ meV/kbar for I_1^{DEEP} and 6.58 ± 0.15 meV/kbar for $I_1^{\text{DEEP-LO}}$. For the "thick" sample, $dE/dp = 6.50 \pm 0.13$ meV/kbar for the dominant free exciton (FE) peak, 6.54 ± 0.13 meV/kbar for I_{20} , and 6.67 ± 0.15 meV/kbar for I' . For the "thin" sample, $dE/dp = 6.48 \pm 0.21$ meV/kbar (FE).

ANALYSIS

The effect of hydrostatic and uniaxial pressure on a semiconductor is to shift the conduction and valence band edges by changing the volume and crystal symmetry. For ZnSe with its direct bandgap at Γ_1 , the conduction band is only subject to hydrostatic components of strain. However, in addition to the effect of hydrostatic strain on shifting the valence bands (Γ_8), tetragonal distortion splits the degeneracy of the four-fold $P_{3/2}$ multiplet into heavy hole (hh: $J = 3/2$; $m_J = \pm 3/2$) and light hole (lh: $J = 3/2$; $m_J = \pm 1/2$) bands. The effect of biaxial stress due to lattice mismatch may therefore be separated into hydrostatic and nonhydrostatic components [14,15], which when considered together with externally applied hydrostatic pressure may be shown to affect energy bandgap shifts, according to:

$$\Delta E_g = -(a_c - a_v) \frac{3p}{C_{11} + 2C_{12}} + \left[2(a_c - a_v) \left(1 - \frac{C_{12}}{C_{11}} \right) + b \left(1 + \frac{2C_{12}}{C_{11}} \right) \right] \epsilon_{xx}^{\text{ZnSe}}(T,p) \quad [1]$$

The first term is the hydrostatic pressure component, while the first component of the second term is due to the hydrostatic portion of the strain and the second component is due to tetragonal deformation, with – for heavy holes and + for light holes. Spin-orbit splitting has been included in the overall bandgap term. Here, a_c and a_v are the hydrostatic deformation potentials for the conduction and valence bands respectively, b is the uniaxial deformation potential for a strain of tetragonal symmetry, and C_{11} and C_{12} are elastic constants for ZnSe. The strain $\epsilon_{xx}^{\text{ZnSe}}(T,p)$ is evaluated for a given temperature and pressure and has the form:

$$\epsilon_{xx}^{\text{ZnSe}}(T,p) = \frac{a_x(T,p_0)}{a_x(T,p_0)} \left(\frac{1 - \frac{p}{C_{11} + 2C_{12}'}}{1 - \frac{p}{C_{11} + 2C_{12}}} \right) - 1 \quad [2]$$

where $a_x(T,p_0)$ is the lattice constant for ZnSe at temperature T and ambient pressure ($p_0 = 1$ bar), and the primed quantities correspond to the respective parameters for GaAs.

The resultant shift in bandgap energy with pressure for a strained layer may be related to $(dE/dp)_{\text{bulk}} = - \{3(a_c - a_v)/(C_{11} + 2C_{12})\}$ for bulk material by:

$$\left(\frac{dE}{dp} \right)_{hh}^{hh} = \left(\frac{dE}{dp} \right)_{bulk} - \left[2(a_c - a_v) \left(1 - \frac{C_{12}}{C_{11}} \right) + b \left(1 + \frac{2C_{12}}{C_{11}} \right) \right] \frac{a_x(T,p_0)}{a_x(T,p_0)} \left[\frac{1}{C_{11} + 2C_{12}'} - \frac{1}{C_{11} + 2C_{12}} \right] \quad [3]$$

The variation of the exciton binding energy with applied hydrostatic pressure is not significant here.

The values for dE/dp may be evaluated using $C_{11} = 929$ kbar, $C_{12} = 562$ kbar, $C_{11}' = 1221$ kbar, $C_{12}' = 566$ kbar [16,17], $a_x(298 \text{ K}, p_0) = 5.6676 \text{ \AA}$, and $a_x'(298 \text{ K}, p_0) = 5.6533 \text{ \AA}$ [5,17]. The elastic constants are for $T = 77 \text{ K}$. For 9 K , the elastic constants are estimated to be 940, 570, 1234, and 577 kbar, respectively, extrapolating from the constants at 77 and 300 K by using an exponential fit. A wide range of deformation potential values are reported in the literature. The values $(a_c - a_v) = -4.17 \text{ eV}$ and $b = -1.20 \text{ eV}$ [3,18] can be used as reference parameters. Then the expected values of dE/dp are 6.09 meV/kbar for bulk crystalline ZnSe, and 6.05 and 5.72 meV/kbar for the hh and lh bands for strained layer ZnSe on GaAs, using the elastic constants at 77 K. At 9 K, the respective values are 6.01, 5.98, and 5.65 meV/kbar. Using the previously determined

experimental values [6] as a second reference, $(a_c - a_v) = -4.87$ eV and $b = -1.05$ eV, the three expected values for dE/dp are 7.11, 7.02, and 6.73 meV/kbar, respectively at 77 K, and 7.02, 6.93, and 6.64 meV/kbar at 9 K. The value of $(a_c - a_v)$ determined here is -4.60 eV, using dE/dp measured for the I_{20} peak in bulk crystalline ZnSe and using the elastic constants estimated for 9 K.

The heavy hole band is higher in energy than the light hole band for compressed films, while for films under tensile stress the light hole band is higher. However, since dE/dp for hh is greater than that for lh, increasing the pressure will cause the bands to cross. Thus films initially under compressive stress, such as "thin" ZnSe films, will become tensile beyond some pressure, and the value of dE/dp will change from the hh to the lh value. The "thick" films, on the other hand, are always either relaxed or under tensile stress, and will therefore follow the lh value throughout.

Low temperatures (9 K) will affect the film strain and the relative energies of the valence bands. Specifically, for ZnSe films on GaAs, a temperature decrease relaxes the compressive strain due to lattice mismatch, since the thermal expansion coefficient for ZnSe is larger than that for GaAs [15]. Nonetheless, the "thin" films here remain compressively strained even at low temperature for $p \leq 41$ kbar, so that the heavy hole band will therefore always be at the higher energy. Hence, the model suggests that dE/dp for the "thin" film hh excitons and for excitons in the bulk should be within 0.1 meV/kbar of each other. Within experimental uncertainty, this is seen here.

The "thick" ZnSe films, however, are always under tensile stress, since it is assumed that the compressive strain has been completely relaxed at room temperature. As a result, dE/dp for these films is expected to be the lh value which, according to the model, is ~ 0.3 - 0.4 meV/kbar lower than the bulk and "thin" film values. Within experimental error, this is consistent with the reported measurements.

CONCLUDING REMARKS

The experimental value obtained for dE/dp for bulk crystalline ZnSe falls within the range of values determined in previous experiments. Moreover, the values of dE/dp obtained for the ZnSe epilayers grown on GaAs are indistinguishable from the bulk result. Work is continuing on examining the effect of pressure on ZnSe films, including potential causes of strain relaxation in films with the application of high pressure.

ACKNOWLEDGMENTS

This work was supported at Columbia by the Joint Services Electronics Program Contract DAAL03-88-C-0009 and at Purdue by the Office of Naval Research Contract

N00014-82-K0563. The authors would like to thank Chris Berzins, Rob Scarmozzino, and Tom Licata for their assistance in data processing, and K. Shahzad for valuable discussions.

REFERENCES

1. J. Kleiman, R.M. Park, and S.B. Qadri, *J. Appl. Phys.* **61**, 2067 (1987).
2. J. Petruzzello, B.L. Greenberg, D.A. Cammack, and R. Dalby, *J. Appl. Phys.* **63**, 2299 (1988).
3. T. Yao, Y. Okada, S. Matsui, K. Ishida, and I. Fujimoto, *J. Crystal Growth* **81**, 518 (1987).
4. T. Yao, *Jpn. J. Appl. Phys.* **25**, L544 (1986).
5. K. Mohammed, D.A. Cammack, R. Dalby, P. Newbury, B.L. Greenberg, J. Petruzzello, and R.N. Bhargava, *Appl. Phys. Lett.* **50**, 37 (1987).
6. R.L. Gunshor, L. A. Kolodziejski, M.R. Melloch, M. Vaziri, C. Choi, and N. Otsuka, *Appl. Phys. Lett.* **50**, 200 (1987).
7. A.L. Edwards, T.E. Slykhouse, and H.G. Drickamer, *J. Phys. Chem. Solids* **11**, 140 (1959).
8. S. Ves, K. Strossner, N.E. Christensen, C.K. Kim, and M. Cardona, *Solid State Commun.* **56**, 479 (1985).
9. P. Jaszczyn-Kopec, B. Canny, G. Syfosse, and G. Hamel, *Solid State Commun.* **49**, 795 (1984).
10. A. Jayaraman, *Rev. Mod. Phys.* **55**, 65 (1983).
11. L. Merrill and W.A. Bassett, *Rev. Sci. Instrum.* **45**, 290 (1974).
12. A.P. Jephcoat, H.K. Mao, and P.M. Bell, *J. Geophys. Res.* **91**, 4677 (1986).
13. R.A. Noack and W.B. Holzapfel, in *High Pressure Science and Technology*, ed. K.D. Timmerhaus and M.S. Barber (Plenum) **1**, 748 (1979).
14. H. Asai and K. Oe, *J. Appl. Phys.* **54**, 2052 (1983).
15. C.G. Van de Walle, K. Shahzad, and D.J. Olego, *J. Vac. Sci. Technol.* **B6**, 1350 (1988).
16. S.S. Mitra and N.E. Massa, in *Handbook on Semiconductors*, ed. T.S. Moss (North Holland) **1**, 91 (1986).
17. Landolt-Bornstein, *Numerical Data and Functional Relationships in Science and Technology* (Springer, New York) Group III, **17a-b**, (1982).
18. D.W. Langer, R.N. Euwema, K. Era, and T. Koda, *Phys. Rev.* **B2**, 4005 (1970).

3d TRANSITION METALS IN II-VI SEMICONDUCTORS

D. HEIMAN, M. DAHL, X. WANG, P.A. WOLFF, P. BECLA, A. PETROU*,
and A. MYCIELSKI**

MIT Francis Bitter National Magnet Lab, Cambridge, MA 02139,

*Physics Department, SUNY Buffalo, NY 14260

**Institute of Solid State Physics, Polish Academy of Science, Warsaw

ABSTRACT

The magnetic and electronic properties of some II-VI semiconductors with 3d transition metals other than Mn are presented. For example, the nonzero orbital moment in Fe^{2+} leads to more complex electronic energy levels than for Mn^{2+} ions. In (Cd,Fe)Se, inelastic light scattering experiments demonstrate that the ground state is nonmagnetic (Van Vleck ion), and directly measures the energy spacing between the three lowest levels. For Sc^{2+} ions the donor level lies above the bottom of the conduction band in the Cd-based materials.

INTRODUCTION

Research on II-VI semiconductors with Mn^{2+} has been quite productive in the past ten years in establishing many of the basic interactions. This is due to the simplicity of both the electronic and magnetic properties of the Mn^{2+} ion. On the other hand, most of the other 3d transition metals are more complex, leading to new effects not found with Mn^{2+} ions. A striking example is the charge ordering of ionized Fe^{3+} donors in (Hg,Fe)Se.[1,2] Here, we will address some new effects and applications of non-Mn 3d transition metals in II-VI semiconductors.

Since Mn^{2+} is the only magnetic 3d ion having a simple spin-only moment ($S=5/2$, $L=0$), its paramagnetic properties are easy to model. In more concentrated material the d-d exchange interaction between the ions significantly modifies the magnetic properties. The mechanisms and effects associated with the d-d exchange have been relatively easy to understand because of the simplicity of the Mn^{2+} ion. Figure 1 displays the quantum numbers for spin (S) and orbital momentum (L) for all the 3d transition metal series. The nonzero orbital moment of all the non-Mn ions leads to more complicated magnetic behavior due to spin-orbit coupling in crystals. This coupling induces a nonmagnetic singlet ground state (Van Vleck ion) for the Fe^{2+} ion.

In addition to the magnetic properties, the energy levels of the 3d transition metals have some interesting interactions. The Mn^{2+} donor level ($2+/3+$) lies deep within the valence band of all the II-VI semiconductors, shown in Fig. 2. In contrast to Mn^{2+} , the donor levels of other 3d ions often lie near the band edges, or even above the conduction band level. Thus some of these ions act as a source of large concentrations of conduction electrons, as with Fe in HgSe. One can also speculate that the transitions $2+ \rightarrow 3+$ might be useful for optical processes, since the donor levels provide an additional level to interact with the existing conduction and valence band states.

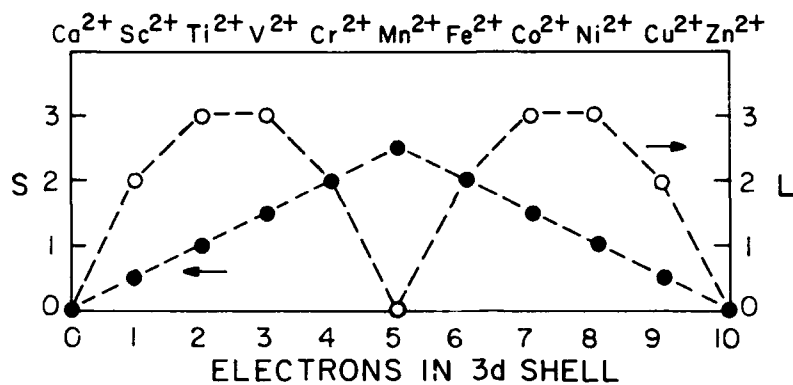


Fig. 1 -- Quantum numbers for spin (S) and orbital (L) momentum for the doubly-ionized 3d transition metals.

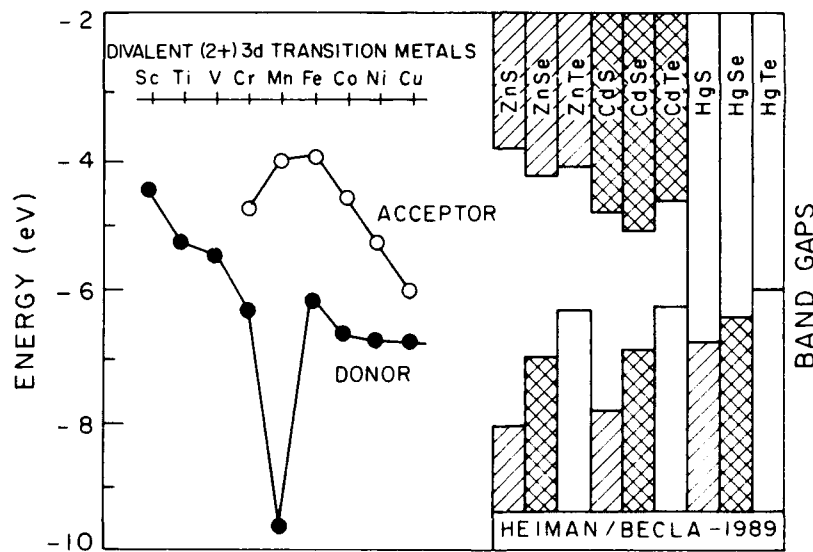


Fig. 2 -- Donor ($2+ \rightarrow 3+$) and acceptor ($2+ \rightarrow 1+$) energy levels for the doubly-ionized 3d transition metal series. On the right are the conduction and valence band edge energies for II-VI semiconductors. The relative band offsets and transition metal levels are uncertain to approximately ± 0.1 eV. See Refs. 9-11 for details.

INELASTIC LIGHT SCATTERING IN (Cd,Fe)Se

The spin-orbit coupling and crystal fields in materials with Fe^{2+} combine to produce a ground state multiplet of electronic energy levels having separations of 1-2 meV. In wurtzite (Cd,Fe)Se the three lowest levels have symmetries A_1 , A_2 and E, respectively. The first observation of these transitions using Raman scattering has recently been published.[3] The transition energies between the A_1 ground state and the two excited states were measured and found to be $E(A_1 \rightarrow A_2) = 1.5$ meV and $E(A_1 \rightarrow E) = 2.0$ meV. Fig. 3 shows these transition energies in magnetic fields to 15 tesla. Subsequent calculations[4] of these energy levels agreed with the measured field-dependent variations, shown as solid lines. Notice the large differences when the magnetic field is applied either parallel or perpendicular to the hexagonal c-axis. This arises from the selection rules for field-induced mixing of the wavefunctions of the interacting states. The lowest energy transition is nearly B-independent for B perpendicular to c, demonstrating that both the A_1 and A_2 levels have equivalent diamagnetic-like shifts. Compare this to the large shift for the same transition but with B parallel to c, demonstrating a large mixing. The highest energy transition in Fig. 3 is an overtone of the latter transition, and is not the ground to third excited state which is expected to lie above 4 meV at B=0.[4]

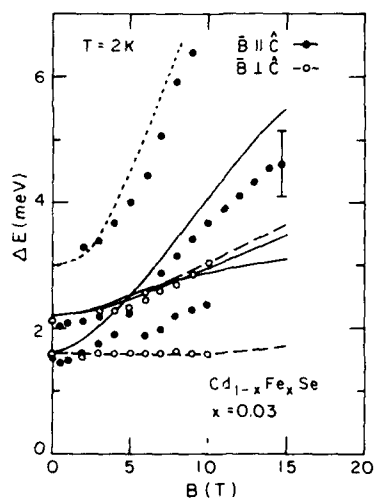


Fig. 3 -- Internal Fe^{2+} transition energies versus applied magnetic field for $\text{Cd}_{1-x}\text{Fe}_x\text{Se}$, $x=0.03$ at $T=2$ K. Raman scattering was used to measure the transitions $A_1 \rightarrow A_2$, $A_1 \rightarrow E$, and $2(A_1 \rightarrow A_2)$ for directions of magnetic field parallel and perpendicular to the hexagonal c-axis, after Ref. 3. Solid lines are calculations from Ref. 4.

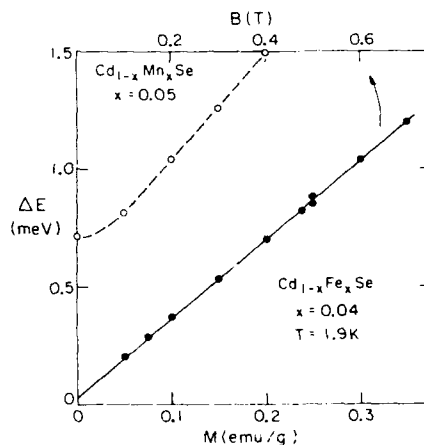


Fig. 4 -- Zeeman splitting of donor-bound electrons versus magnetization for (Cd,Fe)Se and (Cd,Mn)Se, from spin-flip Raman scattering, after Ref. 6. The smaller energy for (Cd,Fe)Se is due to the absence of the bound magnetic polaron, characteristic of the nonmagnetic, induced-moment ground state of Fe^{2+} .

Next, we examine the nonmagnetic ground state of Fe^{2+} in CdSe using spin-flip Raman scattering (SFRS). In Fig. 4, the SFRS from donor-bound electrons is compared for (Cd,Mn)Se and (Cd,Fe)Se. The bound magnetic polaron (BMP) in (Cd,Mn)Se is a well-known example where the localized donor electron experiences a finite exchange field (nonzero Zeeman splitting) even at $B=0$. [5] In remarkable contrast to this, a similar concentration of Fe does not show the BMP effect -- the energy extrapolates to zero as B decreases. [6] This results from the fact that Fe^{2+} ions do not have the large $S=5/2$ moment like Mn^{2+} , they only have a small field-induced moment. In the Mn-material there are only $N \sim 10^2$ stochastically fluctuating spins, giving rise to roughly $N^{1/2}$ net spin alignment at $B=0$. At moderate fields, the induced moment in (Cd,Fe)Se amounts to about one-quarter of the aligned moment in similar concentration (Cd,Mn)Se.

MAGNETIC QUANTUM LIMIT IN $\text{Hg}(\text{Te,Se})\text{:Fe}$

In very high magnetic fields, conduction electrons are expected to form charged rods when the cyclotron energy is much larger than the Fermi energy. Moreover, these rods might order in space perpendicular to the field, forming a Wigner-like lattice. This configuration could be further stabilized, if the background positive charges are mobile, allowing rearrangement of the positive charge along the rods as "pearls on a string". Up to now, such effects have been predicted to occur in exotic systems like neutron stars. However, with the discovery of the mixed valence $\text{Fe}^{2+}/\text{Fe}^{3+}$ phenomenon in HgSe:Fe , it now appears that these collective effects might occur in a laboratory system. [7]

There is a lot of recent experimental evidence [2,8] showing that in HgSe:Fe the Fe^{3+} ionized donors order [1] to some extent. In this situation, when the number of Fe^{2+} ions far exceeds the number of ionized Fe^{3+} ions, the Fe^{2+} "choose" which Fe sites to occupy in order to maximize their distance. Unfortunately, in pure HgSe the Fe^{2+} donor level pins the Fermi level at a large value of $E_F = 220$ meV. Thus the quantum limit ($B > 95$ T) is out of reach of present dc or long-pulse magnets. The pinning level, and hence the quantum limit, can be reduced by alloying with tellurium. [8] Results from high-field transport measurements (Hall- and Shubnikov deHaas-effect) on $\text{HgSe}_{1-y}\text{Te}_y\text{:Fe}$ give $E_F = 135$ meV for $y = 0.12$, and $E_F = 45$ meV for $y = 0.19$. In the latter sample the quantum limit is observed at $B = 14.5$ T.

SCANDIUM DOPED MATERIALS

The highest-lying 3d donor level in Fig. 2 is that of Sc^{2+} . It appears to lie above the bottom of the conduction band in all the Cd compounds. Preliminary SFRS measurements have been made on donor electrons in $\text{Cd}_{1-x}\text{Mn}_x\text{Te}$, $x=0.05$, doped with $\sim 10^{17}$ cm^{-3} Sc. This gives us an opportunity to study the interaction of the Sc^{2+} donor level with the conduction band.

It is a pleasure to acknowledge collaborations with E.D. Isaacs, S.H. Bloom, Y. Shapira, R. Kershaw, K. Dwight, A. Wold, and W. Giriat. This work was supported by Grant NSF-DMR-887419, and the FBNML is supported by the NSF.

References

1. J. Mycielski, Sol. State Commun. 60, 165 (1986).
2. Z. Wilamowski, K. Swiatek, T. Dietl, and J. Kossut (to be published).
3. D. Heiman, E.D. Isaacs, A. Petrou, R. Kershaw, K. Dwight, and A. Wold, Proc. 19th Int. Conf. Phys. Semicond., ed. W. Zawadski (Academy of Science, Warsaw, 1989), p. 1539.
4. D. Scalbert, J. Cernogora, A. Mauger, C. Beniot a la Guillaume, and A. Mycielski, Sol. State Commun. 62, 453 (1989).
5. M. Nawrocki, R. Planel, G. Fishman, and R.R. Galazka, Phys. Rev. Lett. 46, 735 (1981).
6. D. Heiman, A. Petrou, S.H. Bloom, Y. Shapira, E.D. Isaacs, and W. Giriat, Phys. Rev. Lett. 60, 1876 (1988).
7. P.A. Wolff, private communication.
8. A. Mycielski, J. Appl. Phys. 63, 3279 (1988).
9. V.I. Sokolov, Sov. Phys. Solid State 29, 1061 (1987).
10. J.M. Langer, C. Delerue, M. Lannoo, and H. Heinrich, Phys. Rev. B38, 7723 (1988).
11. A. Fazio, M.J. Caldas, and A. Zunger, Phys. Rev. B30, 3430 (1984).

MAGNETIZATION STUDY OF Fe-BASED II-VI DILUTED MAGNETIC SEMICONDUCTORS

W.J.M. DE JONGE*, H.J.M. SWAGTEN*, A. TWARDOWSKI**

*Department of Physics, Eindhoven University of Technology, Eindhoven, The Netherlands

**Institute of Experimental Physics, Warsaw University, Poland

ABSTRACT

The high field magnetization for Fe based Diluted Magnetic Semiconductors has been calculated. It is shown that the low temperature magnetization displays characteristic steps, related to the nearest neighbour exchange interaction J_{NN} , provided that J_{NN} exceeds a critical value.

INTRODUCTION

Up till recently, investigations on Diluted Magnetic Semiconductors (DMS) were almost exclusively devoted to DMS containing Mn^{2+} as a magnetic ion [1]. However, an increasing number of papers nowadays deals with DMS containing other magnetic ions such as Co^{2+} or Fe^{2+} [2].

From a magnetic point of view these ions represent a more general case since also orbital momenta are involved. As was shown before [3] for Fe^{2+} this results in a rather complex energy level scheme with a magnetically inactive ground state, giving rise to a Van Vleck type of magnetic behavior.

For the understanding of the exchange mechanism between the magnetic ions the strength and sign of the nearest neighbour interaction J_{NN} is of utmost importance since it is intimately related to the location of the d electron levels with respect to the band structure [4]. For Mn-DMS the location of steps in the magnetization has been used as a direct probe for the determination of J_{NN} [5], while in Fe-DMS, to which we will restrict ourselves, in this contribution, the d-d interactions can only be estimated from the high temperature susceptibility.

In this paper we will show by calculation that, also in the case of Fe-DMS magnetization steps can be expected which are related to J_{NN} , provided that J_{NN} exceeds a certain critical value.

THE COUPLED Fe PAIR

The energy levels and wave functions of a single Fe ion in a cubic crystal field has been extensively studied by Slack et al [6]. In our calculations we also implemented an isotropic exchange interaction for a pair and an external field:

$$H_{ij} = -2J \vec{S}_i \cdot \vec{S}_j + \mu_B \vec{B} \cdot (\vec{L}_i + 2\vec{S}_i), \quad (1)$$

which is defined on the $^5E \times ^5E$ subspace of the lowest orbital doublet given by the solution of the crystal field Hamiltonian including spin orbit interaction [7].

The magnetization per mole of Fe^{2+} ions can be calculated from:

$$\vec{M} = -R/2 \sum_i \left\{ \frac{\partial E_i}{\partial \vec{B}} \right\} \frac{e^{-E_i/kT}}{\sum_j e^{-E_j/kT}} \vec{B}/|\vec{B}| \quad (2)$$

where E_i represent the eigenvalues obtained from diagonalization of (1). For the calculations we will use the data for ZnFeSe which may be considered as representative for several Fe-DMS from the II-VI group. The crystal field parameters are well

established; $\Delta = 10 Dq = -2930 \text{ cm}^{-1}$, $\lambda = -95 \text{ cm}^{-1}$ [8] and an estimation for the nearest neighbour exchange has been found from high temperature series expansion; $J_{NN} = -22 \text{ K}$ [3].

For isolated ions ($J = 0$) the situation is relatively simple. An external field B induces a mixing of the originally non magnetic ground state with higher states, causing a repulsion of the ground state and an induction of a magnetic moment. For small fields the ground state varies quadratically with field, yielding at low temperatures a temperature independent linear magnetization (so called Van Vleck paramagnetism). The contribution of these isolated Fe^{2+} -ions magnetization is included in fig. 2 and displays no characteristic steps.

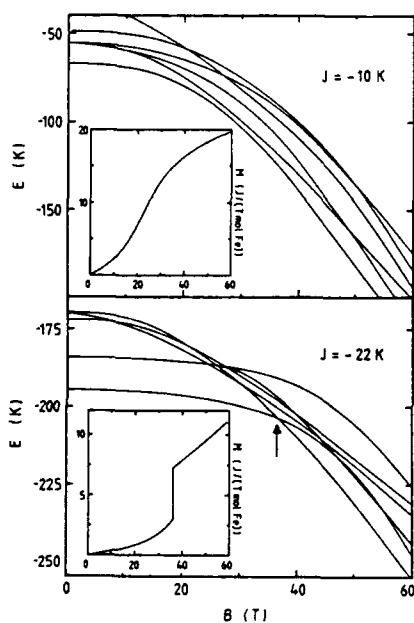


Fig. 1. Field dependence of the lowest levels of an exchange coupled Fe pair in a cubic crystal field for two values of J_{NN} , above and below $J_{\text{crit}} \approx -14 \text{ K}$. The insert shows the appearance of a magnetization step when $J_{NN} > J_{\text{crit}}$.

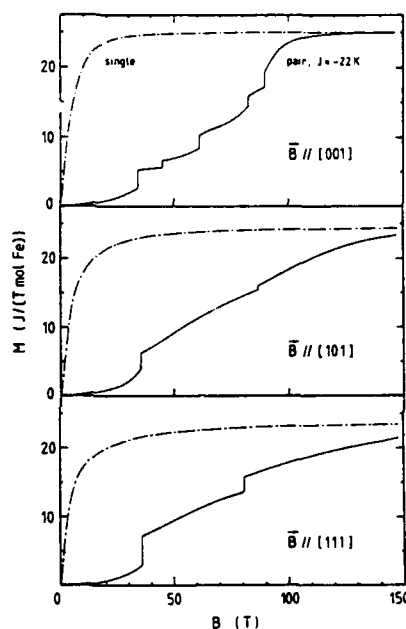


Fig. 2. Magnetization for isolated spins and exchange coupled pairs in three field directions.

A completely different situation arises when antiferromagnetically coupled pairs ($J < 0$) are considered. One may note that for sufficiently large J , i.e. when $|J| \gg \lambda^2/|\Delta|$, the energy scheme becomes analogous to the spin-only situation, where the ground state is intersected by magnetically active states, yielding steps in the magnetization at fields $g\mu_B B_s = rk_B|J|$, with $r = 1.4$ for $S = 2$. We checked that for $J = -100 \text{ K}$ this situation is almost achieved. Lowering the interaction strengths, a critical interaction strength $|J_{\text{crit}}|$ ($J_{\text{crit}} \approx -14 \text{ K}$) is observed, below which no steps in the magnetization are visible. In this case the relatively large degree of mixing bends the ground state in that amount that the excited states cannot intersect. For $J = -10 \text{ K}$ and $J = -22 \text{ K}$ the low-lying energetical structure as well as the inferred low temperature magnetization are plotted in Fig. 1. The contribution of a pair to the magnetization is shown in fig. 2, while the relation between the location of the first step and J_{NN} is

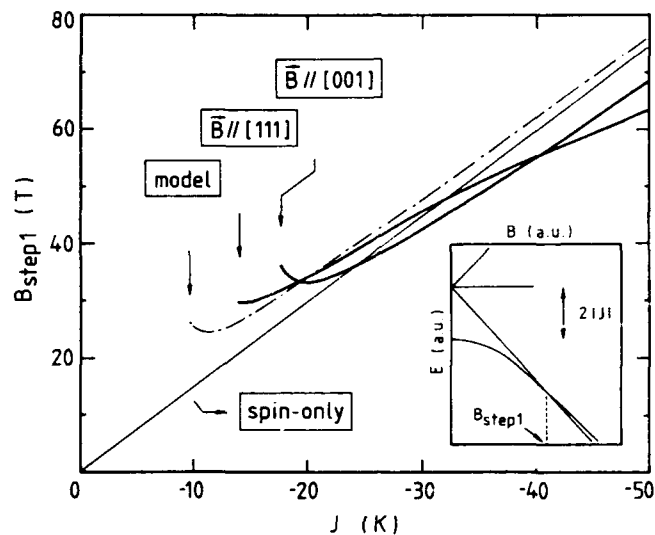


Fig. 3. Relation between the nearest neighbour Fe exchange and the magnetic field at which the first step in the magnetization is observed for two field directions. This relation is also displayed for two simplified models e.g. without crystal field effects ("spin-only") and partial inclusion of crystal field effects as discussed in our text ("model").

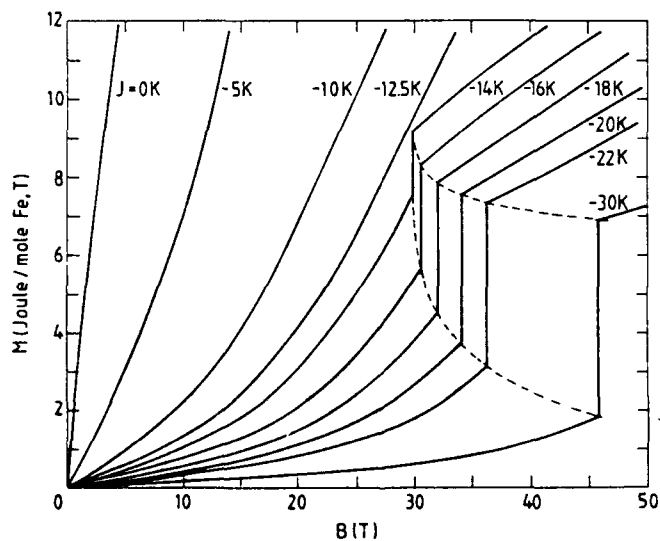


Fig. 4. The magnetization of Fe pairs close to the first step showing the appearance of a critical nearest neighbour exchange.

displayed in fig. 3. The field dependence of the magnetization close to J_{crit} is further illustrated in fig. 4. In general, the position of the steps ($|J| > |J_{crit}|$) depend strongly on the field direction and seem somewhat arbitrary. This is illustrated in Fig. 2, showing that for B along the $[001]$ axis the number of steps is maximal whereas in the $[111]$ direction only two steps are visible. Intuitively this may be due to a minimal degree of overlap between the wave-functions when the external field is applied along one of the principal crystallographic axes.

We would like to emphasize that, despite the complex general behavior, as far as the first step is concerned, the field direction does not influence its position considerably. Only the size of the step is affected. It also appears that a close resemblance with the spin-only situation ($g\mu_B B_s = k_B |J|$) is already obtained for interaction strengths closely approaching J_{crit} . Moreover, variation of the spin-orbit parameter from -95 cm^{-1} to -105 cm^{-1} , which actually increases the single-ion splitting roughly with 25%, induces a step-shift of less than 10%.

SAMPLE MAGNETIZATION

In an actual DMS crystal, the magnetic ions are randomly distributed. For not too large magnetic ion percentages (up to a few percent) we assume that the response of such a system may be described as arising from isolated ions and exchange coupled nearest neighbour pairs, provided that the exchange between the magnetic ions is short ranged. In contrast to Mn-DMS, so far no conclusive evidence about the range of the interaction has been obtained, nor has a clear spin glass transition been observed, which would be indicative for a long-range nature of the d-d exchange interactions [9]. Therefore we feel that the assumption made above is justified. The magnetization of such an array of statistically distributed single ions and pairs can now be calculated on the basis of the results obtained in the foregoing paragraph. Again, we will use ZnFeSe as a representative example. The results for a crystal containing 5% of Fe ions are shown in fig. 5 at different temperatures. It is clear that, due to the thermal population of excited states the steps in the magnetization broaden.

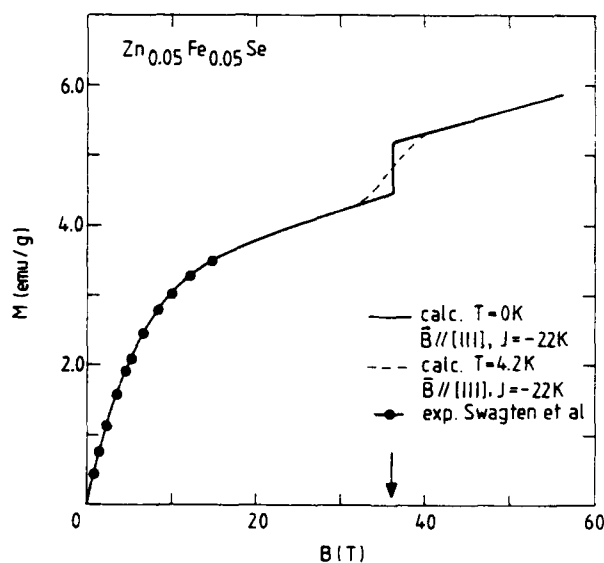


Fig. 5. Total magnetization calculated for $\text{Zn}_{0.95}\text{Fe}_{0.05}\text{Se}$. The data points were taken from Swagten et al. [7].

No experimental data on the magnetization have been reported yet in the field range where according to our calculations the magnetization steps should occur. Data are reported for ZnFeSe [7] and CdFeTe [10] in fields up till 15 T. The data for ZnFeSe are included in figure 5 and seem to be rather well described by the present calculation. However, since these experiments are restricted to low fields we will refrain from further interpretation in the scope of this paper.

DISCUSSION

The existence of a critical exchange strength, J_{crit} , necessary to observe steps in the magnetization, may not be very transparent from the treatment of the full Hamiltonian, but can be understood from the following simplified model for the behavior of the energy gap between ground state and first excited level for an Fe-Fe pair:

$$E_0 - E_1 = \chi_{pair} B^2 + g\mu_B B - 2k_B |J_{NN}|. \quad (3)$$

The first right hand term represents the Van Vleck type variation of the ground state energy; the second term represents the field dependence of the excited state which closely resembles the spin-only eigen state of a pair $E_1 = m_{spair} g\mu_B B$; while the third term represents the zero field offset between the levels which is only valid for spin-only eigen states of a pair. The solution of (3) for $E_0 - E_1 = 0$ is implemented in figure 3 and predicts indeed also a critical exchange strength, though somewhat smaller than observed in the full treatment.

The experimental observation of the magnetization steps may not be as evident as suggested by our calculations. Apart from the fact that, obviously, the exchange interaction should exceed the critical strength J_{crit} , we also did not consider the contribution of clusters of more than two Fe-ions. These clusters, which become important for higher concentrations, will not contribute to the structure near the first step, but will decrease the height. On the other hand broadening may be caused by temperature effects (as we showed in figure 5.) and by additional matrix elements (such as DM anisotropy [11]) which were not considered in the present calculations.

In conclusion, we have shown that in principle, the magnetization of Fe-DMS displays a steplike behaviour. The magnetic field at which these steps occur are determined by the nearest neighbour interaction J_{NN} between Fe^{2+} pairs, provided that this exchange exceeds a certain critical value J_{crit} . Experimental conditions favourable for the observations of these phenomena include: low temperatures (well below 4.2 K) and high fields (order of 50 T); the use of oriented crystals preferably along the [111] axis for ZnFeSe-like II-VI compounds and Fe concentrations of a few percent to maximize the number of nearest-neighbour pairs.

ACKNOWLEDGEMENTS

The authors wish to acknowledge the valuable contribution of C.E.P. Gerrits and C.H.W. Swüste. This work has been financially supported by the Foundation for Fundamental Research on Matter (FOM) which forms part of the Dutch Organization for the Advancement of Research (NWO).

REFERENCES

- [1] J.K. Furdyna, J. Appl. Phys. **64** (4), R29 (1988).
- [2] A. Mycielski, J. Appl. Phys. **63** (8), 3279 (1988).
- [3] A. Twardowski, A. Lewicky, M. Arciszewska, W.J.M. de Jonge, H.J.M. Swagten and M. Demianiuk, Phys. Rev. **B38**, 10749 (1988).
- [4] B.E. Larson, K.C. Hass, H. Ehrenreich and A.E. Carlsson, Phys. Rev. **B37**, 4137 (1988).
- [5] see for instance: S. Foner, Y. Shapira, D. Heiman, P. Becla, R. Kershaw, K. Dwight and A. Wold, Phys. Rev. **B39**, 11793 (1989).
- [6] G.E. Slack, S. Roberts and J.T. Vallin, Phys. Rev. **187**, 511 (1969); W. Low and

- M. Weger, Phys. Rev. 118, 1119 (1960).
- [7] H.J.M. Swagten, A. Twardowski, W.J.M. de Jonge and M. Demianiuk, Phys. Rev. B39, 2568 (1989).
 - [8] M. Hausenblas, L.M. Claessen, A. Wittlin, A. Twardowski, M. von Ortenberg, W.J.M. de Jonge and P. Wyder, to be published in Solid State Commun. (1989).
J.P. Mahoney, C.C. Lin, W.H. Brumage and F. Dorman, J. Chem. Phys. 53, 4286 (1970).
 - [9] W.J.M. de Jonge, A. Twardowski and C.J.M. Denissen, Mat. Res. Soc. Symp. Proc. 89, 153 (1987).
 - [10] C. Testelin, A. Mauger, C. Rigaux, M. Guillot and A. Mycielski, Solid State Commun. 70, 355 (1989).
 - [11] Y. Shapira, S. Foner, D. Heiman, P.A.M. Wolff and C.R. McIntyre, Solid State Commun. 70, 355 (1989).

ENERGY LEVEL SPECTRA OF TRANSITION METAL IONS IN DILUTED MAGNETIC SEMICONDUCTORS

MURIELLE VILLERET*, S. RODRIGUEZ* AND E. KARTHEUSER**

*Department of Physics, Purdue University, West Lafayette, IN 47907

**Institut de Physique, Université de Liège, B-4000 Liège, Belgium

ABSTRACT

We present a study of the low lying energy levels of Fe^{2+} , Co^{2+} , Ni^{2+} and Cu^{2+} in diluted magnetic semiconductors such as $\text{Cd}_{1-x}\text{Co}_x\text{Te}$ and $\text{Cd}_{1-x}\text{Co}_x\text{Se}$ and their counterparts. In the first of these compounds the magnetic ion sits on a site of symmetry T_d while in the second the symmetry is trigonal (C_{3v}). We develop a formulation that permits a continuous variation from T_d to C_{3v} symmetry. Comparison with experimental data in $\text{Cd}_{1-x}\text{Co}_x\text{Se}$ shows that the C_{2v} distortion amounts to about 10% of the crystal potential at the Co^{2+} site. Our study of the energy spectra of Fe^{2+} in T_d and C_{3v} crystal potentials reveals that, even in the cubic field, the levels exhibit an anisotropy which manifests itself in an anisotropy of the magnetization, M , in the regime in which M is not a linear function of the magnetic field B . The study includes all the levels in the lowest terms of the $(3d)^n$ ($n=6,7,8,9$) configurations. The calculations are carried out to second order in the spin-orbit interaction and in B for the lowest orbital states and to first order in B for the excited states. The g-factors of all the levels are obtained including their anisotropy for the Co^{2+} and Cu^{2+} Γ_8 states.

Diluted magnetic semiconductors (DMS's) [1] are materials obtained alloying a II-VI compound AB, where A and B are elements of the groups II and VI of the periodic table of the elements, respectively, with MB where M is a transition metal ion. Usually, the element M enters the structure substitutionally at A sites in the compound AB. The chemical formula of the resulting compound is $\text{A}_{1-x}\text{M}_x\text{B}$, x being the atomic concentration of M. The Mn-based DMS's have, until recently, received the greatest attention. Since the ground state of Mn^{2+} is $^6S_{5/2}$, the crystal field has a negligible effect on its magnetic properties and isolated Mn^{2+} ions in DMS's behave as if they were free. Other doubly-ionized transition metal ions exhibit ground terms possessing orbital as well as spin degeneracies. A systematic investigation of these transition ions in zinc-blende and wurtzite semiconductors has been carried out [2-3]. In the former, the symmetry of the site of the impurity is tetrahedral (group T_d) whereas in the latter a slight distortion along the [111] direction yields trigonal symmetry (group C_{3v}). Excluding Mn^{2+} , all the doubly-ionized iron group ions have ground states that are either D or F terms. The values of L and S are symmetrical with respect to the half-filled 3d shell so that a study of ions whose shell is more than half-filled yields automatically information about those for which the 3d shell is less than half full. However, the order of the crystal-field-split levels is reversed and the spin-orbit coupling constant, λ , changes sign. Therefore, we need only study four of the transition metal ions. We have investigated the energy spectra of $\text{Fe}^{2+}(3d^6)$, $\text{Co}^{2+}(3d^7)$, $\text{Ni}^{2+}(3d^8)$ and $\text{Cu}^{2+}(3d^9)$. Symmetry arguments show that while a D term splits into a doublet Γ_3 and a triplet Γ_5 in the presence of a tetrahedral field [4], F terms split into $\Gamma_2+\Gamma_4+\Gamma_5$. It can be shown [5] that the ground multiplet of an ion in the $(3d)^n$ configuration in a field produced by a tetrahedral arrangement of negatively charged ions is Γ_1 for $n=5$, Γ_2 for $n=2$ and 7, Γ_3 for $n=1$ and 6, Γ_4 for $n=3$ and 8, and Γ_5 for $n=4$ and 9. We expect a fundamental difference between the behavior of Fe^{2+} and Ni^{2+} on the one hand and of Co^{2+} and Cu^{2+} on the other because while the number of electrons in the former is even, in the latter it

is odd. By virtue of Kramers' theorem all eigenstates of Co^{2+} and Cu^{2+} have even degeneracies and thus must always exhibit paramagnetism. Fe^{2+} and Ni^{2+} can have both degenerate and non-degenerate states. It turns out that, in the crystals under study, the ground states of Fe^{2+} and Ni^{2+} are non-degenerate and are, in first approximation non-magnetic. However, in the presence of a magnetic field, the Zeeman interaction mixes the states of the lowest term giving rise to a temperature-independent paramagnetism (Van Vleck paramagnetism).

We first consider the case of a D term in a T_d field. The only significant part of the crystal potential can be expressed as

$$V(T_d) = -a \left[\frac{1}{8}(L_x^2 + L_y^2)^2 + \frac{3}{2}L_z^4 - 6L_z^2 - \frac{12}{5} \right] \quad (1)$$

where $L_{\pm} = L_x \pm iL_y$ and L_x, L_y, L_z are components of the angular momentum operator along the cubic axes x, y and z . The orbital angular momentum states of the free ion are eigenvectors of L_z and are denoted by $|M_L\rangle$ ($M_L = 2, 1, 0, -1, -2$). The orbital states in the presence of the T_d field and their symmetry characterization are:

$$\begin{aligned} \Gamma_3: u_1 &= |0\rangle \\ u_2 &= 2^{-1/2}(|2\rangle + |-2\rangle) \\ \Gamma_5: v_+ &= |-1\rangle \\ v_0 &= 2^{-1/2}(|2\rangle - |-2\rangle) \\ v_- &= -|1\rangle. \end{aligned} \quad (2)$$

u_1, u_2, v_+, v_0 and v_- are taken as the unperturbed wave functions. The spin-orbit coupling and the Zeeman interaction are treated as perturbations.

We write the Hamiltonian operator of the problem as a supermatrix divided into diagonal square blocks of $2(2S+1)$ and $3(2S+1)$ dimensions corresponding to the $2(2S+1)$ $|u_i, M_S\rangle$ states ($i=1, 2; M_S=S, S-1, \dots, -S+1, -S$) generated by the orbital Γ_5 levels. We consider the Hamiltonian

$$H = H_c + H_{s.o.} + H_Z \quad (3)$$

where H_c is the Hamiltonian of the ion in the crystal field excluding the spin-orbit coupling $H_{s.o.} = \lambda \vec{L} \cdot \vec{S}$. The term H_Z is the Zeeman energy in a magnetic field $\vec{B} = B\hat{n}$, i.e.,

$$H_Z = \mu_B B \hat{n} \cdot (\vec{L} + 2\vec{S}). \quad (4)$$

The expression for the Hamiltonian H is

$$H = \begin{pmatrix} E_0(\Gamma_3) + 2\mu_B B \hat{n} \cdot \vec{S} & (\lambda \vec{S} + \mu_B B \hat{n}) \cdot \vec{U} \\ (\lambda \vec{S} + \mu_B B \hat{n}) \cdot \vec{U}^\dagger & E_0(\Gamma_5) + 2\mu_B B \hat{n} \cdot \vec{S} - (\lambda \vec{S} + \mu_B B \hat{n}) \cdot \vec{I} \end{pmatrix} \quad (5)$$

Here $E_0(\Gamma_3)$ and $E_0(\Gamma_5)$ are the unperturbed energies of the Γ_3 and Γ_5 states, respectively. Two new quantities \vec{U} and \vec{I} are introduced, their definition being

$$\langle u_v | \vec{L} | v_{\kappa} \rangle = \vec{U}_{v\kappa} \quad (6)$$

and

$$\langle \vec{L} | v_{\kappa} \rangle = -\vec{I}_{\kappa\kappa} \quad (7)$$

($v=1,2$ and $\kappa, \kappa' = +, 0, -$). The components of \vec{I} obey the commutation relation $\vec{I} \times \vec{I} = i\vec{I}$ and can thus be treated exactly as an angular momentum operator with quantum number $I=1$.

The Schrödinger equation $H\psi = E\psi$ can be rearranged replacing the $5(2S+1)$ -component vector ψ by a composite of two vectors, namely $\psi^{(3)}$ and $\psi^{(5)}$ of dimensions $2(2S+1)$ and $3(2S+1)$, respectively. The Schrödinger equation is equivalent to two coupled equations which can be solved for $\psi^{(3)}$ and $\psi^{(5)}$ by iteration keeping terms up to second order in λ and $\mu_B B$. A similar perturbation formalism can be developed for F terms in a T_d field. The eigenvalues and eigenstates of the spin Hamiltonian are easily determined introducing the operator $\vec{F} = \vec{I} + \vec{S}$. The components of \vec{F} obey commutation rules identical to those of \vec{I} and \vec{S} . The eigenvalues of $\vec{F} \cdot \vec{F}$ are $F(F+1)$ and the energy levels are obtained working in the representation generated by the states

$$|F, M_F\rangle = \sum_{M_S, M_I} |M_S, M_I\rangle \langle M_S, M_I | F, M_F \rangle \quad (8)$$

where $M_I = 1, 0, -1$, $M_S = S, S-1, \dots, -S+1, -S$ and $M_F = F, F-1, \dots, -F+1, -F$. $\langle M_S, M_I | F, M_F \rangle$ is a Clebsch-Gordan coefficient. The trigonal distortion which affects the energy levels and the magnetic properties of the system is described by the additional potential

$$V(C_{3v}) = -b(2-L_z^2) - c \left(\frac{7}{12} L_z^4 - \frac{31}{12} L_z^2 + \frac{6}{5} \right) \quad (9)$$

where L_z is the component of \vec{L} along the trigonal axis. As an example we investigate the magnetic susceptibility of Fe^{2+} in a wurzite semiconductor, such as CdSe.

The differential magnetic susceptibility is defined by

$$\chi_D = nk_B T \lim_{B \rightarrow 0} \left[Z^{-1} (\partial^2 Z / \partial B^2) - Z^{-2} (\partial Z / \partial B)^2 \right] \quad (10)$$

where

$$Z = \sum_i \exp(-E_i / k_B T) \quad (11)$$

is the partition function and n is the number of Fe^{2+} ions per unit volume. We take into account the contributions of the states arising from the lowest orbital multiplet of Fe^{2+} , namely 5T_2 . We calculate the energy levels of the 5T_2 states using second order perturbation theory and assuming that the Zeeman splitting is smaller than the separation between the levels caused by the trigonal field. The results, including all the levels within the lowest orbital states, are displayed in Tables I and II for \vec{B} parallel and

perpendicular to the trigonal axis \hat{z} , respectively. In these tables, $\Delta=6a$ is the crystal field parameter and $3W=2[(3b-c)\lambda]/\Delta$ is the energy splitting of the $\Gamma_2(C_{3v})$ and $\Gamma_3(C_{3v})$ states originating from the $\Gamma_4(T_d)$ level of the lowest orbital state. Figure 1 shows the temperature dependence of the differential magnetic susceptibility of $Cd_{1-x}Fe_xSe$. We note that the susceptibilities when \vec{B} is either parallel or perpendicular to \hat{z} differ considerably below 10K in good qualitative agreement with experimental results [6-7]. The reason for this behavior lies in the fact that the Zeeman interaction giving rise to the Van Vleck paramagnetism mixes the Γ_1 and Γ_2 states when \vec{B} is parallel to \hat{z} and the Γ_1 and Γ_3 states when \vec{B} is perpendicular to this axis.

Table I. Energy eigenvalues of the $^5\Gamma_3$ states of Fe^{2+} in a field of symmetry C_{3v} including terms to second order in the magnetic field $B_{\parallel}\hat{z}$.

T_d	C_{3v}	Energy eigenvalue
Γ_1	Γ_1	$-24\lambda^2\Delta^{-1}-8\mu_B^2B_z^2(6\lambda^2\Delta^{-1}-2W)^{-1}$
Γ_4	Γ_2	$-18\lambda^2\Delta^{-1}-2W+8\mu_B^2B_z^2(6\lambda^2\Delta^{-1}-2W)^{-1}-\mu_B^2B_z^2\Delta/3\lambda^2$
	Γ_3	$-18\lambda^2\Delta^{-1}+W-\mu_B B_z(1+2\lambda\Delta^{-1})-4\mu_B^2B_z^2(6\lambda^2\Delta^{-1}-W)^{-1}-\mu_B^2B_z^2\Delta/12\lambda^2$ $-18\lambda^2\Delta^{-1}+W+\mu_B B_z(1+2\lambda\Delta^{-1})-4\mu_B^2B_z^2(6\lambda^2\Delta^{-1}-W)^{-1}-\mu_B^2B_z^2\Delta/12\lambda^2$
Γ_3	Γ_3	$-12\lambda^2\Delta^{-1}+4\mu_B^2B_z^2(6\lambda^2\Delta^{-1}-W)^{-1}-4\mu_B^2B_z^2(6\lambda^2\Delta^{-1}+W)^{-1}$
Γ_5	Γ_1	$-6\lambda^2\Delta^{-1}-2W-8\mu_B^2B_z^2(6\lambda^2\Delta^{-1}+2W)^{-1}+\mu_B^2B_z^2\Delta/3\lambda^2$
	Γ_3	$-6\lambda^2\Delta^{-1}+W-\mu_B B_z(1-6\lambda\Delta^{-1})+4\mu_B^2B_z^2(6\lambda^2\Delta^{-1}+W)^{-1}+\mu_B^2B_z^2\Delta/12\lambda^2$ $-6\lambda^2\Delta^{-1}+W+\mu_B B_z(1-6\lambda\Delta^{-1})+4\mu_B^2B_z^2(6\lambda^2\Delta^{-1}+W)^{-1}+\mu_B^2B_z^2\Delta/12\lambda^2$
Γ_2	Γ_2	$8\mu_B^2B_z^2(6\lambda^2\Delta^{-1}+2W)^{-1}$

Table II. Energy eigenvalues of the $^5\Gamma_3$ states of Fe^{2+} in a field of symmetry C_{3v} including terms to second order in the magnetic field $B_{\perp}\hat{z}$.

T_d	C_{3v}	Energy eigenvalue
Γ_1	Γ_1	$-24\lambda^2\Delta^{-1}-8\mu_B^2B_z^2(6\lambda^2\Delta^{-1}+W)^{-1}$
Γ_4	Γ_2	$-18\lambda^2\Delta^{-1}-2W-\mu_B^2B_z^2[(3W)^{-1}+4(6\lambda^2\Delta^{-1}+2W)^{-1}+(12\lambda^2\Delta^{-1}+3W)^{-1}]$
	Γ_3	$-18\lambda^2\Delta^{-1}+W+\mu_B^2B_z^2[(3W)^{-1}-2(6\lambda^2\Delta^{-1}-W)^{-1}-(\Delta/6\lambda^2)]$ $-18\lambda^2\Delta^{-1}+W+\mu_B^2B_z^2[8(6\lambda^2\Delta^{-1}+W)^{-1}-2(6\lambda^2\Delta^{-1}-W)^{-1}-(\Delta/6\lambda^2)]$ $-(12\lambda^2\Delta^{-1}-3W)^{-1}]$
Γ_3	Γ_3	$-12\lambda^2\Delta^{-1}+\mu_B^2B_z^2[-4(6\lambda^2\Delta^{-1}-2W)^{-1}+2(6\lambda^2\Delta^{-1}-W)^{-1}-2(6\lambda^2\Delta^{-1}+W)^{-1}]$ $-12\lambda^2\Delta^{-1}+\mu_B^2B_z^2[4(6\lambda^2\Delta^{-1}+2W)^{-1}+2(6\lambda^2\Delta^{-1}-W)^{-1}-2(6\lambda^2\Delta^{-1}+W)^{-1}]$
Γ_5	Γ_1	$-6\lambda^2\Delta^{-1}-2W+\mu_B^2B_z^2[(12\lambda^2\Delta^{-1}-3W)^{-1}+4(6\lambda^2\Delta^{-1}-2W)^{-1}-(3W)^{-1}]$
	Γ_3	$-6\lambda^2\Delta^{-1}+W+\mu_B^2B_z^2[(12\lambda^2\Delta^{-1}+3W)^{-1}+(\Delta/6\lambda^2)+2(6\lambda^2\Delta^{-1}+W)^{-1}-8(6\lambda^2\Delta^{-1}-W)^{-1}]$ $-6\lambda^2\Delta^{-1}+W+\mu_B^2B_z^2[(\Delta/6\lambda^2)+(3W)^{-1}+2(6\lambda^2\Delta^{-1}+W)^{-1}]$
Γ_2	Γ_2	$8\mu_B^2B_z^2(6\lambda^2\Delta^{-1}-W)^{-1}$

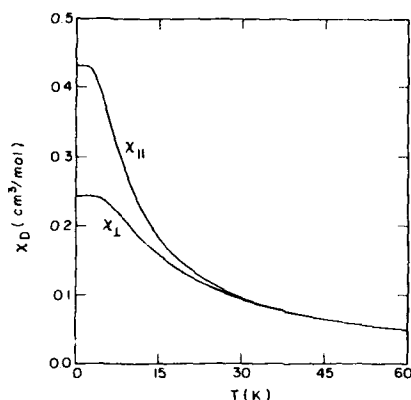


Figure 1. Magnetic susceptibility of $\text{Cd}_{1-x}\text{Fe}_x\text{Se}$ as a function of temperature for small x and weak magnetic fields. The curves are obtained using $\lambda = -81\text{cm}^{-1}$ and $\Delta = 2680\text{cm}^{-1}$ taken from Ref. [6]. The energy separation of the $\Gamma_2(\text{C}_{3v})$ and $\Gamma_3(\text{C}_{3v})$ is selected to be $3W = 7.5\text{cm}^{-1}$ to yield agreement with the experimental data [7]. $\chi_{||}$ and χ_{\perp} are the differential magnetic susceptibilities when \vec{B} is parallel and perpendicular to the trigonal axis, respectively.

ACKNOWLEDGMENTS

This work was supported by the National Science Foundation (Grant No. DMR 86-16787) and by the North Atlantic Treaty Organization (Research Grant No. 0759/87).

REFERENCES

1. Diluted Magnetic Semiconductors in Semiconductors and Semimetals, vol. 25, edited by J.K. Furdyna and J. Kossut (Academic, Boston, 1988).
2. M. Villeret, S. Rodriguez and E. Kartheuser, *Physica B* (to be published).
3. M. Villeret, Ph.D. Thesis, Purdue University, 1989.
4. The group theoretical notation for the point groups and the irreducible representations follows G.F. Koster, J.O. Dimmock, R.G. Wheeler and H. Statz, Properties of the Thirty-Two Point Groups (M.I.T. Press, Cambridge, MA, 1966).
5. A. Abragam and B. Bleaney, Electron Paramagnetic Resonance of Transition Ions (Clarendon Press, Oxford, 1970).
6. J.P. Mahoney, C.C. Lin, W.H. Brumage and F. Dorman, *J. Chem. Phys.* **53**, 4286, 1970.
7. A. Lewicki (private communication).

RAMAN SPECTROSCOPY OF A NOVEL DILUTED MAGNETIC SEMICONDUCTOR: CUBIC $\text{Cd}_{1-x}\text{Mn}_x\text{Se}$.

R. G. ALONSO,* E.-K. SUH,* H. PASCHER,* E. OH,* A. K. RAMDAS,* N. SAMARTH,**
H. LUO,** AND J. K. FURDYNA**

* Purdue University, Dept. of Physics, West Lafayette, IN 47907

** University of Notre Dame, Dept. of Physics, Notre Dame, IN 46556

ABSTRACT

In contrast to the bulk diluted magnetic semiconductor (DMS) $\text{Cd}_{1-x}\text{Mn}_x\text{Se}$ which occurs with the wurtzite structure, its epilayers grown on (001) GaAs substrate by Molecular Beam Epitaxy exhibit the cubic zinc-blende structure. Raman spectroscopy and photoluminescence studies on this novel DMS show (1) a "two-mode" behavior of the zone center optical phonons, (2) the Raman line associated with the spin-flip in the Zeeman split $S = 5/2$ ground state of Mn^{2+} , and (3) large Raman shifts associated with the spin-flip of donor-bound electrons. The large magnetic field dependence in (3) with saturation at high fields and low temperature shows that the s-d exchange interaction characteristic of DMS's is also manifested strikingly in the zinc-blende phase of $\text{Cd}_{1-x}\text{Mn}_x\text{Se}$.

INTRODUCTION

The tetrahedrally coordinated Mn-based II-VI diluted magnetic semiconductors (DMS's) are continuing to attract intense interest in view of their remarkable magnetic and semiconducting properties [1]. More recently DMS's in which Fe^{2+} and Co^{2+} replace the group II element have also become available and their distinctive behavior has been the object of several investigations [1, 2]. We note that the II-VI DMS's typically occur either in the cubic (zinc-blende) or the hexagonal (wurtzite) structure. For example, $\text{Cd}_{1-x}\text{Mn}_x\text{Te}$ and $\text{Cd}_{1-x}\text{Mn}_x\text{Se}$ grown by bulk growth techniques have zinc-blende and wurtzite structure, respectively. Bulk crystal growth appears to restrict the maximum concentration of the magnetic constituent which can be incorporated; for example, $\text{Cd}_{1-x}\text{Mn}_x\text{Te}$ occurs with a maximum x of 0.75. Also, MnTe has NiAs structure, whereas viewed as the "end member" of the $\text{Cd}_{1-x}\text{Mn}_x\text{Te}$ system with $x \rightarrow 1$, it has a zinc-blende structure. It is evident that subtle thermodynamic considerations play a role in determining the structure assumed by the system and in limiting the maximum x which can be incorporated. In this context a non-equilibrium growth technique like molecular beam epitaxy (MBE) offers a mean to increasing x even up to unity [3] and for realizing alternative structures [4, 5].

Recently, Samarth *et al.* [4, 5] demonstrated that CdSe, $\text{Cd}_{1-x}\text{Mn}_x\text{Se}$ and $\text{Cd}_{1-x}\text{Zn}_x\text{Se}$ can be stabilized in the cubic zinc-blende structure by growing epitaxial layers on (001) GaAs substrates using molecular beam epitaxy (MBE). In this paper we describe and discuss the Raman spectra of $\text{Cd}_{1-x}\text{Mn}_x\text{Se}$ epilayers, as well as, $\text{Cd}_{1-x}\text{Zn}_x\text{Se}/\text{Cd}_{1-x}\text{Mn}_x\text{Se}$ and $\text{ZnSe}/\text{Cd}_{1-x}\text{Mn}_x\text{Se}$ superlattices [6]. We have observed zone center optical phonons, Raman electron paramagnetic resonance (ω_{PM} : Raman EPR) of Mn^{2+} and the spin-flip of the donor-bound electrons (ω_{SFR}). We discuss them in the context of the two-mode behavior expected for zone center optical phonons and the large spin-spin exchange between the d-electrons of Mn^{2+} and the s-electrons of the Γ_6 conduction band.

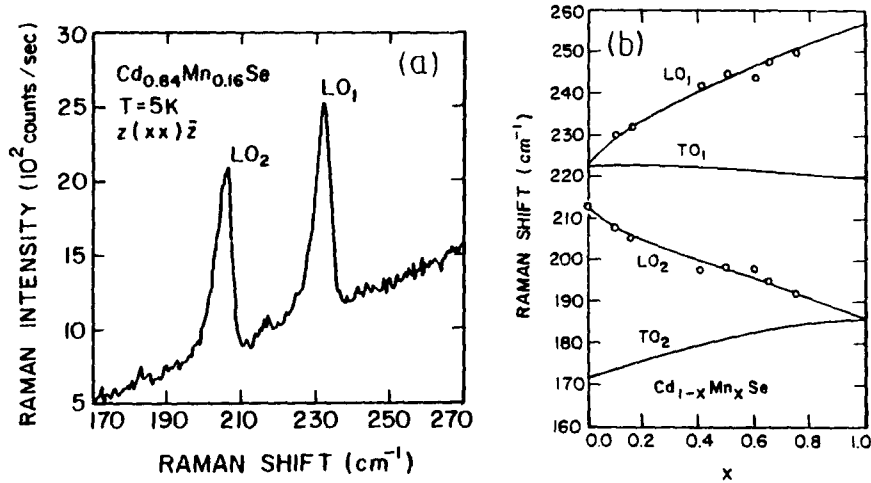


Figure 1: (a) Raman spectrum of the zinc-blende $\text{Cd}_{0.84}\text{Mn}_{0.16}\text{Se}$ epilayer at $T=5\text{K}$. The spectrum was recorded in the backscattering geometry $z(xx)\bar{z}$ with incident wavelength of 6328 \AA . (b) Composition dependence of the zone center optical phonon frequencies in zinc-blende $\text{Cd}_{1-x}\text{Mn}_x\text{Se}$.

II. VIBRATIONAL RAMAN SPECTRA

The Raman spectrum of a (001) epilayer of cubic $\text{Cd}_{1-x}\text{Mn}_x\text{Se}$, $x = 0.16$, recorded in the backscattering geometry $z(xx)\bar{z}$ is shown in Fig. 1a. The spectrum was taken at $T=5\text{K}$ with the 6328 \AA line of a He-Ne laser. As shown in Fig. 1b, the Raman peak labeled LO_2 can be traced to the zone center LO phonon of CdSe as $x \rightarrow 0$. The Raman peak labeled LO_1 corresponds to the line evolving from the local mode of Mn in CdSe as x increases. The TO mode is not observed since it is forbidden in the (001) orientation of the epilayers.

The optical phonons of $\text{Cd}_{1-x}\text{Mn}_x\text{Se}$ show a composition dependence corresponding to a "two-mode" behavior. As shown in Fig. 1b, in the two-mode behavior the modes (LO and TO) of each of the two binary crystals involved in the alloy maintain their character throughout the concentration range. We shall refer to them as "CdSe" modes and "MnSe" modes. The CdSe modes at $x = 0$ converge into the gap mode of Cd in MnSe as $x \rightarrow 1$. Similarly, the MnSe modes at $x = 1$ become the local mode of Mn in CdSe as $x \rightarrow 0$. At $x = 0$ the Mn impurity in CdSe has a higher frequency than the two modes of CdSe, as expected for an impurity with a mass significantly smaller than those of the other constituents. The curves in Fig. 1b were generated from a modified random-element isodisplacement (MREI) model [7, 8].

We have compared the frequencies of the zone center Raman lines as a function of x observed in cubic and uniaxial [9] $\text{Cd}_{1-x}\text{Mn}_x\text{Se}$. Both structures show a similar two-mode behavior. In the cubic zinc-blende (T_d^2) crystals only F_2 optical modes are allowed. In the wurtzite (C_{6v}^4) crystals the Raman active zone center optical phonons consist of $A_1 + E_1 + 2E_2$. The hexagonal crystal field splits the F_2 vibrational modes of the zinc-blende lattice into the A_1 and E_1 modes of the wurtzite structure. Since the frequency of the $F_2(\text{TO})$ and $F_2(\text{LO})$ modes in the zinc-blende epilayers are close to those of the corresponding A_1 and E_1 modes in the wurtzite $\text{Cd}_{1-x}\text{Mn}_x\text{Se}$ throughout the composition range, we conclude that the anisotropy of the crystal field is small.

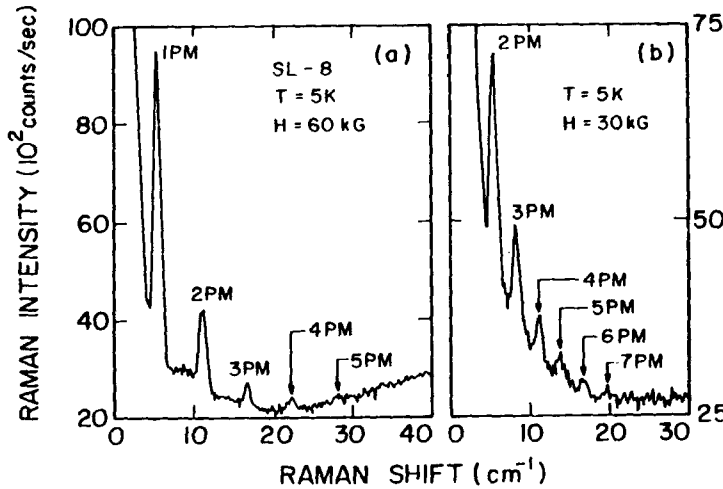


Figure 2: Raman-EPR lines in the $\text{Cd}_{0.9}\text{Mn}_{0.1}\text{Se}/\text{ZnSe}$ superlattice, at $T=5\text{K}$. The Raman lines in (a) correspond to 1PM, 2PM, 3PM, 4PM, and 5PM. They result from transitions within the Zeeman multiplet of Mn^{2+} , with $\Delta m_S=1,2,3,4$, and 5, respectively. This spectrum is obtained in the crossed polarization $z(yx)z$ with magnetic field $H=60\text{ kG}$ along x and incident wavelength of 6764 \AA with 57 mW power. The 5PM line appearing superposed on the photoluminescence shows how closely the resonance condition is fulfilled. The spectrum in (b) shows the additional 6PM and 7PM lines observed at a lower magnetic field. In this spectrum the 1PM line is obscured by the parasitic laser light.

III. RAMAN-ELECTRON PARAMAGNETIC RESONANCE OF Mn^{2+}

In addition to the vibrational modes, the Raman spectra of $\text{Cd}_{1-x}\text{Mn}_x\text{Se}$ show magnetic features typically encountered in DMS's. The Raman line associated with the spin-flip transition within the Zeeman split $3d^5$ multiplet of Mn^{2+} , i.e., the Raman-EPR (PM), has been observed in $\text{Cd}_{1-x}\text{Mn}_x\text{Se}$ and in the $\text{Cd}_{0.9}\text{Mn}_{0.1}\text{Se}/\text{ZnSe}$ superlattice. The intensity of this Raman line is resonantly enhanced when the scattered phonon is close to that of a Zeeman component of the excitonic transition. This resonant enhancement demonstrates [10] that the mechanism for the Raman-EPR involves interband electronic transitions. The Raman-EPR shift, given by $\hbar\omega_{\text{PM}} = g_{\text{Mn}}\mu_B H$, yields a g -factor of 2, as expected for Mn^{2+} .

Figure 2(a) shows the remarkable Raman-EPR spectrum observed in a $\text{Cd}_{0.9}\text{Mn}_{0.1}\text{Se}/\text{ZnSe}$ superlattice, at $T=5\text{K}$, where $\text{Cd}_{0.9}\text{Mn}_{0.1}\text{Se}$ is the well. The observed Raman lines labeled 1PM, 2PM, 3PM, 4PM and 5PM have their origin in the transitions with $\Delta m_S=1,2,3,4$ and 5 within the $S=5/2$ Zeeman multiplet of Mn^{2+} . Figure 3 shows the linear dependence of the Raman-EPR shift as a function of magnetic field where the solid lines correspond to $g_{\text{Mn}^{2+}} = 2$. In Fig. 2(b) we also observe peaks corresponding to 6PM and 7PM (see also Fig. 3). The multiple spin-flip features in a DMS can be accounted for in terms of excitations within neighboring pairs of Mn^{2+} ions coupled antiferromagnetically and assuming an anisotropic exchange interaction between the ground state multiplet of one and the excited state of the other [11].

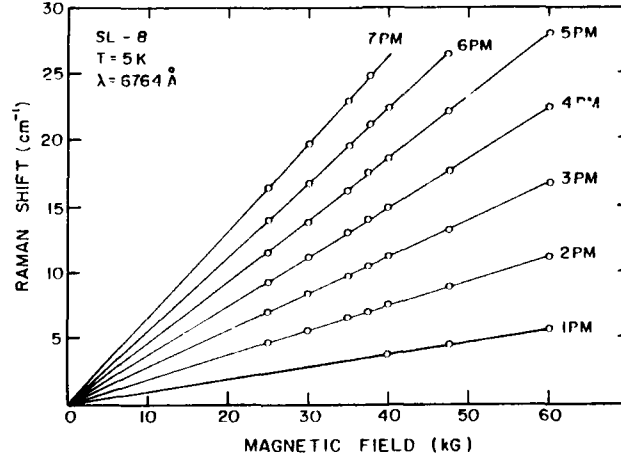


Figure 3: Raman-EPR (PM) shift as a function of magnetic field in the $\text{Cd}_{0.9}\text{Mn}_{0.1}\text{Se}/\text{ZnSe}$ superlattice, at $T=5\text{K}$. The solid lines correspond to the Raman-EPR shift given by $n g_{\text{Mn}^{2+}} \mu_B H$ with $g_{\text{Mn}^{2+}} = 2$ and $n = 1, \dots, 7$.

IV. SPIN-FLIP OF ELECTRONS BOUND TO DONORS

Another Raman feature associated with magnetic excitations encountered in DMS alloys is the spin-flip of electrons bound to donors, enhanced by the s-d exchange interaction. As in a bulk DMS, the Raman shift of the donor spin-flip line exhibits a Brillouin function-like behavior, as can be seen in Fig. 4. Since the spin-flip Raman mechanism also involves inter-band electronic transitions [10], the observed resonant enhancement for incident frequencies close to excitonic excitations is to be expected.

The spin splitting of the donor ground state in DMS's is determined by the macroscopic magnetization of the Mn^{2+} ions and the "intrinsic" Zeeman effect, i.e.,

$$\hbar\omega_{\text{SFR}} = \frac{\alpha}{g_{\text{Mn}^{2+}}} M_o(H) + g^* \mu_B H = g_{\text{eff}} \mu_B H, \quad (1)$$

where α is the exchange integral characterizing the interaction between the spins of Mn^{2+} ions and those of the s-like Γ_6 electrons; μ_B the Bohr magneton; $M_o(H)$ the macroscopic magnetization; $g_{\text{Mn}^{2+}}=2$, the g factor of Mn^{2+} ; g^* the intrinsic g factor of the band electrons, and g_{eff} the effective g factor of the conduction band. Because of the strong s-d exchange interaction, the first term, characterized by the Brillouin function $B_{5/2}(g\mu_B H/k_B T)$, dominates the spin splitting [12].

From the slope of the linear portion of the spin-flip data for $\text{Cd}_{1-x}\text{Mn}_x\text{Se}$, $x=0.10$, shown in Fig. 4, we obtain $g_{\text{eff}} = 94$ at $T=5\text{K}$, within experimental errors, close to that previously observed in bulk $\text{Cd}_{0.9}\text{Mn}_{0.1}\text{Se}$ [12].

In Fig. 4 we also observe the smaller spin-flip Raman shift associated with a higher concentration, $x = 0.75$. At $x = 0.75$ we obtain $g_{\text{eff}} = 20$ at $T = 5\text{K}$ which is considerably smaller than the value given above for $x = 0.10$. The spin-flip Raman shift, which is proportional to the magnetization, increases with x until it reaches a maximum shift at about

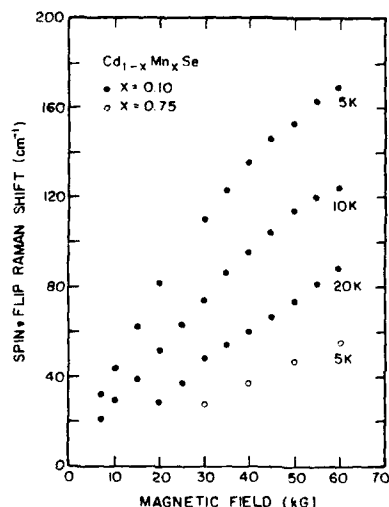


Figure 4: Magnetic field and temperature dependence of the spin-flip Raman shift in $\text{Cd}_{1-x}\text{Mn}_x\text{Se}$ epilayers, $x = 0.1$ and $x = 0.75$, with external magnetic field in the plane of the (001) layers. The spectra were obtained in the cross-polarization $z(xy)\bar{z}$ with incident laser wavelength $\lambda_L = 6471 \text{ \AA}$.

$x = 0.20$. For higher concentrations the antiferromagnetic interaction reduces the effective number of spins contributing to the magnetization. Equation (1) does not reproduce the experimental data at high x which show a much weaker dependence on the temperature. An ansatz [12] that works very well is to replace T by $T + T_{AF}$, where T_{AF} is a phenomenological constant that is inserted to account for antiferromagnetic interactions. We found that T_{AF} steadily increases with x , having a value of about 400 K for $x = 0.75$. These experimental results are in reasonable agreement with Faraday rotation measurements in bulk $\text{Cd}_{1-x}\text{Mn}_x\text{Se}$ ($0.0 \leq x \leq 0.5$), where the magnetization as a function of x behaves quantitatively similar to the g_{eff} [13]. Faraday rotation in $\text{Cd}_{1-x}\text{Mn}_x\text{Te}$ also shows large values of T_{AF} for large x [14].

V. CONCLUDING REMARKS

The Raman scattering confirms the zinc-blende nature of $\text{Cd}_{1-x}\text{Mn}_x\text{Se}$ epilayers grown on (001) GaAs substrates. These new members of the family of II-VI semiconductors and their alloys are zinc-blende counterparts of the wurtzite structure occurring in bulk crystals. As a member of the DMS family of materials, zinc-blende $\text{Cd}_{1-x}\text{Mn}_x\text{Se}$ shows the magnetic excitations characteristic of these materials, namely, Raman-EPR and spin-flip scattering from donor-bound electrons. These features are also seen in $\text{Cd}_{1-x}\text{Mn}_x\text{Se}$ layers incorporated in superlattices. As the growth parameters are brought under better control, features characteristic of superlattices and quantum wells (such as folded acoustic phonons, confined optical phonons, and confined electronic levels) will be explored.

ACKNOWLEDGMENTS

The work reported in this paper was carried out with support from the Defense Advanced Research Projects Agency-University Research Initiative Consortium on "Diluted Magnetic Semiconductors and their Heterostructures," administered by the Office of Naval Research (N00014-86-K-0760). The work at Purdue and University of Notre Dame also received support from the National Science Foundation, Grants No. DMR-86-16787 and DMR-85-09800 respectively. One of us (H.P.) acknowledges a Fulbright Travel Grant which enabled him to participate in the research reported in this paper.

References

1. J. K. Furdyna, *J. Appl. Phys.* **64**, R29 (1988).
2. D. U. Bartholomew, E.-K. Suh, A. K. Ramdas, S. Rodriguez, U. Debska, and J. K. Furdyna, *Phys. Rev.* **B39**, 5865 (1989).
3. L. A. Kolodziejcki, R. L. Gunshor, N. Otsuka, B. P. Gu, Y. Hefetz, and A. V. Nurmikko, *Appl. Phys. Lett.* **48**, 1482 (1986).
4. N. Samarth, H. Luo, J. K. Furdyna, S. B. Qadri, Y. R. Lee, A. K. Ramdas and N. Otsuka, *Appl. Phys. Lett.* **54**, 2680 (1989).
5. N. Samarth, H. Luo, J. K. Furdyna, S. B. Qadri, Y. R. Lee, A. K. Ramdas and N. Otsuka (unpublished).
6. R. G. Alonso, E.-K. Suh, A. K. Ramdas, N. Samarth, H. Luo, and J. K. Furdyna, *Phys. Rev.* **B40**, 3720 (1989).
7. D. L. Peterson, A. Petrou, W. Giriat, A. K. Ramdas, and S. Rodriguez, *Phys. Rev.* **B33**, 1160 (1986).
8. L. Genzel, T. P. Martin, and C. H. Perry, *Phys. Stat. Sol. (B)* **62**, 83 (1974).
9. E.-K. Suh, A. K. Arora, A. K. Ramdas, and S. Rodriguez (unpublished).
10. A. Petrou, D. L. Peterson, S. Venugopalan, R. R. Galazka, A. K. Ramdas, and S. Rodriguez, *Phys. Rev.* **B27**, 3471 (1983).
11. D. L. Peterson, D. U. Bartholomew, A. K. Ramdas, and S. Rodriguez, *Phys. Rev.* **B31**, 7932 (1985).
12. D. L. Peterson, D. U. Bartholomew, U. Debska, A. K. Ramdas, and S. Rodriguez, *Phys. Rev.* **B32**, 323 (1985).
13. E. Oh, D. U. Bartholomew, A. K. Ramdas, J. K. Furdyna, and U. Debska, *Phys. Rev.* **B38**, 13183 (1988).
14. D. U. Bartholomew, J. K. Furdyna, and A. K. Ramdas, *Phys. Rev.* **B34**, 6943 (1986).

FREE EXCITON MAGNETOSPECTROSCOPY OF CdFeSe DILUTED MAGNETIC SEMICONDUCTOR

TWARDOWSKI A*, PAKULA K*, ARCISZEWSKA M** and MYCIELSKI A**

*Institute of Experimental Physics, Warsaw University, Hoza 69, 00681 Warsaw, Poland

**Institute of Physics, Polish Academy of Sciences, Al. Lotnikow 32, 02668 Warsaw, Poland

ABSTRACT

The magnetospectroscopy data of free exciton in hexagonal $\text{Cd}_{1-x}\text{Fe}_x\text{Se}$ are presented for different magnetic field orientation. Combining exciton splitting data with magnetic susceptibility data we estimate p-d exchange integral for CdFeSe valence band.

INTRODUCTION

Most research on Diluted Magnetic Semiconductors [1] has been devoted to Mn-based DMS, which represent rather simple case because of spin-only magnetic moment of Mn ions ($L=0$, $S=5/2$) leading to Brillouin-type paramagnetism. On the other hand the class of Fe-based DMS represents more complex case, since Fe^{2+} ions possess both spin and orbital momenta ($L=2$, $S=2$) [2,3,4]. In this situation the ground state of Fe ions is a singlet resulting in Van Vleck-type (i.e. magnetic field induced) paramagnetism [3,4].

Although recently Fe-based DMS have been intensively investigated [5-17] the available data are still rather poor. In particular the influence of s,p-d exchange interaction on conduction and valence bands has been reported only for ZnFeSe [10] and partially for CdFeSe [11,12,13,14]. Therefore we thought it worthwhile to study free exciton in CdFeSe in some detail.

EXPERIMENTAL

We studied hexagonal $\text{Cd}_{1-x}\text{Fe}_x\text{Se}$ crystals with Fe concentration $x=0.007$, 0.011, 0.032, 0.036, 0.038, 0.044, 0.049, 0.055, 0.068, 0.077 (x determined from the free exciton energy in the absence of magnetic field [13]).

We measured reflectivity and transmission (on the samples of the thickness less than $1\mu\text{m}$) in the free exciton energy range at temperature $T=1.8\text{K}$ and Faraday configuration in circularly polarized light (σ^+ , σ^-). Magnetic field (up to 5T) was oriented relatively to the crystal hexagonal c axis.

In the absence of magnetic field two exciton lines are observed (exciton A and B as expected for hexagonal crystals). These exciton lines are strongly split in magnetic field into 4 lines: a, b, c and d. In Fig.1a, b and c we show representative exciton splittings for different magnetic field orientation. We notice strong anisotropy of exciton splittings while rotating sample relatively magnetic field. General structure of exciton lines in our material is similar to that observed for CdMnSe [15]. The absence of saturation effects for exciton level splittings with magnetic field (observed for CdMnSe) results from Van Vleck type paramagnetism of Fe^{2+} ions.

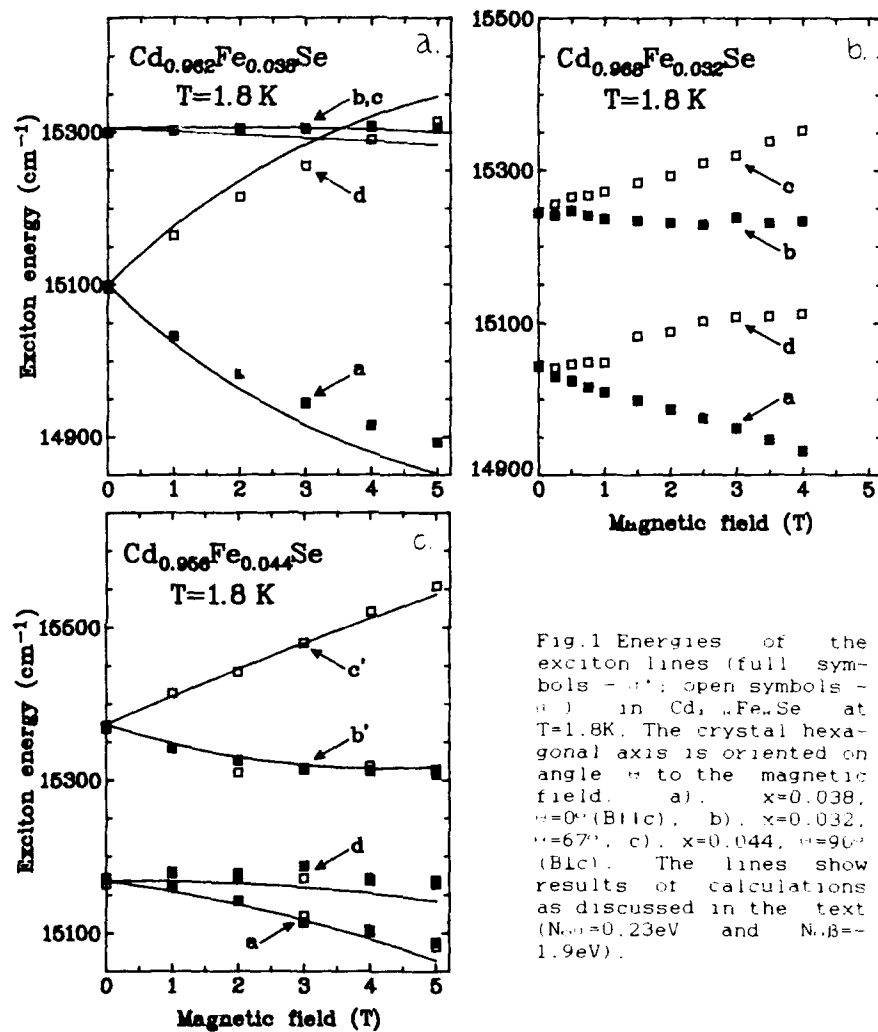


Fig.1 Energies of the exciton lines (full symbols - \bullet ; open symbols - \square) in $\text{Cd}_{1-x}\text{Fe}_x\text{Se}$ at $T = 1.8$ K. The crystal hexagonal axis is oriented on angle θ to the magnetic field. a), $x = 0.032$, $\theta = 0^\circ$ (B||c). b), $x = 0.032$, $\theta = 67^\circ$. c), $x = 0.044$, $\theta = 90^\circ$ (B||c). The lines show results of calculations as discussed in the text ($N_{\alpha\beta} = 0.23$ eV and $N_{\beta\alpha} = -1.9$ eV).

DISCUSSION

The large exciton splitting in magnetic field reflects strong band splittings due to s,p-d exchange interaction between band electrons and Fe ions [1,16]. This interaction is usually described by Heisenberg-type Hamiltonian, which in simplified, mean field approximation reads [16]:

$$(1) \quad H = -J \sum_{i,j} s_{i,j} \langle S_z \rangle \times N_0$$

where $s_{i,j}$ is z component of band electron (hole) spin, $\langle S_z \rangle$ is mean value of magnetic ion spin, N_0 denotes the number of unit cells per unit volume and J is exchange operator resulting in matrix elements $\alpha = \langle S_i | J | S_j \rangle$ and $\beta = \langle X_i | J | X_j \rangle$ for conduction and valence bands, respectively. The Heisenberg-type Hamiltonian is a proper one if interacting states are simple multiplets, as for materials containing Mn^{2+} . Although for Fe^{2+} the situation is more complicated, the exchange Hamiltonian in this case was also assumed in the form (1) having in mind similar exciton behaviour in Mn - and Fe -based materials [10].

The mean spin $\langle S_z \rangle$ was suggested to be expressed by macroscopic magnetization in the form [10]:

$$(2) \quad \langle S_z \rangle = k \langle M_z \rangle = (m/x) (k/\mu_B) M_z$$

where $m = (1-x)m_{CdSe} + xm_{Fe} + m_{FeSe}$ is mass of $CdFeSe$ molecule, M_z is magnetization (per unit mass) and k is prefactor describing the fact that magnetization of Fe^{2+} ions results from both spin and orbital momenta [3]. In the case of $CdSe$: $k=0.444$ (for spin-only case $k=1/2$ [10]). It follows from a $Fe-Fe$ pair calculations [8] that k -factor should be practically the same for noninteracting Fe^{2+} ions as well as for interacting systems for which ENNPA calculations apply ($x < 0.05$, [8]).

The full Hamiltonian describing conduction and valence bands can be obtained in a form similar to the $CdMnSe$ case (see Ref.17, eqs. 1 and 5). We notice that this Hamiltonian is parametrized by $\langle S_z \rangle$ and then by the magnetization. Since experimental magnetization data are not available, we calculated $Cd_{1-x}Fe_xSe$ magnetization for B1c and B1c in the ENNPA approximation [23]. Using parameters $N_{\alpha\beta}$ and $N_{\alpha\beta}$ obtained as described below, we diagonalized Hamiltonian matrix obtaining exciton energy levels. The results are shown in Fig.1. We find satisfactory matching with the experimental data.

Exchange parameters $N_{\alpha\beta}$ and $N_{\alpha\beta}$ can be determined by comparing exciton splitting with magnetization or susceptibility in the configuration B1c. In this case the splitting of lines a and d (Fig.1) reads [17]:

$$(3) \quad \begin{aligned} E_a - E_d &= (N_{\alpha\beta} - N_{\beta\alpha}) m (k/\mu_B) M_z \\ \text{or} \quad d(E_a - E_d)/dB &= (N_{\alpha\beta} - N_{\beta\alpha}) m (k/\mu_B) \chi_m \end{aligned}$$

where χ_m is magnetic susceptibility.

In order to estimate exchange integrals $N_{\alpha\beta}$ and $N_{\beta\alpha}$ we determined numerically derivative of exciton splitting $d(E_a - E_d)/dB$ and we measured susceptibility (both for B1c) of some of our samples. Obtained susceptibility data reveal deviation from expected Van Vleck-type behaviour [4,8]: susceptibility increases monotonously with decreasing temperature instead of being

temperature independent at low temperatures (below at about 4K). Similar situation was also encountered for ZnFeSe [10] and HgFeSe [9,18] and was attributed to the paramagnetic impurities present in the investigated crystals [10,18,19]. We notice that rather small amount of such impurities ($x=10^{-3}$ – 10^{-5} , which corresponds to $N_{\text{imp}}=10^{18}$ – 10^{20} cm^{-3}) is enough to mask completely the temperature independent susceptibility of Fe^{2+} ions at low temperatures [4].

In the spirit of this interpretation we corrected experimental data to remove from susceptibility and exciton splittings contribution of the impurities [20]. Finally $(N_{\text{d-d}}-N_{\text{s-d}})$ may be evaluated using formula (3) for each sample. We found decrease of $(N_{\text{d-d}}-N_{\text{s-d}})$ with increasing Fe concentration. However, in our opinion, experimental accuracy is too poor to derive pertinent conclusions concerning this dependence. Moreover we notice that if the calculated magnetization [23] is used for $(E_{\text{d-d}}-E_{\text{s-d}})$ vs. M_{Fe} plot, one finds $(N_{\text{d-d}}-N_{\text{s-d}})$ independent of concentration ($N_{\text{d-d}}-N_{\text{s-d}}=2.0\text{eV}$ in this case). We believe, that at the present stage the most reasonable estimation of $(N_{\text{d-d}}-N_{\text{s-d}})$ for CdFeSe should be the average value: $(N_{\text{d-d}}-N_{\text{s-d}})=(2.13\pm 0.15)\text{eV}$. Using $N_{\text{d-d}}=0.225\text{eV}$, the value resulting from Raman scattering experiment [11], one finds $N_{\text{s-d}}=(-1.9\pm 0.15)\text{eV}$, the value very close to that reported for ZnFeSe ($N_{\text{s-d}}=(-1.74\pm 0.13)\text{eV}$ [21]). Since the differences in exchange parameters for different materials does not exceed the experimental accuracy, one can hardly conclude about the chemical trends of s,p-d exchange interaction for Fe-type and Mn-type DMS. In general we find similar situation for both families, where s-d as well as p-d exchange parameters are similar for Zn and Cd selenides as shown in Tab.1.

Table 1

material	$N_{\text{d-d}}$ (eV)	$N_{\text{s-d}}$ (eV)	$J_{\text{NN}}/K_{\text{B}}$ (K)
ZnFeSe	0.22 [10]	-1.74 [10]	-22 [22]
CdFeSe	0.225 [11]	-1.9	-19 [23]
HgFeSe			-18 [23]
ZnMnSe	0.26 [24]	-1.31 [24]	-12.6 [25]
CdMnSe	0.23 [15]	-1.26 [15]	-8 [26]
HgMnSe			-11 [28]
			-6 [27]

This situation should be correlated with the d-d exchange interaction for these materials (see Tab.1). Assuming that superexchange is the dominant mechanism of d-d interaction, the stronger p-d exchange (reflecting larger probability of the electron hopping between Fe ions) should lead to stronger interaction between magnetic ions (monitored by J_{NN}) [29]. This trend may be recovered comparing Mn and Fe DMS families (Tab.2). Moreover similar $N_{\text{s-d}}$ values for ZnFeSe and CdFeSe correspond to similar d-d interaction between Fe ions. Unfortunately more detailed analysis of exchange is difficult at the moment since the knowledge about the other parameters involved in the s,p-d and d-d interaction model [29] for ZnFeSe and CdFeSe is rather poor and proper analysis of chemical trends for p-d and d-d interaction still awaits further study.

REFERENCES

1. see: Semiconductors and Semimetals, **25**, "Diluted Magnetic Semiconductors" ed. J.K.Furdyna and J.Kossut, Academic Press (1988) and review paper: J.K.Furdyna, J.Appl.Phys. **64** (4), R29 (1988)
2. W.Low and M.Weger, Phys.Rev. **118**, 1119 (1960)
3. G.A.Slack, S.Roberts and J.T.Wallin, Phys.Rev. **187**, 511 (1969)
4. J.Mahoney, C.Lin, W.Brumage and F.Dorman, J.Chem.Phys. **53**, 4286 (1970)
5. see review paper: A.Mycielski, J. Appl. Phys. **63**, 3279 (1988) and references therein
8. A.Twardowski, H.J.M.Swagten, T.F.H.v.d.Wetering and W.J.M.de Jonge, Solid State Commun. **65**, 235 (1988)
9. A.Lewicki, J.Spalek and A.Mycielski, J.Phys. C, **20**, 2005 (1987)
10. A.Twardowski, P.Glod, W.J.M. de Jonge, M.Demianiuk, Solid State Commun. **64**, 63 (1987)
11. D.Heiman, A.Petrou, S.H.Bloom, Y.Shapira, E.D.Isaacs and W.Giriat, Phys. Rev. Letters, **60**, 1876 (1988)
12. A.Petrou, X.Liu, G.Waytena, J.Warnock and W.Giriat, Solid State Commun. **61**, 767 (1987)
13. D.Scalbert, J.Cernogora, A.Mauger and C.Benoit a la Guillaume and A.Mycielski, Solid State Commun. **69**, 453 (1989) J.A.Gaj, private communication
14. D.Scalbert, J.A.Gaj, A.Mauger, J.Cernogora C.Benoit a la Guillaume, Phys. Rev. Lett. **62**, 2865 (1989)
15. M.Arciszewska and M.Nawrocki, J.Phys.Chem.Solids **47**, 309 (1986)
16. J.A.Gaj, J.Ginter and R.R.Galazka, Phys.Stat.Sol. (b) **89**, 655 (1978)
17. R.L.Aggarwal, S.N.Jasperson, J.Stankiewicz, Y.Shapira, S.Foner, B.Khazai and A.Wold, Phys. Rev. **B28**, 6907 (1983)
18. M.Arciszewska, A.Lenard, T.Diel, W.Plesiewicz, T.Skoskiewicz and W.Dobrowolski, MAGNETIC SUSCEPTIBILITY OF HgFeSe, Acta Physica Polonica, in press (1990)
19. EPR performed on some of our samples revealed the presence of Mn^{++} impurities in our crystals.
20. It should be mentioned here that the discussed effect of impurities is in fact smaller than the experimental error.
21. The value $N_0\beta = -1.57\text{eV}$ reported in [10] resulted from $k=1/2$, obtained in Low & Weger model [2], in better, Slack's model [3] one obtains $k=0.447$ and consequently $N_0\beta = -1.74\text{eV}$.
22. A.Twardowski, A.Lewicki, M.Arciszewska, W.J.M.de Jonge, H.J.M.Swagten, M.Demianiuk, Phys. Rev. **B38**, 10749 (1988)
23. A.Twardowski, H.J.M.Swagten and W.J.M.de Jonge, SPECIFIC HEAT OF HgCdFeSe DMS, to be published
A.Twardowski, Solid State Commun. **68**, 1069 (1988)
24. A.Twardowski, M. von Ortenberg, M.Demianiuk, R.Pauthenet, Solid State Commun. **51**, 849 (1984)
25. T.M.Giebultowicz, J.J.Rhyne, J.K.Furdyna J.Appl.Phys. **61**, 3537 (1987); **61**, 3540 (1987)
26. B.E.Larson, K.C.Hass, R.L.Aggarwal, Phys.Rev. **B33**, 1789 (1986)
27. R.R.Galazka, W.Dobrowolski, J.P.Lascaray, M.Nawrocki, A.Bruno, J.M.Broto and J.C.Ousset, J.of Mag. and Mag. Mat. **72**, 174 (1988)
28. J.Spalek, A.Lewicki, Z.Tarnawski, J.K.Furdyna, R.R.Galazka, Z.Obuszko, Phys. Rev **B33**, 3407 (1986)
29. B.E.Larson, K.C.Hass, H.Ehrenreich and A.E.Carlsson, Solid State Commun. **56**, 347 (1985); Phys. Rev. **B37**, 4137 (1988)

Author Index

- Abele, J.C., 239
 Adams, S.J.A., 153
 Ahlgren, W.L., 63, 351
 Allred, D.D., 33, 109
 Allred, Worth P., 33
 Alonso, R.G., 497
 Amirtharaj, P.M., 27
 Arciszewska, M., 503
 Arnold, D.J., 413
 Ashenford, D., 437
 Auyang, S.Y., 385

 Bartoli, F.J., 397, 403, 413
 Becla, P., 455, 465, 479
 Berding, M.A., 291
 Bhat, I.B., 271
 Biswas, Sambhu N., 371
 Bowers, K.A., 15, 133
 Bowman, Jr., R.C., 251
 Brillson, L.J., 59
 Brinkman, A.W., 357
 Brown, P.D., 357

 Cammack, D.A., 471
 Cavenett, B.C., 153
 Ceccone, G., 297
 Chandra, Dipankar, 303, 313
 Chandrasekhar, H.R., 449
 Chandrasekhar, Meera, 449
 Chaudhuri, J., 83
 Chen, A.-B., 291
 Chen, M.-C., 39
 Cheng, H., 97
 Clifton, P.A., 357
 Compaa, A., 251
 Cook, Jr., J.W., 133, 159, 263, 363, 397, 413

 Dahl, M., 479
 de Jonge, W.J.M., 485
 DeCarlo, J., 377
 DePuydt, J.M., 97
 Dhar, N.K., 27
 Diamond, S.J., 437
 DiMarzio, D., 377
 Doggett, W.O., 217
 Dreifus, D.L., 159, 323
 Dubowski, J.J., 443
 Duncan, W.M., 39

 Endoh, Yasuyuki, 211

 Faurie, J.P., 59
 Finkman, Eliezer, 277
 Fitzpatrick, B.J., 141

 Foner, S., 455
 Franciosi, A., 297, 459
 Fu, Q., 121
 Furdyna, J.K., 427, 497

 Ghandhi, Sorab K., 271, 331
 Ghatak, Kamakhya P., 371
 Giles, N.C., 227, 263
 Glenn Jr., J., 127
 Gonsalves, J., 121
 Gonzalez-Hernandez, J., 33
 Goodwin, Michael W., 313
 Gough, J.S., 285
 Gunshor, R.L., 115, 121, 127, 471

 Haase, M.A., 97
 Hagerott, M., 121
 Hails, J.E., 343
 Haines, M.J.L.S., 153
 Hall, D.O., 357
 Hamilton, Jr., W.J., 63, 351
 Han, J., 121
 Han, J.W., 159, 227, 257, 263, 397
 Hariu, T., 147
 Harper, R.L., 227
 Haugstad, G., 297, 459
 Heiman, D., 455, 465, 479
 Herman, Irving P., 471
 Hoffman, C.A., 397, 403, 413
 Huber, C.A., 465
 Hunter, J.J., 153
 Hwang, S., 133, 159, 245, 263, 363

 Irvine, S.J.C., 285, 343

 Jackman, J.A., 443
 James, J.B., 351
 James, K.M., 45
 Jiang, X.D., 171
 Jin, M.H., 45
 John, D.R., 15
 Johnson, S.M., 3, 63, 351
 Jones, C.E., 45

 Kalisher, M.H., 351
 Kartheuser, E., 491
 Kesselman, M., 377
 Kiele, J.A., 3
 Kimura, R., 177
 Kleebe, H.-J., 63
 Kobayashi, M., 115, 121, 127
 Koestner, R.J., 39

- Kolbas, R.M., 323
 Kolodziejewski, L.A., 471
 Konagai, M., 177
 Konkel, W.H., 3
 Kremer, R.E., 239
 Krishnamurthy, Srinivasan, 291
 Kukimoto, Hiroshi, 91
 Lansari, Y., 159, 257, 263, 363, 413
 Lee, M.B., 377
 Li, D., 115, 127
 Liu, H.-Y., 39
 Lopez-Cruz, Elias, 33
 Lozykowski, H.J., 171
 Lu, Z., 141
 Lunn, B., 437
 Luo, H., 497
 Mahajan, S., 15
 Marfaing, Y., 69
 Martinez, A., 397
 Mathine, D.L., 121
 Mazur, J.H., 443
 McDevitt, S., 15
 Menke, D.R., 115, 121
 Merz, J.L., 45, 171
 Meyer, J.R., 397, 403, 413
 Miotkowski, I., 449
 Mitchell, Richard L., 193
 Moore, F.G., 239
 Mullin, J.B., 285, 343
 Mullins, J.T., 357
 Mycielski, A., 479, 503
 Neumark, G.F., 141
 Newbury, P.R., 141
 Noad, J., 443
 Nurmikko, A.V., 121
 Oh, E., 497
 Oniyama, H., 187
 Otsuka, N., 115, 121, 127
 Pakula, K., 503
 Parat, K.K., 271
 Pascher, H., 497
 Perkins, R.T., 109
 Petrou, A., 479
 Potts, J.E., 97
 Prakash, Maneesha, 449
 Prior, K.A., 153
 Qian, Q.-D., 115
 Qiu, J., 115, 127
 Rai, R.S., 15
 Raisanen, A., 297, 459
 Ramdas, A.K., 449, 497
 Rani, V.K. Madhu Smitha, 51
 Reddy, B.K., 51
 Reddy, D. Raja, 51
 Reichman, Joseph, 165
 Ren, J., 133
 Reyes-Mena, A., 33
 Rodriguez, S., 491
 Rolfe, S., 443
 Royle, Anne, 285
 Ruhle, M., 63
 Samarth, N., 427, 497
 Schacham, Samuel E., 277
 Schetzina, J.F., 15, 133, 159, 217, 227, 245, 257, 263, 323, 363, 397, 413, 419
 Schulman, J.N., 413
 Sen, S., 3
 Sepich, J.L., 15
 Shah, S., 83
 Shaw, J.L., 59
 Sher, A., 291
 Shih, M., 465
 Shone, M., 141, 471
 Shurtleff, J.K., 109
 Sicignano, A., 141
 Sivananthan, S., 59
 Sneed, B.P., 323
 Stannard, J.E., 3
 Steeds, J.W., 437
 Suh, E.-K., 497
 Sui, Zhifeng, 471
 Swagten, H.J.M., 485
 Taguchi, Tsunemasa, 199, 211
 Takahashi, K., 177
 Takemura, Y., 177
 Taskar, N.R., 271
 Teraguchi, N., 177
 Thelander, Michael W., 217
 Thorne, J.M., 109
 Tregilgas, J.H., 39
 Troullier, N., 459
 Tuchman, Judah A., 471
 Twardowski, A., 485, 503
 Ullal, Harin S., 193
 Vaziri, M., 121
 Vijayalakshmi, R.P., 51
 Villeret, Murielle, 491
 Wallace, J.M., 153
 Walrod, D., 385
 Wang, Xiaomei, 455, 479
 Wolff, P.A., 385, 479
 Wrobel, J.M., 443
 Yamada, Yoichi, 199
 Yamaga, S., 187

Yamauchi, S., 147
Yang, Z., 257, 263, 363, 419
Yi, Guan-Jiun, 141
Yoshikawa, A., 187
Youngdale, E.R., 397
Yu, C.F., 141
Yu, Xiaohua, 297, 459
Yu, Z., 257

Zheng, X.L., 465
Zweibel, Kenneth, 193

Subject Index

- $\text{Al}_{1-x}\text{Co}_x\text{B}^{\text{VI}}$ alloys, 427
 $\text{Al}_{1-x}\text{Mn}_x\text{B}^{\text{VI}}$ alloys, 427
 acceptor, 147
 bound magnetic polaron, 447
 aging, 27
 annealing, 33, 141
 atomic layer epitaxy, 109, 177
 attenuation, 83
 blue LED's, 97
 Boltzmann equation, 247
 $\text{Br}_2/\text{CH}_3\text{OH}$, 27
 Bridgman, 3
 bulk CdTe, 15, 27
 C-V, 115
 cadmium
 vacancies, 33
 telluride, 33
 carrier concentrations, 134
 cathodoluminescence, 435
 Cd
 vacancy, 27
 vapor anneal, 33
 $\text{Cd}_{1-y}\text{Zn}_y\text{Te}$, 3
 $\text{Cd}_{1-x}\text{Fe}_x\text{Se}$, 501
 $\text{Cd}_{1-x}\text{Mn}_x\text{Se}$, 495
 $\text{Cd}_{1-x}\text{Mn}_x\text{Te}$, 447, 453, 463
 (Cd,Fe)Se, 477
 CdMnTe-CdTe superlattice, 217
 CdS, 165
 CdTe, 3, 15, 27, 69, 193, 217, 227, 291
 CdTe:As, 323
 CdTe:In, 323
 CdTe-InSb, 127
 $\text{CdTe}_{1-z}\text{Se}_z$, 3
 $\text{Cd}_x\text{Hg}_{1-x}\text{Te}$, 69, 285
 CdZnS-ZnS superlattices, 211
 CdZnTe, 39, 63
 chemical
 approximation, 291
 etching, 27
 vapor deposition, 109
 cleaved, 27
 $\text{Co}^{2+}(\text{3d}^7)$, 489
 complex, 27
 defect, 27
 impedance, 165
 compositional, 39
 convex interface, 3
 crystal field, 489
 $\text{Cu}^{2+}(\text{3d}^9)$, 489
 CuInSe_2 , 193
 curvature effect, 83
 defect characterization, 39
 density measurement, 240
 detector, 217
 device
 fabrication, 27
 processing, 27
 di-
 allyl telluride, 343
 isopropyl telluride, 343
 n-propyl telluride, 343
 t-butyl telluride, 343
 diffusion, 441
 barriers, 291
 dilute magnetic semiconductor, 427, 453, 463, 483, 489, 495, 501
 dislocation density, 303
 doping, 69
 double crystal rocking curves, 377
 doubly-ionized transition metal ions, 489
 elastic strain, 469
 electrical
 characterization, 285
 properties, 245, 363
 electrochemical sulphur cell, 153
 electron
 microscope, 63
 mobility, 247
 structure, 357
 encapsulation, 27
 epitaxial
 growth, 331, 441
 layers, 463
 ZnSe, 115
 etching, 27
 exciton splitting, 501
 excitonic properties, 199
 excitons, 27, 33
 far infrared detectors, 331
 $\text{Fe}^{2+}(\text{3d}^6)$, 489
 Fibonacci sequence, 199
 field emission, 371
 Fourier transform IR, 377
 free-carrier nonlinear process, 385
 free exciton, 501

- freeze, 3
- further-neighbor interactions, 453
- g-factors, 489
- Ga₂Se₃, 115
- GaAs, 63, 115, 187
- Ge-Cd_{1-x}Mn_xTe hetero-structure, 457
- gradient, 3
- Green's function, 291
- Hall
 - effect, 377
 - measurement, 243
 - mobility, 136
- heteroepitaxial, 63
 - HgCdTe/CdZnTe/GaAs/Si, 351
- heterojunction IR detectors, 351
- heterojunctions, 457
- heterostructures, 115
- Hg_{1-x}Cd_xTe, 3, 245, 251, 271, 277
- HgBaTe, 239
- HgBeTe, 239
- HgCaTe, 239
- HgCdTe, 63, 217, 227, 263, 291, 331, 377, 385
- HgCdZnTe, 303
- HgMgTe, 239
- HgSrTe, 239
- HgTe, 291
- HgTe-CdTe superlattice, 257, 264, 363, 371, 397, 403
- HgTe-CdTe multiple quantum wells, 413, 419
- HgTe-ZnTe superlattice, 357
- high field magnetization, 483
- hydrogen-chloride, 147
- hydrostatic pressure, 447, 469
- II-VI semiconductor, 91, 159
- III₂VI₃ compounds, 127
- impurity, 69
- In doped, 27, 303
- inelastic light scattering, 477
- inert atmosphere, 27
- infrared, 3
 - absorption, 257
- integrated diffracted intensity, 83
- interdiffused multilayer process, 285
- interface, 115
 - defects, 63
 - state density, 115
- interfaces, 127
- interfacial compound, 115
- inter-subband transitions, 257
- intrinsic bandgap, 242
- inverted surface layer, 277, 285
- ion-implantation gettering, 45
- IR, 3
 - detector material, 343
 - detectors, 263
- KOH/CH₃OH, 27
- laser, 141
- lattice mismatch, 351, 469
- lifetime, 217
- liquid crystal, 165
- low
 - pressure MOCVD, 211
 - temperature device processing, 323
- LPE, 63, 251, 303, 313
- luminescence, 141
- LWIR HgCdTe, 303, 313
- magnetic
 - field dependence of R_H, 271
 - ion triplets, 453
 - properties, 483
 - quantization, 371
- magneto-transport, 413
- MBE, 115, 133, 377
- MBE-ALE, 177
- measurement of vapor pressure, 343
- metal-insulator-semiconductor, 171
- metallic contacts, 27
- methyl-allyl telluride, 343
- microscopy, 127
- MIS properties, 313
- misfit dislocations, 435
- MOCVD, 63, 91, 251
 - ZnSe-ZnS, 199
- modulation
 - doped superlattice, 227
 - doping, 263, 363
- molecular beam epitaxy, 97, 121, 127, 153
- MOMBE-ALE, 177
- MOVPE, 357
 - layers, 285
 - precursor, 343
- multilayer, 63, 109
 - growth model, 291

- multiple quantum wells, 413
- N_2^- ion, 147
- narrow gap superlattice, 385, 397
- native defects, 27
- next-nearest neighbor exchange, 453
- $Ni^{2+}(3d^8)$, 489
- nitrogen, 147
- nonlinear
 - exciton effect, 211
 - optical effects, 385, 397
- ohmic contacts, 159
- OMVPE, 331
- oxidation, 27
- p-d exchange integral, 501
- p-n junctions, 97, 323
- PAE, 147
- $Pb_{1-x}Sn_xTe$, 397
- perturbation, 27
- photoassisted MBE, 227, 263, 323, 363
- photoelectrochemical cell, 165
- photoluminescence, 27, 33, 39, 121, 165, 447, 469, ???
- polycrystalline thin-film, 193
- primary, 83
- pseudomorphic ZnTe/AlSb/GaSb, 121
- pulsed laser annealing, 251
- quantum
 - alloy, 263
 - confined Stark effect, 211, 419
 - well MODFETs, 323
- Raman
 - scattering, 251
 - spectroscopy, 495
- RHEED, 121
- 16-point Laguerre formula, 246
- scanning electron microscopy, 377
- scattering mechanisms, 247
- Schottky barrier, 27
- Se doping, 121
- Se-N, 147
- secondary extinction, 83
- segregation, 241
- selective-area epitaxy, 159
- self-compensation, 69
- semiconductors, 63, 413
- semimagnetic semiconductors, 457
- Shubnikov-de Haas technique, 277
- single-crystal, 3
- solubility, 69
- spatial
 - Light Modulator, 165
 - resolution, 27
- stability, 27
- stacking faults, 435
- stoichiometry, 109
- surface
 - electrons, 271, 277
 - energies, 291
 - order-disorder transitions, 291
 - passivation, 159
 - region, 27
- susceptibility, 501
- synchrotron radiation
 - photoemission, 297, 457
- 3d transition metals, 477
- tellurium
 - precursors, 343
 - rich melt, 313
- temperature-dependent EXAFS, 377
- tetrahedral symmetry, 489
- thicknesses of thin film, 83
- thin film, 83, 165
- transient photoconductivity, 217
- transmission electron microscopy, 115, 121, 127, 435
- transport, 403
- trigonal symmetry, 489
- twinning, 141
- two-dimensional electron gas, 277
- vacancies, 27
- valence band offset, 457
- Van-Vleck paramagnetism, 501
- wide bandgap, 91
- x-ray, 109
 - diffraction, 83, 351
 - rocking curve, 115
- zinc cadmium telluride, 33
- $ZnCl_2$, 133
- ZnSe, 177, 187
- ZnSe/GaAs, 127

ZnSe, 97, 109, 141, 147, 177,
187, 469
ZnSe-ZnTe strained-layer
superlattices, 177
ZnSe on GaAs, 153
ZnSe:Cl, 133
(ZnSe)₁-(ZnTe)₁ SLS, 177
ZnSe-ZnS superlattice, 199
ZnS_xSe_{1-x} alloys, 153
ZnTe, 177

MATERIALS RESEARCH SOCIETY SYMPOSIUM PROCEEDINGS

ISSN 0272 - 9172

- Volume 1—Laser and Electron-Beam Solid Interactions and Materials Processing, J. F. Gibbons, L. D. Hess, T. W. Sigmon, 1981, ISBN 0-444-00595-1
- Volume 2—Defects in Semiconductors, J. Narayan, T. Y. Tan, 1981, ISBN 0-444-00596-X
- Volume 3—Nuclear and Electron Resonance Spectroscopies Applied to Materials Science, E. N. Kaufmann, G. K. Shenoy, 1981, ISBN 0-444-00597-8
- Volume 4—Laser and Electron-Beam Interactions with Solids, B. R. Appleton, G. K. Celler, 1982, ISBN 0-444-00693-1
- Volume 5—Grain Boundaries in Semiconductors, H. J. Leamy, G. E. Pike, C. H. Seager, 1982, ISBN 0-444-00697-4
- Volume 6—Scientific Basis for Nuclear Waste Management IV, S. V. Topp, 1982, ISBN 0-444-00699-0
- Volume 7—Metastable Materials Formation by Ion Implantation, S. T. Picraux, W. J. Choyke, 1982, ISBN 0-444-00692-3
- Volume 8—Rapidly Solidified Amorphous and Crystalline Alloys, B. H. Kear, B. C. Giessen, M. Cohen, 1982, ISBN 0-444-00698-2
- Volume 9—Materials Processing in the Reduced Gravity Environment of Space, G. E. Rindone, 1982, ISBN 0-444-00691-5
- Volume 10—Thin Films and Interfaces, P. S. Ho, K.-N. Tu, 1982, ISBN 0-444-00774-1
- Volume 11—Scientific Basis for Nuclear Waste Management V, W. Lutze, 1982, ISBN 0-444-00725-3
- Volume 12—In Situ Composites IV, F. D. Lemkey, H. E. Cline, M. McLean, 1982, ISBN 0-444-00726-1
- Volume 13—Laser-Solid Interactions and Transient Thermal Processing of Materials, J. Narayan, W. L. Brown, R. A. Lemons, 1983, ISBN 0-444-00788-1
- Volume 14—Defects in Semiconductors II, S. Mahajan, J. W. Corbett, 1983, ISBN 0-444-00812-8
- Volume 15—Scientific Basis for Nuclear Waste Management VI, D. G. Brookins, 1983, ISBN 0-444-00780-6
- Volume 16—Nuclear Radiation Detector Materials, E. E. Haller, H. W. Kraner, W. A. Higinbotham, 1983, ISBN 0-444-00787-3
- Volume 17—Laser Diagnostics and Photochemical Processing for Semiconductor Devices, R. M. Osgood, S. R. J. Brueck, H. R. Schlossberg, 1983, ISBN 0-444-00782-2
- Volume 18—Interfaces and Contacts, R. Ludeke, K. Rose, 1983, ISBN 0-444-00820-9
- Volume 19—Alloy Phase Diagrams, L. H. Bennett, T. B. Massalski, B. C. Giessen, 1983, ISBN 0-444-00809-8
- Volume 20—Intercalated Graphite, M. S. Dresselhaus, G. Dresselhaus, J. E. Fischer, M. J. Moran, 1983, ISBN 0-444-00781-4
- Volume 21—Phase Transformations in Solids, T. Tsakalakos, 1984, ISBN 0-444-00901-9
- Volume 22—High Pressure in Science and Technology, C. Homan, R. K. MacCrone, E. Whalley, 1984, ISBN 0-444-00932-9 (3 part set)
- Volume 23—Energy Beam-Solid Interactions and Transient Thermal Processing, J. C. C. Fan, N. M. Johnson, 1984, ISBN 0-444-00903-5
- Volume 24—Defect Properties and Processing of High-Technology Nonmetallic Materials, J. H. Crawford, Jr., Y. Chen, W. A. Sibley, 1984, ISBN 0-444-00904-3
- Volume 25—Thin Films and Interfaces II, J. E. E. Baglin, D. R. Campbell, W. K. Chu, 1984, ISBN 0-444-00905-1

MATERIALS RESEARCH SOCIETY SYMPOSIUM PROCEEDINGS

- Volume 26—Scientific Basis for Nuclear Waste Management VII, G. L. McVay, 1984, ISBN 0-444-00906-X
- Volume 27—Ion Implantation and Ion Beam Processing of Materials, G. K. Hubler, O. W. Holland, C. R. Clayton, C. W. White, 1984, ISBN 0-444-00869-1
- Volume 28—Rapidly Solidified Metastable Materials, B. H. Kear, B. C. Giessen, 1984, ISBN 0-444-00935-3
- Volume 29—Laser-Controlled Chemical Processing of Surfaces, A. W. Johnson, D. J. Ehrlich, H. R. Schlossberg, 1984, ISBN 0-444-00894-2
- Volume 30—Plasma Processing and Synthesis of Materials, J. Szekely, D. Apelian, 1984, ISBN 0-444-00895-0
- Volume 31—Electron Microscopy of Materials, W. Krakow, D. A. Smith, L. W. Hobbs, 1984, ISBN 0-444-00898-7
- Volume 32—Better Ceramics Through Chemistry, C. J. Brinker, D. E. Clark, D. R. Ulrich, 1984, ISBN 0-444-00898-5
- Volume 33—Comparison of Thin Film Transistor and SOI Technologies, H. W. Lam, M. J. Thompson, 1984, ISBN 0-444-00899-3
- Volume 34—Physical Metallurgy of Cast Iron, H. Fredriksson, M. Hillerts, 1985, ISBN 0-444-00938-8
- Volume 35—Energy Beam-Solid Interactions and Transient Thermal Processing/1984, D. K. Biegelsen, G. A. Rozgonyi, C. V. Shank, 1985, ISBN 0-931837-00-6
- Volume 36—Impurity Diffusion and Gettering in Silicon, R. B. Fair, C. W. Pearce, J. Washburn, 1985, ISBN 0-931837-01-4
- Volume 37—Layered Structures, Epitaxy, and Interfaces, J. M. Gibson, L. R. Dawson, 1985, ISBN 0-931837-02-2
- Volume 38—Plasma Synthesis and Etching of Electronic Materials, R. P. H. Chang, B. Abeles, 1985, ISBN 0-931837-03-0
- Volume 39—High-Temperature Ordered Intermetallic Alloys, C. C. Koch, C. T. Liu, N. S. Stoloff, 1985, ISBN 0-931837-04-9
- Volume 40—Electronic Packaging Materials Science, E. A. Giess, K.-N. Tu, D. R. Uhlmann, 1985, ISBN 0-931837-05-7
- Volume 41—Advanced Photon and Particle Techniques for the Characterization of Defects in Solids, J. B. Roberto, R. W. Carpenter, M. C. Wittels, 1985, ISBN 0-931837-06-5
- Volume 42—Very High Strength Cement-Based Materials, J. F. Young, 1985, ISBN 0-931837-07-3
- Volume 43—Fly Ash and Coal Conversion By-Products: Characterization, Utilization, and Disposal I, G. J. McCarthy, R. J. Lauf, 1985, ISBN 0-931837-08-1
- Volume 44—Scientific Basis for Nuclear Waste Management VIII, C. M. Jantzen, J. A. Stone, R. C. Ewing, 1985, ISBN 0-931837-09-X
- Volume 45—Ion Beam Processes in Advanced Electronic Materials and Device Technology, B. R. Appleton, F. H. Eisen, T. W. Sigmon, 1985, ISBN 0-931837-10-3
- Volume 46—Microscopic Identification of Electronic Defects in Semiconductors, N. M. Johnson, S. G. Bishop, G. D. Watkins, 1985, ISBN 0-931837-11-1
- Volume 47—Thin Films: The Relationship of Structure to Properties, C. R. Aita, K. S. SreeHarsha, 1985, ISBN 0-931837-12-X
- Volume 48—Applied Materials Characterization, W. Katz, P. Williams, 1985, ISBN 0-931837-13-8
- Volume 49—Materials Issues in Applications of Amorphous Silicon Technology, D. Adler, A. Madan, M. J. Thompson, 1985, ISBN 0-931837-14-6

MATERIALS RESEARCH SOCIETY SYMPOSIUM PROCEEDINGS

- Volume 50—Scientific Basis for Nuclear Waste Management IX, L. O. Werme, 1986, ISBN 0-931837-15-4
- Volume 51—Beam-Solid Interactions and Phase Transformations, H. Kurz, G. L. Olson, J. M. Poate, 1986, ISBN 0-931837-16-2
- Volume 52—Rapid Thermal Processing, T. O. Sedgwick, T. E. Seidel, B.-Y. Tsaur, 1986, ISBN 0-931837-17-0
- Volume 53—Semiconductor-on-Insulator and Thin Film Transistor Technology, A. Chiang, M. W. Geis, L. Pfeiffer, 1986, ISBN 0-931837-18-9
- Volume 54—Thin Films—Interfaces and Phenomena, R. J. Nemanich, P. S. Ho, S. S. Lau, 1986, ISBN 0-931837-19-7
- Volume 55—Biomedical Materials, J. M. Williams, M. F. Nichols, W. Zingg, 1986, ISBN 0-931837-20-0
- Volume 56—Layered Structures and Epitaxy, J. M. Gibson, G. C. Osbourn, R. M. Tromp, 1986, ISBN 0-931837-21-9
- Volume 57—Phase Transitions in Condensed Systems—Experiments and Theory, G. S. Cargill III, F. Spaepen, K.-N. Tu, 1987, ISBN 0-931837-22-7
- Volume 58—Rapidly Solidified Alloys and Their Mechanical and Magnetic Properties, B. C. Giessen, D. E. Polk, A. I. Taub, 1986, ISBN 0-931837-23-5
- Volume 59—Oxygen, Carbon, Hydrogen, and Nitrogen in Crystalline Silicon, J. C. Mikkelsen, Jr., S. J. Pearton, J. W. Corbett, S. J. Pennycook, 1986, ISBN 0-931837-24-3
- Volume 60—Defect Properties and Processing of High-Technology Nonmetallic Materials, Y. Chen, W. D. Kingery, R. J. Stokes, 1986, ISBN 0-931837-25-1
- Volume 61—Defects in Glasses, F. L. Galeener, D. L. Griscom, M. J. Weber, 1986, ISBN 0-931837-26-X
- Volume 62—Materials Problem Solving with the Transmission Electron Microscope, L. W. Hobbs, K. H. Westmacott, D. B. Williams, 1986, ISBN 0-931837-27-8
- Volume 63—Computer-Based Microscopic Description of the Structure and Properties of Materials, J. Broughton, W. Krakow, S. T. Pantelides, 1986, ISBN 0-931837-28-6
- Volume 64—Cement-Based Composites: Strain Rate Effects on Fracture, S. Mindess, S. P. Shah, 1986, ISBN 0-931837-29-4
- Volume 65—Fly Ash and Coal Conversion By-Products: Characterization, Utilization and Disposal II, G. J. McCarthy, F. P. Glasser, D. M. Roy, 1986, ISBN 0-931837-30-8
- Volume 66—Frontiers in Materials Education, L. W. Hobbs, G. L. Liedl, 1986, ISBN 0-931837-31-6
- Volume 67—Heteroepitaxy on Silicon, J. C. C. Fan, J. M. Poate, 1986, ISBN 0-931837-33-2
- Volume 68—Plasma Processing, J. W. Coburn, R. A. Gottscho, D. W. Hess, 1986, ISBN 0-931837-34-0
- Volume 69—Materials Characterization, N. W. Cheung, M.-A. Nicolet, 1986, ISBN 0-931837-35-9
- Volume 70—Materials Issues in Amorphous-Semiconductor Technology, D. Adler, Y. Hamakawa, A. Madan, 1986, ISBN 0-931837-36-7
- Volume 71—Materials Issues in Silicon Integrated Circuit Processing, M. Wittmer, J. Stimmell, M. Strathman, 1986, ISBN 0-931837-37-5
- Volume 72—Electronic Packaging Materials Science II, K. A. Jackson, R. C. Pohanka, D. R. Uhlmann, D. R. Ulrich, 1986, ISBN 0-931837-38-3
- Volume 73—Better Ceramics Through Chemistry II, C. J. Brinker, D. E. Clark, D. R. Ulrich, 1986, ISBN 0-931837-39-1
- Volume 74—Beam-Solid Interactions and Transient Processes, M. O. Thompson, S. T. Picraux, J. S. Williams, 1987, ISBN 0-931837-40-5

MATERIALS RESEARCH SOCIETY SYMPOSIUM PROCEEDINGS

- Volume 75—Photon, Beam and Plasma Stimulated Chemical Processes at Surfaces, V. M. Donnelly, I. P. Herman, M. Hirose, 1987, ISBN 0-931837-41-3
- Volume 76—Science and Technology of Microfabrication, R. E. Howard, E. L. Hu, S. Namba, S. Pang, 1987, ISBN 0-931837-42-1
- Volume 77—Interfaces, Superlattices, and Thin Films, J. D. Dow, I. K. Schuller, 1987, ISBN 0-931837-56-1
- Volume 78—Advances in Structural Ceramics, P. F. Becher, M. V. Swain, S. Sōmiya, 1987, ISBN 0-931837-43-X
- Volume 79—Scattering, Deformation and Fracture in Polymers, G. D. Wignall, B. Crist, T. P. Russell, E. L. Thomas, 1987, ISBN 0-931837-44-8
- Volume 80—Science and Technology of Rapidly Quenched Alloys, M. Tenhover, W. L. Johnson, L. E. Tanner, 1987, ISBN 0-931837-45-6
- Volume 81—High-Temperature Ordered Intermetallic Alloys, II, N. S. Stoloff, C. C. Koch, C. T. Liu, O. Izumi, 1987, ISBN 0-931837-46-4
- Volume 82—Characterization of Defects in Materials, R. W. Siegel, J. R. Weertman, R. Sinclair, 1987, ISBN 0-931837-47-2
- Volume 83—Physical and Chemical Properties of Thin Metal Overlayers and Alloy Surfaces, D. M. Zehner, D. W. Goodman, 1987, ISBN 0-931837-48-0
- Volume 84—Scientific Basis for Nuclear Waste Management X, J. K. Bates, W. B. Seefeldt, 1987, ISBN 0-931837-49-9
- Volume 85—Microstructural Development During the Hydration of Cement, L. Struble, P. Brown, 1987, ISBN 0-931837-50-2
- Volume 86—Fly Ash and Coal Conversion By-Products Characterization, Utilization and Disposal III, G. J. McCarthy, F. P. Glasser, D. M. Roy, S. Diamond, 1987, ISBN 0-931837-51-0
- Volume 87—Materials Processing in the Reduced Gravity Environment of Space, R. H. Doremus, P. C. Nordine, 1987, ISBN 0-931837-52-9
- Volume 88—Optical Fiber Materials and Properties, S. R. Nagel, J. W. Fleming, G. Sigel, D. A. Thompson, 1987, ISBN 0-931837-53-7
- Volume 89—Diluted Magnetic (Semimagnetic) Semiconductors, R. L. Aggarwal, J. K. Furdyna, S. von Molnar, 1987, ISBN 0-931837-54-5
- Volume 90—Materials for Infrared Detectors and Sources, R. F. C. Farrow, J. F. Schetzina, J. T. Cheung, 1987, ISBN 0-931837-55-3
- Volume 91—Heteroepitaxy on Silicon II, J. C. C. Fan, J. M. Phillips, B.-Y. Tsaur, 1987, ISBN 0-931837-58-8
- Volume 92—Rapid Thermal Processing of Electronic Materials, S. R. Wilson, R. A. Powell, D. E. Davies, 1987, ISBN 0-931837-59-6
- Volume 93—Materials Modification and Growth Using Ion Beams, U. Gibson, A. E. White, P. P. Pronko, 1987, ISBN 0-931837-60-X
- Volume 94—Initial Stages of Epitaxial Growth, R. Hull, J. M. Gibson, David A. Smith, 1987, ISBN 0-931837-61-8
- Volume 95—Amorphous Silicon Semiconductors—Pure and Hydrogenated, A. Madan, M. Thompson, D. Adler, Y. Hamakawa, 1987, ISBN 0-931837-62-6
- Volume 96—Permanent Magnet Materials, S. G. Sankar, J. F. Herbst, N. C. Koon, 1987, ISBN 0-931837-63-4
- Volume 97—Novel Refractory Semiconductors, D. Emin, T. Aselage, C. Wood, 1987, ISBN 0-931837-64-2
- Volume 98—Plasma Processing and Synthesis of Materials, D. Apelian, J. Szekeley, 1987, ISBN 0-931837-65-0

MATERIALS RESEARCH SOCIETY SYMPOSIUM PROCEEDINGS

- Volume 99—High-Temperature Superconductors, M. B. Brodsky, R. C. Dynes, K. Kitazawa, H. L. Tuller, 1988, ISBN 0-931837-67-7
- Volume 100—Fundamentals of Beam-Solid Interactions and Transient Thermal Processing, M. J. Aziz, L. E. Rehn, B. Stritzker, 1988, ISBN 0-931837-68-5
- Volume 101—Laser and Particle-Beam Chemical Processing for Microelectronics, D. J. Ehrlich, G. S. Higashi, M. M. Oprysko, 1988, ISBN 0-931837-69-3
- Volume 102—Epitaxy of Semiconductor Layered Structures, R. T. Tung, L. R. Dawson, R. L. Gunshor, 1988, ISBN 0-931837-70-7
- Volume 103—Multilayers: Synthesis, Properties, and Nonelectronic Applications, T. W. Barbee Jr., F. Spaepen, L. Greer, 1988, ISBN 0-931837-71-5
- Volume 104—Defects in Electronic Materials, M. Stavola, S. J. Pearton, G. Davies, 1988, ISBN 0-931837-72-3
- Volume 105— SiO_2 and Its Interfaces, G. Lucovsky, S. T. Pantelides, 1988, ISBN 0-931837-73-1
- Volume 106—Polysilicon Films and Interfaces, C. Y. Wong, C. V. Thompson, K. N. Tu, 1988, ISBN 0-931837-74-X
- Volume 107—Silicon-on-Insulator and Buried Metals in Semiconductors, J. C. Sturm, C. K. Chen, L. Pfeiffer, P. L. F. Hemment, 1988, ISBN 0-931837-75-8
- Volume 108—Electronic Packaging Materials Science II, R. C. Sundahl, R. Jaccodine, K. A. Jackson, 1988, ISBN 0-931837-76-6
- Volume 109—Nonlinear Optical Properties of Polymers, A. J. Heeger, J. Orenstein, D. R. Ulrich, 1988, ISBN 0-931837-77-4
- Volume 110—Biomedical Materials and Devices, J. S. Hanker, B. L. Giammara, 1988, ISBN 0-931837-78-2
- Volume 111—Microstructure and Properties of Catalysts, M. M. J. Treacy, J. M. Thomas, J. M. White, 1988, ISBN 0-931837-79-0
- Volume 112—Scientific Basis for Nuclear Waste Management XI, M. J. Apted, R. E. Westerman, 1988, ISBN 0-931837-80-4
- Volume 113—Fly Ash and Coal Conversion By-Products: Characterization, Utilization, and Disposal IV, G. J. McCarthy, D. M. Roy, F. P. Glasser, R. T. Hemmings, 1988, ISBN 0-931837-81-2
- Volume 114—Bonding in Cementitious Composites, S. Mindess, S. P. Shah, 1988, ISBN 0-931837-82-0
- Volume 115—Specimen Preparation for Transmission Electron Microscopy of Materials, J. C. Bravman, R. Anderson, M. L. McDonald, 1988, ISBN 0-931837-83-9
- Volume 116—Heteroepitaxy on Silicon: Fundamentals, Structures, and Devices, H. K. Choi, H. Ishiwara, R. Hull, R. J. Nemanich, 1988, ISBN: 0-931837-86-3
- Volume 117—Process Diagnostics: Materials, Combustion, Fusion, K. Hays, A. C. Eckbreth, G. A. Campbell, 1988, ISBN: 0-931837-87-1
- Volume 118—Amorphous Silicon Technology, A. Madan, M. J. Thompson, P. C. Taylor, P. G. LeComber, Y. Hamakawa, 1988, ISBN: 0-931837-88-X
- Volume 119—Adhesion in Solids, D. M. Mattox, C. Batich, J. E. E. Baglin, R. J. Gottschall, 1988, ISBN: 0-931837-89-8
- Volume 120—High-Temperature/High-Performance Composites, F. D. Lemkey, A. G. Evans, S. G. Fishman, J. R. Strife, 1988, ISBN: 0-931837-90-1
- Volume 121—Better Ceramics Through Chemistry III, C. J. Brinker, D. E. Clark, D. R. Ulrich, 1988, ISBN: 0-931837-91-X

MATERIALS RESEARCH SOCIETY SYMPOSIUM PROCEEDINGS

- Volume 122—Interfacial Structure, Properties, and Design, M.H. Yoo, W.A.T. Clark, C.L. Briant, 1988, ISBN: 0-931837-92-8
- Volume 123—Materials Issues in Art and Archaeology, E.V. Sayre, P. Vandiver, J. Druzik, C. Stevenson, 1988, ISBN: 0-931837-93-6
- Volume 124—Microwave-Processing of Materials, M.H. Brooks, I.J. Chabinsky, W.H. Sutton, 1988, ISBN: 0-931837-94-4
- Volume 125—Materials Stability and Environmental Degradation, A. Barkatt, L.R. Smith, E. Verink, 1988, ISBN: 0-931837-95-2
- Volume 126—Advanced Surface Processes for Optoelectronics, S. Bernasek, T. Venkatesan, H. Temkin, 1988, ISBN: 0-931837-96-0
- Volume 127—Scientific Basis for Nuclear Waste Management XII, W. Lutze, R.C. Ewing, 1989, ISBN: 0-931837-97-9
- Volume 128—Processing and Characterization of Materials Using Ion Beams, L.E. Rehn, J. Greene, F.A. Smidt, 1989, ISBN: 1-55899-001-1
- Volume 129—Laser and Particle-Beam Modification of Chemical Processes on Surfaces, A.W. Johnson, G.L. Loper, T.W. Sigmon, 1989, ISBN: 1-55899-002-X
- Volume 130—Thin Films: Stresses and Mechanical Properties, J.C. Bravman, W.D. Nix, D.M. Barnett, D.A. Smith, 1989, ISBN: 1-55899-003-8
- Volume 131—Chemical Perspectives of Microelectronic Materials, M.E. Gross, J. Jasinski, J.T. Yates, Jr., 1989, ISBN: 1-55899-004-6
- Volume 132—Multicomponent Ultrafine Microstructures, L.E. McCandlish, B.H. Kear, D.E. Polk, and R.W. Siegel, 1989, ISBN: 1-55899-005-4
- Volume 133—High Temperature Ordered Intermetallic Alloys III, C.T. Liu, A.I. Taub, N.S. Stoloff, C.C. Koch, 1989, ISBN: 1-55899-006-2
- Volume 134—The Materials Science and Engineering of Rigid-Rod Polymers, W.W. Adams, R.K. Eby, D.E. McLemore, 1989, ISBN: 1-55899-007-0
- Volume 135—Solid State Ionics, G. Nazri, R.A. Huggins, D.F. Shriver, 1989, ISBN: 1-55899-008-9
- Volume 136—Fly Ash and Coal Conversion By-Products: Characterization, Utilization and Disposal V, R.T. Hemmings, E.E. Berry, G.J. McCarthy, F.P. Glasser, 1989, ISBN: 1-55899-009-7
- Volume 137—Pore Structure and Permeability of Cementitious Materials, L.R. Roberts, J.P. Skalny, 1989, ISBN: 1-55899-010-0
- Volume 138—Characterization of the Structure and Chemistry of Defects in Materials, B.C. Larson, M. Ruhle, D.N. Seidman, 1989, ISBN: 1-55899-011-9
- Volume 139—High Resolution Microscopy of Materials, W. Krakow, F.A. Ponce, D.J. Smith, 1989, ISBN: 1-55899-012-7
- Volume 140—New Materials Approaches to Tribology: Theory and Applications, L.E. Pope, L. Fehrenbacher, W.O. Winer, 1989, ISBN: 1-55899-013-5
- Volume 141—Atomic Scale Calculations in Materials Science, J. Tersoff, D. Vanderbilt, V. Vitek, 1989, ISBN: 1-55899-014-3
- Volume 142—Nondestructive Monitoring of Materials Properties, J. Holbrook, J. Bussiere, 1989, ISBN: 1-55899-015-1
- Volume 143—Synchrotron Radiation in Materials Research, R. Clarke, J. Gland, J.H. Weaver, 1989, ISBN: 1-55899-016-X
- Volume 144—Advances in Materials, Processing and Devices in III-V Compound Semiconductors, D.K. Sadana, L. Eastman, R. Dupuis, 1989, ISBN: 1-55899-017-8

Recent Materials Research Society Proceedings listed in the front.

MATERIALS RESEARCH SOCIETY CONFERENCE PROCEEDINGS

Tungsten and Other Refractory Metals for VLSI Applications, Robert S. Blewer, 1986; ISSN 0886-7860; ISBN 0-931837-32-4

Tungsten and Other Refractory Metals for VLSI Applications II, Eliot K. Broadbent, 1987; ISSN 0886-7860; ISBN 0-931837-66-9

Ternary and Multinary Compounds, Satyen K. Deb, Alex Zunger, 1987; ISBN 0-931837-57-X

Tungsten and Other Refractory Metals for VLSI Applications III, Victor A. Wells, 1988; ISSN 0886-7860; ISBN 0-931837-84-7

Atomic and Molecular Processing of Electronic and Ceramic Materials: Preparation, Characterization and Properties, Ilhan A. Aksay, Gary L. McVay, Thomas G. Stoebe, J.F. Wager, 1988; ISBN 0-931837-85-5

Materials Futures: Strategies and Opportunities, R. Byron Pipes, U.S. Organizing Committee, Rune Lagneborg, Swedish Organizing Committee, 1988; ISBN 1-55899-000-3

Tungsten and Other Refractory Metals for VLSI Applications IV, Robert S. Blewer, Carol M. McConica, 1989; ISSN 0886-7860; ISBN 0-931837-98-7

Tungsten and Other Advanced Metals for VLSI/ULSI Applications V, S. Simon Wong, Seijiro Furukawa, 1990; ISSN 1048-0854; ISBN 1-55899-086-2

High Energy and Heavy Ion Beams in Materials Analysis, Joseph R. Tesmer, Carl J. Maggiore, Michael Nastasi, J. Charles Barbour, James W. Mayer, 1990; ISBN 1-55899-091-7

Physical Metallurgy of Cast Iron IV, Goro Ohira, Takaji Kusakawa, Eisuke Niyama, 1990; ISBN 1-55899-090-9